PHYSICAL PROPERTIES
OF CRYSTALS

Dedicated to the 60th Anniversary
of the Shubnikov Institute of Crystallography
of the Russian Academy of Sciences

Crystals with Disordered Hydrogen-Bond Networks and Superprotonic Conductivity. Review

A. I. Baranov

Shubnikov Institute of Crystallography, Russian Academy of Sciences, Leninskiǐ pr. 59, Moscow, 119333 Russia
e-mail: baranov@ns.crys.ras.ru
Received June 11, 2003

Abstract—The class of hydrogen-containing salts in which the phases with dynamically disordered hydrogen-bond nets are formed has been considered. Unlike other hydrogen-bonded crystals, the crystals of this class are characterized by delocalized hydrogen bonds producing considerable influence on their physical and physical–chemical properties. The structural transitions between the phases with ordered and disordered hydrogen-bond networks are described with the emphasis being made on the structural mechanisms of anomalously high (superprotonic) conductivity associated with delocalization of hydrogen bonds. The perspectives of the use of crystals with delocalized hydrogen bonds in fuel cells and other electrochemical devices are discussed. © 2003 MAIK "Nauka/Interperiodica".

LIST OF CONTENTS

INTRODUCTION

It is well known that hydrogen in crystals has specific crystallochemical parameters and interacts with the surrounding atoms forming specific hydrogen bonds [1]. The formation of hydrogen bonds considerably influences the structure of crystals, their physical and physicochemical properties, and also the thermodynamic stability of the crystalline state. Since hydrogen bonds (H bonds) are directional, their arrangement in crystals is usually characterized by networks of different geometries, which depend on the structural and chemical characteristics of each compound. The dimension and orientation of networks of hydrogen bonds and also the characteristics of the proton dynamics on an H bond determine the physical properties of crystals such as piezoelectric effect, spontaneous polarization, dielectric nonlinearity, and protonic conductivity [2, 3].

Most of the known crystals have localized hydrogen bonds; i.e., the positions and directions of hydrogen bonds are fixed by the crystal symmetry. However, comparatively recently, crystals with delocalized H bonds have also been found [4–14]. The characteristic feature of these crystals is a disordered sublattice of hydrogen atoms; i.e., the number of structurally and, therefore, energetically equivalent positions of hydrogen atoms forming H bonds exceeds the number of hydrogen atoms in the unit cell. The most important characteristics of crystals with delocalized bonds or crystals with disordered hydrogen-bond networks

Table 1. Phase-transition temperatures T_{sp}, activation enthalpies in phases with DHBNs, and lengths of hydrogen bonds in superprotonic crystals

Crystal	T_{sp}^*, K	Change of symmetry in superionic transition	Length of H bond, Å	H_a, eV
RbHSO$_4$	466**) [111]	$B2_{1/a} \longleftrightarrow$ tetragonal [111]	2.530 2.620	0.32
(NH)$_4$HSO$_4$	496***) [112]	$B2_1/a \longleftrightarrow$ tetragonal [112]	2.514 2.620	0.32
CsHSO$_4$	414 [4]	$P2_1/c \longleftrightarrow I4_1/amd$ [21]	2.57	0.26
CsDSO$_4$	409 [5]	$P2_1/c \longleftrightarrow I4_1/amd$ [21]	2.638	0.27
RbHSeO$_4$	470 [6, 8]	$I2 \longleftrightarrow$ tetragonal [6, 8]	2.53 2.55	0.25
(NH)$_4$HSeO$_4$	428 [6, 8]	$I2 \longleftrightarrow$ tetragonal [6, 8]	2.52 2.56	0.25
CsHSeO$_4$	384 [4, 94]	$P2_1/c \longleftrightarrow I4_1/amd$ [21, 81]	2.57	0.25
K$_3$H(SO$_4$)$_2$	463 [134]	$A2/a \longleftrightarrow$? [134]	2.49	
Rb$_3$H(SO$_4$)$_2$	475 [121, 128]	$C2/c \longleftrightarrow$ cubic [128]	2.486	
(NH$_4$)$_3$H(SO$_4$)$_2$	413 [80]	$A2/a \longleftrightarrow R\bar{3}m$ [121]	2.540	0.23
[(NH$_4$)$_{0.3}$Rb$_{0.7}$]$_3$H(SO$_4$)$_2$	463 [128] 495 [128]	$A2/a \longleftrightarrow R\bar{3}m$ [121] $R\bar{3}m \longleftrightarrow$ cubic [128]		
K$_3$H(SeO$_4$)$_2$	393 [135]	$A2/a \longleftrightarrow R\bar{3}m$ [135]	2.524	
Rb$_3$H(SeO$_4$)$_2$	455 [9]	$A2/a \longleftrightarrow R\bar{3}m$ [9]	2.541	0.26
(NH$_4$)$_3$H(SeO$_4$)$_2$	305 [10, 11]	$A2/a \longleftrightarrow R\bar{3}m$ [122]	2.486	0.27
Cs$_3$H(SeO$_4$)$_2$	451 [10, 11, 136]	$A2/a \longleftrightarrow R\bar{3}m$ [136]	2.71	0.37
Cs$_3$D(SeO$_4$)$_2$	448 [136]	$A2/a \longleftrightarrow R\bar{3}m$ [136]		0.39
(NH$_4$)$_4$H$_3$(SeO$_4$)$_3$	378 [10.11]	$A2/a \longleftrightarrow R\bar{3}m$ [11]		0.11
Cs$_5$H$_3$(SO$_4$)$_4 \cdot x$H$_2$O		$P6_3/mmc$ [23]		0.66
Cs$_5$(H,D)$_3$(SO$_4$)$_4 \cdot x$(H,D)$_2$O		P6$_3$/mmc [23]		0.66
Cs$_5$H$_3$(SeO$_4$)$_4 \cdot$ H$_2$O	346 [35, 94]	$Pbcn \longleftrightarrow P6_3/mmc$ [24]		0.63
K$_9$H$_7$(SO$_4$)$_8 \cdot$ H$_2$O	393 [95]	$P2/c \longleftrightarrow$? [95]		
CsH$_2$PO$_4$	503 [12, 120]	$P2_1/c \longleftrightarrow Pm3m$ [133]	2.48	0.32
β-Cs$_3$H(SO$_4$)$_2$[Hx(P,S)O$_4$]	398 [127]	$C2/c \longleftrightarrow$? [127]		
α-Cs$_3$H(SO$_4$)$_2$[H$_2$(PO$_4$]	390 [126]	$P2_1/n \longleftrightarrow$? [126]		
CsH$_2$AsO$_4$	435 [12]	$P4/ \longleftrightarrow$ cubic [12]		0.3
Cs$_{1.5}$Li$_{1.5}$H$_3$(SeO$_4$)$_2$		[125]		1.0

* For first-order phase transitions the temperature T_{sp} correspond to heating.
** Hydrostatic-pressure-induced phase transition, $p = 0.6$ GPa.
*** Hydrostatic-pressure-induced phase transition, $p = 0.28$ GPa.

(DHBNs) are fast proton diffusion, $D_p \sim 10^{-7}$ cm^2 s^{-1}, and high protonic conductivity, $\sigma \sim 10^{-2} \Omega^{-1}$ cm^{-1} [4–8].

The present review is dedicated to the structural characteristics of crystals with dynamically disordered networks of H bonds and their effect on the physical and physicochemical properties of these crystals. At present, a rather large number of groups of crystals possessing phases with DHBNs are known (Table 1). These are the crystals described by the general formulas MeHAO$_4$, Me_3H(AO$_4$)$_2$, Me_4H$_2$(AO$_4$)$_3$, Me_5H$_3$(AO$_4$)$_4 \cdot x$H$_2$O, Me_9H$_7$(AO$_4$)$_8 \cdot$ H$_2$O (Me = K, Rb, NH$_4$, Cs; A = S, Se), and CsH$_2$BO$_4$ (B = P, As) and the

solid solutions on their basis. At present, we have vast experimental and theoretical material waiting for generalization. In addition to the fundamental aspect—deepening of our knowledge on the nature of H bonds and their effect on the properties of the crystalline substances—crystals with DHBNs are also of great interest as promising materials for practical applications. Because of high protonic conductivity, these crystals are actively studied as possible protonic solid electrolytes for the membranes of fuel cells (electrochemical generators of current) [15–17].

1. GEOMETRY OF HYDROGEN-BOND NETWORKS AND PROTON DISORDER

In a majority of crystals, hydrogen atoms forming H bonds completely occupy one or several crystallographic positions in the crystal structure. In other words, the number of structurally equivalent lattice sites corresponding to the total multiplicity of the crystallographic positions g_p energetically most favorable for the formation of H bonds is equal to the number of hydrogen atoms per unit cell, n_p. This signifies that the centers of hydrogen bonds in these crystal structures are ordered and the hydrogen bonds, being directional, form an ordered hydrogen-bond network (OHBN). The notion of a hydrogen-bond center is introduced because the proton position usually does not coincide with the hydrogen-bond center. As a rule, the latter is characterized by a potential with two minima and two proton positions (not necessarily structurally equivalent). Therefore, it is important to distinguish between proton disorder in a two-minimum potential of an H bond and disorder in the positions of H bonds.

Networks of H bonds in crystals are usually characterized by their dimension. One-, two-, or three-dimensional networks unite structural elements into chains, layers, and three-dimensional structures, respectively. The zero-dimensional networks unite two structural elements into dimers. This classification is rather useful, in particular, in the study of anisotropy of the physical properties of crystals.

Upon the discovery of anomalously high protonic (superprotonic) conductivity in hydrogen-containing crystals of some salts [4], the structural mechanism of this phenomenon was explained based on the concept of dynamically disordered network of hydrogen bonds [5, 6]. According to this mechanism, both the positions of the H-bond centers and orientations of these bonds are dynamically disordered. Further studies confirmed the relation between the superprotonic conductivity and DHBNs in various classes of H-bonded salts (Table 1). According to the structural data, DHBNs can be formed only in the crystal structures where the number of hydrogen atoms per unit cell, n_p, is less than the total multiplicity of g_p positions energetically favorable for hydrogen bonding. In other words, DHBNs are formed in structures with disordered sublattices of hydrogen

atoms. Therefore, the H bonds in these structures are positionally and orientationally disordered. If this disorder is dynamical, then protons and, therefore, hydrogen bonds are delocalized. It should be indicated that, in principle, this characteristic of hydrogen bonds differs from the well-known bifurcated three-center hydrogen bonds whose formation is associated with deficit of protons [1, 18]. This type of hydrogen bonds is beyond the scope of the present review.

The difference between ordered and disordered hydrogen-bond networks is illustrated by Fig. 1, which shows the structures of monoclinic (zero-dimensional ordered network with localized hydrogen bonds) and trigonal (two-dimensional disordered network with disordered hydrogen bonds) phases of the crystals described by the general formula $Me_3H(AO_4)_2$.

2. PROTONIC CONDUCTIVITY AND PROTON DEFECTS IN CRYSTALS WITH ORDERED HYDROGEN-BOND NETWORKS

The experimental data show [13, 14, 19] that the dimension and geometry of H-bond networks produce no effect on anisotropy of protonic conductivity in crystals with OHBNs. Thus, protonic conductivity in the monoclinic phase of a CsH_2PO_4 crystal with the one-dimensional network of hydrogen bonds is almost isotropic (Fig. 2). The protonic conductivity in the monoclinic phases of the $Me_3H(AO_4)_2$ crystals with the zero-dimensional network of H bonds is also three-dimensional but strongly anisotropic (Fig. 3). These facts indicate that proton migration (diffusion) proceeds not only over conventional proton sites but also over interstitials. Taking into account the insignificant difference between the activation energies of conductivity along the chains of hydrogen bonds and in the perpendicular direction (Table 2), one can also state that proton migration over interstitials should be accompanied by the formation and breaking of interstitial "defect H bonds." Unlike an ordered hydrogen-bond network formed by hydrogen atoms located in conventional sites, which, for definiteness, can be called the basic or primary OHBN, the interstitial hydrogen bonds form the secondary network of hydrogen bonds. Obviously, the latter can exist only in crystals with proton defects. The primary and secondary networks of H bonds in the tetragonal phase of a KH_2PO_4 crystal are schematically shown in Fig. 4. Thus, in real crystals, the appearance of proton defects and their migration are associated with delocalization of H bonds and formation of a secondary network of H bonds.

In order to relate the protonic-conductivity tensor with the spectrum of thermally activated proton hoppings, we assume that a proton can occupy s types of proton positions (conventional or interstitial) with the multiplicity g_q, where $q = 1, \ldots, s$. Then, according to Flynn [20], the density of the proton flux from the sites
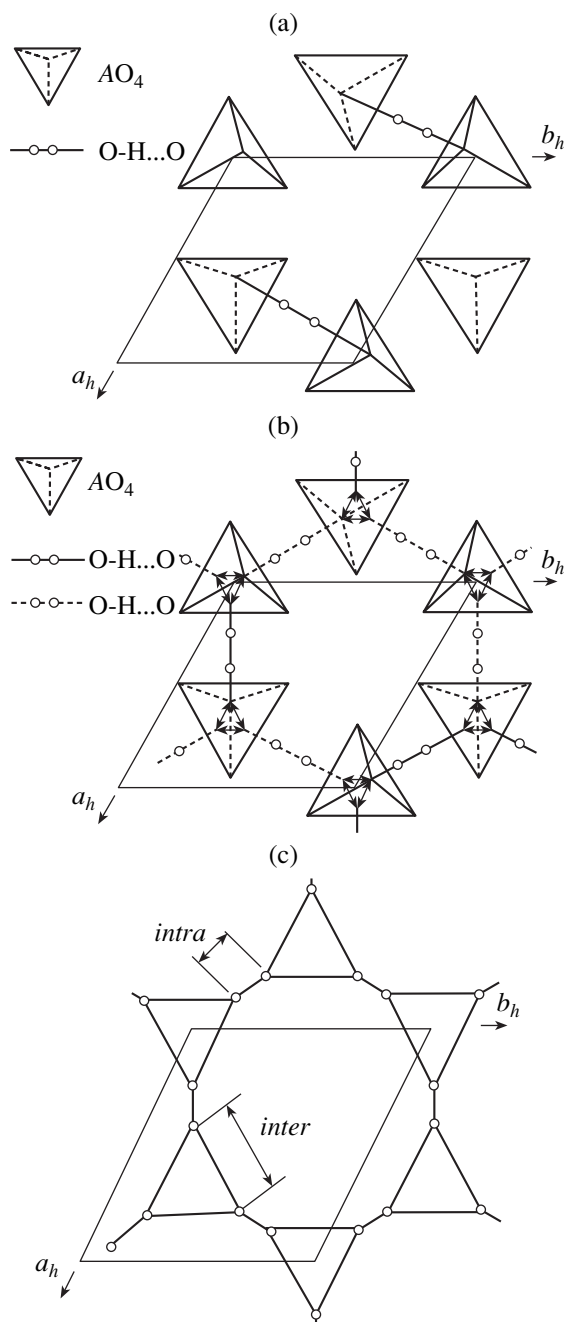
Fig. 1. Schematic projection of the $Me_3H(AO_4)_2$ structure onto the (001) plane. (a) Monoclinic phase, (b) trigonal phase, (c) transport pathways of protons in the trigonal phase. Free structure-equivalent positions of H bonds in Fig. 1b are indicated by dashed lines.

of the position q to the sites of the position k can be written as

$$J^{qk} = en_p c_q (1 - c_k) v^{qk} \mathbf{l}^{qk}, \qquad (1)$$

where e is the electron charge, n_p is the atomic density of mobile protons (the number of protons per formula unit), c_q is the probability of finding a proton in one of
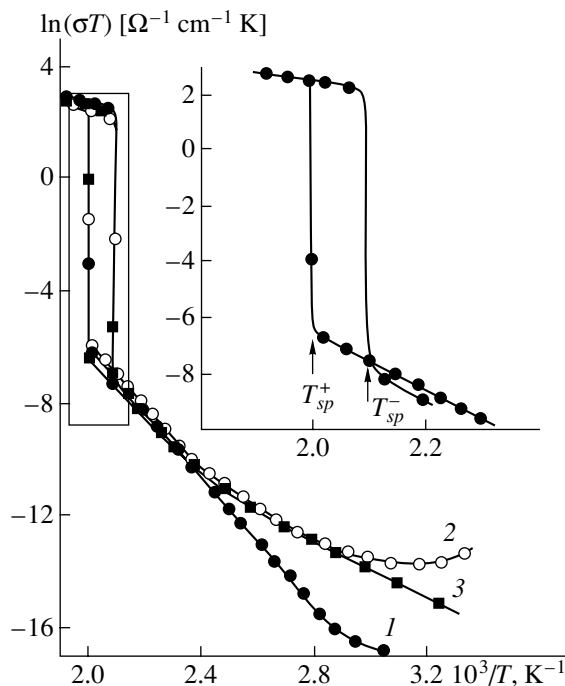

Fig. 2. Temperature dependences of protonic conductivity measured along different crystallographic directions of a CsH_2PO_4 crystal: (1) a^*, (2) b, and (3) c^* [12]. In the inset: temperature dependences obtained during cooling and heating in the vicinity of the superprotonic transition.

the sites of the position q, c_k is the probability of finding the site k closest to the occupied site q empty, and $\mathbf{l}^{qk}$ is the vector between the closest sites of the positions q and k. The frequency of a thermally activated proton hopping between these positions is determined as

$$q^k = v_0^{qk} \exp\left(-\frac{\Phi_a^{qk}}{kT}\right), \qquad (2)$$

where v_0^{qk} is the frequency of proton vibrations in the potential well and Φ_a^{qk} is the change of the thermodynamic potential of a crystal caused by proton hopping to the saddle point of the potential between the nearest sites of the positions q and k.

Each site of the position q has N_q $\mathbf{l}^{qk}$-vectors with the frequency v^{qk} of hoppings between the q and k positions, where $k = 1, 2, \ldots, N_q$. The density of the proton current in an external electric field E is obtained by summation over all N_q sites and s crystallographic positions

$$\mathbf{J} = \sum_{q=1}^{s} \sum_{k=1}^{N_q} en_p c_q (1 - c_k) \Delta v^{\mathbf{qk}} \mathbf{l}^{\mathbf{qk}} = \hat{\sigma} \mathbf{E}, \qquad (3)$$

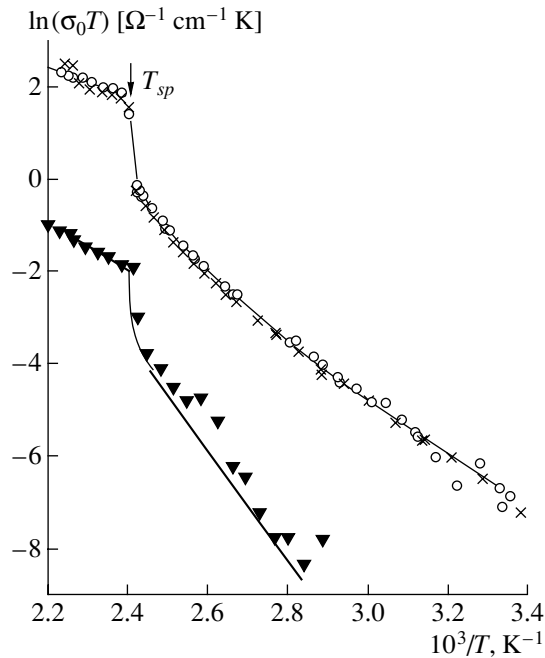where the change in frequency of proton hoppings, Δv^{qk}, between the closest proton sites in the field E is

Fig. 3. Temperature dependences of the protonic conductivity of an $(NH_4)_3H(SO_4)_2$ crystal measured along different crystallographic directions: ($\circ$) $a*$, ($\times$) b, and ($\blacktriangledown$) $c*$ [80].
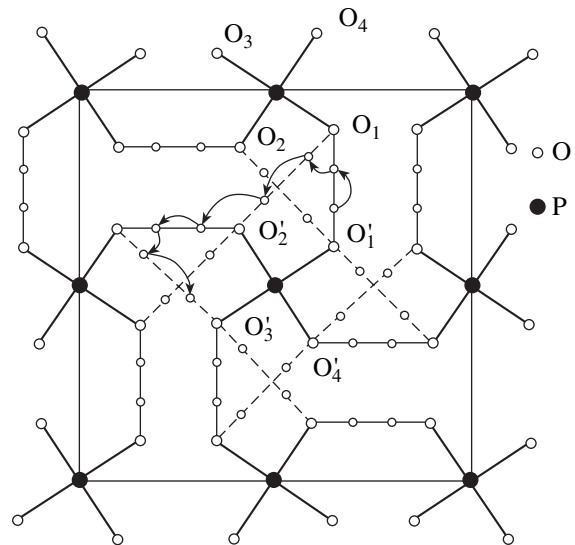

Fig. 4. Primary (solid lines) and secondary (dashed lines) networks of H bonds in the tetragonal KH_2PO_4 phase projected onto the (001) plane. Arrows indicate possible pathways of proton transport [14].

given by the following expression [19]:

$$\Delta v^{qk} \approx v_0^{kl}\left(\frac{e\mathbf{E}\mathbf{l}^{\mathbf{qk}}}{2k_B T}\right)\exp\left(-\frac{\Phi_a^{qk}}{k_B T}\right). \tag{4}$$

Then, the components of the conductivity tensor $\hat{\sigma}$ are determined by the expression

$$\sigma_{ij} = \frac{1}{2}\frac{e^2 n_p}{k_B T}$$
$$\times\left[\sum_{q=1}^{s} c_p \sum_{k=1}^{n_q}(1-c_q)\mathbf{l}_i^{qk}\mathbf{l}_j^{qk}v_0^{qk}\exp\left(-\frac{\Phi_a^{qk}}{k_B T}\right)\right]. \tag{5}$$

In ideal structures with OHBNs, we have $c_q = 1$ for conventional sites and $c_q = 0$ for interstitials, so that, in accordance with Eq. (5), $\sigma = 0$. In real crystals containing intrinsic or extrinsic defects, the probabilities of filling conventional and interstitial positions are different: $c_q < 1$ for conventional positions and $0 < c_q \ll 1$ for interstitial ones. As a result, the multipliers in Eqs. (1), (3), and (5) obey the relationship $c_q(1-c_p) \sim c_q \neq 0$ and, therefore, $\sigma \neq 0$. The introduction into a crystal of impurities with different valences gives rise to the appearance of proton defects which provide the fulfillment of the electroneutrality condition. In this case, the condition $c_q(1-c_k) \sim c_q \ll 1$ is fulfilled, with c_q being independent of the temperature. Depending on the valence ratio of an impurity and the replaced ion, either vacant proton sites or interstitial protons can be formed. Therefore, proton migration (diffusion) proceeds only

over the conventional sites or the interstitial positions. In both cases, the thermodynamic potential Φ_a^{qk} in Eqs. (4) and (5) corresponds to the thermodynamic potential of proton migration, Φ_m^{qk}.

Intrinsic proton defects, which represent a proton vacancy at the site, and an interstitial proton (a pair of Frenkel defects) are formed as a result of a transition of a thermally activated proton from the site q to the interstitial site k. The probability of formation of such a pair of defects depends on the temperature according to the Arrhenius law

$$c_q = \exp\left(-\frac{\Phi_d^q}{2k_B T}\right), \tag{6}$$

where Φ_d^q is the thermodynamic potential of formation of these defects. Therefore, the activation energy of intrinsic protonic conductivity is determined not only by Φ_m^{qk} but also by the thermodynamic potential of defect formation, Φ_d^q. Thus, in crystals with ordered network of H bonds, proton migration and, therefore, protonic conductivity are possible only in the presence of proton defects. It should be noted that, even in the vicinity of the melting point, the concentration of thermally activated defects does not exceed 10^{-19} cm^{-3}.

It follows from Eq. (5) that, in the general case, the temperature dependences of the conductivity-tensor
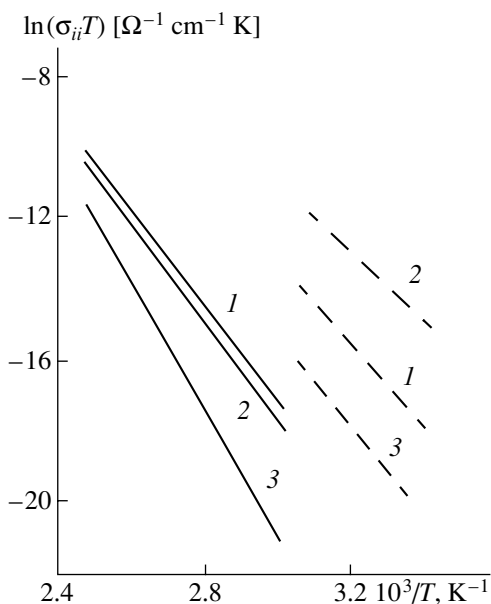
Fig. 5. Temperature dependences of the main components of the proton-conductivity tensor in phases II (solid lines) and III (dashed lines) of a CsHSO$_4$ crystal: (*1*) σ_{11}, (*2*) σ_{22}, and (*3*) σ_{33} [19].

components are the sums of the exponents

$$c_q(1 - c_k)\mathbf{l}_i^{qk}\mathbf{l}_j^{qk}\exp\left(-\frac{\Phi_a^q}{2k_BT}\right) \qquad (7)$$

and, therefore, are not exponential. However, the experimental dependences of conductivity are well approximated by one exponent of type (7) within a rather wide temperature range, i.e., by the Arrhenius law. This signifies that, in real crystals, proton migration proceeds mainly over the sites or interstitials of only one crystal-

lographic position. Figure 5 shows the temperature curves of the main components of the electrical conductivity σ_{ii} in phases III and II of a CsHSO$_4$ crystal characterized by a one-dimensional OHBN. It is seen that the chain of H bonds, which, in these phases, coincides with the twofold axes (component σ_{22}), is not a preferred direction, which confirms the above conclusion about the existence in the crystals with OHBNs of a secondary system of H bonds formed by protons located in interstitials.

Taking into account the geometric properties of the characteristic surface of a second-rank tensor, we can represent Eq. (5), which describes the temperature dependence of conductivity (with due regard for anisotropy), in the form

$$\sigma(\mathbf{n}, T) = \frac{A_0(\mathbf{n})}{T}\exp\left(-\frac{\Phi_a(\mathbf{n})}{k_BT}\right), \qquad (8)$$

where $\mathbf{n}$ is the unit vector of an external field E and $A_0(\mathbf{n})$ is the prefactor defined as

$$A_0(\mathbf{n}) = \frac{1}{2}\frac{n_p e^2}{k_BT}v_0(\mathbf{n})(l(\mathbf{n}))^2. \qquad (9)$$

Taking into account the thermodynamic relationships

$$\begin{aligned}\Phi_a(\mathbf{n}) &= H_a(\mathbf{n}) - TS_a \\ &= E_a(\mathbf{n}) - TS_a(\mathbf{n}) + pV_a(\mathbf{n}),\end{aligned} \qquad (10)$$

we can represent Eq. (8) in the form

$$\begin{aligned}\sigma(\mathbf{n}, T) &= \frac{A(\mathbf{n})}{T}\exp\left(-\frac{H_a(\mathbf{n})}{k_BT}\right) \\ &= \frac{A(\mathbf{n})}{T}\exp\left(-\frac{E_a(\mathbf{n}) + pV_a(\mathbf{n})}{k_BT}\right),\end{aligned} \qquad (11)$$

Table 2. Activation enthalpy and prefactors in Eq. (11) for phases with ordered and disordered hydrogen-bond networks

Crystal	T_{sp}, K	Crystallographic axis	Phase with OHBN			Phase with DHBN		
			sp. gr	H_a, eV	A, Ω^{-1} cm^{-1} K	sp. gr	H_a, eV	A, Ω^{-1} cm^{-1} K
CsHSO$_4$ [19]	414	a^*	$P2_1/c$	0.96	3.6×10^8	$I4_1/amd$	0.25	4.3×10^3
		b		0.73	2.0×10^{11}		0.25	4.3×10^3
		c		0.97	2.1×10^8		0.28	7.3×10^3
CsDSO$_4$ [19]	411	a^*	$P2_1/c$	1.19	3.0×10^{10}	$I4_1/amd$	0.26	3.3×10^3
		b		1.12	1.8×10^{11}		0.26	3.3×10^3
		c		1.42	1.2×10^{15}		0.29	5.7×10^3
Rb$_3$H(SeO$_4$)$_2$ [13]	456	a^*	$A2/a$	1.13	3.1×10^{11}	$R\bar{3}/m$	0.26	1.9×10^3
		b		1.12	3.1×10^{11}		0.26	1.9×10^3
		c		1.42	1.5×10^9		0.49	2.4×10^4
Rb$_3$H(SeO$_4$)$_2$ [13]	504	a^*	$A2/a$	1.13	3.1×10^{11}	$Pm3m$	0.29	2.7×10^3
		b		1.12	3.1×10^{11}		0.29	3.0×10^3
		c		1.42	1.5×10^9		0.31	3.5×10^3

Table 3. Components of H_{ii} and A_{ii} tensors in phases with OHBNs (II and III) and DHBN (I) of $CsHSO_4$ and $CsDSO_4$ crystals [19]

Crystal	Phase	Sp. gr.	Tensor component	H_{ii}, eV	A_{ii}, Ω^{-1} cm^{-1} K
$CsHSO_4$	III	$P2_1/c$	11	0.95 ± 0.05	3.75×10^8
			22	0.74 ± 0.05	1.99×10^6
			33	1.05 ± 0.05	2.19×10^9
$CsDSO_4$	II	$P2_1/c$	11	1.18 ± 0.05	1.09×10^9
			22	1.15 ± 0.05	5.14×10^9
			33	1.55 ± 0.08	5.44×10^{14}
$CsHSO_4$	I	$I4_1/amd$	11	0.26 ± 0.02	4.36×10^3
			22	0.26 ± 0.02	4.36×10^3
			33	0.28 ± 0.02	7.34×10^3
$CsDSO_4$	I	$I4_1/amd$	11	0.27 ± 0.02	3.5×10^3
			22	0.27 ± 0.02	3.5×10^3
			33	0.29 ± 0.02	5.7×10^3

where $E_a(\mathbf{n})$ is the activation energy, $S_a(\mathbf{n})$ is the activation entropy, p is the external pressure, and $V_a(\mathbf{n})$ is the activation volume. The parameters of Eq. (11) that can be determined experimentally are the enthalpy of conductivity activation, H_a, and the prefactor, A. The latter is related to the parameter A_0 in Eqs. (8) and (9) by the formula

$$A(\mathbf{n}) = A_0(\mathbf{n})\exp(-S_a(\mathbf{n})). \quad (12)$$

It should be noted that, under atmospheric pressure, $H_a \simeq E_a$. Therefore, in this case, one can state that the parameter to be determined experimentally is the activation energy E_a. If conductivity is provided by intrinsic proton defects, we have

$$H_a(\mathbf{n}) = H_m(\mathbf{n}) + 1/2H_d(\mathbf{n}),$$
$$S_a = S_m(\mathbf{n}) + 1/2S_d(\mathbf{n}), \quad (13)$$

where $H_m(\mathbf{n})$ and $S_m(\mathbf{n})$ bare the enthalpy and entropy of migration of proton defects and $H_d(\mathbf{n})$ and $S_d(\mathbf{n})$ are the enthalpy and entropy of their formation, respectively. If the protonic conductivity is caused by impurities having different valences, then

$$H_a(\mathbf{n}) = H_m(\mathbf{n}),$$
$$S_a(\mathbf{n}) = S_m(\mathbf{n}). \quad (14)$$

The analysis of the $H_a(\mathbf{n})$ and $A(\mathbf{n})$ parameters shows that, in the majority of hydrogen-bonded crystals with OHBNs, the conductivity at the temperatures $T > 300$ K depends on the intrinsic proton defects. Depending on the structural characteristics of the crystal, the enthalpy of defect formation, H_d, varies within 1.1–1.4 eV, which is considerably higher than the enthalpy of their migration ($0.25 \leq H_m(\mathbf{n}) \leq 0.45$ eV). It should also be indicated that, within the measurement error, the H_d value is independent of $\mathbf{n}$. Therefore, the anisotropy of

the parameters of proton migration $H_a(\mathbf{n})$ and $A(\mathbf{n})$ (Table 3) is determined by anisotropy of the parameters of proton migration $H_m(\mathbf{n})$ and $S_m(\mathbf{n})$, which reflects the difference in the migration pathways of protons along different crystallographic directions.

3. PROTONIC CONDUCTIVITY AND PROTON DYNAMICS IN CRYSTALS WITH DYNAMICALLY DISORDERED HYDROGEN-BOND NETWORKS

It has already been indicated that dynamical disordering of a hydrogen-bond network arises as a result of the dynamical disordering in the sublattice of hydrogen atoms. In accordance with the symmetry of these disordered structures, the multiplicity g_q of the conventional proton position exceeds the number of protons per unit cell, so that the probability of filling conventional proton sites in an ideal structure is

$$c_q = g_q^{-1} < 1. \quad (15)$$

For the known crystal structures with disordered H-bond networks, c_q takes the values 1/3, 1/4, 1/6, and 1/12 [9, 21–24]. Therefore, in these structures, the mobile protons are those which occupy the conventional sites, and the translational hoppings occur between conventional proton sites. It should be emphasized that the translation vectors $\mathbf{l}$ between the sites of one crystallographic position form continuous transport pathways (Fig. 1c) with equal energy barriers between the proton sites both inside the unit cell and between the neighboring unit cells. Thus, the protonic conductivity in crystals with DHBNs is a symmetry property of their structures, which does not depend on defects.

Similar to impurity conductivity in the structures with OHBNs, the enthalpy and entropy of conductivity
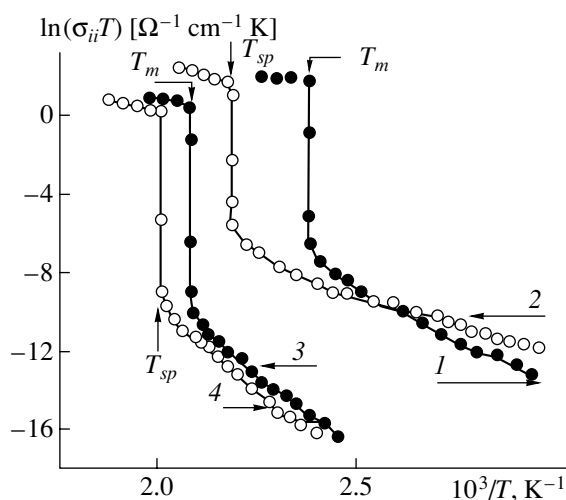
Fig. 6. Temperature dependences of conductivity of (*1*, *2*) $(NH_4)HSO_4$ and (*3*, *4*) $RbHSO_4$ crystals in the Arrhenius coordinates. (*1*, *3*) Atmospheric pressure, (*2*) 1.77 GPa, (*4*) 0.32 GPa [111].

activation in the structures with DHBNs is determined only by the thermodynamic potential of proton migration [Eq. (14)]. It should be emphasized that the characteristic feature of crystals with DHBNs is a high concentration of mobile protons equal to the stoichiometric hydrogen concentration in the crystal ($N_p \sim 10^{22}$ cm^{-3}). Obviously, this concentration exceeds, by several orders of magnitude, the concentration of mobile proton defects in crystals with OHBNs. This is clearly seen in the considerable (by three to five orders of magnitude) difference in the protonic conductivities of phases with DHBNs in comparison with the protonic conductivities of phases with OHBNs (Figs. 2, 3, 6). Analyzing the differences in the transport characteristics of protons in the phases with OHBNs and DHBNs (Tables 2 and 3), one has to note that large values of Φ_a, H_a, and S_a in the phases with OHBNs are explained by the contribution of the energy of defect formation. The considerable differences in the prefactors A are associated mainly with an additional multiplier $\exp(0.5S_d/k_B)$ in Eq. (12), which appears only in the case of impurity conductivity. In this case, the entropy of formation of proton defects, S_d, considerably exceeds the entropy of their migration, S_m [20].

Thus, a high protonic conductivity and a low activation energy in phases with DHBNs are the consequence of characteristic symmetry of their ideal structures, which manifest themselves in delocalization of H bonds. On the other hand, hydrogen bonds in crystals with OHBNs are localized, and the protonic conductivity in these phases is caused by the deviation of the structure from the ideal one caused by the formation of proton defects. Therefore, ideal structures with OHBNs should be protonic insulators. In this connection, one should pay attention to the formal analogy between the

crystals with hydrogen and electron bonds [25]. If electron and hydrogen bonds are localized, the crystals are electronic or protonic insulators. On the other hand, crystals with delocalized electron or hydrogen bonds are electronic or protonic conductors, respectively. In this sense, the well-known metal–dielectric transitions [25] are formal analogs of the structural transitions between the phases with delocalized and localized H bonds considered in this review and can be characterized as the protonic conductor—protonic dielectric transitions.

The dimensions of networks of disordered hydrogen bonds are always higher than the dimensions of disordered ones, and, while the anisotropy of protonic conductivity in the phases with OHBNs shows no correlation with the geometry and dimension of the networks of hydrogen bonds, the dimension and orientation of the disordered networks in the phases with DHBNs necessarily reflects the anisotropy of protonic conductivity. Thus, in the tetragonal MeHAO$_4$ and trigonal Me_3H(AO$_4$)$_2$ phases with two-dimensional DHBNs, the isosurfaces of constant deuteron (Fig. 7) [26] or hydrogen electron density (Fig. 8) [27] indicate the existence of two-dimensional transport pathways of protons in the (001) planes, which manifests themselves in strongly anisotropic proton (deuteron) conductivity $\sigma_{(001)} \gg \sigma_{[001]}$ (Figs. 3 and 9). Two-dimensional transport pathways of protons in the phases with DHBNs in the Me_3H(AO$_4$)$_2$ crystals are schematically shown in Fig. 1c.

4. PROTON TRANSFER AND ENERGY OF HYDROGEN-BOND FORMATION

It is seen from Tables 1 and 2 that the activation enthalpy, H_a, and the prefactor, A, for the crystallographic directions of the maximum protonic conductivity in the Arrhenius law (11) are almost independent of the structural characteristics and chemical composition of crystals. This indicates the common proton-conductivity mechanisms in crystals with DHBNs, which, in turn, reflects the universal nature of hydrogen bonds and proton transport in crystals with hydrogen bonds [1, 28–30]. Hydrogen atoms differ from all the other atoms by their specific interaction with the environment—formation of hydrogen bonds. Therefore, the characteristics of the proton transport can be determined from the known formulas relating the thermodynamic and geometrical parameters of H bonds. These formulas are rather universal and are independent of crystal structure [28–31].

It is known from the theory of hydrogen bond that, if the bond length $R(O\cdots O) \geq 2.40$ Å, then its potential is characterized by two minima [28–31]. Therefore, the process of proton diffusion should consist of two stages (Figs. 1b and 1c):

—Proton transfer between two potential minima of the hydrogen bond $O\cdots H–O \longrightarrow O–H\cdots O$ separated by

the barrier E_{intra}. Depending on the distance between the minima and the E_{intra} value, the proton transport can be either thermally activated or can be caused by proton tunneling [2, 3, 28, 29];

—Breaking of the hydrogen O–H···O bond accompanied by the reorientation of its short shoulder O–H. As a result, a proton moves from one site to a neighboring vacant site, where it forms a new hydrogen bond. This process is thermally activated and is characterized by the energy E_{inter} [29–31].

The two-stage mechanism of protonic conductivity is illustrated by Figs. 1b and 1c for a two-dimensional ordered network of H bonds in the trigonal phases of $Me_3H(AO_4)_2$ crystals.

In the first approximation, the energy of proton migration is determined by the value of a higher potential barrier, E_{intra} or E_{inter}. The dependences of E_{inter} and E_{intra} on $R(O{\cdots}O)$ are shown in Fig. 10. It is seen that the optimum conditions for fast proton migration are fulfilled for hydrogen bonds with the lengths $R(O{\cdots}O) \sim$ 2.65 ± 0.5 Å. In this case, $E_{inter} \sim E_{intra} \sim 0.26 \pm 0.3$ eV. It should also be indicated that these dependences are obtained in the approximation of an isolated linear hydrogen bond [29, 30]. In actual fact, both breaking and formation of H bonds are accompanied by relaxation of atoms surrounding hydrogen and, first of all, by deformation of AO_4 octahedra and the change of their orientations [21, 22, 32–34]. These factors should affect the energies of the breaking and formation of H bonds. Nevertheless, simple model calculations [29, 30] illustrated by Fig. 10 show the good accord with the experimental values of the activation enthalpy and the lengths of hydrogen bonds in the phases with DHBNs (Tables 1–3).

It is seen from Table 1 that, in some hydrate forms of crystals, the activation enthalpy in the phases with DHBNs exceeds 0.3 eV. This can be associated with a more complex network of hydrogen bonds, which includes several crystallographic positions. Thus, in the hexagonal $Cs_5H_3(SO_4)_4 \cdot xH_2O$ and $Cs_5H_3(SeO_4)_4 \cdot xH_2O$ phases, the acid hydrogen bonds are formed in three crystallographic positions, 6(h), 12(k), and 24(l), with the occupancies by protons equal to 1/3, 1/6, and 1/12, respectively [33–35]. The lengths of H bonds for these positions are considerably different: the H bond in the position 6(h) is symmetric, whereas the H bonds in the other two positions are asymmetric [23, 24]. Therefore, the transport pathways of protons in these crystals are characterized by a more complicated potential relief than in crystals with only one system of H bonds. It should also be indicated that, in the hydrate forms of superionic crystals, the contribution of protons from water of crystallization to protonic conductivity is negligible in comparison with the contribution of acid protons [35, 36, 37].
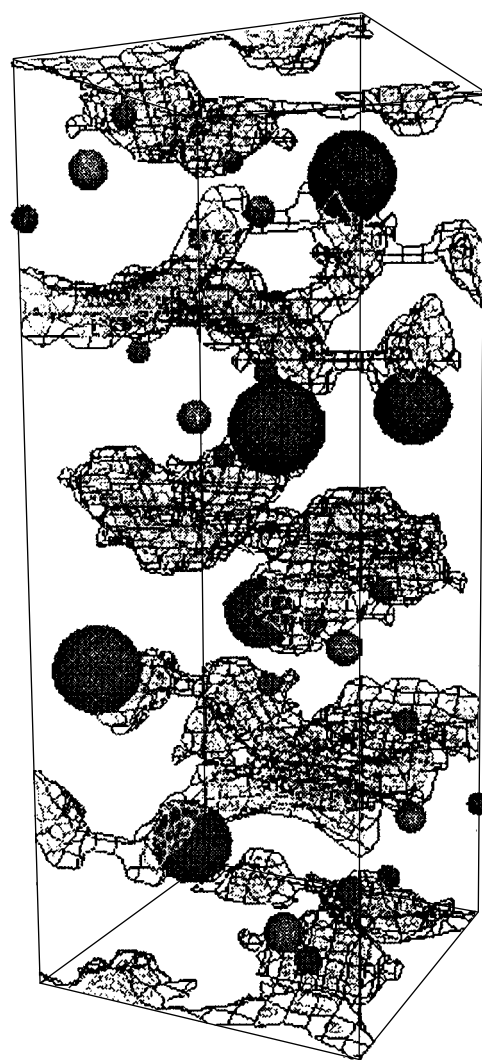

Fig. 7. Surfaces of constant density for deuterons in the superprotonic tetragonal $CsDSO_4$ phase [26].
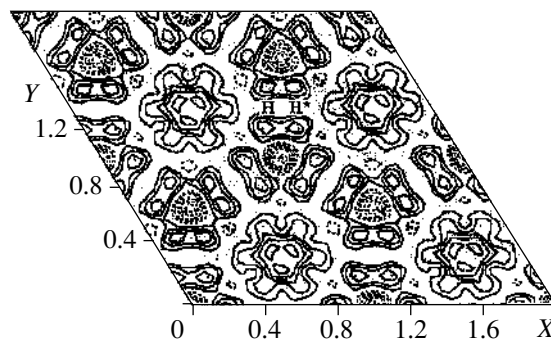

Fig. 8. Map of hydrogen electron density in the plane of dynamically disordered hydrogen bonds in a $[Rb_{0.57}(NH_4)_{0.43}]_3H(SeO_4)_2$ crystal. The symbols H and H* correspond to two proton positions on an H bond [27], $Z = 0.330$.
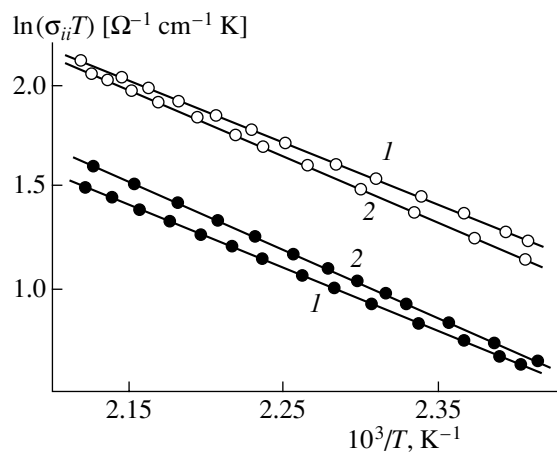
Fig. 9. Temperature dependences of the main components of the protonic-conductivity tensor in superprotonic phases I of (*1*) CsHSO$_4$ and (*2*) CsDSO$_4$ crystals: (○) σ_{11}, σ_{22}, (●) σ_{33} [19].
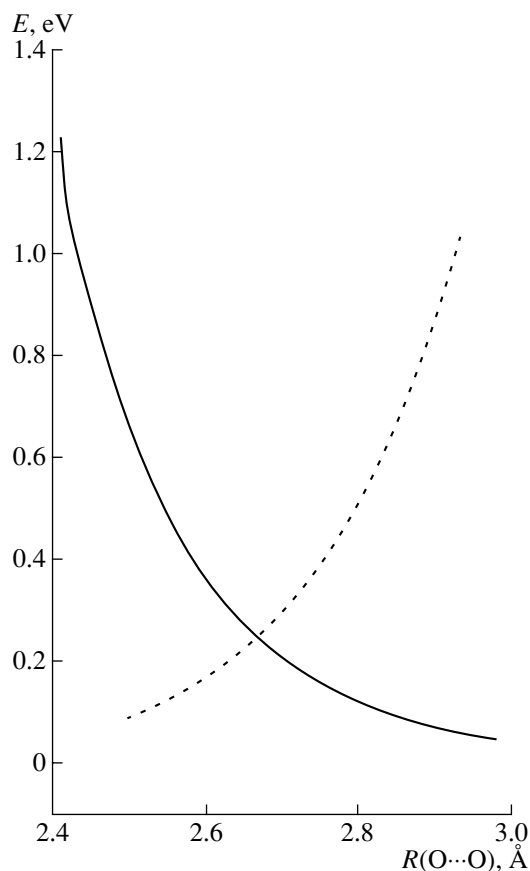

Fig. 10. Energy of formation of an H bond, E_{intra} [29] (solid line), and energy of proton transfer between two potential minima on an H bond, E_{inter} [30] as functions of the length of an H bond, R(O···O).

5. EFFECT OF HYDROSTATIC PRESSURE ON PROTONIC CONDUCTIVITY. ACTIVATION VOLUME OF PROTONS

The effect of pressure on ionic conductivity is characterized by the activation volume V_a in Eq. (11). In the general case, the activation volume is related to the thermodynamic potential of activation as [38]

$$V_a = \left(\frac{d\Phi_a}{dp}\right)_T = \left(\frac{d\Phi_d}{dp}\right)_T + \left(\frac{d\Phi_m}{dp}\right)_T = V_d + V_m, \quad (16)$$

where V_d and V_m are the activation volumes of formation of a proton defect and its migration, respectively. For a majority of metal and ionic crystals, V_a is rather well described by the model of rigid spheres, whose radii correspond to the crystallochemical radii of point defects [38]. However, because of the specific nature of hydrogen bonds formed by protons in a crystal and its zero radius, the validity of such a model is not obvious. Indeed, it is seen from Figs. 11–13 that hydrostatic pressure can produce different effects on the protonic conductivity of various crystals. Thus, for the $Me_3H(AO_4)_2$ phases with OHBNs (Figs. 11a and 11b) and DHBNs (Fig. 11c), protonic conductivity decreases with an increase in pressure. However, the phase with a DHBN of another crystal, CsHSO$_4$ (phase I), shows different behavior (Fig. 12). On the other hand, in ordered phase II of this crystal, protonic conductivity does not depend on pressure within the experimental error (Fig. 13).

In order to interpret this unusual effect of hydrostatic pressure on protonic conductivity, consider Eq. (11) relating the activation volume to the conduc-
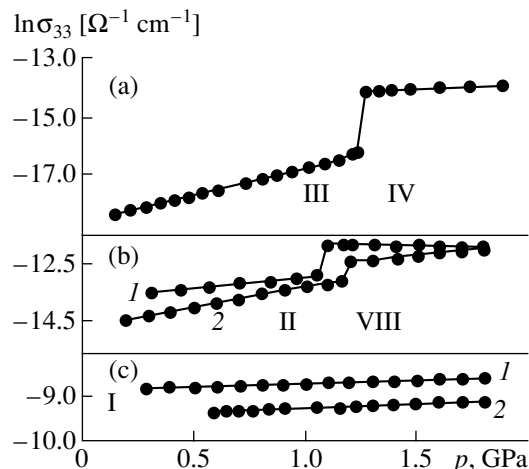

Fig. 11. Baric dependences of proton conductivity σ_{33} of (a) ordered phases III and IV of a Rb$_3$HSeO$_4$ crystal at $T = 314$ K, (b) ordered phases II and VIII of a (NH$_4$)$_3$HSeO$_4$ crystal at (*1*) $T = 291$ K, (*2*) $T = 333$ K; (c) disordered phases of (*1*) Rb$_3$HSeO$_4$ crystals at 423 K and of (NH$_4$)$_3$HSeO$_4$ crystals at (*2*) 402 K [39].

tivity parameters

$$V_a(\mathbf{n}) = -T\left[\left(\frac{\partial \ln \sigma(\mathbf{n})}{\partial p}\right)_T + \left(\frac{\partial \ln A(\mathbf{n})}{\partial p}\right)_T\right]. \quad (17)$$

It follows from this formula that the calculation of $V_a(\mathbf{n})$ requires the knowledge of both isothermal ($\sigma(p)$ at T = const) and isobaric ($\sigma(T)$ at p = const) dependences of conductivity. The analysis of the experimental isobaric dependences shows that the change in the prefactor A in the Arrhenius law in Eqs. (9), (11), (12) under pressures lower than 2 GPa is quite insignificant, whereas the value of the derivative $\partial \ln A/\partial p$ does not exceed $\pm 3 \times 10^{-12}$ cm^2/dyn. Similar values are also obtained for $\partial \ln A/\partial p$ based on the continuum model of diffusion [19, 38]. The corresponding correction in the activation volume associated with the second term in Eq. (17) amounts to 0.22–0.26 cm^3/mol. It follows from Table 4 for the activation volumes of the phases with disordered and ordered H-bond networks that the activation volume of protonic conductivity varies over wide ranges depending on the chemical composition and the structure and can have both positive and negative values [19, 39, 40]. Moreover, similar to other thermodynamic parameters of conductivity, the activation volume is anisotropic and can have considerably different values along different crystallographic directions. Thus, in phase III of a CsHSO$_4$ crystal, the σ_{11} component of the conductivity tensor decreases ($V_a > 0$), whereas the σ_{22} component increases ($V_a < 0$) with pressure (Fig. 12).

It is important to note that, unlike other characteristics of proton conductivity, the activation volumes of the phases with ordered and disordered H-bond networks show no substantial differences. On the other hand, compared with the other transport characteristics of protons, parameter V_a proves to be the most sensitive to the structural and energy characteristics of transport pathways of protons. This fact can be explained proceeding from the two-stage proton transport considered above [19, 39, 40]. In this case, the activation volume can be represented in the form

$$V_a = \frac{\partial E}{\partial p} \approx \frac{\partial E_{inter}}{dp} + \frac{\partial E_{intra}}{\partial p}$$
$$= \left(\frac{\partial E_{inter}}{dR} + \frac{\partial E_{intra}}{\partial R}\right)\left(\frac{\partial R}{\partial P}\right), \quad (18)$$

where E_{inter} and E_{intra} are the heights of the potential barriers for the proton transfer between two minima on the hydrogen bond and its reorientation determined above (Section 4). Since E_{inter} is a decreasing and E_{intra} is an increasing function of R (Fig. 10), their derivatives $\dfrac{\partial E_{inter}}{dR}$ and $\dfrac{\partial E_{intra}}{\partial R}$, have different signs. Therefore, depending on the potential relief in which a proton moves, the contributions of these derivatives to the acti-
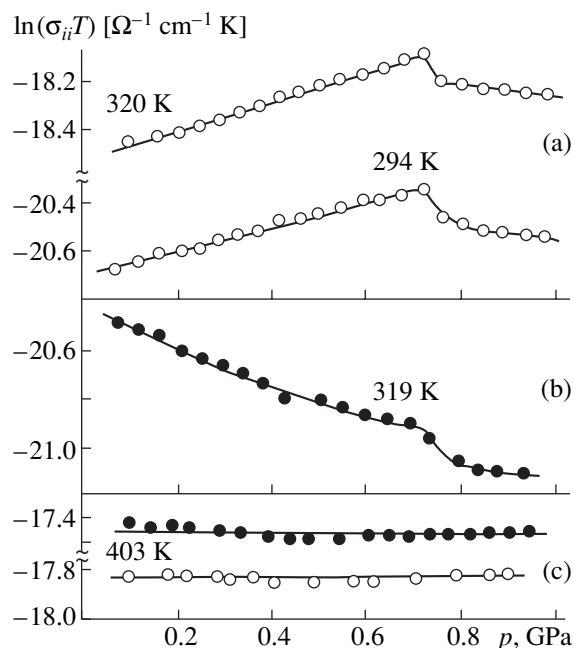

Fig. 12. Baric dependences of protonic conductivity σ_{ii} (a, b) in ordered phase III of a CsHSO$_4$ crystal and (c) phase I with disordered H-bond network of a CsDSO$_4$ crystal along different crystallographic directions: ($\bigcirc$) σ (0$\bar{1}$0), ($\bullet$) σ (100).
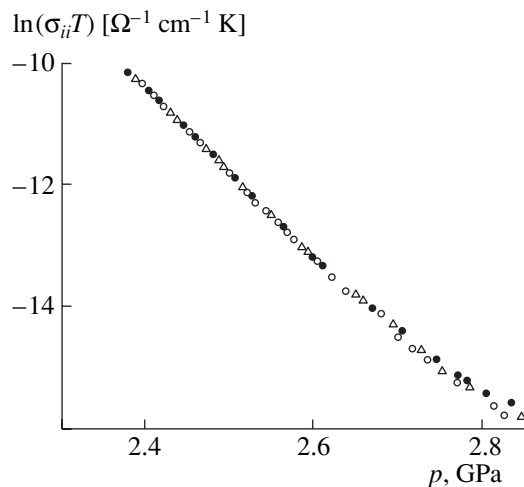

Fig. 13. Temperature dependences of protonic conductivity σ (100) in ordered phase II of a CsHSO$_4$ crystal at different hydrostatic pressures: ($\bullet$) 0.3, ($\triangle$) 0.6, and ($\bigcirc$) 0.9 GPa.

vation volume can be different and the signs of V_a should also be different.

A negative activation volume signifies that the crystal compression giving rise to a decrease in the interatomic distances reduces the thermodynamic potentials of defect formation, Φ_d, and their migration, Φ_m. As a result, the concentration of proton defects, their mobility, and conductivity increase. This fact can hardly be

Table 4. Activation volumes V_a for phases with disordered and ordered H-bond networks of some crystals

Crystal	Phase	Phase characteristic	Crystallographic axis	V_a, cm^3/mol
CsHSO$_4$ [19]	III	OHBN	a^*	2.0 ± 0.03
			b	-1.6 ± 0.03
	III'	OHBN	b	1.4 ± 0.03
	I	DHBN	a^*	0.9 ± 0.03
			c	1.2 ± 0.03
CsDSO$_4$ [19]	II	OHBN	a^*	± 0.03
			c^*	± 0.03
(Rb)$_3$H(SeO$_4$)$_2$ [39]	III	OHBN	c	-5.5 ± 0.3
	IV	OHBN	c	-0.7 ± 0.3
	II	DHBN	c	-1.2 ± 0.3
(NH$_4$)$_3$H(SO$_4$)$_2$ [40]	II	OHBN	c	-2.2 ± 0.3
	VII	OHBN	c	1.5 ± 0.3
	I	DHBN	c	-0.7 ± 0.3
CsH$_2$PO$_4$ [120]	I	DHBN	a^*	2.0

explained for large cations and anions, where the steric factors play the decisive role. However, protons, having the zero ionic radius and a high density of the positive charge, are localized at the sites with the maximum negative density. Therefore, a reduction of interatomic distances with pressure can increase the negative charge density along the transport pathways of protons, thus facilitating their migration.

6. PROTON DYNAMICS IN PHASES WITH DISORDERED HYDROGEN-BOND NETWORKS

The effective method of studying lattice dynamics in phases with DHBNs is nuclear magnetic resonance (NMR) [7, 8, 41–45]. It is advantageous for studying proton diffusion and conductivity because it allows one to directly determine the frequency of proton hoppings. Moreover, NMR also allows one to separate the dynamics of proton motion on an H bond (proton hoppings between two minima on a hydrogen bond) and their diffusion dynamics. It is seen from Fig. 14 that, in the phases with OHBNs of CsHSO$_4$ crystals (phases II and III), where proton diffusion is rather slow, the times of spin-lattice relaxation T_1 and T_2 (characterizing the dynamics of reorientation of HSO$_4^-$ groups) considerably differ from the parameter $T_{1\rho}$ (characterizing the translational diffusion of protons). However, in the phase with a DHBN (phase I), rather fast proton diffusion results in averaging of the dipole–dipole interactions, so that $T_1 = T_2 = T_{1\rho}$ [7, 45].

Fast proton diffusion in phases with DHBNs is confirmed by the direct measurements of the diffusion coefficient of protons by the method of spin pulse echo [7]. The activation enthalpies measured by this method

in phases I of the CsHSO$_4$ and CsHSeO$_4$ crystals are equal to 0.29 and 0.23 eV, respectively, and agree quite well with the H_a values calculated from the conductivity data (Table 1). However, the energy of diffusion activation in phase I of a CsHSO$_4$ crystal calculated from the quasi-elastic neutron scattering turned out to be much lower (~0.1 eV) [46–48]. The diffusion coefficients D_p in CsHSO$_4$ and CsHSeO$_4$ determined from the NMR data depend on temperature; they vary within the range 5×10^{-8}–10^{-6} cm^2/s and agree quite well with the D_p values in the disordered CsHSO$_4$, Rb$_3$H(SeO$_4$)$_2$, and Cs$_3$H(SeO$_4$)$_2$ phases determined by inelastic neutron scattering [48–50]. For the majority of crystals listed in Table 1, the diffusion coefficients in the phases with DHBNs calculated using the experimentaal data on conductivity by the Nernst–Einstein relationship

$$\sigma = \frac{N_p e^2 D_p}{kT}, \qquad (19)$$

where $N_p \simeq 10^{22}$ cm^{-3}, also have values ranging within 10^{-7}–10^{-6} cm^2/s.

Using the diffusion coefficient in the form

$$D_p \approx \frac{l^2}{\tau}, \qquad (20)$$

one can evaluate the time τ of the proton hopping between the closest proton sites. In phase I of a CsHSO$_4$ crystal, where the effective length of the proton hoppings is $l_{ef} \sim 2.3$ Å [48], the τ values vary with the temperature from 5×10^{-8} to 10^{-10} s. It should be noted that, in the general case, the relaxation time τ thus determined is the sum of the lifetime of a hydrogen bond at the proton site, τ_{lf}, and the time necessary for breaking (formation) of this bond, τ_{br}. Taking into account that τ_{lf}

$\gg \tau_{br} \sim 10^{-13}$ s, the above estimates of τ correspond to τ_{lf}. Then, proceeding from the structural mechanism of protonic conductivity considered above, one can draw the conclusion that it is τ_{lf} that limits diffusion and conductivity of phases with DHBNs.

For water and some organic liquids with qualitatively similar dynamics of formation and breaking of H bonds, the τ_{lf} values are less (by two orders of magnitude [51]) than in the known crystals with DHBNs. Therefore, for substances with hydrogen bonds, the coefficient of proton diffusion in water, $D_P \sim 10^{-5}$ cm^2 s^1, can be taken as the limiting value. Lower values, $D_p < 10^{-6}$ cm^2 s^{-1}, attained in the crystals of acid salts with DHBNs can be explained by steric factors—reorientation of large complex HSO_4^-, $HSeO_4^-$, and HPO_4^{2-} anions in diffusion of protons over crystals somewhat hindered in comparison with the reorientation of H_2O molecules in water.

Numerous studies of proton dynamics by NMR [7, 42–44], infrared and Raman spectroscopy [52–59], and inelastic neutron scattering [32, 46, 48, 50] confirm the two-stage mechanism of proton transport in the phases with DHBNs, namely, the proton transport between two proton sites on an H bond and reorientation of its short shoulder O–H. However, the results of these experiments show that reorientation of O–H is accompanied by rotations of AO_4 groups. Therefore, it is more correct to consider reorientation of an HAO_4 complex as a whole. It is seen from Fig. 15 that the spectra of incoherent inelastic neutron scattering in $CsHSO_4$ have a peak at ~25 meV attributed to librations of HSO_4 groups. This peak is considerably spread in phase I with a DHBN in comparison with this peak in ordered phase II. This indicates not only the positional disorder of H bonds but also the positional disorder of oxygen atoms. Anomalously high anharmonism of internal vibrations of HSO_4 groups in phases with DHBNs results in considerable spread of high-frequency peaks at 53, 73, 100, and 165 meV caused by these vibrations [46]. Considerably different lattice modes in the phases with ordered and disordered H-bond networks are also seen in the Raman spectra. In particular, the low-frequency Raman spectrum of disordered phase I of a $CsHSO_4$ crystal has a characteristic intense structureless wing of the Rayleigh line (Fig. 16) and diffuse bands in the vicinity of 100 cm^{-1}, which correspond to librations of sulfate ions.

Specific characteristics of lattice dynamics of phases with DHBNs caused by structural disorder, pronounced anharmonism of atomic vibrations, and fast proton diffusion manifest themselves in high plasticity, low sound velocity, and strong absorption of sonic waves in the megahertz frequency range [60–63]. Thus, the elasticity moduli in the phases with DHBNs of MeHAO$_4$ crystals are lower (by a factor ranging from 1.5 to 2.0) than in phases with OHBNs, whereas sound
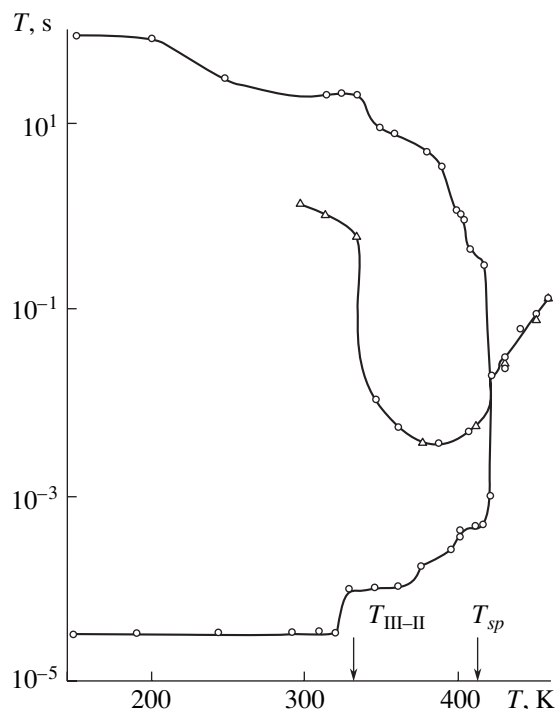

Fig. 14. Temperature dependences of protonic-relaxation time in $CsHSO_4$ [43]: (○) T_1, (□) T_2, and (△) T_{1p}.

absorption attains values ranging within 10–30 Np cm^{-1}. The study of $Rb_3H(SeO_4)$ crystals by the method of Brillouin scattering showed that the phases with DHBNs demonstrate pronounced dispersion of the velocity of acoustic phonons with the frequency ranging from 20 GHz to 20 mHz, whereas the relative sound velocity is changed by almost a factor of three [64, 65]. This dispersion and, in particular, anomalously low velocity of low-frequency phonons are the consequence of strong interactions between mobile protons and phonons (proton–phonon interactions) [61, 62, 64]. In order to explain the observed dispersion, the interaction of an acoustic wave with mobile charge carriers in nonpolar crystals was considered with an invocation of a deformation potential [61]. In this case, the total deformation of a crystal is determined by the elastic part (depending on the external mechanical stress X) and the deviation of the mobile-carrier concentration n_P from a certain mean value $\bar{n}_P$

$$u = cX + a(n - \bar{n}_P), \qquad (21)$$

where c is the modulus of the instantaneous elasticity of the crystal and a is the phenomenological constant. However, the estimates showed that absorption of sound by this mechanism, $\alpha \sim 10^{-3}$ Np/m, is less by several orders of magnitude than absorption observed experimentally, $\alpha \sim 10^3$ Np/m.

Another mechanism of interaction of an elastic wave with mobile protons is based on the well-known
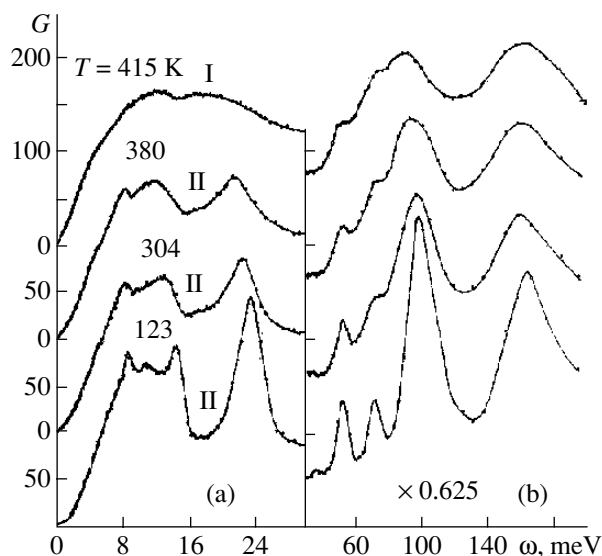
Fig. 15. Weighted density of phonon states $G(\omega)$ for phases I and II of a $CsHSO_4$ crystal at various temperatures [46]: (a) low- and (b) high-frequency spectrum ranges.
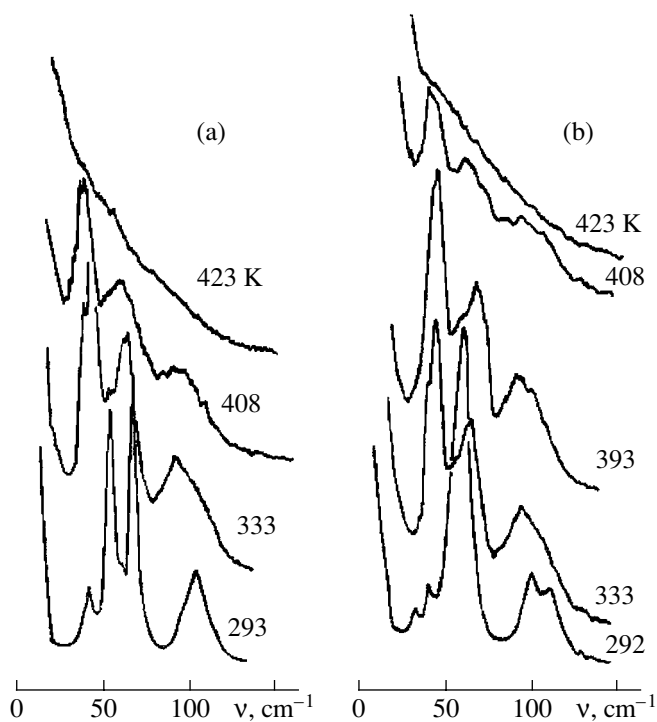

Fig. 16. Low-frequency Raman spectra of the type (a) A_g and (b) B_g of a $CsHSO_4$ crystal. Scattering geometry (a) $Y(XX)Z$ and (b) $Y(ZX)Z$.

Snoek effect [66]—the appearance of instantaneous deformation under the action of uniform mechanical stress [the first term in Eq. (21)], which lowers the crystal symmetry. As a result, the multiplicity g_q of structurally equivalent proton positions is changed and, therefore, their occupancies are also changed. The redistribution of protons gives rise to some additional time-delayed (inelastic) deformation,

$$\frac{\lambda n_p X}{c},\qquad(22)$$

where λ is the phenomenological parameter characterizing the interaction of the mobile-proton subsystem with the crystal lattice. The time necessary for the attainment of a new equilibrium proton distribution and, thus, inelastic deformation is of the order of the characteristic time of proton hoppings between neighboring positions, τ. As was indicated above (Section 6), phases with DHBNs have τ ranging within $\tau \sim 10^{-9}$–10^{-7} s, so that the corresponding relaxation frequencies lie in the megahertz frequency range, where one observes the maximum sound absorption. It was shown in [61] that this mechanism leads to good agreement with the experimental data and allows one to describe both temperature and frequency dependences of the sound velocity and absorption in phases with DHBNs.

7. SUPERPROTONIC PHASE TRANSITIONS

The thermodynamic range of the stability of phases with DHBNs is limited from the high- and low-temperature sides by crystal melting and the transition to phases with OHBNs, respectively. As has already been indicated, in the vicinity of the temperature of transition between the phases with disordered and ordered H-bond networks, T_{sp}, conductivity changes from three to five orders of magnitude (Figs. 2 and 3). On the other hand, in the vicinity of the melting point, T_m, the conductivities of the melt and the phases with DHBNs are of the same order of magnitude (Fig. 6), whereas the anomalies in conductivity during crystal melting and transitions between the phases with disordered and ordered H-bond networks are practically the same. With due regard for these facts and different structural mechanisms of conductivities in these phases, the phases with DHBNs are usually called *superprotonic phases*. The corresponding term *superprotonic phase transition* underlies the specific features of the structural transition between the phases with disordered and ordered H-bond networks.

Superprotonic transitions are characterized by considerable changes in the configurational entropy (Table 5) associated with the positional disorder of hydrogen bonds and orientational disorder of AO_4 tetrahedra in the phases with DHBNs. This manifests itself in pronounced anomalies of specific heat in phase transitions and their high heat values [67–71]. It is seen from Table 5 that the experimental entropy in $Me HAO_4$ and $Me_3H(AO_4)_2$ crystals agrees with the configurational entropy calculated by the formula

$$\Delta S = R\ln w,\qquad(23)$$

Table 5. Experimental values of heat ΔQ_{obs} and entropy of transition $\Delta Q_{obs} \cdot \Delta Q_{calcd}$ is entropy calculated by Eq. (23)

Crystal	T_{sp}, K	ΔQ_{exp}, J mol^{-1}	ΔS_{exp}, J mol^{-1} deg^{-1}	ΔS_{obs}, J mol^{-1} deg^{-1}
CsHSO$_4$	414	4.51×10^3	11 [67]	11.52
CsHSeO$_4$	384	4.3×10^3	16.1 [68]	11.52
Rb$_3$H(SeO$_4$)$_2$	446	4.51×10^3	10.11 [71]	9.13
(NH$_4$)$_3$H(SO$_4$)$_2$	410	4.28×10^3	10.4 [69]	9.13
Cs$_3$H(SeO$_4$)$_2$	446	4.32×10^3	9.4 [70]	9.13
Cs$_5$H$_3$ (SeO$_4$)$_4 \cdot$ H$_2$O	343	1.51×10^4	44.1 [94]	49

where w is the number of possible positions of an H bond in the unit cell of the superprotonic phase. According to the structural data [9, 21, 22, 27], $w = 4$ for MeHAO$_4$ crystals and $w = 3$ for Me_3H(AO$_4$)$_2$ crystals. It is characteristic that the transition entropy for superprotonic phase transitions is comparable to the melting entropy of these salts.

In the vicinity of the superprotonic phase transition, the anomalies of thermal expansion [68, 72] and high-frequency permittivity [60] show no characteristics associated with disordering in the proton subsystem and are similar to the anomalies observed in conventional phase transitions. On the other hand, the anomalies of the sound velocity and absorption in both megahertz (Fig. 17) [60–62] and gigahertz [63, 64] ranges are unusually pronounced, which is associated with the acoustoprotonic interactions considered in Section 6.

In terms of symmetry, superprotonic transitions are improper ferroelastic transitions (Table 1) described by the Landau phenomenological theory of phase transitions. The ferroelastic phase is that with an OHBN and the paraelectric one is the superprotonic phase with a DHBN. Improper ferroelastic transitions with the symmetry changes $I4_1/amd \longrightarrow P2_1/c$ and $R\bar{3}m \longrightarrow C2/c$ are initiated by the irreducible representations of the wave vectors $G_{\mathbf{k}_{13}}$ (X is a point of the Brillouin zone) [73] and $G_{\mathbf{k}_4}$ (L is the point of the Brillouin zone), respectively [74, 75]. This phenomenological theory with the multicomponent order parameter fully describes all the specific features of ferroelastic transitions—anomalies of the physical properties, domain structure, and orientation of domain walls [73–75]. However, in MeHAO$_4$ and Me_3H(AO$_4$)$_2$ crystals, where ferroelastic transitions are simultaneously superprotonic transitions accompanied by ordering or disordering of hydrogen atoms, the theory with one order parameter cannot completely describe the structural changes.

As analysis shows [76–79], the basic functions of the wave-vector representations considered above describe the change in the average occupancy of the proton position in a superprotonic phase transitions $I4_1/amd \longrightarrow P2_1/c$ and $R\bar{3}m \longrightarrow C2/c$ in MeHAO$_4$ and Me_3H(AO$_4$)$_2$ crystals incorrectly. The functions of the

wave vectors $G_{\mathbf{k}_{13}}$ and $G_{\mathbf{k}_4}$ describe the filling of only some proton sites of the position $16(f)$ in the tetragonal MeHAO$_4$ phase and the position $9(e)$ in the trigonal Me_3H(AO$_4$)$_2$ phase, because the symmetry elements of these vectors do not act on the remaining proton sites (the so-called gray sites). This is inessential for the Pb$_3$(PO$_4$)$_2$ ferroelectric, where the position $9(e)$ of the paraelectric phase $R\bar{3}m$ is not occupied [74, 75] but is essential, in particular, for Me_3H(AO$_4$)$_2$ crystals stucturally (but not chemically) isomorphous to Pb$_3$(PO$_4$)$_2$ crystals, where the position $9(e)$ is occcupied by hydrogen atoms with the occupancy $c = 1/3$ [9, 27, 49].

In order to describe the change in the occupancies of the proton positions in superprotonic phase transitions with the change in the symmetry, $I4_1/amd \longrightarrow P2_1/c$ and $R\bar{3}m \longrightarrow C2/c$, a special theory was developed in which these transitions are considered as being initiated by irreducible representations of the symmetry groups
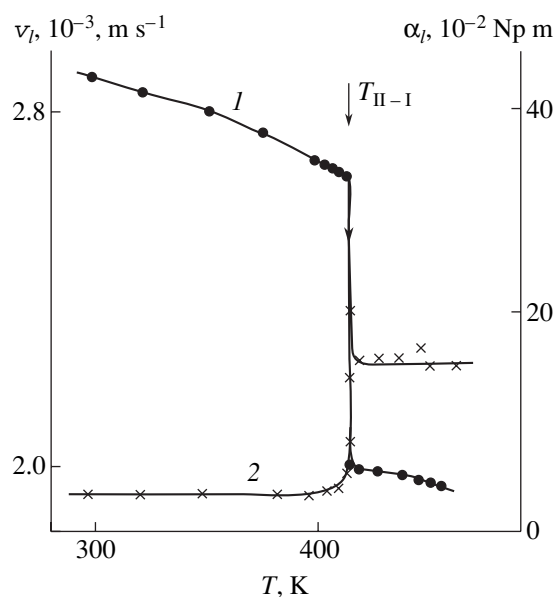

Fig. 17. Temperature dependences of (*1*) velocity v_l and (*2*) the decay coefficient α_l of a quasilongitudinal acoustic wave with the frequency 25 MHz propagating along the *z* axis in phase II of a CsDSO$_4$ crystal.
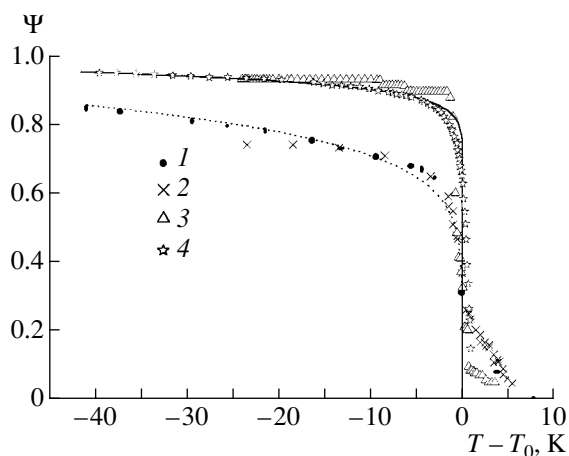
Fig. 18. Temperature dependences of the order parameter of the superprotonic transition in a $(NH_4)_3H(SO_4)_2$ crystal calculated from the data of several experiments: (*1*) protonic conductivity, (*2*) intensity of the (120) reflection, (*3*) high-frequency permittivity, (*4*) optical birefringence. The lines correspond to the approximations by the power law described by Eq. (26): the solid line corresponds to $\beta = 0.04$, and the dashed line, to $\beta = 0.132$ [80].

of two wave vectors $\mathbf{k}_{13} = \mathbf{b}_3/2$ and $\mathbf{k}_{14} = 0$ for MeHAO$_4$ crystals and $\mathbf{k}_4 = \mathbf{b}_3/2$ and $\mathbf{k}_7 = 0$ for Me_3H(AO$_4$)$_2$ crystals [78, 79]. Within the framework of this theory, the free energy can be represented in the approximation of a molecular field as

$$F = -T \ln Z + \gamma \eta^2 + \gamma_1 \xi^2, \qquad (24)$$

where γ and γ_1 are the parameters of the molecular field, η and ξ are the order parameters corresponding to the wave vectors $\mathbf{k}_{13}$ and $\mathbf{k}_{14}$ (for MeHAO$_4$ crystals), or $\mathbf{k}_4$ and $\mathbf{k}_7$ (for Me_3H(AO$_4$)$_2$ crystals), and Z is the statistical sum. It is important to note that the parameter η describes mainly the displacements of heavy atoms, whereas the parameter ξ, the changes in the order of the proton subsystem. Analyzing the equation of free energy, Eq. (24), we see that, in general, the temperature dependences of the parameters η and ξ are different. Moreover, it follows from the theory that these parameters influence the anomalies in various properties differently. Indeed, it is seen from Fig. 18 that the temperature dependences of the order parameter of a $(NH_4)_3H(SO_4)_2$ crystal calculated from the anomalies in permittivity and birefringence differ from the analogous dependences calculated from the anomaly in protonic conductivity and integral intensity of the 120 reflection measured by the method of neutron scattering [80]. In accordance with the theory, the anomalies in high-frequency permittivity and birefringence are determined by the displacements of heavy atoms and, therefore, by the parameter ξ. On the other hand, the temperature anomalies in the protonic conductivity and the intensity of the 120 reflection are determined by the temperature dependence of occupancy of the proton

position and, as was shown in [78, 79], by two parameters—η and ξ.

In some crystals, the transition to the superprotonic paraelectric phase is preceded by the formation of an intermediate phase existing in a narrow temperature range. Thus, in an Rb$_3$H(SeO$_4$)$_2$ crystal, the temperature range of this phase equals $\Delta T \sim 2°C$ [71, 81, 82]. X-ray diffraction analysis showed [82] that the symmetry of the intermediate phase is $C2/m$ and that its structural characteristics differ from those of the ferroelastic phase (symmetry $C2/c$) because of the arrangement of H bonds and orientations of SeO$_4$ groups. The existence of such an intermediate phase in a narrow temperature range ($\Delta T \sim 3°C$) in a CsDSO$_4$ crystal was established from the Raman spectroscopy data and the specific features of the domain structure at $T > T_{sp} - 3$ K [83]. The theory of phase transitions with two interacting parameters considered above allows one to explain the existence of two successive genetically related transitions. With an increase in temperature, the ferroelastic transition with respect to the parameter η takes place, and then, at a higher temperature, the superprotonic transition with respect to the parameter ξ takes place. It should be emphasized that the existence of an intermediate phase in MeHAO$_4$ crystals is also predicted by the phenomenological theory of the $I4_1/amd \longrightarrow P2_1/c$ transition based on the assumption of the existence of a hypothetical parent cubic phase with the symmetry $Fd3m$ [84, 85].

In accordance with the theory developed in [78, 79], the occupancy c of the proton positions, which is a function of the order parameters η and ξ, varies with temperature, so that, upon cooling a crystal below T_{sp}, some conventional proton sites become interstitials. Therefore, in terms of physics, thermally activated hoppings of protons from the remaining proton sites to the positions that became interstitial positions below the temperature T_{sp} indicate the formation of a proton defect with the thermodynamic activation potential Φ_d (see Eq. (6)). Therefore, Φ_d is also a function of the parameters η and ξ and goes to zero at $T \geq T_{sp}$. Thus, the parameters A, Φ_d, and H_d in the expression for conductivity, Eq. (11), are functions of the order parameters, whereas the temperature dependences of conductivity, both above and below T_{sp}, can be described by one equation,

$$\sigma_f(\mathbf{n}, T) = \frac{A_0(\mathbf{n}, \gamma, \xi)}{T}$$
$$\times \exp\left(-\frac{\Phi_m(\mathbf{n}) + 1/2\Phi_d(\mathbf{n}, \eta, \xi)}{k_B T}\right). \qquad (25)$$

Taking into account that the dependence of σ on A_0 is weaker than on Φ_d, the difference in the parameter A_0 above and below T_{sp} can be ignored. Equation (25) can be rewritten in the form convenient for the analysis of

the experimental curves of conductivity

$$\sigma(\mathbf{n}, T) \cong \sigma_{sp}(\mathbf{n}, T)\exp\left(-\frac{\Phi_d(\mathbf{n}, \eta(T), \xi(T))}{2k_B T}\right), \quad (26)$$

where $\sigma_{sp}(\mathbf{n}, T)$ is the conductivity of the paraelastic superprotonic phase.

The general behavior of the anomalies in protonic conductivity in the vicinity of phase transitions described by Eq. (26) are confirmed experimentally [9, 80, 86]. In particular, for second-order phase transitions, the temperature curves of the thermodynamic potential of activation of proton defects calculated by Eq. (26) are rather universal and can be approximated by the power law

$$\Phi_d \propto (T_{sp} - T)^{2\beta}, \quad (27)$$

where β is the critical index of the order parameter. The fulfillment of this law is illustrated by the superprotonic transition in $(NH_4)_3H(SO_4)_2$ (Fig. 19). It is seen that the Φ_d values calculated from the conductivity data along two crystallographic directions coincide and that the $\Phi_d(T)$ curves are approximated well by law (27) over a broad temperature range. It should also be noted that the value $\beta = 0.13$ obtained from the conductivity data agrees with the value of the critical index calculated from the intensity of the 120 reflection (Fig. 18).

It is well known that the specific heat measured experimentally consists of the specific heat of an ideal ordered crystal and the "excessive" specific heat associated with its disordering. Therefore, in the vicinity of the superprotonic phase transition, the anomalies in conductivity and excessive specific heat ΔC_p should be related. It was shown experimentally that this relation for the superprotonic transition in a $Cs_3H(SeO_4)_2$ crystal can be written in the form

$$\frac{\partial \ln \sigma}{\partial T} = \gamma\frac{\Delta C_p}{k_B T_{sp}} + \text{const}. \quad (28)$$

This formula was confirmed theoretically in [87, 88]. The phenomenological constant γ in Eq. (28) does not depend on temperature.

The study of ferroelastic properties of superprotonic $MeHAO_4$ [83, 87, 89, 90] and $Me_3H(AO_4)_2$ [91] crystals show that their symmetry-dependent properties, such as domain structure and tensor of spontaneous deformation, are the same as for conventional ferroelastic crystals symmetrically isomorphous to the crystals under consideration. However, as was shown in the previous sections, the properties of paraelastic superprotonic phases, such as protonic conductivity, specific heat, sound velocity, and plasticity, which are determined by the disordered proton subsystem, are substantially different from the analogous properties of conventional ferroelastics. The characteristic feature of superprotonic ferroelastic crystals is also the slow kinetics of transition and the long-term relaxation. In conventional
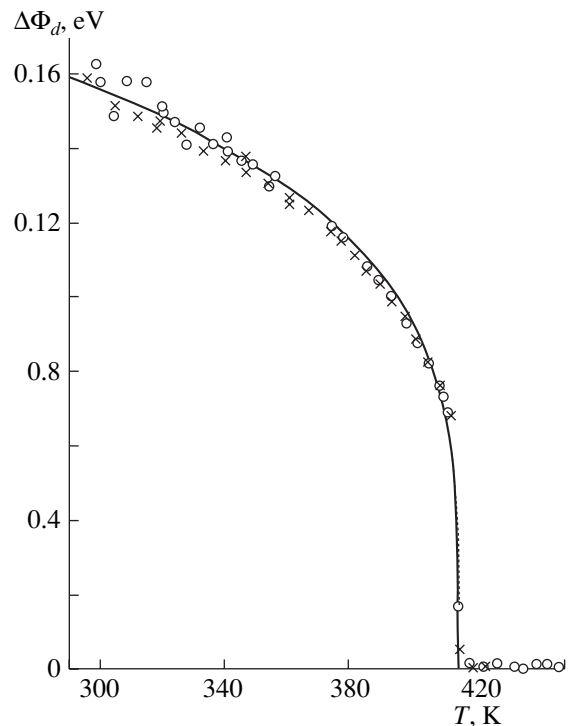

Fig. 19. Temperature dependences of the thermodynamic potential of activation of proton defects (dots) calculated from the experimental temperature dependences of (○) σ_a and (×) σ_b of a $(NH_4)_3H(SO_4)_2$ crystal shown in Fig. 3. The solid line indicates the approximation by the power law described by Eq. (26) at $\beta = 0.132$ [80].

ferroelastic crystals, thermodynamic equilibrium is attained in a time comparable with the decay time of phonons (10^{-13} s), whereas in superprotonic crystals, the time of the attainment of the thermodynamic equilibrium is determined by the time of the attainment of the equilibrium proton distribution,

$$\tau = \tau_0\exp\left(\frac{\Phi_m}{kT}\right), \quad (29)$$

where τ_0 is the quantity having the order of the period of proton vibrations in a potential well, $\tau_0 \sim 10^{-13}$–10^{-14} s. For typical Φ_m values ranging within 0.23–0.3 eV (Table 1), the characteristic relaxation time τ of the proton system estimated using Eq. (29) is of the order of 10^{-9}–10^{-10} s.

One more specific feature of crystals with DHBNs is the occurrence of the phase transitions in the surface layers revealed in $MeHSO_4$ crystals [92, 93] at the temperatures T_{s1} which are lower (by about 20°C) than the temperature T_{sp} of volume superprotonic transitions in $CsHSO_4$ and $CsDSO_4$ or the melting point, T_m, in $RbHSO_4$ and NH_4HSO_4. These transitions manifest themselves in an anomalous increase in surface conductivity (Fig. 20) [92] and the change in the structure of the surface layer [93]. The known experimental data
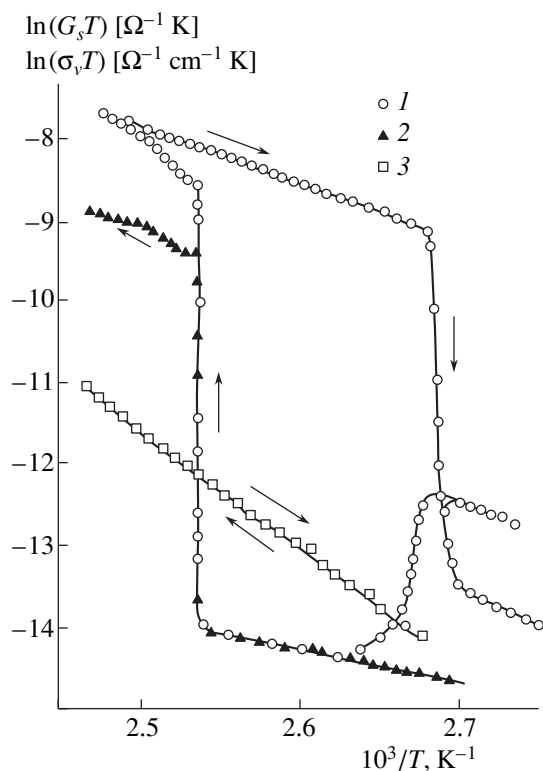
Fig. 20. Temperature dependences of (*1, 2*) surface, G_s, and (*3*) volume, σ_v, conductivities in the vicinity of the temperature of surface phase transition in a CsDSO$_4$ crystal. Measurements were made on the samples *x*-cut in an atmosphere of dry argon at a frequency of 0.1 Hz: (*1*) for a sample kept in an atmosphere of dry air before measurements and (*2*) for the same sample kept for 24 h in an atmosphere of humid air [92].
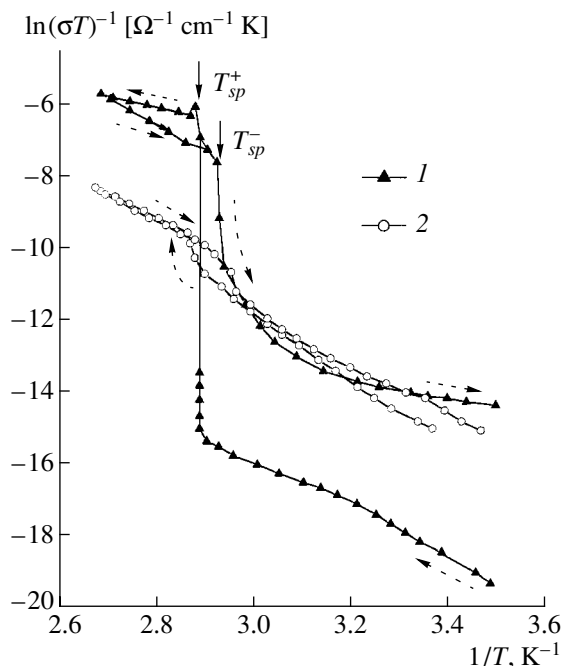

Fig. 21. Temperature dependences of conductivity of Cs$_5$H$_3$(SeO$_4$)$_4 \cdot x$H$_2$O crystals in (*1*) the first and (*2*) sixth heating–cooling cycles [94].

indicate that these transitions are reversible and are not related to the moisture adsorbed on the sample surface. The triple-crystal X-ray diffractometry data for CsDSO$_4$ crystals at $T > T_{s1}$ show the appearance of an additional diffraction maximum coinciding with the 112 Bragg reflection of the superprotonic tetragonal phase [93]. The thickness of the effective layer in which the surface transition takes place was estimated to range within 10 to 20 nm.

8. CHARACTERISTICS OF SUPERPROTONIC PHASE TRANSITIONS IN HYDRATE PHASES OF CRYSTALS WITH DISORDERED HYDROGEN-BOND NETWORKS

We have already indicated that, in the hydrate phases of superprotonic crystals, proton conductivity is provided by acid protons. However, the water of crystallization produces a strong effect on superprotonic phase transitions [35, 37, 94–98]. Figure 21 illustrates the evolution of a superprotonic phase transition in a Cs$_5$H$_3$(SeO$_4$)$_4 \cdot x$H$_2$O crystal during successive heating–cooling cycles. The crystals grown have ordered phases with the stoichiometric water content ($x = 1$). During first heating, one observes an anomaly in conductivity characteristic of superprotonic transitions; however, during cooling, this anomaly considerably decreases and, after several successive cooling–heating cycles, is almost completely suppressed. In another crystal, K$_9$H$_7$(SO$_4$)$_8 \cdot x$H$_2$O, no anomalies in the superprotonic transition are observed after the first cooling from the superprotonic phase (Fig. 22a). A similar temperature behavior is also observed for the anomalies in permittivity and specific heat (Figs. 22b and 22c), which allows one to draw the conclusion about the suppression of the superprotonic transition during thermal cycles [37, 94, 95, 97]. The thermogravimetric [37, 94] and IR spectroscopy [37] data indicate that the superprotonic transitions in these crystals are accompanied by the partial or complete loss of water of crystallization. Thus, stabilization of the superprotonic phases with DHBNs in Cs$_5$H$_3$(SeO$_4$)$_4 \cdot x$H$_2$O and K$_9$H$_7$(SO$_4$)$_8 \cdot x$H$_2$O crystals is associated with their dehydration [37, 94–97].

At temperatures below T_{sp}, the supercooled dehydrated superprotonic phases of these crystals become metastable. In humid atmosphere, the hydration process takes place. This is accompanied by the structural transition to the ordered phase. During hydration, the crystal is in the mixed state, in which the dehydrated phase with a DHBN and the ordered hydrated phase coexist [95, 97]. It is important that the dehydration and hydration processes do not change the state of the samples—they remain single crystals. Visually, the occurring processes are revealed from sample turbidity (dehydration) and clearing (hydration) [37, 95, 97].

Unlike Cs$_5$H$_3$(SeO$_4$)$_4 \cdot x$H$_2$O and K$_9$H$_7$(SO$_4$)$_8 \cdot x$H$_2$O, the Cs$_5$H$_3$(SO$_4$)$_4 \cdot x$H$_2$O crystals are crystallized with

the nonstoichiometric amount of water of crystallization ($x \sim 0.5$). One can assume that, because of this, the $Cs_5H_3(SO_4)_4 \cdot xH_2O$ crystals at room and lower temperatures are in the phase with a DHBN [36]. According to X-ray diffraction data [23], this phase is hexagonal ($P6_3/mmc$) and is structurally isomorphous to the superprotonic hexagonal phase $Cs_5H_3(SeO_4)_4 \cdot xH_2O$ partly dehydrated at temperatures above T_{sp} [23, 24, 35, 36]. The X-ray and neutron diffraction data [99, 100] show that the symmetry of $Cs_5H_3(SO_4)_4 \cdot xH_2O$ crystals remains unchanged in the temperature range from 414 to 4 K. It should be noted that, according to [100], the diffraction patterns of partially deuterated crystals at $T \sim 20$ K show some additional weak maxima that violate the above symmetry. Thus, from a rather long list of superprotonic crystals (Table 1), only $Cs_5H_3(SO_4)_4 \cdot xH_2O$ crystals crystallize in disordered superprotonic phases preserved up to the liquid-helium temperature. It should also be noted that protonic conductivity of thermally activated $Cs_5H_3(SO_4)_4 \cdot xH_2O$ phase at low temperatures is rather low. Therefore, in this case, the term "superprotonic" reflects only the specific feature of proton disordering and the structural mechanism of protonic conductivity but not the absolute value of this conductivity.

Upon cooling of $Cs_5H_3(SO_4)_4 \cdot xH_2O$ crystals below $T_g = 260$ K, the dynamics of hydrogen bonds and orientations of SO_4 groups is considerably changed, which is characteristic of the transition to the phase of protonic (orientational) glass [36, 101–108]. Thus, the Raman spectra at $T < T_g$, indicate the occurrence of pronounced Rayleigh scattering, which is characteristic of molecular scattering associated with the orientational fluctuations of molecular groups [103]. The evolution of the parameters of the spectral lines of Raman scattering [103] and EPR lines [105] with temperature indicates the changes in the orientational disorder of SO_4 groups and water molecules (from dynamical to static) upon cooling below T_g. Another bright example is the transition to the glass phase, which manifests itself in the dielectric dispersion in the range from very low to gigahertz frequencies [36, 65, 101]. The pronounced anisotropy of this dispersion reflects the two-dimensional disorder in the H-bond network. It is seen from Fig. 23 that, like in polymer materials, one can single out two relaxation processes, α and β, in $Cs_5H_3(SO_4)_4 \cdot xH_2O$ crystals with considerably different relaxation characteristics. The low-frequency α relaxation is determined by the frequency-dependent complex conductivity $\sigma^*(\omega)$,

$$\varepsilon_\alpha^*(\omega) = \varepsilon_\alpha'(\omega) + i\varepsilon_\alpha''(\omega)$$
$$= \frac{4\pi\sigma^*(\omega)}{\omega} = B(i\omega)^{-\delta(T)}, \tag{29}$$

where B is the temperature-independent parameter. The exponent δ shows the temperature behavior charac-

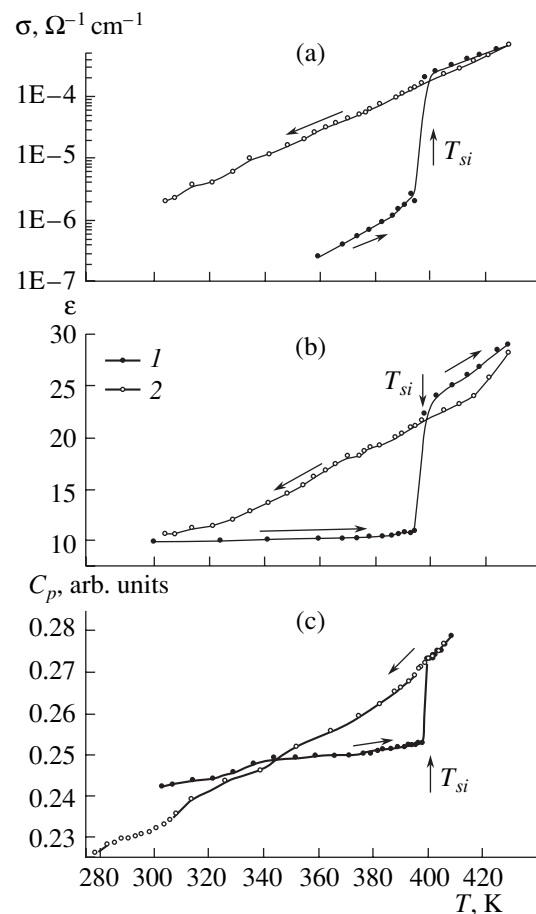**Fig. 22.** Temperature dependences of (a) conductivity and (b) permittivity measured at a frequency of 1 MHz and (c) specific heat for a $K_9H_7(SO_4)_4 \cdot xH_2O$ crystals in the first heating–cooling cycle [37, 95, 96].

istic of the transition from the ergodic to nonergodic state and decreases from 1 to 0 with a decrease in temperature from $T \sim T_g + 10$ to $T \sim T_g - 30$ K [101, 107]. The high-temperature β relaxation is described as

$$\sigma_\beta^* = \varepsilon_{\beta_\infty} + [\varepsilon_{\beta_0} - \varepsilon_{\beta_\infty}]\int\frac{f(E)dE}{1 + i\omega\tau}, \tag{30}$$

where ε_{β_0} and $\varepsilon_{\beta_\infty}$ are the low- and high-frequency limits of dielectric constant, respectively. The function of the activation-energy distribution $f(E)$ is described by the Gauss law with the most probable relaxation time $\bar{\tau}_\beta$, whose temperature dependence is described by the Arrhenius law with the most probable activation energy $\bar{E}_\beta = 0.20$ eV [101].

The transition to the glass phase can also be established from the pronounced anomalies of the velocity and absorption of longitudinal sonic waves in the range of megahertz frequencies (Fig. 24) [65, 105, 107]. However, the temperature anomalies of hypersonic longitudinal phonons in the vicinity of T_g are insignificant
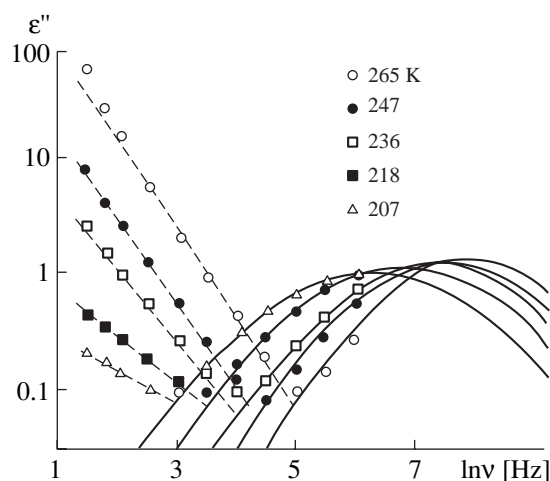
Fig. 23. Frequency dependences of the imaginary part of the dielectric constant ε'' in a $Cs_5H_3(SeO_4)_4 \cdot xH_2O$ crystal measured at different temperatures in the vicinity of T_g. Dashed and solid lines correspond to the approximation of the experimental points by Eqs. (29) and (30), respectively [101].
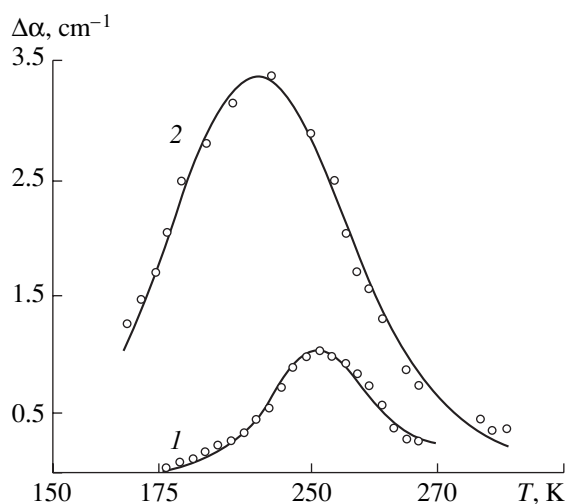

Fig. 24. Temperature dependences of absorption of longitudinal sonic waves (at the frequency 10 MHz) in a $Cs_5H_3(SO_4)_4 \cdot xH_2O$ crystal along (*1*) [001] and (*2*) [100] directions [107].

[102, 108]. This is the consequence of the strong frequency dispersion of acoustic phonons in the transition to the glass phase. The study of the dispersion of transverse acoustic phonons along the [001] direction by the method of inelastic neutron scattering [109] also indicates the change in the phonon frequency in the glass region. The anomalies characteristic of the glass process were also observed in measurements of the specific heat by the method of dynamic calorimetry [104, 105].

It should be noted that the parameters of the β relaxation, $\bar{\tau}_\beta$, $\bar{E}_\beta$, and $f(E)$, for $Cs_5H_3(SO_4)_4 \cdot xH_2O$ crystals

determined from the dielectric and acoustic measurements agree quite well quantitatively [105, 107]. This indicates the common nature of the dipole and elastic relaxation in the transition from the ergodic to nonergodic state. It may be assumed that the structural relaxation is associated with the structural "arrest" of the correlations of the ordered phase. Similar to $Cs_5H_3(SeO_4)_4 \cdot xH_2O$ crystals, the latter phase can have the orthorhombic symmetry. In this connection, we would like to note an unusual size effect observed in the transition of $Cs_5H_3(SeO_4)_4 \cdot xH_2O$ to the phase of protonic glass. According to the X-ray diffraction data, the structural changes in macrocrystals and powders observed during the vitrification process are considerably different [99]. After the first cycle of cooling of the $Cs_5H_3(SO_4)_4 \cdot xH_2O$ powder at $T \sim 220$ K $< T_g$, a mixed phase (consisting of the initial hexagonal phase and a new orthorhombic one) is formed. The following cooling–heating cycles in the temperature range 20–300 K result in an increase in the volume of the orthorhombic phase and a decrease in the volume of the hexagonal one. After approximately the seventh cycle, instead of the transition to the glass phase, a well developed structural transition from the hexagonal to orthorhombic phase is observed at the temperature $T \approx T_g$. Obviously, the different temperature behavior of the powder and the single crystal confirms the hypothesis about the structural arrest of the correlations of the orthorhombic phase in the vicinity of the glass temperature T_g. If the characteristic dimensions of the correlations of the ordered phase become comparable with the grain sizes $\sim 10^{-4}$ cm prior to their structural arrest with a decrease in temperature, then the diffraction patterns should have reflections from the ordered phase. The formation of such ordered macroregions allows one to explain the strong Rayleigh scattering in a $Cs_5H_3(SO_4)_4 \cdot xH_2O$ single crystal arising at $T < T_g$ [103]. However, the estimates of the dimensions of optically inhomogeneous regions based on the Rayleigh scattering data yield values (10^{-7}–10^{-5} cm) lower than the values that could be expected from the data of powder X-ray diffraction [99].

It should be emphasized that freezing of the positional proton disorder and orientational disorder of SO_4 groups in the transition to the glass phase do not lead to infinitely high enthalpy of conductivity activation H_a or a decrease in the protonic conductivity to zero values. In the glass phase, H_a has a certain intermediate value between the H_a values in the disordered and hypothetical ordered phases.

9. EFFECT OF HYDROSTATIC PRESSURE ON SUPERPROTONIC PHASE TRANSITIONS AND THERMODYNAMIC STABILITY OF SUPERPROTONIC PHASES

We have already noted that the phases with DHBNs are characterized by high configurational and vibra-

tional entropies and, therefore, their formation always precedes crystal melting. It is characteristic that the heat and entropy of superprotonic phase transitions for many crystals are comparable with the values of these parameters during melting. The stability range of the phases with DHBNs is limited by the temperature T_{sp} of the superprotonic transition to the ferroelastic phase with an OHBN. The study of the pT phase diagrams of superprotonic crystals [110–120] allows one to draw the conclusion that the hydrostatic pressure increases the temperature range of stability of the phase with a DHBN. This is associated mainly with a sharper increase in melting point T_m (in comparison with T_{sp}) with an increase in pressure ($\partial T_m/\partial p \sim 150$ K/GPa). Depending on the structural characteristics of the crystal, the temperatures of superprotonic phase transitions can either increase or decrease with an increase in pressure. In particular, for MeHAO$_4$ crystals, the $\partial T_{sp}/\partial p$ values vary over a wide range from –40 to 70 K/GPa [110–113]. At higher pressures, new superprotonic phases are formed in these crystals (Fig. 25). In [114], the unit-cell parameters of high-pressure CsHSO$_4$ phases were determined by the neutron diffraction method and their possible symmetry groups were analyzed.

For Me_3H(AO$_4$)$_2$ crystals at $p \leq 1$ GPa, the $\partial T_{sp}/\partial p$ values are negative and range within –40 to –60 K/GPa for different compositions [115–118]. However, at pressures $p \geq 1$ GPa, a new ordered phase is formed and the $\partial T_{sp}/\partial p$ value becomes positive. It should be noted that it is at pressures close to 1 GPa that new ordered high-density phases are formed also in MeHAO$_4$ (phase IV in Fig. 25) [110–113] and CsH$_2$PO$_4$ [119] crystals. Therefore, an increase in $\partial T_{sp}/\partial p$ at $p \geq 1$ GPa is characteristic of all these crystals. The study of the lattice dynamics of high-pressure phases of CsHSO$_4$ by the method of inelastic neutron scattering showed that, with an increase in pressure, the anharmonicity of vibrations in these phases decreases and, in phase V existing at the pressure $p > 1.7$ GPa (Fig. 25), the lattice becomes harmonic [114].

It is also necessary to pay attention to the topological similarity of the pT phase diagrams for each group of crystals. Thus, MeHAO$_4$ crystals obey the so-called principle of chemical pressure: a decrease in the radius of a metal cation or an increase in the size of a complex AO_4 anion are equivalent to an increase in hydrostatic pressure. This manifests itself in the possibility of inducing superprotonic phases by applying hydrostatic pressure to crystals having no such phases under atmospheric pressure (Fig. 6) [111, 112]. In particular, it is seen from Fig. 6 that the anomalies in conductivity observed during melting and superprotonic phase transitions are similar both qualitatively and quantitatively. This fact is an additional argument for singling out superprotonic transitions into an individual class of phase transitions.
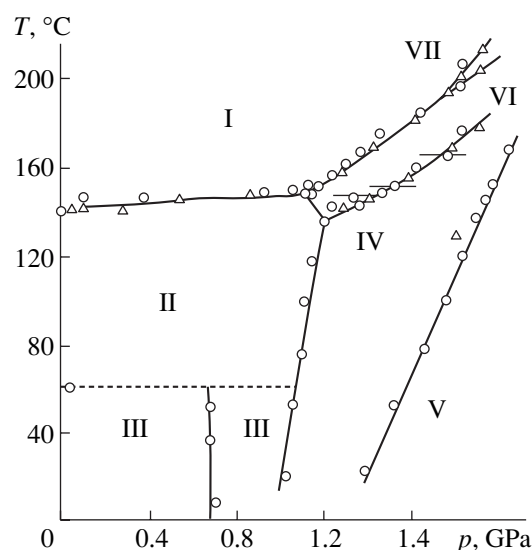

Fig. 25. Phase pT diagram for a CsHSO$_4$ crystal. Disordered (superprotonic) phases I, VI, and VII. Ordered phases II, III, IV, and V with low conductivity [110].

10. EFFECT OF CATIONIC AND ANIONIC SUBSTITUTION ON SUPERPROTONIC PHASE TRANSITIONS AND PROTONIC CONDUCTIVITY

Substitution of cations having close ionic radii, K$^+$–Rb$^+$ and Rb$^+$–(NH$_4$)$^+$, results in the change of both the number of phases formed and their symmetry [121–125]. Thus, the symmetries of the superprotonic phases (initial compositions) in the mixed [(NH$_4$)$_{1-x}$Rb$_x$]H(SO$_4$)$_2$ crystals are different: phase I in [(NH)$_4$]$_3$H(SO$_4$)$_2$ is trigonal and phase I' in Rb$_3$H(SO$_4$)$_2$ is cubic (Fig. 26). The replacement of a spherical Rb$^+$ cation by a steric complex NH$_4^+$ ion results in a decrease in the temperature of transition to phase I and an increase in the temperature of transition to phase I'. For the compositions where $0.6 \leq x \leq 0.95$, both superprotonic phases, I and I', coexist. In [(NH$_4$)$_{1-x}$Rb$_x$]$_3$H(SeO$_4$)$_2$ crystals, where the superprotonic phases with the initial compositions are structurally isomorphous, an increase in the ammonium concentration also decreases the temperature of transition to the superprotonic phase [81].

If the radii of the substituted cations are considerably different, the mixed crystals form phases with the structures considerably different from the structures with the initial compositions. Thus, the chemical composition of a Cs$_{1.5}$Li$_{1.5}$H(SO$_4$)$_2$ crystal [125] allows one to relate it to Me_3H(AO$_4$)$_2$ solid solutions with the trigonal superprotonic phase and a two-dimensional DHBN, whereas a Cs$_{1.5}$Li$_{1.5}$H(SO$_4$)$_2$ crystal (similar to its deuterated analog) in the phase having the cubic symmetry (sp. gr. $I\bar{4}3d$) undergoes no phase transitions up to the temperature of its decomposition at about
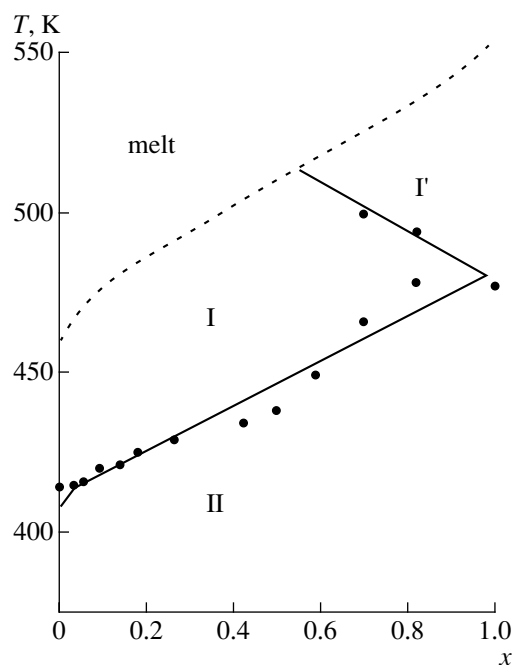
Fig. 26. Phase xT diagram of mixed $[(NH_4)_{1-x}Rb_x]_3H(SO_4)_4$ crystals [127]. I and I' are superprotonic phases with DHBNs; II is a low-conductive phase with OHBN.

470 K. In this structure, hydrogen atoms occupy the position $48(e)$ with the occupancy 1/6 [125], so that the H bonds formed in this position are disordered. However, a high enthalpy of conductivity activation, $H_a = 1.01$ eV, is characteristic not of the superprotonic but of the ordered phases with intrinsic protonic conductivity (Table 2.) This experimental fact can be explained by weak H bonds ($R(O{\cdots}O) \sim 3.3$ Å) formed in the position $48(e)$ in $Cs_{1.5}Li_{1.5}H(SO_4)_2$ and, therefore, also by a high potential barrier E_{intra} between the two proton positions on this bond. In this case, $E_{intra} \geq 1$ eV, in accordance with the model of proton transport (Fig. 10) discussed in Section 4. Another explanation of the high enthalpy of activation is the existence of one-dimensional –H–SO$_4$–H chains oriented along the body diagonals of the cube and also the absence of three-dimensional pathways of proton migration. In the CsHSO$_4$–CsH$_2$PO$_4$ system, new mixed crystals were synthesized, α-Cs$_3$(HSO$_4$)$_2$H$_2$(PO)$_4$ [126] and β-Cs$_3$(HSO$_4$)$_2$(H$_x$(P,S)O$_4$ [127], which possess the phases with superprotonic conductivity. The thermodynamic parameters of the superprotonic transitions in these crystals only slightly differ from the corresponding parameters of the transitions in the crystals with the initial compositions. However, conductivity in the ordered phase β-Cs$_3$(HSO$_4$)$_2$H$_x$(P,S)O$_4$ is much higher than in the CsHSO$_4$ and CsH$_2$PO$_4$ crystals.

The effect of cationic substitution on the transport characteristics of protons was studied in $[(NH_4)_{1-x}Rb_x]_3H(SO_4)_2$ mixed crystals [128]. The measurements were made along the [001] direction normal to the plane of the disordered H-bond network of the trigonal phase. With an increase in x from 0 to 0.6, the activation enthalpy H_a increases nonlinearly from 0.43 to 0.6 eV. Taking into account that, in this case, the ionic radii are practically equal, the considerable change in H_a after the $(NH_4)^+ \longrightarrow Rb^+$ substitution can be explained by the steric characteristics of ammonium ions and the formation of weak N–H$\cdots$O bonds. Obviously, in this case, the libration vibrations of $(NH_4)^+$ ions affect the dynamics of $(HSO_4)^-$ groups and, thus, the transport characteristics of acid protons.

11. ISOTOPIC EFFECTS IN H–D SUBSTITUTIONS

As is well known [2, 3], the isotopic $H \longrightarrow D$ substitution in the phase transitions induced by proton ordering–disordering in a two-minimum potential of a hydrogen bond results in an increase of the temperatures of these transitions by more than 100°C. However, for transitions between the phases with disordered and ordered H bonds, this effect has the negative value; i.e., the temperature T_{sp} decreases during deuteration [13, 14, 19, 125]. Quantitatively, this decrease is much less than in the first case and does not exceed 3 to 4°C irrespectively of the structural characteristics and chemical compositions of the crystals. Thus, different mechanisms of phase transitions occurring with the ordering–disordering processes in a two-minimum potential of a hydrogen bond and the transitions with ordering–disordering of an H-bond network manifest themselves in quite different isotopic effects with respect to the phase-transition temperatures. At present, there is no reliable theoretical interpretation of the negative isotopic effect with respect to the temperatures of superprotonic phase transitions. One can only assume that this effect is associated with the change of the interaction constants responsible for the superprotonic transitions because of an increase in the hydrogen-bond length during deuteration (geometric isotopic effect) [28].

An increase in the bond length in the $H \longrightarrow D$ substitution correlates with the isotopic effect with respect to conductivity (Fig. 9). The results obtained in [13, 14, 19, 125] indicate that in such a substitution, the parameter A in Eq. (11) decreases and the parameter H_a increases in both phases with OHBNs and those with DHBNs. It is characteristic that, in all the crystals studied, the A_H/A_D ratio ranges from 1.3 to 1.5. The same result was also observed with the use of the structural model of protonic conductivity considered in Sections 2 and 3. It follows from Eqs. (9) and (12), relating the parameter A to the microscopic parameters of the crystal, that

$$\frac{A_H}{A_D} \approx \frac{\nu_0^H}{\nu_0^D} \approx \sqrt{\frac{m_D}{m_H}} \approx 1.44, \qquad (31)$$

where m_D and m_H are the proton and deuteron masses, respectively. Thus, the change of the prefactor A during deuteration is associated mainly with the change of the mobile-ion mass. A slight increase in H_a (from 0.01 to 0.05 eV) in the $H \longrightarrow D$ substitution can be explained by the geometric isotopic effect mentioned above, which results in an increase of the potential barrier E_{intra}.

12. PRACTICAL APPLICATIONS OF SUPERPROTONIC CRYSTALS AND SYNTHESIS OF NEW PROTONIC SOLID ELECTROLYTES

Superprotonic crystals are not only important for fundamental science, they are also of interest for various practical applications. Because of a high purely protonic conductivity (the transport number of proton is $t_p \cong 10.0$) in the temperature range from 100 to 220°C, they are also promising solid electrolytes for proton-exchange membranes [15–17]. In particular, this temperature range is the most advantageous, both economically and energetically, for fuel cells. The first experience in the use of $CsHSO_4$ crystals as membranes of a fuel cell showed that, along with very high electrochemical parameters (open-circuit voltage 1.1 V and short-circuit current density 44 mA/cm^2), these elements are also stable to the action of atmospheric moisture [15]. However, a more detailed study of their thermal stability during long-term exploitation in various electrochemical devices is still an important problem.

The synthesis of new protonic solid electrolytes based on known superprotonic crystals is another practically important task. In particular, it is expedient to create nanocomposites based on superprotonic salts which would possess high protonic conductivity [129–131]. This would allow one not only to improve the technological characteristics of protonic electrolytes but also to modify the transport characteristics of protons [131].

Another interesting aspect is creation of new oxide-based protonic electrolytes with crystal structures symmetrically isomorphous to the structures of superprotonic salts. Under certain crystallochemical conditions, incorporation of hydrogen into these oxides would result in filling of the crystallochemical positions characteristic of stoichiometric hydrogen in the structure of a symmetrically isomorphous salt. Thus, one can also expect that the transport characteristics of protons in these chemically different materials would be similar. Thus, lead orthophosphate $Pb_3(PO_4)_2$ undergoes the ferroelastic phase transition ($C2/c \longrightarrow R\bar{3}m$), which is symmetry-isomorphous to the superprotonic transitions observed in the $Me_3H(AO_4)_2$ crystals. However, the position $9(e)$ of the trigonal phase with the occupancy 1/3 in the $Me_3H(AO_4)_2$ crystals is not occupied in $Pb_3(PO_4)_2$ crystals [74, 75].

The crystallochemical analysis shows that, in a hydrogen-doped $Pb_3(PO_4)_2$ crystal, the $9(e)$ position is energetically favorable for the formation of an H bond. Indeed, the first studies of a hydrogen-doped $Pb_3(PO_4)_2$ crystal showed that protonic conductivity of its protonic phase is as anisotropic as protonic conductivity in the trigonal phases with DHBNs of $Me_3H(AO_4)_2$ crystals [132]. Moreover, the activation enthalpies in the disordered (001) planes of H bonds in lead orthophosphate and $Me_3H(AO_4)_2$ crystals have the same values ranging within $H_a = 0.24 \pm 0.1$ eV (Table 1). These facts confirm the common nature of the structural mechanisms of proton conductivity in lead orthophosphate and the structurally isomorphous superprotonic salts. At temperatures below 200°C, the lower conductivity of lead orthophosphate in comparison with the conductivity of the isostructural salts is explained by a lower proton concentration in lead orthophosphate. However, this fact favors various practical applications of lead orthophosphate because of its high chemical and thermal stability up to temperatures of about 500°C, at which its conductivity in the (001) plane is as high as 10^{-3} Ω^{-1} cm^{-1}.

CONCLUSIONS

The reviewed material shows the obvious progress in understanding the nature and structural mechanisms of protonic conductivity. It should be emphasized that some of the above results are also applicable to a larger class of crystalline and amorphous objects. The study of crystals with DHBNs allows one to better understand the nature of hydrogen bonding and to deepen the knowledge of proton diffusion in hydrogen-containing materials. One can expect that, under certain conditions, e.g., under high hydrostatic pressures, protons in phases with DHBNs would also manifest some quantum mechanical properties and, in particular, tunnel diffusion.

It is also important to emphasize that delocalization of hydrogen bonds and superprotonic conductivity in acid salts cannot be explained by the presence of defects in these crystals, because these are the properties inherent in ideal crystal structures. Moreover, the structural phase transitions between the phases with disordered and ordered hydrogen-bond networks obey the symmetry relationships. Therefore, these crystals can be considered as model objects for the study of elementary processes of proton transfer and the main characteristics of proton conductivity in hydrogen-containing materials. As was shown above, the results of such studies would help in the search for new protonic electrolytes with desirable characteristics.

ACKNOWLEDGMENTS

REFERENCES

1. G. C. Pimentel and A. L. McClellan, *The Hydrogen Bond* (Freeman, San Francisco, 1960; Mir, Moscow, 1964).

2. V. G. Vaks, *Introduction to the Microscopic Theory of Ferroelectrics* (Nauka, Moscow, 1973).

3. R. Blinc and B. Zeks, *Soft Modes in Ferroelectrics and Antiferroelectrics* (North-Holland, Amsterdam, 1974; Mir, Moscow, 1975).

4. A. I. Baranov, L. A. Shuvalov, and N. M. Shchagina, Pis'ma Zh. Éksp. Teor. Fiz. **36**, 381 (1982) [JETP Lett. **36**, 459 (1982)].

5. A. I. Baranov, L. A. Shuvalov, and N. M. Shchagina, Kristallografiya **29** (5), 1203 (1984) [Sov. Phys. Crystallogr. **29**, 706 (1984)].

6. A. I. Baranov, R. M. Phedosyuk, N. M. Shchagina, and L. A. Shuvalov, Ferroelectr. Lett. Sect. **2**, 25 (1984).

7. R. Blinc, P. Dolinsek, B. Lahainar, *et al.*, Phys. Status Solidi B **123**, K83 (1984).

8. Yu. P. Moskvich, A. A. Sukhovskiĭ, and O. V. Rozanov, Fiz. Tverd. Tela (Leningrad) **26**, 38 (1984) [Sov. Phys. Solid State **26**, 21 (1984)].

9. A. I. Baranov, I. P. Makarova, L. A. Muradyan, *et al.*, Kristallografiya **32** (3), 682 (1987) [Sov. Phys. Crystallogr. **32**, 400 (1987)].

10. A. A. Baranov, A. V. Tregubchenko, L. A. Shuvalov, and N. M. Shchagina, Fiz. Tverd. Tela (Leningrad) **29**, 2513 (1987) [Sov. Phys. Solid State **29**, 1448 (1987)].

11. Cz. Pawlaczyk, F. E. Salman, A. Pawlowski, *et al.*, Phase Transit. **8**, 9 (1988).

12. A. I. Baranov, V. P. Khiznichenko, V. A. Sandler, and L. A. Shuvalov, Ferroelectrics **81**, 183 (1988).

13. A. I. Baranov, B. V. Merinov, A. V. Tregubchenko, and L. A. Shuvalov, Ferroelectrics **81**, 187 (1988).

14. A. I. Baranov, V. P. Khiznichenko, and L. A. Shuvalov, Ferroelectrics **100**, 135 (1989).

15. S. M. Haile, D. A. Boysen, C. R. I. Chisolm, and R. V. Merle, Nature **410**, 910 (2001).

16. T. Norby, Nature **410**, 877 (2001).

17. R. Fitzergerald, Phys. Today **54**, 21 (2001).

18. R. D. Parra, S. Bulusu, and X. C. Zeng, J. Chem. Phys. **118**, 3499 (2003).

19. V. V. Sinitsyn, E. G. Ponyatovskiĭ, A. I. Baranov, *et al.*, Zh. Éksp. Teor. Fiz. **100**, 386 (1991) [Sov. Phys. JETP **73**, 386 (1991)].

20. G. P. Flynn, *Point Defects and Diffusion* (Clarendon, Oxford, 1972).

21. B. V. Merinov, A. I. Baranov, L. A. Shuvalov, and B. A. Maksimov, Kristallografiya **32** (1), 86 (1987) [Sov. Phys. Crystallogr. **32**, 47 (1987)].

22. A. V. Belushkin, L. A. Shuvalov, W. I. F. David, and R. M. Ibberson, Acta Crystallogr., Sect. B: Struct. Sci. **47**, 161 (1991).

23. B. V. Merinov, A. I. Baranov, L. A. Shuvalov, *et al.*, Solid State Ionics **74**, 53 (1994).

24. B. V. Merinov, A. I. Baranov, L. A. Shuvalov, *et al.*, Solid State Ionics **69**, 153 (1997).

25. O. Madelung, *Introduction to Solid State Theory. Localized States* (Springer, Heidelberg, 1978; Nauka, Moscow, 1985).

26. A. V. Belushkin, R. L. McGreevy, P. Zetterstrom, and L. A. Shuvalov, Physica B (Amsterdam) **241–243**, 323 (1998).

27. B. Merinov, G. Bourenkov, and U. Bismayer, Phys. Status Solidi B **218**, 365 (2000).

28. M. Ichikawa, Acta Crystallogr., Sect. B: Struct. Crystallogr. Cryst. Chem. **34**, 2074 (1978).

29. S. Yomosa and M. Hasegawa, J. Phys. Soc. Jpn. **29**, 1329 (1970).

30. E. Lippincott and R. Shroeder, J. Chem. Phys. **23**, 1099 (1955).

31. I. D. Brown, Acta Crystallogr., Sect. A: Cryst. Phys., Diffr., Theor. Gen. Crystallogr. **32**, 24 (1976).

32. A. V. Belushkin, C. J. Carlile, and L. A. Shuvalov, J. Phys.: Condens. Matter **4**, 389 (1992).

33. B. V. Merinov and L. A. Shuvalov, Kristallografiya **39** (3), 469 (1994) [Crystallogr. Rep. **39**, 414 (1994)].

34. B. V. Merinov, Solid State Ionics **84**, 89 (1996).

35. B. V. Merinov, A. I. Baranov, L. A. Shuvalov, and N. M. Shchagina, Kristallografiya **36** (3), 584 (1991) [Sov. Phys. Crystallogr. **36**, 321 (1991)].

36. A. I. Baranov, O. A. Kabanov, B. V. Merinov, *et al.*, Ferroelectrics **127**, 257 (1992).

37. A. I. Baranov, V. V. Sinitsyn, V. Yu. Vinnichenko, *et al.*, Solid State Ionics **97**, 153 (1997).

38. R. Keiss, *Solids under Pressure*, Ed. by W. Paul and D. Warschauer (McGraw-Hill, New York, 1963; Mir, Moscow, 1966).

39. V. V. Sinitsyn, A. I. Baranov, E. G. Ponyatovsky, and L. A. Shuvalov, Solid State Ionics **77**, 118 (1995).

40. V. V. Sinitsyn, A. I. Baranov, E. G. Ponyatovsky, and L. A. Shuvalov, Ferroelectrics **167**, 67 (1995).

41. J. Dolinsék, R. Blinc, A. Novak, and L. A. Shuvalov, Solid State Commun. **60**, 877 (1987).

42. D. Abramič, J. Dolinsék, R. Blinc, and L. A. Shuvalov, Phys. Rev. B **42**, 442 (1990).

43. D. Arcon, R. Blinc, J. Dolinsék, and L. A. Shuvalov, Phys. Rev. B **55**, 8961 (1997).

44. G. Lahajanar, R. Blinc, J. Dolinsék, *et al.*, Solid State Ionics **97**, 141 (1997).

45. A. Damyanovich, M. M. Pintar, R. Blinc, and J. Slak, Phys. Rev. B **56**, 7942 (1997).

46. A. V. Belushkin, I. Natkaniec, N. M. Plakida, *et al.*, J. Phys. C: Solid State Phys. **20**, 671 (1987).

47. A. V. Belushkin, C. J. Carlie, W. I. F. David, *et al.*, Physica B (Amsterdam) **174**, 268 (1991).

48. A. V. Belushkin, C. J. Carlile, and L. A. Shuvalov, J. Phys.: Condens. Matter **4**, 389 (1992).

49. A. V. Belushkin, J. Tomkinson, and L. A. Shuvalov, J. Phys. II **3**, 217 (1993).

50. P. Zetterstrom, A. V. Belushkin, R. L. McGreevy, and L. A. Shuvallov, Solid State Ionics **116**, 321 (1999).

51. T. Kosztolanyi, I. Bako, and G. Palinkas, J. Chem. Phys. **118**, 4546 (2003).

52. M. Pham-Thi, Ph. Colomban, A. Novak, and R. Blinc, Solid State Commun. **55**, 265 (1985).

53. V. P. Dmitriev, M. Klanynek, L. T. Latush, *et al.*, Kristallografiya **31** (4), 695 (1986) [Sov. Phys. Crystallogr. **31**, 410 (1986)].

54. V. P. Dmitriev, V. V. Loshkarev, L. M. Rabkin, *et al.*, Kristallografiya **31** (6), 1138 (1986) [Sov. Phys. Crystallogr. **31**, 673 (1986)].

55. V. P. Dmitriev, V. V. Loshkarev, L. M. Rabkin, *et al.*, Fiz. Tverd. Tela (Leningrad) **29**, 1225 (1987) [Sov. Phys. Solid State **29**, 699 (1987)].

56. Ph. Colomban, J. S. Lasseguest, A. Novak, *et al.*, *Dynamics of Molecular Crystals* (Elsevier, Amsterdam, 1991), p. 269.

57. V. Zelezny, J. Petzelt, A. Pawlowski, *et al.*, Ferroelectrics **107**, 139 (1990).

58. Yu. I. Yuzyuk, V. P. Dmitriev, L. M. Rabkin, *et al.*, Solid State Ionics **91**, 145 (1996).

59. Yu. I. Yuzyuk, V. P. Dmitriev, V. V. Loshkarev, and L. M. Rabkin, Ferroelectrics **167**, 53 (1995).

60. R. Mizeris, J. Grigas, V. Samulionis, *et al.*, Phys. Status Solidi A **110**, 429 (1988).

61. B. V. Shchepetil'nikov, A. I. Baranov, L. A. Shuvalov, and V. A. Dolbinina, Fiz. Tverd. Tela (Leningrad) **32**, 254 (1990) [Sov. Phys. Solid State **32**, 142 (1990)].

62. B. V. Shchepetil'nikov, A. I. Baranov, L. A. Shuvalov, and N. M. Shchagina, Fiz. Tverd. Tela (Leningrad) **32**, 2885 (1990) [Sov. Phys. Solid State **32**, 1676 (1990)].

63. R. Mizaras, J. Grigas, V. Samulionis, *et al.*, Ferroelectrics **155**, 201 (1994).

64. S. G. Lushnikov and I. G. Siny, Ferroelectrics **106**, 237 (1990).

65. S. G. Lushnikov and L. A. Shuvalov, Ferroelectrics **124**, 409 (1991).

66. L. Snoek, Physica (Amsterdam) **8**, 711 (1941).

67. M. Komukae, T. Osaka, Y. Makita, *et al.*, J. Phys. Soc. Jpn. **50**, 31 (1981).

68. S. Yokota, N. Takanonashi, T. Osaka, and Y. Makita, J. Phys. Soc. Jpn. **51**, 199 (1982).

69. S. Suzuki, Y. Oshino, K. Gesi, and Y. Makita, J. Phys. Soc. Jpn. **47**, 874 (1979).

70. B. Hilczer and A. Pawlowski, Ferroelectrics **104**, 383 (1990).

71. R. A. Dilanyan, V. V. Sinitsyn, V. Sh. Shekhtman, *et al.*, Kristallografiya **39** (3), 484 (1994) [Crystallogr. Rep. **39**, 428 (1994)].

72. V. Sh. Shekhtman and R. A. Dylanyan, Ferroelectrics **167**, 115 (1995).

73. J. C. Toledano and P. Toledano, Phys. Rev. B **21**, 1139 (1980).

74. J. Torres, Phys. Status Solidi B **71**, 145 (1975).

75. E. Salje and V. Devarajan, J. Phys. C: Solid State Phys. **14**, L1029 (1981).

76. N. M. Plakida and V. S. Shakhmatov, Izv. Akad. Nauk SSSR, Ser. Fiz. **51**, 315 (1987).

77. N. M. Plakida and W. Saleida, Phys. Status Solidi B **148**, 473 (1988).

78. W. Salejda and N. A. Dzhavadov, Phys. Status Solidi B **158**, 119 (1990).

79. W. Salejda and N. A. Dzhavadov, Phys. Status Solidi B **158**, 475 (1990).

80. L. Schwalowsky, V. Vinnichenko, A. Baranov, *et al.*, J. Phys.: Condens. Matter **10**, 3019 (1998).

81. B. V. Merinov, U. Bismayer, V. V. Synitsyn, and A. I. Baranov, Phase Transit. **69**, 453 (1999).

82. B. V. Merinov, S. M. Haile, and U. Bismayer, Solid State Ionics **146**, 355 (2002).

83. L. Kirpichnikova, M. Polomska, and B. Hilcher, Ferroelectrics **221**, 85 (1999).

84. V. S. Shakhmatov, Kristallografiya **36** (1), 1021 (1991) [Sov. Phys. Crystallogr. **36**, 575 (1991)].

85. V. S. Shakhmatov, Kristallografiya **38** (6), 176 (1993) [Crystallogr. Rep. **38**, 805 (1993)].

86. A. I. Baranov, Izv. Akad. Nauk SSSR, Ser. Fiz. **51**, 2146 (1987).

87. R. A. Vargas, M. B. Salamon, and C. P. Flynn, Phys. Rev. Lett. **37**, 1550 (1976).

88. R. A. Vargas, M. B. Salamon, and C. P. Flynn, Phys. Rev. B **17**, 269 (1978).

89. L. Kirpichnikova, M. Polomska, J. Wolak, and B. Hilczer, Solid State Ionics **97**, 85 (1997).

90. T. Ozaki, K. Itoh, and E. Nakamura, J. Phys. Soc. Jpn. **51**, 213 (1982).

91. T. Kishomoto, T. Osaka, M. Komukae, and Y. Makita, J. Phys. Soc. Jpn. **56**, 2070 (1987).

92. A. I. Baranov, V. V. Sinitsyn, E. G. Ponyatovskiĭ, and L. A. Shuvalov, Pis'ma Zh. Éksp. Teor. Fiz. **33**, 824 (1988).

93. A. A. Lomov, N. V. Shitov, V. A. Bushuev, and A. I. Baranov, Pis'ma Zh. Éksp. Teor. Fiz. **55**, 297 (1992) [JETP Lett. **55**, 296 (1992)].

94. V. V. Sinitsyn, A. I. Baranov, A. F. Gurov, *et al.*, Solid State Ionics **97**, 171 (1997).

95. A. I. Baranov, E. D. Yakushkin, D. J. Jones, and J. Roziere, Solid State Ionics **125**, 99 (1999).

96. A. I. Baranov, Ferroelectrics **265**, 87 (2002).

97. E. D. Yakushkin and A. I. Baranov, Fiz. Tverd. Tela (St. Petersburg) **42**, 1474 (2000) [Phys. Solid State **42**, 1517 (2000)].

98. A. M. Faidiga-Bulat, G. Lahajanar, *et al.*, Solid State Ionics **77**, 22 (1995).

99. B. V. Merinov, R. E. Melzer, R. E. Lechner, *et al.*, Solid State Ionics **97**, 161 (1997).

100. S. G. Lushnikov, A. V. Belushkin, S. N. Gvasaliya, *et al.*, Physica B (Amsterdam) **276–278**, 2197 (2000).

101. A. I. Baranov, O. A. Kabanov, and L. A. Shuvalov, Pis'ma Zh. Éksp. Teor. Fiz. **58**, 542 (1993) [JETP Lett. **58**, 548 (1993)].

102. S. G. Lushnikov, A. V. Belushkin, and A. I. Beskrovnyi, Solid State Ionics **125**, 119 (1999).

103. Yu. I. Yuzyuk, V. P. Dmitriev, L. M. Rabkin, *et al.*, J. Phys.: Condens. Matter **8**, 3965 (1996).

104. V. N. Anisimova, A. I. Baranov, and E. D. Yakushkin, Izv. Ross. Akad. Nauk, Ser. Fiz. **60**, 80 (1996).

105. E. D. Yakushkin and A. I. Baranov, Fiz. Tverd. Tela (St. Petersburg) **39**, 89 (1997) [Phys. Solid State **39**, 77 (1997)].

106. S. Waplak, W. Bernadski, A. I. Baranov, and L. A. Shuvalov, J. Phys.: Condens. Matter **9**, 4813 (1997).

107. A. I. Baranov, L. A. Shuvalov, E. D. Yakushkin, and V. V. Synitsyn, Ferroelectrics **199**, 307 (1997).

108. S. G. Lushnikov, A. I. Fedoseev, and L. A. Shuvalov, Fiz. Tverd. Tela (St. Petersburg) **42**, 2197 (2000) [Phys. Solid State **42**, 2265 (2000)].

109. A. I. Belushkin, M. Bull, C. Carlile, *et al.*, Physica B (Amsterdam) **241–243**, 484 (1998).

110. E. G. Ponyatovskiǐ, V. I. Rashchupkin, V. V. Sinitsyn, *et al.*, Pis'ma Zh. Éksp. Teor. Fiz. **41**, 114 (1985) [JETP Lett. **41**, 139 (1985)].

111. A. I. Baranov, E. G. Ponyatovskiǐ, V. V. Sinitsyn, and L. A. Shuvalov, Kristallografiya **30** (6), 1121 (1985) [Sov. Phys. Crystallogr. **30**, 653 (1985)].

112. V. V. Sinitsyn, E. G. Ponyatovskiǐ, A. I. Baranov, *et al.*, Fiz. Tverd. Tela (Leningrad) **30**, 2838 (1988) [Sov. Phys. Solid State **30**, 1636 (1988)].

113. M. Freizel, B. Baranovski, and A. Lunden, Solid State Ionics **35**, 85 (1989).

114. A. V. Belushkin, M. A. Adams, S. Hull, *et al.*, Physica B (Amsterdam) **213–214**, 1034 (1995).

115. V. V. Sinitsyn, A. I. Baranov, and E. G. Ponyatovskiǐ, Fiz. Tverd. Tela (St. Petersburg) **37**, 2059 (1995) [Phys. Solid State **37**, 1121 (1995)].

116. V. V. Sinitsyn, A. I. Baranov, E. G. Ponyatovsky, and L. A. Shuvalov, Ferroelectrics **167**, 67 (1995).

117. V. V. Sinitsyn, A. I. Baranov, E. G. Ponyatovsky, and L. A. Shuvalov, Solid State Ionics **77**, 118 (1995).

118. V. V. Sinitsyn, A. I. Baranov, and E. G. Ponyatovsky, Solid State Ionics **136**, 167 (2000).

119. E. Rapoport, J. B. Clark, and P. W. Richter, J. Solid State Chem. **24**, 423 (1978).

120. D. A. Boysen, S. M. Haile, H. Liu, and R. A. Secco, Chem. Mater. **15**, 727 (2003).

121. A. I. Baranov, V. V. Dolbinina, E. D. Yakushkin, *et al.*, Ferroelectrics **217**, 285 (1998).

122. T. Mhiri and Ph. Colomban, Solid State Ionics **44**, 235 (1991).

123. B. V. Merinov, D. J. Jones, J. Roziere, and T. Mhiri, Solid State Ionics **91**, 323 (1996).

124. B. V. Merinov, D. J. Jones, J. Roziere, and T. Mhiri, Solid State Ionics **69**, 53 (1994).

125. B. V. Merinov, C. R. I. Chisholm, D. A. Boysen, and S. M. Haile, Solid State Ionics **145**, 185 (2001).

126. S. M. Haile, G. Lentz, K. D. Kreuer, and J. Maier, Solid State Ionics **77**, 128 (1995).

127. S. M. Haile, P. M. Galkins, and D. I. Boysen, Solid State Ionics **97**, 145 (1997).

128. V. Yu. Vinnichenko, Candidate's Dissertation in Physics and Mathematics (Inst. of Crystallography, Russian Academy of Sciences, Moscow, 1998).

129. V. G. Ponomareva and G. V. Lavrova, Solid State Ionics **106**, 137 (1998).

130. V. G. Ponomareva, G. V. Lavrova, and L. G. Simonova, Solid State Ionics **118**, 317 (1999).

131. V. G. Ponomareva, G. V. Lavrova, and L. G. Simonova, Solid State Ionics **119**, 295 (1999).

132. A. I. Baranov, V. M. Duda, D. J. Jones, *et al.*, Solid State Ionics **145**, 241 (2001).

133. W. Bronowska, J. Chem. Phys. **114**, 611 (2001).

134. C. R. I. Chisholm and S. M. Haile, Solid State Ionics **145**, 179 (2001).

135. T. Osako, Y. Makita, and K. Gesi, J. Phys. Soc. Jpn. **49**, 593 (1980).

136. A. I. Baranov, B. V. Merinov, A. V. Tregubchenko, and L. A. Shuvalov, Ferroelectrics **81**, 187 (1988).

Translated by L. Man

PHYSICAL PROPERTIES
OF CRYSTALS

Ordinary Electromagnetic Waves in Absorptive Crystals

V. I. Alshits and V. N. Lyubimov

Shubnikov Institute of Crystallography, Russian Academy of Sciences, Leninskiĭ pr. 59, Moscow, 119333 Russia
e-mail: alshits@ns.crys.ras.ru
Received January 27, 2003

Abstract—It is shown that "switching-on" of absorption in a continuum of the directions of propagation of ordinary electromagnetic waves in transparent triclinic crystals results in the "survival" of only a discrete number of these directions. The relationships for the angular coordinates of these directions are obtained in terms of the components of a complex permittivity tensor. © *2003 MAIK "Nauka/Interperiodica".*

It is well known that, in general, the directions of the phase and group velocities of an electromagnetic or acoustic wave in anisotropic media do not coincide. However, for some particular directions of wave propagation, these directions coincide. According to the definition given in [1, 2], these waves should be ordinary waves. The optical properties of a crystal are determined by permittivity tensor $\boldsymbol{\varepsilon}$, whereas its acoustic properties, by the tensor of elastic moduli, **c**. In the absence of energy dissipation, both tensors are real. In the general case of a triclinic crystal, tensor **c** is invariant only with respect to the center of inversion, and ordinary acoustic waves propagate only along some particular discrete directions. As follows from [3], there are at least three such directions. In optics, the situation is different in principle: tensor $\boldsymbol{\varepsilon}$ for transparent triclinic crystals is characterized by orthorhombic symmetry

and is invariant with respect to reflection in three mutually orthogonal planes. As was proven in [4], ordinary electromagnetic waves in these crystals can propagate only in the symmetry planes of tensor $\boldsymbol{\varepsilon}$. These waves exist only in those planes of the continuum of propagation directions which correspond to circular sections of the refractive-index surface (Fig. 1a). Then, a question may arise as to what can happen to the continuum of ordinary waves during "switching-on" of absorption when the tensor $\boldsymbol{\varepsilon}$ acquires a small imaginary part $i\boldsymbol{\varepsilon}'$. We consider here the general case, where all the three eigenvalues of tensor $\boldsymbol{\varepsilon}$ are different and a crystal is triclinic and optically biaxial. Hereafter, we use the crystallophysical coordinate system in which tensor $\boldsymbol{\varepsilon}$ is diagonal. Then, the three planes in which the coordinate axes lie turn out to be symmetry planes of the tensor $\boldsymbol{\varepsilon}$ but not of the tensor $\boldsymbol{\varepsilon}'$. In the general case, all the
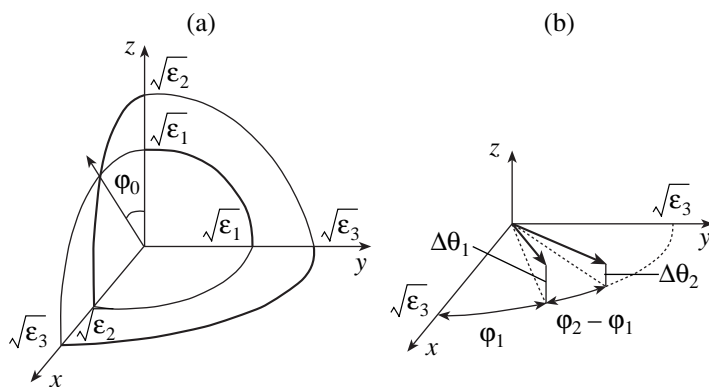
Fig. 1. Directions of propagation of ordinary waves in triclinic crystals. (a) Transparent crystals. Fragments of the sections of the refractive-index surface by symmetry planes. Solid lines indicate the circular sections corresponding to the continuum of directions of ordinary-wave propagation. An arrow indicates the direction of the optic axis at $\varepsilon_1 < \varepsilon_2 < \varepsilon_3$. (b) Absorptive crystals. Two isolated directions of propagation of ordinary waves in the vicinity of the *xy* plane at nonzero value of ε_{13} and $\varepsilon_{23} \neq 0$.

components of the tensor $\boldsymbol{\varepsilon}'$ in the chosen coordinate system have nonzero values. As a result, the complex permittivity tensor $\boldsymbol{\varepsilon} + i\boldsymbol{\varepsilon}'$ becomes invariant only with respect to the center of inversion. The continuum of the directions of propagation ordinary wave of in a triclinic crystal breaks, and only discrete directions "survive." Our goal is to reveal and describe these discrete directions.

In transparent crystals, the dependence of the refractive index n of electromagnetic waves on the direction of their propagation $\mathbf{m}$ ($\mathbf{m}^2 = 1$) can be described by the following equation [1]:

$$n^4 \mathbf{m} \cdot \boldsymbol{\varepsilon}\mathbf{m} - n^2(\mathrm{Sp}\,\bar{\boldsymbol{\varepsilon}} - \mathbf{m} \cdot \bar{\boldsymbol{\varepsilon}}\mathbf{m}) + \det \boldsymbol{\varepsilon} = 0. \quad (1)$$

Here, $\bar{\boldsymbol{\varepsilon}}$ and $\boldsymbol{\varepsilon}$ are interdependent tensors. The phase velocity of an electromagnetic wave is parallel to the vector $\mathbf{m}$, whereas the direction of the group velocity is parallel to the surface normal, $n(\mathbf{m})$. At the extremum points of this surface, the group velocity is parallel to the phase velocity, which determines ordinary waves. Using the spherical angular coordinates θ and φ, which set the direction of $\mathbf{m}$, one can readily show that, irrespectively of the propagation direction in the xy plane ($\theta = \pi/2$ and $0 \le \varphi < 2\pi$), we obtain for ordinary waves (Fig. 1a)

$$n = \sqrt{\varepsilon_3}, \quad \partial n/\partial\theta = \partial n/\partial\varphi = 0. \quad (2)$$

Now, consider how this continuum of propagation directions of ordinary waves changes under the action of a certain perturbation, i.e., upon the substitution $\varepsilon \longrightarrow \varepsilon + i\varepsilon'$ and $n \longrightarrow n + in'$ in Eq. (1) (here, n' is the absorption coefficient). Perturbation changes the n value. This change in the vicinity of the xy plane is a function of angles $\theta = \pi/2 + \Delta\theta$ and φ, i.e., $\Delta n(\theta, \varphi)$. A rather cumbersome procedure of the search for extrema of this function allows one to express the angular coordinates of the extreme directions in terms of the components of the complex permittivity tensor. In the vicinity of the xy plane, there exist two extreme directions with the angular coordinates $(\Delta\theta_1, \varphi_1)$ and $(\Delta\theta_2, \varphi_2)$ (Fig. 1b). The coordinates $\varphi_{1,2}$ are given by the following expressions

$$\varphi_1 = \frac{1}{2}(\varphi_+ - \varphi_-), \quad \varphi_2 = \frac{\pi}{2} + \frac{1}{2}(\varphi_+ + \varphi_-),$$

$$\varphi_+ = \arctan\frac{b}{a_+}, \quad \varphi_- = \arctan\frac{c}{a_-}. \quad (3)$$

Here, the following notation was used:

$$a_\pm = (\varepsilon'_{13})^2 A_1 \pm (\varepsilon'_{23})^2 A_2,$$

$$b = \varepsilon'_{13}\varepsilon'_{23}B, \quad c = \varepsilon'_{13}\varepsilon'_{23}C; \quad (4)$$

$$A_1 = \varepsilon_2 d_{23}, \quad A_2 = \varepsilon_1 d_{31}, \quad B = \varepsilon_1 d_{23} + \varepsilon_2 d_{13},$$

$$C = \varepsilon_3 d_{12}, \quad d_{ij} = \varepsilon_i - \varepsilon_j. \quad (5)$$

Then, we obtain for the coordinates

$$\Delta\theta_{1,2} = \left(\frac{\varepsilon_1\varepsilon_2}{\varepsilon_3}\right)\frac{(a_{12}\cos\varphi_{1,2} + b_{12}\sin\varphi_{1,2})\cos^2\varphi_{1,2} + (a_{21}\sin\varphi_{1,2} + b_{21}\cos\varphi_{1,2})\sin^2\varphi_{1,2}}{A_1 A_2 (B - C\cos 2\varphi_{1,2})}. \quad (6)$$

Above, we used the notation

$$a_{12} = \varepsilon'_{13}(2\varepsilon'_{11}\varepsilon_3 - \varepsilon'_{33}\varepsilon_1)d_{23}^2 + 2\varepsilon'_{12}\varepsilon'_{23}d_{23}\varepsilon_1\varepsilon_3, \quad (7)$$

$$b_{12} = \varepsilon'_{23}[2(\varepsilon'_{11}d_{32}\varepsilon_3 + \varepsilon'_{22}d_{13}\varepsilon_1)\varepsilon_3$$
$$+ \varepsilon'_{33}(2d_{21}\varepsilon_2 + d_{13}d_{32})\varepsilon_1] + 2\varepsilon'_{12}\varepsilon'_{13}d_{32}\varepsilon_3(2\varepsilon_3 - \varepsilon_1). \quad (8)$$

Upon the subscript change $1 \longleftrightarrow 2$ in the components ε'_{ij}, ε_i, and d_{ij}, the following correspondence of the coefficients in Eq. (6) exists: $a_{12} \longrightarrow a_{21}$ and $b_{12} \longrightarrow b_{21}$. It follows from Eqs. (3)–(8) that the transformation of the continuum described here takes place if at least one of the two perturbation parameters, ε'_{13} or ε'_{23}, has a nonzero value. The angle between the extreme directions considered above, $\varphi_2 - \varphi_1 = \varphi_- + \pi/2$, is right if $\varepsilon'_{13} = 0$ or $\varepsilon'_{23} = 0$ (where $\varphi_- = \varphi_+ = 0$). In the particular case $\varphi_- = -\pi/2$ (where $c/a_- \longrightarrow -\infty$), degeneracy takes place, $\varphi_+ = \varphi_-$. One can readily see that, in this case, the circumference under the action of perturbation simply

changes its radius, whereas the continuum of particular directions remains unchanged.

Consider specific instability of the positions of the above extrema. The coordinates $\varphi_{1,2}$ in Eq. (3) are determined by the ratio of small quantities. In this case, even slight changes in small parameters lead to considerable changes in their ratios (in the limit, we have indeterminacy of the 0/0 type). As a result, the coordinates $\varphi_{1,2}$ considerably change despite the smallness of perturbations. Pairs of extreme directions also exist in the vicinity of the two other coordinate planes—yz and zx. The above relationships also describe these cases. Thus, in order to describe the extreme directions in the vicinity of the yz plane, angle θ should be measured from the x axis, whereas angle φ, from the y axis in the yz plane. All the above relationships remain valid if one makes the cyclic permutation of subscripts $1 \longrightarrow 2 \longrightarrow 3 \longrightarrow 1$ in the parameters ε'_{ij}, ε_i, d_{ij}, a_{ij}, and b_{ij}. In order to describe the extreme directions in the vicinity of the zx plane, angle θ is measured from the y axis, and angle φ, from the z axis in the zx plane. Then, the

cyclic permutation $1 \longrightarrow 3 \longrightarrow 2 \longrightarrow 1$ should be made.

Thus, there are six directions of propagation of ordinary waves in an absorptive triclinic crystal. Only one exotic case remains to be considered—a random combination of the material constants, which results in the situation where the constant angle φ_1 or φ_2 in Eq. (3) turns out to be close to the direction of the optic axis of an initial transparent crystal. These axes usually lie in one of three symmetry planes of the crystal [1, 2] (Fig. 1a). In the situation where the optic axes lie in the zx plane, angle φ_0, which determines the orientations of these axes (at $\boldsymbol{\varepsilon}' = 0$), satisfies the relationship

$$\cos 2\varphi_0 - B/C = 0. \tag{9}$$

At $\varphi_{1,2} - \varphi_0 = \Delta\varphi \ll 1$, formula (6) has no sense any more. The range of angles in which our approach based on the standard perturbation theory is invalid is rather narrow, $\Delta\varphi \sim (\varepsilon')^2$.

Considering the analogous characteristics of absorptive monoclinic crystals, one should remember that one of their coordinate planes remains a symmetry plane. Thus, the xy plane is a symmetry plane if $\varepsilon'_{13} = \varepsilon'_{23} = 0$. In this case, the continuum of ordinary waves in this planes described by Eq. (2) is not changed, whereas the extreme directions in the vicinity of the yz and zx planes are the same as in triclinic crystals. In orthorhombic crystals, all three coordinate planes are symmetry planes. The continuum of the directions of propagation of ordinary waves in all the three planes is exactly the same as for transparent crystals. Absorption does not change the existence range of the continuum of ordinary waves for optically uniaxial crystals, where these waves exist on the whole sphere of the propagation directions, $\mathbf{m}^2 = 1$.

REFERENCES

1. F. I. Fedorov, *Theory of Gyrotropy* (Nauka i Tekhnika, Minsk, 1976).

2. Yu. I. Sirotin and M. P. Shaskol'skaya, *Fundamentals of Crystal Physics*, 2nd ed. (Nauka, Moscow, 1979; Mir, Moscow, 1982).

3. I. I. Kolodner, J. Acoust. Soc. Am. **40** (3), 730 (1966).

4. V. I. Alshits and V. N. Lyubimov, Kristallografiya **46** (2), 340 (2001) [Crystallogr. Rep. **46**, 296 (2001)].

Translated by L. Man

========= **NANOMATERIALS** =========

Dedicated to the 60th Anniversary
of the Shubnikov Institute of Crystallography
of the Russian Academy of Sciences

Lasing and Refractive Indices of Nanocrystalline Ceramics of Cubic Yttrium Oxide Y_2O_3 Doped with Nd^{3+} and Yb^{3+} Ions

A. A. Kaminskiĭ*, K. Ueda**, A. F. Konstantinova*, H. Yagi***, T. Yanagitani***,
A. V. Butashin*, V. P. Orekhova*, J. Lu**, K. Takaichi**, T. Uematsu**, M. Musha**,
and A. Shirokava**

* *Shubnikov Institute of Crystallography, Russian Academy of Sciences, Leninskiĭ pr. 59, Moscow, 119333 Russia*
e-mail: AFKonst@ns.crys.ras.ru
** *Institute for Laser Science, University of Electro-Communications, Chofu, Tokyo 182, Japan*
e-mail: lu@ils.uec.ac.jp
*** *Takuma Works, Konoshima Chemical Co., Ltd., 80 Kouda, Takuma, Mitoyo, Kagawa 769, Japan*
Received April 3, 2003

Abstract—A continuous-wave lasing at 1 μm was excited by the radiation of semiconductor laser diodes at room temperature in nanocrystalline ceramics Y_2O_3 doped with Nd^{3+} and Yb^{3+} ions. The refractive indices of the undoped nanocrystalline Y_2O_3 ceramics were measured in the wavelength range 0.4–9 μm. © *2003 MAIK "Nauka/Interperiodica".*

Single crystals of cubic rare-earth oxides RE_2O_3: Ln^{3+} (RE = Y, Sc, and Ln) doped with Ln^{3+} ions have for many years attracted the attention of specialists as laser materials with high thermal conductivity (see, e.g., [1–3]). Unfortunately, their high melting point (~2400°C) has hindered the use of the well-known methods of growing of large crystals of high optical quality. In the first laser experiments with rare-earth oxides, the crystalline elements made of these materials were about a millimeter in size (Y_2O_3 doped with Nd^{3+} ions [4] and Er_2O_3 doped with Ho^{3+} and Tm^{3+} ions [5, 6]). In recent years, in view of the development of the technique of semiconductor laser pumping, interest in RE_2O_3 : Ln^{3+} compounds doped with Ln^{3+} ions (and especially with Nd^{3+} and Yb^{3+} ions) has increased significantly. Recently, Sc_2O_3, Y_2O_3, and Lu_2O_3 single crystals doped with Tm^{3+} and Yb^{3+} ions have been grown, and lasing in these crystals was obtained by semiconductor laser pumping [7, 8]. Although rhenium crucibles were used to grow RE_2O_3 single crystals in these studies, no substantial progress in increasing the crystal size has been made so far.

The existing nanoceramic vacuum technology of producing large (tens of centimeters in size) $Y_3Al_5O_{12}$ lasing crystals doped with Nd^{3+} and Yb^{3+} ions [9, 10] has been modified recently and used to obtain highly transparent ceramics based on cubic Y_2O_3 yttrium

oxide doped with Nd^{3+} and Yb^{3+} ions. The results of lasing experiments with these ceramic materials were published in [11, 12].

In continuation of these studies, we present here new results on lasing at 1 μm in these materials (the $^4F_{3/2} \longrightarrow {}^4I_{11/2}$ transition for Nd^{3+} ions and the $^2F_{5/2} \longrightarrow$
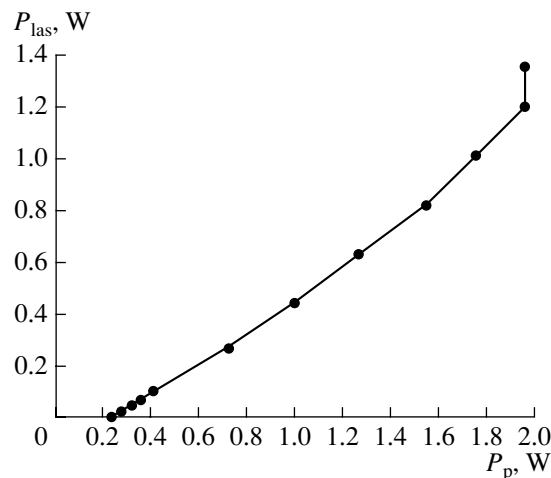

Fig. 1. Output power P_{las} of CW lasing as a function of absorbed power P_p for a laser based on the nanocrystalline Y_2O_3 : Yb^{3+} ceramics (C_{Yb} ~ 4 at. %, λ_p ~ 0.926 μm, d = 800 μm).

Refractive indices n of Y_2O_3 ceramics

λ, μm	n
0.405	1.9590
0.436	1.9467
0.491	1.9310
0.546	1.9205
0.579	1.9158
0.615	1.9104
0.633	1.9093
0.691	1.9042
1.064	1.8903
2	1.8803
3	1.8701
4	1.8568
5	1.8388
6	1.8148
7	1.7827
8	1.7394
8.6	1.7061

$^2F_{7/2}$ transition for Yb^{3+} ions). Using a conventional scheme of end pumping by semiconductor laser diodes at 300 K, we obtained a continuous-wave (CW) lasing power as high as 0.16 W for the Y_2O_3 : Nd^{3+} ceramics and 1.4 W for the Y_2O_3 : Yb^{3+} ceramics with an efficiency of 40 and ~70%, respectively (see Fig. 1). Further improvement of the lasing parameters of these materials will involve the use of new semiconductor diodes with an emission spectrum exactly corresponding to the strongest absorption bands of the Nd^{3+} and Yb^{3+} ions in the Y_2O_3 ceramics.

As far as we know, the refractive indices n of Y_2O_3 ceramics have not been measured so far. The value of n
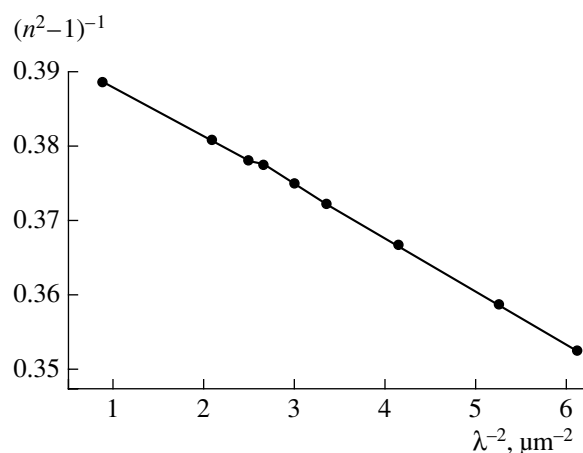
for single-crystal Y_2O_3 was reported in [13]; the refractive indices of crystalline films, in [14].

In our experiments, the refractive indices of undoped Y_2O_3 ceramics were measured by the minimum deviation method with a GS-5 goniometer [15] in the wavelength range from 0.405 to 1.064 μm at room temperature. The prism fabricated had refracting angle $\alpha = 40.02854°$ and a 1-cm^2 aperture. The light sources were a PRK-4 mercury lamp, a He–Ne laser ($\lambda = 0.633$ μm), and an $Y_3Al_5O_{12}$: Nd^{3+} laser ($\lambda = 1.064$ μm). The measured refractive indices are listed in the table. In the range 0.436–0.633 μm, the refractive indices were measured with an accuracy of ±0.0002. At $\lambda = 0.405$ and 1.064 μm, the accuracy was lower (±0.0008).

In the noted spectral region, the refractive indices n of the Y_2O_3 ceramics were approximated by the one-term Sellmeier dispersion formula

$$n^2 - 1 = K\lambda^2/(\lambda^2 - \lambda_0^2), \qquad (1)$$

where $K = 2.529212$ is the coefficient, $\lambda_0 = 0.133058$ μm is the corresponding characteristic wavelength, and λ is the wavelength of the incident light in μm. Figure 2 shows the dependence of $1/(n_i^2 - 1)$ on $f(1/\lambda^2)$. It is clearly seen that this dependence is linear and, thus, can be well approximated by a straight line in this spectral region.

In the IR spectral region, the refractive indices were measured by the interference method, which was described by us earlier [16]. Samples were cut from the Y_2O_3 ceramics in the form of polished plane-parallel plates with thickness $d = 103$ μm. The plane parallelism was no worse than 10″. The transmission spectra were measured with a resolution of 1 cm^{-1} with a Brooker (IFS-25) spectrometer in the range 9000–500 cm^{-1}. The entire transmission spectrum of the ceramics is shown in Fig. 3. The order of interference for the oscillating curve was determined at $\lambda = 1.669$ μm, and the disper-

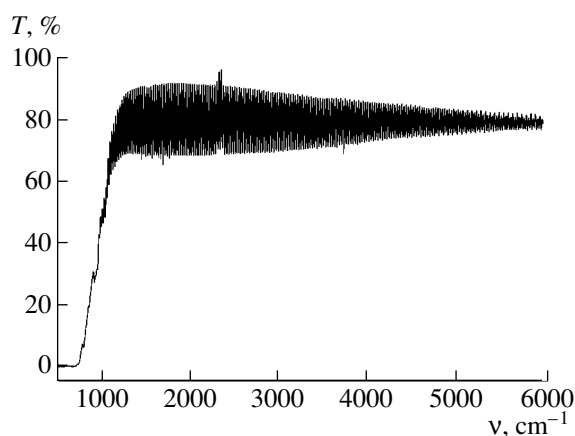**Fig. 2.** Dependence of $1/(n^2 - 1)$ on $1/\lambda^2$ for Y_2O_3 ceramics.

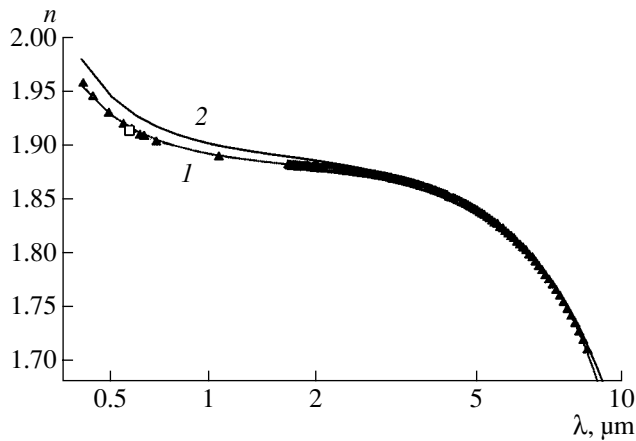**Fig. 3.** Transmission spectrum of Y_2O_3 ceramics in the IR range ($d = 103$ μm).

Fig. 4. Dispersion dependence of the refractive indices of Y_2O_3: (▲) experimental data for ceramics, (*1*) calculation for ceramics by formula (3), and the data for single crystals from (*2*) [13] and (□) [1].

sion dependence $n(\lambda)$ was finally calculated by the formula

$$2dn = m\lambda, \qquad (2)$$

where n is the refractive index, d is the thickness of the sample studied, λ is the wavelength of the incident light, and m is the order of interference [17]. The measurement accuracy in this spectral region was ±0.001.

The refractive indices of Y_2O_3 ceramics in the entire range studied are shown in Fig. 4. The entire dispersion dependence $n(\lambda)$ can be approximated by the function (curve *1*)

$$n^2 - 1 = A\lambda^2/(\lambda^2 - B) + C\lambda^2/(\lambda^2 - D), \qquad (3)$$

where $A = 2.5503$, $B = (0.12626)^2$, $C = 1.5839$, $D = (16.031)^2$, and λ is measured in μm.

The value of the refractive index of single-crystal Y_2O_3 reported in [1] ($n = 1.915$ at $\lambda = 0.57$ μm) is almost the same as the value we obtained. Figure 4 also shows the refractive indices of single-crystal Y_2O_3 taken from [13] (curve *2*). Comparison shows that, in the visible range, the refractive indices of ceramics are noticeably lower than those reported in [13], whereas the relevant data are almost the same for the IR region. Since the values of the refractive indices of the ceramics obtained by us are much (by ~0.01) higher than those for thin crystalline Y_2O_3 films [14], we can assume that the structure and optical properties of the ceramics, single crystals, and crystalline films depend on the preparation procedure.

Thus, efficient lasing at 1 μm of the Nd^{3+} (the $^4F_{3/2} \longrightarrow {}^4I_{11/2}$ transition) and Yb^{3+} (the $^2F_{5/2} \longrightarrow {}^2F_{7/2}$ transition) ions in Y_2O_3 ceramics was obtained, and the refractive indices of Y_2O_3 ceramics were measured over a wide spectral range.

REFERENCES

1. A. A. Kaminskii, *Laser Crystals, Their Physical Properties*, 2nd ed. (Springer, Berlin, 1990).

2. A. A. Kaminskii, *Crystalline Lasers: Physical Processes and Operating Schemes* (CRC Press, Boca Raton, 1996).

3. M. J. Weber, *Handbook of Laser Wavelengths* (CRC Press, Boca Raton, 2000).

4. R. H. Hoskins and B. H. Soffer, Appl. Phys. Lett. **4**, 22 (1964).

5. R. H. Hoskins and B. H. Soffer, IEEE J. Quantum Electron. **2**, 527 (1966).

6. R. H. Hoskins and B. H. Soffer, Appl. Phys. Lett. **6**, 200 (1965).

7. L. Fornasiero, T. Max, V. Peters, *et al.*, Ceram. Int. **26**, 589 (2000).

8. V. Peters, E. Max, L. Fornasiero, *et al.*, Laser Phys. **10** (2), 417 (2000).

9. T. Yanagitani, H. Yagi, and M. Ichikawa, Jpn. Patent No. 10-101333 (1998).

10. T. Yanagitani, H. Yagi, and Y. Hiro, Jpn. Patent No. 10-101411 (1998).

11. J. Lu, J. Lu, T. Murai, *et al.*, Jpn. J. Appl. Phys. **40** (12), L1277 (2001).

12. J. Lu, K. Takaichi, T. Uematsu, *et al.*, Jpn. J. Appl. Phys. **41** (12), L1373 (2002).

13. Y. Nigara, Jpn. J. Appl. Phys. **7** (4), 404 (1968).

14. D. F. Bezuidenhout and R. Pretorius, Thin Solid Films **139**, 121 (1986).

15. N. M. Melankholin, *Methods for Studying Optical Properties of Crystals* (Nauka, Moscow, 1970).

16. A. A. Kaminskiĭ, K. Ueda, A. F. Konstantinova, *et al.*, Kristallografiya **48** (5), 729 (2003) [Crystallogr. Rep. **48**, 868 (2003)].

17. M. Born and E. Wolf, *Principles of Optics: Electromagnetic Theory of Propagation, Interference, and Diffraction of Light*, 2nd ed. (Pergamon Press, Oxford, 1964; Nauka, Moscow, 1970).

Translated by A. Zolot'ko

CRYSTAL
GROWTH

Growth and Structure of Barium Sodium Orthoborate NaBaBO$_3$ Crystals

N. G. Kononova*, A. E. Kokh*, T. B. Bekker*, N. G. Furmanova**, B. A. Maksimov**,
V. N. Molchanov**, and P. P. Fedorov**

* Institute of Mineralogy and Petrography, Siberian Division, Russian Academy of Sciences,
Universitetskiĭ pr. 3, Novosibirsk, 630090 Russia
** Shubnikov Institute of Crystallography, Russian Academy of Sciences, Leninskiĭ pr. 59, Moscow, 119333 Russia
e-mail: ppf@newmail.ru
Received February 6, 2003

Abstract—Crystals of NaBaBO$_3$ were grown by spontaneous crystallization on a platinum loop from the BaO–B$_2$O$_3$–Na$_2$O system using the flux technique. The crystals have a highly disordered block structure. X-ray diffraction study (λMoK$_\alpha$, 518 independent reflections, $R = 0.0272$) demonstrated that the structure of these crystals is identical with that established previously by other researchers for a sample prepared by cooling a stoichiometric melt. © 2003 MAIK "Nauka/Interperiodica".

INTRODUCTION

Crystals of a low-temperature modification of barium metaborate β-BaB$_2$O$_4$ (BBO) are of paramount importance in nonlinear optics and are used for converting the laser frequency in the UV–Vis spectral region. BBO single crystals are most often grown from a flux in the BaO–B$_2$O$_3$–Na$_2$O system [1]. When studying phase equilibria in this system [2], we isolated and characterized the NaBaBO$_3$ compound with a melting point of 1271°C. The formation of this compound at the crystallization front stops the crystal growth of BBO. The crystal structure of this compound was established previously [3]. However, the method for the synthesis of single crystals by cooling a stoichiometric melt from 1053 to 803 K, which was described in [3], disagrees with the data on the thermal stability of NaBaBO$_3$ [2]. Since the difference in the melting points is typical of different polymorphs, it could not be excluded that different modifications of NaBaBO$_3$ were studied in [2, 3], despite the fact that the specimens studied had similar X-ray-diffraction characteristics. Hence, the aim of the present study was to grow single crystals of NaBaBO$_3$ and establish their structure.

SYNTHESIS OF NaBaBO$_3$

The reagents BaCO$_3$, Na$_2$CO$_3$, and H$_3$BO$_3$ of high-purity grade were used as starting compounds. A powder-like sample of NaBaBO$_3$ was prepared by two-step solid-phase synthesis from a mixture of starting reagents in a platinum crucible 40 mm in diameter. The ratio between the components and their amounts were calculated to prepare 5 g of the final product. In the first stage of the synthesis performed at 180°C for 16–20 h, the initial blend was dehydrated. In the second stage performed at 700°C for five days, sodium and barium carbonates completely decomposed to release CO$_2$. In the first stage, the time of exposure was monitored gravimetrically by observing the weight loss of H$_2$O corresponding to the calculated value. The second stage of the process was carried out until phase equilibrium was reached, which was determined by powder X-ray diffraction analysis. The X-ray diffraction data were measured on a DRON-3 diffractometer using CuK$_\alpha$ radiation. Generally, X-ray diffraction patterns of nonequilibrium samples have reflections not only from the main phase but also from BaCO$_3$ impurity as the initial component of the blend. To achieve the equilibrium, the

Table 1. Compositions of the fluxes of the BaO–B$_2$O$_3$–Na$_2$O system (mole fractions), from which spontaneous single crystals were grown, and the temperatures t (°C) at which spontaneous crystallization started

Run no.	BaO	B$_2$O$_3$	Na$_2$O	t
1	0.485	0.34	0.175	970
2	0.475	0.35	0.175	930
3	0.45	0.36	0.19	940
4	0.38	0.38	0.25	880

synthesis must be accompanied by repeated grinding of intermediate products. The absence of even very weak reflections corresponding to $BaCO_3$ in X-ray patterns serves as a criterion for the completeness of the solid-phase reaction. It should be noted that, at $t > 700°C$, the components began to have a corrosive effect on the platinum crucible.

The samples synthesized rapidly degrade in air, and they must be stored in a dessicator. The X-ray diffraction patterns of $NaBaBO_3$ powders measured after their prolonged storage in air had reflections corresponding to impurity $Ba(OH)_2 \cdot H_2O$.

SINGLE-CRYSTAL GROWTH

Crystals of $NaBaBO_3$ were grown by spontaneous crystallization from the $BaO–B_2O_3–Na_2O$ system using the flux technique. The compositions listed in Table 1 correspond to the region of primary crystallization of $NaBaBO_3$, which we found previously [2]. The table also lists the temperatures at which spontaneous crystallization started.

Single crystals were grown in a platinum crucible after performing the two-step solid-phase synthesis described above. The synthesis product (40 g) was heated to 950–1000°C and kept for 16 h to achieve homogenization. Since the chemical reactions, which were completed in the solid phase, did not occur in the melt, the melting process was not accompanied by melt foaming. After homogenization, a platinum rod with a loop was placed in the central region of the melt surface, and the temperature was lowered at a rate of 10 K/h. Once the onset of crystallization was visually observed, the melt was cooled at a rate of 1–2 K/day for 15–20 days. After completion of the process, the outgrowth on the platinum loop was withdrawn from the melt and cooled. Then, a high-quality material without inclusions was selected. This procedure made it possible to prepare single-crystal samples as rounded lenses with a weight of 1.5–2 g, up to 18 mm in diameter, and up to 1.5 mm thick. In runs 1–3, intergrowths of well-faceted isometric crystals ~1 mm in size (Fig. 1) appeared on the surface of crystal boules. In run 4, the lens formed showed no pronounced faceting. Note that spontaneous crystals become coated with a white layer in air; hence, they must be stored in a dessicator.
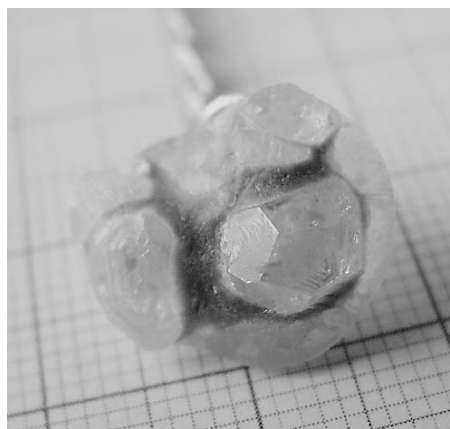

Fig. 1. Photograph of the grown single crystal of $NaBaBO_3$.

Chemical analysis of the crystals was carried out by flame atomic absorption spectroscopy and atomic emission spectroscopy. The results of analysis were as follows (wt %): Na_2O, 14.3; BaO, 71.0. The standard deviation $S_T = 0.02–0.03$. For $NaBaBO_3$, the calculated data are as follows (wt %): Na_2O, 14.3; BaO, 70.0.

X-RAY DIFFRACTION STUDY

Several crystalline samples were chosen for X-ray diffraction study (a CAD-4 Enraf-Nonius diffractometer, λMoK_α). However, it appeared that all these crystals had a block structure. The X-ray data were collected from an irregularly shaped sample of ~0.40 × 0.30 × 0.22 mm^3 in size. This sample contained at least three pronounced blocks. For these blocks, the intensity ratio of diffraction reflections with the same indices was ~10 : 1 : 1. The experimental data ($\theta/2\theta$ scanning technique in the scan-angle range $\theta \le 30°$, 518 independent reflections with $I > 2\sigma(I)$) were collected from the block that gave maximum intensities of diffraction reflections.

The unit-cell parameters were determined and refined using 16 reflections: $a = 9.562(2)$ Å, $b = 5.561(1)$ Å, $c = 6.173(1)$ Å, and $\beta = 98.95(2)°$. The sp. gr. $C2/m$ was established in the course of structure solution: $d_{calcd} = 4.487$ g/cm^3, $\mu = 125.22$ cm^{-1}, $Z = 4$.

Table 2. Atomic coordinates and equivalent isotropic thermal parameters

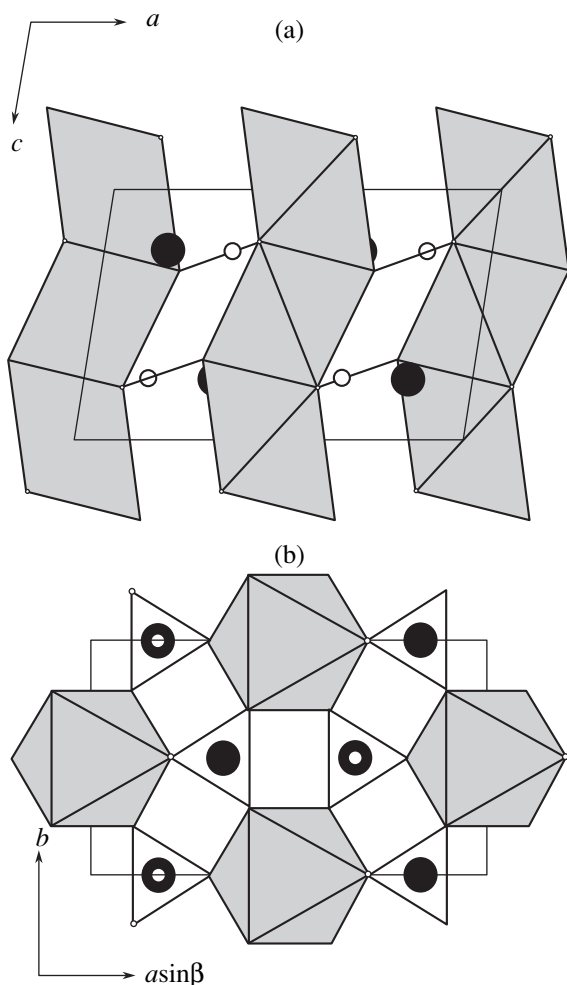| Atom	Position	x	y	z	U_{eq}, Å^2
Ba	4i	0.16655(4)	0	0.24335(7)	0.0129(1)
Na(1)	2b	0	0.5	0	0.020(1)
Na(2)	2d	0	0.5	0.5	0.019(1)
B	4i	0.8321(9)	0	0.2426(12)	0.014(2)
O(1)	4i	0.7022(6)	0	0.3205(10)	0.017(1)
O(2)	8j	0.8978(4)	0.7876(8)	0.2096(7)	0.019(1)

Fig. 2. Structure of NaBaBO$_3$ projected along the (a) [010] and (b) [001] directions. Large filled and small empty circles represent Ba and B atoms, respectively.

The structure was solved by the heavy-atom method and refined anisotropically by the least-squares method to $R1 = 0.0272$ and $wR2 = 0.0708$, 36 parameters to be refined, and $S = 1.163$. All calculations were carried out using the AREN [4] and SHELXL93 [5] software packages. The absorption correction was applied using the DIFABS program [6]. The atomic coordinates and equivalent isotropic thermal parameters are listed in Table 2.

The crystal structure established in the present study appeared to be identical to that described in [3]. The main characteristic feature of this crystal structure is the presence of columns linked by shared faces of the NaO$_6$ octahedra. The octahedra are linked through the planar BO$_3$ triangles to form a framework, whose cavities are occupied by large Ba^{2+} cations (Fig. 2). The powder X-ray diffraction pattern calculated from the structural data is in agreement with the experimental pattern and the data reported previously [2]. Therefore, the same modification of NaBaBO$_3$ was examined in this study and in [2, 3]. However, the thermal stability of the compound under consideration is much higher than that reported in [3]. Judging from the unit-cell parameters, this compound is, apparently, isostructural with monoclinic potassium–sodium carbonate KNaCO$_3$ [7]. The presence of isolated planar BO$_3$ groups in the NaBaBO$_3$ structure is consistent with the Raman scattering data [2].

The results of this study and of [3] cast doubt upon the existence of the Na$_2$BaB$_2$O$_5$ compound, which was first mentioned in [8] and then in [9]. In the latter study, this compound was prepared by the solid-phase synthesis; the parameters of the monoclinic unit cell calculated on the basis of the powder X-ray diffraction data coincide with the parameters determined by us for the NaBaBO$_3$ compound accurate to 0.2%.

REFERENCES

1. P. P. Fedorov, G. A. Kokh, and N. G. Kononova, Usp. Khim. **71** (8), 741 (2002).
2. P. P. Fedorov, N. G. Kononova, G. A. Kokh, *et al.*, Zh. Neorg. Khim. **47** (7), 1150 (2002).
3. J.-M. Tu and A. Keszler, Acta Crystallogr., Sect. C: Cryst. Struct. Commun. **51**, 1962 (1995).
4. V. I. Andrianov, Kristallografiya **32** (1), 228 (1987) [Sov. Phys. Crystallogr. **32**, 130 (1987)].
5. G. M. Sheldrick, *SHELXL-93. Program for the Refinement of Crystal Structures* (Univ. of Göttingen, Germany, 1993).
6. N. Walker and D. Stuart, Acta Crystallogr., Sect. A: Found. Crystallogr. **39**, 158 (1983).
7. M. Chistmann and G. Papni, Rev. Chim. Miner. **16**, 485 (1979).
8. Q.-Z. Huang and J. K. Liang, Acta Phys. Sin. **30**, 559 (1981).
9. J. Bedson, R. W. Lawrence, and P. J. Picone, J. Mater. Chem. **4**, 571 (1994).

Translated by T. Safonova

CRYSTAL GROWTH

Hydrothermal Crystallization in the KF–ZrO₂–SiO₂–H₂O System at 400°C: Phase Equilibria and Modeling of ZrSiO₄, K₂ZrSi₆O₁₅, K₂ZrSi₃O₉, K₃ZrF₇, and ZrO₂ Crystal Structures

G. D. Ilyushin

Shubnikov Institute of Crystallography, Russian Academy of Sciences, Leninskiĭ pr. 59, Moscow, 119333 Russia
e-mail: ilyushin@ns.crys.ras.ru
Received October 30, 2002

Abstract—The phase equilibria in the KF–ZrO₂ (nanocrystals)–SiO₂–H₂O system are studied for the ZrO₂ : SiO₂ molar ratio ranging from 2 : 1 to 1 : 6 and the KF concentration C_{KF} ranging from 3 to 36 wt % under 0.1 GPa at 400°C. We established crystallization of three silicates—ZrSiO₄ (zircon), K₂ZrSi₆O₁₅ (deleite), K₂ZrSi₃O₉ (wadeite)—and K₃ZrF₇ fluoride and ZrO₂ and SiO₂ oxides. The structures of K- and Zr-based silicates obtained can be represented as an open framework formed by M octahedra (ZrO₆) that share vertices with T tetrahedra (SiO₄). With the increase of KF concentration, silicates "substitute" each other in the following sequence: ZrSiO₄ ⟹ K₂ZrSi₆O₁₅ ⟹ K₂ZrSi₃O₉. Depending on the ZrO₂ : SiO₂ ratio and C_{KF} concentration, K₃ZrF₇ fluoride is formed simultaneously with K₂ZrSi₃O₉ and K₂ZrSi₃O₉ + K₂ZrSi₆O₁₅. The characteristic features of formation of Zr-containing phases are discussed in the framework of the model of the matrix assembly of crystal structures from subpolyhedral structural units—clusters of cyclic type. The features of the phase formation in the system are compared with the characteristics determined earlier for the KOH–ZrO₂ (nanocrystals)–SiO₂–H₂O system at 400°C. © 2003 MAIK "Nauka/Interperiodica".

INTRODUCTION

Earlier, the correlation between the chemical composition, structure, and the number of formed compounds was established for KOH–ZrO₂ (nanocrystals)–SiO₂–H₂O, KOH–ZrO₂ (crystals)–SiO₂–H₂O and KOH–ZrSiO₄ (zircon)–H₂O systems at 400°C [1].

It was shown [2] that the hydrothermal treatment of ZrO₂ + 3SiO₂ under 0.07 GPa at 600°C leads to crystallization of K₂ZrSi₃O₉ in the solutions containing the KOH, K₂CO₃, or KMnO₄ components. The use of other components (KCl, K₂Cr₂O₇, KAl(SO₄)₂ · 12H₂O, and KAlSi₃O₈) resulted in formation of only zircon ZrSiO₄.

In the KOH–ZrO₂–SiO₂–H₂O system, five K,Zr-based silicates are formed [3, 4]—three anhydrous phases, K₂ZrSi₆O₁₅ (deleite, sp. gr. $P\bar{1}$ [5], *DEL*-type framework [4]), K₂ZrSi₃O₉ (wadeite, sp. gr. $P6_3/m$ [6], *BAD*-type framework [4]), K₂ZrSi₂O₇ (khibinskite, sp. gr. $P2_1/b$ [7], *KHI*-type framework [4]), and two hydrates with the same chemical composition, K₂ZrSi₃O₉ · H₂O (umbite, sp. gr. $P2_12_12_1$ [8], *UMB*-type framework [4]) and K₄Zr₂Si₆O₁₈ · 2H₂O (kostylevite, sp. gr. $P2_1/b$ [9], *KOS*-type framework [4]). All these silicates have *MT* frameworks of different topol-

ogy formed by M octahedra (ZrO₆) and T tetrahedra (SiO₄) sharing their vertices.

The structures of anhydrous K,Zr-based silicates (*DEL*, *BAD*, and *KHI*) containing invariant subpolyhedral structural units (SSU precursors) were revealed. These units are membered six-polyhedron cyclic M_2T_4 clusters. Hydrated K,Zr-based silicates (*UMB* and *KOS*), crystallizing only at low temperatures, are built by four-polyhedron chains of M_2T_2 clusters [3].

The synthesis and the study of zirconosilicates and germanates [10–13] with open frameworks [10–13] is of great interest because of their possible application as solid electrolytes, selective adsorbents, and molecular sieves.

The present paper was aimed at studying the effect of KF solvent on the phase composition of the products of the hydrothermal reactions and comparing the phase formation with the corresponding characteristics in the KOH–ZrO₂ (nanocrystals)–SiO₂–H₂O system studied earlier at 400°C [1].

This work is a continuation of studies [1, 3, 4, 10, 14–16] and analysis of the geometry and topology characterizing the structure of crystalline phases and the simulation of self-organization processes in the *AOH*–

MeO_2–TO_2–H_2O systems, where A = Li, Na, and K; Me = Zr, Ti, Hf, Si[6], Ge[6], and Sn; T = Si[4] and Ge[4].

EXPERIMENTAL

The phase equilibria in the KF–ZrO_2 (nanocrystals)–SiO_2–H_2O system were studied under conditions of direct temperature gradient under 0.1 GPa at 400°C [1]. The experiment duration was 240 h. The temperature was automatically maintained within an accuracy of ±2 K at the outer wall of the autoclave. The vertical temperature gradient was 1.5 K/cm. The experiments were performed in 15-cm^3 copper ampules mounted inside 130-cm^3 lined steel autoclaves.

The initial charge consisted of SiO_2 (silica gel) and ZrO_2 (nanocrystals) produced by the technology reported in [17] in the form of nanocrystalline three-dimensional associate formed by 30-Å-particles with the fluorite (CaF_2) structure. The surface area of particles was about 100 m^2/cm^3. The $ZrO_2 : SiO_2$ molar ratio ranged from 2 : 1 to 1 : 6. The concentration of KF solvent varied from 3 to 36 wt %. The solid insoluble products of the reaction were rinsed with hot water and dried at room temperature.

The structural identification of the phases was performed by the X-ray phase analysis (DRON-2 and Rigaku D-Max 1500 diffractometers, CuK_α radiation) using the ICDD (International Center for Diffraction Data) [18] and ICSD (Inorganic Crystal Structure Database) databases [19].

RESULTS

Depending on the synthesis conditions, the products of crystallization in the KF–ZrO_2 (nanocrystals)–SiO_2–H_2O system were either single crystals (0.1–1 mm in size) or fine-grained crystalline powders. X-ray phase analysis (see table) showed that, according to crystal chemistry, the compounds crystallizing in this system can be divided into five groups. These groups are distinguished by the types of the simplest structural units:

—SiO_2 dioxide (quartz-type structure, structural units are SiO_4 tetrahedra);

—ZrO_2 dioxide (fluorite-type structure, structural units are ZrO_8 cubes [14, 20]);

—K,Zr-based fluoride K_3ZrF_7 (randomly disordered structure described in [21]);

—Zr-based silicate $ZrSiO_4$ (zircon, structural units are ZrO_8 dodecahedra and SiO_4 tetrahedra);

—K,Zr-based silicates $K_2ZrSi_6O_{15}$ (*DEL*) $K_2ZrSi_3O_9$ (*BAD*) (structural units are ZrO_6 octahedra and SiO_4 tetrahedra).

The $ZrSiO_4$ silicate (zircon) belongs to orthotetrahedral structures. The K,Zr-based silicates have the following *T*-condensed structures: $K_2ZrSi_6O_{15}$ contains infinite [Si_6O_{15}] ribbons and $K_2ZrSi_3O_9$ has three-membered [Si_3O_9] rings. The K_3ZrF_7 fluoride has statistically disordered Zr, K, and F sublattices ([21], the data obtained in 1938). The structural model of the analogous Hf-based compound K_3HfF_7 ([22], the data obtained in 1988) is statistically disordered only in the F sublattice.

It was found that, at a $ZrO_2 : SiO_2$ ratio of 2 : 1 (experiments 1–5 in table), the main phase in the whole range of KF concentrations studied is $ZrSiO_4$ silicate. With an increase the solvent concentration, along with $ZrSiO_4$, the following phases are formed:

$$K_2ZrSi_6O_{15} \Rightarrow K_2ZrSi_3O_9 + K_3ZrF_7.$$
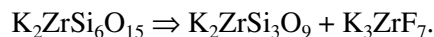
At C_{KF} = 3%, along with zircon $ZrSiO_4$, ZrO_2 was also crystallized. The broadening of the X-ray reflection profiles indicated the existence of 120-Å-large crystallites (the calculation technique was discussed in [17]).

It is seen from the table that a decrease in ZrO_2 content in the mixture ($ZrO_2 : SiO_2$ = 1 : 1–1:6) results in the formation of the following crystallization fields:

—$ZrSiO_4$ + $K_2ZrSi_6O_{15}$ (in the form of isometric single crystals of the spherical shape) + $K_2ZrSi_3O_9$ in 15% solutions of KF at $ZrO_2 : SiO_2$ = 1 : 1 and 1 : 2;

—$ZrSiO_4$ + ZrO_2 + SiO_2 (quartz in the form of needlelike single crystals) in 3–7% solutions of KF, at $ZrO_2 : SiO_2$ = 1 : 2;

—SiO_2 + $ZrSiO_4$ + $K_2ZrSi_6O_{15}$ in 3–10% solutions of KF at $ZrO_2 : SiO_2$ = 1 : 3;

—K_3ZrF_7 + $K_2ZrSi_6O_{15}$ + $K_2ZrSi_3O_9$ in 15–36% solutions of KF at $ZrO_2 : SiO_2$ = 1 : 3.

Thus, in the KF system, the formation of $ZrSiO_4$, $K_2ZrSi_6O_{15}$, $K_2ZrSi_3O_9$ silicates and K_3ZrF_7 fluoride was established. With an increase of the solvent concentration, the phases are formed according to the following scheme:

$$ZrSiO_4 \Rightarrow K_2ZrSi_6O_{15} \Rightarrow K_2ZrSi_3O_9 + K_3ZrF_7$$

$$\Rightarrow \text{(at } ZrO_2 : SiO_2 = 1 : 1 - 1 : 2\text{)},$$

$$ZrSiO_4 \Rightarrow K_2ZrSi_6O_{15} \Rightarrow K_2ZrSi_6O_{15} + K_2ZrSi_3O_9$$

$$+ K_3ZrF_7 \text{ (at } ZrO_2 : SiO_2 = 1 : 3 - 1 : 6\text{)}.$$
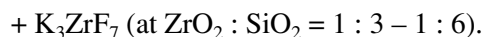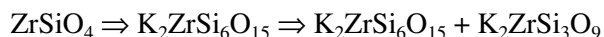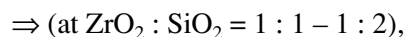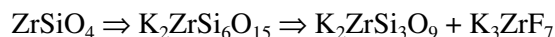
Now, compare the phase compositions of silicates formed in the KF system with the phase compositions of silicates synthesized earlier in the KOH systems with different Zr-containing components—ZrO_2 (nanocrystals) and $ZrSiO_4$ (zircon) [1].

In the KOH–ZrO_2 (nanocrystals)–SiO_2–H_2O system at the given ratio $ZrO_2 : SiO_2$ = 1 : 1, crystallization of $ZrSiO_4$ and of two alkaline K,Zr-based silicates is observed: $K_2ZrSi_3O_9$ and $K_2ZrSi_2O_7$. With an increase

Experimental data on crystallization fields in the $KF–ZrO_2–SiO_2–H_2O$ system at 400°C

Exper-iment	Composition of the initial charge, g		KF, wt %	$ZrO_2 : SiO_2$, (molar ratio)	Phase composition of crystallization products					
	ZrO_2	SiO_2			SiO_2	ZrO_2	$ZrSiO_4$	$K_2ZrSi_6O_{15}$	$K_2ZrSi_3O_9$	K_3ZrF_7
1	2.11	0.51	3	2 : 1	–	+*	+ (max)	–	–	–
2	2.11	0.51	7	2 : 1	–	+*	+ (max)	+	–	–
3	2.11	0.51	10	2 : 1	–	–	+	+	–	–
4	2.11	0.51	15	2 : 1	–	–	+	+	–	–
5	2.11	0.51	36	2 : 1	–	–	+	+	+	+
6	1.61	0.80	3	1 : 1	–	+*	+ (max)	–	–	–
7	1.61	0.80	7	1 : 1	–	+*	+	–	–	–
8	1.61	0.80	10	1 : 1	–	–	+	+	–	–
9	1.61	0.80	15	1 : 1	–	–	+	+	+	–
10	1.61	0.80	36	1 : 1	–	–	–	–	+	+
11	1.11	1.09	3	1 : 2	+	+*	+	–	–	–
12	1.11	1.09	7	1 : 2	+	+*	+	+	–	–
13	1.11	1.09	10	1 : 2	–	–	+	+	–	–
14	1.11	1.09	15	1 : 2	–	–	+	+	+	–
15	1.11	1.09	36	1 : 2	–	–	–	–	+	+
16	0.84	1.23	3	1 : 3	+	–	+	+	–	–
17	0.84	1.23	7	1 : 3	+	–	+	+	–	–
18	0.84	1.23	10	1 : 3	+	–	+	+	–	–
19	0.84	1.23	15	1 : 3	–	–	–	+	+	+
20	0.84	1.23	36	1 : 3	–	–	–	+	+	+
21	0.50	1.44	3	1 : 6	+	–	+	–	–	–
22	0.50	1.44	7	1 : 6	+	–	+	+	–	–
23	0.50	1.44	10	1 : 6	+	–	+	+	–	–
24	0.50	1.44	15	1 : 6	–	–	–	+	+	+
25	0.50	1.44	36	1 : 6	–	–	–	+	+	+

* Microcrystalline powder with 120-Å-large crystallites.

in the KOH concentration, the following changes of the phase composition are observed:

$$ZrSiO_4 + ZrO_2 \Rightarrow ZrSiO_4 + K_2ZrSi_3O_9 + ZrO_2$$

$$\Rightarrow K_2ZrSi_3O_9 + ZrO_2 \Rightarrow K_2ZrSi_2O_7 + ZrO_2.$$

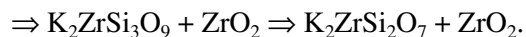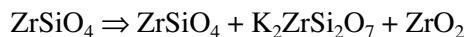In the $KOH–ZrSiO_4$ (zircon)$–H_2O$ system, crystallization of both $ZrSiO_4$ and $K_2ZrSi_2O_7$ was observed. The following crystallization fields are formed with an increase in the KOH concentration:

$$ZrSiO_4 \Rightarrow ZrSiO_4 + K_2ZrSi_2O_7 + ZrO_2$$

$$\Rightarrow K_2ZrSi_2O_7 + ZrO_2.$$

Therefore, in the KF system studied, we did not observe $K_2ZrSi_2O_7$ crystallization characteristic of the most concentrated KOH solutions. In fluoride solutions, instead of the expected crystallization field

$K_2ZrSi_2O_7 + ZrO_2$ (typical of KOH systems), we observed the formation of a new phase, K_3ZrF_7 fluoride, never formed in KOH solutions.

The results obtained indicate that the phase composition in the systems under discussion is determined by the $ZrO_2 : SiO_2$ molar ratio and chemical nature of either the KOH or KF solvent. Fluorine atoms together with K and Zr atoms form a new type of SSU precursor, whose evolution results in the formation of the K,Zr-based fluoride. This is accompanied by the suppression of the channel of evolution of the $K_2ZrSi_2O_7$ phase in the KF system.

The crystallochemical interpretation of the results obtained based on the simulation of crystallization processes occurring according to the mechanism of the matrix (complementary) assembly is given below.

THEORETICAL ANALYSIS

The KF system studied can be regarded as a system of very high rank of chemical complexity, $R_{chem} = 6$, which is determined by the number of chemically different components in the system [4], namely, K, Zr, Si, O, F, and H.

In this system, K,Zr-based silicates with a very complex topology of bonds between M and T polyhedra in the three-dimensional MT frameworks are formed. However, among numerous representatives of the family of K,Zr-based fluorides and oxyfluorides [18, 19], we observed only the formation of a phase with the structure of cubic K_3ZrF_7.

Nucleation and growth of crystals in any system with such a level of chemical complexity occurs at the suprapolyhedral level. In multicomponent systems, the processes of spontaneous self-organization of chemically different polyhedral structural units (suprapolyhedral clusters) take place. The structures are assembled from these ready structural fragments—SSU precursors [10, 14–17].

Based on the developed methods of crystallochemical analysis [10, 14–16] such as the method of local crystallostructural intersection of symmetry groups, two-color decomposition of structural graphs into primary and secondary contours, and the method of determining equivalent coordination sequences, we can identify the type of geometric and topologic characteristic of the SSU–precursors.

The algorithm of self-assembly of a three-dimensional structure from SSU–precursors according to the principle of their maximum boundedness at the transition to a higher level of structural self-organization was discussed in [10, 14–17].

Now compare the programs of structure assembly of K_3ZrF_7, ZrO_2, and $K_2ZrSi_2O_7$ in order to understand what characteristic features of the structure of the SSU–precursor of K_3ZrF_7 fluoride are the most probable cause of the suppression of the channel of evolution of the $K_2ZrSi_2O_7$ silicate. It should be noted that, among all K,Zr-based silicates, the $K_2ZrSi_2O_7$ phase is characterized by the highest formation rate and the simplest program of the matrix assembly [14–16]. The $K_2ZrSi_2O_7$ structure (with Si/Zr = 2) is represented in [16] as a packing of the SSU–precursors whose chemical composition $K_2M_2T_4$ (with Si/Zr = 2) determines the lower limit of silicon content in the three-dimensional framework structures of the K,Zr-based silicates.

The crystal structures of the K_3ZrF_7 and ZrO_2 phases discussed below are characterized by the cubic symmetry and the same space group. First, we consider the model of assembly of the ZrO_2 phase (fluorite CaF_2 type), then the model of K_3ZrF_7 fluoride, and, finally, compare all the types of the SSU–precursors for the K–Zr–Si–O–F–H system.

ASSEMBLY OF THE ZrO_2 STRUCTURE

General features of the structure. The structure of ZrO_2 dioxide is characterized by the cubic sp. gr. $Fm\bar{3}m$ (no. 225). The lattice constant $a = 5.129$ Å [20], $Z = 4$; Zr atoms occupy the $4a$ position (Wyckoff notation) with the local symmetry $m\bar{3}m$; O atoms occupy the $8c$ position with the local symmetry $\bar{4}3m$.

We describe the structure of ZrO_2 dioxide (Fig. 1a) as a set of two-dimensional layers which form topologically equivalent layers–networks of type 4^4 both for Zr and O atoms

$$
\begin{array}{ccccccccc}
/ \text{Zr} & - & \text{O} & - & \text{Zr} & - & \text{O} & // & \text{Zr} & - & \text{O} & - & \text{Zr} & - & \text{O} & /\ldots \\
00 & & 0.25 & & 0.50 & & 0.75 & & 1.00 & & 1.25 & & 1.50 & & 1.75 \\
S_1 & & S_2 & & S_3 & & S_4 & & S_5 & & S_6 & & S_7 & & S_8
\end{array}
\tag{1}
$$

The Schloefly symbol 4^4 indicates the existence of four squares forming each node of the network.

The first S_1 and the fifth S_5 layers in the structure are related by a translation vector (Fig. 1a). The layers from S_1 to S_4 and from S_5 to S_8 in Eq. (1) are combined into repeating blocks; the layers S_1, S_4, S_5, and S_8 are the block boundaries. The density of nodes of the O network (with O–O distances equal to 2.565 Å) is twice as high as the density of nodes in the Zr network (with Zr–Zr distances equal to 3.627 Å). The sides of the squares forming different networks are rotated with respect to each other by an angle of 45°.

The "shear packing" of Zr networks determines the type of cubic Bravais F lattice and the magnitudes of the translation vectors $a = 5.129$ Å [20]. The networks of O atoms form a primitive cubic lattice with the lattice constant $a' = a/2 = 2.565$ Å.

In ZrO_2, the polyhedral structural unit is a ZrO_8 cube.

Cluster substructure (SSU Identification). For the planar networks, the existence of a cluster substructure can be revealed by the two-color decomposition into elementary cycles [14]. Within the framework of this method, planar networks consisting of SU nodes are considered as *packings* of equivalent N-link cyclic SSU clusters (N is the number of structural units). The struc-
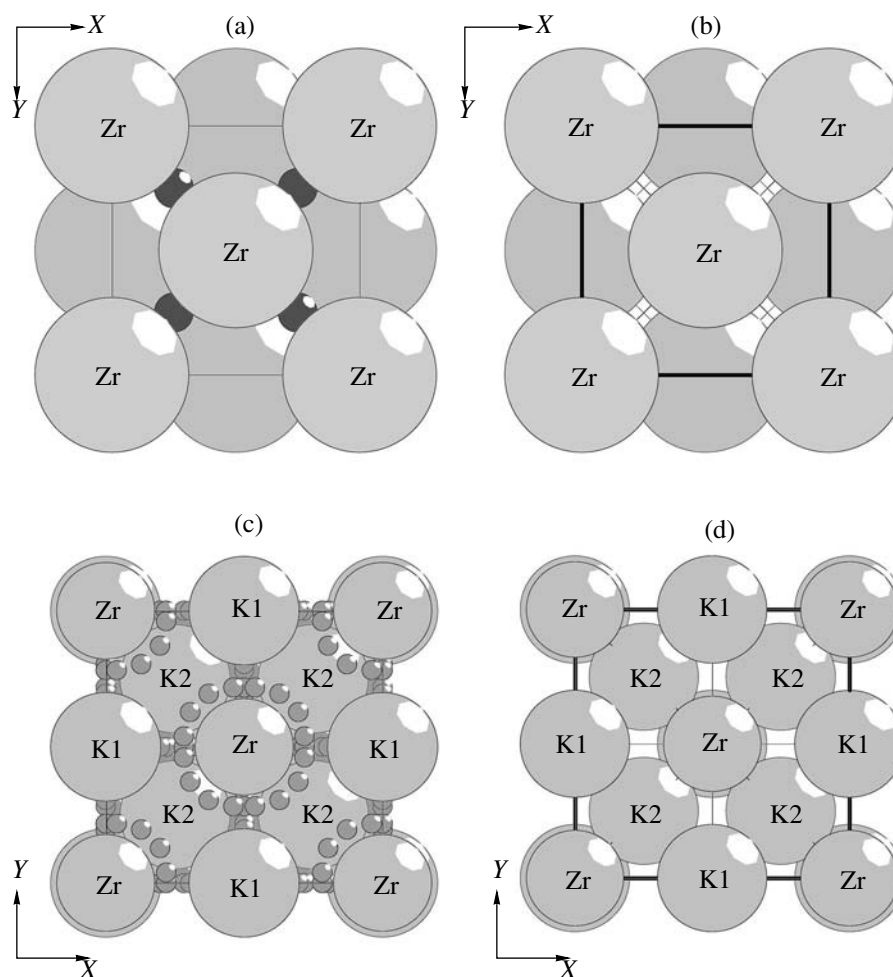
Fig. 1. Structural fragments of Zr-based phases: (a) ZrO_2, (b) Zr sublattice in ZrO_2, (c) K_3ZrF_7, (d) K,Zr sublattice in K_3ZrF_7.

ture of a planar network can be represented as a packing of cyclic clusters if any node of the network can belong to one and only one SSU.

If a network (chemical graph) can be completely decomposed into equivalent elementary cycles (*main contours* of the network), these cycles marked by different colors can be regarded as isolated islands.

The use of the two-color decomposition technique of planar Zr networks singled out in the ZrO_2 structure (Fig. 1b) allowed us to establish the following features of their geometry (Fig. 2a):

—Network 4^4, which is one of the three regular Shubnikov networks, is obtained as a result of condensation of four atomic cyclic square clusters, with each of them being a *primary contour* of the network [14]. In Fig. 2a, these clusters (in the form of islands) are shown by gray color.

—The topology of bonds in the *secondary contour* of the network, which reflects the specific features of the condensation mechanism of primary contours, is also a square. Such a type of secondary contour formed

during condensation of the square four-atom cyclic clusters is not the only possible one. Other types of the secondary contours in two-dimensional half-regular Shubnikov networks built by square clusters are discussed in [14].

—The distances between the centers of primary square contours correspond to the face diagonal of the unit cell (Fig. 2a).

Thus, we singled out the cluster substructure in the Zr network—a ring of four Zr atoms—and determined the mechanism of their binding by a translation along the face diagonal of the cubic unit cell.

Polyhedral structure of SSU. The allowance for O atoms transforms a four-atom square cluster into a polyhedral one consisting of four ZrO_8 cubes. The neighboring cubes in the cluster share edges (Fig. 3a). The cluster center (black sphere in Fig. 3a) is located at the vacant $4b$ position having, similar to the $4a$ position, the local symmetry $m\overline{3}m$. The cluster centers are the centers of the Delaunay domains of the 4^4 Zr network.

Fig. 2. Substructure of clusters (differently shaded) in the 4^4 layers: (a) four-atom clusters in square lattices formed by Zr atoms in ZrO_2, (b) four-atom clusters in square lattices formed by K1 and Zr atoms in K_3ZrF_7.

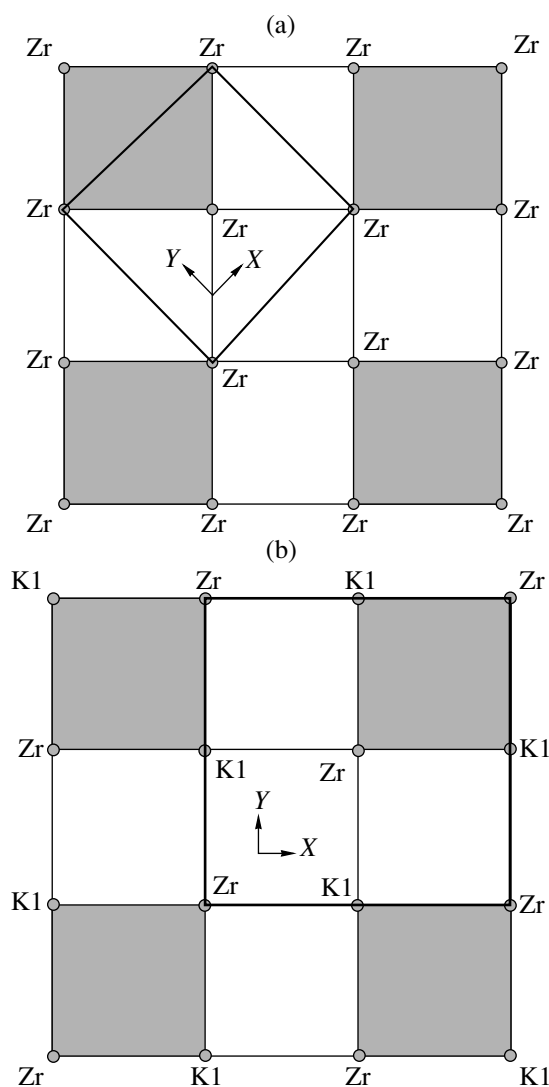*Structural mechanism of assembly.* The mechanism of reconstruction of the three-dimensional topology of bonds from the local structural fragment in accordance with the principle of the maximum boundedness of SSU–precursors is characterized by the following.

—Formation of one-dimensional periodic structures (*primary chains*) occurs via bonding of SSUs along the face diagonal in the cubic cell (in the *XY* plane in Fig. 4a). Any two neighboring SSU–precursors share two edges.

—The condensation of parallel chains into the plane results in the formation of a layer shown in Fig. 5a. The chains share the maximum possible number of edges.

—Bonding of layers is accompanied by their displacement by a half of the body diagonal of the cubic

unit cell. The local coordination number of each ZrO_8 polyhedron in the multilayer block with respect to similar structural units is equal to 12. One such polyhedron is shown by gray color in Fig. 6a. Four polyhedral units are the neighboring ZrO_8 polyhedra of a two-dimensional basal layer (Fig. 5a). Four other polyhedra are located in the upper and lower adjacent layers. The first and third Zr layers (Fig. 6a) are translationally equivalent, see scheme (1).

ASSEMBLY OF K_3ZrF_7 STRUCTURE

General features of the structure. Similar to ZrO_2, K_3ZrF_7 fluoride is crystallized in sp. gr. $Fm\bar{3}m$. In a more complex chemical compound K,Zr-based K_3ZrF_7 fluoride, the lattice constant *a* of the cubic unit cell is equal to 8.951 Å [21]. It exceeds the lattice constant of ZrO_2 (5.129 Å) by a factor of 1.74 [20].

The number of crystallographically independent positions in the K_3ZrF_7 structure is six [21] (in contrast to two in ZrO_2). All the atoms (Zr, K1, K2, or F1) occupy the 32*f* positions with the local symmetry 3*m*; the F2 and F3 atoms occupy the general 192*l* crystallographic positions. All the atoms are statistically distributed over their positions with the occupancies 0.25 (K1 atom), 0.125 (Zr, K2, and F1 atoms), and 0.063 (F2 and F3 atoms). The center of each split position (except for that of fluorine atoms) is close to the special position within the unit cell. In the later identification of the isostructural Hf-based phase [22], these particular positions were taken to be the positions of the corresponding unsplit atoms.

In simulating the assembly of the K_3ZrF_7 crystal structure, we used refined data [22]. The number of crystallographically independent atoms is five. All the atoms occupy special positions (Fig 1c). The Zr, K1, and K2 atoms fully occupy the 4*a*, 4*b*, and 8*c* positions with the local symmetry $m\bar{3}m$, $m\bar{3}m$, and $\bar{4}3m$, respectively. Note that, in the cubic ZrO_2 structure discussed above, Zr atoms also occupy the 4*a* position (Fig. 1b).

The F1 and F2 atoms are statistically distributed over the crystallographic 96*j* positions with the local symmetry *m*. The occupancies of these positions are 0.187 (F1 atoms) and 0.104 (F2 atoms).

In the description of K_3ZrF_7 as a set of two-dimensional layers built by framework-forming Zr and K1 (in the 4*a* and 4*b* positions) and K2 (in the 8*c* positions) atoms, the crystal structure can be considered as pack-
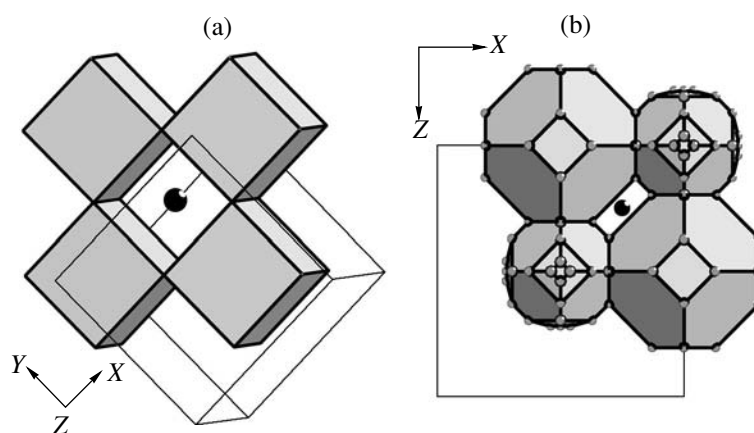
Fig. 3. Polyhedral precursors consisting of (a) four Zr-based polyhedra in ZrO_2 and (b) two Zr-based and two K-based polyhedra in K_3ZrF_7. Hereinafter, small black circles indicate crystallographic centers of clusters.
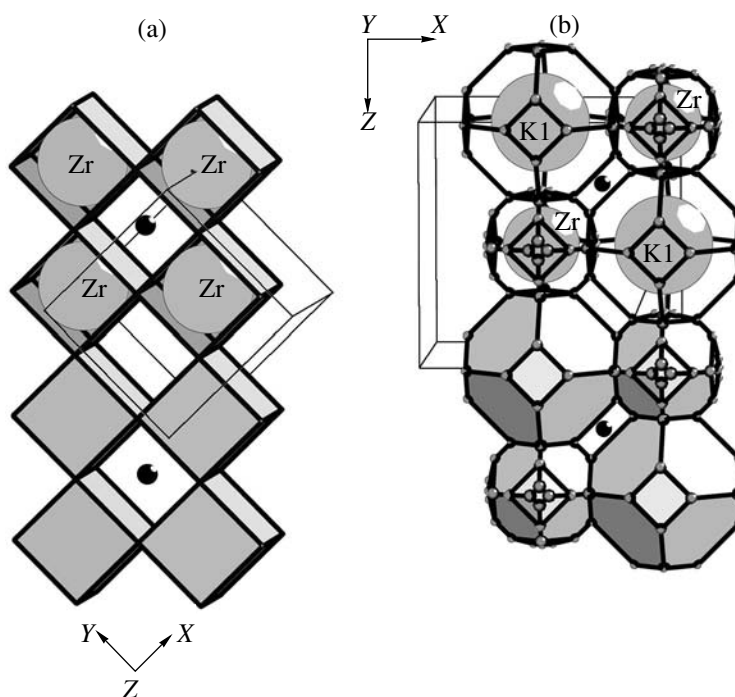
Fig. 4. Assembly of a chain from two SSU–precursors in (a) ZrO_2 and (b) K_3ZrF_7.

ing of layers with the following atomic composition (Fig. 1d):

$$
\begin{array}{cccccccc}
/\ (Zr + K1) - & K2 & - (Zr + K1) - & K2 & //\ (Zr + K1) - & K2 & - (Zr + K1) - & K2\ /... \\
00 & 0.25 & 0.50 & 0.75 & 1.00 & 1.25 & 1.50 & 1.75 \\
S_1 & S_2 & S_3 & S_4 & S_5 & S_6 & S_7 & S_8
\end{array}
\tag{2}
$$

The first S_1 and fifth S_5 layers in the structure are related by the translation vector (Fig. 1d). The layers from S_1 to S_4 and from S_5 to S_8 in Eq. (2) and in Eq. (1) are combined into repeating blocks; the layers S_1, S_4,

S_5, and S_8 are the block boundaries. The density of nodes in the K1 + Zr and K2 networks are the same.

The "shear packing" of K1 + Zr networks determines the type of cubic Bravais lattice and the magni-

(a)

(b)
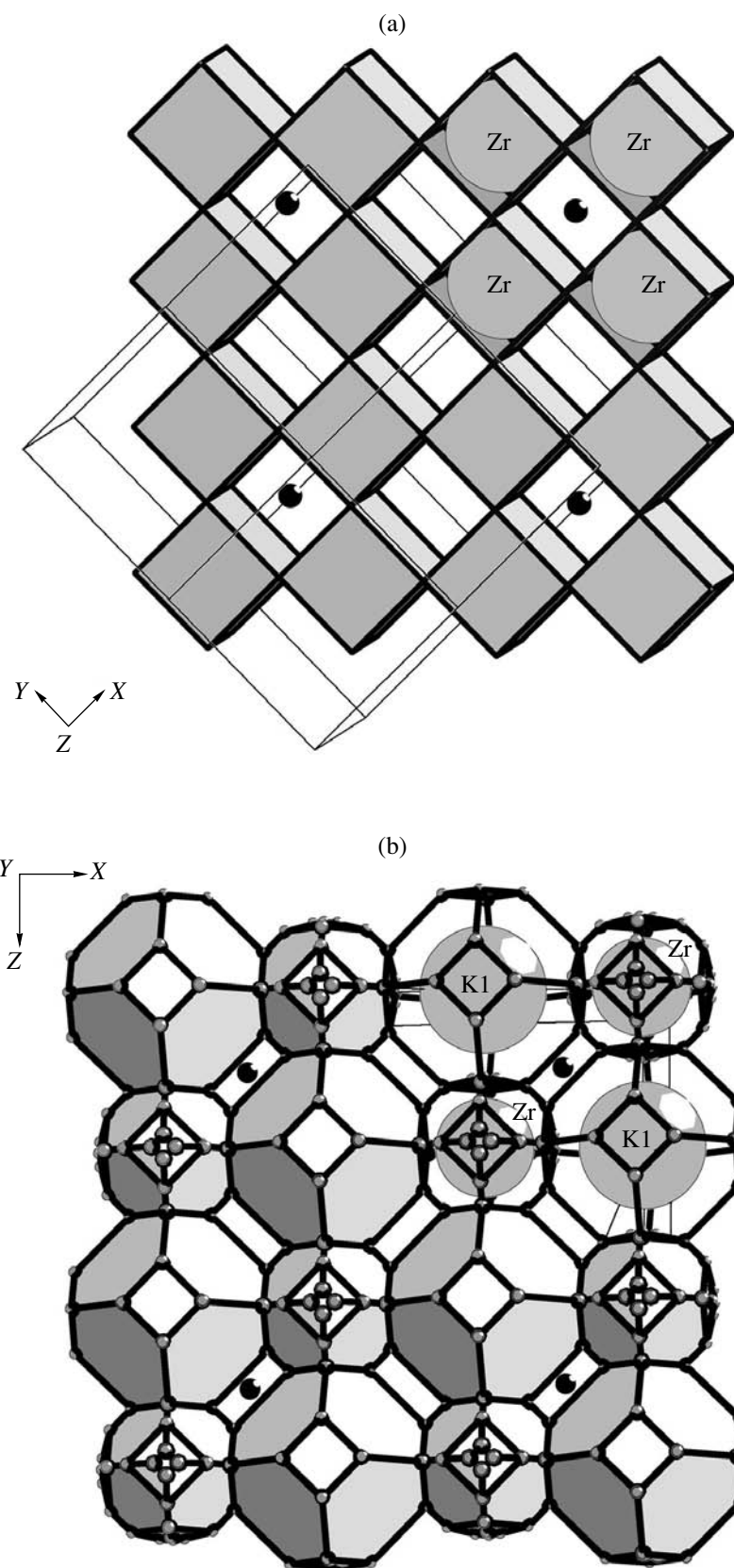
Fig. 5. Assembly of a layer from four SSU–precursors in (a) ZrO_2 and (b) K_3ZrF_7.
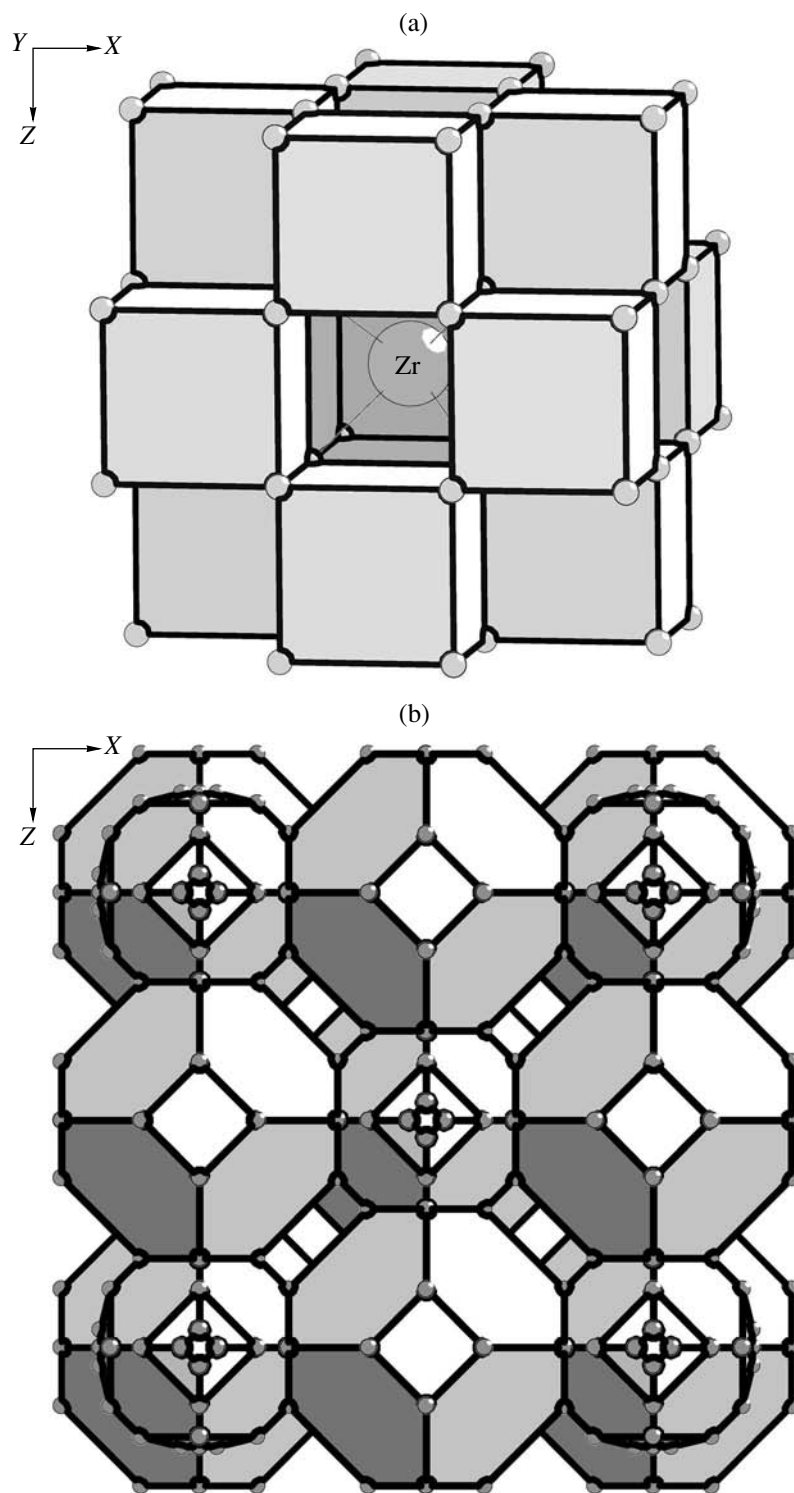
Fig. 6. Three-dimensional structural fragments: (a) three-layer packing of polyhedra in ZrO_2 and (b) two-layer packing of polyhedra in K_3ZrF_7.

tudes of the translation vector a = 8.951 Å [21]. The networks of K2 (Fig. 1d), as well as O networks in ZrO_2 (Fig. 1a) form a primitive cubic lattice with the lattice constant a' = $a/2$ = 4.472 Å.

Cluster substructure (SSU identification). For planar networks formed by K1 + Zr atoms, the existence of the cluster substructure can be revealed by the two-color decomposition into elementary

cycles in a way similar to that used for the ZrO_2 structure.

For the K,Zr networks (Fig. 1b), we established the following.

—After removal of superstructural chemical order of Zr and K atoms over the nodes of the network, this network becomes square one of the 4^4 type in a way similar to the Zr network in the ZrO_2 structure.

—The network 4^4 is formed as a result of condensation of four square atomic cyclic clusters of the composition 2K + 2Zr, which are *primary contours*. In Fig. 2b, these clusters (in the form of islands) are shown by gray color.

—The distances between the centers of primary square contours determine the magnitude of the translation vector (Fig. 2b).

Thus, we singled out the cluster substructure in the K,Zr-based network—a cycle of four alternating Zr and K atoms (Fig. 2b).

Polyhedral structure of SSU. The allowance for statistically disordered F atoms transforms a cyclic four-atom cluster into a four-polyhedron cluster (Fig. 3b). The center of the cluster (black sphere with the coordinates 0, 0.25, 0.25 in Fig. 3b) is located at the vacant 24d position with the local symmetry *mmm*. The cluster centers are the centers of the Delaunay domains in the 4^4 K1 + Zr network.

Extending the local fragment of the unit cell of the K_3ZrF_7 fluoride (with the center of this fragment in the 24d position) containing four-polyhedron SSU–precursors built by Zr- and K1-based polyhedra, we see that the K2 atoms are located above and under the SSU center (Fig. 7b).

Structural mechanism of assembly. The reconstruction mechanism of the three-dimensional topology of bonds from the given local fragment of the structure based on the principle of the maximum boundedness of SSU–precursors in the of K_3ZrF_7 structure is characterized by the following:

—the formation of one-dimensional periodic structures (*primary chains*) via bonding of SSUs along the edge of the cubic unit cell (Fig. 4b);

—the condensation of parallel chains into a plane results in the formation of a layer shown in Fig. 5b; all the polyhedra from different chains participate in the condensation during layer formation;

—bonding of layers is accompanied by the displacement of the layers by a half of the body diagonal of the cubic unit cell. The first and the third K1 + Zr layers are translationally equivalent (see scheme (2)). The voids thus formed in the $KZrF_7$ framework incorporate K2 atoms (Figs. 1c, 1d, and 7b), and the structure as a whole acquires the composition K_3ZrF_7.

THE TYPES OF GEOMETRY AND TOPOLOGY CHARACTERISTIC OF SSU–PRECURSORS IN ZrO_2, K_3ZrF_7, $ZrSiO_4$, AND K,Zr-BASED SILICATES

Structures with R_{chem} = 2 and 3. The models of formation of ZrO_2 and K_3ZrF_7 phases (these phases are formed in the systems with R_{chem} = 2 and 3) discussed above are described by simple assembling algorithms: successive packing of the cyclic-type four-polyhedron SSU into chains, layers, and framework.

Such a type of cyclic SSU–precursor consisting of two Zr-based polyhedra connected by two SiO_4 tetrahedra was determined in the course of simulation of assembly of the $ZrSiO_4$ (zircon) crystal structure (Fig. 7c). For scheelite $ZrGeO_4$, the SSU–precursor is a cluster consisting of two Zr-based polyhedra connected by two Ge-based tetrahedra (Fig. 7d). The difference in their structures reduces to the edge contacts of Zr-based polyhedra with "small" SiO_4 tetrahedra and the absence of such contacts after condensation of Zr-based polyhedra with larger GeO_4 tetrahedra.

In the $ZrSiO_4$ and $ZrGeO_4$ phases discussed above, the formation of SSUs (in contrast to K_3ZrF_7 with two additional atoms lying above and under the plane of a cyclic cluster) proceeds without participation of other atoms (Figs. 7c and 7d). Therefore, in the KF system containing two phases, $ZrSiO_4$ and K_3ZrF_7, with the same chemical complexity R = 3, the simplest (and shortest) program of formation of a crystal structure is characteristic of SSU–precursors of zircon, the main phase in the system at ZrO_2:SiO_2 = 2:1 to 1:2.

Structures with R_{chem} = 4. In contrast to ZrO_2, K_3ZrF_7, $ZrSiO_4$, and $ZrGeO_4$ phases (with R_{chem} = 2 and 3), all anhydrous K,Zr-based silicates (R_{chem} = 4) are formed from six-polyhedron precursors (Fig. 7a). Such invariant SSU–precursors of the K,Zr-based silicates (R_{chem} = 4) contain two K atoms lying above and under the plane of a cyclic cluster (Figs. 7a and 7b), like SSUs in K_3ZrF_7. The difference between the structures of obtained K,Zr-based silicates, $K_2ZrSi_3O_9$ and $K_2ZrSi_6O_{15}$, reduces to different numbers of binding SiO_4 tetrahedra drawn in by the SSU–precursors at higher levels of the self-organization of the system [16].

It is evident that cyclic SSUs with a smaller number of structural units (four in the phases with R_{chem} = 2 and 3) have some advantages—a higher formation rate in comparison with the formation rate of other SSU–precursors, are formed from a larger number of structural units in the same crystal-forming medium, namely, six in the K,Zr-based silicates.

Thus, the structures of the first group (ZrO_2, K_3ZrF_7, $ZrSiO_4$, and $ZrGeO_4$) differ from those of the second group (three K,Zr-based silicates), first and foremost, by the number of polyhedral links in cyclic SSU–precursors, four and six links, respectively. As a consequence, the program of formation of an SSU–precursor in $K_2ZrSi_2O_7$ becomes more complicated in
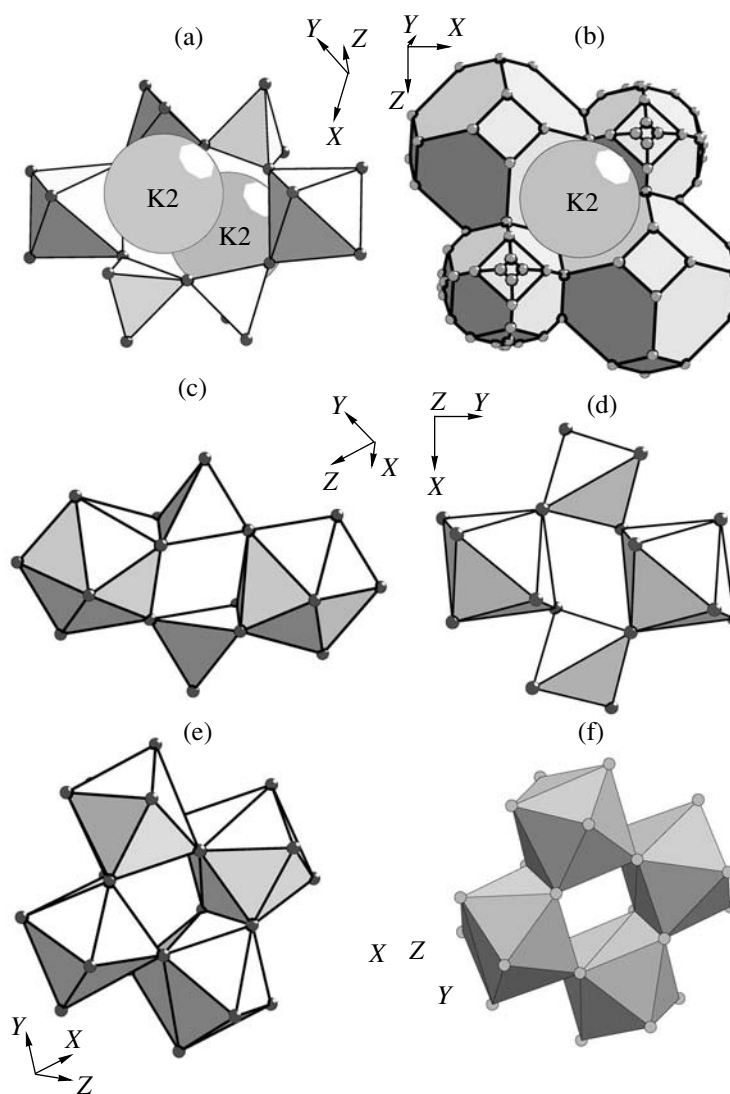
Fig. 7. SSU precursors of crystalline structures: (a) $K_2ZrSi_2O_7$, (b) $K_3HfF_7(K_3ZrF_7)$, (c) $ZrSiO_4$, (d) $ZrGeO_4$, (e) $[Zr_4(OH)_8 \cdot 16H_2O]$ (for $[Zr_4(OH)_8Cl_4 \cdot 16H_2O] \cdot 4Cl \cdot 12H_2O$, (f) $[Zr_4F_8 \cdot 16F]$ (for $(CN_4H_8)ZrF_6 \cdot H_2O$).

comparison with the programs of any phase with $R_{chem} = 2$ and 3. A new phase, K_3ZrF_7 (with $R_{chem} = 3$), formed in the KF system results in suppression of the evolution channel of $K_2ZrSi_2O_7$.

Chemical factor. Note that, with an increase in concentration C_{KF} in the KF solution, the simplest polyhedral structural units in the SSU–precursors are chemically modified; that is, the OH groups in the Zr-based polyhedra are partially substituted by F atoms. This rules out the participation of these SSU–precursors in the structure formation in oxygen-containing silicates.

In the same way, precursors of K,Zr-based fluoride cannot participate in the assembly of the K_3ZrF_7 structure with the modified coordination sphere of Zr-based polyhedra (some F atoms are replaced by oxygen from OH groups).

The K_3ZrF_7 structure can form only in a medium with an elevated concentration of K and F atoms. In this case, the invariant six-polyhedron precursors of K,Zr-based silicates and their structural derivatives in such media cannot complete with a rapidly forming four-polyhedron SSU in K_3ZrF_7. The cocrystallization of K_3ZrF_7 in the crystallization fields of $K_2ZrSi_3O_9$ and $K_2ZrSi_3O_9 + K_2ZrSi_6O_{15}$ (in the solutions with reduced ZrO_2 content in the mixture) is consistent with the concept of behavior of K_3ZrF_7 precursors 7 in the solutions.

Two factors (structural and chemical) discussed above provide the suppression of the evolution channel of SSU–precursors of the $K_2ZrSi_2O_7$ phase occurring with the replacement of the KOH solvent in the system by KF. Note also that, in the sequence of the crystallizing phases $K_2ZrSi_6O_{15} \longrightarrow K_2ZrSi_3O_9 \longrightarrow K_2ZrSi_2O_7$, the crystallization field of $K_2ZrSi_2O_7$ corresponds to the

most concentrated KOH solutions for the Zr-based systems under discussion. Hence, this phase will be the first to be replaced by K_3ZrF_7 in concentrated KF solutions.

In conclusion, we should like to note that the SSU–precursor established for ZrO_2 is an *island-like* four-polyhedron precursor $[Zr_4(OH)_8 \cdot 16H_2O]$ of the salt of aqueous zirconium oxychloride $[Zr_4(OH)_8Cl_4 \cdot 16H_2O] \cdot 4Cl \cdot 12H_2O$ [23] incorporated into the three-dimensional structure of the dioxide (according to the maximum boundedness mechanism) (Fig. 7e). The zirconium salt was crystallized from a solution with the addition of concentrated HCl.

In terms of topology, the structure of the SSU–precursor of aqueous zirconium oxychloride is fully reproduced in the form of island-like four-polyhedron cluster $[Zr_4F_8 \cdot 16F]$ (Fig. 7f) of the $(CN_4H_8)ZrF_6 \cdot H_2O$ crystal structure obtained in fluoride solutions [24]. The study of the $(NH_4)_3Zr_2F_9SO_4 \cdot 2H_2O$ crystal structure and its isostructural K-based analogue $K_3Zr_2F_9SO_4 \cdot 2H_2O$ [25] showed that such Zr–F-based clusters in the bound state form isolated two-dimensional layers.

ACKNOWLEDGMENTS

REFERENCES

1. G. D. Ilyushin and L. N. Dem'yanets, Neorg. Mater. **38** (6), 739 (2002).
2. R. Caruba, A. Baumer, and C. Turco, Chem. Geol. **11** (1), 49 (1973).
3. G. D. Ilyushin and L. N. Dem'yanets, Kristallografiya **42** (6), 1124 (1997) [Crystallogr. Rep. **42**, 1047 (1997)].
4. G. D. Ilyushin and B. A. Blatov, Acta Crystallogr., Sect. B: Struct. Sci. **58** (2), 198 (2002).
5. S. Fleet, Z. Kristallogr. **121** (5–6), 349 (1965).
6. D. Henshaw, Miner. Mag. **30** (2), 585 (1955).
7. A. N. Chernov, B. A. Maksimov, V. V. Ilyukhin, *et al.*, Dokl. Akad. Nauk SSSR **193** (6), 1293 (1970) [Sov. Phys. Dokl. **15**, 711 (1970)].
8. G. D. Ilyushin, Neorg. Mater. **29** (7), 971 (1993).
9. G. D. Ilyushin, Z. V. Pudovkina, A. A. Voronkov, *et al.*, Dokl. Akad. Nauk SSSR **257** (3), 608 (1981) [Sov. Phys. Dokl. **26**, 257 (1981)].
10. G. D. Ilyushin and L. N. Dem'yanets, *Germanates of Tetravalent Metals* (VINITI, Moscow, 1989).
11. S. R. Jale, A. Ojo, and F. R. Fitch, Chem. Commun., No. 5, 411 (1999).
12. D. M. Poojary, A. I. Bortun, L. N. Bortun, and A. Clearfield, Inorg. Chem. **36** (14), 3072 (1997).
13. J. Rocha and M. W. Anderson, Eur. J. Inorg. Chem. **2000** (5), 801 (2000).
14. G. D. Ilyushin and L. N. Dem'yanets, *Structural Studies of Crystals* (Nauka, Moscow, 2002), p. 98.
15. G. D. Ilyushin and L. N. Dem'yanets, Kristallografiya **46** (5), 875 (2001) [Crystallogr. Rep. **46**, 801 (2001)].
16. G. D. Ilyushin and L. N. Dem'yanets, Zh. Neorg. Khim. **47** (8), 1480 (2002).
17. G. D. Ilyushin and L. N. Dem'yanets, *Hydrothermal Synthesis and Growth of Single Crystals* (Nauka, Moscow, 1982), p. 229.
18. *Inorganic Crystal Structure Database (ICSD)* (Gmelin-Inst. fur Anorganische Chemie and FIC, Karlsruhe, 2002).
19. International Center for Diffraction Data (ICDD). 12 Campus Boulevard Newtown Square, PA 19073-3273, USA.
20. U. Martin, H. Boysen, and F. Frey, Am. Crystallogr. Assoc.: Program and Abstracts **49**, 403 (1993).
21. G. C. Hampson and L. Pauling, J. Am. Chem. Soc. **60**, 2702 (1938).
22. J. Granzin and H. Saalfeld, Z. Kristallogr. **183**, 71 (1988).
23. C. W. Mak, Can. J. Chem. **46**, 3491 (1968).
24. A. V. Gerasimenko, B. V. Bukvetskiĭ, R. L. Davidovich, and I. P. Kondratyuk, Koord. Khim. **15** (1), 130 (1989).
25. V. Ya. Kuznetsov, A. I. Gusev, E. B. Chuklanova, *et al.*, Kristallografiya **36** (3), 600 (1991) [Sov. Phys. Crystallogr. **36**, 330 (1991)].

Translated by K. Kugel

====== **CRYSTAL** ======
====== **GROWTH** ======

Dedicated to the 60th Anniversary
of the Shubnikov Institute of Crystallography
of the Russian Academy of Sciences

Optimization of the Local Crystallization Processes of Preparing Chiral Drugs in Periodic Crystallizers

N. K. Tolochko*, I. A. Yadroĭtsev*, A. Z. Myal'dun*, V. A. Kuznetsov**, T. M. Okhrimenko**, and P. York***

* *Institute of Technical Acoustics, Belarussian Academy of Sciences, pr. Lyudnikova 13, Vitebsk, 210717 Belarus*
e-mail: lkm_ita@vitebsk.by
** *Shubnikov Institute of Crystallography, Russian Academy of Sciences, Leninskiĭ pr. 59, Moscow, 119333 Russia*
e-mail: kuznetsov@ns.crys.ras.ru
*** *Bradford University, Bradford BD7 1DP, England*
Received May 16, 2003

Abstract—The regularities of periodic processes of local crystallization of enantiomers and the kinetics of nucleation and growth of crystals are considered. The criteria for optimization of technological processes of preparing chiral drugs with the aim of attaining the maximum yield of final products with a required optical purity are formulated on the basis of experimental data. © *2003 MAIK "Nauka/Interperiodica".*

INTRODUCTION

Almost half the drugs manufactured throughout the world belong to the class of chiral compounds. One of the promising processes of their preparation is the so-called preferential or local crystallization of enantiomers. This process involves local crystallization of individual enantiomers (*L* or *D* forms) on seed crystals in a supersaturated racemic solution, which provides direct separation of racemates into enantiomers [1, 2].[1]

The mechanisms of local crystallization of enantiomers are similar to those of bulk crystallization of solutions with the participation of seed crystals [3]. In both cases, the crystalline product is formed by particles of two types: crystals grown on seeds preliminarily introduced into the solution and crystals grown from nuclei spontaneously formed in the solution. At the same time, there is a significant difference between these processes. The traditional crystallization results in the formation of crystals with identical physicochemical properties, and, hence, their ratio in the final crystalline product does not affect its properties. The properties of the crystals formed upon local crystallization of enantiomers differ radically. Seed crystals and crystals growing on them represent an enantiomer with the best functional characteristics (for example, the highest pharmacological activity in the case of chiral drugs), whereas spontaneously growing crystals of

racemates are side (inactive or harmful) components of the final product. In the case of chiral drugs, these components either have no noticeable medicinal effect or have a damaging effect on one's health [1, 2]. The end aim of local crystallization of enantiomers is to ensure a high yield of the final product with a maximum content of the required enantiomer.

Experience in manufacturing chiral drugs through local crystallization of enantiomers shows that an increase in the yield of the crystalline product is necessarily accompanied by a decline in enantiomeric purity (i.e., by a decrease in the content of the required enantiomer). This can be explained by the fact that the crystallization conditions providing an increase in the content of crystals of the required enantiomer (most frequently, an increase in the supersaturation or the duration of the process) are also favorable for an increase in the amount of racemic crystals contaminating the final product. In this respect, the optimization of local crystallization of enantiomers with the aim of achieving the maximum yield of the product with the observance of medical requirements for enantiomeric purity is a very important problem. However, at present, this problem is far from resolved. This is associated with both technical and fundamental difficulties, because systematic investigations into the processes of synthesizing chiral drugs have been performed only in the last 15–20 years [1].

The local crystallization of enantiomers can proceed in periodic or continuous regimes. The continuous

---

[1] A racemate is the compound formed by enantiomers taken in equal proportions. A racemic solution is a solution of a racemate.

crystallization ensures a higher enantiomeric purity of the product. This process can be conducted, for example, in a crystallizer in the form of an open flow-type system. A racemic solution is fed from below into the crystallizer and passes through a crystallization chamber. Seed crystals of the required enantiomer are introduced into the chamber in which they are in a suspended state in a rising stream of the solution. The growth of crystals is attended by an increase in their weight. As a result, the crystals tend to settle to the bottom of the crystallizer and are then discharged from it. Concurrently, small-sized racemate crystals formed in the solution accumulate at the top of the crystallizer and are removed from it together with the solution. Consequently, crystals of different types are continuously separated in the crystallizer. There exist other variants of continuous crystallization. However, these processes have a serious disadvantage associated with the necessity of strictly controlling the flow rate of the solution. Moreover, the implementation of these variants requires the use of rather complex crystallization equipment.

The periodic crystallization occurs within a limited period of time in a crystallizer being a closed system. Initially, seed crystals of the required enantiomer are introduced in the racemic solution in the crystallizer. Once the crystals have grown to a specified size, they are removed from the crystallizer. However, racemate crystals are also removed from the crystallizer, provided the spontaneous crystallization takes place simultaneously with the crystal growth on seeds. Then, the solution is saturated with the racemate and the crystallization on seed crystals of the opposite enantiomer is performed. These procedures are repeated many times, which makes it possible to prepare the required enantiomer in considerable amounts. A serious disadvantage of the periodic crystallization is the necessity of strictly controlling the supersaturation of the solution in order to minimize or completely suppress spontaneous precipitation of racemic crystals and to ensure the high optical purity of the final product. The sizes of enantiomer crystals grown on seeds can be larger than those of spontaneously formed racemic crystals. In this case, they can be mechanically separated from the final product. However, most frequently, crystals of different types are sufficiently close in size to each other. As a consequence, their separation becomes extremely difficult or even impossible.

The local crystallization of enantiomers is characterized by a complex dependence of the yield and the enantiomeric purity of the final product on the parameters of the process (the induction period of nucleation, the number and sizes of introduced seed crystals, etc.).

In this work, we considered the regularities of periodic local crystallization of enantiomers and possible methods of optimizing this process with the aim of increasing the yield of the crystalline product with a high enantiomeric purity.

ANALYSIS OF LOCAL CRYSTALLIZATION OF ENANTIOMERS

The equation of material balance for periodic local crystallization of enantiomers can be written in the compact form

$$M_S + M_{R_0} = M_{GS} + M_R + M_{GN}. \tag{1}$$

Here, M_S is the initial mass (kg) of seed crystals of the required enantiomer in the solution, M_{R_0} is the initial mass (kg) of the dissolved racemate, M_{GS} is the mass (kg) of the required enantiomer crystals grown on seeds at the instant of time τ, M_R is the mass (kg) of the dissolved racemate at the instant of time τ, M_{GN} is the mass (kg) of the racemate crystals grown on nuclei in the solution at the instant of time τ, and τ is the crystallization time (min).

The enantiomeric (or optical) purity P and the yield Y (kg) of the crystalline product can be determined from the following formulas (under the assumption that the contents of L and D enantiomers in the spontaneously crystallized racemate with mass M_{GN} are equal to each other):

$$P = (M_{GS} - M_{GN})/(M_{GS} + M_{GN}), \quad Y = M_{GS} + M_{GN}. \tag{2}$$

According to relationships (2), the enantiomeric purity P increases with an increase in M_{GS} and a decrease in M_{GN}. In turn, the yield of the crystalline product Y increases with an increase in M_{GS} and M_{GN}. Therefore, in order to obtain the maximum yield Y at a high enantiomeric purity P, it is necessary to determine the optimum ratio between M_{GS} and M_{GN}.

Let us consider a simplified model of the crystallization process. We assume that the solution contains a fixed number n_S of seed crystals with identical initial sizes r_{S_0} (m) and a fixed number n_N of spontaneous nuclei with identical initial sizes r_{N_0} (m). The seed crystals were introduced into the solution at the instant of time $\tau = 0$, and the spontaneous nuclei arose at the instant of time τ_N (min). Here, τ_N is the induction period of nucleation, i.e., the time elapsed from the onset of crystallization to the crystal nucleation. In this case, the process of forming the crystalline product can be treated as consisting of two concurrent processes, namely, the crystal growth on seeds and the crystal growth from nuclei. It is also assumed that crystals of both types do not undergo multiplication and agglomeration in the course of growth; i.e., the numbers of crystals of both types remain unchanged during the growth. Then, the masses M_{GS} and M_{GN} can be approximately determined from the expressions

$$M_{GS} = n_S F \rho_c r_s^3(\tau); \quad M_{GN} = n_N F \rho_c r_N^3(\tau), \tag{3}$$

where F is the form factor; ρ_c is the density (kg/m^3) of the crystalline material; and $r_S(\tau)$ and $r_N(\tau)$ are the cur-

rent sizes (m) of crystals growing on seeds and from nuclei, respectively.

In the framework of the model proposed, the growth rate G_S of crystals on seeds and the growth rate G_N of crystals from nuclei are the most important kinetic parameters of crystallization. As a rule, the sizes of crystals grown on seeds do not exceed tenths of a millimeter [4]. In turn, crystals grown from nuclei have even smaller sizes. For such small crystals, the growth rate depends on the crystal size: the larger the crystal size, the higher the growth rate of crystals [5, 6]. The experimentally determined dependence of the crystal size on the time [6] is plotted in Fig. 1. With due regard for this dependence and by assuming that the supersaturation (directly affecting the crystallization rate) remains constant, the growth of crystals on seeds and from nuclei can be described, to a first approximation, by the equations

$$r_S(\tau) = K(\tau + (r_{S_0}/K)^{1/2})^\alpha, \quad r_N(\tau) = K(\tau - \tau_N)^\alpha, \quad (4)$$

where $K = 2.5 \times 10^{-12}$ m/s^2 and $\alpha = 2$ (the chosen parameters give the best fit to the experimental data on the time dependence of the crystal size [6]).

In the equation for the growth of crystals from nuclei, the initial sizes of nuclei (at τ_{N_0}) can be ignored because of their smallness. With allowance made for Eqs. (4), the values of M_{GS} and M_{GN} can be determined from the relationships

$$M_{GS} = n_S F \rho_c [K(\tau + (r_{S_0}/K)^{1/2})^\alpha]^3,$$
$$M_{GN} = n_N F \rho_c [K(\tau - \tau_N)^\alpha]^3. \quad (5)$$

The dependences $r_S(\tau)$ and $r_N(\tau)$ described by Eqs. (4) and the dependences $M_{GS}(\tau)$ and $M_{GN}(\tau)$ described by relationships (5) are shown in Fig. 2. The variant with the initial size of seed crystals $r_{S_0} = 0.05$ mm, the induction period of nucleation $\tau_N = 30$ min, the number of introduced seeds $n_S = 3 \times 10^4$, and the number of formed nuclei $n_N = 8 \times 10^4$ is used as the starting model. The induction period of nucleation $\tau_N = 30$ min is chosen with due regard for the experimental data on the local crystallization of glutamic acid on seeds of the D enantiomer [7]. In all cases, the crystallization duration is taken to be equal to 180 min, because the rate of growth of crystals from spontaneously formed nuclei depends on the crystal size [6] over this period of time. For simplicity, the numerical values of F and ρ_c are taken to be equal to unity. The nucleation parameters are chosen so that the optical purity P after the completion of the process falls in the range 80–95%.

It can be seen from Fig. 2 that, under the chosen conditions, the size of spontaneously grown crystals toward the end of the process remains approximately three times smaller than the size of crystals grown on seeds and the mass of the former crystals does not
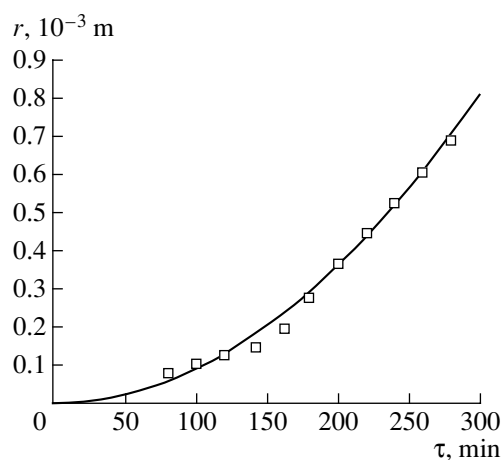
Fig. 1. Experimental dependence of the crystal size on the time [6] (open squares) and its interpolation (solid line).
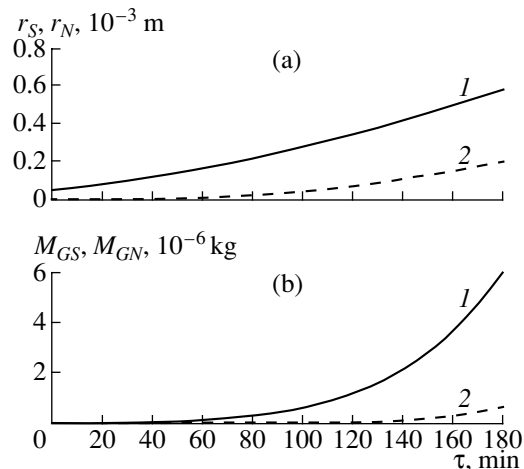
Fig. 2. Time dependences of (a) the size and (b) the mass of (1) seed crystals and (2) nuclei. $r_{S_0} = 0.05$ mm, $\tau_N = 30$ min, $n_S = 3 \times 10^4$, and $n_N = 8 \times 10^4$.

exceed ~5% of the total mass of the crystallized product. For the first 30 min (induction period of nucleation), crystals grow only on introduced seeds of the required enantiomer in the solution, which leads to the formation of the product with an optical purity of 100%. It seems likely that an increase in the induction period of nucleation should make it possible to obtain the pure product for longer time intervals. The influence of the induction period of nucleation on the product yield Y and the enantiomeric purity P of the product is illustrated in Fig. 3. As can be seen from this figure, a twofold increase in the induction period of nucleation τ_N (from 30 to 60 min) leads to an increase in the optical purity P of the crystallized product from 80 to 95%. At the same time, the total yield of the product almost does not depend on the induction period of nucleation τ_N (Fig. 3a). This is explained by the aforementioned

Fig. 3. Time dependences of (a) the yield and (b) the optical purity of the crystalline product at different induction periods of nucleation $\tau_N = $ (*1*) 30, (*2*) 45, and (*3*) 60 min.

small contribution of spontaneously nucleated crystals to the total mass of the crystalline product (Fig. 2).

For the same reason, an increase in the number n_N of spontaneous nuclei (by a factor of four in our calculations) virtually does not affect the total yield of the final product (Fig. 4a). On the other hand, the effect of the number n_N of spontaneous nuclei on the optical purity of the final product is significant and opposite to that of the induction period of nucleation τ_N: an increase in n_N is attended by a drastic decrease in the optical purity (Fig. 4b) (an increase in n_N by 1% results in a decrease in P by ~2%). This effect is associated with the nonlin-

ear dependence of the optical purity P on M_{GN} at constant M_{GS}.

Thus, the analysis of the results obtained demonstrates that an increase in the induction period of nucleation τ_N is an efficient way to increase the yield and the enantiomeric purity of the product. It is well known that the induction period of nucleation τ_N strongly depends on the crystallization temperature and decreases as this temperature increases. For example, according to our data, the induction period of nucleation τ_N increases from 10–15 min to 2–20 h with a decrease in the crystallization temperature from 40–42 to 25–20°C upon crystallization of drugs such as levomycetin, synthomycin, and camphor in water–alcohol solutions. Consequently, a decrease in the temperature of the local crystallization of enantiomers is an efficient way of increasing the enantiomeric impurity of the prepared products.

Another way to increase the optical purity of products is to decrease the supersaturation of solutions, because the induction period of nucleation τ_N is inversely related to the supersaturation. However, this approach necessarily leads to a substantial decrease in the product yield.

The third way to increase the optical purity is to introduce special additives suppressing spontaneous nucleation in solutions. This process can also be accompanied by an appreciable retardation of the growth on seed crystals.

The parameters r_{S_0} and n_S can affect the yield Y and the optical purity P of the final product as follows. An increase in the initial sizes of seed crystals r_{S_0} and their number results in a proportional increase in the yield Y

Fig. 4. Time dependences of (a) the yield and (b) the optical purity of the crystalline product at different numbers of spontaneously formed nuclei $n_N = $ (*1*) 2×10^4, (*2*) 4×10^4, and (*3*) 8×10^4.
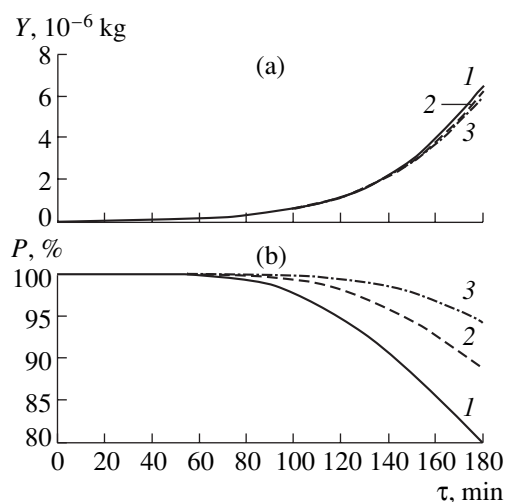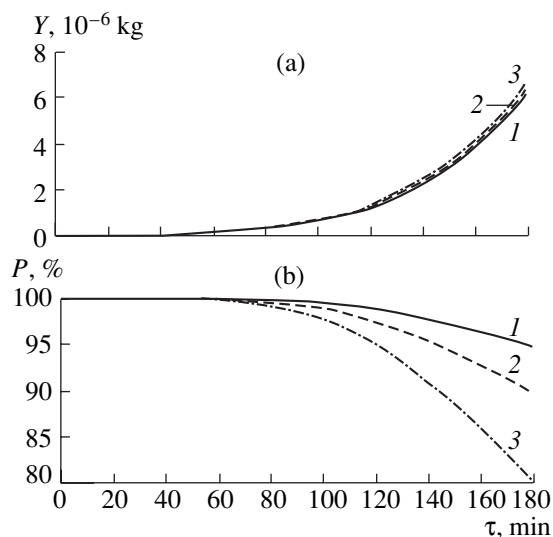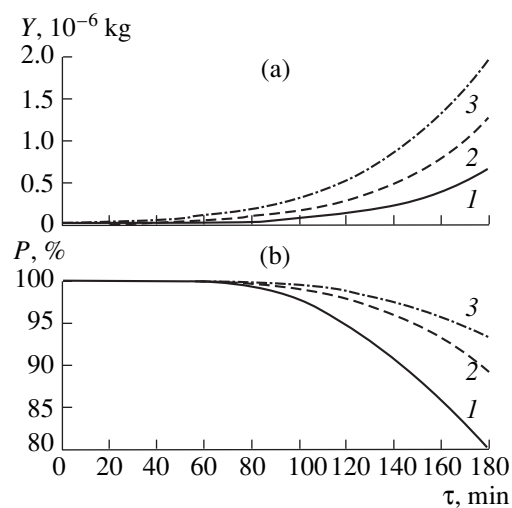

Fig. 5. Time dependences of (a) the yield and (b) the optical purity of the crystalline product at different initial sizes of seed crystals $r_{S_0} = $ (*1*) 0.05, (*2*) 0.10, and (*3*) 0.15 mm.

(Fig. 5). The parameters r_{S_0} and n_S have an almost identical effect. This indicates once again that seed crystals make a decisive contribution to the total mass of the product. On the other hand, the optical purity P increases in a nonlinear manner. Indeed, a twofold increase in the number n_S of seed crystals with respect to the initial value (3×10^4) leads to an increase in the optical purity from 80 to ~90%, and a further twofold increase in n_S to 1.2×10^5 is attended by an increase in P by only 5%. This can be explained by the nonlinear dependence of the optical purity on M_{GS} at constant M_{GN}.

CONCLUSIONS

Thus, in this work, we analyzed the influence of the main variable parameters on the yield and the enantiomeric purity of the products formed upon local crystallization of enantiomers. It was demonstrated that an increase in the induction period of nucleation τ_N is the most efficient way to increase the purity of crystallization products. This can be achieved both by a decrease in the crystallization temperature or supersaturation and by the introduction of special additives (for example, nucleation inhibitors) into solutions. However, this leads to a decrease in the product yield. Among the above approaches, the first approach seems to be more efficient in practical applications, because even a small decrease in the crystallization temperature (within a few degrees) can result in a considerable increase in the induction period of nucleation τ_N with an insignificant decrease in the yield Y. In this case, the decrease in the yield Y can be compensated for by an increase in the crystallization time.

An increase in both the number of seed crystals introduced into solutions and their sizes leads to an increase in the yield of crystallization products and their enantiomeric purity. However, if the induction period of nucleation τ_N remains relatively short, the crystallization time should be reduced as much as possible in order to retain the high purity P (more than ~95%).

By applying the proposed investigation technique and using the results of preliminary experiments, the conditions of conducting the technological process of crystallization in each specific case can be chosen in such a way as to provide the maximum yield of drugs at a specified optical purity satisfying pharmacological requirements.

REFERENCES

1. B. Yu. Shekunov and P. York, J. Cryst. Growth **211**, 122 (2000).
2. Z. J. Li and D. J. W. Grant, J. Pharm. Sci. **86**, 1073 (1997).
3. V. V. Klubovich and N. K. Tolochko, *Methods of Crystal Growth from Solutions* (Nauka i Tekhnika, Minsk, 1991).
4. E. V. Khamskiĭ, *Crystallization in Chemical Industry* (Khimiya, Moscow, 1969).
5. N. K. Tolochko, I. A. Yadroĭtsev, V. A. Yanusov, *et al.*, in *Proceedings of III International Conference on Crystals: Growth, Properties, Real Structure, and Application, Aleksandrov, 1997* (VNIISIMS, 1997), Vol. 1, p. 208.
6. A. S. Tolochko, V. A. Yanusov, A. Z. Myal'dun, and I. A. Yadroĭtsev, Kristallografiya **44** (6), 1132 (1999) [Crystallogr. Rep. **44**, 1061 (1999)].
7. UK Patent No. 829939 (Patent Office, London, 1960).

Translated by O. Borovik-Romanova

=========== **CRYSTAL** ===========
GROWTH

Morphological Effects in Liquid Phase Epitaxy
(the $C_8H_5O_4K$–$C_8H_5O_4Rb$–H_2O System)

A. É. Voloshin*, A. É. Glikin**, S. I. Kovalev*, and E. B. Rudneva*

* Shubnikov Institute of Crystallography, Russian Academy of Sciences, Leninskiĭ pr. 59, Moscow, 119333 Russia
e-mail: voloshin@ns.crys.ras.ru
** St. Petersburg State University, Universitetskaya naberezhnaya, St. Petersburg, 199164 Russia
Received December 27, 2002

Abstract—The results of the complex study of the morphology and defect state of the crystals of the isomorphous potassium acid phthalate–rubidium acid phthalate (KAP–RbAP) series formed in aqueous solutions are presented. The crystals are characterized by heteroepitaxial porous and solid textures formed as a result of the exchange reaction between the crystals and solution. The interaction of the KAP and RbAP crystals with saturated RbAP and KAP aqueous solutions is studied both *in situ* and *in vitro* under optical and atomic force microscopes. The results obtained are used to create a theoretical model of formation of characteristic morphological textures in liquid phase epitaxy, including their formation from the aqueous solutions of the respective salts. © *2003 MAIK "Nauka/Interperiodica".*

INTRODUCTION

The formation of isomorphously mixed crystals in solutions is an individual important problem which is being solved within the framework of the studies of the crystallization processes of complex (multiphase and multicomponent) systems. Its solution is necessary for controlled growth of these crystals and interpretation of the genesis of minerals, most of which are characterized by varying compositions.

For the first time, the unusual phenomena during the isothermal contact of a multicomponent liquid phase with a crystal having the composition nonequilibrium with respect to this phase (substrate dissolution, growth of a new phase with the simultaneous dissolution of the substrate, metastable equilibrium of two phases under certain supercooling) were observed in liquid phase heteroepitaxy of solid solutions of the A_3B_5 compounds. These unusual phenomena were interpreted based on the suggested model of the formation of a stressed diffusion layer (skin layer) on the substrate surface [1–3]. Almost simultaneously with these studies, similar effects have also been observed since 1983 in growth of mixed crystals from aqueous solutions at St. Petersburg University [4–14]. Despite the similarity of the phenomena occurring in solutions and in liquid phase epitaxy in melts, the morphological effects in crystallization from solutions are usually more pronounced than in liquid phase epitaxy (LPE) in melts.

The model of a stressed skin layer describes the experimentally observed metastable equilibrium between the supercooled melt and the substrate rather satisfactorily. Moreover, Bolkhovityanov [1–3] indicated the relation between the lattice parameters of the substrate and the epitaxial layer grown on it and the character of the surface morphology. At the same time, this model fails to reliably explain the formation of morphological textures during interaction of a growing crystal with the liquid phase whose composition is not in equilibrium with respect to the composition of the crystal.

Based on numerous observations of the processes occurring in aqueous solutions, it is shown that there exists a relation between the forming surface morphology and the solubility ratio of the system components. A model of isomorphous replacement based on the physicochemical analysis of the phase interaction was suggested and developed in a number of studies [4–11]. The model allowed one to relate the mechanism and kinetics of the process to the type of a formed morphological structure.

The most important characteristic of this model is the allowance for the changes in the compositions of the solid and liquid phases caused by their exchange interaction during the process (reaction of isomorphous replacement). During the isothermal interaction of a crystal and a saturated solution with the composition nonequilibrium with respect to the composition of the crystal, the whole process reduces to this reaction. Supercooling or overheating of the solution can give

rise to the appearance of a driving force (solution super- or undersaturation) of growth of a new crystalline phase or the dissolution of the initial crystal. At sufficiently high values of supercooling or overheating, either free growth or dissolution is observed, with the exchange reaction being practically fully suppressed. These important characteristics of formation of mixed crystals were established in aqueous systems with the $(Mg,Ni)SO_4 \cdot 7H_2O$, $(Fe,Ni)SO_4 \cdot 7H_2O$, $(Co,Ni)(NH_4)_2(SO_4)_2 \cdot 6H_2O$, $(Cr,Al)K(SO_4)_2 \cdot 12H_2O$, $K_2(SO_4,CrO_4)$, etc., salts.

The concept developed in [4–11] allows one to interpret and predict many characteristic features of the interaction of a crystal and a liquid phase with the composition nonequilibrium with respect to the crystal composition. Nevertheless, to date, there is no detailed model of the mechanism of this process that can describe its main stages and determine its unique relation to the system parameters. Experiments show that the general characteristics of the above effects are the same in different systems, but the process details can be different. Below, we discuss the general characteristics of liquid phase epitaxy of the salts of the potassium acid phthalate–rubidium acid phthalate (PAP–RbAP) series, consider some of their characteristic features, and suggest the general model of formation of an interface between the initial crystal (substrate) and the epitaxial layer.

EXPERIMENTAL

The dynamics of the long-term development of morphological textures was studied on flat samples. The $7 \times 5 \times 0.25$-mm-large (010) cleavage of a plate of a KAP or RbAP crystal was placed between the object carrier and the cover glass glued along their perimeters with a vacuum lubricant (Fig. 1a). The volume of the solution was determined using the sample thickness (0.25–0.30 mm) and the dimensions of the cover glass (15×15 mm). The observations were made under an optical microscope.

The experiments made on a microcrystallization setup (Fig. 1b) under controllable conditions [15] were undertaken to study the dynamics of the initial stages of the interaction between KAP and RbAP crystals and the solutions of a component–partner (another salt of the ternary system). The constancy of the solution composition during the experiment was ensured by the use of a large volume of the solution (50 ml), small dimensions of a seed (not exceeding $2 \times 2 \times 2$ mm), and the absence of spontaneous nucleation in the crystallizer volume. The *in situ* studies of the solution of a set composition in reflected or transmitted light at temperatures in the vicinity of the saturation point showed the signs either of growth or dissolution on the crystal surface (sharp or rounded edges, motion of macrosteps, directions of convective flows, etc.). We also studied different stages of the evolution of a seed surface and determined their duration.

In situ studies on a Nanoscope 3 atomic force microscope (AFM) showed the changes of the surface mor-

phology of RbAP crystals interacting with the KAP solution. A $3 \times 3 \times 2.6$-mm-large RbAP crystal was placed into an AFM cell filled with a KAP solution saturated at a temperature of 28°C. The (010) surface of the crystal was studied. The experiments were performed in the constant-force mode; the visual field had the dimension $L = 10$ μm. Scanning frequency was $H = 10.1725$ Hz at the number of scans per frame $S = 512$.

RESULTS

Exchange of Isomorphous Components between Crystals and Solutions

The observation of the dynamics of the processes of isomorphous replacement occurring between the initial KAP and RbAP crystals and the solution of the component–partner showed that they were similar. Figure 2 shows the photographs of the Y cuts of KAP and RbAP crystals at various moments of their interaction with the RbAP and KAP solutions, respectively. In all the cases, the process begins with crystal dissolution. Five minutes after the beginning of the interaction, the peripheral region of both samples acquired clearly seen defect zones formed due to the processes taking place at the end faces of the crystal. Such a defect zone consists of a network of thin channels penetrating to a considerable depth of the crystal and contains inclusions of the solution. One can also see the formation of islands on the (010) faces of both crystals, although the face of the KAP crystal is covered with the layer almost completely, whereas a considerable part of the surface of the RbAP crystal remains uncovered.

The differences in the processes occurring on the surface of KAP and RbAP crystals gradually disappear. After 1.5 h, the surface of the KAP crystal is completely covered with a inhomogeneous solid layer of a new formation, whereas the surface area of the RbAP crystal covered with the islands of the new phase considerably increases despite the fact that there still exist some small island-free regions of the substrate. At the same time, the formation of a porous structure at the end surfaces of the RbAP crystal continues, whereas the analogous process on the KAP crystal almost ceases. After 170 h, the surfaces of both crystals become practically indistinguishable; all their faces are covered with similar overgrown epitaxial formations, whose shape depends on the type of the sample face.

We would like to draw attention to the fact that, in the $C_8H_5O_4K$–$C_8H_5O_4Rb$–H_2O system considered here, porous and island textures are substantially different from those observed in other systems [4, 5]. In the systems described earlier, porous structures are formed only if the crystal substance has the solubility exceeding the solubility of the dissolved component–partner. In this case, the porous texture rapidly propagates over the whole volume of the crystal (several days or even hours) and uniformly, and this is the final stage of the process. On the contrary, autoepitaxial island textures

(a)

0.5–1.5 cm

1 *2* *3* *4* *5* *6*

3–5 cm

(b)

1 *2* *3*

7
6
5
4
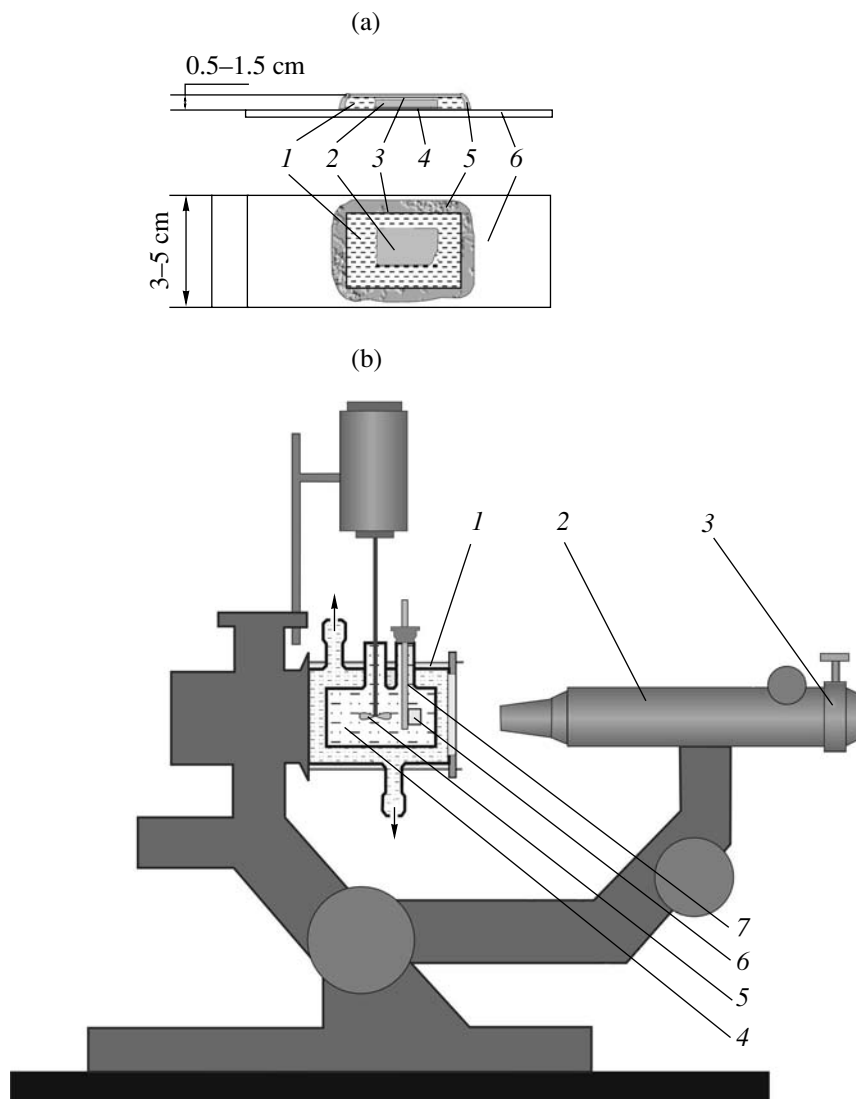
Fig. 1. Schematic illustrating *in situ* observations. (a) Flat samples: *1*, solution, *2*, sample, *3*, cover glass, *4*, varnish layer, *5,* vacuum lubricant, *6,* object carrier; (b) microcrystallization setup: *1,* quartz vessel connected with a thermostat, *2,* optical microscope, *3,* device for mounting a videocamera, *4,* internal volume of the vessel with the solution, *5,* mixer, *6,* seed, and *7,* crystal holder.

are formed only if the substance of the crystal has a lower solubility than the solubility of the dissolved component–partner. In this case, the island texture is limited by a thin subsurface zone of the crystal and the substitution proceeds in the crystal very slowly (about 0.5 mm/month). In our case, despite the fact that the solubility of rubidium acid phthalate exceeds the solubility of potassium acid phthalate, porous textures at the initial stage were formed on both RbAP and KAP substrates. Then, no pore formation was observed, and the main part was played by growth of a crystalline layer.

In situ Atomic Force Microscopy

At the first stage (first three to four minutes), we observed very intense layer-by-layer dissolution of the sample because of fast motion of echelons of macrosteps. Since for the time of the frame development (50 s) the sample thickness decreased by a value exceeding the cantilever path along the surface normal (3 μm), it was impossible to measure the normal dissolution rate. According to our estimates, the rate of the sample dissolution at the initial stage was about 5 μm/min. After the next five minutes, the dissolution rate considerably decreased, which allowed us to determine the velocity of the macrostep motion from a pair of successive frames (Fig. 3) taken along the opposite scanning directions. In this case, the velocity of the step motion is calculated from the change of the tilt angle of the images obtained during upward and downward motion of the cantilever.
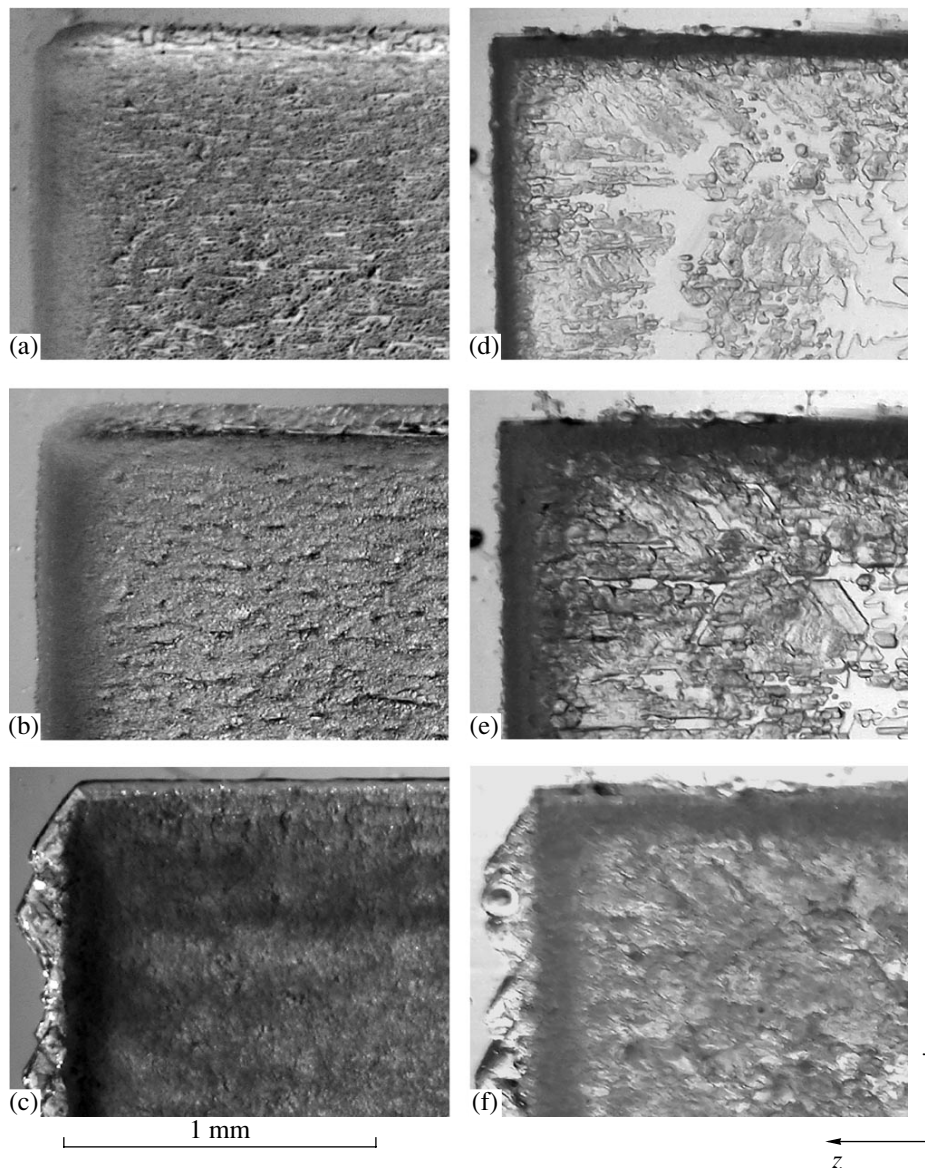
Fig. 2. Illustrating the changes in the surface morphology during interaction of flat samples with the solution of the component–partner: (a–c) *Y* cut of a KAP crystal in the RbAP solution; (d–f) *Y* cut of a RbAP crystal in the KAP solution; (a, d) five minutes, (b, e) 1 h 20 min, and (c, f) 170 h after the introduction of the solution.

Figure 3a shows two types of macrosteps—relatively low macrosteps *1* and high macrosteps *2* and *3* moving in the opposite directions. Their velocities and orientations are indicated in the table.

Knowing the mean tilt of the surface to the singular face, *p*, and the tangential velocity of step motion, *V*, one can calculate the normal dissolution rate as

$$R = pV. \qquad (1)$$

The *p* value measured along the *aa* (Fig. 3a) and *bb* (Fig. 3b) segments on relatively smooth regions of the surface is ~0.7° (Figs. 3c, 3d). Thus, the normal dissolution rate is $R \sim 0.5$ μm/min; i.e., within 10 min, it decreases by an order of magnitude.

Figure 4 shows the initial AFM images obtained in the constant-force mode and the corresponding reconstructed three-dimensional images of the surface inside the channels between the primary islands shown in Fig. 5. It follows from Figs. 4a–4c that, at the first stage, the channels are formed due to fluctuations. As a result, ledge *1* is formed at the left-hand side of the channel, and pit *2*, at its bottom (Fig. 4d). Then, the channel gradually deepens because of the continuing dissolution of the substrate between the islands and simultaneous narrowing of the channels because of island growth (Figs. 4e, 4f). Growth of the layer on the right-hand side of the channel (*3*) slowly proceeds upward along the [010] direction. The left-hand side of the channel remains rather smooth for the whole time of
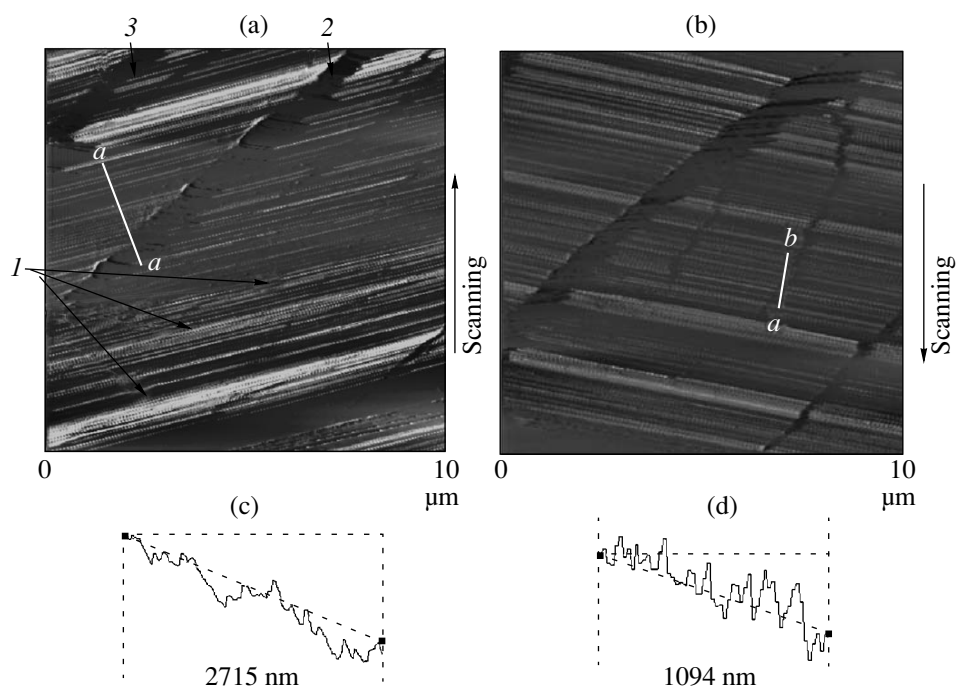
Fig. 3. AFM images of the (010) surface of the RbAP crystal interacting with the KAP solution: (a) 2 min and (b) 2 min 50 s after the introduction of the solution and the surface profiles along the (c) *aa* and (d) *bb* lines; *1–3* are macrosteps of different kinds.

observation, with the thickness of a grown layer on the right-hand side considerably exceeding the layer thickness on the left-hand side. This difference can probably be explained by the specific characteristics of the distribution of convective flows in the channel.

Crystallization under Controllable Conditions

A RbAP seed introduced into the KAP solution starts immediately dissolving, which is seen from rounding-off of the vertices and edges and appearance of etch pits. One to two minutes later, the first signs of growth are observed—the formation of flat regions on the surface, layer polygonization, and appearance of ascending convective flows. This stage is followed by autoepitaxial growth of islands. Some time later, the islands cover almost the whole surface except for channels between the islands preserved intact during the whole experiment (Fig. 5).

Parameters of macrosteps shown in Fig. 3

Macrostep	Velocity, μm/s	Angle formed with the vertical axis measured in the clockwise direction
1	0.790	−29.5°
2	0.008	48.5°
3	0.035	48.5°

DISCUSSION

Reaction of Isomorphous Replacement

All the interpretations of the reaction of isomorphous replacement [1–14] are based on the fact that the contact between the liquid phase and the crystal, whose compositions are not in equilibrium, results in crystal dissolution, solution supersaturation, and crystallization of a new phase. This phenomenon was theoretically interpreted in [2, 3], where growth of epitaxial semiconductor films in the $A^{III}B^{V}$ systems was studied and it was shown that the interaction between the liquid and solid phases with mutually nonequilibrium compositions results in an increase (in comparison with the equilibrium state) of the thermodynamic potential of the system and, as a result, in crystal dissolution. Isomorphous replacement in water–salt systems was studied in [4–14], where the process was interpreted qualitatively as a particular case of the salting-out reaction.

The change of the solution composition because of the substrate dissolution and its supersaturation in a thin diffusion subsurface layer results in crystallization of a new phase—a solid solution of the salt components of the system with a composition different from the composition of the initial crystal. In essence, the reaction of isomorphous replacement reduces to crystal dissolution and crystallization of new layers with the phase compositions being gradually shifted toward the equilibrium. In other words, the reaction proceeds until the compositions of the crystal and solution would attain equilibrium at the given temperature. Further
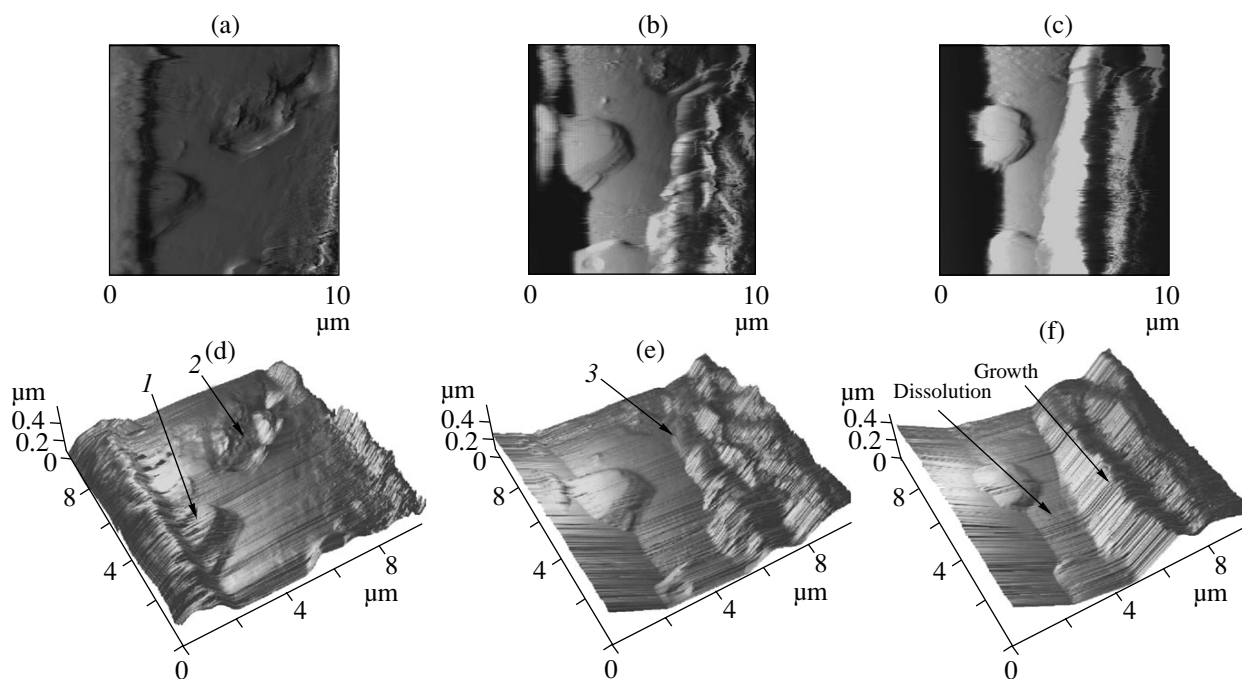
Fig. 4. (a–c) AFM images and (d–f) three-dimensional reconstruction of the (010) surface of an RbAP crystal interacting with the KAP solution: (a, d) 14, (b, e) 24, and (c, f) 28 min after the introduction of the solution.

growth of the crystal is possible only after the attainment of the solution supersaturation because of the lowering of the temperature, evaporation of water, or feeding of the solution.

The initial dissolution of the substrate giving rise to further crystallization of the isomorphous substance on it is the key moment of the whole process, which is confirmed by the AFM data. The intense layer-by-layer dissolution of the substrate at the initial moments of its contact with the solution of the component–partner (from several seconds to several minutes) was observed on both optical and atomic force microscopes. Thus, the results of the present study can be considered as the first direct experimental confirmation of the models of the process suggested in [1–5].

The specific characteristic of the reaction of isomorphous replacement is its occurrence under the action of constant external factors (temperature and pressure). Therefore, the necessary condition for the reaction occurrence is the ability of the system to reach equilibrium because of the changes in the compositions of the contacting phases, i.e., the existence of at least one degree of freedom. In accordance with the Gibbs phase rule, in this case, the two-phase system should consists of at least three components. The simplest example of such systems is solutions. As will be shown later, in this case, it is possible to develop an analytical model of morphological changes and formulate a comparatively simple criterion of the volume effect of the reaction.

Morphological Effect of the Reaction of Isomorphous Replacement

In accordance with the models of substrate transformation during its interaction with the liquid phase with the composition nonequilibrium with respect to the substrate composition discussed in [1–5], the whole process can be divided into three stages (Fig. 6). These are the primary dissolution of the substrate and forma-
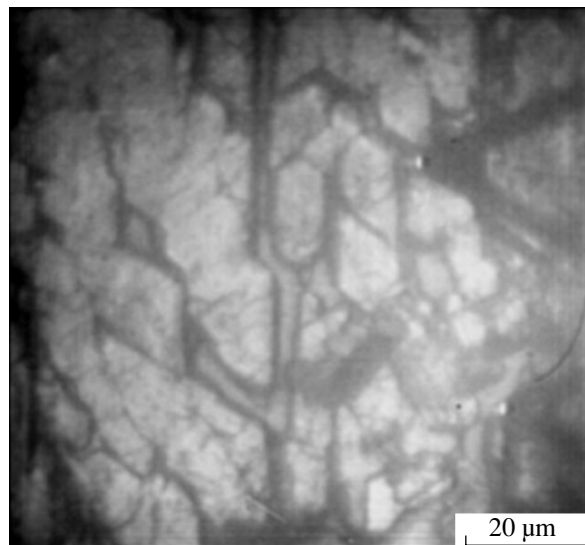
Fig. 5. A part of the (010) surface of an RbAP crystal 12 min after its interaction with the RbAP solution (optical microscope).
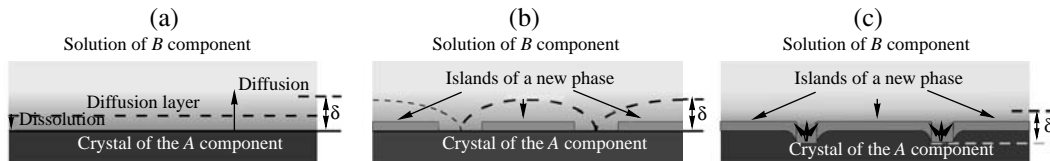
Fig. 6. Stages of formation of epitaxial structures: (a) initial dissolution of the substrate, (b) deposition of islands, (c) further growth of islands due to substrate dissolution.
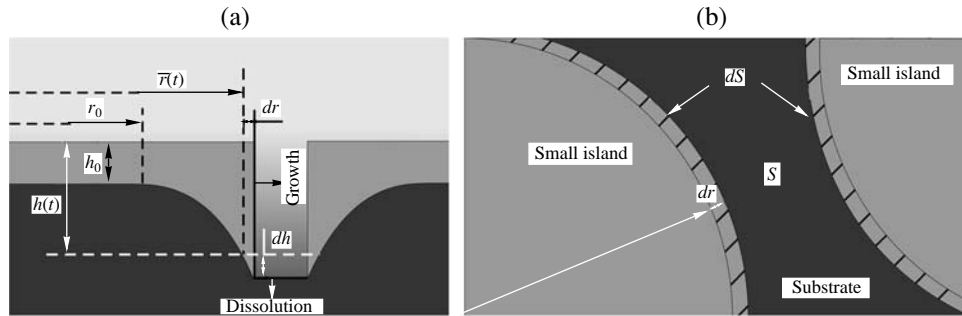
Fig. 7. Schematic illustrating tangential growth of islands during dissolution of the substrate between these islands: (a) section, (b) view from above.

tion of the layer of the supersaturated solution at the interface; deposition and fast growth of islands; and further slow growth of the islands already formed due to dissolution of the substrate between these islands. The first two stages are common for all the types of the contact between the crystal and the liquids with non-equilibrium compositions with respect to the composition of the crystal. The third stage is the most important one for the formation of a characteristic morphological texture, because it is at this stage that the channels (pores) are formed in the substrate or islands coalesce into a solid epitaxial layer.

Island deposition begins after the attainment of the supersaturation in the subsurface layer of the substrate because of the primary dissolution of the substrate. This supersaturation should be sufficient for heterogeneous nucleation of a new phase on the substrate surface. At this stage, the process is associated with fluctuations because of the great importance of the local variations in the supersaturation caused by concentration convection and of the defects present on the crystal surface and facilitating nucleation.

Supersaturation in the vicinity of the nucleated islands decreases, and growth of islands proceeds by the spiral mechanism. New islands are formed up to the moment when the diffusion fields of neighboring islands start overlapping, because then the supersaturation at all the points above the surface becomes insufficient for heterogeneous nucleation. At the same time, the substrate dissolution between the islands continues (this is confirmed by the AFM data). However, now the process proceeds in the steady-state mode and can be characterized by a certain space–time dependence

relating the processes of substrate dissolution, crystallization of a new phase, and diffusion of the dissolved substance in the solution.

Consider the model of this process in more detail. The main assumption consists in the following. Upon cessation of the deposition of new islands, growth of the already existing islands proceeds solely because of the dissolution of the substrate between these islands, and all the excessive substance is deposited on the end surfaces of the islands. In other words, the transport of the substance outside the channels between the islands and growth of islands along the surface normal of the substrate are ignored. We also assume that the process occurs at the constant temperature and that the crystalline components of the system form a continuous series of solid solutions.

Let the specific area of the surface free of islands (per unit area of the interface) at a certain moment of time be S and the mean depth of channels formed by this moment be h (Fig. 7). Consider the material balance in the process (the further analysis is also performed per unit area of the interface). Let a layer of thickness dh be dissolved in the channels between islands within a certain time interval. Then, the volume of the crystalline phase equal to Sdh goes to the solution, thus giving rise to an additional supersaturation of the solution and crystallization of a layer with the thickness dr at the channel walls (end surface of the islands) (Fig. 7b). Then, the area of the free surface of the substrate changes by $-dS$ and the volume of the layer crystallized because of the dissolution of the volume Sdh of the substrate becomes equal to hdS. However, the compositions of the substrate and the crystallized layer

would be different because of the mutual nonequilibrium of the compositions of the initial crystal and the solution. This requires the introduction into the material balance equation of a certain coefficient ω taking into account the change in the volume and solubility of the crystalline phase with the change of its composition. Finally, the material equation balance takes the form

$$\omega S dh = -h dS,$$
$$S = S_0|_{h = h_0}, \quad (2)$$

where S_0 is the area of the free surface and h_0 is the mean height of islands at the initial moment. Solving problem (2), we obtain

$$S = S_0\left(\frac{h_0}{h}\right)^{\omega}. \quad (3)$$

In this case, $S \longrightarrow 0$ at $h \longrightarrow \infty$, because $0 < \omega < \infty$. This signifies that, according to this strongly idealized model, the process would continue infinitely, because the formation of a solid layer ($S = 0$) requires the formation of infinitely deep channels. Then, the channel width would tend to zero, which is physically impossible.

Nevertheless, one can evaluate the substrate volume, V, which should be dissolved to provide island coalescence and formation of a solid epitaxial layer. Within the duration of the process (the time necessary for the development of channels, i.e., an increase of h_0 to ∞), this volume is

$$V = \int_{h_0}^{\infty} S dh = S_0 h_0^{\omega}\int_{h_0}^{\infty}\frac{dh}{h^{\omega}} = \begin{cases} \dfrac{h_0 S_0}{\omega - 1}; & \omega > 1 \\ \infty; & \omega \leq 1. \end{cases} \quad (4)$$

In other words, at $\omega > 1$, growth of an epitaxial layer proceeds faster than the substrate dissolution. In this case, a continuous layer can be formed only if a certain finite volume of the substrate is dissolved. If $\omega \leq 1$, one has to dissolve an infinite volume of the substrate, which may be interpreted as impossibility of the formation of a solid epitaxial layer.

Thus, the above analysis shows that the morphological textures characteristic of the reaction of isomorphous replacement are formed because of multiple nucleation of islands of a new phase and continuous dissolution of the substrate (either growth or dissolution proceeds at a higher rate). Then, the value of the parameter ω can serve as a criterion of impossibility of the formation of a solid epitaxial layer.

Now, estimate the geometry of the layer–substrate interface. We assume that the islands have the cylindrical shape, their mean radius equals r, and the number of islands per unit surface equals ρ. Then, $S = 1 - \rho\pi r^2$, and

Eq. (3) yields

$$h = h_0\left(\frac{1 - \rho\pi r_0^2}{1 - \rho\pi r^2}\right)^{1/\omega}. \quad (5)$$

Figure 8a shows the shape of the channels calculated at $\omega = 1/2$ and 2 (in our calculations, we assumed that $\pi\rho = 10\,000$ mm^{-2}, $h_0 = 3$ μm, and $r_0 = 3$ μm). Using the same parameters and the value $\omega = 4$, we find that the layer–substrate interface has the shape shown in Fig. 8b. For comparison, Fig. 8c shows the photograph of the transverse cut of the epitaxial structure borrowed from [1]. The similarity of the profiles of the layer–substrate interfaces in these figures gives ground to believe that the above mechanism also works in epitaxy from melt.

Volume Effect of Reaction of Isomorphous Replacement

Analyzing the structure of Eq. (1), one can see that, in fact, the parameter ω is the ratio of the volume ΔV_l of the epitaxial layer (grown during the dissolution during the reaction) to the substrate volume ΔV_c, i.e., describes the change in the volume of the crystalline phase during
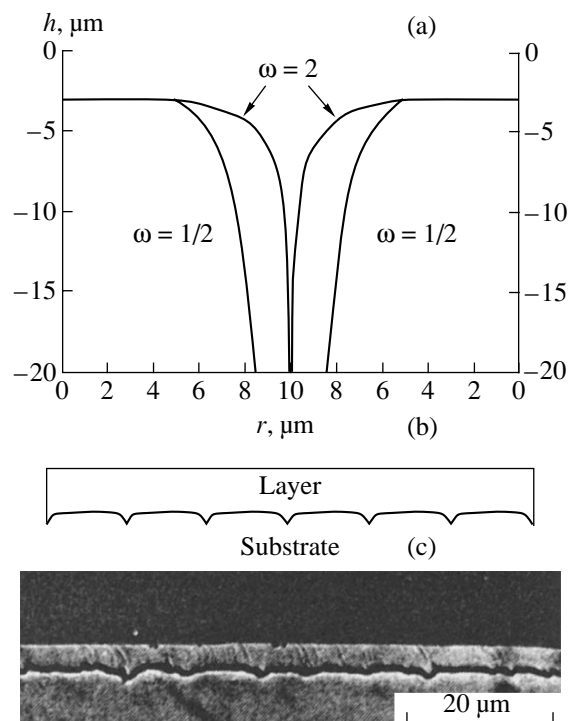

Fig. 8. Layer–substrate interface: (a) shape of channels formed between islands calculated at the volume factors $\omega = 2$ and 1/2; (b) layer–substrate interface calculated at $\omega = 4$; (c) region of the transverse section of the In–As/GaP (111)B structure formed during the contact of the saturated melt with the binary substrate (see [1], Fig. 7).

isomorphous replacement and, thus, characterizes the volume effect of the reaction,

$$\omega = \frac{\Delta V_l}{\Delta V_c}. \tag{6}$$

At $\omega < 1$, the reaction occurs with a decrease in the volume of the crystalline phase (replacement with deficit in volume), and at $\omega > 1$, with an increase in the volume (replacement with excess in volume). Obviously, this parameter depends on the specific features of the phase diagram of the system and also on the ratio of specific (or molar) volumes of the crystalline phases. It was shown [4–8] that such interactions can be conveniently considered in the modified Schreinmakers concentration coordinates, where the ordinate indicates the volume of the crystalline phase dissolved in a fixed amount (e.g., in 100 cm^3) of the solvent.

Prior to further statement of the problem, consider some properties of the Schreinmakers diagrams. Each point corresponding to the solution of a certain composition on this diagram can be considered as a vector of the two-dimensional normalized space R_1^2 with a norm (vector length $\mathbf{a} = (x, y)$) $|\mathbf{a}| = |x| + |y|$ and the metrics (distance between the points (x_1, y_1) and (x_2, y_2)) equal to $\rho = |x_1 - x_2| + |y_1 - y_2|$. Then, the length of the vector outgoing from the coordinate origin on the diagram shows the total volume content of the salts in the solution calculated per 100 cm^3 of the solvent and the distance between any two points shows the total change in the solution composition (also calculated per 100 cm^3 of the solvent) in the transition from one figurative point to another. The compositions of the crystalline phases are depicted by straight lines. The angle of the straight-line inclination to the abscissa for the phase containing x volume fractions of the A component is
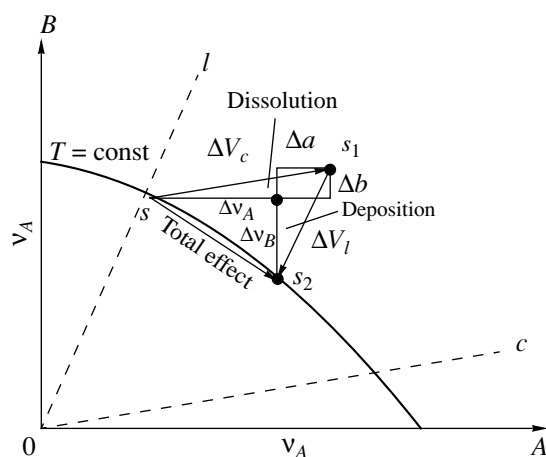
Fig. 9. Solubility isotherm for a hypothetic ternary *A–B–*solvent system: compositions of the *s* initial, s_1 supersaturated, and s_2 final solutions, *c* is the composition of the initial crystal, and *l* is the composition of the crystalline phase in equilibrium with the solution of the composition s_2.

equal to $\arctan((1 - x)/x)$. Such a straight line passing though the figurative point showing the solution composition indicates the composition of the solid phase crystallizing from this solution.

Consider a hypothetical binary system of water-soluble isomorphous compounds *A* and *B*. Figure 9 shows the solubility isotherm of this system at a certain temperature *T* in the modified Schreinmakers coordinates. The straight lines *Oc* and *Ol* correspond to the compositions of the crystalline phases with the volume fractions of the *A* component equal to *c* (initial crystal) and *l* (crystalline phase with the composition in the equilibrium with respect to the composition of a certain composition *s*).

We assume that a crystal of the composition *c* is placed into the solution of the composition *s*. As was shown above, the crystal is dissolved in the solution at a certain rate. We assume that isomorphous replacement is a continuous process, and the character of this process is close to equilibrium. Let a crystal volume ΔV_c be dissolved during an elementary event of the process, so that the solution composition is displaced from the point *s* to the point s_1 in such a way that the segment $[s\,s_1]$ would be parallel to the straight line *Oc* and $|s\,s_1| = \Delta V_c$. In accordance with the phase diagram of solubility, in the supersaturated solution s_1, the volume of the solid phase crystallized is ΔV_l and the composition of this phase is in equilibrium with the composition of the solution s_1. As a result, the solution composition becomes equal to s_2. We assume that the value of ΔV_c is sufficiently small, so that we can assume that the composition of the phase crystallized from the solution of the composition s_1 is constant and only slightly different from *l*. Then, in the vicinity of the point *s*, the composition of the supersaturated solution varies along the segment $[s_1 s_2]$ parallel to the straight line *Ol*.

Thus, as a result of dissolution, the volume of the initial crystal is changed by $-\Delta V_c$, and, as a result of the crystallization of a new layer, by ΔV_l. The vector $\mathbf{ss_2}$ represents the effect resulting from the occurrence of the replacement reaction in the solution, and the vector $\mathbf{s_2s}$ having the opposite direction represents this effect in the crystalline phase, which loses Δv_A cm^3 of the component *A* during crystal dissolution and acquires Δv_B cm^3 of the *B* component during layer crystallization. In this case, Δa cm^3 of the *A* component and Δb cm^3 of the *B* component, first, are transferred to the solution during dissolution and, then, are crystallized into a new layer.

With due regard for the above remarks on the properties of the Schreinmakers diagram, one can write a number of obvious equations that follow from the

scheme shown in Fig. 9:

$$\Delta V_c = \Delta v_A + \Delta a + \Delta b; \quad \Delta V_l = \Delta v_B + \Delta b + \Delta a;$$

$$\Delta a = l\Delta V_l; \quad \Delta b = (1-c)\Delta V_c; \quad (7)$$

$$\Delta v_A + \Delta a = c\Delta V_c; \quad \Delta(v_B + \Delta b) = (1-l)\Delta V_l.$$

Using the above equations, one can transform Eq. (6) to the form

$$\omega = \frac{1 + c(\Delta v_B/\Delta v_A - 1)}{1 + l(\Delta v_B/\Delta v_A - 1)}. \quad (8)$$

If the volume of the dissolved crystal, ΔV_c, tends to zero, the direction of the vector $\mathbf{s_2s}$ tends to the direction of the tangent to the solubility isotherm at the point s. Then, with due regard of the fact that the derivative at each point of the curve t is negative, Eq. (8) acquires the following final form:

$$\omega = \frac{1 - c(dv_B/dv_A + 1)}{1 - l(dv_B/dv_A + 1)}. \quad (9)$$

In the case of the interaction between pure components of the system ($c = 1$, $l = 0$), Eq. (9) is transformed into

$$\omega = -dv_B/dv_A. \quad (10)$$

Thus, the volume effect of the reaction of isomorphous replacement depends on the difference in the compositions of the crystalline phases and the ratio of the component solubilities at the solution point. Thus, the tangent to the curve t at the point s in Fig. 9a is inclined to the abscissa at an angle less than 45°. Therefore, in the interaction between a crystal enriched with the A component and the solution enriched with the B component, the volume factor is less than unity, $\omega < 1$, i.e., replacement proceeds with a deficit in volume.

It should be noted that the use of the Schreinmakers coordinates requires the fulfillment of the additivity condition for the molar volumes of the crystalline phases. In this case, the dependence of the lattice parameters of the crystal on its composition should obey the Retgers rule (the parabolic dependence of the third degree on the molar composition of the solid solution). However, in practice, this dependence is observed rather seldom. Therefore, estimating the volume effect of the reaction, one should necessarily take into account the deviation of the volume of the crystalline phase from the additivity property. This can be done by introducing into Eq. (6) the following coefficients: $p_c = \dfrac{\Omega_c}{c\Omega_A + (1-c)\Omega_B}$ and $p_l = \dfrac{\Omega_l}{l\Omega_A + (1-l)\Omega_B}$, where Ω_i ($i = c, l, A, B$) are the experimentally measured values of the unit-cell volumes of the crystalline phases with the respective compositions

$$\omega = \frac{\Delta V_l}{\Delta V_c}K_V, \quad K_V = \frac{p_l}{p_c}. \quad (11)$$

It should be noted that the latter correction only slightly affects the final value of ω, because, usually, the deviation of the dependence of the lattice parameters from the Retgers rule does not exceed 1%, whereas the solubilities of the salt components of the system can differ from one another up to a factor of about ten.

Thus, the above consideration shows that, in the first approximation, there exist the direct correlation between the morphological effect of the reaction of isomorphous replacement and the ratio of the volume solubilities of the system components. The difference in the lattice parameters (or molar volumes) is usually much less pronounced than the difference in the solubilities of the components and, therefore, the lattice mismatch should manifest itself in the case, where the molar solubilities of the components are either close or equal.

At the same time, one should remember that criterion (8) is only approximate since, in its derivation, some factors were ignored, e.g., the relationship of the dissolution rates, growth, and diffusion in the liquid phase, the anisotropy of the growth rates of different faces, the effect of stresses caused by lattice mismatch, etc. When estimating the reaction kinetics and its total morphological effect, one should take into account that these quantities are determined by the ratio of the amounts of the crystal and solution, which, in turn, determines the magnitude and velocity of the displacement of the solution and crystal compositions in the course of the reaction.

Specific Characteristics of the KAP–RbAP System

All the cases of isomorphous replacement in the aqueous solution of binary salt systems studied and described in [4–14] demonstrate a certain dependence of the surface morphology on the volume effect of the reaction: the formation of porous textures at $\omega < 1$ and the formation of island textures or a solid crystalline layer at $\omega > 1$. The system studied here demonstrates a more complicated behavior associated, first of all, with the alternation of the mechanisms characteristic of the substitution with deficit or the excess in the volume.

The KAP–RbAP system possesses a number of important characteristics in comparison with the systems studied earlier. First of all, it is characterized by a convex solubility isotherm (Fig. 10) [11]. Second, the system components have close values of the volume solubility in water (about 10% difference). Third, the differences in the lattice parameters of KAP and RbAP along different unit-cell axes have different signs.

In the (K,Rb)AP series, with an increase in the content of both K and Rb in the solution, the modulus of the derivative of the solubility function varies from values less than unity to values higher than unity. This is observed in the range of mean compositions, where the angles between the tangents to the solubility curve and the coordinate axes vary from values exceeding 45° to

RbAP, cm^3/100 g H$_2$O
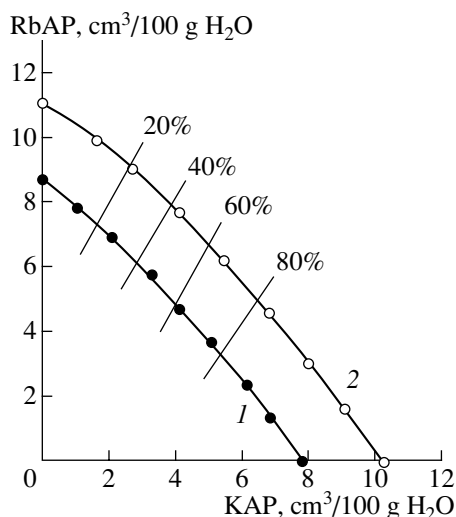
Fig. 10. Solubility isotherms for the C$_8$H$_5$O$_4$K–C$_8$H$_5$O$_4$Rb–H$_2$O system measured at (*1*) 29 and (*2*) 39°C [13]. Straight lines connect the compositions of the solutions in which the solid phase with the same KAP/RbAP ratio (percent) is crystallized.

values less than 45° (Fig. 10). Therefore, at the initial stage of the interaction of KAP and RbAP crystals with the solutions of the components–partners, the replacement with a deficit in volume is observed in both cases. It manifests itself in the formation of the aforementioned characteristic defect zones on the end faces of the samples and growth of islands on the (010) faces with the preservation of the regions without islands of the initial crystal. In the course of the long-term interaction of KAP and RbAP crystals with the solutions of the component–partner, the continuous dissolution of the substrate and feeding of the solution with the crystal substance lead to the change of the mechanism with deficit in volume to the mechanism with an excess in volume. This is seen from healing of the gaps between islands and continuous overgrown formations on the end faces. The change of the mechanisms on the KAP samples proceeds within a shorter time, because the point on the solubility curve where its slope to the coordinate axes is equal to 45° is shifted toward the RbAP-enriched solutions.

Note one more important feature of the system studied. The differences in the lattice parameters of KAP and RbAP crystals along different axes have different signs: the lattice parameters *a* and *b* of KAP crystals are less than those of RbAP crystals, whereas the parameter *c* of KAP crystals is larger than that of RbAP crystals.

Lattice parameters of KAP crystals are *a* = 6.47 Å, *b* = 9.61 Å, *c* = 13.26 Å; lattice parameters of RbAP crystals, *a* = 6.58 Å, *b* = 10.81 Å, *c* = 12.84 Å [16].

Considering the conclusions made in [2], one may think that, in principle, the formation of epitaxial layers on the (100) and (010) faces should differ from the process occurring on the (001) face (e.g., if a porous texture is formed on the (100) and (010) faces, one should expect the formation of a solid layer on the (001) face, and vice versa). However, the experiments showed no obvious differences in the mechanisms of formation of the morphological textures on different faces (Fig. 2). This confirms the conclusion drawn above about the secondary role of the lattice mismatch in the formation of an epitaxial layer.

CONCLUSIONS

The mechanisms of formation of epitaxial layers in the C$_8$H$_5$O$_4$K–C$_8$H$_5$O$_4$Rb–H$_2$O system have been studied by the methods of optical and *in situ* atomic force microscopy. It is shown that the formation of the characteristic morphological structures on the surface of crystals interacting with the solutions of the component–partner is associated with the intensity ratio of the processes of growth of the islands of a new phase and dissolution of the substrate between the islands. The decisive role in the process is played by dissolution of the substrate associated with the nonequilibrium compositions of the initial crystal and the solution. For the first time, an analytical model of the process of layer formation in the case of the liquid phase heteroepitaxy is suggested. It is shown that, in the first approximation, the possibility of formation of a continuous layer in the isothermal process is determined by the solubility ratio of the system components. These conclusions are of a general character and, thus, are also applicable to the epitaxial processes occurring not only in aqueous solutions but also in solutions–melts in the case where layer deposition proceeds via two-dimensional nucleation on the substrate.

REFERENCES

1. Yu. B. Bolkhovityanov, J. Cryst. Growth **55**, 591 (1981).
2. Yu. B. Bolkhovityanov, *Crystal Growth* (Nauka, Moscow, 1990), No. 18, p. 158.
3. Yu. V. Bolkhovityanov, *Materials of Electronic Technology, 1. Physical–Chemical Foundations of the Methods of Their Synthesis* (Nauka, Novosibirsk, 1983), p. 63.
4. A. É. Glikin and M. Yu. Sinaĭ, Zap. Vseross. Mineral. O–va, No. 6, 742 (1983).
5. A. É. Glikin and M. Yu. Sinaĭ, Zap. Vseross. Mineral. O–va, No. 1, 3 (1991).

6. A. É. Glikin, O. A. Leont'eva, and M. Yu. Sinaĭ, Zh. Strukt. Khim., No. 5, 79 (1994).

7. A. É. Glikin, Zap. Vseross. Mineral. O–va, No. 5, 125 (1995).

8. A. É. Glikin, Zap. Vseross. Mineral. O–va, No. 5, 103 (1996).

9. A. É. Voloshin, A. É. Glikin, S. I. Kovalev, *et al.*, in *Abstracts of 9th National Conference on Crystal Growth* (Moscow, 2000), p. 361.

10. L. Yu. Kryuchkova, A. É. Glikin, A. É. Voloshin, and S. I. Kovalev, Zap. Vseross. Mineral. O–va, No. 3, 62 (2002).

11. A. É. Glikin, S. I. Kovalev, E. B. Rudneva, *et al.*, J. Cryst. Growth **255**, 150 (2003).

12. C. M. Pina, C. Putnis, K. Pollok, *et al.*, in *Abstracts of the 14th Konegsberg Seminar on Spatio–Temporal Patterns in the Earth, Norway, 2001*, p. 31.

13. C. Putnis, C. M. Pina, K. Pollok, and A. Glikin, in *Abstracts of the 11th Annual Goldschmidt Conference, Hot Springs, Virginia, USA, 2001*, p. 3555.

14. A. Putnis, Mineral. Mag. **66** (5), 689 (2002).

15. T. G. Petrov, E. B. Treĭvus, Yu. O. Punin, and A. P. Kasatkin, *Growth of Crystals from Solutions* (Nedra, Leningrad, 1983).

16. *Acoustic Crystals*, Ed. by M. P. Shaskol'skaya (Nauka, Moscow, 1982).

Translated by L. Man

CRYSTAL
GROWTH

Study of Correlation between Morphological Structures and Composition Inhomogeneity for $Ca_{0.9}Ho_{0.1}F_{2.1}$ Crystals

V. A. Meleshina* and V. A. Smirnova**

* Shubnikov Institute of Crystallography, Russian Academy of Sciences,
Leninskiĭ pr. 59, Moscow, 119333 Russia

** Central Scientific and Research Institute for Machine-Building Technology,
Sharikopodshipnikovskaya ul. 4, Moscow, 109088 Russia

Received October 20, 2002

Abstract—Optical methods and local X-ray spectroscopic analysis were used to study the correlation between the morphological structures and the composition inhomogeneity for $Ca_{0.9}Ho_{0.1}F_{2.1}$ crystals. It is found that, at two nearby points, the characteristics of uniformity of the Ca and Ho distribution (the homogeneity criterion $S_c/2\sigma$, the coefficient of variation $S_c/\overline{N}$, and the level of homogeneity W_{95}/C) may differ by more than two orders of magnitude if these points belong to morphologically different regions with different prehistory. © 2003 MAIK "Nauka/Interperiodica".

The composition, phase, and structural disturbances which accompany the loss of stability by the growth front in crystals of $La_{1-x}Sr_xF_{3-x}$ solid solutions were investigated in [1] for the case when the average melt composition, being close to eutectic, controls the front stability. It is of interest to find out how the local composition of a crystal changes when the growth front loses its stability under the conditions of crystallization near the dystectic point, where, according to the equilibrium phase diagram, the ratio of distribution $k \approx 1$.

In this study, the variations in the composition were investigated by an example of ionic $Ca_{1-x}Ho_xF_{2+x}$ crystals with the fluorite structure. The dystectic point of these solid solutions is in the vicinity of the $Ca_{0.9}Ho_{0.1}F_{2.1}$ composition [2]. The latter served as the initial mixture composition for growing crystals by the Bridgman–Stockbarger method [3].

The features of the Ca–Ho substitution, i.e., the variations in the contents of these elements, were studied by local X-ray spectral microanalysis using continuous recording modes and step-by-step scanning by point and linear probes. The samples were prepared for investigation using conventional techniques: grinding, polishing, vacuum deposition of a thin conducting layer (gold), and coating the faces of an entire crystal with a silver paste. The final correlation between the regions under study and the internal morphology of the samples was established using traces of an electron probe (spots of hydrocarbon deposit). To increase the reliability of the data collected, we investigated either two or three

parallel lines (JXA-50A, MS-46, and Camebax microanalysers were used).

Special consideration was given to the variations in the composition that accompanied the sequence of transitions of the growth front when it lost stability and transformed from the planar isothermal into the cellular (Fig. 1a) and then cellular–globular form (Fig. 1b). Such transitions were revealed in the end crystal regions after constant (on the average) composition of the crystal was established by the end of crystallization (Fig. 2). As will be shown below, the local composition changed noticeably in a rather regular way at these transitions.

The uniformity of the Ca and Ho distribution was evaluated according to the schemes accepted in [4]. The data obtained on the homogeneity criterion $S_c/2\sigma$ and coefficient of variation $S_c/\overline{N}$, as well as the calculated and experimental levels of homogeneity W_{95}/C for the 95% confidence level, are listed in the table. The parameters noted are given by the expressions

$$S_c = \left[\sum (N_i - \overline{N})^2/(n-1) \right]^{1/2},$$

$$\sigma = \overline{N}^{1/2},$$

$$W_{95}/C = \pm 2t_{n-1}^{95}/(n^{1/2}\overline{N}^{1/2}) \text{ (calculated level)},$$

$$W_{95}/C = \pm t_{n-1}^{95} S_c/(n^{1/2}\overline{N}) \text{ (experimental level)},$$

(a)

(b)

200 μm
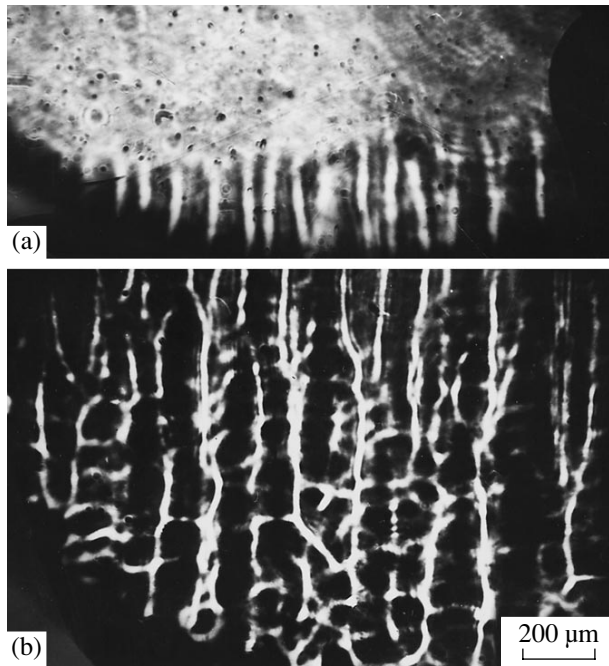
Fig. 1. Morphologically different regions corresponding to the loss of stability and the transition from (a) the isothermal to cellular and (b) the cellular to cellular–globular crystallization front. The transitions (a) and (b) were observed at $g \sim 0.8$ (see Fig. 2).

Fig. 2. Distribution of Ca and Ho along the crystal length. Step-by-step scanning in the plane of central cross section (step 1–2 mm, probe diameter 5 μm).

where N_i is the number of pulses of characteristic X-ray radiation in the ith measurement, $\overline{N}$ is the average number of pulses in a given series of measurements, n is the number of regions analyzed by the point probe, C is the actual weight concentration of the element analyzed, and t_{n-1}^{95} is Student's coefficient for the 95% confidence level and $n-1$ degrees of freedom.

Both elements show highest inhomogeneity when the path passing through the boundary between the regions of isothermal and cellular growth is studied (see table). The morphological picture of the transition region and the scan paths for different microanalyzers are shown in Fig. 3. Figure 4 shows the results of these independent measurements by probes with different cross-section shapes. As can be seen from Fig. 4, when the isothermal-growth front loses its stability, an abrupt decrease in the concentration of the host cation (Ca) is observed in both independent measurements with scanning along paths I and II.

As noted in [5], weak modulations of the Ca content at the boundaries of cells to be formed are observed in

Morphological structures and characteristics of boundaries between them

Morphological structures and boundaries between them	Characteristic-emission line	Homogeneity criterion $S_c/2\sigma$	Coefficient of variation $S_c/\overline{N}$, %	Level of homogeneity W_{95}/C, wt %	
				calculated	experimental
Cellular structure (along the normal to the cell boundaries)	CaK_α	7.6	19.5	±0.35	±2.7
	HoL_α	0.3	2.1	±0.32	±0.34
Along the normal to the boundary separating the isothermal and cellular growth stages	CaK_α	18.1	8.2	±0.10	±2.4
	HoL_α	23.6	34.8	±0.42	±9.9
In the plane of the growth layer in the initial crystallization region	CaK_α	1.1	0.5	±0.33	±0.36
	HoL_α	1.4	1.6	±0.82	±1.12
In the plane of the growth layer in the intermediate crystallization region	CaK_α	2.2	1.0	±0.34	±0.74
	HoL_α	1.2	3.1	±0.90	±1.12
In the plane of the growth layer in the end crystallization region	CaK_α	1.2	0.6	±0.32	±0.39
	HoL_α	1.2	1.6	±0.96	±1.15

Fig. 3. Region of transition from the isothermal to the cellular growth. B is the boundary separating the regions with visually revealed cellular structure and without it; I is the path of step-by-step scanning by a linear probe (band 50 × 10 μm² in size, step 20 μm, 64 portions); II is the path of step-by-step scanning by a point probe (probe diameter 5 μm, step 10–20 μm); III is the path of additional step-by-step scanning by a point probe.
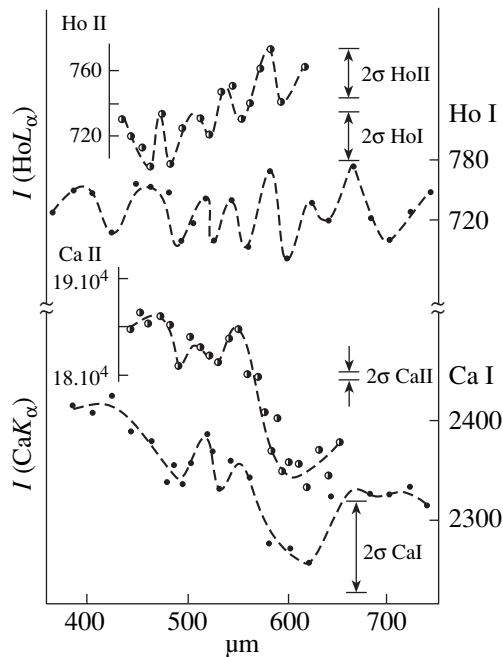
Fig. 4. Distribution of Ca and Ho along the growth direction in the region of transition from the isothermal to cellular growth: Ca I and Ho I are obtained by a linear probe, and Ca II and Ho II are obtained by the point probe. The Ca content is minimum at the boundary separating the regions of different growth. The scan paths are shown in Fig. 3.

modulated with $S_c/2\sigma \sim 7.6$. This modulation is bound to the cell boundaries [5].

Thus, starting with weak modulations, the Ca content responses to the perturbations of the growth-surface relief, which precede the partition of the growth-front into cells [5]. At the instant when discernible cells are formed, a significant deficit of Ca before the front is observed (Fig. 4). At the same time, the content of Ho is almost insensitive to the cell formation: both in the initial stage and after the visual appearance of cells, oscillations of the Ho content are periodic, but they are not bound to the cell boundaries. Scanning across cells reveals almost uniform Ho distribution with $S_c/2\sigma \sim 0.3$. At the transition from the isothermal to the cellular growth (Fig. 3), the Ho content does not suffer abrupt changes at the boundary of the transition region, nevertheless demonstrating significant oscillations along the growth direction both before and after the boundary (Fig. 4).

When scanning along the normal to the growth axis (in the plane of the growth layer), it was established that the value of S_c/N for Ho is about three times larger than for Ca (see table). This circumstance, along with the aforementioned behavior of the Ho content near the cell boundaries, suggests that the heavier dopant Ho contributes to the composition inhomogeneity mainly through the microlayer substructure along the tangential direction with respect to the growth layers. Along the normal direction, the Ho content may remain surprisingly constant within sections up to ~350 μm long, whereas the Ca content suffers periodic oscillations close to sinusoidal.

It is possible that the difference in the behavior of Ca and Ho revealed in this study is related to the different buoyancies of the Ca and Ho complexes (which have different specific weights) in the melt [6] and physico-chemical melt exfoliation before the crystallization front [7].

It is also possible that these effects manifest themselves successively; i.e., the layers formed near the growth front after the melt exfoliation, which are enriched with the lighter element Ca, rise, depleting the region directly before the crystallization front with this element (Fig. 4).

the continuous-recording mode in the stage of isothermal growth up to the instant when optically discernible cells appear. When the cellular structure becomes optically discernible, the content of Ca becomes noticeably

REFERENCES

1. V. A. Meleshina, O. I. Lyamina, E. A. Krivandina, *et al.*, Kristallografiya **38** (1), 177 (1993) [Crystallogr. Rep. **38**, 94 (1993)].

2. B. P. Sobolev and P. P. Fedorov, J. Less-Common Met. **60** (6), 33 (1978).

3. A. Z. Arakelyan, Candidate's Dissertation in Physics and Mathematics (Inst. of Physical Research, Academy of Sciences of Armenia, Ashtarak, 1981).

4. J. Colby and J. Goldstein, in *Practical Scanning Electron Microscopy: Electron and Ion Microprobe Analysis*, Ed. by J. I. Goldstein and H. Yakowitz (Plenum, New York, 1975; Mir, Moscow, 1978).

5. P. P. Fedorov, T. M. Turkina, V. A. Meleshina, and B. P. Sobolev, in *Crystal Growth* (Nauka, Moscow, 1988), Vol. 17, p. 198.

6. G. W. Young and S. H. Davis, Phys. Rev. B **34**, 3388 (1986).

7. V. A. Meleshina and E. S. Nikolaevskiĭ, Kristallografiya **39** (5), 900 (1994) [Crystallogr. Rep. **39**, 820 (1994)].

Translated by Yu. Sin'kov

═══ **JUBILEES** ═══

Petr Grigor'evich Pozdnyakov
(On the Occasion of His Ninetieth Birthday)

Petr Grigor'evich Pozdnyakov, Doctor of Technical Sciences, Professor, winner of the Lenin Prize of the USSR, Honored Inventor of the RSFSR, a full member of the International Academy of Information Science, the follower of academic A.V. Shubnikov, is one of the founders and organizers of domestic piezoelectronics. Being a real innovator and creator, Pozdnyakov made a great contribution to its development. He is the author of more than one hundred publications and about one hundred inventions, most of which were realized in practice. Most results of his studies are implemented in real devices, which were used, in particular, in control systems of space vehicles in the 1950s–1970s.

Petr Grigor'evich Pozdnyakov was born on December 4, 1912 (November 20 under the old calendar), in Orel. Pozdnyakov's grandfather was a great organizer and an enterprising man. Born a peasant, he made his way in the world and became a first-guild merchant. The father of P.G. Pozdnyakov was a art teacher; his mother, the daughter of a lady of the manor (of peasant origin), finished gymnasium with a medal. Pozdnyakov left school in Orel in 1929 (the period of "great break"). Then, he worked as electrician to gain a three-year seniority (required to enter high school) and studied at the rabfak (faculty for the working youth). In 1932, Pozdnyakov entered the Moscow Energy Institute and in 1939 graduated from the Electrophysical Department with the qualification of an electrical engineer in the field of radio equipment production. The subject of his diploma thesis was the design of a frequency standard on the basis of a quartz crystal, using a frequency standard produced by a US company as a prototype. At that tragic period of our history, it was practically impossible for a man of merchant origin, whose parents were subjected to repression in 1937, to get a job as an engineer. Only by lucky chance, he managed to get a job at the Central Scientific Research Laboratory (CSRL) of Applied Crystallography of Trust 13 (organized by Shubnikov) in 1939. Under the supervision of Alekseĭ Vasil'evich Shubnikov, Pozdnyakov studied all stages of processing various crystals, including quartz. Shubnikov thought it necessary that all research assistants could carry out any operations in the processing, preparation, and measurement of crystals with their own hands. G.G. Lemmleĭn, a well-known crystallographer (who also worked under supervision of Shubnikov), helped Pozdnyakov to master the fundamentals of practical crystallography, in particular, the specific features of orienting of natural quartz crystals. Shubnikov's school was an excellent basis for further practical, creative, and organizational activity of Pozdnyakov.

At the beginning of 1941, Shubnikov recommended Pozdnyakov to be appointed the head of the CSRL to organize production of crystals of Rochelle salt, which was used as basic material in hydroacoustic devices abroad.

When the Great Patriotic War began, it became necessary to organize a plant on the basis of the CSRL. The aim was to produce Rochelle salt crystals and devices based on this material. Pozdnyakov, who was appointed an acting director, and the main engineer A.S. Shein managed it successfully.

In December 1941, Pozdnyakov and a small group of experts, together with a part of equipment, were evacuated to Tashkent to organize an alternate plant.

This plant, at which Pozdnyakov was appointed a main engineer and worked successfully throughout the whole war, produced Rochelle salt crystals and devices on their basis. Shein, staying at the Moscow plant, diligently produced new devices based on Rochelle salt. Rochelle salt piezoelectric elements were used in pickups, loudspeakers, and hydroacoustic devices for the Navy. During the Great Patriotic War, soviet submarines were equipped with Mars hydrophones based on hydrophone piezoelectric stacks (PB-20 piezoelectric batteries). There were no sonars then. It was noted in a report from the North Fleet, published in the newspaper Krasnaya Zvezda, that, due to the high sensitivity of PB-20 piezoelectric batteries, a sound technician in a soviet submarine could hear the sound of a enemy German submarine much earlier than the enemy could, which made it possible to attack the enemy submarine before it could detect the danger.

The largest scale product based on Rochelle salt crystals was a PK-1 microphone with a bimorph piezoelectric element, which was used in military field telephones. Among commercial products, there were piezoelectric stethoscopes, systems for communication between a sound technician on a submarine and the submarine captain and for controlling the sound technician operation, two-agent airplane communication systems without batteries, systems for communication between a diver and the boat board, Neva telephone stations for divers, telephones without batteries for communication in railway transport, telephones without batteries for communication in regions liberated from the temporary occupation (which provided communication at distances as large as 30–50 km in air and 10–15 km by cable communication lines).

When the war was over, Pozdnyakov came back to work at the Moscow plant as a main engineer. There he organized the research work on analysis and growth of new piezoelectric crystals. The practical result of these studies was the development of commercial technology of growing water-soluble crystals of ammonium and potassium phosphates, potassium tartrates, and ethylenediamine. For example, successful application of potassium tartrate crystals as resonators in multi-channel communication systems made it possible to reduce consumption of high-quality quartz raw material. This was of importance, because the production of artificial quartz crystals was not developed at that time.

In 1949, P.G. Pozdnyakov and A.A. Shternberg started research work on the growth of quartz crystals and fabrication of piezoceramic. The small plant was not appropriate for this important work. Under Pozdnyakov's initiative, the plant was reorganized into the Central Scientific Research Laboratory of Piezoelectrics, where Pozdnyakov became the Deputy Chief of Research.

In 1952, Pozdnyakov was appointed the Main Engineer of the Central Administrative Board at the Ministry of Industry of Communication Means (MICM). One of the most important results of his activity in the Central Administrative Board and its scientific and technical section of piezoelectrics was the decision about merging quartz workshops that belonged to different administrative boards and creation of the All-Union Scientific Research Institute of Piezoelectrics (in future, VNIISIMS in Aleksandrov).

In May 1953, P.G. Pozdnyakov, who was anxious for creative work, moved to NII-885 of MICM, in which systems and complex equipment for radio control of ballistic rockets were developed. N.A. Pilyugin and M.S. Ryazanskiĭ were the main designers. On the basis of a laboratory, which looked rather like a workshop, Pozdnyakov organized the well-equipped Complex Quartz Laboratory, in which many original scientific and applied studies were carried out.

The Quartz Laboratory was reinforced with engineering and technical staff. An experienced expert in quartz problems, I.G. Vasin, and a young specialist, who graduated from Moscow State University, M.I. Yaroslavskiĭ, were recruited to work there.

In 1954, the technical specifications on the resonators developed in NII-885 were supplemented for the first time with requirements for frequency changes due to the action of various climatic and mechanical factors and storage and operation conditions, including requirements for frequency changes during long operation time, i.e., aging. In addition, hermetically sealed resonators in metal cases and vacuum resonators in glass bulbs (which were used in electron tubes) were designed and fabricated in 1954. Such studies were performed for the first time in the domestic industry, and the results obtained were widely implemented in series production at all the plants in our country in which there were quartz workshops.

To produce these reliable resonators, a quartz workshop was organized at the pilot plant of NII-885. Since the production capacity of the workshop was limited, series production of the quartz resonators developed in the Laboratory was started at the Kozitskiĭ factory in Leningrad (now St. Petersburg), the workshops of NII-20 in Moscow, plant 210 in Omsk, and the NII in Sverdlovsk (now Yekaterinburg).

Since 1955, the Quartz Laboratory of NII-885 under the direction of Pozdnyakov has become the leading laboratory in the country in constructing and fabricating quartz resonators. The rate of development of systems and devices in the NII was very high, and the requirements for reliability and frequency stability of the resonators designed, as well as their frequency range, were constantly increasing.

In 1956, not only resonators comparable in quality with the best foreign analogous devices were developed and fabricated in the Laboratory but also resonators with no foreign equivalent were designed (resonators operating as torsional vibration absorbers at different frequencies, a class of slotted resonators, combined and

hybrid piezoelectric elements and integrated piezoelectric devices, and so on).

The technical documentation developed in the Quartz Laboratory of NII-885 was transferred in 1959 to the NII of Piezoelectronics, and, on the basis of this documentation, production of standard resonators of conventional types was started. Many specialists from the Quartz Laboratory of NII-885 passed to the NII of Piezoelectronics and became main specialists there.

Pozdnyakov also organized the development of integrated piezoelectric devices—monolithic quartz filters, integrated and hybrid oscillators and filters, thermally stable resonators, precise quartz oscillators with integrated thermally stable resonators, semiconductor and hybrid integrated circuits.

In 1964, Pozdnyakov and his coworkers were awarded the Lenin Prize for the results obtained in the design and scale-up of quartz resonators intended for special devices.

Pozdnyakov always paid much attention to rationalization and, especially, invention. He is the holder of more than 100 inventor's certificates and he has the title of Honored Inventor of the RSFSR.

In 1967, Pozdnyakov brilliantly defended his Candidate thesis in the form of a complex report on his studies and immediately after that, the Scientific Council awarded him a degree of Doctor of Technical Sciences by repeated voting. He is a full professor.

On January 5, 2001, at the meeting on the occasion of the 30th anniversary of the Morion plant in St. Petersburg, in the presence of domestic civil and military representatives and foreign experts, Pozdnyakov was awarded the title of Honorary Veteran of Piezoelectronics for his prominent contribution to the development of domestic piezoelectronics, his real innovation, doubtless and long-term leadership in this field of science and technique.

Pozdnyakov edited Handbook on Quartz Resonators (Moscow: Svyaz', 1978, 288 pp.) and Piezoelectric Resonators (Moscow: Radio i Svyaz', 1992, 392 pp.).

Presently, Pozdnyakov is a unique expert who remembers well all the stages in the development of domestic piezoelectronics, pays much interest to its modern status, and is in correspondence with veterans of piezoelectronics in various towns of Russia.

Specialists in piezoelectronics and the Editorial Board of Kristallografiya (Crystallography Reports) congratulate Petr Grigor'evich Pozdnyakov—the eldest domestic expert in quartz—on his ninetieth birthday and wish him good health and new success in his work.

Translated by Yu. Sin'kov

Dedicated to the 60th Anniversary
of the Shubnikov Institute of Crystallography
of the Russian Academy of Sciences

To the 150th Anniversary of the Birth of Evgraf Stepanovich Fedorov (1853–1919)
Irregularities in the Fate of the Theory of Regularity

R. V. Galiulin[1]

Shubnikov Institute of Crystallography, Russian Academy of Sciences, Leninskiĭ pr. 59, Moscow, 119333 Russia
e-mail:galiulin@ns.crys.ras.ru

There are two world-class geometers in our country—
Lobachevskii and Fedorov.
B.N. Delaunay

All will be regular, regularity underlies the world.
Woland[2]

E.S. Fedorov

Mankind has been guided by the notion of regularity since ancient times. Platonic and Archimedean bodies, Mauritanian ornaments, parquets, Kepler snowflakes, Hauy mineralogy, Galois' theory, Lobachevskii geom-

etry, and the Mendeleev Table are examples of the exhaustive interpretation of the particular manifestations of regularity. However, the general meaning of regularity as a universal and natural law, even in human thought, was first realized by the prominent thinker, humanist, and Russian patriot Evgraf Stepanovich Fedorov (December 10, 1853–May 21, 1919). In its essence, science is unified, and, therefore, Fedorov's theory of regularity covers all knowledge accumulated by mankind throughout its entire existence. The 21st century began with the triumph of Fedorov's ideas in both the world of quarks and the global structure of the Universe and in the new school handbooks on geometry.

Fedorov's life was far from easy. He became interested in geometry in his childhood and, being only sixteen years old, started writing a book which, to a large extent, anticipated the development of geometry. He failed to enter the Medical–Surgical Academy (1874), and entered the Technological Institute, where he carefully studied *Foundations of Chemistry* by D.I. Mendeleev (1834–1907), one of the most important scientific books written in the 19th century. Fedorov combined these studies with revolutionary activity—he was a member of the organization *Land and Freedom*. It is believed that it was Italian (Fedorov's conspiratorial name) who was the excellent violinist who helped famous revolutionary P.A. Kropotkin to escape from the Peter and Paul Fortress in 1876. In 1880, Fedorov, who intuitively realized the fundamental importance of crystallography in the development of geometry, started his studies at the Mining Institute. Since then, all Fedorov's weekdays, joys, and troubles were associated with this institute. Fedorov, a Member of the Academy, died of starvation in 1919.

[1] Fedorov Prize winner, 1997.
[2] From Bulgakov's *Master and Margarita*.

His coffin was carried high in people's hands for the whole way from the Mining Institute (Gorny) to the Smolensk cemetery [1].

FEDOROV'S *ELEMENTS*

Fedorov recollected [2] that in 1863 he came across his elder brother's handbook on elementary geometry written by Shul'gin for military schools. He looked through its first pages and the contents gave rise to such an emotion that he was carried away. A ten year old boy had got through Shulgin's planimetry in two days. Six years later, being a cadet of the St. Nicholas Military Engineering School, Fedorov started writing his first book, *The Elements of the Study of Configurations* [3].

The St. Nikolas Military Engineering School was located at the Mikhailovsky (Engineering) Castle. It seems that the spirit of the former owner of the castle, Emperor Paul I, brought him to the concepts of regularity and order, which Paul I tried to establish in Russia. The book was completed in 1879 but was published only in 1885 with the help of general of artillery and Professor of physics A.V. Gadolin (1828–1892), the author of the most progressive method of derivation of 32 crystal classes [4].

Fedorov's book was preceded by two famous treatises—Euclid's *Elements* and Newton's *Principia*. Here, the question may arise as to how a young scientist could dare to choose such a title for his first book. However, by this time (1878), Fedorov was already an organizer of an illegal socialist newspaper *Nachala* (elements, principles), which criticized the existing social system and had the aim to unite all kinds of socialists for writing a revolutionary program. In this newspaper, Fedorov supervised the column *Chronicles of the Socialist Motion in the West*. The police made all possible efforts to find its anonymous publishers. After the successful self-liquidation of the newspaper office located at Kirochnaya ulitsa (in the house of A.A. Panyutina, a landowner from the Perm district and the mother of Fedorov's future wife), Fedorov directed all his revolutionary ardor to *The Elements of the Study of Configurations*. He wrote that this extremely elegant section of elementary geometry was still almost unstudied despite the fact that the need in this theory was so urgent that many representatives of other natural sciences, and first of all mineralogists, made numerous attempts to create such a theory. However, all these attempts failed, because the authors considered only those aspects of the problem which were necessary for solving their own specific problems. As a result, their spontaneously developed theories lacked satisfactory nomenclature and integrity, whereas mathematicians, usually unaware of the results obtained in other branches of science, formulated the problem quite differently.

The distinctive feature of Fedorov's geometry, which distinguishes it from all the other geometries, is the use of the concept of regularity—a configuration composed by equivalent parts, with each of these parts being surrounded in the same way with other equivalent parts. Only such systems can possess the minimum energy [5]. Thus, the finite state of any varying system is the crystalline state, because it is only in an ideal crystal that the particles are absolutely equivalent, i.e., cannot be distinguished from one another [6]. Similar speculations brought Fedorov to the Mining Institute, from which he graduated in 1883 at the top of his class. According to the rules, he had to be sent on probation work to Germany, but he never went there, because he considered it to be humiliating to plead for something that should be granted according to the rules.

Today, Fedorov's *Elements* is considered to be one of the deepest monographs on elementary geometry (elementary in the sense fundamental and not simplest). More exactly, the largest part of *Elements* is dedicated to planimetry and not only to Euclidean but also spherical planimetry. Stereometry is considered only in the sections dealing with division of space (parallelohedra and stereohedra).

Now, consider the different sections of *Elements*. Such a consideration can also be included into all modern handbooks on geometry, including school handbooks.

Euclidean planimetry is planimetry on a Euclidean plane, i.e., conventional planimetry. The unusual aspect of the Fedorov planimetry is that it is based on regularity. It is regular division that reveals the fundamental properties of space. Fedorov called a planigon any polygon that could divide a plane in a regular way. Already the first studies of planigons gave very interesting results. Thus, it turned out that only triangles, tetra-, penta-, and hexagons can be planigons (dashed polygons in Fig. 1), that any tetragon (including nonconvex one) is a planigon, etc. Today, these results are included even in school handbooks on geometry [7]. The exhaustive theory of planigons was developed by outstanding geometer B.N. Delaunay (Delauné) (1890–1980) [8].

A division dual to the division of a plane into planigons (the apices of this division form a regular system, Fig. 1) were considered in 1916 by outstanding crystallographer A.V. Shubnikov (1887–1970) in the solution of the following problem [9]. Let each atom in the plane possess the same number of bonds with other atoms. Then, how many atomic networks are formed? Since the problem was solved by topological methods using the generalized Euler formula, it followed that two-dimensional crystallography was a purely topological science. In other words, growth of a two-dimensional crystal did not necessarily require that the bond lengths and the bond angles formed by these bonds be fixed. At the first stages of growth, they can be arbitrary. The main requirement is that these patterns could be transformed into regular patterns forming new bonds and breaking old ones. These results were generalized by Delaunay [8], who showed that all such networks can
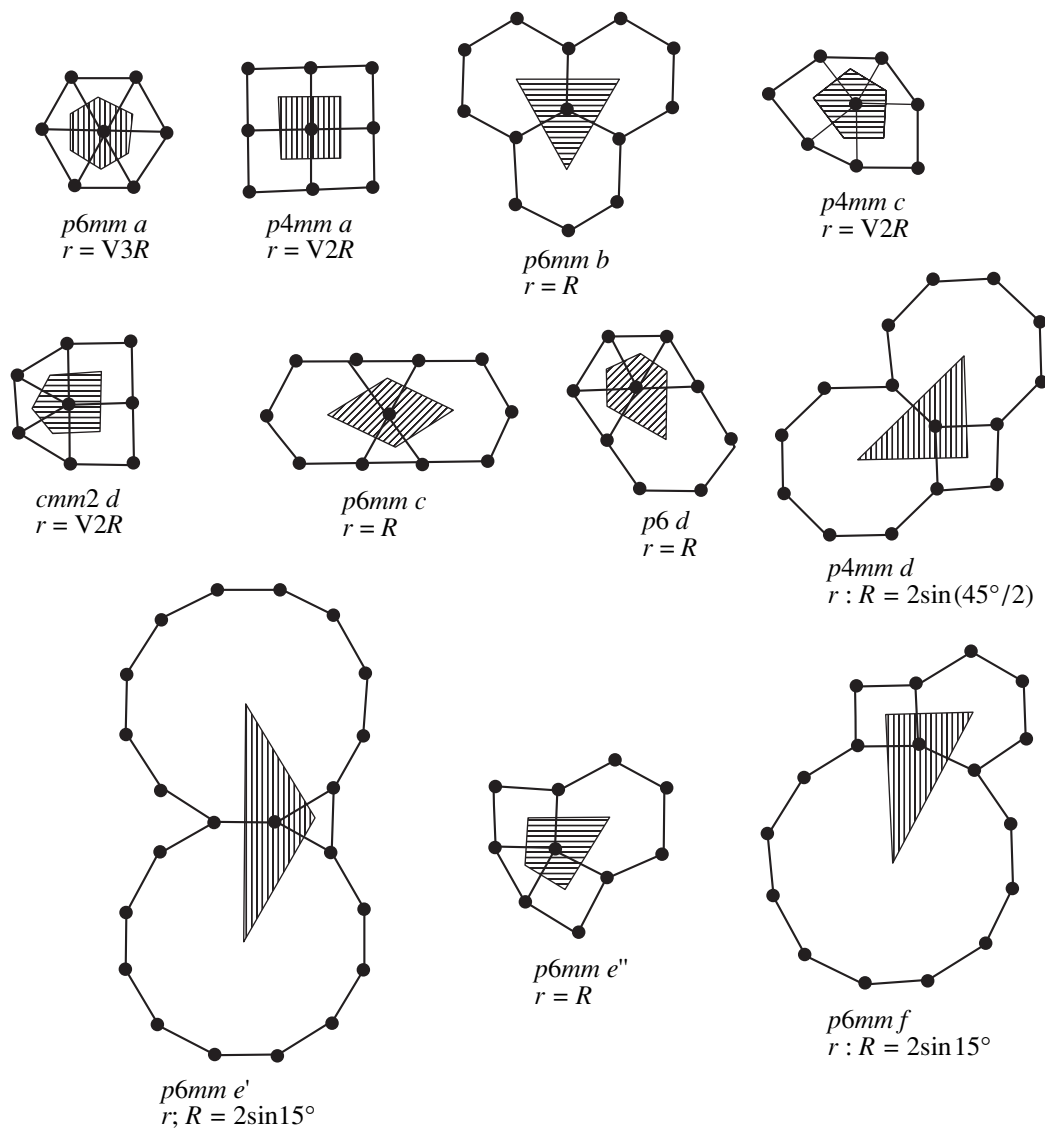
Fig. 1. 11 Kepler–Shubnikov–Delaunay networks and the corresponding Dirichlet planigons. Each infinite regular network is represented by a star of regular polygons converging at the network point. The corresponding Dirichlet planigon (composed of the points of the plane that are closer to the given lattice point than to any other point) is represented by the etched polygon. For each network, the symbol of its two-dimensional Fedorov group is indicated as well as the corresponding Wyckoff position in this group, and the ratio of the discreteness radius in this network, r, to the radius of its coverage, R.

be constructed only from regular polygons (Fig. 1) and that two-dimensional crystallography has a purely topological basis. Thus, Delaunay related the theory of planigons with the Kepler parquetry from his *World's Harmony.*

The most outstanding recent achievement of the theory of planigons is the Shtogrin theorem (the idea of this theorem was suggested by the author of the present article), according to which each regular system on a Euclidean plane is defined locally, i.e., by the same environment of any point of the system with other points of this system lying within a sphere of a fixed radius [10]. It follows from Shtogrin's theorem that long-range order is the consequence of the short-range

order. The long-range order can exist only in crystal structures.

Fedorov's planigons have not been considered as yet in traditional handbooks on crystallography. In this respect, the school handbooks of geometry turned out to be more progressive [7, 11, 12].

Spherical planimetry deals with regular division of a two-dimensional sphere, i.e., a sphere's surface. All topologically nonequivalent divisions are exhausted by Platonic and Catalani bodies and two infinite series of bipyramids and deltahedra (Fig. 2). These polyhedra are called isohedra. Polyhedra dual to isohedra are called isogons. All the topologically nonequivalent polyhedra are exhausted by Platonic and Archimedean

Platonic bodies

Tetrahedron
4i3m-24

Cube (hexahedron)
m3m-48

Octahedron
m3m-48

Icosahedron
53m-120

Dodecahedron
53m-120

Archimedean bodies

Truncated
tetrahedron
4i3m-24

Truncated
cube
m3m-48

Truncated
octahedron
m3m-48

Cuboctahedron
m3m-48

Rhombocuboctahedron
m3m-48

Snub
cube
432-24

Truncated
cuboctahedron
m3m-48

Truncated
dodecahedron
53m-120

Truncated
icosahedron
53m-120

Icosidodeca-
hedron
53m-120

Rhombicosido-
decahedron
53m-120

Snub
dodecahedron
532+60

Truncated
icosidodecahedron
53m-120

Prisms
6i2m-12

Antiprisms
8im2-16

Catalani Bodies

Trigon-
tritetrahedron
4i3m-24

Trigon-
trioctahedron
m3m-48

Tetra-
hexahedron
m3m-48

Rhombidodeca-
hedron
m3m-48

Tetragon-
trioctahedron
m3m-48

Pentagon-
trioctahedron
432-24

Hexaocta-
hedron
m3m-48

Trigontri-
icosahedron
53m-120

Hexadodeca-
hedron
53m-120

Rhombitriacon-
tetrahedron
53m-120

Tetragontri-
icosihedron
53m-120

Pentagontri-
icosahedron
532-60

Hexa-
cosahedron
53m-120

Bipyramids 6i2m-12

Deltahedra 8im2-16

Fig. 2. Regular and semiregular convex polygons. Regular polygons: 5 Platonic bodies. Semiregular isogons: 13 Archimedean bodies and two infinite series of prisms and antiprisms. Semiregular isohedra: 13 Catalani bodies and two infinite series of bipyramids and deltahedra. For each polygon, its symmetry is indicated.

bodies and two infinite series of prisms and antiprisms (Fig. 2). In fact, isogons and isohedra form the basis of the theory of polyhedra. Therefore, the latter theory should be related not to stereometry but rather to planimetry on a sphere.

Proceeding from the consideration above, school geometry [7] should rather be called planimetry and should be complemented with the elementary data on a Lobachevskii plane (sum of the angles of a triangle is less than 180°, each regular polygon can regularly
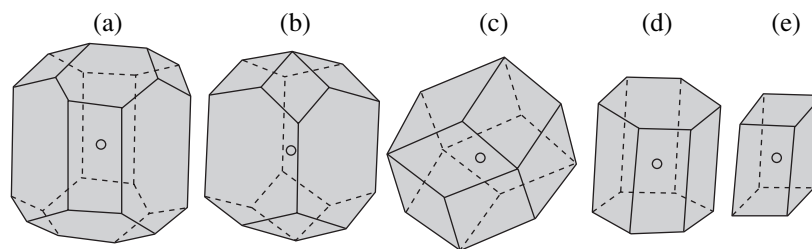
Fig. 3. Fedorov bodies: 5 combinatorially different parallelohedra for the points of three-dimensional lattices. (a) General 14-face polygon, (b) Fedorov dodecahedron, (c) parallelogrammatical dodecahedron, (d) hexagonal prism, (e) parallelepiped.

divide the Lobachevskii plane). This is already used in practice when nesting blanks in the shoe industry [13]: soles are sewn from regular hexagons, heels, from pentagons, and shin, from heptagons.

STEREOMETRY

Delaunay was the first to compare Fedorov with Plato and Archimedes [14], because it was Fedorov who composed the complete list of all the combinatorially different polyhedra that can fill the space being in parallel positions, the so-called Fedorov parallelohedra. Delaunay called these five polyhedra the Fedorov bodies (Fig. 3). Four of these bodies (the first, third, fourth and fifth ones) have been known since ancient times. The second parallelohedron can be justly called the Fedorov dodecahedron.

The division of the Euclidean space into parallelohedra (in the case of a plane, into Fedorov parallelogons) is one of its basic properties. This property is inherent only in spaces with the zero curvature. Other spaces of a constant curvature (it is only in these spaces that matter can be crystallized, i.e., form absolutely equivalent and indistinguishable particles) cannot be divided into parallelohedra. A Euclidean observer cannot move rectilinearly in these spaces. It should also be indicated that many other mathematicians arrived at parallelohedra, but their derivation gave rise to serious difficulties even for advanced mathematicians [15, 16]. Despite this, Delaunay included parallelohedra in his school book on geometrical problems [17].

The fifth chapter of *Elements*, dedicated to nonconvex polyhedra, has still not received due attention despite the fact that Russian mathematicians recently reported important results obtained in the theory of nonconvex polyhedra [18].

Elements is a versatile work, the best handbook on regularity necessary not only for mathematicians and natural scientists but also for any educated person. I was surprised to see Newton's "Principia" and Fedorov's *Elements* side by side at the honorary place in the personal library of Marutaev, a well-known musician. It shows that people with humanitarian education also realize the necessity of a mathematical picture of the world.

REGULARITY OF ATOMIC AND NUCLEAR ORBITALS

After completion of *Elements* (1869–1879), Fedorov presented to D.I. Mendeleev (1834–1907) his new manuscript (1880) in which he first stated his new idea—to consider the Periodic Law in terms of the theory of regularity. At that time, he published only the abstract of this work [19]. The manuscript of the complete work was found in Mendeleev's Archives many years later [20] and was published only in 1955 [21].

Fedorov writes [21] that the human brain always seeks regularity in everything, which is quite understandable, because a man can be oriented in his search for an appropriate work only considering regularly grouped materials and only if this regularity does not give rise to any doubt, so that he can be satisfied and become a master of this new field.

To explain the sequence of atomic weights of elements in the Mendeleev Table, Fedorov put forward the hypothesis of a planetary structure of an atom. Fedorov writes [21] that the atomic surface is the most important factor providing the occurrence of a chemical reaction. This signifies that small bodies forming an atom are not arranged continuously but, similar to planets, are spaced from one another by sufficiently large distances. Thus, at the very beginning of his scientific carrier (1880), Fedorov came to the concept of divisibility of an atom. Fedorov had an inclination for physics. He wrote a large manuscript on the theory of electricity but refused to publish it without its experimental verification. However, fate seemed to be against it—Fedorov had no chance to use equipment of any physical laboratory and, gradually, he left physics. Only at the beginning of the new 19th century did he realized that the theory he developed a quarter of century before was, in essence, the theory of an electron.

The theory of atomic orbitals fully confirmed his conjecture—the structure of an atom is regular! The equivalent charges on a sphere could be stable only if they form a regular system. All the possible configurations (within an accuracy of the combinatorial equivalence) are exhausted by the Platonic and Archimedean bodies and two infinite series of prisms and antiprisms (Fig. 2) [22]. With due regard for quantum constraints, each electronic level (*s*, *p*, *d*, and *f*) can be represented
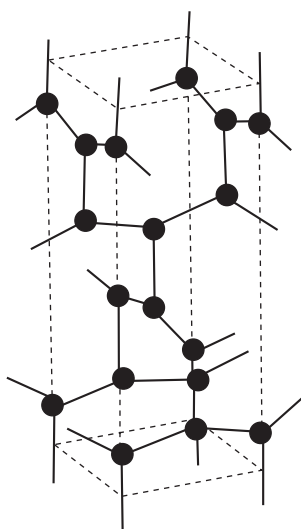
Fig. 4. Bravais parallelepiped of the hypothetical carbon structure described by the Fedorov group *I4r/amd*.

by two centrosymmetric simplexes of the four-dimensional space—the *s* level, by a segment; the *p* level, by a regular octahedron; the *d* level, by a pentagonal antiprism; and the *f* level, by a regular heptagonal antiprism.

It should be indicated that the atoms at the *d* and *f* levels have the symmetry forbidden for crystal structures in the Euclidean space. This results in partial destruction of the regularity of these levels in atoms that form a crystal structure with the Euclidean metrics [23]. The crystals consisting of such atoms have no defects only in the spherical, Lobachevskii, and Euclidean spaces with the dimension not exceeding three [24]. Therefore, the crystals with *d* and *f* elements in the Euclidean three-dimensional space should always contain defects (e.g., quasicrystals).

Only regular systems can be stable. Fersman, who dreamed of an institute of crystallography still in 1932 [25], wrote that everything which is not crystalline cannot be stable and should gradually be transformed into crystals. A crystal is such an ideal state of matter, a deep internal order to which nature strives… [26]. It should also be noted that any defect in a crystal is influenced by the gradient of the crystalline field and, therefore, such a defect would either be pushed out from the crystal or form a regular system with other similar defects [27]. In this way, the crystal "cures" itself.

The representation of the orbitals of chemical elements in the Mendeleev Table corresponds to their lowest energy level. The concrete physical conditions give rise to the corresponding displacements of electrons to other admissible levels [28]. Possibly, under certain extreme conditions, all the electrons of a carbon atom can fill the 2*p* level. Then, an extremely strong carbon modification is formed with multiple bonds [29] (Fig. 4). Possibly, the solid part of the earth's core consists of this carbon modification and is a fractal penetrating the iron–nickel melt [30].

It should also be indicated that all the regular features of the atomic shell are regularly reflected into the atomic nucleus, which should also have a regular structure. This is confirmed by the empirically determined magic numbers of protons and neutrons in the most stable nuclei—2, 8, 20, 50, 82, and 126. However, the nuclei are characterized not by spherical but by the hyperbolic regularity, and the heavier the nucleus, the more pronounced the absolute curvature of the corresponding Lobachevskii space. For example, the nuclei of the most stable isotopes of the inert gases can possess a diamond-like structure (because of the regular arrangement of the α particles constituting these nuclei [29]). The nuclei in which the regularity in the arrangement of α particles is violated are less stable. It is the solution of the problem of the atomic-nucleus structure which is based on the three theories developed by three Russian scientists—Lobachevskii (1792–1859), Mendeleev, and Fedorov—whose works predetermined the development of the world's science in the 21st century. It is most probable that the problem of low-temperature nuclear synthesis would also be solved via dissymmetrization of atomic nuclei.

FEDOROV GROUPS

It was fated that, instead of working with Mendeleev, Fedorov worked for ten years in the Geological Committee, where he composed geological maps of northwest Russia. As usual, Fedorov found brilliant solutions to routine geological problems, e.g., he developed a universal theodolite method in mineralogy and petrography (1893). He also designed a special device, the so-called Fedorov's stage, which allowed him to study by the latter method the optical properties at any point along any direction of a thin section of a rock.

The most famous Fedorov's work is associated with regularity in crystal structures. Fedorov was the first to derive 230 discrete groups of motion of the Euclidean space with a finite independent domain (1890) [31]. In Russia, these groups are justly called Fedorov groups. The story of their derivation was initiated by outstanding French mathematician Jordan (1838–1922) and German physicist Sohncke (1842–1897), a follower of Neumann (1798–1859), a prominent expert in crystal physics from Köenigsberg. Jordan in his memories entitled *On Groups of Motion* first stated that the discovery made by Galois (1811–1832) can also be interpreted as the discovery of groups of motion. At that time, Jordan had two students, Lie (1842–1899) and Klein (1849–1925), who "divided" the theory of groups into two parts—continuous groups were studied by Lie, and discrete groups, by Klein. These two theories were developed along different lines, so that today they can hardly be unified.

Jordan described in his memoirs [32] 174 groups of motion. Zohncke singled out from these groups the discrete groups directly related to the arrangement of atoms in crystal structures and found that the list of these groups was not complete. In 1874, Zohncke derived infinite regular systems of points on a Euclidean plane [33]. In 1869, he published the list of discrete groups of motion with the finite independent domain in the Euclidean space which consisted only of the first-order symmetry transformations [34]. However, he mistakenly included into this list one group twice. This mistake was revealed by his post graduate student Arthur Schönflies (1853–1928), who established that the groups can also be derived by using second-order transformations. Schönflies started their derivation and published intermediate results obtained. Fedorov paid attention to these publications and decided to complete the derivation of such groups started still in *Elements*. He sent his results to Schönflies and indicated some inaccuracies in Schönflies' derivation. In turn, Schönflies made the same. From this moment on, they entered into a lively correspondence, which concluded with the derivation of 230 groups by both scientists. Fedorov completed his derivation somewhat earlier [31]. This derivation had become a landmark in the development of natural sciences. Thus, finally, Mankind rigorously established that crystals are regular atomic formations which, by definition, should be described by the Fedorov groups.

The Schönflies monograph [35] received wide recognition in Europe and since then the Schönflies notation has been widely used. Even Russian crystallographers use this notation although it is important only for crystal classes. Germans did not forget Fedorov either. In 1896, Fedorov, an unknown laboratory assistant from the Geological Committee, was elected a Corresponding Member of the Bavarian Academy of Sciences. Klein was going to address the Russian Tzar and to ask him to make Fedorov also a member of the Russian Academy. Only Fedorov's resolute protest prevented Klein from doing so. Fedorov's colleagues working with him in Krasnotyr'insk (where Fedorov rather successfully prospected new copper deposits) could not believe the fact that they worked with a member of a German academy.

Neither Fedorov nor Schönflies made use of the lattice classification suggested by Bravais, who had made the first steps in group–theoretical crystallography. The results obtained by Bravais can be considered as the derivation of all the Fedorov groups possessed by lattices [36]. Altogether, there are 14 such groups. Another interpretation of the Bravais results is the derivation of all the different groups of the integral automorphisms of positive quadratic forms (arithmetic holohedry [36]), which seems to be the deepest meaning of the above classification. The best lattice classification should be based on the Fedorov theory of parallelohedra [37]. Delaunay completed this classification and made it extremely elegant by dividing all the lattices into 24 kinds [38]. This classification is the most appropriate for solving a number of applied problems (the unique choice of the main frame of reference in the lattice, the rigorous description of ideal habits of crystals according to Wulff, combinatorial–symmetric classification of the first Brillouin zones [39], etc.). It should be noted that modern handbooks on crystallography consider the types of the Bravais lattices insufficiently rigorously [40].

Fedorov's classification of all the space groups is much deeper than Schönflies' classification. Fedorov divided all the groups into symmorphic (whose crystal class is the stabilizer of the Fedorov group), hemisymmorhic (in which the axial hemihedry is the maximum stabilizer of the Fedorov group), and asymmorphic (all the remaining groups). This classification of groups considerably facilitated their derivation. Also, it turned out that this classification has a rather deep mathematical sense: there is a one-to-one correspondence between the symmorphic and finite groups of integral matrices. It is not accidental that D.K. Faddeev, a well-known expert in algebra, used Fedorov's classification as the basis for the table of representations of the Fedorov groups [41]. Faddeev's classification is more natural for crystallography than the classification suggested in [42], which is confirmed by [43]. We believe that it is necessary to publish a new edition of Faddeev's tables which would be based on the modern crystallographic nomenclature of the Fedorov groups [44]. The innovations introduced into the nomenclature in [45] seem to be excessive. The nomenclature of the Fedorov groups convenient for computer work is given in [46]; it is also useful for making compact tables of these groups (Table 1) [47].

Fedorov also derived regular systems purely algebraically. This derivation was then repeated by the mathematician Bogomolov [48]. The most widespread purely algebraic method of derivation of the Fedorov groups was suggested by Zassenhaus [49]. The method was used to derive all the four-dimensional Fedorov groups [50]. Geometrization of this algorithm made in [51] resulted in the compact analytical representation of the vector systems–the complete set of vectors in any crystal structure (Galiulin–Delone formula [52]).

However, not all of Fedorov's contemporaries realized the meaning of the Fedorov groups, the convenient classification of regular point systems following from these groups, and the crystal structures composed of such systems. Thus, Vernadsky (1843–1945) in his lectures on physical crystallography delivered at the Physics Faculty of Moscow State University in 1908 stated that crystallography can confine itself only to 32 crystal classes [53]. Fedorov was also criticized by Wulff (1863–1925) [54]. As a result, the Department of Crystallography of the Physics Faculty of Moscow State University made a much more modest contribution to the development of crystallography than the Department of Crystallography of the Mining Institute

Table 1. 219 abstractly different Fedorov groups

Pi		*P1+.*		
P2/m	*P2s/m*	*P2.*	*Pm.*	
P2/b	*P2s/b*	*P2s+.*	*Pb+.*	
I2/m	*I2.*		*Im.*	
I2/b			*Ib+.*	

> $219_{sym} = 73_{sym} + 54_{hemisym} + 2_{asym}$
> $(230 = 73 + 54 + 103)$
> * – enantiomorphic (11)
> + – uniform (10)
> . – degenerate (53)
> " – caleidoscopic (7)
> ' – Molnar (22)
>
> **32 CRYSTAL CLASSES OF MEROHEDRY**
>
> | | | | | | | | |
> |---|---|---|---|---|---|---|---|
> | *i* | 1 | | | | | | |
> | *2/m* | 2 | *m* | | | | | |
> | *mmm* | 222 | *mm2* | | | | | |
> | *4/mmm* | 422 | *4mm* | *4i2m* | *4/m* | 4 | | *4i* |
> | *6/mmm* | 622 | *6mm* | *6i2m* | *6/m* | 6 | | *6i* |
> | | | | | *3im* | 32 | *3m* | *3i* 3 |
> | *m3m* | 432 | | *4i3m* | *m3* | 23 | | |

Pmmm"	*Pmma*	*P222*	*Pmm2.*	*Pmc2s.*
Pccm	*Pmna*	*P222s*	*Pcc2.*	*Pmn2s.*
Pban	*Pbam*	*P2s2s2*	*Pma2.*	*Pca2s+.*
Pnnn	*Pmmn*	*P2s2s2s+*	*Pnc2.*	*Pna2s+.*
	Pnnm		*Pnn2.*	
	Pcca		*Pba2.*	
	Pnna			
	Pbcm			
	Pbcn			
	Pccn			
	Pnma			
	Pbca			
Cmmm'	*Cmcm*	*C222*	*Cmm2.*	*Cmc2s.*
Cccm	*Cmca*	*C222s*	*Ccc2.*	
Cmma			*C2mm.*	
Ccca			*C2mb.*	
			C2cm.	
			C2cb.	
Immm'	*Imma*	*I222*	*Imm2.*	
Ibam	*Ibca*	*I2s2s2s*	*Ima2.*	
			Iba2.	
Fmmm'		*F222*	*Fmm2.*	
Fddd			*Fdd2*	

P4/mmm"	*P4/mbm'*	*P422*	*P4mm.*	*P4smc.*	*P4i2m*	*P4i2sm*	*P4/m*	*P4s/m*	*P4.*	*P4i*
P4/mcc	*P4/nmm*	*P422s*	*P4cc.*	*P4snm.*	*P4i2c*	*P4i2sc*	*P4/n*	*P4s/n*	*P4s.*	
P4/nbm	*P4/mnc*	*P4s22*	*P4bm.*	*P4scm.*					*P4r+**	
P4/nnc	*P4s/mmc'*	*P4s22s*	*P4nc.*	*P4sbc.*	*P4im2*					
	P4s/mcm'	*P4r22**	*P4ic2*							
	P4s/nnm	*P4r22s**	*P4ib2*							
	P4s/mnm'	*P4in2*								
	P4s/nmc									
	P4/ncc									
	P4s/nbc									
	P4s/ncm									
	P4s/mbc									
I4/mmm'	*P4r/amd*	*I422*	*I4mm.*	*I4rmd*	*I4i2m*	*I4i2d*	*I4/m*	*I4r/a*	*I4.*	*I4i*
I4/mcm'	*I4r/acd*	*I4r22*	*I4cm.*	*I4rcd*	*I4im2*				*I4r*	
					I4ic2					

P6/mmm"	*P6s/mcm'*	*P622*	*P6mm.*	*P6smc.*	*P6i2m'*			*P6/m*	*P6s/m*	*P6.*		*P6i*	
P6/mcc	*P6s/mmc'*	*P6s22*	*P6cc.*	*P6scm.*	*P6i2c*					*P6s.*			
		P6rr22*			*P6im2"*					*P6rr**			
		P6r22*			*P6ic2*					*P6r*+*			
					P3im1					*P321*	*P3m1.*	*P3i*	*P3.*
					P3ic1					*P3r21**	*P3c1.*		*P3r*+*
					P3i1m					*P312*	*P31m.*		
					P3i1c					*P3r12**	*P31c.*		
					R3im					*R32*	*R3m*	*R3i*	*R3*
					R3ic						*R3c*		

Pm3m"	*Pm3n'*	*P432*		*P4i3m'*		*Pm3'*	*Pa3*	*P23*
Pn3n	*Pn3m'*	*P4s32*		*P4i3n'*		*Pn3*		*P2s3*
		P4r32*						
Im3m'	*Ia3d*	*I432*		*I4i3m'*	*I4i3d*	*Im3*	*Ia3*	*I23*
		I4r32						*I2s3*
Fm3m"	*Fd3m'*	*F432*		*F4i3m"*	*Fm3'*	*F23*		
Fm3c'	*Fd3c*	*F4r32*		*F4i3c*	*Fd3*			

Note: *s* is a twofold screw axis, *r* is a right-handed screw axis, and *i* is an inversion axis.

founded by Fedorov. The outstanding results of the Physics Faculty of Moscow State University were obtained by noncrystallographers. Thus, Vlasov (1908–1975) predicted the existence of long-range order in plasma [55] and bending of space by a growing crystal [56]. Ivanenko (1904–1994), together with Heisenberg, predicted the proton–neutron model of a nucleus (1932) and, together with Pomeranchuk, the synchrotron radiation (1945), formulated the problem of regularity of the global structure of the Universe (1994) [57]. A high level of crystallography at the Geology and Chemistry Faculties of Moscow State University was achieved by Fedorov's followers Bokii (1909–2001) [58], Belov (1891–1992) [59], Popov (1905–1963) [60], and Livinskaya (1920–1994) [61]. High level of crystallographic studies at the Moscow Institute of Steel and Alloys is also associated with the Leningrad school and its representative Shaskol'skaya (1913–1983) [62]. An important role in the development of Russian crystallography was also played by *Crystallographic University* created by Shubnikov, Bokii, and Shaskol'skaya [58].

The situation with the 17 two-dimensional Fedorov groups was quite different. They were derived by Fedorov in 1891 [63], although, in fact, all these groups can be found in Medieval Mauritanian ornaments [64]. Arabs decorated their mosques with such ornaments; they symbolized for Moslems infinite regular paths to Allah [65]. Unfortunately, there is still no handbook on two-dimensional crystallography, which seems to be a considerable gap in education, because many crystallographic problems can readily be understood in the two-dimensional case. As a result, two-dimensional crystallography is less used in practice than three-dimensional crystallography.

Table 2 lists the Bravais parallelograms for the 17 two-dimensional Fedorov groups. The independent domain of the group is hatched. Latin letters indicate the Wyckoff positions corresponding to this group. The symbol of the general Wyckoff position is given along with the symbols of the special positions, which are indicated at the corresponding symmetry elements (mirror planes and rotation axes). Table 2 has six columns. The first two columns correspond to holohedry and contain both symmorphic and nonsymmorphic groups in the order of a decrease in holohedry (along the vertical); the third, fourth, and fifth columns correspond to hemihedry (axial, symmorphic, and nonsymmorphic (*pb*) groups); the sixth column corresponds to tetartohedry (*p,* the sixth row).

To the merit of school teaching [7], which, in some instances, is better than teaching in modern higher schools, the elements of two-dimensional crystallography are considered in modern school handbooks. The level of understanding of crystallography and its relation to other sciences, and, first of all, to mathematics, physics, chemistry, and biology, is determined by realization of the meaning of the Fedorov groups.
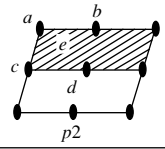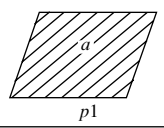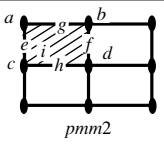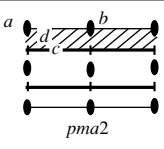
PERFECTIONISM
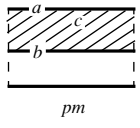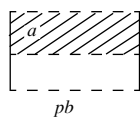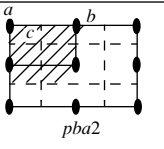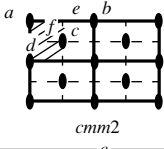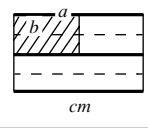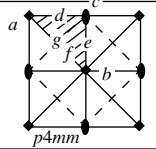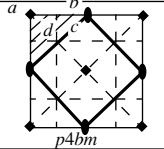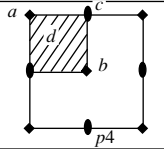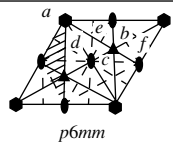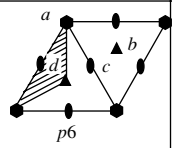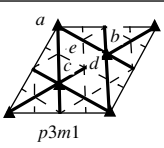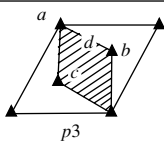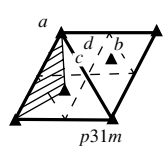
Fedorov started his philosophical work on perfectionism in 1872 and continued writing it for many years [66]. His wife, Ludmila Vasil'evna Fedorova, recollects the time before her marriage [1]: "… He told us his theory of perfectionism, which I then rewrote for him. Unfortunately, it was published with considerable censure gaps in those places where he mentioned Germans as perfectionists and predicted their future failure." The term perfectionism was coined by Fedorov and signifies the strive for perfection. Fedorov shows the universal nature of the main laws of evolution, which describe the development of the most diverse phenomena. Using the laws established in natural sciences (physics, in the broad sense), he considered the specific features of biology, psychology, and sociology. Fedorov believes that evolution can never be ended with the attainment of perfection, it can only strive for perfection. The most elegant and perfect elements, which are formed in the process of evolution, unavoidably disappear and make space for new even more perfect and harmonic elements. Perfection and harmony are attained only at the moments of their disappearance. When life is in full swing, only its unstable forms can develop. Life deals only with unstable forms.

Now, we draw your attention to the fact that double helix of DNA is associated with the action of a tenfold axis [67]. It is this axis that "protects" DNA from crystallization in the Euclidean space in a way similar to the *d* shell of an atom having the shape of a pentagonal antiprism (Fig. 5), which prevents the growth of an ideal crystal [23]. The crystal structure is uniquely reconstructed from its nucleus. It can have no mutations, so necessary for life. Thus, crystals signify death. I heard about this Fedorov concept from Alan MacKay, an English crystallographer, the founder of the theory of quasicrystals [68], who in turn referred to his teacher John Bernal (1901–1971). Bernal, the founder of protein crystallography planned to state his original position in understanding symmetry (the addition of a five-fold axis [69]) at the 7th International Congress of Crystallographers in Moscow in 1966, but he could not do it because of his illness. Instead, the Congress was addressed by Shubnikov, who, in Fedorov's spirit, called the crystallographers to keep the banner of pure crystallography [70].

The Fedorov groups form the main criterion separating crystal structures from all the other atomic formations, cannot be generalized. In the mathematical sense, Shubnikov's black and white groups and Belov's color groups are the subgroups of the Fedorov groups and, in fact, are the mathematical interpretations of these groups.

The latter studies of global crystal formation [71] allow one to emphasize the above thought of Fedorov and to state that only crystals signify depth. Other systems, e.g., quasicrystals, cannot be uniquely reconstructed and they have no long-range order. Therefore,

Table 2. Two-dimensional Fedorov groups

Holohedry		Hemihedry			Tetartohedry
nonsymmorphic	symmorphic	axial	planar symmorphic	planar nonsymmorphic	
p2		*p1*			
pmm2	*pma2*		*pm*	*pb*	
	pba2				
cmm2			*cm*		
p4mm	*p4bm*	*p4*			
p6mm		*p6*	*p3m1*		*p3*
			p31m		

they possess the ability (although only limited) to accommodate. One can reveal some primitive elements of life in these systems. A crystal with defects also has some primitive elements of life, because defects are always subjected to the action of a force—an electric field gradient [27, 72]. Formation of twins (considered in one of the first of Fedorov's articles [73]), OD structures [74] (whose theory is consistent with the theory of twinning (Fig. 6) and unique local continuation [75]), and the Penrose-like model of a quasicrystal [76] are some examples of the attempts of matter to avoid the attainment of any stable state. In all the occasions, these attempts are stopped by Pauling's approximants, ideal

crystal structures which, within the experimental accuracy, can be assigned noncrystallographic symmetry.

The simplest way of introducing mutations into a crystal is *twinning*, formation of a set of crystal structures related by symmetry transformations (twinning operations) not contained in the Fedorov group that describes the crystal structure. The atomic structure at the contact surface is another polymorphic modification of the structure (diamond–lonsdaleite, sphalerite–wurtzite, calcite–aragonite, pyrite–marcasite, etc.). Therefore, the study of the twinning laws is the most promising way of searching for new phases of a substance. Any plane of a crystal structure can play the part of a twinning plane. The axial polysynthetic twins are

formed due to multiple reflection in such planes. The surface separating individuals in a twin is called a *twin boundary* (contact surface). If the intergrowth surface is a plane dividing the twin structure into two parts, the twinned structures formed are called *contact twins*; otherwise, they are called *penetration twins*. The contact surface can have fractal indices.

Composition (contact) plane in twins may either coincide with the twinning plane (*mirror twin*) or not coincide with it. If a twinning axis lies in the composition plane, the twins are called *parallel*. If the twinning axis is perpendicular to the composition plane, the twins are called *normal*. If the composition planes are parallel to one another, the twins are called polysynthetic; otherwise, they are called cyclic. A twin is rational if the twinning operation in the Bravais reference system is written by rational numerals. These twins are ideal crystals, because they are described by the Fedorov group, which is a subgroup of the initial group.

The most widespread type of twins are *merohedral twins* in which the twinning operations are the symmetry operations of the holohedry of the individual that are not contained in its crystal class. In this case the corresponding groups of parallel translations of individuals are the same. Sometimes, the twin symmetry can be higher than the symmetry of an individual. These are the mimetic twins. The processes of twinning in crystals can be considered as elementary events of life.

> What is life? Fedorov wrote [66]: "Thorough consideration of the conditions of development always shows that evolution is not a continuous upward band, it is similar to branching observed in crystallization from solutions. Not all the branches of the crystalline substance propagate uniformly, the situation is quite different. Almost all the branches disappear one after another, i.e., stop growing immediately after the formation of more favorable conditions for crystallization. The vital branches are those which, because of the conditions of the solution drying, would continuously maintain the highest growth rate, and these are always the most miserable shapeless crystallizing (but not crystallized) masses. To some extent, everybody can observe this phenomenon in water freezing on a window. Of course, as soon as a delicate flakelike mass of growth figures is brought into contact with a saturated solution with an introduced well-shaped little crystal, the whole flakelike mass disappears at an amazing rate, and, instead, the introduced crystal starts growing. This fact is even more emblematic of the general law of development: delicate unstable growth figures are emblematic of motion, life, and eternal and continuous changes, whereas a crystal is emblematic of death, equilibrium, and immobility. No doubt, death is stronger than life, and the attainment of the constant conditions of mobility indicates the
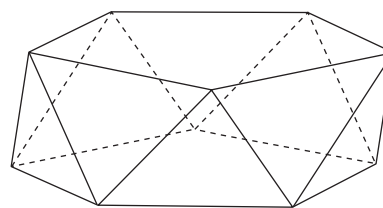
Fig. 5. Semiregular pentagonal antiprism.

moment of death and beginning of perfect crystallization."

Living matter cannot be stable. It seems that Nature created Man in the search for new ways of its own further development. Man differs from animals because of his strive for intellectual activity as necessary for him as food. Therefore, he must pay for being able to perform such an activity [77] in the way he pays for bread and meat. This is exactly what Fedorov himself did. Fedorov organized the Department of Crystallography at the Mining Institute with his own money despite the fact that at that time he was a Director, and a progressive one. "…Progress cannot be based on binding or unbinding hands of individual citizens, providing the most favorable conditions for an individual and the removal of all the obstacles in the development of the already accumulated forces" [66]. Fedorov was not appointed a Director by the order of the administration, he was selected by students. From 1895 to 1905, Fedorov was a Professor of geology at the St. Peter Academy at Petrovskoe–Razumovskoe (Now Timiryazev Agricultural Academy in Moscow). For ten years of his professorship, he was never invited to deliver a lecture on crystallography at Moscow University. Instead, once a week, the Moscow–St. Petersburg train stopped at the Petrovsko-Razumovskoe station to take a sole passenger, Professor Fedorov, who went to St. Petersburg to deliver one of his regular lectures on crystallography at the Mining Institute.

Up to the very end of his life, Fedorov was a Russian patriot. Because of the war with Germany, he refused to publish in German his work "The Realm of Crystals" [78], where he stated that goniometric data allows one to characterize crystals and draw some conclusions on their atomic structure. This work is still disputed by crystallographers throughout the world. English crystallographer Thomas Barker visited Fedorov to master this method. However, without Fedorov, this work had not been concluded.

UNITY OF SCIENCE BASED ON REGULARITY

Fedorov always stated that science is unified. This thought is also shared by modern scientists [79, 80]. And science can be unified only based on regularity. The most successful step in understanding the importance of such a science was made by Fedorov. The future of science lies in its unity. As an example of the

Figures 1–21

fruitful influence of such unity, we mention here the proof of the famous Fermat theorem by the mathematician Faddeev, who invoked for this almost all the branches of modern mathematics [81]. The solution was found by considering two theories—those of elliptic functions and modulated forms [82]. Both these theories are associated with the finite groups of integral matrices, i.e., lead to crystallography. Attempts of finding purely crystallographic (i.e., regularity-based) proof of this theorem were also undertaken by crystallographers [83].

It should also be noted that the Fedorov groups (discrete groups with finite independent domains) exist in all the spaces of constant curvatures [84–88], in particular, in Lobachevskii spaces. Fedorov deeply respected Lobachevskii. He wrote that Lobachevskii destroyed the artificial obstacle between mathematics and natural sciences by proving that geometry is based not on the indisputable truth but on the truth, which requires its experimental verification and confirmation [89].

This attitude to mathematics formulated still in the 19th century turned out to be extremely important not only for modern mathematics but even for teaching of

Fig. 6. Crystal twinning. Type of twins most often encountered and the symbols of twinning operations and composition planes.

No.	Twin	Twinning operation and composition plane
1	Manebach twin of orthoclase $KAlSi_3O_8$	$m(001)/(001)$
2	Baveno twin of orthoclase	$m(021)/(021)$
3	Right Carlsbad twin of orthoclase	$2[001]/(010)$
4	Left Carlsbad twin of orthoclase	–
5	Swallow tail (gypsum $CaSO_4 \cdot 2H_2O$)	$m(100)/(100)$
6	Polysynthetic plagioclase twin	$(001)/(001)$
7	Kalomine twin $Zn_4(Si_2O_7)(OH)_2 \cdot H_2O$	$m(001)/(001)$
8	Pseudohexagonal antigrowth twins of chrysoberyl $BeAl_2O_4$	–
9	Staurolite $Fe[OH]_2 \cdot 2Al_2SiO_5$	$m(032)/(032)$
10	Staurolit	$m(232)/(232)$
11	Cassiterite type (rutile TiO_2)	$m(101)/(101)$
12	Aragonite law (agaronite $CaCO_3$)	$m(110)/(110)$
13	ZnO twin	$m(001)/(001)$
14	Dophin'e twin of quartz SiO_2	$6[001]/(101)$
15	Brazilian twin of quartz	$m(110)/(110)$
16	Twin along pinacoid (Iceland spar)	$6[001]/(001)$
17	Diamond twin	–
18	Diamond twin along octahedron	$m(111)/(111)$
19	Spinel twins with respect to octahedron	$m(111)/(111)$
20	Iron cross (pyrite FeS_2)	$m(110)/(100)$
21	Maltese cross (pyrite FeS_2)	$m(110)/(100)$

mathematics in school. According to Arnol'd [90], mathematics is a part of physics and, similar to physics, is an experimental science. In the well-known article *Mathematics and Natural Sciences* (1930), Gilbert wrote that geometry is a part of physics. However, there is also an opinion that mathematics and physics have nothing in common. This brought the conclusion that geometry may be excluded from all the mathematical courses. And indeed, such an attempt has already been made in Russia [90, p. 11]. It is timely to compare the negative attitude of Chebyshev (1821–1894), one of the most prominent mathematicians of the 19th century, to Fedorov's *Elements*, who wrote that the modern science has no interest in such a geometry, with the first epigraph to the present article and Delaunay's words that "Geometry is a difficult science in which one has to think at every step." As follows from Fedorov's and Delaunay's works, one cannot state modern geometry and mathematics, in general, without invocation of regularity, i.e., crystallography.

CONCLUSIONS

To E.S. Fedorov

Deep in beautiful vials,
Similar to a sculptor–magician,
Colorless dense solutions
Create for us beautiful crystals.

Based on the vague entangling
Of thoughts, expectations, and dreams,
The human brain endlessly sculptures
Visions of fantastic creations.

The World of ethereal ideas
Is close to the mineral realm,
Shining like crystal faces
The dreams are instilled in our hearts.

January 2, 1919
N.A. Morozov "Crystals. Star Songs"
Books 1, 2. Moscow 1920–1921

These verses addressed to Fedorov, written on January 2, 1919, by N.A. Morozov (1854–1946), imprisoned for 23 years (1881–1905) in the Schliesselburg Fortress, provoke deep thinking. What is the crystal civilization? What contribution did crystallography make to World's history? What is Future in the light of the opposition of Life and Crystal? How deeply is Fedorov understood by our contemporaries? Mankind should always be grateful to Fedorova (1851–1936) for the memoirs about her husband [1], which, in fact, should be regarded as a literary masterpiece. Probably, Fedorov would have never become the Fedorov we know without the understanding and constant support of his wife. We are lacking Bokii, who brought us as closer to Fedorov. Just imagine that, being a child,

Bokii sat on Fedorov's knee! We should also be grateful to Nina Georgievna Furmanova, Bokii's daughter, who made a precious gift to us all— the reprints of the majority of Fedorov's articles collected by her grandfather and father and two volumes of the "Fundamentals of Differential and Integral Calculus" written by Fedorov [91, 92] still never mentioned in any of his bibliographies. The penetration into the crystallographic meaning of Fedorov's ideas was also facilitated by Shafranovskiĭ (1907–1994) and Frank-Kamenetskiĭ (1912–1994) [93].

The modern tendency of integration of various sciences made the restoration of the Fedorov Institute (created by Fedorov's brightest student, Boldyrev (1883–1946)) quite timely [94]. This Institute should be an international organization performing the studies in all the natural and humanitarian sciences under the UNESCO supervision.

ACKNOWLEDGMENTS

REFERENCES

1. L. V. Fedorova, *Our Workdays, Sorrows, and Joys. Memoirs Scientific Heritage* (Nauka, Moscow, 1992), Vol. 20.

2. E. S. Fedorov, *The Symmetry of Real Systems of Configurations. Imperial Petersburg Academy of Sciences. Scientific Heritage* (Nauka, Moscow, 1991), Vol. 16, p. 168.

3. E. S. Fedorov, *The Elements of the Study of Configurations. Transactions of the St. Petersburg Mineralogical Society* (1885), Part 21.

4. A. V. Gadolin, *Derivation of All Crystallographic Systems and Their Subsystems from One Common Origin* (Akad. Nauk SSSR, Moscow, 1954).

5. R. P. Feynman, R. B. Leighton, and M. Sands, *The Feynman Lectures on Physics* (Addison-Wesley, Reading, Mass., 1966; Mir, Moscow, 1977), Vol. 7.

6. R. V. Galiulin, Priroda (Moscow), No. 12, 20 (1991).

7. I. M. Smirnova and V. A. Smirnov, *Geometry. Handbook for the 7–9 Grades of Primary Schools* (Prosveshchenie, Moscow, 2001).

8. B. N. Delone, Izv. Akad. Nauk SSSR, Ser. Mat., No. 23, 365 (1959).

9. A. V. Shubnikov, Izv. Imp. Akad. Nauk, Ser. 6 **10** (9), 757 (1916).

10. R. V. Galiulin, Kvant, No. 11, 10 (1983).

11. I. M. Smirnova, *In the World of Polyhedra* (Prosveshchenie, Moscow, 1995).

12. I. M. Smirnova, *Geometry* (Prosveshchenie, Moscow, 1997).

13. A. N. Golovanova and R. V. Galiulin, in *Proceedings of International Conference on Mineralogy and Life* (Syktyvkar, 2000), p. 172.

14. B. N. Delone, Tr. Inst. Istor. Estestvozn. Tekh. Akad. Nauk SSSR **10**, 5 (1956).

15. P. N. Antonyuk, in *Proceedings of VII All-Russian School on Modern Problems of Gas Dynamics* (Moscow, 1991), p. 87.

16. M. Sh. Yakupov, in *Proceedings of International Conference on Geometrization of Physics* (Kazan, 1992), p. 1.

17. B. Delone and O. Zhitomirskiĭ, *Book on Geometrical Problems* (GITTL, Moscow, 1952).

18. I. Kh. Sabitov, Priroda (Moscow), No. 4, 19 (2000).

19. E. S. Fedorov, Zh. Russ. Fiz.–Khim. O–va **13** (4), 244 (1881).

20. S. A. Shchukarev and R. B. Dobrotin, *Crystallography* (Leningr. Gorn. Inst., Leningrad, 1955), No. 3, p. 81.

21. E. S. Fedorov, *Crystallography* (Leningr. Gorn. Inst., Leningrad, 1955), No. 3, p. 85.

22. R. V. Galiulin, Zh. Vychisl. Mat. Mat. Fiz. **43** (6), 791 (2003).

23. T. F. Veremeĭchik and R. V. Galiulin, in *Proceedings of International Conference on Crystal Genesis and Mineralogy* (St. Petersburg, 2001), p. 409.

24. R. V. Galiulin, in *Proceedings of International Conference on Carbon, Syktyvkar, 2003* (in press).

25. A. E. Fersman, Nauka Rabot. (Petersburg), No. 1, 13 (1920).

26. A. E. Fersman, Tr. Inst. im. M.V. Lomonosova, Ser. Obshch., No. 1, 39 (1932).

27. T. F. Veremeĭchik and R. V. Galiulin, Neorg. Mater. **38** (9), 1110 (2002).

28. A. A. Marakushev, *Periodic System of Extremum States of Chemical Elements* (Nauka, Moscow, 1987).

29. R. V. Galiulin, in *Proceedings of 2nd International Conference on Carbon: Fundamental Problems of Science, Materials Science, Technology* (Mosk. Gos. Univ., Moscow, 2003).

30. R. V. Galiulin, Vestn. Nizhegorod. Univ. im. N.I. Lobachevskogo, Fiz. Tverd. Tela, No. 1 (4), 152 (2001).

31. E. S. Fedorov, Zap. Imp. S.-Peterb. Mineral. O–va, No. 28 (2), 1 (1891).

32. C. Jordan, Ann. Math. Ser. 2 **2**, 167 (1868/1869); Ann. Math. Ser. 2 **2**, 322 (1868/1869).

33. L. Sohncke, J. Reine Angew. Math. **77**, 48 (1874).

34. L. Sohncke, *Entwickelung Einer Theorie der Kristallstruktur* (Tuebner, Leipzig, 1869).

35. A. Schönflies, *Kristallsystem und Kristallstruktur* (Teubner, Leipzig, 1891).

36. R. V. Galiulin and S. S. Ryshkov, *Problems in Crystallology* (Mosk. Gos. Univ., Moscow, 1971), p. 290.

37. E. S. Fedorov, Abh. K. Bauer Akad. Wiss. **11**, 465 (1899).

38. B. N. Delone, *Science and Mankind* (Znanie, Moscow, 1981), p. 160.

39. R. V. Galiulin, Kristallografiya **29** (4), 638 (1984) [Sov. Phys. Crystallogr. **29**, 378 (1984)].

40. B. K. Vaĭnshteĭn and R. V. Galiulin, in *Physical Encyclopedia* (1988), Vol. 1, p. 226.

41. D. K. Faddeev, *Tables of the Main Unitary Representations of the Fedorov Groups* (Akad. Nauk SSSR, Moscow, 1961; Pergamon Press, Oxford, 1964).

42. O. V. Kovalev, *Irreducible Representations of Space Groups* (Akad. Nauk Ukr. SSR, Kiev, 1961).

43. M. I. Aroyo and H. Wondratschek, Z. Kristallogr. **210**, 243 (1995).

44. *International Tables for X-ray Crystallography* (Kynoch, Birmingham, 1952), Vol. 1.

45. *International Tables for Crystallography*, Vol. A: *Space-Group Symmetry*, Ed. by T. Hahn (Reidel, Dordrecht, 1983).

46. R. V. Galiulin, Kristallografiya **40** (3), 461 (1995) [Crystallogr. Rep. **40**, 421 (1995)].

47. S. A. Bogomolov, *Derivation of Regular Systems by the Fedorov Method* (KUBUCh, Leningrad, 1932), Part 1; (ONTI, Leningrad, 1934), Part 2.

48. R. V. Galiulin, Kristallografiya **32** (3), 769 (1987) [Sov. Phys. Crystallogr. **32**, 452 (1987)].

49. H. Zassenhaus, Commun. Math. Helv. **21**, 117 (1948).

50. H. Brown, R. Bulow, J. Neubusser, H. Wondratschek, and H. Zassenhaus, *Crystallographic Groups of Four-Dimensional Space* (Wiley, New York, 1978).

51. R. V. Galiulin, *Matrix–Vector Method of Deviation of the Fedorov Group*, Available from VINITI, Moscow, No. 1094-69.

52. R. V. Galiulin and B. N. Delone, Dokl. Akad. Nauk SSSR **210** (1), 85 (1973) [Sov. Phys. Dokl. **18**, 285 (1973)].

53. V. I. Vernadsky, *Selected Works. Crystallography* (Nauka, Moscow, 1988), p. 66.

54. Y. V. Wulff, Z. Kristallogr. **45**, 433 (1908).

55. A. A. Vlasov, Vestn. Mosk. Univ., Nos. 3–4, 63 (1946).

56. L. S. Kuz'menkov, *Prosesses of Real Crystal Formation* (Nauka, Moscow, 1977), p. 221.

57. D. D. Ivanenko and R. V. Galiulin, in *Proceedings of 17th Workshop Dedicated to the 140th Birth Anniversary of Henri Poincare, Protvino, 1995*, p. 180.

58. G. B. Bokiĭ, *Problems of Crystallology* (GEOS, Moscow, 1999), p. 31.

59. N. V. Belov, *Structural Crystallography* (Akad. Nauk SSSR, Moscow, 1951).

60. G. M. Popov and I. I. Shafranovskiĭ, *Crystallography* (Vysshaya Shkola, Moscow, 1972).

61. Yu. G. Zagal'skaya, G. P. Litvinskaya, R. V. Galiulin, and V. S. Kovalenko, *Problems of Crystallology* (Mosk. Gos. Univ., Moscow, 1971), p. 284.

62. M. P. Shaskol'skaya, *Crystallography* (Vysshaya Shkola, Moscow, 1984).

63. E. S. Fedorov, Zap. Imper. S.-Peterb. Mineral. O–va, No. 28 (2), 345 (1891).

64. N. V. Belov, Kristallografiya **1** (5), 612 (1956) [Sov. Phys. Crystallogr. **1**, 482 (1956)].

65. Kh. S. Mamedov, Comput. Math. Appl. **128**, 511 (1986).

66. E. S. Fedorov, Izv. S.-Peterb. Biol. Lab. **8** (1), 25 (1906); Izv. S.-Peterb. Biol. Lab. **8** (2), 9 (1906).

67. M. D. Frank-Kamenetskiĭ, *The Most Important Molecule* (Nauka, Moscow, 1983).

68. A. L. Mackay, Kristallografiya **26** (5), 910 (1981) [Sov. Phys. Crystallogr. **26**, 517 (1981)].

69. J. D. Bernal and S. H. Carlise, Kristallografiya **13** (5), 927 (1968) [Sov. Phys. Crystallogr. **13**, 811 (1968)].

70. R. V. Galiulin, Usp. Fiz. Nauk **172**, 229 (2002).

71. R. V. Galiulin, in *Proceedings of Scientific Seminar on Nontraditional Problems of Geology* (Moscow, 2002), p. 52.

72. O. V. Konovalov and R. V. Galiulin, Kristallografiya **34** (3), 731 (1989) [Sov. Phys. Crystallogr. **34**, 435 (1989)].

73. E. S. Fedorov, Zap. S.-Peterb. Mineral. O–va, Ser. 2, No. 17, 381 (1882).

74. K. Dornberger-Schiff, *Lehrgang über OD-Strukturen* (Akademie, Berlin, 1966; Mosk. Gos. Univ., Moscow, 1966).

75. R. V. Galiulin, Kristallografiya **43** (2), 366 (1998) [Crystallogr. Rep. **43**, 332 (1998)].

76. D. Gratia, Usp. Fiz. Nauk **156** (2), 347 (1988).

77. V. M. Vil'chek, *Algorithms of History* (Prometeĭ, Moscow, 1989).

78. E. S. Fedorov, *The Realm of Crystals. Tables for Crystallochemical Analysis* (Zap. Akad. Nauk Fiz.–Mat. Otd., 1920), Vol. 36.

79. V. I. Arnol'd, Izv. Ross. Akad. Nauk, Ser. Yaz. Lit. **56** (2), 63 (1997).

80. V. I. Arnol'd, Usp. Fiz. Nauk **169** (12), 1311 (1999) [Phys. Usp. **42**, 1205 (1999)].

81. L. D. Faddeev, Chto Novogo Nauke Tekh., No. 2 (4), 112 (2003).

82. S. Singh, *Fermat's Enigma: the Epic Quest to Solve the World's Greatest Mathematical Problem* (Anchor Books, New York, 1998; Mosk. Tsentr Neprer. Mat. Obraz., Moscow, 2000).

83. I. A. Sheremet'ev, Kristallografiya **46** (2), 199 (2001) [Crystallogr. Rep. **46**, 161 (2001)].

84. V. V. Nikulin and I. R. Shafarevich, *Geometries and Groups* (Nauka, Moscow, 1983).

85. S. V. Rudnev, Comput. Math. Appl. **16** (5–8), 597 (1988).

86. R. V. Galiulin, Sci. Spectra **14**, 54 (1998).

87. R. V. Galiulin, Usp. Fiz. Nauk **172** (2), 229 (2002).

88. R. V. Galiulin and T. F. Veremeĭchik, in *Proceedings of International Conference Dedicated to M.P. Shaskol'-skaya, Moscow, 2003* (in press).

89. E. S. Fedorov, Zap. S.-Peterb. Mineral. O–va, Ser. 2, No. 30, 455 (1893).

90. V. I. Arnol'd, *What is Mathematics?* (Mosk. Tsentr Neprer. Mat. Obraz., Moscow, 2002).

91. E. S. Fedorov, *Fundamentals of Differential and Integral Calculus* (Imper. Akad. Nauk, St. Petersburg, 1903).

92. E. S. Fedorov, *Fundamentals of Differential and Integral Calculus, Drawings* (Imper. Akad. Nauk, St. Petersburg, 1903).

93. E. S. Fedorov, *Scientific Heritage* (Nauka, Leningrad, 1991), Vol. 16.

94. I. I. Shafranovskiĭ, *Crystallography in the USSR, 1917–1991* (Nauka, St. Petersburg, 1996).

Translated by L. Man

STRUCTURE
OF INORGANIC COMPOUNDS

Twin Orthorhombic Structure of Haüyne from Sakrofano (Italy)

N. B. Bolotina*, R. K. Rastsvetaeva*, A. N. Sapozhnikov**, and A. A. Kashaev***

* Shubnikov Institute of Crystallography, Russian Academy of Sciences,
Leninskiĭ pr. 59, Moscow, 119333 Russia
e-mail: rast@ns.crys.ras.ru
** Vinogradov Institute of Geochemistry and Analytical Chemistry, Siberian Division,
Russian Academy of Sciences, ul. Favorskogo 1a, Irkutsk, 664033 Russia
*** Irkutsk State University of Transport Communications, Irkutsk, Russia

Received April 8, 2003

Abstract—The structure of haüyne from Sakrofano (Italy) is solved using the superstructure reflections, which double the unit cell parameters in three directions. The cubic symmetry of the diffraction pattern of haüyne results from the twinning of the equidimensional orthorhombic components by the [111] threefold axis. The structure is refined in the orthorhombic space group $Pba2$ with the unit cell parameters $a = b = 12.872(7)$ Å and $c = 9.102(3)$ Å in the anisotropic approximation to $R = 0.043$ for 1737 reflections. Compared to high-potassium haüyne from Arissia (Italy), the mineral studied contains potassium in smaller amounts and the distribution of K, Na, and Ca atoms over four body diagonals of the cell is ordered, which apparently causes the lowering of symmetry from cubic to orthorhombic. © 2003 MAIK "Nauka/Interperiodica".

INTRODUCTION

Haüyne belongs to the sodalite group of aluminosilicate minerals. The ideal sodalite framework has cubic symmetry. The $(Al_6Si_6O_{24})^{6-}$ rings formed by six tetrahedra alternate parallel to each other along the $\langle 111 \rangle$ axis of the unit cell with a parameter of ~9 Å. The centers of the rings lie on the body diagonals of the cube, and the large cavities of the framework are occupied by large cations (Na, K, Ca) and anions or anionic groups (SO_4^{2-}, S^{2-}, Cl^-). The shape and size of the cavities can vary through rotations of the framework tetrahedra for better fitting to ions or ionic groups of different sizes. Sodalite $Na_8(Al_6Si_6O_{24})Cl_2$ has a stoichiometric composition, and the symmetry of its structure is described by the cubic space group $P\bar{4}3n$ [1]. A more complex situation occurs with sulfate derivatives of sodalite minerals (such as haüyne, nosean, and lazurite) with the general formula $(Na,Ca,K)_8(Al_6Si_6O_{24})(SO_4,S,Cl)_2$, because almost all these minerals are nonstoichiometric and have vacancies at the sites of the framework ions. The same mineral often has several varieties that differ in physical properties (for example, isotropic and anisotropic lazurites), visual appearance (color and shape of the specimens), and, what is more important in this context, in the type of diffraction pattern: almost all the patterns contain superstructure or satellite reflec-

tions, or their combination, in addition to the main reflections of the cubic sodalite structure.

Interest in the structure of sulfur-containing sodalites is largely associated with the diversity of structural modifications of a particular mineral from different deposits. Haüyne of the general formula $(Na,Ca,K)_8(Al_6Si_6O_{24})(SO_4,Cl)_2$ is not an exception to this rule. The present work continues a series of our investigations [2–8] aimed at systematizing available structural data for sulfur-containing sodalites and establishing correlations between the composition and structure of these minerals. We studied the structure of haüyne from the Cavalluccio deposit (Sakrofano, Italy). The specimens were kindly placed at our disposal by Prof. A. Maras (Rome University).

EXPERIMENTAL

The mineral is represented by colorless transparent isotropic crystals with the refractive index $n = 1.507$. The chemical composition was determined by microprobe analysis. The formula calculated for $Z = 2$ is $(Na_{4.44}K_{1.09}Ca_{2.36})(Si_{5.82}Al_{6.18})O_{24}(SO_4)_{1.96}Cl_{0.01}$.[1] Weak superstructure reflections are observed in rotating-crystal and reciprocal-lattice X-ray photographs indicating the doubling of the lattice period $a = 9.118 \times 2 = 18.236$ Å

---

[1] A minor excess of positive charge (+0.14) is most likely associated with the experimental error.

and fitting the space groups $I23$, $I2_13$, and $I432$. The most intense superstructure reflections observed in reciprocal-lattice and powder X-ray photographs were 431 and 433 with interplanar distances $d = 3.58$ and 3.13 Å, respectively.

The diffraction pattern and the set of systematic absences indicate that the crystal is cubic (Laue class $m3$), its symmetry is $Ia3$, and the unit cell parameter is twice as large as that of the sodalite cell. However, our earlier attempts to determine the structure of the mineral were unsuccessful, since they resulted in an R factor larger than 20%. We recommended the studies after our recent determination of the structure of lazurite from the Baĭkal region [7, 8], which is known as isotropic cubic lazurite. The diffraction pattern of this mineral with due regard for numerous satellites, which are incommensurate to the period of the sodalite lattice, also corresponds to the $m3$ point symmetry. It was found that the real symmetry of the modulated lazurite is lower than the cubic symmetry. The cubic symmetry of the diffraction pattern was explained by the twinning of three equidimensional orthorhombic components by the [111] axis of the cubic lattice. We assumed that the observed cubic symmetry of the diffraction pattern of haüyne also stems from the twinning of equidimensional orthorhombic components by the [111] axis.

First, a set of 1747 measured reflections with intensities $I > 3\sigma(I)$, which was obtained on an Enraf–Nonius diffractometer (Mo radiation), was indexed in the cubic I-centered cell with the parameter $a = 18.204(1)$ Å. The unit cells of the first, second, and third components of the twin are related to the cubic cell as follows:

$$\mathbf{a}_1 = (\mathbf{a}_{cub} - \mathbf{b}_{cub})/2; \quad \mathbf{b}_1 = (\mathbf{a}_{cub} + \mathbf{b}_{cub})/2; \quad \mathbf{c}_1 = \mathbf{c}_{cub}/2;$$

$$\mathbf{a}_2 = (\mathbf{a}_{cub} - \mathbf{c}_{cub})/2; \quad \mathbf{b}_2 = \mathbf{b}_{cub}/2; \quad \mathbf{c}_2 = (\mathbf{a}_{cub} + \mathbf{c}_{cub})/2;$$

$$\mathbf{a}_3 = \mathbf{a}_{cub}/2; \quad \mathbf{b}_3 = (\mathbf{b}_{cub} - \mathbf{c}_{cub})/2; \quad \mathbf{c}_3 = (\mathbf{b}_{cub} + \mathbf{c}_{cub})/2,$$

where $\mathbf{a}_{cub}$, $\mathbf{b}_{cub}$, $\mathbf{c}_{cub}$ is the cubic cell basis and $\mathbf{a}_i$, $\mathbf{b}_i$, $\mathbf{c}_i$ ($i = 1, 2, 3$) is the basis of the corresponding twin component. The parameters of the new unit cell are $a = b = 12.872(7)$ Å, $c = 9.102(3)$ Å, and $\alpha = \beta = \gamma = 90°$. The transformation of the reflection indices follows the same rule as the transformation of the basis vectors of the cubic cell; that is,

$$h_1 = (h_{cub} - k_{cub})/2; \quad k_1 = (h_{cub} + k_{cub})/2; \quad l_1 = l_{cub}/2;$$

$$h_2 = (h_{cub} - l_{cub})/2; \quad k_2 = k_{cub}/2; \quad l_2 = (h_{cub} + l_{cub})/2;$$

$$h_3 = h_{cub}/2; \quad k_3 = (k_{cub} - l_{cub})/2; \quad l_3 = (k_{cub} + l_{cub})/2.$$

All the (h_{cub}, k_{cub}, l_{cub}) reflections with three even indices are indexed in the basis of each component, and their intensities are equal to the sums of intensities of the corresponding overlapped reflections. All the remaining reflections have one even and two odd indices in the I-centered cubic lattice. The reflections with an even l_{cub}, k_{cub}, or h_{cub} index are indexed only in the basis of the first, second, or third lattice and generated by the corresponding twin component. According to the requirements of the JANA program [9], which was used for the structural calculations, each reflection was preliminarily reindexed in its own lattice and provided with the component number. The reflections that are common for all components can be indexed in the lattice of any component (for example, the first component), and the component number is of no significance for them. Since we can average in this case only the nonoverlapping symmetry-equivalent reflections separately for each component, the symmetry group is chosen based on the results of the refinement of the structural parameters in different groups.

The atomic coordinates of the lazurite structure [8] were transformed from the cubic cell with the a parameter into the orthorhombic cell with the $a\sqrt{2}$, $a\sqrt{2}$, and a parameters and used as starting atomic coordinates for haüyne. Among the orthorhombic space groups satisfying the systematic absences, $Pba2$ was the only space group in which a small R factor was obtained. Although some weak reflections in the data set violated the systematic absence $h0l$: $h = 2N$, the refinement in the $Pmm2$ and $P222$ orthorhombic groups without systematic absences resulted in a large R factor. The R factor close to that obtained in the $Pba2$ group was also attained in the $P2$ group, but, in this case, the number of atoms was twice as large because of lower symmetry.

Note that, in the $P\bar{4}$ group, the F_{calcd} values of the reflections $h0l$: $h = 2N + 1$, which should be absent in the $Pba2$ group, coincide rather closely with the F_{obs} values. However, the R factors in the tetragonal group $P\bar{4}$ are larger than those in the $Pba2$ group. We assume that, similar to lazurite [8], this mineral is inhomogeneous in structure and part of its domains is described by the tetragonal group of symmetry better than by the orthorhombic group. Nonetheless, we finally decided in favor of the $Pba2$ group.

The ten worst reflections, for which $|F_{obs} - F_{calcd}| > 20\sigma(F_{obs})$, were rejected from the data set with $I > 3\sigma(I)$. The remaining 1737 reflections were included in the least-squares procedure. The structural parameters were refined in the anisotropic approximation of thermal vibrations on the F criterion using the weighting scheme $w(F_{obs}) = 1/\sigma^2(F_{obs})$ to the weighted factor $wR = 0.043$. The refined atomic coordinates and equivalent thermal parameters are listed in Table 1. The interatomic distances are given in Tables 2 and 3.

RESULTS AND DISCUSSION

The structure of haüyne in the projections onto the (001) and (100) planes is shown in Figs. 1 and 2, respectively. The T positions are located at the centers of the oxygen tetrahedra of the framework. Their population with silicon and aluminum is only in part ordered in distinction to haüynes from Arissia [2], which have a close composition, and lazurites with an ordered framework [3, 4]. As follows from the interatomic distances (Table 2), the $T(1)$ and $T(2)$ positions are occupied

BOLOTINA *et al.*

Table 1. Atomic coordinates, thermal parameters U_{eq}, and site occupancies q

Position	x	y	z	U_{eq}, Å^2	q
$T(1)$	0.2568(4)	0.2513(5)	0.250(1)	0.007(2)	1
$T(2)$	0.7497(5)	0.7410(6)	0.751(1)	0.017(2)	1
$T(3)$	0.1193(5)	0.8793(7)	0.498(1)	0.005(2)	1
$T(4)$	0.6308(6)	0.3718(9)	0.505(1)	0.021(3)	1
$T(5)$	0.3718(6)	0.8864(8)	−0.006(1)	0.017(2)	1
$T(6)$	0.8760(6)	0.3720(8)	0.009(1)	0.013(2)	1
O(1)	0.198(1)	0.144(2)	0.348(2)	0.049(9)	1
O(2)	0.647(1)	0.701(2)	0.642(2)	0.039(8)	1
O(3)	0.187(1)	0.830(2)	0.366(2)	0.021(6)	1
O(4)	0.661(1)	0.315(1)	0.661(2)	0.009(5)	1
O(5)	0.351(2)	0.003(1)	0.032(3)	0.032(8)	1
O(6)	0.008(1)	0.350(2)	−0.039(2)	0.010(6)	1
O(7)	0.150(1)	−0.001(1)	0.540(2)	0.012(6)	1
O(8)	−0.001(1)	0.149(2)	0.474(2)	0.020(7)	1
O(9)	0.344(1)	0.815(2)	0.156(3)	0.039(8)	1
O(10)	0.814(2)	0.330(2)	0.867(3)	0.064(10)	1
O(11)	0.837(1)	0.305(2)	0.125(2)	0.014(5)	1
O(12)	0.315(1)	0.850(2)	0.840(2)	0.018(6)	1
Ca(1)	0.327(1)	0.010(2)	0.318(2)	0.044(8)	0.35
Ca(2)	0.5004(7)	0.786(2)	0.711(2)	0.260(13)	1
Na(1)	0.262(1)	−0.011(2)	0.264(2)	0.026(6)	0.65
Na(2)	−0.001(1)	0.232(1)	0.230(2)	0.006(3)	0.6
Na(3)	0.715(1)	0.497(1)	0.786(2)	0.100(1)	1
K	−0.002(1)	0.171(2)	0.173(2)	0.028(6)	0.4
S(1)	0	0	−0.045(3)	0.39(5)	1
O(13)	0.018(3)	−0.059(6)	0.077(6)	0.22(4)	1
O(14)	−0.044(4)	0.075(7)	−0.136(9)	0.32(5)	1
S(2)	0.5	0	0.494(8)	0.37(7)	1
O(15)	0.516(4)	0.112(7)	0.384(7)	0.10(3)	0.5
O(16)	0.413(3)	0.022(3)	0.389(5)	0.04(1)	0.5
O(17)	0.406(10)	−0.068(13)	0.566(11)	0.7(2)	1

Note: The T positions are populated as follows: $T(1)$ and $T(2)$ contain Al; $T(3)$ and $T(6)$, Si; $T(4)$, (0.75Al + 0.25Si); $T(5)$, (0.75Si + 0.25Al). The Ca(1) position contains 0.2Ca + 0.15K.

Table 2. Interatomic T–O distances in the framework tetrahedra

$T(1)$–O(1)	1.81(2)	$T(2)$–O(2)	1.73(2)	$T(3)$–O(2)	1.70(2)
O(3)	1.63(2)	O(4)	1.70(2)	O(3)	1.62(2)
O(9)	1.76(2)	O(10)	1.76(3)	O(7)	1.63(2)
O(11)	1.70(2)	O(12)	1.64(2)	O(8)	1.58(2)
	⟨1.72⟩		⟨1.71⟩		⟨1.63⟩
$T(4)$–O(1)	1.69(2)	$T(5)$–O(5)	1.56(2)	$T(6)$–O(5)	1.66(2)
O(4)	1.65(2)	O(6)	1.65(2)	O(6)	1.77(2)
O(7)	1.72(2)	O(9)	1.77(3)	O(10)	1.61(3)
O(8)	1.74(2)	O(12)	1.64(2)	O(11)	1.46(2)
	⟨1.70⟩		⟨1.65⟩		⟨1.62⟩

mainly by Al, the $T(3)$ and $T(6)$ tetrahedra are occupied by Si, and the $T(4)$ and $T(5)$ tetrahedra accommodate Al and Si in comparable amounts with the prevalence of Al in the former tetrahedron and Si in the latter tetrahedron.

The origin of structural modifications in sodalite minerals is not entirely clear. However, it was found [10] that, in these minerals, the high potassium content prevents the formation of modulated structures. In haüynes from Sakrofano [11], Monte Somma [12], and Arissia [2], whose structures were studied earlier, the potassium content lies in the range from 0.9 to 1.4 atoms per formula unit (the maximum amount of potassium was found in the specimen from Arissia).

Table 3. Interatomic distances for intraframework cations

Ca(1)–O(1)	2.41(3)	Ca(2)–O(2)	2.28(2)	Na(1)–O(1)	2.29(3)	Na(2)–O(1)	3.00(2)
O(3)	2.98(3)	O(4)	2.50(2)	O(3)	2.44(3)	O(3)	2.81(2)
O(5)	2.62(2)	O(6)	2.43(3)	O(5)	2.41(3)	O(6)	2.88(3)
O(9)	2.93(3)	O(8)	2.79(3)	O(7)	2.90(3)	O(8)	2.46(3)
O(11)	2.96(3)	O(10)	2.83(3)	O(9)	2.67(3)	O(9)	2.39(2)
O(15)	2.82(6)	O(12)	2.78(2)	O(16)	2.30(4)	O(11)	2.47(2)
O(15)	2.63(7)	O(17)	2.6(2)			O(13)	2.64(8)
O(17)	2.67(12)					O(15)	2.46(9)
Na(3)–O(4)	2.69(3)	K–O(3)	2.95(2)	S(1)–O(13)	1.4(1) × 2	S(2)–O(15)	1.8(1) × 2
O(5)	2.84(3)	O(8)	2.75(3)	O(14)	1.4(1) × 2	O(16)	1.5(1) × 2
O(7)	2.39(3)	O(9)	2.76(3)			O(17)	1.6(1) × 2
O(10)	2.61(3)	O(11)	2.72(3)				
O(12)	2.40(3)						
O(14)	2.53(6)						

Note: For S(2), the statistical environment is given at the 50% probability level.

Their structures differ mainly in the number of orientations adopted by sulfate groups and in the distribution of intraframework cations. For example, in haüyne studied in [11], all the S tetrahedra show the same orientation, whereas high-potassium haüyne [2] and the haüyne described in [12] are characterized by two orientations. Large K, Ca, and Na cations are uniformly distributed over all the body diagonals of the cube; thus, the cubic symmetry is retained in all three specimens.

The structure of the specimen from the Cavalluccio deposit differs substantially from the structures of the haüynes described earlier. For simplicity of the refinement, we located both independent sulfur atoms in special positions. In reality, these positions split into several subpositions, which are related by the twofold axis. The difference Fourier synthesis calculated for the set of atomic coordinates not including the sulfur atoms and the oxygens of the sulfur environment revealed the following features. At the S(1) site, three pairs of split subpositions are observed, namely, (±0.035, 0, 0.04), (0, ±0.05, 0.04), and (0, ±0.04, −0.04). At the S(2) site, there exist two pairs of subpositions, (0.5, ±0.037, 0.475) and (±0.53, 0, 0.525). The positions of the oxygen atoms in the sulfur environment are even less definite, as indicated by large values of their thermal parameters. The oxygen maxima are hardly distinguished in the electron-density clouds around the sulfur positions. Therefore, the positions of the oxygen atoms of the sulfur environment given in Table 1 are conventional and allow us to estimate the situation around the sulfur atoms qualitatively rather than quantitatively. The tetrahedra around the S(1) atoms degenerate into distorted squares, and the ellipsoids of thermal vibrations of both the S(1) atom and the oxygen atoms in its environment are large and flatten: they actually degenerate into ellipses perpendicular to the plane of the square. For the oxygen atoms surrounding S(2), Table 1 presents the positions of two equally probable orientations of tetrahedra, which are contracted along directions perpendicular to the c axis of the unit cell.

The $(Na_{4.5}K_{1.1}Ca_{2.4})_{\Sigma 8}$ composition of the intraframework cations obtained in the refinement agrees with the empirical formula. The large cations are distributed over four independent structural positions, two of which are split into two positions each [Na(1)–Ca(1) and Na(2)–K]. The K atoms are located in large polyhedra formed by four oxygen atoms of the framework. The K–O distances are equal to 2.72–2.95 Å. A number of potassium atoms are also located at the Ca(1) position in the eight-vertex polyhedron, which
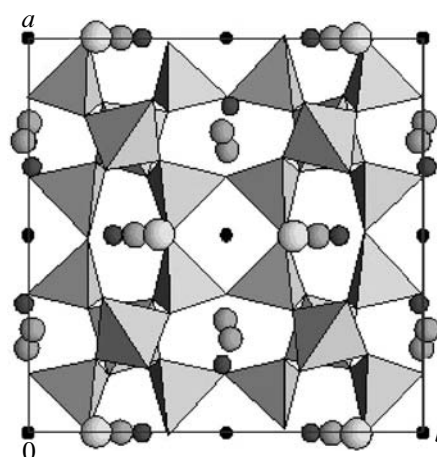

Fig. 1. Haüyne structure in the projection onto the (001) plane. The K, Na, and Ca positions are indicated by large open circles, medium-size shaded circles, and small closed circles, respectively. The positions of sulfur atoms are indicated by the smallest closed circles.
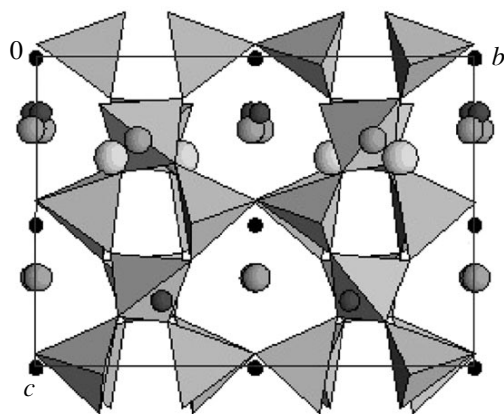
Fig. 2. Haüyne structure in the projection onto the (100) plane. The designations are the same as in Fig. 1.

includes the O atoms of the S(2) environment. The cation-to-anion distances are 2.41–2.98 Å. Four body diagonals in the structure studied are inequivalent because of the positional displacements of the intraframework atoms and different occupancies of their positions. Most of the potassium and calcium atoms lie on two diagonals and occupy positions similar to those in the structure of haüyne from Arissia. The two other diagonals are populated mainly with sodium atoms and contain also small amounts of Ca and K, so that potassium completely substitutes for sodium at the position found in the structure of haüyne from Arissia. Thus, the ordering of the Na and K (Ca) intraframework cations is apparently responsible for the lowering of symmetry of haüyne from cubic to orthorhombic.

REFERENCES

1. I. Hassan and H. D. Grundy, Acta Crystallogr., Sect. B: Struct. Sci. **40** (1), 6 (1984).

2. V. G. Evsyunin, A. N. Sapozhnikov, R. K. Rastsvetaeva, and A. A. Kashaev, Kristallografiya **41** (4), 659 (1996) [Crystallogr. Rep. **41**, 622 (1996)].

3. V. G. Evsyunin, A. N. Sapozhnikov, A. A. Kashaev, and R. K. Rastsvetaeva, Kristallografiya **42** (6), 1014 (1997) [Crystallogr. Rep. **42**, 938 (1997)].

4. R. K. Rastsvetaeva, A. N. Sapozhnikov, V. L. Tauson, and A. A. Kashaev, Dokl. Akad. Nauk **356** (6), 773 (1997).

5. V. G. Evsyunin, R. K. Rastsvetaeva, A. N. Sapozhnikov, and A. A. Kashaev, Kristallografiya **43** (6), 1057 (1998) [Crystallogr. Rep. **43**, 999 (1998)].

6. R. K. Rastsvetaeva, N. B. Bolotina, A. N. Sapozhnikov, *et al.*, Kristallografiya **47** (3), 449 (2002) [Crystallogr. Rep. **47**, 404 (2002)].

7. N. B. Bolotina, R. K. Rastsvetaeva, A. N. Sapozhnikov, *et al.*, Kristallografiya **48** (1), 14 (2003) [Crystallogr. Rep. **48**, 8 (2003)].

8. N. B. Bolotina, R. K. Rastsvetaeva, A. N. Sapozhnikov, *et al.*, Kristallografiya **48**, 779 (2003) [Crystallogr. Rep. **48**, 721 (2003)].

9. V. Petricek and M. Dusek, *JANA98: The Crystallographic Computing System (User Manual)* (Inst. of Physics, Academy of Sciences of the Czech Republic, Praha, 2000).

10. D. Tailor, Contrib. Mineral. Petrol. **16**, 172 (1967).

11. I. Hassan and H. D. Grundy, Can. Mineral. **29**, 123 (1991).

12. J. Lohn and H. Schulz, Neues Jahrb. Mineral., Abh. **109** (3), 201 (1968).

Translated by I. Polyakova

STRUCTURE
OF INORGANIC COMPOUNDS

Dedicated to the 60th Anniversary
of the Shubnikov Institute of Crystallography
of the Russian Academy of Sciences

Synthesis and Crystal Structure of Low Ferrialuminosilicate Sanidine

Yu. S. Lebedeva[1], D. Yu. Pushcharovsky[1,2], M. Pasero[3], S. Merlino[3], A. A. Kashaev[4],
V. K. Taroev[4], J. Goettlicher[5], H. Kroll[6], H. Pentinghaus[5], L. F. Suvorova[7],
H. Wulf-Bernodat[5], and V. V. Lashkevich[4]

[1] *Department of Geology, Moscow State University, Vorob'evy gory, Moscow, 119992 Russia*
e-mail: dmitp@geol.msu.ru

[2] *Shubnikov Institute of Crystallography, Russian Academy of Sciences, Leninskiĭ pr. 59, Moscow, 119333 Russia*

[3] *Dipartimento de Scienze della Terra, Universita de Pisa, v. S. Maria 53, Pisa, 56126 Italy*

[4] *Institute of the Earth's Crust, Siberian Division, Russian Academy of Sciences,*
ul. Lermontova 128, Irkutsk, 664033 Russia

[5] *Institut für Technishe Chemie, Berech Wasser- und Geotechnologie (ITC–WGT), Abteilung Technishe Mineralogie Geb. 42,*
P.O. Box 3640, Karlsruhe, D76344 Germany

[6] *Westfalische Wilhelms Universität, Munster Institut für Mineralogie,*
Correnssrabe 24, Munster, D48149 Germany

[7] *Institute of Geochemistry, Siberian Division, Russian Academy of Sciences, ul. Favorskogo 1a, Irkutsk, 664033 Russia*

Received December 30, 2002

Abstract—Iron-containing potassium feldspar crystals are prepared using the hydrothermal synthesis in an alkaline medium at temperatures ranging from 500 to 526°C. The crystal structure of the synthetic potassium feldspar is refined [Ital Structures diffractometer, MoK_α radiation, 1327 unique reflections with $|F| > 4\sigma(F)$, anisotropic approximation, $R(F) = 0.044$]. It is established that, under the given preparation conditions, the synthesis leads to the formation of the monoclinic modification with the following unit-cell parameters: $a = 8.655(7)$ Å, $b = 13.101(9)$ Å, $c = 7.250(8)$ Å, $\beta = 116.02(2)°$, space group $C2/m$, and $Z = 4$. The cation distribution over crystallographically inequivalent tetrahedral positions $T(1)$ and $T(2)$ is determined and justified using X-ray diffraction data. According to this distribution, the iron-containing potassium feldspar is assigned to the low ferrialuminosilicate sanidine. The proposed structural formula $K_{A=0.99}(Si_{1.2}Fe_{0.5}Al_{0.3})_{\Sigma T(1)=2}(Si_{1.81}Al_{0.19})_{\Sigma T(2)=2}O_8$ agrees well with the data of the electron microprobe analysis. It is revealed that iron occupies the $T(1)$ position and manifests itself as a majority rather than minority impurity element with respect to aluminum. © *2003 MAIK "Nauka/Interperiodica".*

INTRODUCTION

Feldspars belong to the group of the most important rock-forming minerals. These are framework silicates of the general formula AT_4O_8, where A stands for alkali and alkaline-earth cations (Na$^+$, K$^+$, Rb$^+$, Ca^{2+}, NH$_4^+$) located in large-sized holes in the structure and T represents small-sized tetrahedrally coordinated cations (Si^{4+}, B^{3+}, Al^{3+}, Fe^{3+}, Ga^{3+}, Ge^{4+}, P^{5+}).

As early as 1933, Taylor [1] used sanidine as an example and was the first to determine the main features of the crystal structure of minerals in this group. At present, a large number of structural studies have dealt with feldspars. The majority of these works are concerned primarily with the investigation into the specific features of the distribution of silicon and aluminum cations over tetrahedral positions, i.e., with the analysis of the structural state of the crystals.

It is known that the lowering of symmetry of feldspars is due to ordering of tetrahedrally coordinated cations. A completely disordered modification with a uniform distribution of aluminum and silicon between two eightfold positions $T(1)$ and $T(2)$, namely, the end-member high sanidine, is characterized by monoclinic symmetry. A completely disordered high sanidine of this type at an equal aluminum content in both tetrahedral positions was first described by Ferguson *et al.* [2]. When going over to more ordered feldspars (such as orthoclase and microcline), the symmetry changes from monoclinic to triclinic and aluminum at different contents is disordered over four cation positions [$T(1o)$,

$T(1m)$, $T(2o)$, $T(2m)$] in such a way that the maximum aluminum content is observed at the $T(1o)$ position [3].

However, the specific features in the distribution over the aforementioned tetrahedral positions of other atoms contained in smaller amounts (as compared to aluminum and silicon atoms) are not as well understood. Among the trivalent cations involved in natural feldspars, second in importance to aluminum is Fe^{3+}. The mean Fe^{3+} content, as a rule, does not exceed 0.5 wt % [4] and, only in some samples, reaches several percent. It is worth noting that the maximum Fe_2O_3 content in potassium feldspars is higher than that in plagioclases and amounts to 4 and 1–2 wt %, respectively [5]. An example of natural iron-containing feldspars is provided by iron orthoclases (Madagascar) with an Fe_2O_3 content of ~3 wt % [6].

At present, more reliable data on the distribution of cations over the tetrahedral positions $T(1)$ and $T(2)$ in iron-containing feldspars have been obtained using fine investigative techniques, such as X-ray diffraction analysis, electron paramagnetic resonance (EPR) spectroscopy, and Mössbauer spectroscopy.

In particular, Mössbauer investigations of synthetic feldspars of the composition $KFeSi_3O_8$ were carried out by Annersten [7] and Vylegzhanin *et al.* [8]. It was demonstrated that iron involved in the $KFeSi_3O_8$ structure resides in a trivalent state. Moreover, it was noted that tetrahedral Fe^{3+} is redistributed over the $T(1)$ and $T(2)$ positions upon the transition from a monoclinic modification (sanidine) to a triclinic modification (microcline).

In a number of works [9–12], the impurity distribution over tetrahedral positions was determined from the results of the interpretation of the EPR spectra. According to these data, Fe^{3+} impurity cations in low albite—an ordered triclinic modification of $NaAlSi_3O_8$—occupy only the $T(1o)$ position, which is typical of Al^{3+} cations; furthermore, the Fe^{3+} impurity cations are retained in this position even upon subsequent disordering of aluminum and silicon cations [9]. In natural sanidine of the composition $KAlSi_3O_8$, impurity iron cations also tend to occupy just the $T(1)$ [$T(1o) + T(1m)$] tetrahedral position [10, 11]. For the $KFeSi_3O_8$ structure, Wones and Appleman [12] noted the limiting case of the complete isomorphic replacement $Al^{3+} \longrightarrow Fe^{3+}$ in the $T(1)$ position.

However, in disordered feldspar modifications, Fe^{3+} cations can be isomorphically incorporated into other tetrahedra [$T(1m)$, $T(2o)$, or $T(2m)$] by replacing not only Al^{3+} but also, in part, Si^{4+} cations [5, 13]. According to the results of EPR measurement performed in [14, 15], Fe^{3+} cations in the sanidines studied are located at two inequivalent positions, $T(1)$ and $T(2)$, simultaneously.

Unfortunately, reliable information on the mechanism and kinetics of replacements such as $Al^{3+} \longleftrightarrow$ Fe^{3+} and $Fe^{3+} \longleftrightarrow Si^{4+}$ in the structure is lacking. This is especially true in regard to intermediate stages of partial distribution of three types of cations simultaneously over tetrahedral positions in silicates generally and feldspars in particular.

In the present work, we carried out a structural investigation of iron-rich potassium feldspar crystals synthesized under hydrothermal conditions. The main objective of this study was to elucidate the character of the distribution of iron and aluminum cations over positions of the tetrahedral framework.

EXPERIMENTAL

Synthesis Conditions

In two series of experiments, we prepared crystals of ferrialuminosilicate feldspars through hydrothermal synthesis. The crystals synthesized appeared to be stable at temperatures of 500–526 and 600°C (P_{H_2O} = 100 MPa in KOH solutions). Crystals of $K(Al,Fe)Si_3O_8$ solid solutions were prepared according to the procedure worked out earlier in [16].

The initial batch was composed of the following oxides: SiO_2, Fe_2O_3, and Al_2O_3. Aqueous solutions containing up to 15.25 wt % KOH were used as mineralizers. The concentration ratio of Fe_2O_3 and Al_2O_3 was varied in different experiments. The synthesis was performed in autoclaves with a volume of 200 cm^3, which were fabricated from a 1Kh18N10T stainless steel and fitted out copper swimming reaction vessels. The use of the copper vessels made it possible to maintain the oxygen potential of the system at a constant level corresponding to a copper–cuprite (Cu–Cu$_2$O) buffer, which is particularly important for the experiments with iron as an element characterized by a variable valence. For this purpose, copper oxide CuO, which is capable of transforming into cuprite Cu$_2$O under the conditions of our experiment, was added to the copper vessels. The precipitation of CuFeO$_2$ delafossite crystals occurred with an increase in the iron content in the initial batch under conditions of the Cu–Cu$_2$O buffer association. Delafossite was observed in the form of scaly platelike precipitates up to 0.1 mm in diameter. Neither delafossite nor cuprite could introduce an uncertainty into the results of X-ray microanalysis, because the sizes of these inclusions were not very small and the interfaces with feldspar crystals were clearly defined.
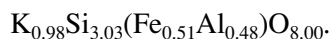
Chemical Composition
(Electron Microprobe Analysis)

The chemical analysis of the crystals synthesized was carried out on Jeol JCXA-733 and Camebax SX-50 (Cameca) microanalyzers (accelerating voltage, 20 kV; microprobe current, 20 nA). The detection limit for iron was 0.1 wt %. The copper content in the crystals under investigation, as a rule, was less than detection limit

for copper (<0.08 wt %). The reference samples (Jeol, Japan) used in these measurements were as follows: albite (Al), orthoclase (Si and K), and pyrope (Fe).

The averaged chemical composition of the crystals studied in this work (experiment G-78/500) includes the following components (wt %): K_2O, 15.80; Fe_2O_3, 13.80; Al_2O_3, 8.30; SiO_2, 62.10; $\Sigma = 100.0$. According to these data, we calculated the formula coefficients (in the anion basis [32(O)]) and obtained the empirical formula

$$K_{0.98}Si_{3.03}(Fe_{0.51}Al_{0.48})O_{8.00}.$$

In parallel with the determination of the chemical composition, we revealed that the crystals synthesized are characterized by a uniform distribution of iron with a strictly constant concentration.

X-ray Diffraction Analysis

The crystallographic characteristics, data collection, and refinement parameters for the studied structure are presented in Table 1. It is established that, under the given preparation conditions, the synthesis leads to the formation of the monoclinic modification of iron-containing potassium feldspar. The parameters of the monoclinic unit cell were determined in the course of the least-squares refinement with the use of the angular parameters for 12 reflections in the range $30° \leq 2\theta \leq 37°$. Correction for absorption was introduced using the ψ scan mode.

The crystal structure was refined with the use of the atomic coordinates taken from [3]. The refinement was performed in the space group $C2/m$ within the anisotropic approximation to $R(F) = 0.044$ for 1327 unique reflections with $I_o > 2\sigma(I_o)$. The calculations were carried out with the SHELX97 software package [17]. At the next stage, we refined the electron content of three inequivalent cation positions, namely, A, $T(1)$, and $T(2)$.

The distribution of the isomorphic cations over these inequivalent positions were determined on the basis of the refinement of the electron content, the correspondence between the structural formula and the results of the electron microprobe analysis, and the electroneutrality of the chemical formula.

However, in the case under consideration, there were a number of constraints in the refinement of the joint occupancy of the tetrahedral positions in the structure. Since aluminum and silicon are virtually indistinguishable in scattering power, the replacement of one cation by the other has little if any effect on the reflection intensities. On this basis, it was expedient to refine the distribution of Al^{3+} and Si^{4+} cations over inequivalent positions under the condition that the mean interatomic distances are approximately equal to the sum of ionic radii of the cation and the anion in the corresponding tetrahedra.

The final coordinates of the atoms and the parameters of atomic displacements are listed in Table 2. The

Table 1. Crystal data, data collection, and refinement parameters for the studied structure

Unit cell parameters, Å	$a = 8.655(7)$, $b = 13.101(9)$, $c = 7.250(8)$, $\beta = 116.02(2)°$
Space group, Z	$C2/m$; 4
Unit cell volume V, Å^3	738.7(1)
Calculated density ρ_{calcd}, g/cm^3	2.632
Absorption coefficient μ, mm^{-1}	2.22
Molecular weight	1170.44
Crystal size, mm	$0.14 \times 0.16 \times 0.20$
F_{000}	578.0
Diffractometer	Ital Structures
Wavelength, Å	0.71069
Maximum 2θ angle, deg	69.96
Total number of reflections measured	1498
Number of unique reflections	1407
Number of unique reflections with $\lvert I_o \rvert > \lvert 2\sigma(I_o) \rvert$	1327
R_{av}, %	0.0189
Refinement method	Least-squares, on F^2
Number of parameters refined	94
Final $R(F)$ factor	0.044
$R(F)$ for all unique reflections	0.048
wR (F^2)	0.117
$S = GOF$	1.084
$\Delta\rho_{max}$, e/Å^3	0.92
$\Delta\rho_{min}$, e/Å^3	−0.76

distribution of the cations over positions and the mean interatomic distances in the $T(1)$ and $T(2)$ tetrahedra and the A nine-vertex polyhedra are presented in Table 3.

Figure 1 shows the projection of the structure of low ferrialuminosilicate sanidine, which was drawn using the ATOMS program [18].

DESCRIPTION OF THE STRUCTURE AND DISCUSSION

According to Smith and Brown [5], the unit cell parameters of feldspars depend not only on the thermodynamic conditions of crystallogeny (T and P) but also on the composition of the crystals and their structural state. A similar analysis based on the construction of different-type diagrams in which the unit cell parameters are plotted along the axes of coordinates makes it possible to determine the crystalline modification of the studied sample and, moreover, to elucidate how the unit cell size is affected by the isomorphic impurities involved in the composition of the feldspars under investigation. For example, as was shown in [5], an

Table 2. Final coordinates of the atoms and the parameters of atomic displacements

Position	x/a	y/b	z/c	$U_{eq} \times 10^2$, Å^2
A	0.2857(1)	0.0	0.1387(1)	3.4(1)
$T(1)$	0.0082(1)	0.1855(1)	0.2226(1)	1.74(2)
$T(2)$	0.7092(1)	0.1177(1)	0.3441(1)	1.79(1)
$O(1)$	0.0	0.1459(2)	0.0	3.64(6)
$O(2)$	0.6396(4)	0.0	0.2853(5)	3.8(1)
$O(3)$	0.8266(3)	0.1473(2)	0.2257(5)	4.1(1)
$O(4)$	0.0354(3)	0.3118(2)	0.2587(3)	3.25(4)
$O(5)$	0.1799(3)	0.1261(2)	0.4058(3)	3.22(4)

increase in the size of the tetrahedral cation in potassium feldspars upon substitution of gallium and iron for aluminum brings about an increase in the unit cell parameters *b* and *c*.

For monoclinic potassium feldspars, the angle of monoclinity β varies in the range 115.58°–116.07° [5] and slightly increases upon replacement of potassium by a cation with a larger radius and (or) due to ordering of tetrahedral cations.

Judging from the *b–c* diagrams constructed for iron-containing feldspars, it is possible to assign the studied sample to a particular series of ordered solid solutions. In the *b–c* diagram (Fig. 2), the point corresponding to the refined parameters of the monoclinic unit cell of the studied sample lies in the region between the aluminosilicate and ferrisilicate series and appears to be closer (as compared to the samples studied earlier in [4]) to the parameters of ferrialuminosilicate sanidine. As is shown by arrows in the diagram, the unit cell parameters *b* and *c* increase regularly in the series $KAlSi_3O_8$–$KGaSi_3O_8$–$KFeSi_3O_8$ (which corresponds to the aluminosilicate, gallosilicate, and ferrisilicate modifications of potassium feldspars) due to an increase in the radius of the trivalent tetrahedral cation: $r^{[4]}Al^{3+} = 0.39 < r^{[4]}Ga^{3+} = 0.47 < r^{[4]}Fe^{3+} = 0.49$ Å [19]. Furthermore, we obtained similar results in the study of the large variety of mixed $K(Al,Fe)Si_3O_8$ crystals synthesized in the temperature range 400–600°C according to the procedure described in [16]. It was found that both the lat-

tice parameters and the unit cell volume of the potassium feldspar under investigation increase linearly with an increase in the mole fraction of the iron minal [20].

Tetrahedral Positions T(1) and T(2)

It should be noted that, in nature, Fe^{3+} substitutes for Al^{3+} in aluminum-rich silicates and oxides and manifests itself as an impurity ion. In feldspars, the possibility of Fe^{3+} and Al^{3+} cations simultaneously locating in common tetrahedra is determined by their large sizes as compared to pure silicon tetrahedra $[r^{[4]}Si^{4+} = 0.26$ Å]. A comparison of the mean interatomic distances in the structure of the studied crystals shows that the $T(1)$ tetrahedron is larger than the $T(2)$ tetrahedron: $\langle T(1)-O\rangle = 1.67$ Å and $\langle T(2)-O\rangle = 1.64$ Å. At the final stage of the structural investigation, the main problem was to determine the distribution of Si, Al, and Fe atoms over these positions.

Among the variants of the occupation of the tetrahedral positions $T(1)$ and $T(2)$, which were simulated with mixed atomic scattering functions (Fe and Si), the lowest value $R(F) = 4.4\%$ (Table 3) corresponds to a cation distribution such that iron completely occupies the $T(1)$ position. This distribution of cations agrees well with the results of Mössbauer investigations of similar synthetic iron-containing feldspars [8] in which all iron resides in a trivalent state and in a tetrahedral coordination.

The ratio Si/Al in the tetrahedral positions $T(1)$ and $T(2)$ (3.01Si and 0.49Al *afe* without regard for iron) is in agreement with the data of electron microprobe analysis. The mean distance $\langle T(2)-O\rangle = 1.64$ Å is somewhat larger than the sum of ionic radii of the cation and the anion at this position (Si–O = 1.61 Å) but, nonetheless, falls in the range of mean bond lengths for the feldspars studied earlier in [3, 13] and does not exceed the bond length equal to 1.66 Å, which, according to the data reported in [5], corresponds to a transformation from the monoclinic modification into the triclinic modification.

Bychkov *et al.* [21] established that, in feldspars crystallizing in alkaline solutions, the maximum rates of ordering of silicon and aluminum in albite are approximately ten times higher than those in potassium feldspars and, moreover, the rates of structural transformations in ferrisilicate samples exceed those in alumi-

Table 3. Distribution of the cations over positions in the studied structure

Position	Electron content	Site occupancy*	$\langle M-O\rangle^{**}_{calcd}$	$\langle M-O\rangle_{exp}$
$T(1)$	33.70	$1.2Si + 0.5Fe^{3+} + 0.3Al$	1.69	1.67
$T(2)$	27.82	$1.81Si + 0.19Al$	1.62	1.64
A	18.81	0.99K	2.90	3.00

* The number of atoms per formula unit.
** *M* is a cation, and O is a ligand (in our case, oxygen). The calculation is performed by summing the relevant ionic radii according to the data taken from [19].
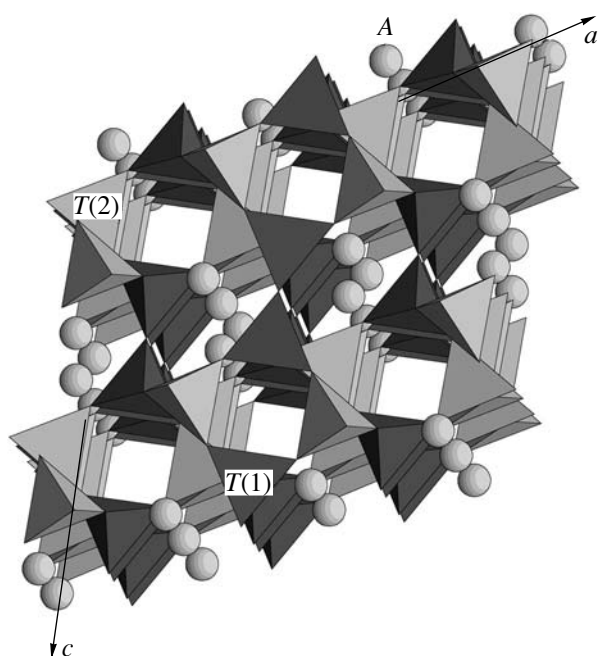
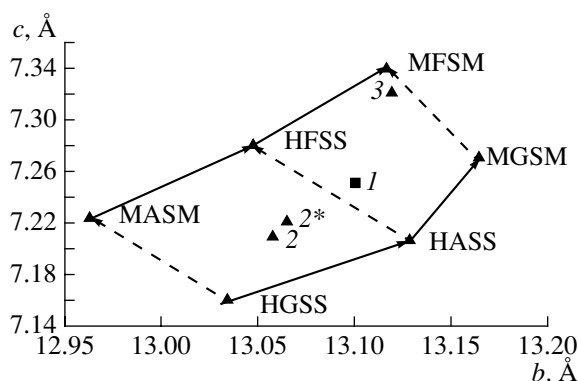**Fig. 1.** Structure of low ferrialuminosilicate sanidine.

Fig. 2. The b–c diagram for potassium feldspars with different tetrahedral cations: (*1*) the studied sample, (*2*) high ferrialuminosilicate sanidine according to the powder data [3], (*2**) high ferrialuminosilicate sanidine according to the single-crystal data [3], and (*3*) ferrisanidine [11]. Designations: MASM is maximum aluminosilicate microcline [12], HASS is high aluminosilicate sanidine [12], HFSS is high ferrisilicate sanidine [19], MFSM is maximum ferrisilicate microcline [19], MGSM is maximum gallosilicate microcline [19], and HGSS is high gallosilicate sanidine [19].

nosilicate samples by a factor of 1000. These results indicate that the rate of ordering of tetrahedral cations substantially depends on the composition of the studied feldspar. In the ferrisanidine under investigation, the iron content in the tetrahedral position $T(1)$ is considerably higher than the aluminum content. Consequently, in the course of the synthesis, iron atoms undergo a more rapid ordering than aluminum atoms against the background of the general tendency for these atoms to occupy the $T(1)$ position. Therefore, we can conclude that the rate of the $Fe^{3+} \longleftrightarrow Si^{4+}$ replacement exceeds the rate of the $Al^{3+} \longleftrightarrow Si^{4+}$ replacement during crystallization of ferrialuminosilicate feldspars, even though both processes proceed simultaneously.

Structural Position A

The aluminum–silicon–oxygen framework of the structure under consideration involves large-sized holes that are occupied by the *A*-type cations lying in the mirror-reflection planes. The results obtained using X-ray diffraction in combination with an electron microprobe analysis demonstrated that, in the ferrialuminosilicate sanidine sample, the structural position *A* is almost entirely occupied by K cations [$r^{[9]}K^+ = 1.55$ Å]. The AO_9 polyhedra are characterized by different A–O distances. However, the mean distance $\langle A$–$O \rangle = 3.00$ Å is in agreement with the relevant distances in the structures of the sanidine samples studied earlier: $\langle A$–$O \rangle = 3.00$ Å [22] and $\langle A$–$O \rangle = 3.05$ Å [4].

It was found that the change in the degree of ordering of silicon and aluminum affects the shape of the

holes occupied by large-sized cations [3]. An increase in the size of the $T(1)$ tetrahedra in sanidine due to the incorporation of larger sized cations (in our case, Fe^{3+}) is accompanied by a change in the shape of the *A* polyhedra. This manifests itself in a decrease in the longest A–O distances and an increase in the shortest A–O distances: $(A$–$O)_{max} = 3.14$ Å and $(A$–$O)_{min} = 2.77$ Å. In our previous work [4], we showed that, in the ferrisanidine characterized by a lower iron content in the $T(1)$ position (0.20Fe *afe*), the *A* polyhedra are distorted more significantly: $(A$–$O)_{max} = 3.39$ Å and $(A$–$O)_{min} = 2.69$ Å.

The refined crystal chemical formula of the synthetic low ferrisanidine accounts for the composition of the cation positions in the structure:

$$K_{A = 0.99}(Si_{1.2}Fe_{0.5}Al_{0.3})_{\Sigma T(1) = 2}(Si_{1.81}Al_{0.19})_{\Sigma T(2) = 2}O_8.$$
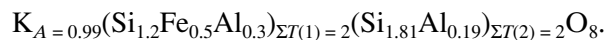
CONCLUSIONS

Thus, the results of the present work and the data obtained earlier in [4] allowed us to conclude that there exists a continuous monoclinic series of $KAlSi_3O_8$–$K(Fe,Al)Si_3O_8$ solid solutions in which iron manifests itself as a majority rather than minority impurity element with respect to aluminum and exhibits a tendency to occupy predominantly the $T(1)$ position.

ACKNOWLEDGMENTS

REFERENCES

1. W. H. Taylor, Z. Kristallogr. **85**, 425 (1933).

2. R. B. Ferguson, N. A. Ball, and P. Cerny, Can. Mineral. **29**, 543 (1991).

3. F. Liebau, *Structural Chemistry of Silicates: Structure, Bonding, and Classification* (Springer, New York, 1985; Mir, Moscow, 1988).

4. T. N. Nadezhina, D. Yu. Pushcharovsky, V. K. Taroev, *et al.*, Kristallografiya **38** (6), 77 (1993) [Crystallogr. Rep. **38**, 753 (1993)].

5. J. V. Smith and W. L. Brown, *Feldspar Minerals*, 2nd ed. (Springer, Berlin, 1988), Vol. 1.

6. D. S. Coombs, Miner. Mag. **30** (226), 409 (1954).

7. H. Annersten, Neues Jahrb. Mineral. 337 (1976).

8. K. V. Vylegzhanin, V. G. Izotov, V. P. Kal'chev, *et al.*, in *Program and Abstracts of IV Meeting on Nuclear Spectroscopic Investigations of Ultrafine Interactions* (Mosk. Gos. Univ., Moscow, 1991), p. 113.

9. Iv. Petrov, Yu. Fu, L. V. Bershov, *et al.*, Am. Mineral. **74**, 604 (1989).

10. Iv. Petrov and S. S. Hafner, Am. Mineral. **73**, 97 (1988).

11. Yu. Fu, Iv. Petrov, and S. S. Hafner, Acta Mineral. Sin. **9**, 97 (1989).

12. D. R. Wones and D. E. Appleman, US Geol. Surv. Prof. Pap., No. 424-C, 309 (1961).

13. H. Kroll and P. H. Ribbe, Am. Mineral. **72**, 491 (1987).

14. Iv. Petrov and S. S. Hafner, Fortschr. Mineral. **63**, 180 (1985).

15. A. M. Haffneister and G. R. Rossman, Phys. Chem. Miner. **11**, 213 (1984).

16. V. K. Taroev, V. L. Tauson, L. F. Suvorova, *et al.*, Dokl. Akad. Nauk **337** (2), 246 (1994).

17. G. M. Sheldrick, *SHELX97: Program for the Solution and Refinement of Crystal Structures* (Siemens Energy and Automation, Madison, WI, 1997).

18. E. Dowty, *Atoms 3.2: A Computer Program for Displaying Atomic Structures* (Kingsport, TN, 1995).

19. R. D. Shannon, Acta Crystallogr. Sect. A: Cryst. Phys., Diffr., Theor. Gen. Crystallogr. **32** (5), 751 (1976).

20. V. K. Taroev, J. Goettlicher, V. V. Lashkevich, *et al.*, Dokl. Akad. Nauk **387** (1), 95 (2002).

21. A. M. Bychkov, N. S. Vasil'ev, I. G. Vorob'eva, and É. É. Senderov, *Experiment in Mineralogy* (Nauka, Moscow, 1988), p. 125.

22. W. F. Cole, H. Sorum, and O. Kennard, Acta Crystallogr. **2**, 280 (1949).

Translated by O. Borovik-Romanova

<div align="center">

STRUCTURE
OF INORGANIC COMPOUNDS

</div>

<div align="right">

Dedicated to the 60th Anniversary
of the Shubnikov Institute of Crystallography
of the Russian Academy of Sciences

</div>

Structure and Properties of Single Crystals of Tin-Doped Potassium Titanyl Phosphate

O. D. Krotova*, N. I. Sorokina**, I. A. Verin**, V. I. Voronkova*,
V. K. Yanovskiĭ*, and V. I. Simonov**

* Moscow State University, Vorob'evy gory, Moscow, 119992 Russia
** Shubnikov Institute of Crystallography, Russian Academy of Sciences,
Leninskiĭ pr. 59, Moscow, 119333 Russia
e-mail: nsor@ns.crys.ras.ru
Received January 29, 2003

Abstract—Single crystals with the compositions $KTi_{0.47}Sn_{0.53}OPO_4$ and $KTi_{0.25}Sn_{0.75}OPO_4$ were grown by spontaneous crystallization from flux in the K_2O–TiO_2–SnO_2–P_2O_5 quaternary system, and their structures were established from precision X-ray diffraction data. The incorporation of tin into the crystals lowers the asymmetry of cation positions in the $(Ti,Sn)O_6$ octahedra. The addition of even a small amount ($x < 0.4$) of tin to the $K(Ti_{1-x}Sn_x)OPO_4$ crystals causes fast symmetrization of the octahedra. The process slows down with an increase in the tin content until the attainment of the composition $KSnOPO_4$ and localization of tin in the centers of octahedra. It is these structural features that are responsible for a decrease in the optical nonlinearity of the crystals and in the intensity of second harmonic generation by laser radiation in these crystals. © 2003 MAIK "Nauka/Interperiodica".

INTRODUCTION

In recent years, physical properties and atomic structures of potassium titanyl phosphate $KTiOPO_4$ (KTP), where titanium is either partially or completely replaced by tin, were repeatedly studied [1–7]. Potassium stannyl phosphate $KSnOPO_4$ (KSP) is isostructural to KTP [8, 9], and these two compounds form a continuous series of solid solutions, $KTi_{1-x}Sn_xOPO_4$ (KTSP). The properties of KSP crystals and their solid solutions were reported in [1, 2, 4, 6, 7]. The data on the ferroelectric properties and conductivity of KTSP crystals were published in [6, 7]. According to the results of these studies, the temperature of the ferroelectric phase transition for pure KSP is 387°C, which is somewhat lower than the temperature determined earlier [4]. With an increase of the tin content in the crystal, T_c decreases

monotonically. Like the intensity of second harmonic generation (SHG), T_c decreases most rapidly with the attainment of a tin concentration in the crystal up to $x = 0.40$. At $x > 0.40$, both the SHG intensity in the KTSP crystals and T_c continue decreasing and approach zero, if a large amount of titanium is replaced by tin. It should be noted that the ferroelectric properties (determined, primarily, by the potassium positions) are retained.

Precision X-ray diffraction studies allow one to reveal correlations between the structure and physical properties of crystals at the atomic level. The atomic structure of $KTi_{1-x}Sn_xOPO_4$ single crystals with a low Sn content ($x \approx 0.06$–0.07) was established by X-ray diffraction analysis in [5]. It was noted that Ti^{4+} cations (ionic radius 0.68 Å) are irregularly replaced by slightly

Table 1. Compositions of the melts and characteristics of the $KTi_{1-x}Sn_xOPO_4$ crystals

Experiment	Compositions of melts, mol %				Sn/(Ti + Sn)		Compositions of crystals determined by microanalysis	Crystal dimensions, mm³
	K_2O	TiO_2	SnO_2	P_2O_5	in melt	in crystal		
1	45	10	5	35	0.5	0.4	$K_{0.93}Ti_{0.6}Sn_{0.4}P_{0.97}O_{4.9}$	$4 \times 3 \times 2$
2	50	10	10	35	0.67	0.5	$K_{0.9}Ti_{0.5}Sn_{0.5}P_{0.97}O_{4.9}$	$2 \times 3 \times 2$

Table 2. Characteristics of X-ray data collection and details of refinement

Chemical composition	$KTi_{0.47}Sn_{0.53}OPO_4$	$KTi_{0.25}Sn_{0.75}OPO_4$
Radius of the sample, mm	0.13(1)	0.14(1)
μ, cm^{-1}	46.32	48.78
Diffractometer	Enraf-Nonius CAD-4F	
Radiation	MoK_α	
Monochromator	Graphite	
Scanning technique	$\omega/2\theta$	
Sp. gr.	$Pna2_1$	
Ranges of h, k, l	$-25 \le h \le 25$	$-21 \le h \le 21$
	$0 \le k \le 12$	$0 \le k \le 10$
	$0 \le l \le 21$	$0 \le l \le 17$
θ_{max}, deg	45	35
Total number of measured reflections, $|F|_{hkl}$	7277	4314
Number of independent reflections, $|F|_{hkl} > 3\sigma_{|F|hkl}$	3742	1979
$R_{int}(|F|_{hkl})$, %	1.88	2.0
Structure type	$KTiOPO_4$	
Program for calculations	JANA98	
Weighting scheme	$1/\sigma^2$	
Number of parameters in the refinement	272	262
Reliability factors R/R_w	0.027/0.029	0.016/0.020

larger Sn^{4+} cations (ionic radius 0.71 Å), with the latter being located predominantly in the Ti(2) positions.

The present study is a continuation of the research of atomic structures of crystals of the KTSP series grown by crystallization from flux. The results of the study of structures and properties of tin-doped KTP crystals are generalized.

Table 3. Unit-cell parameters and unit-cell volumes of KTP crystals with different Sn contents

	a, Å	b, Å	c, Å	V, Å^3
KTP [5]	12.819(1)	6.399(1)	10.584(1)	868.2(1)
KTP–6% Sn	12.831(1)	6.410(1)	10.584(1)	870.5(1)
KTP–53% Sn	12.993(1)	6.471(1)	10.661(1)	896.4(1)
KTP–75% Sn	13.076(1)	6.504(1)	10.690(1)	909.6(1)
KSP [5]	13.145(1)	6.526(1)	10.738(1)	921.2(1)

EXPERIMENTAL

Single crystals of $KTi_{1-x}Sn_xOPO_4$ with two different compositions were grown by spontaneous crystallization from flux [6] in the $K_2O–TiO_2–SnO_2–P_2O_5$ system. The chemical compositions of the compounds were determined on a Cameca SX-50 X-ray microanalyzer. The compositions of the staring melts and crystals grown are given in Table 1.

Optically homogeneous crystals chosen for X-ray diffraction study were ground to spheres. The samples of the shape closest to spherical were used in the subsequent investigation and gave the best X-ray diffraction patterns. Spherical single crystals with radii of 0.13 and 0.14 mm were studied in experiments 1 and 2, respectively. The conditions of X-ray data collection and details of the structure refinement are given in Table 2. The parameters of the orthorhombic unit cell were refined by the least-squares method based on 25 reflections. The complete sets of reflection intensities were collected on a CAD-4F Enraf-Nonius diffractometer equipped with a graphite monochromator.

Table 4. Atomic coordinates, occupancies of positions q, and equivalent thermal parameters B_{eq} (Å^2) in the $KTi_{0.94}Sn_{0.06}OPO_4$ structure

Atom	x/a	y/b	z/c	q	B_{eq}
Ti(1)	0.37252(9)	0.5001(2)	0.00000	0.983(4)	0.439(7)
Sn(1)	0.37252	0.5001	0.00000	0.017	0.439(7)
Ti(2)	0.24632(9)	0.2653(2)	0.2513(2)	0.897(5)	0.441(6)
Sn(2)	0.24632	0.2653	0.2513	0.103	0.441(6)
K(1)	0.1055(2)	0.6989(4)	0.0649(3)	1.000	1.54(2)
K(2)	0.3788(2)	0.7807(3)	0.3108(3)	1.000	1.45(2)
P(1)	0.4983(2)	0.3369(3)	0.2580(3)	1.000	0.39(1)
P(2)	0.1805(2)	0.5021(3)	0.5099(3)	1.000	0.41(1)
O(1)	0.4855(2)	0.4871(5)	0.1471(4)	1.000	0.78(4)
O(2)	0.5103(2)	0.4659(5)	0.3799(4)	1.000	0.76(4)
O(3)	0.4006(4)	0.1989(9)	0.2766(7)	1.000	0.63(4)
O(4)	0.5932(2)	0.1938(4)	0.2365(4)	1.000	0.73(4)
O(5)	0.1121(5)	0.3123(9)	0.5376(6)	1.000	0.66(4)
O(6)	0.1117(2)	0.6924(4)	0.4839(4)	1.000	0.82(4)
O(7)	0.2527(2)	0.5381(6)	0.6241(4)	1.000	0.78(4)
O(8)	0.2523(2)	0.4627(5)	0.3959(4)	1.000	0.81(4)
O(9)	0.2238(5)	0.0430(10)	0.3867(6)	1.000	0.73(4)
O(10)	0.2252(2)	−0.0316(5)	0.6388(3)	1.000	0.70(4)

Table 5. Atomic coordinates, occupancies of positions q, and equivalent thermal parameters B_{eq} (Å^2) in the $KTi_{0.47}Sn_{0.53}OPO_4$ structure

Atom	x/a	y/b	z/c	q	B_{eq}
Ti(1)	0.37208(6)	0.4998(1)	0.00000	0.645(3)	0.444(4)
Sn(1)	0.37208	0.4998	0.00000	0.355	0.444
Ti(2)	0.24624(5)	0.2565(1)	0.2480(2)	0.304(4)	0.425(3)
Sn(2)	0.24624	0.2565	0.2480	0.696	0.425
K(1)	0.1059(2)	0.6982(4)	0.0602(3)	1.000	1.81(2)
K(2)	0.3791(2)	0.7806(4)	0.3063(3)	1.000	1.69(2)
P(1)	0.49907(7)	0.3403(1)	0.2536(2)	1.000	0.41(1)
P(2)	0.17842(5)	0.5030(1)	0.5038(2)	1.000	0.48(1)
O(1)	0.4841(3)	0.4881(5)	0.1425(4)	1.000	0.78(5)
O(2)	0.5117(3)	0.4704(6)	0.3733(4)	1.000	0.81(5)
O(3)	0.4035(2)	0.2017(5)	0.2732(4)	1.000	0.73(4)
O(4)	0.5914(2)	0.1968(5)	0.2307(3)	1.000	0.78(5)
O(5)	0.1095(2)	0.3144(5)	0.5288(4)	1.000	0.70(4)
O(6)	0.1103(3)	0.6926(5)	0.4822(4)	1.000	0.99(5)
O(7)	0.2501(3)	0.5302(7)	0.6178(5)	1.000	0.95(6)
O(8)	0.2508(3)	0.4683(7)	0.3922(4)	1.000	0.87(6)
O(9)	0.2287(3)	0.0405(6)	0.3790(4)	1.000	0.94(5)
O(10)	0.2265(3)	−0.0241(6)	0.6326(4)	1.000	0.97(5)

Table 6. Atomic coordinates, occupancies of positions q, and equivalent thermal parameters B_{eq} (Å^2) in the $KTi_{0.25}Sn_{0.75}OPO_4$ structure

Atom	x/a	y/b	z/c	q	B_{eq}
Ti(1)	0.37306(5)	0.4983(1)	0.00000	0.262(7)	0.328(4)
Sn(1)	0.37306	0.4983	0.00000	0.738	0.328(4)
Ti(2)	0.24758(7)	0.2549(1)	0.2494(2)	0.244(7)	0.340(4)
Sn(2)	0.24758	0.2549	0.2494	0.756	0.340(4)
K(1)	0.1080(2)	0.6944(5)	0.0611(4)	1.000	1.86(3)
K(2)	0.3769(2)	0.7789(4)	0.3038(4)	1.000	1.56(3)
P(1)	0.5003(3)	0.3412(4)	0.2499(6)	1.000	0.35(2)
P(2)	0.1770(2)	0.5026(5)	0.5028(5)	1.000	0.39(2)
O(1)	0.4859(5)	0.4876(8)	0.1376(7)	1.000	0.88(9)
O(2)	0.5124(4)	0.4759(9)	0.3671(6)	1.000	0.79(9)
O(3)	0.4058(3)	0.2032(6)	0.2694(5)	1.000	0.87(8)
O(4)	0.5922(3)	0.2000(7)	0.2270(5)	1.000	0.69(7)
O(5)	0.1074(3)	0.3155(6)	0.5253(5)	1.000	0.78(7)
O(6)	0.1077(4)	0.6884(6)	0.4772(5)	1.000	0.92(8)
O(7)	0.2475(5)	0.5297(9)	0.6145(7)	1.000	1.01(9)
O(8)	0.2488(8)	0.469(2)	0.390(1)	1.000	0.80(9)
O(9)	0.2334(5)	0.0370(9)	0.3737(6)	1.000	0.84(8)
O(10)	0.2255(7)	−0.020(2)	0.6350(9)	1.000	0.88(9)

Both crystal structures were refined by the least-squares method using the JANA98 program [10]. The atomic coordinates determined in the refinement of the $KTi_{0.93}Sn_{0.07}OPO_4$ structure [5] using the PROMETHEUS program package were taken as the starting model for the refinement. We also re-refined the structure of $KTi_{0.93}Sn_{0.07}OPO_4$ single crystals using the experimental data published earlier [5] and the JANA98 program package. In the refinement of the three structures, all extinction models included into the JANA98 program were tested. The best results were obtained with the use of the Becker–Coppens extinction correction taking into consideration the Lorentz distribution of disoriented mosaic blocks in the crystal. The structural parameters were refined on the assumption that Ti and Sn atoms simultaneously occupy one position in all the crystallographically nonequivalent octahedra, and the total occupancies of these positions were taken to be equal to 100%. The strongly correlated structural parameters were refined by step-by-step scanning [11].

RESULTS AND DISCUSSION

The unit-cell parameters of KTP, KSP, and three single crystals of KTSP solid solutions studied are given in Table 3. The a, b, and c parameters and unit-cell volumes correlate with the ionic radii of the Sn^{4+} and Ti^{4+} cations. The coordinates of the basis atoms in the structures of KTSP single crystals with three different compositions, occupancies of crystallographic positions q, and equivalent atomic thermal displacements B_{eq} are listed in Tables 4–6. As can be seen from these tables, the Sn atoms isomorphically replace Ti atoms in both nonequivalent positions. At low tin concentrations, tin atoms largely occupy the second octahedral position. In the crystal containing 75% Sn, the occupancies of both positions are the same and the compositions of these positions are described by the formulas $Ti_{0.262}Sn_{0.738}$ and $Ti_{0.244}Sn_{0.756}$ (see Table 6). According to the results of microanalysis (Table 1), there is some deficit in K, P, and O atoms in the structures under study. This phenomenon has not been observed in $KTiOPO_4$-type solid solutions investigated earlier. We attempted to refine the occupancies of these atomic positions. Difference electron density syntheses calculated based on models with partial occupancies of the K(1), K(2), P(1), and P(2) positions revealed residual density peaks in the vicinity of these atomic positions (Figs. 1 and 2). These sections of the electron density maps are indicative of possible splitting of the K and P positions. However, all attempts to take into account this splitting in the KTSP
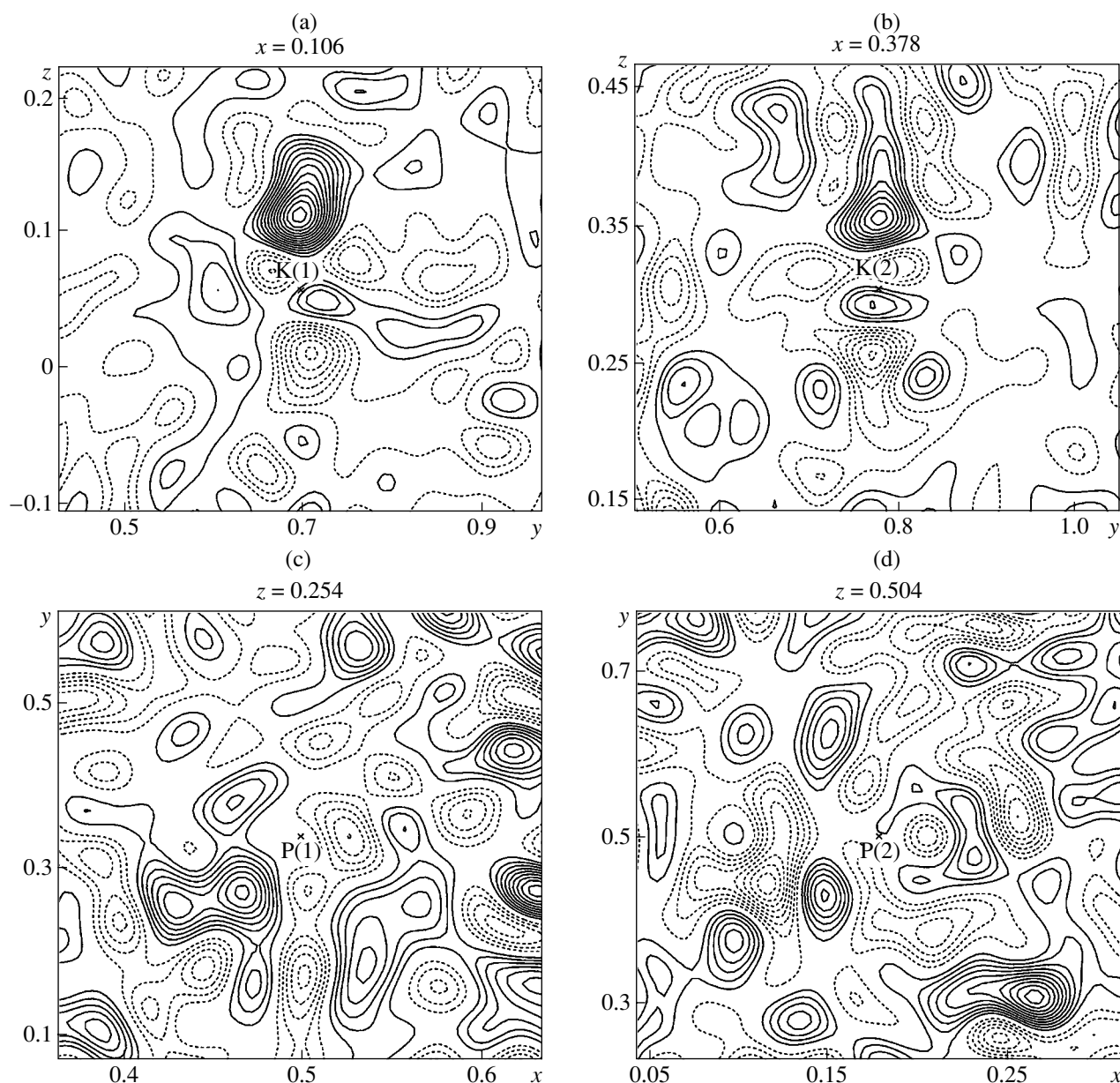
Fig. 1. Crystals structure of $KTi_{0.47}Sn_{0.53}OPO_4$. Difference electron-density maps in the vicinity of the atomic positions: (a) K(1), (b) K(2), (c) P(1), and (d) P(2). Isolines on maps (a) and (b) are spaced by 0.15 e/$Å^3$; those on maps (c) and (d), by 0.09 e/$Å^3$.

structures failed. This may be attributed either to the fact that the residual-density peaks are located in the vicinity of the main atomic positions or to the influence of twinning typical of ferroelectrics. The accuracy of our X-ray diffraction data did not allow us to give an unambiguous answer to this question. Based on the X-ray diffraction data, the following chemical formula of the crystals can be written: $KTi_{0.47}Sn_{0.53}OPO_4$ (experiment 1) and $KTi_{0.25}Sn_{0.75}OPO_4$ (experiment 2). It should be noted that the tin content in the crystals (Table 1) determined by electron probe analysis was substantially underestimated compared to the structure-refinement data. Apparently, the probable deficit of K,

P, and O in the KTPS single crystals is associated with the fact that these crystals were grown at very high temperatures (1200–800°C). However, this assumption calls for further investigation.

The KTSP crystal structure can be described as a three-dimensional framework consisting of the $(Ti,Sn)O_6$ octahedra and $[PO_4]$ tetrahedral sharing their vertices. The framework contains wide helical channels along the c axis. The channels are occupied by potassium cations. The principal interatomic distances in the structures of the three KTSP single crystals studied here and those in the known KTP and KSP crystals are listed in Table 7. Analysis of the interatomic distances

Table 7. Interatomic distances (Å) in the $KTiOPO_4$ (1), $KTi_{0.94}Sn_{0.06}OPO_4$ (2), $KTi_{0.47}Sn_{0.53}OPO_4$ (3), $KTi_{0.25}Sn_{0.75}OPO_4$ (4), and $KSnOPO_4$ (5) structures

| Distances	1	2	3	4	5
Ti(1)–O(1)	2.154(1)	2.135(3)	2.106(4)	2.085(7)	2.091(7)
O(2)	1.955(1)	1.976(3)	2.035(4)	2.070(6)	2.093(7)
O(5)	2.046(1)	2.047(3)	2.072(3)	2.096(4)	2.111(6)
O(6)	1.987(1)	1.990(3)	2.011(3)	2.046(4)	2.064(5)
O(9)	1.716(1)	1.744(3)	1.857(4)	1.955(6)	1.978(6)
O(10)	1.985(1)	1.948(3)	1.915(4)	1.940(10)	1.975(7)
Average	1.974	1.973	1.999	2.032	2.052
$\Delta_{|O(10)-O(9)|}$	0.269	0.194	0.058	0.015	0.003
Ti(2)–O(3)	2.042(1)	2.045(3)	2.092(3)	2.107(4)	2.134(5)
O(4)	1.980(1)	1.988(3)	2.043(3)	2.067(4)	2.102(5)
O(7)	1.964(1)	1.977(3)	2.018(5)	2.057(7)	2.051(6)
O(8)	1.998(1)	1.995(3)	2.061(5)	2.050(10)	2.076(7)
O(9)	2.099(1)	2.046(3)	1.989(5)	1.952(6)	1.957(5)
O(10)	1.736(1)	1.792(3)	1.911(4)	1.940(10)	1.961(5)
Average	1.970	2.004	2.019	2.029	2.047
$\Delta_{|O(9)-O(10)|}$	0.363	0.254	0.078	0.012	0.004
P(1)–O(1)	1.518(1)	1.520(3)	1.534(4)	1.544(8)	1.562(6)
O(2)	1.551(1)	1.547(3)	1.538(4)	1.538(8)	1.535(7)
O(3)	1.546(1)	1.542(3)	1.546(3)	1.541(5)	1.530(5)
O(4)	1.541(1)	1.541(3)	1.537(3)	1.532(5)	1.506(6)
Average	1.539	1.538	1.539	1.539	1.533
P(2)–O(5)	1.538(1)	1.535(3)	1.537(3)	1.539(5)	1.535(5)
O(6)	1.529(1)	1.527(3)	1.530(4)	1.536(5)	1.529(6)
O(7)	1.550(1)	1.546(3)	1.541(5)	1.518(5)	1.527(8)
O(8)	1.535(1)	1.534(3)	1.533(5)	1.543(1)	1.545(7)
Average	1.538	1.536	1.535	1.534(10)	1.534
K(1)–O(1)	2.675(1)	2.682(3)	2.719(4)	2.737(7)	2.995(7)
O(2)	2.983(1)	2.982(3)	3.067(5)	3.183(7)	2.753(4)
O(3)	3.044(1)	3.047(1)	3.062(5)	3.124(7)	2.845(5)
O(4)	3.117(1)	3.125(1)	3.143(4)	3.126(6)	3.148(1)
O(5)	2.804(1)	2.802(3)	2.820(4)	2.842(5)	3.005(4)
O(7)	2.919(1)	2.905(3)	2.915(5)	2.942(7)	3.042(4)
O(8)	3.047(1)	3.050(1)	3.119(5)	3.169(10)	2.770(7)
O(9)	3.058(1)	3.062(1)	3.064(5)	3.060(7)	2.955(5)
O(10)	2.763(1)	2.750(3)	2.722(5)	2.703(10)	2.611(6)
Average	2.934	2.934	2.959	2.987	2.903
K(2)–O(1)	2.891(1)	2.894(3)	2.914(5)	2.962(7)	2.736(6)
O(2)	2.763(1)	2.740(3)	2.740(5)	2.735(7)	3.256(8)
O(3)	2.711(1)	2.725(3)	2.766(4)	2.810(5)	3.123(7)
O(5)	2.869(1)	2.891(3)	2.970(5)	2.993(6)	2.856(6)
O(7)	3.055(1)	3.056(1)	3.076(5)	3.067(8)	2.987(6)
O(8)	2.756(1)	2.755(3)	2.776(5)	2.779(10)	3.182(7)
O(9)	2.723(1)	2.719(3)	2.692(5)	2.627(7)	2.664(5)
O(10)	2.994(1)	2.997(1)	3.033(5)	2.970(10)	3.059(7)
Average	2.845	2.847	2.871	2.868	2.983
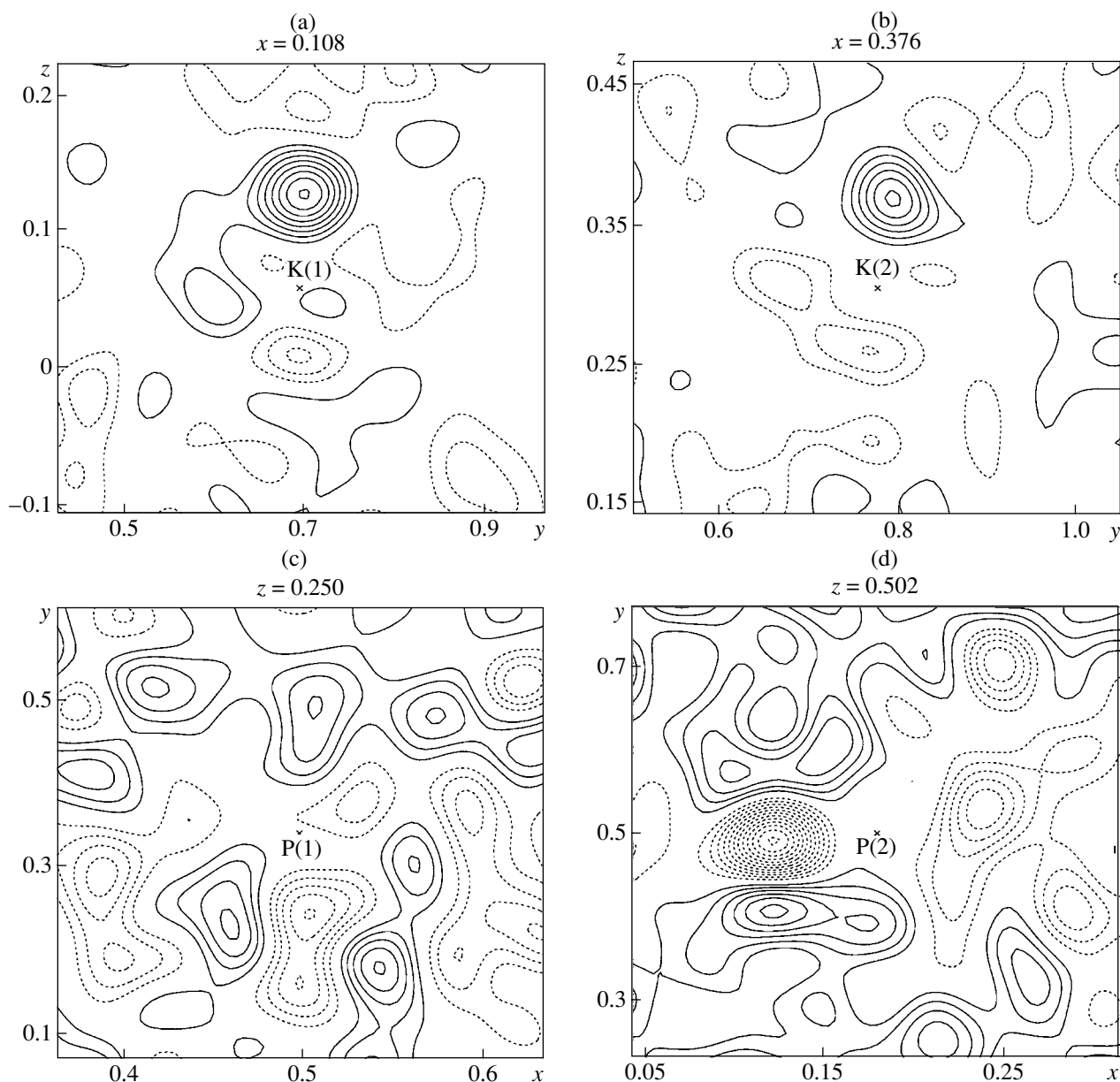
Fig. 2. Crystals structure of $KTi_{0.25}Sn_{0.75}OPO_4$. Difference electron-density maps in the vicinity of the atomic positions: (a) K(1); (b) K(2); (c) P(1); and (d) P(2). Isolines on maps (a) and (b) are spaced by 0.15 e/$Å^3$; those on maps (c) and (d), by 0.09 e/$Å^3$.

shows that the $(Ti,Sn)O_6$ octahedra, whose configuration is responsible for the nonlinear optical properties of crystals, become more symmetric with an increase of tin content in crystals. It should be noted that less distorted $(Ti,Sn)O_6$ octahedra $(\Delta_{|O(10)-O(9)|})$ are observed in crystals containing up to 50% Sn. This fact is consistent with a dramatic decrease in the intensity of second harmonic generation by laser radiation in the crystals of KTSP solid solutions, where the atomic coefficients of Sn vary from 0 to 0.4 [6]. A further increase in the tin content leads to a decrease in the SGH intensity almost to zero. The P–O distances in the $[PO_4]$ tetrahedra and the K–O distances in the $[KO_8]$ and $[KO_9]$ polyhedra only slightly depend on the Sn content.

ACKNOWLEDGMENTS

REFERENCES

1. P. A. Thomas, A. M. Glazer, and B. E. Watts, Acta Crystallogr. Sect. B: Struct. Sci. **46**, 333 (1990).

2. M. L. F. Phillips, W. T. A. Harrison, and G. D. Stucky, Inorg. Chem. **29**, 3247 (1990).

3. S. J. Crennell, J. J. Owen, and A. K. Cheetham, Eur. J. Solid State Inorg. Chem. **28**, 397 (1991).

4. Sh. Furusawa, H. Yanagisawa, and Y. Ishibashi, J. Phys. Soc. Jpn. **62** (11), 4150 (1993).

5. Liu Wen, N. I. Sorokina, V. I. Voronkova, *et al.*, Kristallografiya **45** (3), 429 (2000) [Crystallogr. Rep. **45**, 386 (2000)].

6. Liu Wen, V. I. Voronkova, V. K. Yanovskiĭ, *et al.*, Neorg. Mater. **37** (3), 359 (2001).

7. V. K. Yanovskiĭ, V. I. Voronkova, T. Yu. Losevskaya, *et al.*, Kristallografiya **48** (2), 219 (2003) [Crystallogr. Rep. **48**, 205 (2003)].

8. V. I. Voronkova and V. K. Yanovskiĭ, Neorg. Mater. **25** (9), 1579 (1989).

9. N. S. Slobodyanik, P. G. Nagornyĭ, V. V. Skorenko, and E. S. Lugovskaya, Zh. Neorg. Khim. **32** (7), 1724 (1987).

10. V. Petricek and M. Dusek, in *JANA98, Crystallographic Computing System* (Inst. of Physics, Praha, 1998).

11. L. A. Muradyan, S. F. Radaev, and V. I. Simonov, *Methods of Structural Analysis* (Nauka, Moscow, 1989), p. 5.

Translated by T. Safonova

STRUCTURE
OF INORGANIC COMPOUNDS

Dedicated to the 60th Anniversary
of the Shubnikov Institute of Crystallography
of the Russian Academy of Sciences

X-ray Diffraction Study of Cerium- and Thulium-Doped (Sr,Ba)Nb$_2$O$_6$ Single Crystals

T. S. Chernaya*, T. R. Volk*, B. A. Maksimov*, M. K. Blomberg**, L. I. Ivleva***,
I. A. Verin*, and V. I. Simonov*

* *Shubnikov Institute of Crystallography, Russian Academy of Sciences, Leninskiĭ pr. 59, Moscow, 119991 Russia*
e-mail: chert@ns.crys.ras.ru

** *Department of Physics, University of Helsinki, Siltavuorenpenger 20 I, P.O. Box 9, Helsinki, FIN-00014 Finland*

*** *Institute of General Physics, Russian Academy of Sciences, ul. Vavilova 38, Moscow, 117942 Russia*

Received May 20, 2003

Abstract—The structural models of cerium- and thulium-doped $(Sr_{0.61}Ba_{0.39})Nb_2O_6$ solid solutions were established and refined on the basis of single-crystal X-ray diffraction data. The dopants were located, and their concentrations in the specimens were refined. The effect of the Sr/Ba ratio and doping with rare earth elements on the structural characteristics of $(Sr_xBa_{1-x})Nb_2O_6$ crystals was analyzed. © *2003 MAIK "Nauka/Interperiodica".*

INTRODUCTION

$(Sr_xBa_{1-x})Nb_2O_6$ $(0.25 < x < 0.75)$ crystals [1] are of interest because of their physical characteristics and opportunities for targeted control of their optical properties by varying the Sr/Ba ratio and doping solid solutions with rare earth elements. The crystals belong to oxygen-octahedral ferroelectrics with the general formula AB_2O_6 and the structure of tetragonal tungsten bronzes.

The physical properties of crystals of this type can be changed as desired due to variations in the arrangement of Sr and Ba atoms in the channels of the structure [1–4]. A specified ratio between the concentrations of strontium and barium in the structure leads to a particular distribution of structural defects (vacancies), which represent an essential feature of such structures [5–7]. In addition, the physical properties of $(Sr,Ba)Nb_2O_6$ solid solutions can be changed by doping them with small amounts of rare earth cations [8, 9]. The aim of the present study was to carry out a high-precision X-ray diffraction study of $(Sr_{0.61}Ba_{0.39})Nb_2O_6$: Ce and $(Sr_{0.61}Ba_{0.39})Nb_2O_6$: Tm single crystals and to reveal the influence of Ce and Tm on the crystal structure. Finally, we analyzed the structural characteristics of the $(Sr,Ba)Nb_2O_6$ solid solutions, depending on the Sr/Ba ratio. This analysis was performed using the previous high-precision X-ray data on single-crystal solid solutions with the following compositions:

$(Sr_{0.75}Ba_{0.25})Nb_2O_6$ [6], $(Sr_{0.61}Ba_{0.39})Nb_2O_6$ [5], $(Sr_{0.50}Ba_{0.50})Nb_2O_6$ [7], and $(Sr_{0.33}Ba_{0.67})Nb_2O_6$ [10].

X-RAY DIFFRACTION STUDY
AND STRUCTURE REFINEMENT

$(Sr_{0.61}Ba_{0.39})Nb_2O_6$: Ce and $(Sr_{0.61}Ba_{0.39})Nb_2O_6$: Tm single crystals were grown by the Czochralski method. The presence of Ce and Tm in the crystals was confirmed by electron-probe analysis on a Camebax microanalyzer. For a spherical cerium-doped sample (0.15 mm in diameter), the integrated intensities were measured on an Enraf-Nonius X-ray diffractometer by the ω-scan technique using MoK_α radiation ($\lambda = 0.7106$ Å, graphite monochromator) within a full sphere of reciprocal space up to $\sin\theta/\lambda \leq 1.2$ Å^{-1}. The intensities of a total of 14 350 diffraction reflections were measured, and 1987 independent reflections with $I > 3\delta(I)$ were obtained by merging symmetry-equivalent reflections ($R_{int} = 2\%$).

For a thulium-doped sample (0.26 mm in diameter), the integrated intensities were measured on a four-circle HUBER 5042 diffractometer (MoK_α radiation, graphite monochromator) by the $\Omega/2\theta$-scan technique within two octants of reciprocal space ($\pm h, k, l$; $\sin\theta/\lambda \leq 1.00$ Å^{-1}). A total of 4188 reflections were measured, and 1655 independent reflections with $I > 3\delta(I)$ were obtained by merging equivalent reflections ($R_{int} = 1.9\%$).

The intensities of diffraction reflections were converted to structure-factor amplitudes with regard to the kinematic and polarization factors and X-ray absorption in the samples. For the cerium- and thulium-doped crystals, the linear absorption coefficients for MoK_α radiation are 139.7 and 142.8 cm^{-1}, respectively. The structures were refined using the coordinates of basis atoms in a $(Sr_{0.61}Ba_{0.39})Nb_2O_6$ crystal [5] as a starting model. The diffraction symmetry $4/mmmP-/-b-$, which was found by analyzing the experimental structure-factor amplitudes for cerium- and thulium-doped crystals, corresponds to the following three space groups: $P4/mbm$, $P\bar{4}b2$, and $P4bm$. Further analysis confirmed that the structures of doped crystals, as well as the structures of $(Sr,Ba)Nb_2O_6$ solid solutions established previously, belong to the noncentrosymmetric group $P4bm$. The parameters of the tetragonal unit cell are as follows: $a = 12.454(1)$ Å, $c = 3.932(2)$ Å and $a = 12.458(1)$ Å, $c = 3.935(2)$ Å for the cerium- and thulium-doped crystals, respectively. The structures were refined by the full-matrix least-squares method taking into account the experimental weighting factors with the use of the PROMETHEUS software package [11] (which was also used in all the other calculations) to the reliability factors $R = 2.1\%$, $R_w = 2.4\%$ and $R = 1.8\%$, $R_w = 2.0\%$ for the cerium- and thulium-doped crystals, respectively. The atomic scattering curves and the corrections for anomalous scattering $\Delta f'$ and $\Delta f''$ were taken from [12]. The correction for the secondary extinction was applied with the use of the Becker–Coppens formalism.

The reliable location of the dopants in the structure and the refinement of their concentrations in the samples under investigation were the central problems of this study. A comparison of the ionic radii (both classical and physical [13]) shows that the radii of cerium and thulium are smaller than the radius of strontium and are substantially smaller than the radius of barium. Hence, it is reasonable to assume that, in the structures under consideration, the rare earth elements isomorphously replace strontium in its positions. The verification of this hypothesis based on the X-ray diffraction data not only confirmed this assumption but also indicated that cerium and thulium replace strontium atoms in the Sr(1) positions rather than in the Sr(2) positions. The occupancies of the Sr(1) positions by strontium and, correspondingly, cerium or thulium were refined by the step-by-step scanning method [14]. In the cerium-doped sample, strontium and cerium atoms statistically occupy one Sr(1) position on the fourfold symmetry axis with probabilities of 69.7(3) and 2.8(3)%, respectively. In the thulium-doped sample, the occupancies of this position are 69.0(3) and 3.5(3)%, respectively.

$(Sr_{0.61}Ba_{0.39})Nb_2O_6$: Ce AND $(Sr_{0.61}Ba_{0.39})Nb_2O_6$: Tm STRUCTURES

The model of the structures under consideration is shown in the figure. This model represents a three-dimensional framework, which consists of Nb octahedra sharing oxygen vertices. The structure of the $[NbO_6]$ octahedra is decisive for the optical properties of these crystals. The specific structural feature of these octahedra is that the *trans*-oxygen atoms, which form the –O–Nb–O–Nb–O– chains parallel to the fourfold symmetry axis of the crystal, are split and occupy two nearby positions with probabilities of 50%. In Nb(1) octahedra located at the intersection of the symmetry planes m, the split positions are related by the mirror plane. In Nb(2) octahedra located in a general position, the two similar positions are independent. In both chains, the shortened and elongated Nb–O bonds alternate with each other. The four equatorial Nb–O bonds located in the planes parallel to the (001) plane of the crystal structure have intermediate values. According to [6], the optical characteristics correlate with the displacements of Nb atoms in octahedra. The degree of deviation of NbO$_6$ octahedra from the central symmetry is associated with the optical nonlinearity of $(Sr,Ba)Nb_2O_6$ solid solutions. This asymmetry can be characterized by the differences between the short and long Nb–O distances in these octahedra. The framework contains channels of three types parallel to the fourfold axis. Narrow channels with a triangular cross section are empty. Medium-sized channels with a tetragonal cross section are occupied by Sr(1) atoms (which statistically occupy their positions with a probability of ~72.0% in all the known structures with different Sr/Ba ratios). The wide channels with a pentagonal cross section are statistically occupied by Ba and Sr atoms. In these channels, barium atoms are located in positions with a multiplicity of four in the mirror planes m. The split strontium position is displaced from the plane m to a general position and is located at a distance of about 0.3 Å from the Ba position.

The arrangement of barium and strontium atoms in the structure of a $Sr_{0.61}Ba_{0.39}Nb_2O_6$ crystal that had the same barium-to-strontium ratio but contained no impurities of rare earth elements was determined in [5]. In this compound, strontium atoms are located in tetragonal channels with a probability of 72.5%. It should be noted that the occupancies of the tetragonal channels in all the structures of $(Sr,Ba)Nb_2O_6$ solid solutions studied previously were no higher than the above value. The total occupancy of pentagonal channels by barium and strontium atoms varied from 88.1 to 89.1%. The doped structures were initially refined without considering the rare earth elements. This refinement revealed enhanced X-ray scattering from atoms located in Sr(1) positions. As was mentioned above, the subsequent refinement of the models in which cerium and thulium atoms, respectively, were placed in this position gave better agree-
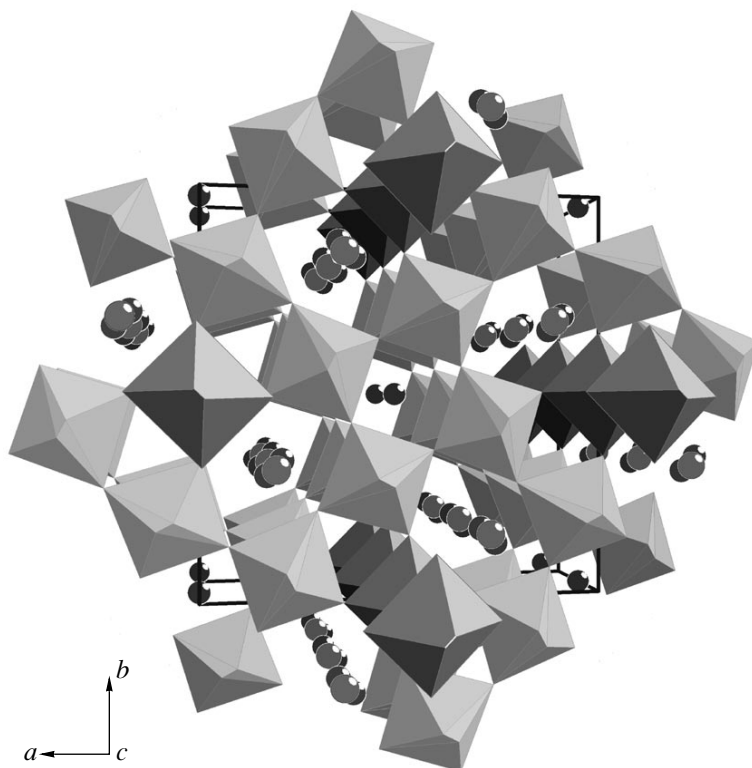
Three-dimensional presentation of the structure of $(Sr_xBa_{1-x})Nb_2O_6$ along the c axis. The dark and light polyhedra represent the (Nb(1)–O) and (Nb(2)–O) octahedra, respectively.

ment between the experimental and calculated structure factors.

The results of the final structure refinement of $Sr_{0.61}Ba_{0.39}Nb_2O_6$: Ce and $Sr_{0.61}Ba_{0.39}Nb_2O_6$: Tm are listed in Table 1. For convenience, this table presents not only the position occupancies, coordinates, and effective thermal vibrations of the basis atoms of the structures but also the symmetries and multiplicities of all the atomic positions. The main interatomic distances for the structures are listed in Table 2. In addition, this table includes the corresponding distances for the structure of $Sr_{0.61}Ba_{0.39}Nb_2O_6$ crystals containing no rare earth dopants [5]. When analyzing the coordination polyhedra of cations in the structures, one should take into account the splitting of the atomic positions O(4), O(4') and O(5), O(6).

The polyhedra of Sr(1) atoms, which incorporate rare earth cations, are of most interest. Each Sr(1) atom is located on the fourfold rotation axis. The coordination environment of this atom is a twelve-vertex polyhedron. As viewed along the c axis, the strontium polyhedron is bounded at the top and bottom by regular squares formed by translationally identical O(2) atoms. The equatorial plane of the polyhedron is formed by four atoms located in split positions. Each of these four split positions may be occupied by either O(5) or O(6) atoms with equal probability. The Sr(1)–O(5) distance

is 2.692 and 2.684 Å in the cerium- and thulium-doped structures, respectively. If O(6) atoms are located in the equatorial plane, the corresponding distances are 2.766 and 2.768 Å. It should not be excluded that atoms in these structures obey the fourfold symmetry only statistically. It is well known that the solid solutions under consideration always contain structural defects in the form of vacancies in the positions of Ba and Sr atoms. In this case, five polyhedra are possible for Sr(1) atoms. In these polyhedra, the average Sr(1)–O distances are 2.737, 2.743, 2.749, 2.755, and 2.761 Å. The probabilities of occurrence of these polyhedra in the structures are 1/16, 4/16, 6/16, 4/16, and 1/16, respectively. These estimates indicate that Ce and Tm ions may choose polyhedra of suitable size to occupy them. Unfortunately, X-ray diffraction analysis always deals with unit cells averaged over the whole crystal and, thus, cannot be used to solve local structural problems.

CRYSTAL STRUCTURE OF $(Sr,Ba)Nb_2O_6$ SOLID SOLUTIONS

It is of interest to compare the occupancies of the strontium and barium positions by corresponding atoms in $(Sr,Ba)Nb_2O_6$ crystals with different Sr/Ba ratios, which were refined in the studies cited above. These data are summarized in Table 3. Their analysis

Table 1. Coordinates and effective parameters of thermal vibrations of the basis atoms in the structures of $Sr_{0.61}Ba_{0.39}Nb_2O_6$: Ce and $Sr_{0.61}Ba_{0.39}Nb_2O_6$: Tm

Atom	Symmetry of the position	Multiplicity of the position	$Sr_{0.61}Ba_{0.39}Nb_2O_6$: Ce					$Sr_{0.61}Ba_{0.39}Nb_2O_6$: Tm				
			occupancy of the position, %	x/a	y/b	z/c	B_{eq}, Å^2	occupancy of the position, %	x/a	y/b	z/c	B_{eq}, Å^2
Nb(1)	*mm*	2	100	0.0	0.5	0.0	0.92	100	0.0	0.5	0.0	0.79
Nb(2)	1	8	100	0.0744(1)	0.2114(1)	−0.0094(7)	0.87	100	0.0746(1)	0.2114(1)	−0.0051(13)	0.70
Sr(1)	4	2	69.7(3)	0.0	0.0	0.4868(8)	0.68	69.0(3)	0.0	0.0	0.4879(18)	0.58
Ce or Tm	4	2	2.8(3)	0.0	0.0	0.4868(8)		3.5(3)	0.0	0.0	0.4879(18)	
Sr(2)	1	8	19.9(1)	0.1532(5)	0.6852(9)	0.4967(19)	1.47	20.1(3)	0.1532(3)	0.6844(6)	0.4974(25)	1.34
Ba	*m*	4	48.6(1)	0.1733(1)	0.6733(1)	0.4886(7)	1.35	48.5(3)	0.1733(1)	0.6733(1)	0.4898(15)	1.25
O(1)	1	8	100	0.3436(1)	0.0060(1)	−0.0441(24)	2.52	100	0.3434(1)	0.0064(1)	−0.0472(20)	2.15
O(2)	1	8	100	0.1394(2)	0.0686(2)	−0.04237(22)	2.20	100	0.1387(2)	0.0685(1)	−0.0473(22)	1.90
O(3)	*m*	4	100	0.2814(2)	0.7814(2)	−0.0202(22)	1.76	100	0.2814(1)	0.7814(1)	−0.0173(42)	1.47
O(4)	*m*	4	50	0.0128(8)	0.5128(8)	0.4849(24)	2.81	50	0.0124(8)	0.5124(8)	0.4740(47)	3.30
O(5)	1	8	50	0.3058(5)	0.4052(6)	0.4700(22)	1.17	50	0.3070(3)	0.4048(4)	0.4777(39)	1.23
O(6)	1	8	50	0.2848(6)	0.4449(7)	0.4689(18)	1.73	50	0.2845(4)	0.4438(5)	0.4710(39)	1.56

Table 2. Main interatomic distances (Å) in the structures of $Sr_{0.61}Ba_{0.39}Nb_2O_6$ (**I**), $Sr_{0.61}Ba_{0.39}Nb_2O_6$: Ce (**II**), and $Sr_{0.61}Ba_{0.39}Nb_2O_6$: Tm (**III**)

	I	II	III
Nb(1) octahedron			
Nb(1)–O(4)	2.127(1)	2.037(1)	2.081(1)
–O(1) × 4	1.958(1)	1.956(1)	1.960(1)
–O(4')	1.833(1)	1.920(1)	1.878(1)
Nb(2) octahedron			
Nb(2)–O(2)	1.956(1)	1.958(1)	1.958(1)
–O(2)	2.001(1)	1.998(1)	2.006(1)
–O(5) × 1/2	1.900(1)	1.914(1)	1.930(1)
–O(6) × 1/2	1.891(1)	1.896(1)	1.888(1)
–O(1)	1.927(1)	1.931(1)	1.936(1)
–O(3)	1.994(1)	1.996(1)	1.995(1)
–O(5) × 1/2	2.089(1)	2.073(1)	2.063(1)
–O(6) × 1/2	2.076(1)	2.065(1)	2.074(1)
Sr(1) polyhedron			
–O(4) × 4	2.679(1)	2.676(1)	2.673(1)
–O(2) × 4	2.839(1)	2.842(1)	2.843(1)
–O(5) × 2	2.692(1)	2.692(1)	2.684(1)
–O(6) × 2	2.764(1)	2.766(1)	2.768(1)

Table 3. Occupancies of atomic positions and the Sr–Ba distances in the crystals of $(Sr,Ba)Nb_2O_6$ solid solutions with different Sr/Ba ratios

Sr/Ba ratio	Atom	Pentagonal channels			Tetragonal channels		
		multiplicity of the position	occupancy, %	vacancies, %	multiplicity of the position	occupancy, %	vacancies, %
Sr0.75/Ba0.25	Sr	8 × 1/2	28.6 + 28.6	11.9	2	71.5	28.5
	Ba	4	30.9				
Sr0.61/Ba0.39	Sr	8 × 1/2	20.2 + 20.2	10.9	2	72.5	27.5
	Ba	4	48.7				
Sr0.61/Ba0.39 : Ce	Sr	8 × 1/2	19.9 + 19.9	11.6	2	69.7	27.5
	Ba	4	48.6				
	Ce				2	2.8	
Sr0.61/Ba0.39 : Tm	Sr	8 × 1/2	20.1 + 20.1	11.3	2	69.0	27.5
	Ba	4	48.5				
	Tm				2	3.5	
Sr0.50/Ba0.50	Sr	8 × 1/2	13.1 + 13.1	11.7	2	72.0	28.0
	Ba	4	62.2				
Sr0.33/Ba0.67	Sr	4		16.0	2	70.5	29.5
	Ba	4	84.0				

showed that the occupancy of the square channels varies from 70 to 72.5%. Taking into account that the strontium position in square channels has a multiplicity of two and that the unit cell contains five $(Sr,Ba)Nb_2O_6$

formula units, we can estimate the limits of existence of solid solutions with this structure. Let us assume that 0.7 is the minimum amount of strontium in the position with a multiplicity of two. Hence, the unit cell contains

Table 4. Dependence of the structural parameters on the composition of $(Sr_xBa_{1-x})Nb_2O_6$ solid solutions

Composition (values of x are listed)	$\Delta[Nb(1)-O]$, Å	$\Delta[Nb(2)-O]$, Å	Distances, Å				Unit-cell volume V, Å³
			O(4)–O(4)	O(5)–O(6)	Sr–Ba	Sr–Sr	
Sr/Ba–0.33	0.35	0.28	0.388	0.510			616.75(4)
Sr/Ba–0.50	0.34	0.25	0.407	0.521	0.335	0.605	613.28(11)
Sr/Ba–0.61	0.29	0.19	0.458	0.567	0.300	0.584	609.38(11)
Sr/Ba–0.61(Ce)	0.10	0.16	0.448	0.558	0.293	0.564	609.47(15)
Sr/Ba–0.61(Tm)	0.20	0.16	0.437	0.562	0.288	0.549	610.14(12)
Sr/Ba–0.75	0.13	0.10	0.561	0.635	0.262	0.510	604.16(12)

1.4 Sr atoms. Then, the number of Sr atoms per formula unit is 1.4 : 5 = 0.28; i.e., $x \approx 0.28$. The data from Table 3 allow one to estimate the numbers of vacancies in the square and pentagonal channels, which are necessary for the existence of structures of this type.

The differences in the distances $\Delta[Nb(1)-O]$ and $\Delta[Nb(2)-O]$ and the interatomic distances for all the pairs of split atomic positions in the structures under consideration are listed in Table 4. Each value in this table characterizes the imperfection of the $(Sr_xBa_{1-x})Nb_2O_6$ solid solutions studied. All these values depend on the amounts of strontium and barium in the crystals.

CONCLUSIONS

Crystals with a minimum strontium content exhibit the strongest nonlinearity of optical properties [1–3]. All structural characteristics listed in Table 4 change monotonically as the strontium content increases. In other words, the structural parameters and optical properties of $(Sr,Ba)Nb_2O_6$ solid solutions can be changed as desired by specifying a particular ratio of strontium to barium in crystals of these compounds. Our study demonstrated that, in the case of fixed concentrations of strontium and barium in $(Sr,Ba)Nb_2O_6$ crystals, their doping with early or late rare earth elements is equivalent to an effective increase in the amount of strontium in a sample, which manifests itself in symmetrization of Nb octahedra and changes in the other structural parameters.

ACKNOWLEDGMENTS

REFERENCES

1. L. I. Ivleva and Yu. S. Kuz'minov, Preprint No. 93, FIAN SSSR (Physical Inst., USSR Academy of Sciences, Moscow, 1977), p. 14.
2. M. E. Lines and A. M. Glass, *Principles and Applications of Ferroelectrics and Related Materials* (Oxford Univ. Press, Oxford, 1977; Mir, Moscow, 1981), p. 89.
3. L. E. Cross, Ferroelectrics **76**, 241 (1987).
4. M. P. Trubelja, E. Ryba, and D. K. Smith, J. Mater. Sci. **31**, 1435 (1996).
5. T. S. Chernaya, B. A. Maksimov, I. A. Verin, *et al.*, Kristallografiya **42**, 421 (1997) [Crystallogr. Rep. **42**, 375 (1997)].
6. T. S. Chernaya, B. A. Maksimov, T. R. Volk, *et al.*, Fiz. Tverd. Tela (St. Petersburg) **42**, 1668 (2000) [Phys. Solid State **42**, 1716 (2000)].
7. T. S. Chernaya, T. R. Volk, I. A. Verin, *et al.*, Kristallografiya **47** (1), 249 (2002) [Crystallogr. Rep. **47**, 213 (2002)].
8. Th. Woike, U. Dorfler, T. Grazow, *et al.*, Kristallphysik (AK5) **19** (39) (2002).
9. T. Granzov, U. Dorfler, Th. Woike, *et al.*, Kristallphysik (AK5) **19** (37) (2002).
10. A. E. Andreĭchuk, L. M. Dorozhkin, Yu. S. Kuz'minov, *et al.*, Kristallografiya **29** (6), 1094 (1984) [Sov. Phys. Crystallogr. **29**, 641 (1984)].
11. U. Zuker, K. Perenthalter, W. F. Kuhs, *et al.*, J. Appl. Crystallogr. **16**, 358 (1983).
12. P. B. Jamison, S. C. Abrahams, and J. L. Bernstein, J. Chem. Phys. **42**, 5048 (1968).
13. *Modern Crystallography. Structure of Crystals*, Ed. by B. K. Vaĭnshteĭn, V. M. Fridkin, and V. L. Indenbom (Nauka, Moscow, 1979), Vol. 2, p. 75.
14. E. A. Belokoneva, V. K. Garanin, and G. Kudryavtseva, Dokl. Akad. Nauk SSSR **242** (2), 330 (1978) [Sov. Phys. Dokl. **23**, 626 (1978)].

Translated by T. Safonova

STRUCTURE
OF INORGANIC COMPOUNDS

Dedicated to the 60th Anniversary
of the Shubnikov Institute of Crystallography
of the Russian Academy of Sciences

Crystal Structure of Zdenekite NaPbCu$_5$(AsO$_4$)$_4$Cl · 5H$_2$O

N. V. Zubkova[1], D. Yu. Pushcharovsky[1,2], H. Sarp[3], S. J. Teat[4], and E. J. MacLean[4]

[1] *Moscow State University, Department of Geology, Vorob'evy gory, Moscow, 119992 Russia*
e-mail: dmitp@geol.msu.ru
[2] *Shubnikov Institute of Crystallography, Russian Academy of Sciences, Leninskiĭ pr. 59, Moscow, 119333 Russia*
[3] *Department of Mineralogy, Museum of Natural History of Geneva,*
route de Malagnou 1, CH-1208 Geneva, Switzerland
[4] *CCLRC Daresbury Laboratory, Daresbury, Warrington, WA4 4AD Cheshire, UK*
Received April 11, 2003

Abstract—The crystal structure of the mineral zdenekite NaPbCu$_5$(AsO$_4$)$_4$Cl · 5H$_2$O was established (Bruker SMART CCD diffractometer, synchrotron radiation, $\lambda = 0.6843$ Å, $R = 0.096$ for 1356 reflections). Single-crystal X-ray diffraction study demonstrated that zdenekite belongs to the monoclinic system with the unit-cell parameters $a = 10.023(7)$ Å, $b = 19.55(1)$ Å, $c = 10.023(6)$ Å, $\beta = 90.02(1)°$, sp. gr. $P2_1/n$, $Z = 4$. The structure consists of polyhedral layers parallel to the (010) plane. These layers are formed by Cuφ_5 polyhedra (φ = O, Cl, H$_2$O) and AsO$_4$ tetrahedra. Distorted Na octahedra and Pb 7-vertex polyhedra and H$_2$O molecules coordinated to these metal atoms are located between the layers. © *2003 MAIK "Nauka/Interperiodica"*.

INTRODUCTION

The mineral zdenekite NaPbCu$_5$(AsO$_4$)$_4$Cl · 5H$_2$O was discovered in the northern region of the Cap Garrone copper–lead mine (France). Two-thirds of this mineral consists of secondary minerals (generally, copper arsenates) [1]. More than a hundred new mineral species were first discovered in this mine. The preliminary single-crystal X-ray diffraction study of zdenekite on a precession X-ray camera (Burger method) revealed that this mineral belongs to the tetragonal system with the unit-cell parameters $a = 10.066(1)$ Å, $c = 39.39(4)$ Å, $V = 3991.41(4)$ Å^3, $Z = 8$ and indicated the possible space groups $P4_1 22$ or $P4_3 22$. It was suggested that zdenekite is a tetragonal Pb-containing analogue of orthorhombic lavendulan NaCaCu$_5$(AsO$_4$)$_4$Cl · 5H$_2$O discovered in 1837 [2]. Until recently, the structure of lavendulan remained unknown. Although eight years elapsed after the discovery of zdenekite, all attempts to establish its structure failed, because X-ray diffraction patterns from its thin platelike single crystals, which are easily cleaved, were of poor quality. New possibilities of X-ray diffraction experiments associated with the use of synchrotron radiation stimulated the X-ray diffraction study of the structure of zdenekite. Here, we present the results of this investigation.

EXPERIMENTAL

X-ray diffraction data were collected from a zdenekite single crystal $0.06 \times 0.04 \times 0.01$ mm^3 in size. Since it was impossible to use a standard X-ray diffractometer for collecting experimental data for zdenekite because of the small sizes and flattened shape of its crystals, the experimental set of intensities was obtained on an automated Bruker AXS SMART CCD diffractometer using synchrotron radiation ($\lambda = 0.6883$ Å) at the Daresbury Synchrotron Radiation Source Station 9.8 (UK) [3]. A total of 3068 reflections were collected in a hemisphere of reciprocal space using the ω-scan technique [4]. Based on the results of processing X-ray diffraction data, it was concluded that the crystals most likely belong to the monoclinic system (averaging of equivalent reflections yielded $R_{int} \sim 0.05$, whereas averaging within the tetragonal system gave $R_{int} \sim 0.20$), in which the unit-cell parameter b is halved. The main characteristics of the crystal and the details of X-ray-diffraction experiment are listed in Table 1. The systematic absences in the three-dimensional X-ray-diffraction data set indicate the sp. gr. $P2_1/n$. The structure was solved directly using the SHELX97 software package [5]. Simultaneously, several possible space groups were tested. The most adequate model was obtained within the sp. gr. $P2_1/n$, which confirms the validity of its choice based on systematic absences of corresponding reflections. Analysis of the model obtained and the residual electron-density map, which contained a large

Table 1. Main crystallographic characteristics and experimental data

Formula	$NaPbCu_5(AsO_4)_4Cl \cdot 5H_2O$
Unit-cell parameters, Å	$a = 10.023(7)$, $b = 19.55(1)$, $c = 10.023(6)$, $\beta = 90.02(1)°$
Space group; Z	$P2_1/n$; 4
Unit-cell volume V, Å^3	1964.6
Calculated density ρ, g/cm^3	4.16
Measured density ρ, g/cm^3*	4.08
Absorption coefficient μ, mm^{-1}	20.80
Molecular weight	1229.1
F_{000}	2260
Diffractometer	Bruker AXS SMART CCD
Radiation; wavelength, Å	Synchroton radiation; 0.6843
Total number of reflections	3068
Number of reflections used in the final stage of the least-squares procedure	1356
Software package for structure solution by direct methods	SHELX97
Software package for structure refinement	JANA2000
Number of parameters in refinement	130
R_{hkl}	0.096
$\Delta\rho_{max}$, e/Å^3	3.18
$\Delta\rho_{min}$, e/Å^3	–2.63

* The measured density is given according to [1].

number of peaks in the vicinity of atomic positions, provided evidence for crystal twinning. The crystal structure of zdenekite was further refined using the JANA2000 program [6]. The weight coefficients of individual components, which were refined using the twin matrices [0 0 1 / 0 1 0 / 1 0 0], [0 0 1 / 0 1 0 / $\bar{1}$ 0 0], and [1 0 0 / 0 1 0 / 0 0 $\bar{1}$], are 0.30(1), 0.166(6), 0.172(6), and 0.365(7). The positions of water molecules were revealed from the difference electron-density map. The model was refined with isotropic thermal parameters, except for the lead atoms, which were refined with anisotropic thermal parameters. The thin platelike shape of the crystal hindered the application of the absorption correction. This fact, together with the poor quality of X-ray diffraction data (all reflections had diffusion tails) and a complex system of twinning, led to negative isotropic atomic thermal displacements for a number of oxygen atoms and water molecules. The coordinates of two oxygen atoms (O(15) and O(16)) and three water molecules (W(1), W(3), and W(5)), which were revealed from the residual electron-density map, were fixed in the course of refinement. The noted reasons also led to deviations of a number of As–O distances from standard values, with the result that the positions of five oxygen atoms (O(2), O(7), O(9), O(11), and O(12)) were somewhat shifted relative to their positions in the difference electron-density map, and these positions were also fixed in the final stage of structure refinement. The average As–O dis-

tances in four nonequivalent AsO_4 tetrahedra (1.77, 1.65, 1.78, and 1.69 Å) are close to the standard values.

The coordinates and atomic thermal displacements for the cations and Cl atoms are given in Table 2. The figures were drawn with the use of the ATOMS program [7].

DESCRIPTION AND DISCUSSION OF THE STRUCTURE

The structure of zdenekite is shown in Figs. 1 and 2. It consists of heteropolyhedral layers parallel to the (010) plane. These layers are formed by $Cu\phi_5$ 5-vertex polyhedra (ϕ = O, Cl, H_2O) and AsO_4 tetrahedra (Fig. 1). In these layers, one can distinguish clusters consisting of four edge-sharing $Cu\phi_5$ 5-vertex polyhedra linked by AsO_4 tetrahedra. In the clusters, four $Cu\phi_5$ 5-vertex polyhedra (distorted tetragonal pyramids) share a vertex occupied by the Cl atom. In all $Cu\phi_5$ 5-vertex polyhedra, the Cu–Cl distance exceeds the Cu–O distances (the average Cu–O distance and the Cu–Cl distance for four $Cu\phi_5$ 5-vertex polyhedra are 1.96 and 2.76 Å, respectively). The AsO_4 tetrahedra are linked to each cluster of four $Cu\phi_5$ 5-vertex polyhedra (four tetrahedra below and four tetrahedra above). Each tetrahedron shares two vertices with two $Cu\phi_5$ 5-vertex polyhedra of one cluster and one vertex with a $Cu\phi_5$ 5-vertex polyhedron from the adjacent cluster. The

fourth vertex of each AsO_4 tetrahedron is linked to the fifth $Cu\varphi_5$ 5-vertex polyhedron, which does not belong to clusters. Like the four 5-vertex polyhedra considered above, the latter copper polyhedron is also a 5-vertex polyhedron and also represents a distorted tetragonal pyramid. However, the latter copper atom is coordinated (along with four oxygen atoms) by the water molecule rather than Cl atom. The water molecule is oriented toward the interlayer space. The average Cu–O distance in this 5-vertex polyhedron is 1.93 Å. The Cu–H_2O distance is elongated to 2.26(5) Å. All the oxygen atoms in this tetragonal pyramid are located in its base and simultaneously serve as vertices of the AsO_4 tetrahedra.

According to [8], the $Cu^{2+}\varphi_5$ tetragonal pyramids differ in the displacement of the copper atom with respect to the square base. This displacement can be characterized by the O–Cu–O angles formed by the O atoms located in the bases of the pyramids. With regard to these values, the fifth CuO_4H_2O 5-vertex polyhedron is somewhat different from the other four CuO_4Cl 5-vertex polyhedra, because the O–Cu–O angles in the former 5-vertex polyhedron are closer to 180°. This circumstance allows us to consider the copper atom in this 5-vertex polyhedron as located virtually in the plane of the square base.

Potassium atoms are located in distorted octahedra and lead atoms are located in 7-vertex polyhedra (the average Na–O and Pb–O distances are 2.35 and 2.52 Å, respectively). These polyhedra and the water molecules coordinated to these metal atoms are located in the interlayer space (Fig. 2). It should be noted that each layer in the zdenekite structure can be described within the tetragonal symmetry with the sp. gr. *P*4, which is consistent with the preliminary data on this mineral obtained by the photographic method [1]. However, the adjacent polyhedral layers are shifted upon their rotation about the twofold screw axis relative to each other, which leads to lowering of the zdenekite symmetry to monoclinic. The structural formula of zdenekite is in complete agreement with its idealized composition reported previously [1].

The correctness of the proposed structural model is additionally supported by the calculations of the valence balance for anions (Table 3). The deviations of the interatomic distances from standard values did not allow us to calculate the local valence balance. However, the formal valence balance for the O^{2-} anions seems to be quite reasonable. The exception is the Cl^- anion, which forms elongated bonds with four surrounding copper atoms. The latter circumstance must be taken into account to correctly estimate the valence balance. This is why the formal valence balance for the chloride anion is overestimated, and this value is not given in Table 3.

The formation of mixed layers consisting of $[Cu\varphi_5]$ tetragonal pyramids and $[AsO_4]$ tetrahedra in the struc-

Table 2. Coordinates of the basis atoms and thermal displacements for the cations and Cl^- anion in the crystal structure of zdenekite

Atom	x	y	z	U_{iso}
Pb	0.362(1)	0.5891(4)	0.2160(9)	0.050(2)*
As(1)	0.152(2)	0.8361(6)	0.919(1)	0.007(3)
As(2)	0.148(3)	0.8473(9)	0.503(2)	0.050(5)
As(3)	0.066(1)	0.6598(7)	0.424(1)	0.006(3)
As(4)	0.060(1)	0.6641(7)	0.010(1)	0.009(4)
Cu(1)	0.128(1)	0.7151(5)	0.714(1)	0.001(3)
Cu(2)	−0.138(2)	0.7838(7)	0.989(1)	0.010(4)
Cu(3)	0.081(2)	0.794(1)	0.207(2)	0.035(6)
Cu(4)	0.364(2)	0.7094(8)	0.946(1)	0.017(4)
Cu(5)	−0.143(3)	0.5931(5)	0.215(2)	0.027(3)
Na	−0.135(7)	0.604(2)	0.707(6)	0.027(9)
Cl	0.634(5)	0.367(1)	0.289(4)	0.026(5)
O(1)	0.235(4)	0.671(2)	0.372(5)	0.001
O(2)	0.271	0.164	0.460	0.001
O(3)	0.541(3)	0.854(2)	0.096(3)	0.001
O(4)	−0.013(5)	0.739(3)	0.375(5)	0.001
O(5)	−0.022(3)	0.826(2)	0.901(4)	0.001
O(6)	0.014(4)	0.657(2)	0.834(4)	0.001
O(7)	0.820	0.160	0.918	0.001
O(8)	0.211(4)	0.770(2)	0.580(5)	0.001
O(9)	0.780	0.241	0.148	0.001
O(10)	0.235(5)	0.909(2)	0.563(5)	0.001
O(11)	0.820	0.157	0.660	0.001
O(12)	0.502	0.090	0.430	0.001
O(13)	0.002(4)	0.863(3)	0.537(5)	0.001
O(14)	0.204(6)	0.916(3)	0.828(6)	0.001
O(15)	−0.008	0.723	0.081	0.001
O(16)	−0.044	0.597	0.364	0.001
W(1)	0.206	0.504	0.148	0.001
W(2)	−0.172(5)	0.479(3)	0.233(8)	0.001
W(3)	−0.142	0.538	0.558	0.001
W(4)	0.035(8)	0.994(4)	0.657(7)	0.001
W(5)	0.390	0.522	0.412	0.001

* The parameter U_{iso} for the Pb atom was calculated based on anisotropic thermal displacements.

ture of zdenekite corresponds to a Cu/As ratio of 1.25 [9]. Mixed layers consisting of Cu polyhedra and As tetrahedra were found in a large group of minerals, among which are pushcharovskite $CuAsO_3(OH) \cdot 1.5H_2O$ [10], geminite $Cu(AsO_3OH) \cdot H_2O$ [11], yvonite $Cu(AsO_3OH) \cdot 2H_2O$ [12], and fluckite $CaMn(AsO_3OH)_2 \cdot 2H_2O$ [13]. The largest distance between the adjacent mixed layers
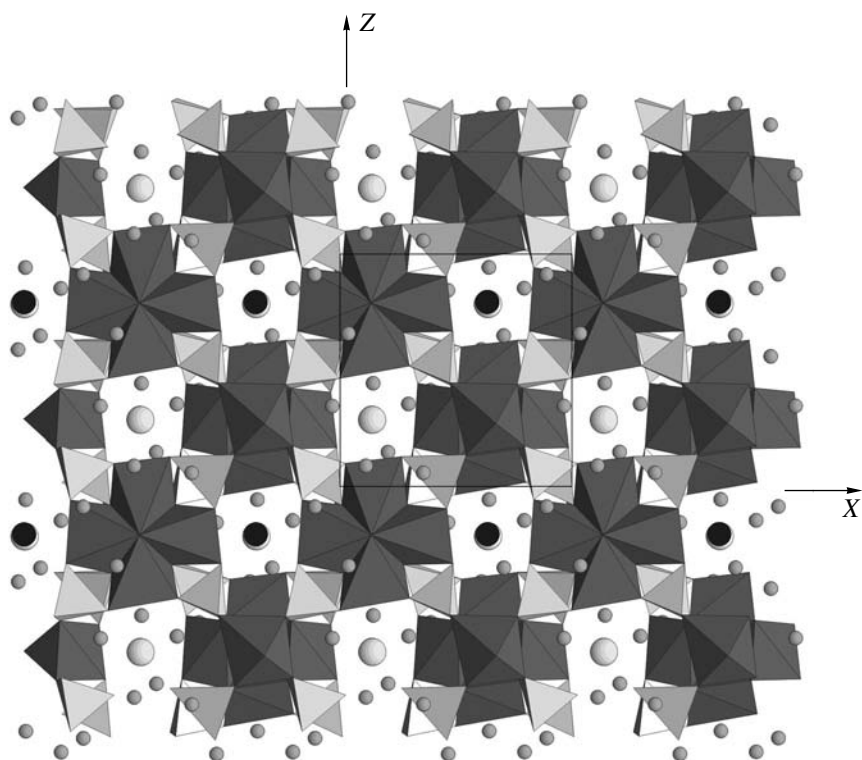
Fig. 1. Polyhedral layer in the structure of zdenekite projected onto the (010) plane [7]. The copper polyhedra and AsO$_4$ tetrahedra are dark-gray and light-gray, respectively. The Pb and Na atoms are represented by large gray and black circles, respectively. The water molecules are indicated by small gray circles.
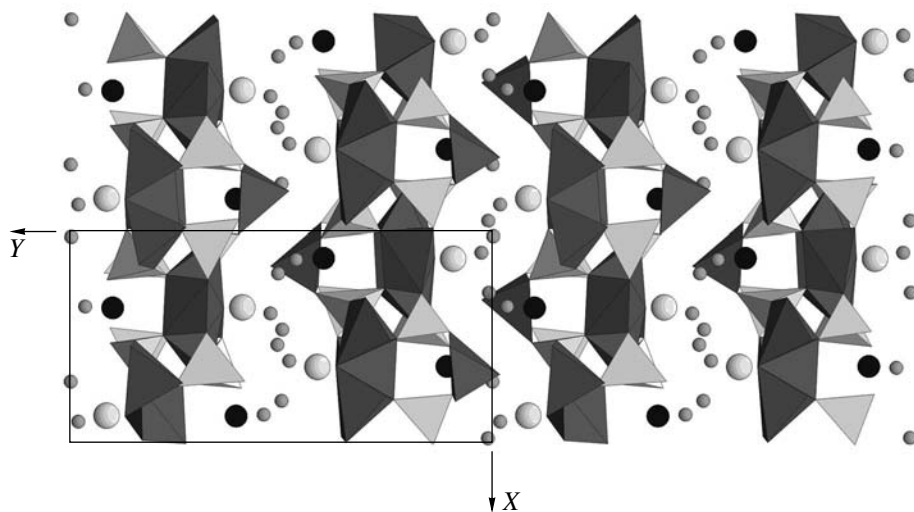

Fig. 2. Crystal structure of zdenekite projected along the [001] direction. For notations, see Fig. 1.

(10.90 Å) was found in pushcharovskite, whereas these distances in the other aforementioned minerals are in the range 7.613–7.822 Å. Like in pushcharovskite, the polyhedral layers and interlayer spaces are rather bulky in the structure of zdenekite. Hence, the distances between these layers are rather large (~9.78 Å).

Until recently, none of the representatives of the lavendulan group have been structurally studied. In addition to the parent mineral lavendulan, this group includes zdenekite and sampleite NaCaCu$_5$(PO$_4$)$_4$Cl · 5H$_2$O. As in the case of lavendulan, the orthorhombic symmetry has been suggested initially for sampleite.

Table 3. Formal valence balance for the anions in the structure of zdenekite

	Na	Pb	As(1)	As(2)	As(3)	As(4)	Cu(1)	Cu(2)	Cu(3)	Cu(4)	Cu(5)	Σ
O(1)		0.29			1.25			0.40				1.94
O(2)		0.29				1.25				0.40		1.94
O(3)	0.17				1.25		0.40					1.82
O(4)					1.25				0.40	0.40		2.05
O(5)		0.29	1.25					0.40				1.94
O(6)	0.17					1.25	0.40					1.82
O(7)	0.17		1.25						0.40			1.82
O(8)				1.25			0.40	0.40				2.05
O(9)			1.25				0.40			0.40		2.05
O(10)				1.25							0.40	1.65
O(11)	0.17			1.25					0.40			1.82
O(12)						1.25					0.40	1.65
O(13)		0.29		1.25						0.40		1.94
O(14)			1.25								0.40	1.65
O(15)						1.25	0.40		0.40			2.05
O(16)					1.25						0.40	1.65
W(1)	0.17	0.29										0.46
W(2)											0.40	0.40
W(3)	0.17											0.17
W(4)		0.29										0.29
W(5)		0.29										0.29

However, in the course of studying zdenekite, it was discovered that the crystal structures of lavendulan and one of the forms of sampleite also belong to the monoclinic system with the sp. gr. $P2_1/n$ and have structures similar to that of zdenekite (unpublished data by G. Giester, P. Williams, and U. Kolitsch). In addition, according to the data of these researchers, another polymorph of sampleite exists, whose structure was established within the sp. gr. $P2_1/c$. Correspondingly, the latter structure is characterized by another alternation of the polyhedral layers. The "tails" of diffraction reflections of zdenekite extended along the [010] direction are indicative of possible violation of the alternation of the polyhedral layers in the zdenekite structure, which suggests that this mineral is characterized by a more complex polytypism.

REFERENCES

1. P. J. Chiappero and H. Sarp, Eur. J. Mineral. **7**, 553 (1995).
2. C. Guillemin, Bull. Soc. Fr. Mineral. Crystallogr. **79**, 7 (1956).
3. R. J. Cernik, W. Clegg, C. R. A. Catlow, *et al.*, J. Synchrotron Radiat. **4**, 279 (1997).
4. W. Clegg, M. R. J. Elsegood, S. J. Teat, *et al.*, J. Chem. Soc. Dalton Trans., 3037 (1998).
5. G. M. Sheldrick, *SHELX97: Program for the Solution and Refinement of Crystal Structures* (Siemens Energy and Automation, Madison, WI, 1997).
6. V. Petricek and M. Dusek, *JANA2000: Crystallographic Computing System for Ordinary and Modulated Structures* (Inst. of Physics, Academy of Sciences of the Czech Republic, Praha, 2003).
7. E. Dowty, *Atoms 5.0. A Computer Program for Displaying Atomic Structures* (Kingsport, 1999), TN 37663.
8. H. Effenberger, Z. Kristallogr. **188**, 43 (1989).
9. R. K. Eby and F. C. Hawthorne, Acta Crystallogr., Sect. B: Struct. Sci. **49**, 28 (1993).
10. D. Yu. Pushcharovsky, S. J. Teat, V. N. Zaitsev, *et al.*, Eur. J. Mineral. **12**, 95 (2000).
11. M. A. Cooper and F. C. Hawthorne, Can. Mineral. **33**, 1111 (1995).
12. H. Sarp and R. Černý, Am. Mineral. **83**, 383 (1995).
13. M. Catti, G. Chiari, and G. Ferraris, Bull. Mineral. **103**, 129 (1980).

Translated by T. Safonova

<div align="center">

STRUCTURE
OF INORGANIC COMPOUNDS

</div>

<div align="right">

Dedicated to the 60th Anniversary
of Shubnikov Institute of Crystallography
of the Russian Academy of Sciences

</div>

$Ba_{1-x}R_xF_{2+x}$ Phases (R = Gd–Lu) with Distorted Fluorite-type Structures—Products of Crystallization of Incongruent Melts in the BaF_2–RF_3 Systems (R = Gd–Lu). III. Defect $Ba_{0.75}Lu_{0.25}F_{2.25}$ Structure. A New {$Lu_8[Ba_6F_{71}]$} Supercluster of Defects

B. P. Sobolev*, A. M. Golubev**, L. P. Otroshchenko*, V. N. Molchanov*,
R. M. Zakalyukin*, E. A. Ryzhova*, and P. Herrero***

* Shubnikov Institute of Crystallography, Russian Academy of Sciences, Leninskiĭ pr. 59, Moscow, 119333 Russia
e-mail: fluorides@ns.crys.ras.ru
** Bauman State Technical University, Vtoraya Baumanskaya ul. 5, Moscow, 107005 Russia
*** Instituto de Ciencia de Materiales, Madrid, Spain
Received September 9, 2002

Abstract—The structure of $Ba_{0.75}Lu_{0.25}F_{2.25}$ crystals grown from melt has been studied by X-ray diffraction analysis (4729 measured reflections, 269 independent reflections with $I > 3\sigma(I)$, $R = 1.1\%$, $R_w = 0.7\%$). The crystals are crystallized in the cubic system, sp. gr. $Pm\bar{3}m$, with the lattice parameter $a = 5.9870(9)$ Å. A new complex of defects is singled out—a supercluster of the composition {$R_8[Ba_6F_{71}]$}. This supercluster differs from the well-known rare earth octahedral supercluster of the composition {$Ba_8[R_6F_{68-69}]$} because its nucleus is formed not by RE cations but by an alkali earth cation, Ba. The {$R_8[Ba_6F_{71}]$} supercluster has a configuration close to that of the [$B_{14}F_{64}$] fragment of the fluorite structure and can replace the latter isomorphously. The model of the $Ba_{0.75}Lu_{0.25}F_{2.25}$ crystals consisting of coherently intergrown isostructural microphases having different chemical compositions is characterized by the good agreement of the calculated and experimentally determined occupancies of the F^{1-} positions. The comparison of the $Ba_{0.8}Yb_{0.2}F_{2.2}$ (phase studied earlier) and $Ba_{0.75}Lu_{0.25}F_{2.25}$ structures demonstrates the evolution of the defect structure along the series of rare earths with the corresponding change of the sp. gr. $Fm\bar{3}m$ by the sp. gr. $Pm\bar{3}m$. © 2003 MAIK "Nauka/Interperiodica".

INTRODUCTION

Numerous studies of various single crystals show that, similar to fluorite, the nonstoichiometric $M_{1-x}R_xF_{2+x}$ phases (M = Ca, Sr, Ba, Cd, Pb; R = RE) are crystallized in the sp. gr. $Fm\bar{3}m$. Their structures are characterized by the formation of associates of ions at which structural defects are concentrated. These associates are called clusters and superclusters. The difference between the two consists in the following: clusters always consist of one type of defects, whereas superclusters sometimes consist of several types of defects. According to the structural studies of $Ba_{1-x}R_xF_{2+x}$ crystals, they have [R_6F_{36}] groups of highly charged rare earth cations [1]. Hereafter, we call the R^{3+} ions in the positions of Ba^{2+} ions the "substitution defects." They are surrounded by anionic vacancies and interstitial fluoride ions. The R^{3+} ions occupy the

vertices of an octahedron and, therefore, this group is called a *rare earth octahedral cluster*. In addition to the above defects, the $Ba_{1-x}R_xF_{2+x}$ structure also has Ba^{2+} ions in the anionic environment not characteristic of the fluorite structure type. These ions should also be considered as structural defects. The attachment of these eight cations to an [R_6F_{36}] cluster results in the formation of a *rare earth octahedral* {$Ba_8[R_6F_{68-69}]$} *supercluster.*

The methods of X-ray and neutron diffraction analysis applied to the crystals with partly disordered (defect) structures give averaged diffraction patterns. The dimensions of some octahedral RE superclusters may exceed the unit-cell dimensions of the $Ba_{1-x}R_xF_{2+x}$ phase. Therefore, in the structural studies, several superclusters can be simultaneously projected onto one unit cell of this structure. As a result, the cationic positions in the structure turn out to be statistically

filled with Ba^{2+} and R^{3+} cations. In the anionic motif, defects are represented by vacancies and interstitial F ions. The vacancies are formed in the main anionic position $8c$ (1/4, 1/4, 1/4) of the sp. gr. $Fm\overline{3}m$. Interstitial fluoride ions occupy two additional positions. Thus, F^{1-} ions occupy the positions $48i(1/2, y, y)$ and form $\{F_{12}\}$ cuboctahedra in the centers of RE superclusters. The remaining F^{-1} anions occupy the $4b$ (1/2, 1/2, 1/2) position and are located either inside $\{F_{12}\}$ cuboctahedra or in the centers of $\{F_8\}$ cubes of the fluorite matrix. The $4b$ position is often called the Goldschmidt position, because it was the only position suggested by Goldschmidt for interstitial F^{1-} ions in the model of yttrofluorite $Ca_{1-x}Y_xF_{2+x}$ [2]. The anions located inside $\{F_{12}\}$ cuboctahedra and $\{F_8\}$ cubes can be displaced from the $4b$ position toward the $32f(x, x, x)$ position. The F^{1-} anions in the latter position are called relaxed anions. The presence of defects in the main anionic position and the existence of two (or three) additional (interstitial) anionic positions is considered as evidence of the formation of $\{Ba_8[R_6F_{68-69}]\}$ superclusters in the structure of disordered $Ba_{1-x}R_xF_{2+x}$ phases.

Earlier (part II of this series of articles [3]), it was established that two phases are simultaneously formed during crystallization of $Ba_{1-x}Yb_xF_{2+x}$ ($x \sim 0.2$) from the melt, the so-called P and F phases. The P phase of $Ba_{1-x}Yb_xF_{2+x}$ became the first representative of the family of nonstoichiometric $M_{1-x}R_xF_{2+x}$ phases crystallized in the sp. gr. $Pm\overline{3}m$. The F phase of $Ba_{1-x}Yb_xF_{2+x}$ (sp. gr. $Fm\overline{3}m$) is somewhat different from the phases studied earlier, namely, all the Yb^{3+} cations are displaced along the [111] direction, whereas some F^{1-} anions are displaced along the threefold axis toward the unit-cell vertex. The formation of a new phase $M_{1-x}R_xF_{2+x}$ with M = Ba and R = Yb can be associated with almost limiting difference between the ionic radii of these cations having different valences, which gives rise to structural rearrangement. If this assumption is true, the transition from $Ba_{1-x}Lu_xF_{2+x}$, to Lu would lead to crystallization from the melt of the phase described by the sp. gr. $Pm\overline{3}m$.

The present article describes the study of the evolution of the defect $Ba_{1-x}R_xF_{2+x}$ structure at the short end of the RE series (from Yb to Lu). With this aim, we determined the defect structure of the phase crystallized from the melt of the composition $Ba_{0.75}Lu_{0.25}F_{2.25}$ and compared this structure with the $Ba_{0.8}Yb_{0.2}F_{2.2}$ structure studied earlier [3].

EXPERIMENTAL

The crystals were grown by the Bridgman technique in a setup with a graphite heater. The growth conditions, the characteristics of the initial reagents, and their purification from the oxygen impurity were described earlier [4]. Like in the preceding articles of this series, the term "as grown crystal" is applied to crystals grown from melt and not subjected to any additional thermal treatment. As was indicated earlier [4], the $Ba_{0.75}Lu_{0.25}F_{2.25}$ boule (having only the $Ba_{0.75}R_{0.25}F_{2.25}$ composition with R = Gd–Lu), when being cooled and taken away from the crucible, disintegrates into transparent blocks with a diameter ranging from 1 to 3 mm, which resembles the effect of a phase transformation during cooling. The blocks do not scatter laser beams, i.e., do not contain any finely dispersed second phase. Unlike all the other crystals of the composition $Ba_{0.75}R_{0.25}F_{2.25}$ (R = Gd–Yb) [4], the small dimensions of these blocks did not allow us to study the inhomogeneity in their composition either in polarized or in transmitted light.

Phase composition of the crystals grown was studied on a powder Siemens D-500 diffractometer ($CuK_{\alpha 1, 2}$ radiation), an INEL diffractometer ($CuK_{\alpha 1}$ radiation), and an HZG-4 diffractometer ($CuK_{\alpha 1, 2}$ radiation). The details of the experiments were described earlier [4]. The X-ray diffraction pattern of an as grown $Ba_{0.75}Lu_{0.249}Er_{0.001}F_{2.25}$ crystal was also considered in [4]. The sample studied was a mixture of small blocks of the boule. The X-ray diffraction pattern had the 110 reflection forbidden in the sp. gr. $Fm\overline{3}m$; the other reflections were considerably distorted. A year after the synthesis, the sample gave a somewhat different diffraction pattern. The refinement of the cubic unit cell over 13 most intense reflections (powder method) gave the lattice parameter $a = 5.987(1)$ Å, coinciding with the lattice parameter $a = 5.9870$ Å of single crystals. It should be indicated that, unlike neutron diffraction analysis, X-ray diffraction analysis of single crystals can be performed on a relatively small amount of the material and, thus, is more preferable for studying multiphase systems with finely dispersed phases similar to as grown $Ba_{1-x}R_xF_{2+2}$ (R = Gd–Lu) boules.

The homogeneity of the composition of a $Ba_{1-x}Lu_xF_{2+x}$ boule was evaluated only indirectly—from the coefficient of Lu distribution in the directed crystallization of the $Ba_{0.75}Lu_{0.25}F_{2.25}$ melt calculated from the phase diagram [5]. This coefficient turned out to be close to unity, 0.95. For all the RE elements in $Ba_{0.75}R_{0.25}F_{2.25}$, except for Ce, Pr, and Nd, this coefficient considerably differs from unity. One can expect that the variation of the composition over the boule during crystallization of the $Ba_{0.75}R_{0.25}F_{2.25}$ melt would be minimal. This is confirmed by the crystal composition obtained based on the lattice parameter determined from the powder and single-crystal data.

Chemical composition of the crystals was set by the charge composition, because the coefficient of the RE distribution in this system is close to unity. The composition determined from the dependence of the lattice parameter on the content of the RE fluoride (powder
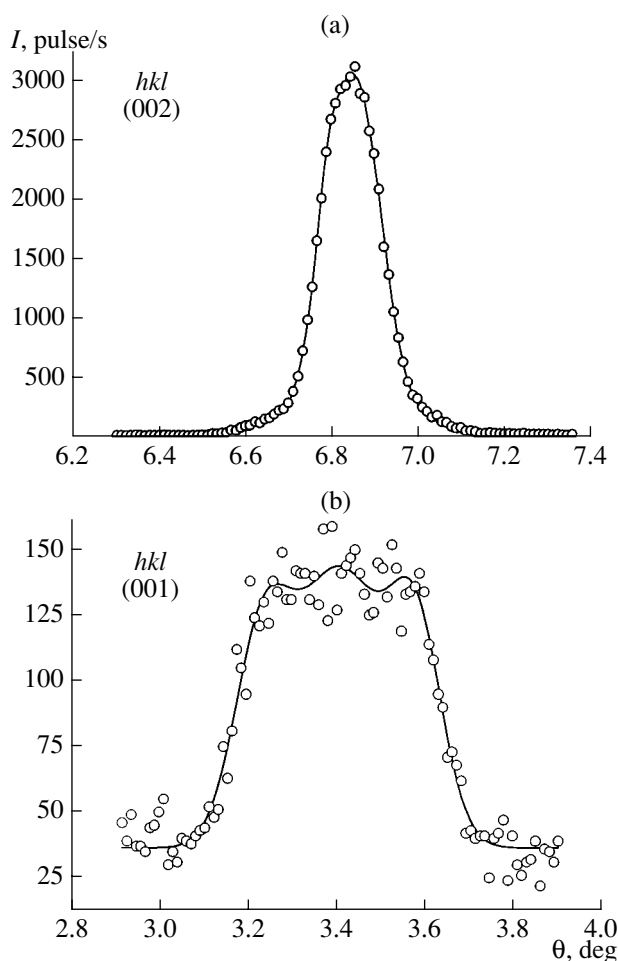
Fig. 1. Typical profiles of diffraction reflections from a $Ba_{0.75}Lu_{0.25}F_{2.25}$ single crystal (a) with and (b) without F centering.

data) only slightly differed from the charge composition. This difference can be explained by the fact that the crystal structure of single crystals grown from melts under nonequilibrium conditions differs from the structure of polycrystal samples obtained by prolonged annealing of the powder mixture of the components below the melting point. In the structural computations, we ignored the presence of 0.1 mol % ErF_3 in the crystals.

Selection of samples and determination of lattice parameters. Since the boule disintegrated into fragments, when being extracted from the crucible, any fragment from any part of the boule could be chosen as a sample for further study. The blocks chosen were rolled into spheres with a diameter ranging from 0.1 to 0.2 mm. Their appropriateness for further study was checked on a diffractometer. The crystal studied showed the extinctions forbidden for the F cell. Therefore, when determining the unit cell parameter of a $Ba_{0.75}Lu_{0.25}F_{2.55}$ crystal, we paid special attention to the search for any deviations from the crystal metrics. The

lattice parameters were determined from the angular position of 24 reflections from the range of θ angles from 26.8° to 29.1°. The α, β, and γ angles turned out to be equal to 90°, and the lattice parameters *a*, *b*, and *c* were equal to one another within the standard deviations (±0.01° and ±0.0009 Å). Thus, the lattice metrics is cubic. The lattice parameters were refined over the groups of high-angle reflections of two types. The first group consisting of 24 equivalent {337} reflections with θ = 29.01° did not violate F centering. The second group of 24 equivalent {037} reflections with θ = 26.87° violated F centering. The lattice parameter determined from these two groups of reflections coincided within 3σ.

EXPERIMENTAL RESULTS

Analysis of the complete set of reflections indicates the absence of general systematic extinctions and, therefore, the unit cell can only be primitive, *P*. The test for centrosymmetricity and the absence of special systematic extinctions indicates the sp. gr. $Pm\bar{3}m$. Thus, the symmetry of an as grown $Ba_{0.75}Lu_{0.25}F_{2.25}$ crystal cannot be described by the sp. gr. $Fm\bar{3}m$. The reflections corresponding to the F cell have clearly shaped profiles. The reflections violating F centering have approximately 100 times lower intensities and are considerably broadened. The FWHM (full width on half-height of the maximum) value for the reflections of the first group is constant at angles θ < 20° and only slightly increases with an increase in θ. Figure 1 shows the typical diffraction–reflection profiles for these two types of reflections. The FWHM value for the reflections of the second group exceeds the value for the reflections of the first group more than twofold. The dependence of FWHM on θ is anomalous: with an increase in the reflection angle, the reflection width decreases and approaches the width of the first-group reflections. This is most clearly seen on the 00*l* reflections violating F centering (Fig. 2) and 11*l* reflections (Fig. 3). The origin of this anomaly requires an additional study. One of the possible explanations can be X-ray diffuse scattering associated with crystal micro-inhomogeneity, which allows one to consider these crystals as nanostructured materials [4].

When recalculating the intensities into the structure-factor moduli, we took into account the polarization and the Lorentz factors and the corrections for absorption by spherical samples and performed averaging within the sp. gr. $Pm\bar{3}m$. The main crystallographic characteristics and the conditions for performing X-ray diffraction experiments on $Ba_{0.75}Lu_{0.25}F_{2.25}$ crystals are indicated in Table 1. The unit-cell parameters were refined using the most intense 337 reflection.
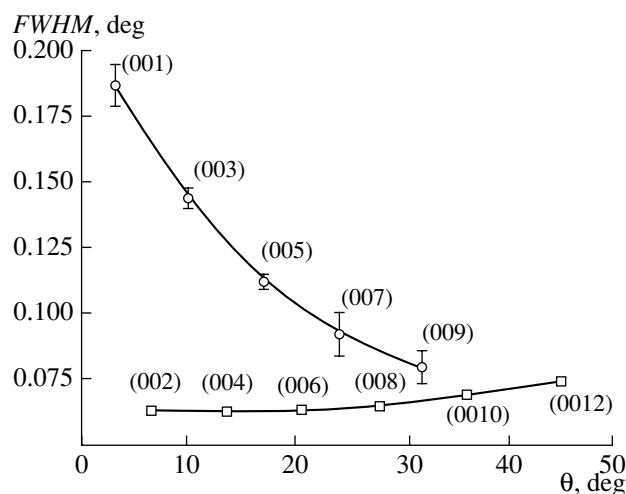
Fig. 2. Width of 00*l* reflections as a function of scanning angle θ.

Fig. 3. Width of 11*l* reflections as a function of scanning angle θ.

REFINEMENT OF Ba$_{0.75}$Lu$_{0.25}$F$_{2.25}$ ATOMIC STRUCTURE

The full matrix LS refinement was performed using the PROMETHEUS program [6]. The initial model for the refinement of the structure parameters was that of the fluorite structure containing only cations. With lowering of the symmetry down to $Pm\overline{3}m$, the cationic position 4*a* (000) of the fluorite structure is split into two positions—1*a* (0 0 0) and 3*c* (0 1/2 1/2). Since the composition of the crystal studied is close to Ba$_3$LuF$_9$ (Ba : Lu = 3 : 1), the Lu cations were placed into the 1*a* position, and the Ba cations, into the 3*c* position. The *R* factor at this stage of the refinement was 8.4%. The electron-density maps also indicated splitting of the cationic 3*c* position. The refinement of the position of the Ba cation in the anisotropic approximation reduced the *R* factor to 7.2%.

To localize F^{1-} anions, the difference electron-density maps were calculated. These maps had a more intense peak in the 8*g* (*x*, *x*, *x*) position at *x* ~ 0.22 (<1/4) and a less intense peak in the 1*b* (1/2 1/2 1/2) position (Fig. 4). The allowance for F^{1-} anions in these positions reduced the *R* factor to 2.9%. The difference electron-density maps constructed at this stage of the refinement revealed one more anionic position—8*g* with *x* ~ 0.28 (>1/4). The allowance for this position reduced the *R* factor even more, to 2.1%.

The cations in the 3*c* position were refined in the anisotropic approximation. The parameters of atomic displacements toward the 6*f* (*x*, 1/2, 1/2) position exceeded the analogous parameters along the perpendicular direction by a factor of 2.6. Therefore, we refined the cations in the 6*f* and not the 3*c* position. This procedure reduced the *R* factor from 2.1 to 1.9%. At the following stage of the refinement, the cationic positions were considered as mixed ones and their composition was refined. This procedure resulted in *R* = 1. 1% and
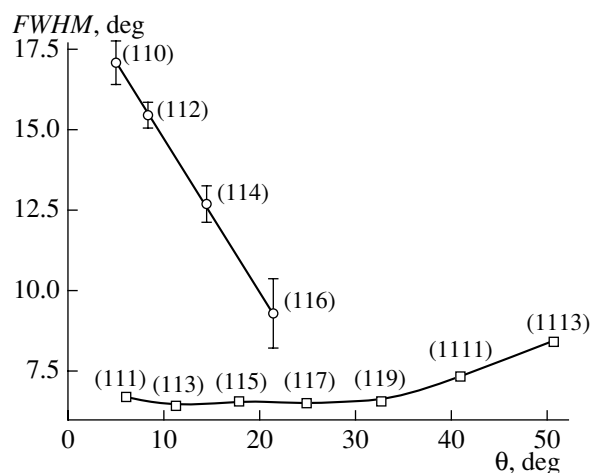
R_W = 0.7%. The concluding stage of the refinement was performed in the isotropic approximation of atomic thermal vibrations with due regard for the extinction correction (Becker–Coppens type 1, *E* = 5.7(2) × 10^{-6} cm). None of the attempts to take into account the anisotropy and ahnarmonism of thermal vibrations reduced the *R* factor.

The refined data are listed in Table 2. The sum of the occupancies of the anionic positions per formula unit is 2.198. The remaining fraction of F anion (0.052) seems to be localized in the vicinity of the 3*d* (1/2 0 0) or 6*e*

Table 1. Main crystallographic characteristics and parameters of diffraction experiments for an as grown Ba$_{0.75}$Lu$_{0.25}$F$_{2.25}$ crystal

Sp. gr.	$Pm\overline{3}m$
a, Å	5.9870 (90)
V, Å^3	214.58 (6)
Z	4
ρ_{calcd}, g/cm^3	5.836
Sample	Sphere, *d* = 0.156 mm
Diffractometer	Enraf-Nonius CAD-4F
Radiation	MoK$_\alpha$; 50 kV; 20 mA
m (MoK$_\alpha$), cm^{-1}	262, 12
Monochromator	Graphite
h, *k*, *l* ranges	±*h*, ±*k*, +*l*
(sinθ/λ)$_{max}$, Å^{-1}	1.15
Scanning	ω/2θ
Number of measured reflections	4729
Number of independent reflections	269, *I* > 3σ(*I*)
R_{av}(*F*)	0.0153
Temperature of experiment	295 K

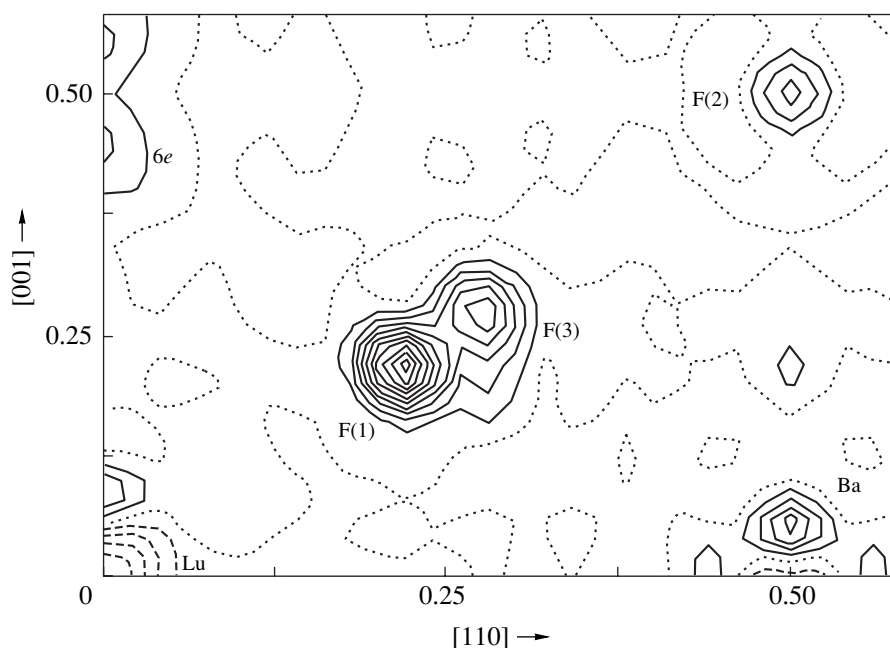**Fig. 4.** Difference (after subtraction of cations) electron-density map for a $Ba_{0.75}Lu_{0.25}F_{2.25}$ structure. Isolines are spaced by 0.05 e/Å^3.

$(x, 0, 0)$ position. The difference electron-density maps show weak peaks in the vicinity of these positions. The refinement of F anions in these positions did not reduce the R factor any more and gave no admissible occupancies of these positions and parameters of atomic thermal vibrations.

DISCUSSION

A new {$Lu_8[Ba_6F_{71}]$} *supercluster of structural defects in* $Ba_{0.75}Lu_{0.25}F_{2.25}$ *crystals.* The data obtained in this study on the defect $Ba_{0.75}Lu_{0.25}F_{2.25}$ structure indicate a new mechanism of the incorporation of additional F^{1-} anions into the structure in comparison with the mechanisms known for the $Ba_{1-x}R_xF_{2+x}$ phases (R = La–Yb) studied earlier (Fig. 5a). The anion positions determined (Fig. 5b) do not correspond to cuboctahedra of anions, whereas the filling of the cationic positions indicate the formation of the octahedra of Ba ions and not of rare earth ions. The displacements of anions to the $1a$ position correlate with the prevalent

filling of this position with Lu cations. The arrangement of six Ba cations in the face centers of the cubic unit cell and eight Lu cations at its vertices, with seven F cations located at the centers of the octahedral cavities of the cationic packing, can be interpreted as the formation of *a new configuration of structural defects—a* {$R_8[Ba_6F_{71}]$} *supercluster* (Fig. 6a). The cation ratio Ba : R in isolated superclusters is equal to 3 : 4. Upon agglomeration of such superclusters, this ratio increases, attaining a value of 3 : 1 (Ba_3RF_9 composition) in the close packing. This corresponds to the $Ba_{0.75}Lu_{0.25}F_{2.25}$ composition of the phase studied. The Ba : R ratio increases with a decrease in the concentration of isolated superclusters in the BaF_2 matrix tending, in the limit, to BaF_2.

Considering the configurations of highly charged cations (RE R^{3+}), we managed to single out two types of rare earth superclusters—octahedral and tetrahedral ones [1]. These superclusters have cationic "cores" of octahedral and tetrahedral configurations, with the vertices occupied (in the limit, completely) by RE ions.

Table 2. Results of structure refinement of an as grown $Ba_{0.75}Lu_{0.25}F_{2.25}$ crystal

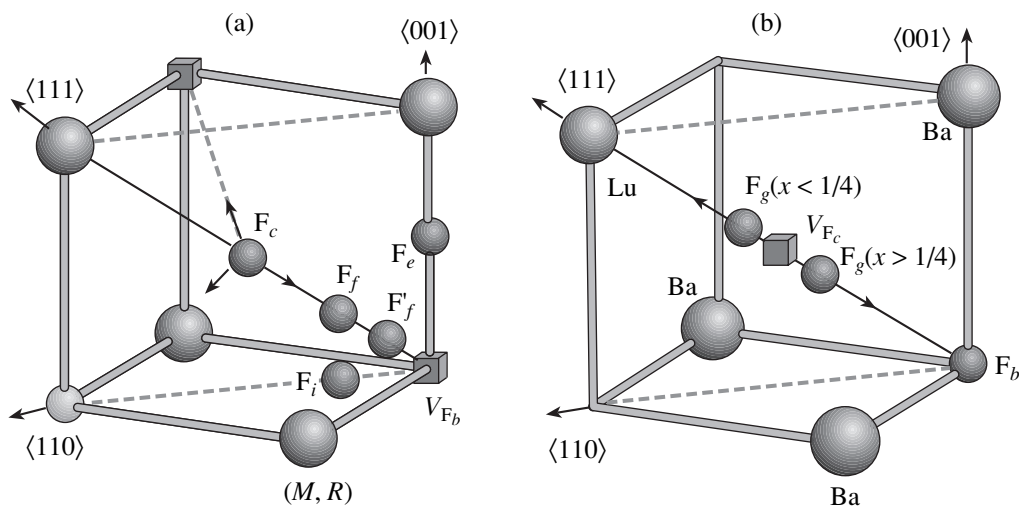| Ion	Position	g	x/a	y/b	z/c	B
Lu, Ba (0.85, 0.15)	$1a$	1	0	0	0	0.25(1)
Ba, Lu (0.475, 0.025)	$6f$	6	0.0138(5)	1/2	1/2	0.45(2)
F(1)	$8g$	6.72(4)	0.220(2)	x	x	0.85(5)
F(2)	$1b$	0.79(3)	1/2	1/2	1/2	1.6(2)
F(3)	$8g$	1.28(4)	0.26(3)	x	x	3.8(1.0)

Fig. 5. Cation and anion positions in the unit cell of the $M_{1-x}R_xF_{2+x}$ phases crystallized in the (a) sp. gr. $Fm\bar{3}m$ and (b) sp. gr. $Pm\bar{3}m$. The subscripts indicate the type of the crystallographic position, e.g., F_f indicates fluoride ions in the $32f$ position, etc. Symbol V indicates the vacancies in the positions of fluoride ions. The arrows indicate the direction of the displacements of fluoride ions from the main position.
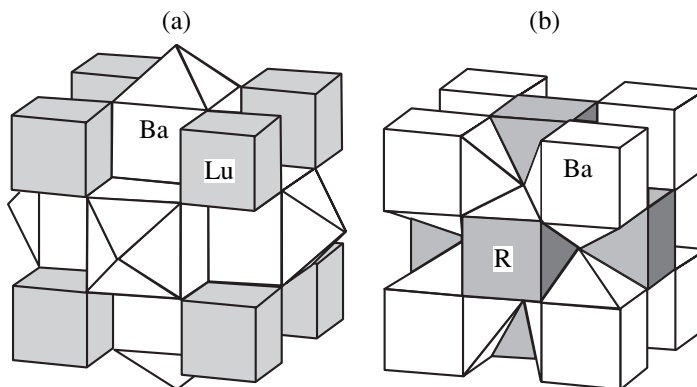

Fig. 6. (a) Octahedral alkali earth $\{R_8[Ba_6F_{71}]\}$ (R = Yb, Lu) supercluster as a combination of $[BaF_{10}]$ and $[RF_8]$ polyhedra and (b) rare earth $\{Ba_8[R_6F_{69}]\}$ (R = Y, La–Yb) supercluster.

The configuration of structural $\{R_8[Ba_6F_{71}]\}$ defects in $Ba_{1-x}R_xF_{2+x}$ crystals with R = Lu represents the third type of superclusters of cationic defects in nonstoichiometric $M_{1-x}R_xF_{2+x}$ phases discovered since 1969. The configuration of cations in the cores allows one to relate this cluster to the octahedral type. The characteristic feature of the cluster is that the octahedral core is formed by alkali earth cations—barium. Therefore, we suggest calling the configuration of $\{R_8[Ba_6F_{71}]\}$ defects (Fig. 6a) an *octahedral alkali earth supercluster.*

When studying the structure of disordered $Ba_{1-x}R_xF_{2+x}$ phases with fluorite-like structure and searching for $\{R_8[Ba_6F_{71}]\}$ superclusters in the cases of the sp. gr. $Pm\bar{3}m$, we established the existence of two anionic positions—$8g$ (with $x < 1/4$) and $1b$ (Figs. 4 and 5b). The equivalent positions in the sp. gr. $Fm\bar{3}m$ are

the $32f$ (with $x < 1/4$) and $4b$. In all the $Ba_{1-x}R_xF_{2+x}$ phases studied earlier, the additional F^{1-} ions in the $32f$ position were characterized by the parameter $x > 1/4$, which corresponds to their *displacement toward the center of an empty* $\{F_8\}$ *cube*—the Goldschmidt position $4b$. In the formation of $\{R_8[Ba_6F_{71}]\}$ superclusters, the anions *are displaced toward the* R^{3+} *cation* (Fig. 5b). This differs the structure of the studied $Ba_{0.75}Lu_{0.25}F_{2.25}$ crystals from the structures of $Ba_{1-x}R_xF_{2+x}$ crystals studied earlier despite the formal coincidence of the crystallographic positions of interstitial F^{1-} ions.

The analysis of the $Ba_4R_3F_{17}$ (R = Yb, Y) structures described in our earlier publication [7] showed that it is possible to single out in these structures a fragment consisting of six Ba^{2+} ions grouped around a fluorine-centered $\{F_9\}$ cube. Thus, we proved structurally the

formation not only of the octahedral rare earth $\{Ba_8[R_6F_{68-69}]\}$ supercluster (Fig. 6b) but also of a fragment of its inverted analogue—alkali earth (with respect to the cationic core) $\{R_8[Ba_6F_{71}]\}$ supercluster (Fig. 6a).

A $\{Lu_8[Ba_6F_{71}]\}$ supercluster includes anions in the $8g$ F(1) and $1b$ F(2) positions (Table 2). Coordination polyhedra of Lu cations are cubes and those of Ba cations, two-capped tetragonal prisms. The Lu–F distances are equal to 2.276 Å and practically coincide with the sum of ionic radii of Lu^{3+} and F^{1-} (2.287 Å) calculated at the coordination numbers 8 (Lu) and 4 (F) using the Shannon system of effective ionic radii [8]. The displacement of Ba^{2+} from the special position in the center of the face leads to four groups of Ba–F distances. For two of these groups, four distances to the vertices of the tetragonal prism are equal to 2.675 and 2.756 Å. For two more F^{1-} ions of the cap, these distances are equal to 2.910 and 3.077 Å. The average Ba–F distance in the coordination polyhedron is 2.771 Å, which is close to the sum of the effective ionic radii of Ba^{2+} and F^{1-} (2.850 Å) at coordination numbers 10 and 6, respectively [8]. Similar to the octahedral rare earth $\{Ba_8[R_6F_{68-69}]\}$ supercluster, the octahedral "alkali earth"$\{R_8[Ba_6F_{71}]\}$ supercluster has a configuration close to that of the $[Ba_{14}F_{64}]$ fragment of the fluorite structure, which includes 14 coordination polyhedra having the shapes of $[BaF_8]$ cubes.

The introduction into the composition of this structural fragment of triply charged cations instead of doubly charged ones requires the introduction of eight additional F anions to compensate the excessive positive charge. A new $\{R_8[Ba_6F_{71}]\}$ supercluster has seven additional F^{1-} ions. However, in the combination of these superclusters, the number of R^{3+} ions per supercluster decreases. Thus, the electroneutrality of the structure is preserved. Similar to the case of $\{R_8[Ba_6F_{71}]\}$ superclusters, the charges of $\{Ba_8[R_6F_{68-69}]\}$ superclusters can be compensated by the incorporation into the structure of one additional F^{1-} ion in the vicinity of the supercluster into the octahedral cavity of the cationic packing. This mechanism of charge compensation was established experimentally in the structure of the ordered $Ba_4Yb_3F_{17}$ phase [7].

On the model of $Ba_{1-x}R_xF_{2+x}$ *solid solutions as coherent intergrowth of the superclusters and the crystalline fluorite matrix.* Recently [9], we suggested to consider the nonstoichiometric fluorite $M_{1-x}R_xF_{2+x}$ phases as a heterogeneous nanophase system. A crystal consists of at least two *isostructural microphases* with considerably different chemical compositions that can *intergrow coherently.* Compared to pure fluorite, MF_2, the microphases having RE-enriched compositions contain all the types of structural defects: RE cations (substitution defects), anionic vacancies in the main position, and interstitial fluoride ions. An isolated complex of these defects forms an octahedral rare earth

supercluster. Isolated $\{M_8[R_6F_{68-69}]\}$ superclusters have nanometer dimensions and are dispersed in the MF_2 matrix. It seems that these superclusters can be combined into larger formations. The $M_{1-x}R_xF_{2+x}$ phases are unique because, even in the case of large associates, they have the form of single crystals and, because of the coherent intergrowth of isostructural microphases, behave as single crystals in X-ray, neutron, and electron diffraction experiments [9]. Such a representation opens new possibilities—fluorite $M_{1-x}R_xF_{2+x}$ phases can be treated as a set of various microphases having different chemical compositions, whose cationic motif remains the same over the whole crystal volume. We use this model to interpret the occupancies of the cationic and anionic positions determined.

A large part of the structure of the $Ba_{0.75}Lu_{0.25}F_{2.25}$ phase (about 85% of the total volume) is a close packing of $\{Lu_8[Ba_6F_{71}]\}$ superclusters and corresponds to the composition Ba_3LuF_9 (microphase I). In accordance with the occupancy of the cationic positions determined, the remaining part (microphase II) consists of Ba cations in the $1a$ position and Lu and Ba cations (in the ratio 1 : 2) in the $6f$ position. The composition of this microphase is also Ba_3LuF_9. The anions in microphase II occupy the $8g$ F(3) position (with $x > 1/4$) (Table 2) and, probably, the $3d$ or $6e$ positions (Figs. 4, 5b). The arrangement of F^{1-} anions in the 1b position would have led to an inadmissibly short distance to the position occupied by F(3) (2.276 Å). The calculated interatomic distances confirm this assumption. The $Ba(1a)$–$F(8g)$ distances are equal to 2.748 Å, which is close to the sum of ionic radii, 2.730 Å [8]. Eight distances of the second cationic position, $3c$, to the anionic position $8g$ occupied by F(3) form two groups of distances, 2.493 and 2.598 Å (average distance 2.545 Å). Theoretically, the average Ba–F and Lu–F distances are equal to 2.509 Å.

Thus, the structure of the disordered $Ba_{0.75}Lu_{0.25}F_{2.25}$ phase can be represented as a coherent intergrowth of two microphases with the same compositions. The differences in the crystal structures of these phases are associated with different filling of the analogous cationic positions and the existence of different anionic positions. The theoretically calculated occupancies of the anionic positions for this model are practically equal to the their experimental values (Table 3).

We believe that the interpretation of the structural data for $Ba_{0.75}Lu_{0.25}F_{2.25}$ can also be applied to the *P* phase of $Ba_{0.80}Yb_{0.20}F_{2.20}$ [3, 10]. The latter phase also crystallizes in the sp. gr. $Pm\bar{3}m$. The anionic positions indicated in Table 3 allow one to interpret (with due regard for the cationic composition) the latter phase as the structure based on the model consisting of two types of superclusters, $\{Yb_8[Ba_6F_{71}]\}$ and $\{Ba_8[Yb_6F_{69}]\}$, and the fluorite BaF_2 matrix. The $Ba_{0.8}Yb_{0.2}F_{2.2}$ composition can be represented as $Ba_3YbF_9 + BaF_2 =$

Table 3. Observed and calculated occupancies of the positions filled with F anions in the structures of the $Ba_{1-x}R_xF_{2+x}$ phases with R = Lu and Yb

Composition of crystals	$Ba_{0.75}Lu_{0.25}F_{2.25}$	$Ba_{0.80}Yb_{0.20}F_{2.20}$
Sp. gr.	$Pm\bar{3}m$	$Pm\bar{3}m$
Position	Position occupancy	
	Obs/calc	Obs/calc
$8g$ ($x < 1/4$)	6.72/6.8	5.636/5.600
$8g$ ($x > 1/4$)	1.28/1.2	0.204/0.226
$6e + 1b$		0.84/0.728
$1b$	0.79/0.85	
$3d + 6e$	0.0/0.15	
$12j$		0.28/0.20

$Ba_4YbF_{11} = 5(Ba_{0.8}Yb_{0.2}F_{2.2})$. The ordered phase with the composition closest to $Ba_{0.8}Yb_{0.2}F_{2.2}$ and containing $\{Ba_8[Yb_6F_{69}]\}$ superclusters is the hypothetic $Ba_7Yb_3F_{23}$ phase [11]. The composition of the $Ba_{0.8}Yb_{0.2}F_{2.2}$ solid solution containing the $Ba_7Yb_3F_{23}$ phase can be written as $15(Ba_{0.8}Yb_{0.2}F_{2.2}) = Ba_{12}Yb_3F_{33} = 3(Ba_4YbF_{11}) = Ba_7Yb_3F_{23} + 5BaF_2$. The representation of the solid solution as a set of structures with two types of superclusters leads one to the formula $[Ba_3YbF_9 + BaF_2]_{0.175}[Ba_7Yb_3F_{23} + 5BaF_2]_{0.0083}$. The occupancies of the anionic positions calculated on this assumption demonstrate the satisfactory agreement between the experimental and calculated values (Table 3). The use of the sum of the $6e$ and $1b$ positions in the calculations is explained by the fact that they both correspond to the anions located in the centers of the $\{F_8\}$ cubes or the $\{F_{12}\}$ octahedra.

The comparison of the above models of two phases with close concentrations of RE cations (Yb and Lu) shows that their structures are different. In the $Ba_{0.8}Yb_{0.2}F_{2.2}$ phase, the Yb^{3+} ions are distributed over the superclusters of both $\{Ba_8[Yb_6F_{59}]\}$ and $\{Yb_8[Ba_6F_{71}]\}$ types. In the $Ba_{0.75}Lu_{0.25}F_{2.25}$ phase, there are no octahedral RE superclusters and all the Lu^{3+} ions are concentrated mainly in the superclusters of the new type—octahedral alkali earth $\{Lu_8[Ba_6F_{71}]\}$ superclusters.

Evolution of the defect structure of as grown $Ba_{1-x}R_xF_{2+x}$ *phases along the RE series.* As was shown in this study, the replacement of disordered $Ba_{1-x}R_xF_{2+x}$ phases in the defect structure revealed in [3, 10] with the change of large RE ions of the Ce subgroup (beginning and middle of the La–Nd–Tm series) by small RE ions of the Y subgroup (Yb, Lu) is seen from the transformation of a defect $\{Ba_8[R_6F_{69}]\}$ supercluster into a $\{R_8[Ba_6F_{71}]\}$ supercluster. There are three very important differences between these superclusters:

—The core of the first supercluster consists of six RE cations concentrated around the $\{F_{13}\}$ cuboctahe-

dron, whereas the core of the second supercluster consists of six Ba^{2+} cations located around the centered $\{F_9\}$ cube.

—The coordination RE polyhedra in the first cluster are one-capped square antiprisms (c.n. = 9), whereas in the second cluster, these are cubes (c.n. = 8). Thus, there is an obvious tendency to a decrease in the coordination number of an RE cation.

—The coordination polyhedra of a Ba^{2+} ion in both first and second superclusters are 10-vertex polyhedra. But in the first supercluster, they are sphenocrowns, whereas in the second one, they are two-capped tetragonal prisms.

The differences in the relative sizes of the Ba^{2+} and R^{3+} ions in the RE series increase in the direction from La to Lu because of the lanthanide contraction. At the same time, the coordination numbers of R^{3+} also decrease along the same direction. In the series of RE trifluorides, this is seen from a decrease in the coordination number from 12 (11) for La^{3+} in the tysonite LaF_3 structure [12] to 9 (possibly to 6) in the β-YF_3 structure [13]. A similar decrease in the coordination number of RE ions at the end of the series with a simultaneous increase in the coordination number of Ba^{2+} was observed in our earlier studies [5, 14, 15] in the morphotropic transition of the monoclinic BaR_2F_8 with the structure of the β-$BaTm_2F_8$ (R = Dy–Tm) type to the orthorhombic phase with the structure of the α-$BaLu_2F_8$ (R = Yb, Lu) type. A decrease in the coordination number of R^{3+} in the BaR_2F_8 phases occurs in the same part of the RE series (Yb, Lu) as for the $Ba_{1-x}R_xF_{2+x}$ phases. It seems that the "driving force" of the morphotropic transitions in both series of phases is the effect of lanthanide contraction of RE ions.

It has already been noted that the relation between two forms of the $Ba_{1-x}Yb_xF_{2+x}$ phases (sp. gr. $Fm\bar{3}m$ and $Pm\bar{3}m$) has not been established in [3, 10]. In the present study, we showed that the $Ba_{0.75}Lu_{0.25}F_{2.25}$

phase described by the sp. gr. $Pm\bar{3}m$ is formed from the melt, i.e., is a high-temperature phase. Being annealed, it changes the space group to $Fm\bar{3}m$ (powder X-ray data [4]). The crystallochemical transformations of the BaR_2F_8 structure with an RE ion from the end portion of the RE series (Yb, Lu) can also be extended to the relation between the two forms (P and F) of the $Ba_{1-x}R_xF_{2+x}$ phases (R = Yb, Lu). If this analogy is correct, then there should exist polymorphous relationships between the P and F forms of the $Ba_{1-x}R_xF_{2+x}$ phase with the fixed RE cations, i.e., the forms described by the sp. gr. $Pm\bar{3}m$ and $Fm\bar{3}m$. The change of RE element along the series and a decrease in the R^{3+} radius after Lu^{3+} should result in the morphotropic transitions to the P form stable at all the temperatures. In our next article, we shall show that, in fact, this is not the case, and the P-$Ba_{0.75}Lu_{0.25}F_{2.25}$ after annealing is transformed into the F form. The morphotropic transition is not completed because of the termination of the RE series at lutecium and because there is no RE cation having a smaller radius. It seems that, in $Ba_{1-x}R_xF_{2+x}$ phases with R = Yb, Lu, one deals with the morphotropic change of the defect (cluster) structure "extended" by the temperature factor for two elements (Yb, Lu) and not completed because of the termination of the RE series.

ACKNOWLEDGMENTS

REFERENCES

1. B. P. Sobolev, *Rare Earth Trifluorides* (Inst. d'Estudis Catalans, Barcelona, 2001), Part 2.
2. V. M. Goldschmidt, T. Barth, G. Lunde, and W. Zachariasen, Skr. Nor. Vidensk. Akad. Kl. 1: Mat.–Naturvidensk. Kl. **1** (2), 1 (1926).
3. B. A. Maksimov, Yu. B. Gubina, E. L. Belokoneva, *et al.*, Kristallografiya **47** (3), 417 (2002) [Crystallogr. Rep. **47**, 372 (2002)].
4. B. P. Sobolev, A. M. Golubev, E. A. Krivandina, *et al.*, Kristallografiya **47** (2), 237 (2002) [Crystallogr. Rep. **47**, 201 (2002)].
5. B. P. Sobolev and N. L. Tkachenko, J. Less-Common Met. **85** (12), 155 (1982).
6. U. H. Zucker, E. Perenthaler, W. F. Kuhs, *et al.*, J. Appl. Crystallogr. **16** (3), 358 (1983).
7. B. A. Maksimov, Kh. Solans, A. P. Dudka, *et al.*, Kristallografiya **41** (1), 51 (1996) [Crystallogr. Rep. **41**, 50 (1996)].
8. R. D. Shannon, Acta Crystallogr., Sect. A: Cryst. Phys., Diffr., Theor. Gen. Crystallogr. **32** (5), 751 (1976).
9. B. P. Sobolev, A. M. Golubev, and P. Herrero, Kristallografiya **48** (1), 148 (2003) [Crystallogr. Rep. **48**, 141 (2003)].
10. B. A. Maksimov, Yu. B. Gubina, E. L. Belokoneva, *et al.*, in *Abstracts of 1st National Conference on Crystal Chemistry* (Chernogolovka, 1998), Part 1, p. 133.
11. A. M. Golubev, Koord. Khim. **18** (12), 1232 (1992).
12. K. Schlyter, Ark. Kemi **5** (1), 73 (1953).
13. L. S. Garashina, B. P. Sobolev, V. B. Aleksandrov, and S. S. Vishnyakov, Kristallografiya **25** (2), 294 (1980) [Sov. Phys. Crystallogr. **25**, 171 (1980)].
14. O. E. Izotova, V. B. Aleksandrov, B. P. Sobolev, and L. S. Garashina, in *Abstracts of 2nd All-Union Symposium on Chemistry of Inorganic Fluorides* (Nauka, Moscow, 1970), p. 116.
15. B. V. Bukvetskiǐ, L. S. Garashina, N. L. Tkachenko, *et al.*, in *Abstracts of 4th All-Union Symposium on Chemistry of Inorganic Fluorides, Dushanbe* (Nauka, Moscow, 1975), p. 47.

Translated by L. Man

STRUCTURE
OF MACROMOLECULAR COMPOUNDS

Dedicated to the 60th Anniversary
of the Shubnikov Institute of Crystallography
of the Russian Academy of Sciences

Three-Dimensional Structure of *Saccharomyces cerevisiae* Inorganic Pyrophosphatase Complexed with Cobalt and Phosphate Ions

I. P. Kuranova*, K. M. Polyakov*, E. A. Smirnova*, W. E. Höhne**, V. S. Lamzin***, and R. Meijer***

* *Shubnikov Institute of Crystallography, Russian Academy of Sciences,*
Leninskiĭ pr. 59, Moscow, 119991 Russia
e-mail: inna@ns.crys.ras.ru
** *Institute of Biochemistry, University Clinics Charité, Humboldt University,*
Hessischestrasse 3-4, Berlin, 10115 Germany
e-mail: wolfgang.hoehne@charite.de
*** *European Molecular Biology Laboratory, EMBL Hamburg Outstation, c/o DESY,*
Notkestrasse 85, Hamburg, 22603 Germany
e-mail: victor@embl-hamburg.de
Received May 26, 2003

Abstract—Crystals of *Saccharomyces cerevisiae* inorganic pyrophosphatase suitable for X-ray diffraction study were grown by cocrystallization of the enzyme with cobalt chloride and imidodiphosphate. *Saccharomyces cerevisiae* is a metal-dependent enzyme which catalyzes hydrolysis of inorganic pyrophosphate to orthophosphate. The three-dimensional structure of this enzyme was solved by the molecular-replacement method and refined at 1.8 Å resolution to an *R* factor of 19.5%. Cobalt and phosphate ions were revealed in the active centers of both identical subunits (*A* and *B*) of the pyrophosphatase molecule. In subunit *B*, a water molecule was found between two cobalt ions. It is believed that this water molecule acts as an attacking nucleophile in the enzymatic cleavage of the pyrophosphate bond. It was demonstrated that cobalt ions and a phosphate group occupy only part of the potential binding sites (two chemically identical and crystallographically independent subunits have different binding sites). The arrangement of ligands and the structure of the nucleophile-binding site are discussed in relation to the mechanism of action of the enzyme and the nature of the metal activator. © 2003 MAIK "Nauka/Interperiodica".

INTRODUCTION

Inorganic pyrophosphatases belong to metal-activated enzymes catalyzing hydrolysis of inorganic pyrophosphate to orthophosphate. These enzymes are involved in processes providing important stages of cellular metabolism, including biosynthesis of proteins and nucleic acids and the energy conversion in living organisms [1]. Soluble inorganic pyrophosphatases are assigned to family **I** or **II**, depending on the type of the three-dimensional structure and the nature of the most efficient metal activator [2]. *Saccharomyces cerevisiae* (SC) inorganic pyrophosphatase, which exists as a dimer of two chemically identical subunits, is the most studied representative of soluble pyrophosphatases of family **I** and serves as a convenient model for detailed elucidation of the mechanism of enzymatic transfer of phosphate groups.

Divalent metal ions necessary for catalysis by pyrophosphatase differ noticeably in their ability to activate the enzyme. The efficiency of metal ions as activators of pyrophosphatase decreases in the series $Mg^{2+} > Zn^{2+} > Co^{2+} > Mn^{2+} > Cd^{2+}$. Ca^{2+} ions inhibit the enzyme [3].

The modern concepts of the mechanism of action of pyrophosphatase are to a large extent based on the results of kinetic and X-ray diffraction studies of this enzyme. The three-dimensional structures of the apoenzyme, the complex of pyrophosphatase with activating manganese ions, the complex with phosphate and manganese ions (the enzyme–product complex), and the enzyme complex with pyrophosphate, manganese ions, and inhibiting fluoride ions were established [4–8]. Based on the results of X-ray diffraction studies, the

Characteristics of the X-ray diffraction data set, details of refinement, and parameters of the cobalt–phosphate pyrophosphatase complex

Number of crystals	1
Synchrotron outstation, EMBL, Hamburg	XII
Wavelength, Å	0.91
Resolution, Å	17.59–1.77
Number of independent reflections	63474
Number of measured reflections	318512
Redundancy	4.65
Completeness of the set, %	99.9
$R(I)$merge, %	3.7
R, %	19.53
R_{free}, %	24.40
Number of protein atoms	4552
Number of phosphate groups	2
Number of cobalt ions	6
Number of solvent molecules	667
Rms deviation from ideal bond angles, deg	2.5
Rms deviation from ideal bond lengths, Å	0.017

proposed schemes of enzymatic catalysis have been considered at the atomic level.

It was demonstrated that the active center of the enzyme, along with the region in which pyrophosphate or phosphate groups formed upon hydrolysis of pyrophosphate are bound, contains four binding sites for the metal ions involved in catalysis. The metal ions are bound by coordination with the carboxyl groups of residues of dicarboxylic amino acids, which are located in the cavity of the active center. Two activating metal ions are bound by the enzyme in both the presence and absence of the substrate, whereas the third and fourth metal ions are bound only together with the substrate (pyrophosphate) or phosphate groups. It was hypothesized that hydrolysis of pyrophosphate occurs by the associative S_N2 mechanism, and the water molecule located between the metal ions serves as a nucleophile that cleaves the pyrophosphate bond [7].

In spite of the fact that the rate of the reaction catalyzed by pyrophosphatase depends substantially on the nature of the metal ion, the high-resolution three-dimensional structure of the enzyme was established only for enzyme complexes with manganese ions serving as activators. It is still unclear how sensitive the three-dimensional structure of pyrophosphatase is to the nature of the bound metal ion, whether the nature of the metal ion influences the conformations of the amino acid residues in the active center, and whether metals of different nature occupy the same positions.

In this study, we report the three-dimensional structure of *Saccharomyces cerevisiae* inorganic pyrophosphatase complexed with cobalt and phosphate ions. The three-dimensional structure of this complex is compared with the known three-dimensional structures of the enzyme complexed with manganese ions and the enzyme complexed with manganese and phosphate ions using the model described in [7].

EXPERIMENTAL

The protein was prepared according to the procedure described previously [9]. The enzymatic activity, determined by the known procedure [10], was 600–640 U/mg at 25°C.

Crystals of pyrophosphatase were grown by vapor diffusion. The enzyme with a concentration of 16 mg/ml and specific activity of 640 U/mg, dissolved in 30 mM MES buffer (pH 6.5), was crystallized in the presence of 1 mM imidodiphosphate and 1 mM cobalt chloride at 4°C using a 25% 2-methyl-2,4-pentanediol solution as a precipitating agent. The crystals up to $0.3 \times 0.25 \times 0.20$ mm in size, with the unit-cell parameters $a = 51.69$ Å, $b = 93.23$ Å, $c = 69.84$ Å, $\beta = 99.74°$, belong to the sp. gr. $P2_1$.

The three-dimensional set of diffraction reflections was collected at 1.77 Å resolution from one crystal using synchrotron radiation at 100 K in the European Molecular Biology Laboratory (EMBL, Hamburg, Germany) on the DESY synchrotron equipped with an MAR-345 two-dimensional detector. The X-ray diffraction data were processed using the DENZO and SCALEPACK programs.

The three-dimensional structure of the enzyme was solved by the molecular-replacement method using the atomic model of pyrophosphatase complexed with manganese and phosphate ions [6] and refined at 1.8 Å resolution using the REFMAC program. Both subunits were refined independently. The atomic model was improved using the FRODO program. The statistics of data collection and details of refinement are listed in the table.

The electron-density maps revealed 283 of 3286 amino acid residues in each subunit of the enzyme molecule. For the three C-terminal residues, the electron density was absent. Six amino acid residues in subunit *A* (Lys21, Ser106, Gln136, Lys167, Asp217, Lys227) and ten amino acid residues in subunit *B* (Lys10, Thr60, Lys76, Arg78, Val80, Asp147, Asn161, Leu168, Lys198, Asn211) adopt two conformations each. The rms deviation between the C_α atoms of both subunits is 0.31 Å. The maximum deviations were observed for the regions 238–240 and 147–148 (2.38 and 1.75 Å, respectively). The refined model was compared with other three-dimensional structures of pyrophosphatase using the LSQKAB program.

RESULTS AND DISCUSSION

As described above, enzyme crystals were prepared by cocrystallization of pyrophosphatase with cobalt
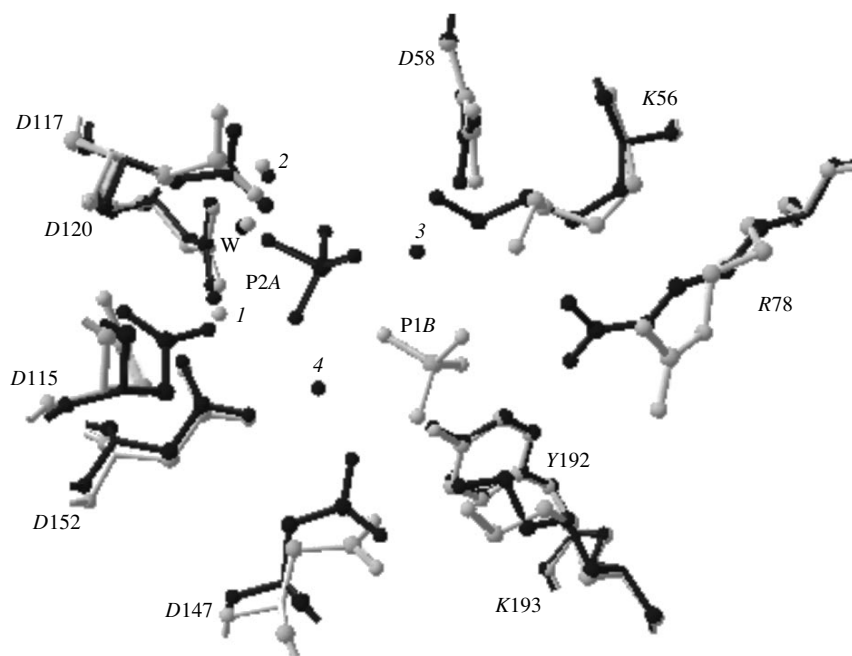
Fig. 1. Comparison of subunits *A* (black) and *B* (gray) of a cobalt–phosphate pyrophosphatase complex. Fragments of the active center with cobalt ions and phosphate and the amino acid residues involved in the coordination sphere of the metal ions and phosphate groups are shown. The positions of the cobalt ions are denoted by *1–4*. The black and gray tetrahedra represent the phosphate groups in the P2*A* and P1*B* sites, respectively. The amino acid residues are represented by one-letter codes.

chloride and imidodiphosphate (a substrate analogue). Compared to magnesium, which is the best activator, cobalt is an order of magnitude less efficient and in this respect is similar to manganese [3]. At the same time, cobalt and magnesium carboxylate complexes have virtually identical geometric parameters, which are somewhat different from the parameters of manganese carboxylates [11]. Imidodiphosphate is cleaved by pyrophosphatase rather slowly, especially when cobalt ions serve as the activator instead of magnesium ions [12, 13].

Initially, we attempted to prepare crystals of the enzyme complexed with imidodiphosphate. For this purpose, we added imidodiphosphate to the mother liquor immediately before freezing crystals. However, this procedure led to cracking of the crystals. Because of this, the sets of X-ray diffraction data were collected from the enzyme crystals incubated with imidodiphosphate during crystal growth. Analysis of the structure demonstrated that the imidodiphosphate molecule was absent in the active center of the enzyme. Apparently, imidodiphosphate was hydrolyzed during crystal growth to phosphate and phosphamide. It is impossible to distinguish the latter two compounds in the electron-density maps at a 1.8 Å resolution. Hence, we described the groups located in the phosphate-binding sites of the enzyme as phosphates.

Previously, it was demonstrated that either of the two active centers of the dimeric pyrophosphatase mol-

ecule can bind four metal ions [4–7] and a maximum of two phosphate groups: one group in the high-affinity site and the other in the low-affinity site (denoted by P1 and P2, respectively). Unlike the pyrophosphatase complex with manganese ions and phosphate, in which ligands occupy all binding sites, the potential binding sites in the enzyme complexed with cobalt are occupied only partially, different sites being occupied in two chemically identical and crystallographically independent subunits of the enzyme.

The fragments of the active centers of subunits *A* and *B*, which were superimposed by least-squares fitting of C_α atoms, are shown in Fig. 1 together with the bound ligands. It can be seen that certain amino acid residues of the active center, which play an important role in catalysis, adopt somewhat different conformations in the two subunits. For example, Lys56 in subunit *A* forms a hydrogen bond with phosphate in the P2 site, whereas this residue in subunit *B* forms a hydrogen bond with phosphate in the P1 site. The residue Arg78 also has different conformations in the two subunits. In subunit *B*, its side chain occupies two positions, one of which is rotated toward the enzyme surface. Apparently, this conformational mobility plays a significant role in the catalysis by pyrophosphatase.

In subunit *A*, cobalt ions are located in all four binding sites (denoted by Co1*A*–Co4*A*). The Co1*A* and Co2*A* sites, which belong to the metal cofactors, are occupied completely ($Z = 1$), whereas the Co3*A* and

Co4*A* sites are only half-occupied. The only phosphate group is located in the P2*A* site, whereas the P1 site does not contain phosphate at all. The coordination sphere of the P2*A* phosphate group contains all four metal ions and the amino group Lys56. One of the oxygen atoms of the phosphate group, namely, O4, is located between the cobalt atoms in the Co1*A* and Co2*A* positions at equal distances from them. This oxygen atom forms a hydrogen bond with the carboxyl group of Asp117.

A different situation is observed for subunit *B* (Fig. 1, gray color). Of four metal-binding sites, only sites 1 and 2, which belong to metal cofactors, are occupied by cobalt ions. A water molecule is located between the Co1*B* and Co2*B* ions. After superposition of subunits *A* and *B*, the position of this water molecule almost coincides with that of the O4 atom of the P2*A* phosphate group. The phosphate group with an occupancy $Z = 0.7$ was found only in the P1*B* site. In the P2 site, the phosphate group is absent. The coordination sphere of the P(1) phosphate group is formed by two nitrogen atoms of the guanidine group of Arg78 and the ε-amino groups of the residues Lys56 and Lys193. The fact that basic groups prevail in this coordination sphere indicates that the P1 site most likely binds phosphate rather than phosphamide. The negative charge of phosphamide is one unit less than that of phosphate, and, consequently, phosphamide has lower affinity for basic groups.

Analysis of the binding of phosphate by pyrophosphatase in the presence of manganese ions demonstrated that the P1 and P2 sites differ in the affinity for phosphate. The P1 site was indicated as the site characterized by the highest affinity [14]. The absence of phosphate in the P1 site of subunit *A* of the cobalt complex is inconsistent with the assumption that this site has a higher affinity for phosphate. Apparently, the relative affinities of the P1 and P2 sites for phosphate vary depending on the degree of occupancy of the metal-binding sites. If all four sites are occupied by metal ions, phosphate is more strongly bound in the P2 site. In the presence of only two metal cofactors, the phosphate P1, which forms hydrogen bonds with the guanidine group of arginine and the amino groups of two lysine residues, is bound more strongly than the phosphate P2. Contrary to the assumption made in [7], the coordination of phosphate to four metal ions is stronger than its binding through hydrogen bonds. Experiments with isotopic exchange of oxygen between the phosphate group and water molecule confirmed the assumption of stronger binding of phosphate in the P2 site [15].

The active centers of subunits *A* and *B* were compared with those in the subunits of the manganese–phosphate pyrophosphatase complex by superimposing their C_α atoms. For this purpose, we used the coordinates of the enzyme complexed with the reaction products [7], in which all metal- and phosphate-binding sites are occupied. Three of four metal ions occupy vir-

tually identical positions in subunit *A* of the cobalt complex and in the manganese–phosphate enzyme complex. The largest distance (0.8 Å) was observed between the metal ions occupying site 4, with the Co4*A* atom displaced toward the P2*A* phosphate group. This displacement occurs, most likely, due to the absence of phosphate in the P1*A* site. In addition, it should be noted that the metal–oxygen distances in the complexes under consideration have different values. The Co–O distances vary from 2.01 to 2.42 Å, and the corresponding Mn–O distances vary from 2.37 to 3.46 Å.

The complexes under consideration differ most significantly in the orientation of the phosphate group in the P2 site (Fig. 2). In both complexes, three oxygen atoms of the P2 phosphate groups lie nearly in the same plane, whereas the fourth oxygen atoms are in apical positions with respect to each other. In other words, the P2 phosphate groups in the *A* subunits of the cobalt and manganese–phosphate enzyme complexes have opposite configurations, thus forming a mirror pair. The distance between the central phosphorus atoms in these two structures is 0.65 Å. The difference in the configurations of the phosphate groups and the absence of phosphate in the P1 site of subunit *A* suggest that the pyrophosphatase complexes under comparison reflect the state of the enzyme, in which it may exist in different stages of the enzymatic reaction. It is generally agreed that the pyrophosphatase-catalyzed cleavage of the pyrophosphate bond occurs by the associative S_N2 mechanism through the attack of a nucleophile (in the case under consideration, of a water molecule or a hydroxy anion) at the electrophilic phosphorus atom. The P2 phosphate group containing the electrophilic phosphorus atom is subjected to the attack, whereas the P1 phosphate group is a leaving group [7, 16]. Subunit *A* simulates the state of the enzyme after binding of the nucleophile and removal of the P1 phosphate group, whereas the manganese–phosphate complex prepared by cocrystallization of the enzyme with phosphate and manganese (the enzyme–product complex) reflects the state of the enzyme after the free and enzyme-bound phosphates come to equilibrium.

The stability of the conformation of the P2*A* phosphate group, which corresponds to an intermediate state during the catalysis, can be attributed to the absence of phosphate in the P1*A* site. As a result, all four metal ions are involved in binding of only one phosphate group. The arrangement of the oxygen atoms of the phosphate in the anion-binding site between the metal ions becomes favorable. In the manganese–phosphate complex, the change in the configuration of the P2 phosphate group gives rise to an eight-membered ring, which involves metal ions in sites 3 and 4 and both phosphates. This configuration is stabilized by coordination bonds between the phosphate groups and metal ions as described in [17]. The energy gain upon the ring formation facilitates a change in the configuration of the P2 phosphate group. It is remarkable that both conformations of the P2 phosphate group were simulta-
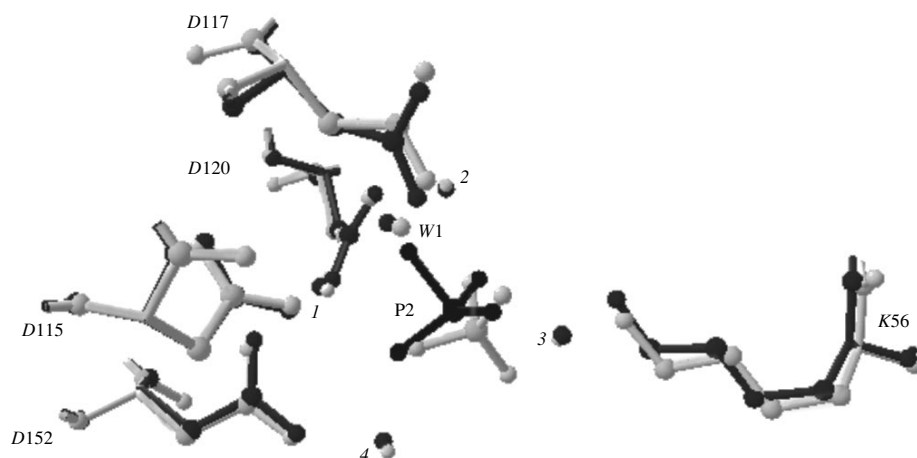
Fig. 2. Comparison of subunit *A* of the cobalt–phosphate pyrophosphatase complex (black) and subunit 1 of the manganese–phosphate pyrophosphatase (gray). The position of the water molecule, which presumably acts as a nucleophile, is denoted by *W*1. The amino acid residues involved in binding of the metal ions and phosphate are shown. In the comparison, the coordinates of the model described in [7] are used.

neously observed in the manganese–phosphate complex established at 1.15 Å resolution [8]. In this complex, the P1 phosphate group occupies two positions. It is partially involved in the ring and partially located at the exit from the active center, thus being removed from the P2 phosphate group.

In subunit *B*, in which two metal ions (Co1 and Co2) are located, the structure of the nucleophile-binding site is of interest (Fig. 3). As noted above, one water molecule is located between the Co1*B* and Co2*B* metal cofactors. It was suggested in [7, 18] that the water molecule (Wat1) located between the metal activators serves as a nucleophile attacking the pyrophosphate bond. The nucleophilic properties of the water molecule in this position are enhanced due to the coordination to two metal ions and donor hydrogen bonding with the carboxyl group of Asp117 [8]. Subunit *B* of the cobalt complex, in which phosphate is absent in the P2 site, is functionally similar to the pyrophosphatase complex containing two manganese ions [7]. The difference is that two water molecules are located between the manganese ions. Based on this fact, it was assumed that the final formation of the nucleophile-binding site accompanied by the removal of the excessive water molecule occurs after the substrate is added [8]. Apparently, in the case of activation of the enzyme with cobalt ions, the nucleophilic center is formed prior to the addition of the substrate, and the above step of the reaction does not occur. Such differences in the structure of the nucleophilic center can influence the efficiency of metal activators and be responsible for the differences in the reaction rate observed in the presence of metals of different nature. In the cobalt complex, the shorter *M*–O distances in the coordination sphere around the

P2 phosphate group may also affect the catalysis efficiency.

The superposition of subunits *A* and *B* of the cobalt complex demonstrated that the position of the water molecule (a nucleophile in subunit *B*) almost coincides with the position of the O4 atom of the P2*A* phosphate group (Fig. 1). Taking into account the S_N2 mechanism
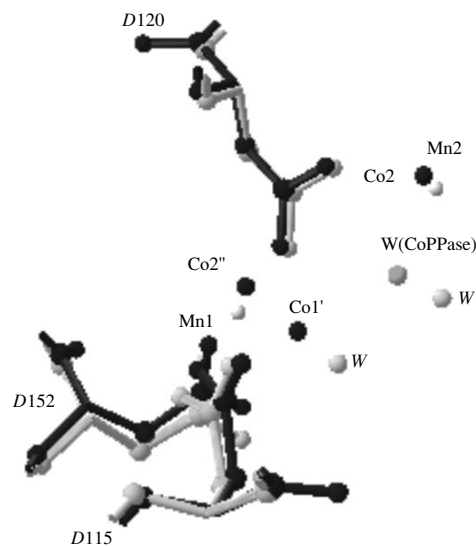

Fig. 3. Comparison of subunit *B* of the cobalt pyrophosphatase complex (black) and subunit 1 of the enzyme complex containing two manganese ions (gray). The fragments of the active centers involving the metal activators (Co and Mn, respectively) coordinating their amino acid residues, the water molecule located between the cobalt ions (*W* CoPPi), and two water molecules between the manganese ions (*W*) are presented. The coordinates of the model described in [7] are used.

of the reaction, we conclude that it is the O(4) atom that previously belonged to the attacking nucleophile and was bound to the P(2) phosphate group as the entering group upon cleavage of the pyrophosphate bond. Since the position of the oxygen atom remains unchanged after its addition to phosphate, it should be assumed that the new P–O bond is formed due to the motion of the central phosphorus atom of the P(2A) phosphate group in the direction of the attack, as was suggested in [5].

Analysis of the structure of the cobalt pyrophosphatase complex showed that the functional ligands are asymmetrically bound in the chemically identical and crystallographically independent subunits *A* and *B* of the enzyme. As a result, each subunit reflects the state of the enzyme in different stages of catalysis. Analogous asymmetry was observed upon binding of ligands in the manganese–phosphate complex of the D115N mutant of pyrophosphatase [18]. The asymmetric binding in the wild-type enzyme indicates that this behavior is not caused by mutation. The manganese–phosphate and cobalt enzyme complexes are crystallized in different space groups ($P2_12_12_1$ and $P2_1$, respectively), in which subunits have different environments. The asymmetric behavior of the subunits was also found previously in a solution in the presence of some reagents [19]. Hence, the asymmetric binding can hardly be attributed only to the influence of the crystallographic environment. This fact is more likely to be the characteristic feature of the functioning of the enzyme itself.

Certain differences in the structures of the manganese and cobalt pyrophosphatase complexes (different distances in the coordination spheres around the metal ions and the difference in the structure of the nucleophilic center) may influence the efficiency of catalysis in the presence of different metal ions.

ACKNOWLEDGMENTS

REFERENCES

1. A. Kornberg, *Horizons in Biochemistry*, Ed. by M. Kasha and B. C. Pullman (Academic, New York, 1962), Vol. 439, p. 263.

2. L. G. Butler, *Enzymes*, Ed. by P. D. Boyer (Academic, New York, 1971), Vol. 4, p. 529.

3. I. P. Kuranova, S. S. Terzyan, A. A. Voronova, *et al.*, Bioorg. Khim. **9**, 1611 (1983).

4. É. G. Arutyunyan, I. P. Kuranova, S. S. Terzyan, *et al.*, Bioorg. Khim. **10**, 1469 (1984).

5. E. H. Harutyunyan, I. P. Kuranova, B. K. Vainshtein, *et al.*, Eur. J. Biochem. **239**, 220 (1996).

6. P. Heikinheimo, Y. Lehtonen, A. Baykov, *et al.*, Structure (London) **4**, 1491 (1996).

7. P. Heikinheimo, V. Tuominen, A.-K. Ahonen, *et al.*, Proc. Natl. Acad. Sci. USA **98**, 3121 (2001).

8. B. S. Cooperman, N. Y. Chiu, R. H. Bruchmann, and G. P. McKenna, Biochemistry **12**, 1665 (1973).

9. T. A. Rapoport, W. E. Hohne, J. G. Reich, *et al.*, Eur. J. Biochem. **26**, 237 (1972).

10. C. J. Carrel, H. L. Carrel, J. Erlebacher, and J. P. Glusker, J. Am. Chem. Soc. **110**, 8651 (1988).

11. I. N. Smirnova, A. A. Baykov, and S. M. Avaeva, FEBS Lett. **206**, 121 (1986).

12. I. N. Smirnova, N. A. Kudryashova, S. V. Komissarenko, *et al.*, Arch. Biochem. Biophys. **267**, 280 (1988).

13. D. I. Hamm and B. S. Cooperman, Biochemistry **17**, 4033 (1978).

14. A. B. Zyryanov, P. Pohjanjoki, V. N. Kasho, *et al.*, J. Biol. Chem. **276**, 17629 (2001).

15. B. S. Cooperman, Methods Enzymol. **87**, 526 (1982).

16. I. P. Kuranova and V. I. Sokolov, Bioorg. Khim. **12**, 749 (1986).

17. T. Salminen, J. Kapila, P. Heikinheimo, *et al.*, Biochemistry **34**, 782 (1995).

18. V. Tuominen, P. Heikinheimo, T. Kajander, *et al.*, J. Mol. Biol. **284**, 1565 (1998).

19. I. E. Svyato, V. A. Sklyankina, S. M. Avaeva, and T. I. Nazarova, FEBS Lett. **167**, 269 (1984).

Translated by T. Safonova

STRUCTURE
OF MACROMOLECULAR COMPOUNDS

Dedicated to the 60th Anniversary
of the Shubnikov Institute of Crystallography
of the Russian Academy of Sciences

Database for Rapid Protein Classification Based on Small-Angle X-ray Scattering Data

A. V. Sokolova[1], V. V. Volkov[1], and D. I. Svergun[1,2]

[1] *Shubnikov Institute of Crystallography, Russian Academy of Sciences,*
Leninskiĭ pr. 59, Moscow, 119333 Russia
e-mail: vvo@ns.crys.ras.ru
e-mail: anna.sokolova@embl-hamburg.de
[2] *European Molecular Biology Laboratory, c/o DESY,*
Notkestrasse 85, Hamburg, 22603 Germany
Received April 9, 2003

Abstract—A method was developed for rapid protein classification based on comparison of the experimental small-angle X-ray scattering data with scattering curves calculated for proteins with known structures. For this purpose, a database was compiled from about 1500 theoretical scattering curves for proteins with known structures. The potential of this method was illustrated by its application to analysis of the experimental scattering data from sperm whale myoglobin. © 2003 MAIK "Nauka/Interperiodica".

INTRODUCTION

Studies of structure–function relationships for biological macromolecules is a fundamental problem of modern molecular biology. It is more probable that proteins with similar three-dimensional structures fulfill similar functions rather than proteins, which are similar only in the primary sequence. Hence, databases developed in the last decade for the analysis of the structure–function relationships, such as SCOP [1] and CATH [2], employ algorithms that search for homologies in the spatial distribution of polypeptide chains in high-resolution structures. This approach allows one to obtain more information on the possible protein functions compared to the analysis of the similarity of only primary sequences. However, this approach cannot, evidently, be used for molecules with unknown atomic structures. In the present paper, we describe a method for the classification of proteins with unknown atomic structures based on small-angle X-ray scattering (SAXS) from their solutions.

The SAXS intensity $I(s)$ from dilute monodisperse particle solutions is a smooth decreasing function of the momentum transfer $s = 4\pi\sin\theta/\lambda$, where 2θ is the scattering angle and λ is the X-ray radiation wavelength. The spatial resolution D is determined by the angle range of experimental data and is related to the momentum transfer s by the equation $s = 2\pi/D$. In the range of the momentum transfer up to 9 nm^{-1}, the intensity corresponds to a resolution of 0.7 nm. Due to the random

orientations of particles in solution, the functions $I(s)$ are isotropic. At higher resolution, the scattering curves from for different proteins are virtually indistinguishable [3]. Information on the quaternary structure of a molecule (resolution up to approximately 4 nm) is provided by the values of s ranging from 0 to 1.5 nm^{-1}. Information on the internal, i.e., secondary and tertiary structure (resolution from 1.5 to 0.7 nm), can be extracted in a range of the momentum transfer from 4 to 9 nm^{-1} (Fig. 1). To classify proteins on the basis of SAXS data, two portions of the curves, which are called the internal ($0 < s < 1.5$ nm^{-1}) and medium ($4 < s < 9$ nm^{-1}) parts, were analyzed. This approach to the construction of a database enables one to independently analyze information on the shape and internal structure of a particle.

EXPERIMENTAL

Atomic Models and Comparison Criteria for Scattering Curves

Presently, the database of structures for which we calculated the small-angle scattering curves includes about 1500 atomic-resolution models of biologically active oligomers taken from the Brookhaven Protein Data Bank (PDB) [4]. We chose the protein models with the sequence lengths varying from 50 to 3000 amino acid residues, whose structures were established by X-ray crystallography. Since the standard
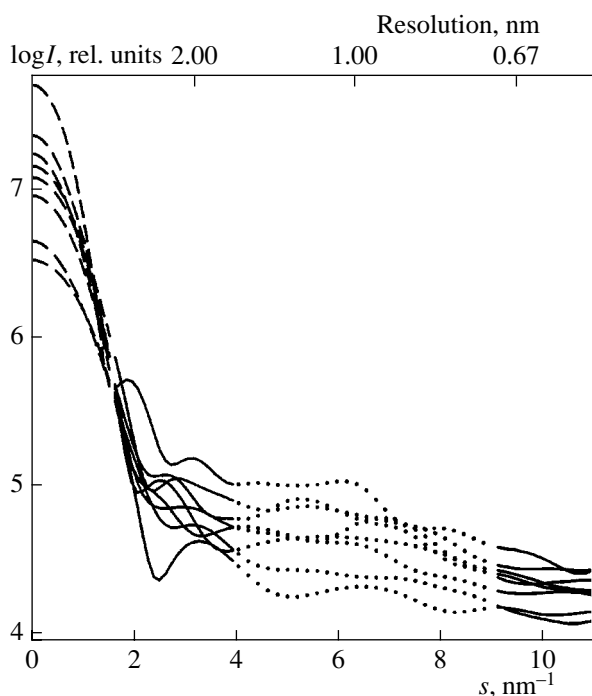
Fig. 1. Eight scattering curves from for proteins, whose molecular weights vary from 100 to 300 kDa. The internal and medium parts of the scattering curves are dashed and dotted, respectively.

PDB files often contain only atomic coordinates of the asymmetric unit and transformation matrices necessary for the generation of the structure of the entire biologically active molecule, we developed computer programs to analyze and apply symmetry operations described in PDB files. Therefore, our database contains models of biologically active oligomers, i.e., of proteins actually expected to exist in solution. When choosing protein models from the PDB, structural homologues (according to the criteria of the PDB) were excluded to minimize the percentage of models with a high degree of homology in the database.

The behavior of SAXS curves depends heavily on the molecular weight of a protein. To exclude this effect on the results of analysis and calculations, all structures were divided into 26 sets. In each set, proteins differ in molecular weight by no more than 50 kDa. All model calculations were carried out with the use of scattering curves calculated from atomic-resolution structures using the CRYSOL program [5].

As mentioned above, SAXS curves are rapidly decreasing functions of the momentum transfer, and a comparison of such curves is a complex problem. In the general form, the mathematical criterion (*R* factor) for the comparison of two one-dimensional scattering

curves $I_1(s)$ and $I_2(s)$ can be written as follows:

$$R_{I_1(s), I_2(s)} = \frac{\sum_{i=1}^{N}(W(s_i)(FI_2(s_i) - I_1(s_i)))^2}{\sum_{i=1}^{N}I_1(s_i)FI_2(s_i)W(s_i)^2},$$

where *F* is the scale factor providing the best fit of two curves to each other by the least-squares method,

$$F = \frac{\sum_{i=1}^{N}I_1(s_i)I_2(s_i)W(s_i)^2}{\sum_{i=1}^{N}(I_2(s_i)W(s_i))^2},$$

and $W(s_i)$ is the weighting function, choice of which depends on the problem solved. We analyzed several functional relationships, namely, $W(s) = s$, $W(s) = s^2$, and a comparison on the logarithmic scale. The *R* factor appeared to be most sensitive to changes in $I(s)$, when the weighting function was equal to *s* (this value is used in the Kotel'nikov theorem on the information content of SAXS data [6]). It was shown that, in this case, the *R* factor can be used for analyzing both the internal and medium parts of SAXS curves. Herein, the *R* factors for these ranges are denoted by *RfI* and *RfM*, respectively.

Internal Part of SAXS Data Defines the Protein Shape

In the analysis of the internal part of SAXS data, the first questions to be answered were whether there are molecules with different shapes, which give identical scattering curves, and what is the maximum value of *RfI* corresponding to molecules with virtually identical shapes.

In the first step, we calculated *RfI* for each pair of scattering curves within each of the 26 sets. Simultaneously, the quantitative measure of shape similarity for each pair of molecules was calculated using the SUPCOMB program [7]. Two arbitrary three-dimensional structures represented as point sets were arranged in a space with the use of the SUPCOMB program by minimizing the parameter called the normalized spatial discrepancy (NSD). The latter is calculated as follows. For each point from the first model, the distances to each point in the second model are calculated and their minimum value is found. Then the same procedure is carried out for each point in the second model. All values thus determined are summed and normalized to the average distances between the adjacent points in each
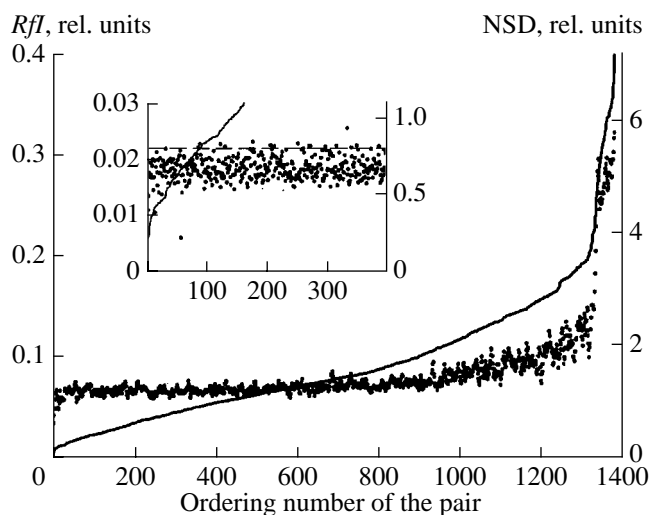
Fig. 2. Values of *RfI* (solid curve) and NSD (dots) for 1378 pairs of SAXS curves for 53 proteins with molecular weights varying from 35 to 40 kDa. The data are arranged in order of increasing *RfI*. In the inset, the initial region of the plot is shown on an enlarged scale.

model. Therefore, NSD yields a quantitative measure of dissimilarity between tree-dimensional objects. For similar structures, NSD should be close to or smaller than unity.

To reduce the computer time, NSD were calculated for models consisting of densely packed spheres (dummy atoms) 0.3–0.4 nm in diameter rather than for atomic-resolution structures. This operation retains the general shape of particles and gives NSD values that adequately represent the discrepancy between low-resolution shapes.

The correlation between *RfI* and NSD shown in Fig. 2 leads to the following conclusions:

(1) the maximum value of *RfI* corresponding to the definitely similar low-resolution structures (NSD < 0.8) is 0.02;

(2) values of *RfI* higher than 0.05 correspond to substantially different external shapes of protein molecules.

Figure 3 shows two pairs of proteins with similar (NSD = 0.96, *RfI* = 0.02) and substantially different (NSD = 1.8, *RfI* = 0.149) quaternary structures and the corresponding calculated SAXS curves.

Interestingly, we found no examples where two scattering curves for substantially different particles (NSD > 1.4) were characterized by low *RfI* (lower than 0.02). In other words, SAXS data containing information on low-resolution structures nearly unambiguously determine the particle shape. This result is nontrivial, because a large portion of structural information is lost due to a random orientation of particles in a solution, and *I*(*s*) is a one-dimensional function of the momen-
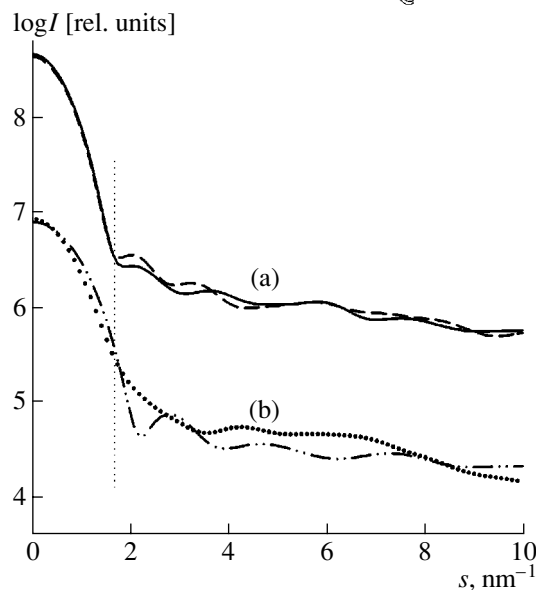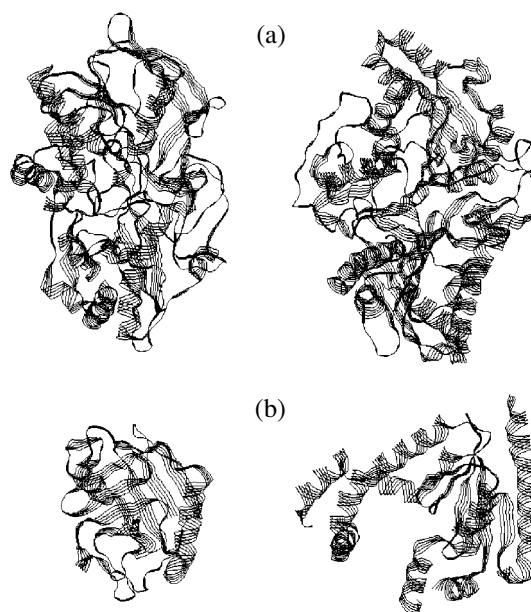

Fig. 3. (a) Proteins having similar shapes, 1B4V.pdb (at the left) and 1FOI.pdb (at the right), and the corresponding theoretical scattering curves (1B4V.pdb and 1FOI.pdb are shown by solid and dashed curves, respectively); (b) proteins having different shapes, 1LOP.pdb (left) and 1JJV.pdb (right), and the corresponding theoretical scattering curves (1LOP.pdb and 1JJV.pdb are shown by dash-and-dot and dotted curves, respectively).

tum transfer due to averaging. The fact that there is a one-to-one correspondence between the particle shape and the initial region of the scattering curve is in good agreement with the possibility of the shape reconstruction by direct methods of analysis of SAXS data [8, 9]. At the same time, no clear correlation with *RfI* was observed for some overall structure parameters, e.g., for the maximum diameter of particles.
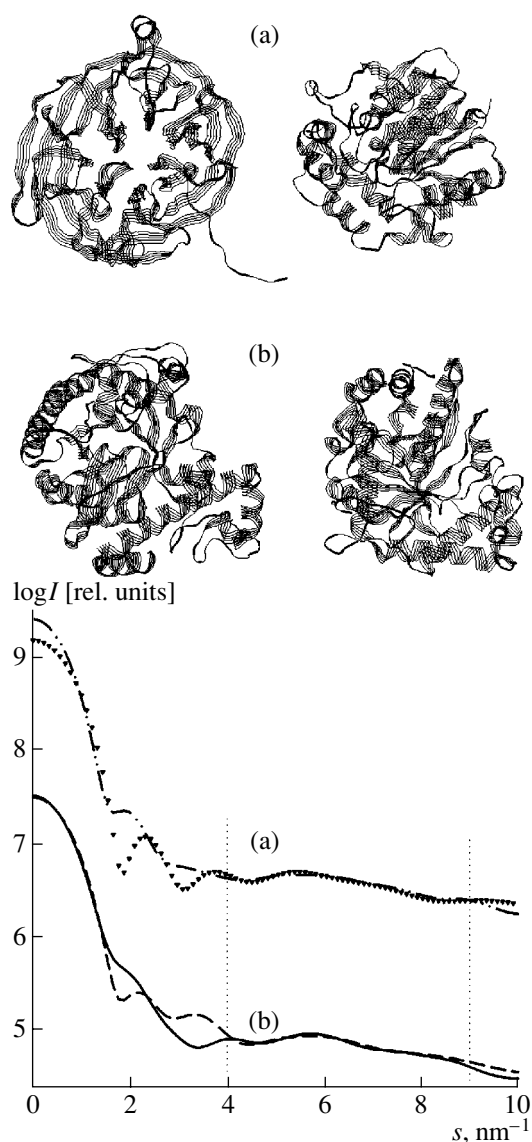
$\log I$ [rel. units]

Fig. 4. (a) Proteins belonging to different classes (2BBK.pdb, class α, and 2HAD.pdb, class β, are shown at the left and right, respectively) and the corresponding scattering curves ($RfM = 0.038$); 2BBK.pdb and 2HAD.pdb are indicated by triangles and a dash-and-dot curve, respectively; (b) homologous proteins according to the DALI classification (1J9Y.pdb is shown at the left, and 1PUD.pdb is shown at the right, $Z = 10.5$) and the corresponding theoretical scattering curves ($RfM = 0.046$); 1J9Y.pdb and 1PUD.pdb are shown by dashed and solid curves, respectively.

Medium Part of SAXS Data: Analogues in Domain Structure

In the analysis of the medium part of SAXS data, the first question to be answered was on the range of *RfM* corresponding to the scattering curves of proteins with similar internal structures. By analogy with the procedure described in the previous section, *RfM* values were calculated for all pairs of structures. It was found that

the scattering curves of proteins having substantially different internal structures are characterized by the value of *RfM* larger than 0.15. Hence, we excluded such pairs from the subsequent consideration.

Generally, the proteins characterized by similar medium parts of scattering curves ($RfM < 0.15$) actually appear to be similar at low resolution. Nevertheless, either quantitative or statistical criteria are required to describe this similarity. We attempted to find a correlation between *RfM* and the secondary structures of protein molecules using the Class, Architecture, Topology, and Homologous (CATH) superfamily database, which represents a hierarchical classification of 18 577 biomacromolecules and their domains according to their correspondence to evolutionary families and structural groups. The class is the upper (first), roughest, level of the classification, which is determined only by the percentage of α helices and β strands. According to the CATH database, there are the following three main structural classes: structures formed only by α helices (α class), only by β strands (β class), and by combinations of these two elements ($\alpha + \beta$ class). Using this classification, all 1500 of the SAXS curves in our database were divided into three groups. For each group, we calculated the average curves $I_\alpha(s)$, $I_\beta(s)$, and $I_{\alpha+\beta}(s)$, which should reflect the characteristic features of the behavior of the scattering curves for proteins belonging to a particular structural class. With the use of the OLIGOMER program, each scattering curve $I(s)$ was represented as a linear combination of the $I_\alpha(s)$, $I_\beta(s)$, and $I_{\alpha+\beta}(s)$ functions:

$$I(s) = w_\alpha I(s)_\alpha + w_\beta I(s)_\beta + w_{\alpha+\beta} I(s)_{\alpha+\beta},$$

where w_α, w_β, and $w_{\alpha+\beta}$ are the weighting coefficients for $I_\alpha(s)$, $I_\beta(s)$, and $I_{\alpha+\beta}(s)$, respectively, in the expansion of the curve $I(s)$. The values of these coefficients vary from 0 to 1.

In most cases, a particular protein can be unambiguously assigned to a structural class; i.e., the corresponding weighting coefficient of the expansion w_i is equal to unity. However, this observation is not valid for some structures (the medium part of the scattering curve of a protein from the α class may coincide with that of a protein from the β class, as shown in Fig. 4a). Evidently, the reliable analysis of higher classification levels of CATH cannot be performed based on SAXS data.

For several arbitrarily chosen pairs of proteins characterized by similar medium-angle regions of scattering curves ($RfM < 0.15$), the level of homology was estimated using the DALI structural comparison method [10]. In particular, the DALI algorithm determines a quantitative statistical criterion denoted by Z for two atomic-resolution macromolecular structures. Values of Z smaller than 2 correspond to definitely different structures, the range $2 \le Z < 10$ corresponds to structures with low homology, and $Z \ge 10$ correspond to definitely similar structures. There is a certain corre-
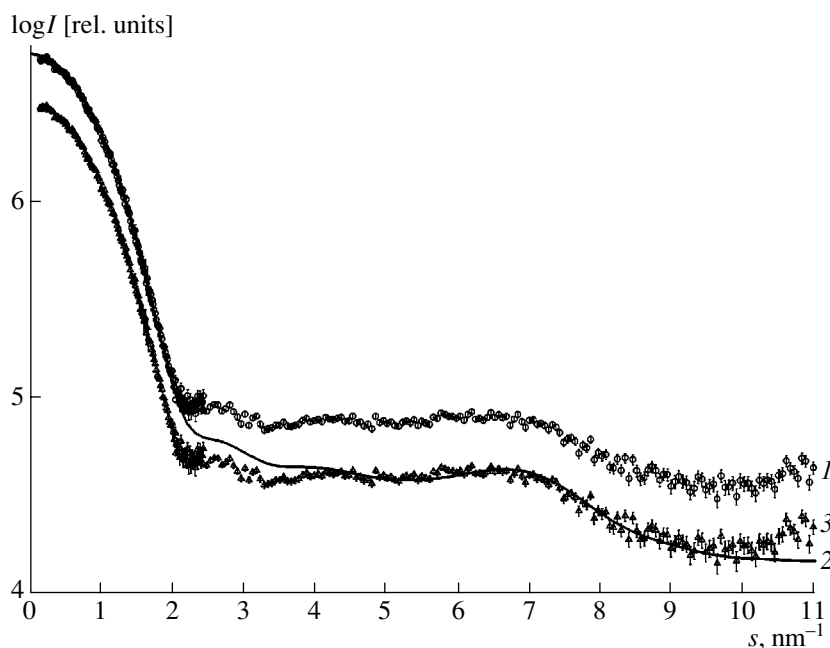
Fig. 5. (*1*) Experimental (scattered circles) and (*2*) theoretical (solid line) scattering curves for myoglobin. Curve *3* is a least-squares superposition of the experimental data and the theoretical curve after multiplication by the scale factor and subtraction of the constant in the *s* range from 4 to 9 nm^{-1}.

lation between *RfM* and *Z*. Thus, *RfM* = 0.06 ± 0.03 for similar structures (*Z* > 2), and *RfM* = 0.12 ± 0.06 for different structures (*Z* < 2). In most cases, the medium parts of SAXS data corresponding to homologous structures (*Z* ≥ 10) are similar (*RfM* < 0.06) (Fig. 4). However, there are structural homologues with *Z* > 4 characterized by *RfM* larger than 0.1.

Therefore, an unambiguous correlation between *RfM* and the degree of homology in databases of high-resolution protein structures could not be established. Nevertheless, the fact that the medium regions of the scattering curves coincide indicates that proteins are structurally similar at low resolution. Visually, proteins with low *RfM* are actually similar in appearance, but this similarity manifests itself at the level of domain structures rather than at the levels of the tertiary or secondary structures.

Example of the Use of the Database

We used the experimental scattering curve of sperm whale myoglobin, which was measured in the range of the momentum transfer *s* up to 12 nm^{-1} on a small-angle D24 camera at the LURE synchrotron facility in Orsay (France), as a test experimental example of searching for similar structures with the use of our database. The experimental scattering data deviate from the theoretical curve calculated for the crystal structure of myoglobin (1DUO.pdb) at large angles (Fig. 5) by the CRYSOL program. This difference is possibly due to the uncertainty of subtraction of the background from the experimental data and also to the fact that the predicted scattering curves in the database were calculated using the CRYSOL program for standard values of the excluded volume of the particle and the density of its hydration shell. For real proteins, these values may vary, resulting in systematic deviations. At large scattering angles, these deviations can be accurately taken into account by adding a constant to the scattering intensity. Hence, all subsequent calculations of the *R* factors were performed with the automatic addition of the constant term to one of the data sets that were compared. As can be seen from Fig. 5, this procedure enables one to fit the theoretical scattering curve to the experimental data for myoglobin in the angle range used for calculating *RfM*.

To choose the structural analogues of myoglobin, we calculated the factors *RfI* and *RfM* in the region between the experimental scattering curve, which was preprocessed using the GNOM program [11] to eliminate random errors of measurements, and the theoretical curves calculated for 638 proteins with molecular weights varying from 15 to 18 kDa. We found 182 proteins, including 12 homologues of myoglobin, which are characterized by *RfI* < 0.02 and have a shape similar to that of myoglobin (NSD < 1). Out of 24 proteins with *RfM* < 0.1, eight proteins appeared to be sequence homologues of myoglobin. The typical structures of the remaining proteins analogous in the medium-angle region of the scattering curve are shown in Fig. 6.
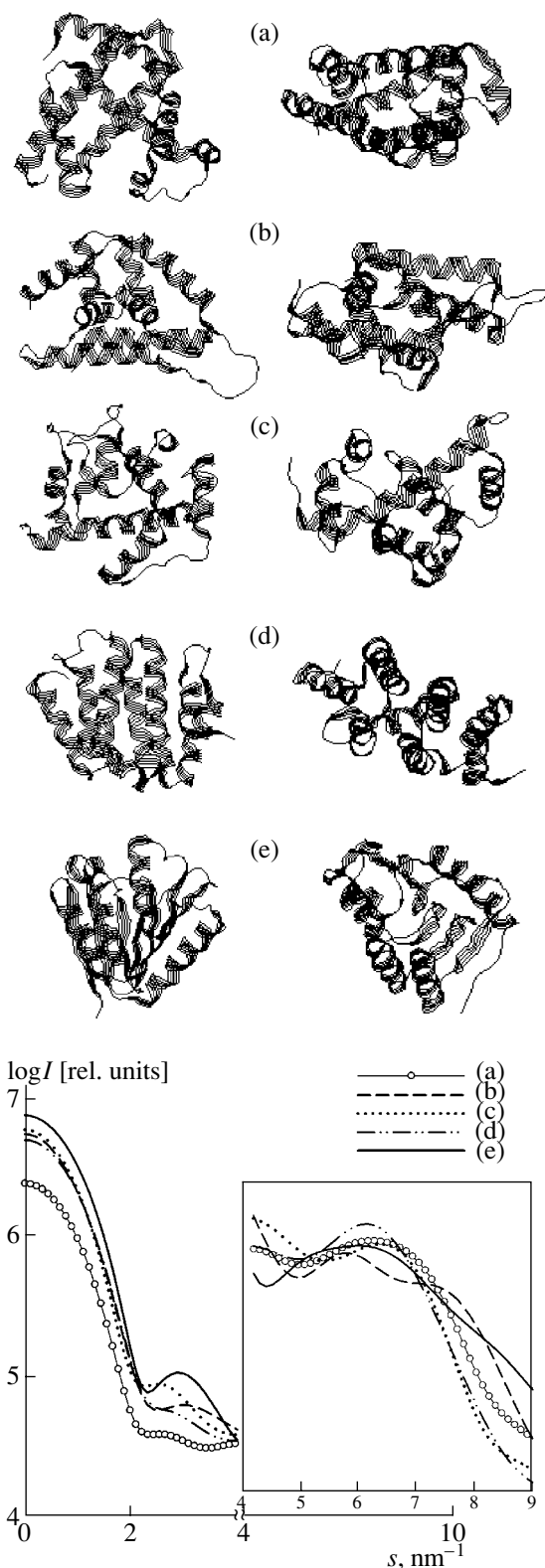
Fig. 6. Typical structures of analogues: (a) 1DUO.pdb; (b) 1K6K.pdb; (c) 1SRA.pdb; (d) 1JWF.pdb; and (e) 1BYR.pdb (structures at the right of the figure are rotated by 90° about the horizontal axis) and the corresponding scattering curves. In the additional plot, the medium-angle curves are scaled by a factor of 5.

This comparison clearly demonstrates that the structural similarity determined from the medium regions of SAXS curves depends largely on the regularities in the overall organization of proteins rather than on the secondary-structure elements (although most of the analogues found, like myoglobin itself, also belong to the α class).

Interestingly, all structures characterized by similar medium parts of the scattering curves ($RfM < 0.1$) also have similar low-resolution shapes ($RfI < 0.03$). Hence, the similarity of low-resolution structures is a necessary prerequisite for the similarity of the scattering curves in the range of the momentum transfer from 4 to 9 nm^{-1}, which suggests that a medium-angle scattering pattern may provide important information (in addition to the low-angle data) on low-resolution structures for proteins with similar molecular weights.

CONCLUSIONS

In this study, we propose a new approach to analyzing SAXS data for solutions of proteins with the use of a database of theoretical scattering curves for known structural models. This database allows one to rapidly find proteins with similar shapes (based on the internal parts of scattering curves) and analogues in domain structures (based on the medium-angle parts of scattering curves). Presently, the database includes 1500 structures. We plan to extend this database and design a Web portal intended for its use via the Internet. The developed approach may be useful in classifying proteins based on SAXS data. This is particularly important in the context of the progress in structural genomics, primarily for proteins, whose structures cannot be solved at high resolution.

ACKNOWLEDGMENTS

REFERENCES

1. A. G. Murzin, S. E. Brenner, T. Hubbard, and C. Chothia, J. Mol. Biol. **247**, 536 (1995); http://scop.berkeley.edu.

2. F. M. G. Pearl, D. Lee, J. E. Bray, *et al.*, Nucleic Acids Res. **28** (1), 277 (2000); http://www.biochem.ucl.ac.uk/bsm/cath_new.

3. D. I. Svergun, M. V. Petoukhov, and M. H. J. Koch, Biophys. J. **80**, 2946 (2001).

4. F. C. Bernstein, T. F. Coetzle, G. J. B. Williams, *et al.*, J. Mol. Biol. **112**, 535 (1977); http://www.rcsb.org.

5. D. I. Svergun, C. Barberato, and M. H. J. Koch, J. Appl. Crystallogr. **28**, 768 (1995).

6. V. A. Kotel'nikov and A. M. Nikolaev, *Fundamentals of Radiotechnics* (Svyaz'izdat, Moscow, 1950).

7. M. B. Kozin and D. I. Svergun, J. Appl. Crystallogr. **34**, 33 (2001).

8. D. I. Svergun, Biophys. J. **76**, 2879 (1999).

9. D. I. Svergun, V. V. Volkov, M. B. Kozin, and H. B. Stuhrmann, Acta Crystallogr., Sect. A: Found. Crystallogr. **52**, 419 (1996).

10. L. Holm and C. Sander, J. Mol. Biol. **233**, 123 (1993); http://www2.ebi.ac.uk/dali.

11. D. I. Svergun, J. Appl. Crystallogr. **25**, 495 (1992).

Translated by T. Safonova

REAL STRUCTURE
OF CRYSTALS

Dedicated to the 60th Anniversary
of the Shubnikov Institute of Crystallography
of the Russian Academy of Sciences

Deformation of Covalent Crystals in the Vicinity of the Yield Drop

B. V. Petukhov

Shubnikov Institute of Crystallography, Russian Academy of Sciences, Leninskiĭ pr. 59, Moscow, 119333 Russia
e-mail:petukhov@ns.crys.ras.ru
Received June 2, 2003

Abstract—The theory for description of the stress peak (yield drop) on the stress–strain curves of covalent crystals with low and zero dislocation densities has been developed. The kinetics of the variation of the dislocation density and the shape of the stress peak in the vicinity of the upper yield stress is described analytically within the framework of the generalized Alexander–Haasen model. The character of the elastoplastic transition is analyzed in detail and the model is compared with the experimental data for silicon. © *2003 MAIK "Nauka/Interperiodica".*

INTRODUCTION

Extremely pure covalent crystals play an important role as model materials for studying dislocation dynamics. There are numerous experimental data on the mobility of individual dislocations in these crystals [1–6]. In recent years, the needs of semiconductor microelectronics considerably increased the interest in the study of the processes of dislocation multiplication. New experimental possibilities for studying dislocation sources are provided by the use of synchrotron radiation [7].

The present study is aimed at the theoretical description of deformation of covalent crystals which, in the initial state, are characterized by low or even zero dislocation densities. As is known, the stress–strain curves of these crystals possess an interesting characteristic—the stress peak in the vicinity of the transition from elastic deformation to plastic flow or the so-called yield drop. This peak can be quite high, so that the difference between the upper and the lower yield stresses observed in the experiments can attain hundreds of percent [1]. Today, the yield drop is extensively studied [1–3, 8–12] because of the importance of the boundary of intense dislocation generation and beginning of the plastic flow of materials for the technology of production and exploitation of semiconductor chips.

Below, we describe the deformation processes using the well-known Alexander–Haasen model [1, 3] developed along two lines. First, the generalized model allows one to describe the practically important case of deformation of dislocation-free silicon crystals [2, 6, 13] with due regard for the presence of dislocation

sources, without which the Alexander–Haasen model cannot be used to describe the deformation of initially dislocation-free crystals because, in this case, it would predict an unrealistic infinitely large value of the upper yield stress. Second, it allows one to describe the shape of the stress peak on the stress–strain curve (i.e., the yield drop) analytically, which, in turn, provides a more detailed comparison of the theory and the experiment. The study of the yield drop is especially interesting in light of the fact that, as is shown below, despite the fact that the problem has a large number of parameters characterizing the properties of the material and the conditions of its deformation, the shape of the yield drop depends only on one combined parameter. This universal character of the peak shape makes it a characteristic sign of the concrete model of dislocation multiplication that can be verified experimentally.

DESCRIPTION OF THE MODEL

The variation in stress with time along the stress–strain curve obeys the so-called "machine equation,"

$$\dot{\varepsilon} = \dot{\varepsilon}_p + \dot{\tau}/S. \qquad (1)$$

Here, ε is the total deformation, which is the sum of the plastic, ε_p, and elastic, τ/S, deformations; τ is the applied stress; S is the combination of the elastic moduli of the sample and the testing machine; and the dot indicates differentiation with respect to time. The rate of plastic deformation in Eq. (1) is set by the Orovan equation $\dot{\varepsilon}_p = NbV$, where N is the dislocation density, b is the magnitude of the Burgers vector of dislocations,

and V is the velocity of their motion. In pure covalent crystals, the dislocation velocity is described by the empiric equation

$$V = B\tau^m, \qquad (2)$$

where B includes the temperature dependence (usually of the Arrhenius type), $B = V_0 \exp(-E/kT)$, E is the activation energy, k is the Boltzmann constant, and T is the temperature [1–6]. The kinetic equation that describes the evolution of an ensemble of dislocations in this model has the form

$$\frac{dN}{dt} = w\tau_e NV + I, \qquad (3)$$

where τ_e are the effective stresses obtained from τ by subtraction of the internal stresses τ_i, I is the stress-dependent rate of dislocation generation by sources, and w is the coefficient of dislocation self-multiplication. The presence of sources in Eq. (3) generalizes the original Alexander–Haasen model [1], which takes into account only the dislocation self-multiplication. As is shown below, the modification of this equation is important only at the initial stage of deformation, because, at the later stages, the self-multiplication of the already existing dislocations prevails over their generation by the sources. This allows us to reduce the problem described by Eq. (3) to the original Alexander–Haasen model under the renormalized initial conditions, which allows one to obtain physically reasonable values of the upper yield stress also for initially dislocation-free crystals.

To simplify the formulas, we introduce into consideration scaling multipliers for stress τ_*, time t_*, and dislocation density N_*:

$$\tau_* = \left(\frac{S\dot{\varepsilon}}{wB}\right)^{1/(m+2)},$$

$$t_* = (wB)^{-1/(m+2)}(S\dot{\varepsilon})^{-(m+1)/(m+2)}, \qquad (4)$$

$$N_* = \frac{1}{b}\left(\frac{\dot{\varepsilon}}{B}\right)^{2/(m+2)}\left(\frac{w}{S}\right)^{m/(m+2)}.$$

Now, consider the initial stage of deformation, where the total density of the initial and newly formed dislocations is still rather low, so that their contribution to the internal stress τ_i can be ignored. The elastic deformation prevails over the plastic deformation, so that $\tau \approx S\dot{\varepsilon}\,t$. Then, the linear equation, which follows from Eq. (3), can readily be solved to yield the following growth law for the dislocation population

$$N = \exp\left[\frac{1}{m+2}\left(\frac{t}{t_*}\right)^{m+2}\right]$$

$$\times \left\{N_0 + \int_0^t dt'\, I(S\dot{\varepsilon}t')\exp\left[-\frac{1}{m+2}\left(\frac{t'}{t_*}\right)^{m+2}\right]\right\}. \qquad (5)$$

It is natural to consider I as an increasing function of stress, $I(\tau)$; however, we assume that this function grows more slowly than $\exp[(\tau/\tau_*)^{m+2}/(m+2)]$. If this condition is fulfilled, the integral in Eq. (5) converges and, upon a certain initial period of time t_{in}, the upper limit of this integral can be taken to be infinity, so that the dislocation density would vary according to the law

$$N \approx N_{01}\exp\left[\frac{1}{m+2}\left(\frac{t}{t_*}\right)^{m+2}\right], \qquad (6)$$

where $N_{01} \equiv N_0 + \int_0^\infty dt\, I\exp\left[-\frac{1}{m+2}\left(\frac{t}{t_*}\right)^{m+2}\right]$.

Equation (6) is valid at $t \gg t_{in}$. In this time interval, the exponential self-multiplication of the already existing dislocations prevails over their generation by the sources. At this stage, we can ignore the term I in the right-hand side of Eq. (3) and, thus, return back to the original Alexander–Haasen model [1]. The only difference associated with the existence of the dislocation sources consists in the modification of the initial condition by making the change $N_0 \longrightarrow N_{01}$. This allows us to preserve all the results obtained earlier and to describe the case of initially dislocation-free crystals.

It is timely to make a remark on the source distributions both in space and in the spectrum of the critical stresses. Since the presence of sources in Eq. (3) is important only at the initial stage of the process, where the equation is reduced to linear one, it is also possible to perform averaging over the source distribution (and, thus, distribution of the initial dislocations) and to consider N_{01} as such an averaged quantity.

SHAPE OF THE YIELD DROP

As experiments show, with a decrease in the initial dislocation density, the yield-drop height increases. Rather perfect initially dislocation-free or almost dislocation-free crystals allow one to compare the model computations of the yield-drop shape with the experimental data. Therefore, it is expedient to describe the deformation in the vicinity of the yield drop of covalent crystals in more theoretical detail, which would provide better understanding of the mechanism of elastoplastic transitions in these materials.

The perfection condition for the initial crystal can be written quantitatively by the inequality $N_{01}/N_* \ll 1$, whose fulfillment provides the low value of the dislocation density up to the upper yield stress, so that, in a certain vicinity of this stress, the strain strengthening can still be ignored. Although this range is rather narrow, the phenomena occurring in it are rather interesting. A rapid growth of the dislocation population predicted by Eq. (6) initiates the transition from prevalent elastic deformation of the sample to prevalent plastic deformation. This decelerates an increase in the deforming stress or leads to its drop, depending on the character of

the influence of the stress variation on a further increase in the dislocation density. The approach that allows one to describe the evolution of the dislocation population with due regard for this feedback was developed elsewhere [14]. The solution that refines Eq. (6) obtained in [14] shows the nontrivial behavior in the vicinity of the upper yield stress. This segment of the stress–strain curve (including the yield drop) was described analytically [14]. We use this description in the present article

after its simple generalization based on the change $N_0 \longrightarrow N_{01}$, increasing its applicability range.

The description reduces to two relationships. The first one gives the correlation between the deforming stress and the dislocation density,

$$\tau(N) = \tau_*\{[(m + 2)\ln(N/N_{01})]^{2/(m+2)} - 2N/N_*]^{1/2}. \quad (7)$$

The second relationship describes the kinetics of dislocation multiplication

$$t = t_* \int_0^{\ln(N/N_0)} \frac{d\varphi}{\{[(m + 2)\varphi]^{2/(m+2)} - 2N_0\exp(\varphi)/N_*\}^{(m+1)/2}}. \quad (8)$$

We use Eqs. (7) and (8) to obtain some additional results and comparing the theory with the experimental data for silicon.

Equation (7) illustrated by Fig. 1 is represented by a curve with the maximum corresponding to the upper yield stress. The position, N_m, and the height, τ_u, of this maximum can readily be found numerically with any degree of accuracy from the equation $d\tau/dN = 0$, which can be reduced to

$$\frac{N_m}{N_*}\left[(m + 2)\ln\left(\frac{N_m}{N_{01}}\right)\right]^{m/(m+2)} = 1. \quad (9)$$

At low values of N_{01}/N_*, this equation can readily be solved using the iteration procedure by replacing N_m under the logarithm sign by its approximate values, beginning, e.g., with $N_m \longrightarrow N_*$. Within an accuracy
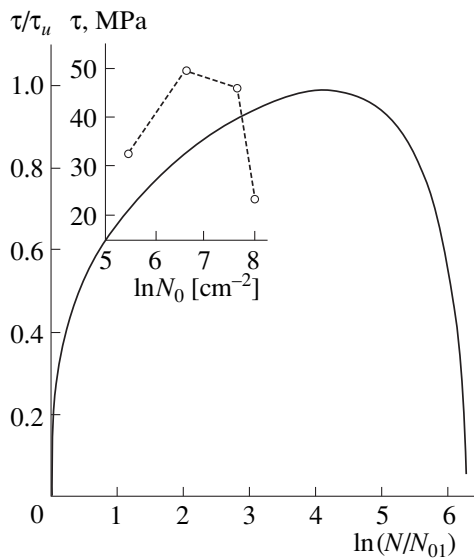
sufficient for our consideration, we can stress ourselves to the results obtained in the first iteration

$$N_m = \frac{N_*}{[(m + 2)\ln(N_*/N_{01})]^{m/(m+2)}}. \quad (10)$$

This expression confirms and, in particular, specifies the above statement on a low dislocation density in the vicinity of the upper yield stress, because the denominator in Eq. (10) is rather large. The substitution of N_m into Eq. (7) yields τ_u. In applications, it is more convenient to use a simplified numerical approximation of τ_u,

$$\tau_u \approx \tau_*[(m + 2)\ln(C_m N_*/N_{01})]^{1/(m+2)}, \quad (11)$$

where $C_m \approx 0.1375/m^{0.7}$.

To illustrate the effect of the work of dislocation sources, consider the model dependence $I(\tau)$ having the threshold form: $I(\tau) = 0$ at $\tau < \tau_0$, $I(\tau) = I_1 = $ const at $\tau > \tau_0$, where $\tau_0 > \tau_*$. In this case, we have

$$N_{01} = N_0 + I_1 t_* \int_{\tau_0/\tau_*}^{\infty} \exp\left(-\frac{1}{m+2}x^{m+2}\right)dx \approx N_0$$

$$+ I_1 t_* \left(\frac{\tau_*}{\tau_0}\right)^{m+1} \exp\left[-\frac{1}{m+2}\left(\frac{\tau_*}{\tau_0}\right)^{m+2}\right]. \quad (12)$$

The latter equation describes the competition between the role of the initial dislocations and the role of the dislocation sources. In the initially dislocation-free crystals ($N_0 = 0$), the parameter $(m + 2)\ln(N_*/N_{01})$ determining the upper yield stress takes the form $(m + 2)\ln[(\tau_0/\tau_*)^{m+1}N_*/It_*] + (\tau_0/\tau_*)^{m+2}$. If a threshold stress is not too high and the rate of dislocation generation I_1 is low, the dependence of the upper yield stress on all the parameters is close (within the logarithmic corrections) to the dependence that takes place in the situation where the initial dislocations play the most important role; otherwise (at a high threshold stress), the upper yield stress is close to the threshold stress τ_0 and the dependence on the other parameters (T, $\dot{\varepsilon}$, etc.)

Fig. 1. Correlation between the applied stress τ and the dislocation density N ($m = 1$, $\ln(N_*/N_{01}) = 5$). For the sake of comparison, the inset shows the experimental data for silicon [9] at $t = 800°C$ and $\dot{\varepsilon} = 6 \times 10^{-4}$ s^{-1}.
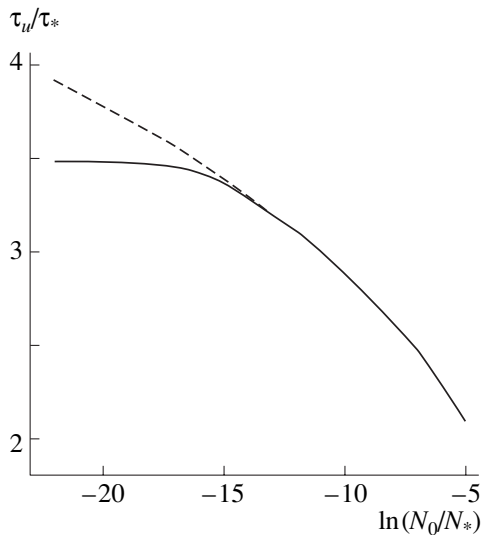
Fig. 2. Dependence of the upper yield stress on the initial density of dislocations calculated at $m = 1$. Solid line corresponds to the source density $I_1 = 10^{-7}N_*/t_*$ at $\tau_0/\tau_* = 3$; dashed line corresponds to pure crystals in the absence of any sources.
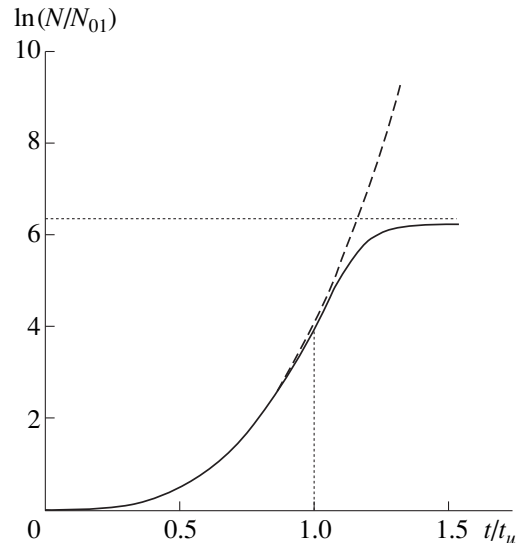

Fig. 3. Increase in dislocation population $(\ln(N_*/N_{01}) = 5)$. Dashed line corresponds to the approximate law given by Eq. (6). The vertical dashed line corresponds to the point of the upper yield stress; the horizontal dashed line shows the maximum possible growth in dislocation density in the vicinity of the yield drop.

becomes weaker. Figure 2 illustrates the dependence of τ_u on the initial dislocation density, N_0. In the absence of dislocations, with a decrease in N_0, τ_u infinitely decreases (dashed line), whereas in the presence of dislocation sources, τ_u attains a certain finite value (solid line).

Equations (7) and (8) become inapplicable if the dislocation density exceeds a certain limiting value N_M at which $\tau(N)$ in Eq. (7) goes to zero. In the approximation used in the derivation of Eq. (10) for N_m, we can also find the approximate equation for N_M,

$$N_M \approx 0.5N_*[(m + 2)\ln(N_*/N_{01})]^{2/(m + 2)}. \quad (13)$$

The dislocation density given by (13) is rather high and considerably exceeds the value at the point of the upper yield stress, $N_M/N_m \approx 0.5(m + 2)\ln(N_*/N_{01})$. It should be noted that this increase is observed only in a narrow range of deformations in the vicinity of the yield drop.

Of special interest is the case where $m = 1$, which corresponds, e.g., to silicon. Here, the integral in Eq. (8) is calculated approximately with the use of the expansion in small parameter N_{01}/N_*. As a result, we obtain

$$t \approx t_*\left\{\left[3\ln\left(\frac{N}{N_{01}}\right)\right]^{1/3} - z_0\ln\left(1 - 2z_0\frac{N}{N_*}\right)\right\}. \quad (14)$$

Here, $z_0 \approx [3\ln(N_*/N_{01}) + 2\ln(\ln(N_*/N_{01})) + 0.5855]^{-2/3}$. The dependence described by Eq. (14) is illustrated by Fig. 3. A rapid increase in the dislocation population gives rise to a dramatic decrease in the deforming stress

after the point of the upper yield stress. This, in turn, results in a dramatic deceleration of dislocation generation in comparison with the initial generation described by the law given by Eq. (6) (Fig. 3). The maximum increase in the dislocation density corresponding to the applicability boundary of (14) is $N_M = 0.5N_*/z_0 \approx 0.5N_*[3\ln(N_*/N_{01})]^{2/3}$. In actual fact, this value can never be attained, because an increase in the dislocation density intensifies the role of the strain strengthening and changes the character of the above characteristics. The description of the subsequent stages of deformation is beyond the scope of the present article.

Over quite a long time, the Alexander–Haasen model has been verified mainly by measuring the upper yield stress and its dependence on temperature and deformation rate [1–3, 9–12]. Recently, attempts have been made to determine the appropriate law of dislocation multiplication and depletion in covalent crystals with the aim to describe the stress–strain curve of germanium over a wide deformation range [15, 16]. Equations (7) and (8) describe the shape of the peak of the stress–strain curve, which is determined only by the law of dislocation multiplication. Therefore, in principle, these equations can allow one to verify the Alexander–Haasen model of dislocation multiplication without considering the models of strain strengthening and dislocation depletion. To be able to make it independent of measurement of the upper yield stress, one has to normalize, $\tau(\varepsilon)$ by τ_u and ε by ε_u, the values corresponding to the point of the upper yield stress. Such a normalization reduces the number of problem parameters and retains the dependence on only one combined
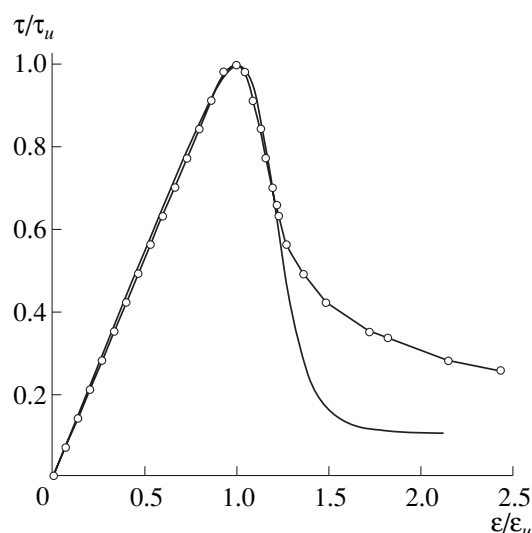
Fig. 4. Stress–strain curve in the reduced coordinates. Solid curve indicates the theoretical dependence described by Eqs. (7)–(14) at $m = 1$, $\ln(N_*/N_{01}) = 5$. The line with circles indicates the experimental data for initially dislocation-free silicon at $t = 800°C$ and $\dot{\varepsilon} = 6.6 \times 10^{-5}$ s^{-1} [13].

parameter, N_{01}/N_*. This allows one to consider the peak shape as a universal characteristic of the model. The renormalized theoretical dependence described by Eqs. (7)–(14) and the experimental dependence for initially dislocation-free silicon [13] are compared in Fig. 4. The circles on the experimental curve are drawn arbitrarily in order to be able to distinguish this curve from the calculated one. The agreement observed at $\ln(N_*/N_{01}) = 5$ for the considerable portion of the peak in the vicinity of the upper yield stress, where the strain strengthening is rather low, seems to be quite satisfactory. Thus, one may draw the conclusion that the Alexander–Haasen model is quite efficient. The detailed experimental data on the shapes of rather pronounced stress peaks on the stress–strain curves of covalent materials would make this conclusion more reliable and, in particular, would allow the unique choice from the competing models [15, 17, 18].

CONCLUSIONS

Because of a certain interest in the specific nature of the transition from elastic to plastic deformation in covalent crystals, attempts are made to explain qualitatively the phenomenon of the yield drop. This could hardly be made in a simple form. Therefore, we made an attempt to describe the qualitative aspect of this phenomenon and find the prerequisites of its practical observation based on the analytical solution of the problem obtained.

At a low value of the initial density of dislocations, their generation in the quantities necessary for the occurrence of developed plastic deformation takes longer and shifts the elastoplastic transition toward higher stresses. The law of dislocation multiplication described by Eq. (3) results in an exponential increase in the dislocation population. The existence of additional multipliers V and τ in the right-hand side of Eq. (3) results in the fact that, in the range of higher stresses, the rate of variation of the dislocation density dN/dt is higher than the N value (in dimensionless variables obtained with the use of Eq. (4)). In a similar way, the rate of an increase in plastic deformation would become higher than the rate of increase of elastic deformation $\dot{\varepsilon}_{el}$ within a shorter time than the time necessary for the value of ε_p to exceed ε_{el}. As a result, the unloading stress $\tau_{re} = S\varepsilon_p$ turns out to be relatively low, so that it cannot considerably reduce the deforming stress. Since the dislocation motion is controlled by the stress value, the rate of dislocation multiplication is approximately constant. At the same time, the velocity of the τ_{re} variation becomes comparable with $S\dot{\varepsilon}$, so that $\dot{\tau}$ goes to zero. This specific inertia of dislocation multiplication associated with the delayed feedback via stress results in "overgeneration" of dislocations, which, in turn, leads to a dramatic decrease in the deforming stress (the yield drop on the stress–strain curves).

Thus, the prerequisites for the formation of the yield drop are a low value of the initial dislocation density (and the density of dislocation sources) and an increase in the total coefficient of dislocation multiplication, $wV\tau_e$, with an increase in the stress. These qualitative speculations show that, to make the plastic deformation (corresponding to the unloading stress) low, so that it would not lead to noticeable strain strengthening and suppress of the yield drop, the initial dislocation density should also be low (with a corresponding reserve). The quantitative criterion of the yield-drop formation, obtained in [14] based on the Taylor model of strain strengthening $\tau_i = \alpha N^{1/2}$, agrees with this conclusion and confirms it.

Thus, the main results of this study can be formulated as follows:

—The Alexander–Haasen model for the description of the deformation of covalent crystals having initially low dislocation densities is extended to the case of dislocation-free crystals.

—It is shown that the shape of the yield drop on the stress–strain curves is rather universal because it depends only on one combined parameter. Numerous other parameters characterizing the properties of the material and the conditions of its deformation can be eliminated using the scaling transformation.

—The kinetics of the dislocation population and the yield-drop shape is described analytically. This allows one to compare the calculated and experimental data and, thus, to verify the applicability of the model of dislocation multiplication.

REFERENCES

1. H. Alexander and P. Haasen, Solid State Phys. **22**, 27 (1968).

2. K. Sumino, in *Defects and Properties of Semiconductors: Defect Engineering*, Ed. by J. Chikawa *et al.* (KTK Sci., Tokyo, 1987), p. 227.

3. H. Alexander, in *Dislocations in Solids*, Ed. by F. R. N. Nabarro (North-Holland, Amsterdam, 1986), Vol. 7, Chap. 35, p. 113.

4. V. I. Nikitenko, in *Dynamics of Discolations* (Naukova Dumka, Kiev, 1975), p. 7.

5. V. I. Nikitenko, B. Ya. Farber, and Yu. L. Iunin, Zh. Éksp. Teor. Fiz. **93**, 1314 (1987) [Sov. Phys. JETP **66**, 738 (1987)].

6. A. George and J. Rabier, Rev. Phys. Appl. **22**, 941 (1987).

7. F. Vallino, A. Jacques, and A. Georges, Phys. Status Solidi B **222**, 51 (2000).

8. M. G. Mil'vidskiǐ and V. V. Osvenskiǐ, *Structural Defects in Single Crystals of Semiconductors* (Metallurgiya, Moscow, 1984).

9. I. Yonenaga and K. Sumino, Phys. Status Solidi A **50**, 685 (1978).

10. M. Suezawa, K. Sumino, and I. Yonenaga, Phys. Status Solidi A **51**, 217 (1979).

11. J. Rabier and A. George, Rev. Phys. Appl. **22**, 1327 (1987).

12. W. Schröter, H. G. Brion, and H. Siethoff, J. Appl. Phys. **54**, 1816 (1983).

13. J. R. Patel, Discuss. Faraday Soc. **38**, 201 (1964).

14. B. V. Petukhov, Kristallografiya **46** (5), 909 (2001) [Crystallogr. Rep. **46**, 835 (2001)].

15. J. Fikar, B. Viguer, T. Kruml, and C. Dupas, J. Phys.: Condens. Matter **14**, 12887 (2002).

16. C. Dupas, N. Zuodar, O. Coddet, *et al.*, J. Phys.: Condens. Matter **14**, 12989 (2002).

17. V. G. Govorkov, V. L. Indenbom, V. S. Papkov, and V. R. Regel', Fiz. Tverd. Tela (Leningrad) **6**, 1039 (1964) [Sov. Phys. Solid State **6**, 802 (1964)].

18. B. V. Petukhov, Zh. Tekh. Fiz. **71** (11), 42 (2001) [Tech. Phys. **46**, 1389 (2001)].

Translated by L. Man

REAL STRUCTURE
OF CRYSTALS

Dedicated to the 60th Anniversary
of the Shubnikov Institute of Crystallography
of the Russian Academy of Sciences

Influence of Preliminary Thermomagnetic Treatment on the Yield Point of NaCl : Ni Crystals

A. E. Smirnov*, N. N. Bekkauer**, and V. V. Sadchikov***

* Shubnikov Institute of Crystallography, Russian Academy of Sciences, Leninskiĭ pr. 59, Moscow, 119333 Russia
e-mail: asmir@ns.crys.ras.ru
** Peoples Friendship University, ul. Miklukho-Maklaya 6, Moscow, 117198 Russia
*** Bardin Central Research Institute for the Iron and Steel Industry,
Vtoraya Baumanskaya ul. 9/23, Moscow, 107005 Russia
Received January 30, 2003

Abstract—The influence of preliminary annealing (3 h, 1000 K), subsequent quenching in liquid nitrogen, and short magnetization in a constant magnetic field (0.5 h, 0.48 T) prior to deformation on the yield point of NaCl : Ni crystals is discovered. The effect depends on the time of sample storage between quenching and magnetization and is maximal 40 h after quenching. © 2003 MAIK "Nauka/Interperiodica".

The macroscopic magnetoplastic effect in nonmagnetic crystals consisting in plasticization of the samples under the action of a constant magnetic field (up to 0.48 T) under active loading was studied in detail in [1–6]. The influence of magnetization on the yield point and kinetics of microplasticity of NaCl [1, 2], LiF [3, 4], and PbS [5] crystals and the effect of preliminary magnetization on the plasticity of NaCl : Ni crystals [6] were studied. It was established that magnetic field promotes depending of dislocations from paramagnetic stoppers. This fact determines the important role of the state of point defects in a crystal, which can be changed by preliminary thermal treatment creating the nonequilibrium state necessary for manifestation of sensitivity of the plastic properties of material to a magnetic field. In particular, the magnetic field affects the state of impurities (magnetosensitive complexes of point defects). The kinetics of nucleation and disappearance of magnetosensitive complexes was studied by example of NaCl : Eu crystals [7]. In this case, microhardness of the samples was considered as an indicator of the impurity state that depends on the thermal treatment and the magnetic field. It was shown that, after 2-h-annealing at 920 K and quenching, the microhardness changes nonmonotonically with the storage time of samples between quenching and switching on of a magnetic field (7 T, 10 μs) before indentation. The maximum effect was observed at $t = 30$ h.

Below, we present the results of the study of the influence of preliminary thermal and magnetic treatment on the yield point of NaCl : Ni crystals.

We studied NaCl crystals grown by the Kyropoulos method with an addition into the charge of 0.05 wt % nickel chloride. The total concentration of foreign inclusions did not exceed 10^{-3} wt %. The cleaved $2 \times 3 \times 8$-mm samples were subjected to a preliminary thermal activation. According to the experimental conditions, the samples were annealed for 3 h at $T = 1000$ K without the application of a magnetic field, quenched in liquid nitrogen, and then stored for different times—from 0 to 240 h. After that, each group of samples was treated in a constant magnetic field applied immediately for 0.5 h prior to loading. Thus, thermoactivated and magnetized crystals were deformed at a rate of 1.4×10^{-5} s^{-1} on a testing machine by the method described in [1]. The presence of magnetoplasticity was detected by measuring the yield point.

The experimental data are listed in the table. Each point is averaged over four measurements.

During the experiments, it was found that the dependence of the yield point of NaCl : Ni crystals subjected to preliminary quenching on the storage time before short magnetization and deformation is nonmonotonical. The yield point does not change during the first

Dependence of the yield point ε of preliminarily quenched NaCl : Ni crystals on the time t of sample storage between quenching and magnetization preceding deformation

t, h	0	24	40	48	72	240
ε, Pa	2.30	2.35	1.60	2.30	3.15	3.10

24 h of the sample storage, at $t = 40$ h, it drops, and then, with an increase in the storage time, increases again. Thus, the maximum plastification effect is observed at the storage time $t = 40$ h. This correlates with the data in [7] and, apparently, indicates that the preliminary thermal and magnetic treatment allows one to obtain the magnetosensitive state fixed in time.

The experiments on the influence of preliminary quenching, storage time, and magnetization of the samples on the yield point allowed us to draw the following conclusion. Without preliminary treatment, the impurity structure of the crystal is not magnetosensitive. Annealing leads to the first transformation of the initial structure—decomposition of impurity complexes (paramagnetic centers) responsible for deceleration of dislocation. The next technological stage (quenching) leads to a "freezing" of the decomposed impurity centers. A further multihour storage of samples changes the "frozen" impurity structure because of diffusion— the formed small paramagnetic centers (dislocation stoppers) grow in size, which is accompanied by the formation of a number of varying states. The "first" and "last" states are still magnetically insensitive like the initial state. Therefore, too fast or too slow application of a magnetic field would result in the magnetically insensitive state. Only if the storage between quenching and magnetization is optimal ($t = 40$ h, in our case), the impurity structure formed by that moment and unstable relative to spin-dependent electron transitions can respond to magnetic excitation and the spin transition can take place, which, in turn, makes the electron transition possible. As a result, the complex configuration and its every interaction with dislocation dramatically change; the energy barrier of the complex (impurity center) which is a a dislocation stopper decreases, the activation energy drops, the dislocation is liberated from the lock, and the structure is plasticized. Experimentally, this process is accompanied by a decrease in the yield point.

As was mentioned above, a similar approach to the formation of the magnetosensitive states was also used in [7]; the objects were NaCl crystals doped with europium. The detector of varying states of the impurity structure was the microhardness value.

ACKNOWLEDGMENTS

REFERENCES

1. V. I. Al'shits, N. N. Bekkauer, A. E. Smirnov, and A. A. Urusovskaya, Zh. Éksp. Teor. Fiz. **115** (3), 951 (1999) [JETP **88**, 523 (1999)].

2. A. A. Urusovskaya, V. I. Alshits, N. N. Bekkauer, and A. E. Smirnov, Fiz. Tverd. Tela (St. Petersburg) **42** (2), 267 (2000) [Phys. Solid State **42**, 274 (2000)].

3. A. A. Urusovskaya, V. I. Alshits, A. E. Smirnov, and N. N. Bekkauer, Pis'ma Zh. Éksp. Teor. Fiz. **65** (6), 470 (1997) [JETP Lett. **65**, 497 (1997)].

4. V. I. Alshits, A. A. Urusovskaya, A. E. Smirnov, and N. N. Bekkauer, Fiz. Tverd. Tela (St. Petersburg) **42** (2), 270 (2000) [Phys. Solid State **42**, 277 (2000)].

5. A. A. Urusovskaya, A. E. Smirnov, and N. N. Bekkauer, Vestn. Tambov. Univ., Ser.: Est. Tekh. Nauki, No. 5, 389 (2000).

6. A. A. Urusovskaya, A. E. Smirnov, and N. N. Bekkauer, in *Proceedings of XXXVI International Seminar on Current Problems of Strength* (Vitebsk, 2000), Vol. 1, p. 294.

7. R. B. Morgunov and A. A. Baskakov, Fiz. Tverd. Tela (St. Petersburg) **43** (9), 1632 (2001) [Phys. Solid State **43**, 1700 (2001)].

Translated by T. Dmitrieva

PHYSICAL PROPERTIES
OF CRYSTALS

Dedicated to the 60th Anniversary
of the Shubnikov Institute of Crystallography
of the Russian Academy of Sciences

New Laser Crystals of Complex Oxides Doped with Ions of *d* Elements with Variable Valence and Different Structural Localization. Review

T. F. Veremeĭchik*, E. V. Zharikov**, and K. A. Subbotin**

* Shubnikov Institute of Crystallography, Russian Academy of Sciences, Leninskiĭ pr. 59, Moscow, 119991 Russia
e-mail: tomver@online.ru
** Laser Materials and Technology Research Center, Institute of General Physics, Russian Academy of Sciences,
ul. Vavilova 38, Moscow, 119991 Russia
e-mail:soubbot@lsk.gpi.ru
Received June 11, 2003

Abstract—Ions of *d* elements in complex oxides with olivine and phenakite structures exhibit diverse structural localization and may incorporate into crystals in various oxidation states. The complexity of the structure of these materials requires a complex approach in investigation of their spectroscopic characteristics with regard to the type of optical center and the growth conditions. The method of estimation of the distribution of an activator ion over crystallographically non-equivalent cationic positions on the basis of the symmetry analysis of the structure of these positions with regard to the spatial distribution of the activator-ion electron density is described. The results of experimental studies of the spectroscopic characteristics of vanadium and chromium ions in the crystals with the olivine (Mg_2SiO_4, Ca_2GeO_4, and $CaMgSiO_4$) and phenakite ($LiGaSiO_4$, $LiAlGeO_4$, and Zn_2SiO_4) structures performed by us (some experimental data are reported for the first time) are analyzed with regard to the growth conditions. Data in the literature are also analyzed. In order to estimate the structural and valence states of the *d* ions, a number of other experimental techniques were used, and the experimental data were compared with the calculated energy-level diagrams for activator ions in centers of various types. This approach made it possible to adequately describe the possibilities of complex oxides Mg_2SiO_4, Ca_2GeO_4, $CaMgSiO_4$, $LiGaSiO_4$, $LiAlGeO_4$, and Zn_2SiO_4 doped with *d* ions, regarded as new laser media. © *2003 MAIK "Nauka/Interperiodica".*

CONTENTS

INTRODUCTION

Single crystals of complex oxides doped with ions of transition 3*d* elements in various oxidation states, including unconventional ones, are of much interest as potential laser media. Single crystals emitting in a wide spectral range are widely used as active media in tunable solid-state [1, 2] and femtosecond [3, 4] lasers. Large oscillator strengths of the transitions and short relaxation times of excitation also make it possible to use these crystals as laser saturable absorbers [5].

Generally, these crystals are characterized by strong broad absorption bands, which makes efficient the optical pumping of active media based on such crystals by sources of almost any type (including conventional commercially available flash lamps and laser diodes).

Generally, the local symmetry of cationic positions in complex oxides corresponds to the lowest symmetry point groups. This circumstance leads to extension of the range of laser-frequency tuning and to interaction with a large number of vibrational modes. As a result, these crystals have a rich phonon spectrum, which also extends the luminescence frequency range. However, the nonradiative multiphonon relaxation may be so efficient in these crystals that it often becomes the dominant mechanism of relaxation of excited states. In this case, the luminescence quantum yield significantly decreases. Development of crystals with a sufficiently

high luminescence lifetime and rich phonon spectrum is a problem that can be solved by searching complex oxides that would be optimal crystalline hosts for activator ions of the iron group.

A characteristic feature of the crystal chemistry of complex oxides is the variety of possible valence states and structural locations of activator ions. In most crystals of this type, the activator ions of d elements may be simultaneously in two, three, or more oxidation states and can be located in cationic positions with different coordination numbers and different degrees and types of distortion of corresponding coordination polyhedra. The examples illustrating the variety of optical centers in such crystals are alexandrite Cr : $BeAl_2O_4$, in which the Cr^{3+} ion is located in two structurally nonequivalent octahedrically coordinated positions; forsterite Mg_2SiO_4, which contains chromium in the form of Cr^{4+} ions in tetrahedral positions and Cr^{3+} ions in two structurally nonequivalent octahedral positions; and beryllium hexaaluminate $BeAl_6O_{10}$, in which the Cr^{4+} ion is located in six different tetrahedrally coordinated positions.

The ratio of concentrations of the dopant in different valence states and structural locations in the crystal may be significantly varied, depending on the growth method used and various parameters of the growth process. Among the latter parameters are the atmosphere of growth and subsequent annealing of crystals; the solvent composition (when the flux or hydrothermal techniques are used); the introduction of additional optically inactive dopants, which play the role of a charge compensator or a buffer, into the blend composition; and so on [6]. The variety of valence states and structural locations may lead both to improvement of lasing characteristics (in particular, to broadening of the frequency-tuning range or to the appearance of new lasing ranges) and to undesirable phenomena, such as optical absorption (from the ground and excited states) of one of optical centers in the range of possible lasing of another center. Thus, identification of all types of valence states and structural locations of activator ions typical of each specific crystal and determination of the ratio of concentrations of centers of each of these types and their dependencies on the process parameters of the growth are of key importance in characterization of laser crystals based on complex oxides. However, this problem does not always receive proper attention. It is necessary to have such data and understand the processes occurring upon doping laser materials by ions of d elements to be able to control these processes and create materials with good operating characteristics.

The problem of structural and valence identification of an activator ion in correlation with the spectroscopic and lasing characteristics and the growth conditions arises in investigation of a variety of doped hosts of such structural classes as, for example, olivine (Mg_2SiO_4, $CaMgSiO_4$, Ca_2GeO_4, $BeAl_2O_4$; sp. gr. *Pnma*); phenakite (LiGaSiO$_4$, LiAlGeO$_4$, LiGaGeO$_4$,

Zn_2GeO_4; sp. gr. $R3$ or $R\bar{3}$, depending on the degree of order of distribution of cations over structurally nonequivalent positions); $BeAl_6O_{10}$ crystals (sp. gr. *Pcam*); $Sr_3Ga_2Ge_4O_{14}$ and $Ca_3Ga_2Ge_4O_{14}$ crystals (sp. gr. D_3^2); and other crystals doped with d ions. Many studies were devoted to alexandrite [7–11] and germanates $Sr_3Ga_2Ge_4O_{14}$ and $Ca_3Ga_2Ge_4O_{14}$ [12–17], which have been well known for a long time. In this review, we consider the valence states and structural location of $3d$ ions, as well as their spectroscopic properties in some new crystals of complex oxides with the olivine (forsterite Mg_2SiO_4, monticellite $CaMgSiO_4$, Ca_2GeO_4) and phenakite (Zn_2SiO_4, LiGaSiO$_4$, LiAlGeO$_4$) structures. Some data on these materials are reported for the first time.

1. DISTRIBUTION OF ACTIVATOR IONS OVER STRUCTURAL POSITIONS WITH IDENTICAL COORDINATION NUMBERS

The most widespread and well-known to date approach to describing and predicting the character of distribution of activator ions both between a crystal and a melt and over different structurally nonequivalent cationic positions in the crystal is based on taking into account mainly crystallochemical factors, such as the relationship between the geometrical size of the activator ion and the corresponding positions and the type of substitution (either isovalent or heterovalent). In this context, we should mention [18], where the character of distribution of a large number of divalent and trivalent ions between the forsterite crystal and the forsterite melt was analyzed and classified on the basis of such an approach. At the same time, as applied to d ions, in which the electron cloud of the d orbital directly interacts with the crystal field of the anionic environment, such an approach is often too rough and cannot be used to describe experimental results with sufficient accuracy, as was shown in [19, 20] by the example of the Cr^{3+} ion in rare earth–scandium–gallium garnets. In such cases, it is necessary to take into account a number of other factors, which are considered below.

The effect of crystal structure on the distribution of an activator ion over structurally nonequivalent positions with lowest symmetry, which are characterized by identical coordination numbers but different sets of interatomic distances and valence angles, was estimated for the first time in [21] with the use of space-group theory and the gradient of the intracrystalline-field potential. Notably, the trend of preferred incorporation of an activator ion into one or another position is governed by the fact that, all other factors being the same, the system of regular points of the preferred position has higher spatial symmetry. In the structure, this trend is realized by the crystal-field gradient, i.e., by the force acting on the activator ion. This gradient is radically different in the positions of different point symmetry of the lowest order.

(a)

(b)

Tetrahedrically coordinated
cations (Si^{4+}, Ge^{4+}, Be^{2+})

Octahedrically coordinated
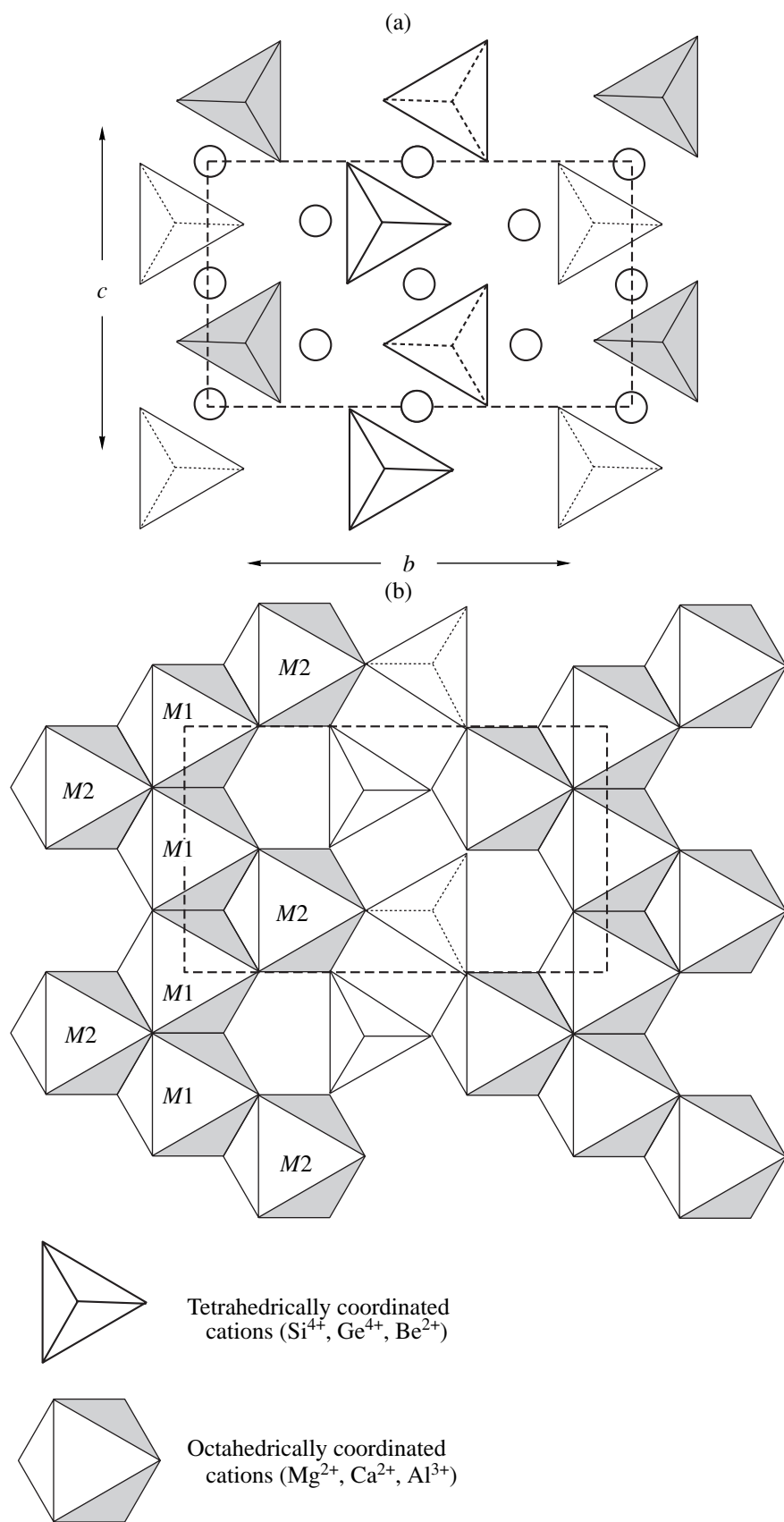cations (Mg^{2+}, Ca^{2+}, Al^{3+})

Fig. 1. Olivine structure (the view plane is perpendicular to the *a* axis): (a) tetrahedral cationic positions and (b) octahedral cationic positions.

The essence of the method is that, first of all, the structures forming when the activator ion occupies only one position among all possible nonequivalent cationic positions should be determined. The structures obtained correspond to different subgroups with small indices of the initial Fedorov group. Then, Brown's principle of maximum symmetry should be applied: "A structure will adopt the highest symmetry consistent with the constraints acting upon it" [22, 23].

Let us consider this technique as applied to crystals with the olivine structure (Fig. 1). This structure contains two structurally nonequivalent octahedrically coordinated cationic positions, which are distorted in comparison with the correct octahedron in such a manner that, in one of them, the only symmetry element is the inversion center (the symmetry C_i) and, in the other position, the only symmetry element is the symmetry plane (C_s) [24]. These positions are conventionally denoted as octahedra $M1$ and $M2$, respectively. Notably, $M2$ is somewhat larger. The olivine structure also contains distorted tetrahedral cationic positions of the same type with the local symmetry C_s and belongs to the Fedorov group $Pnma$ (D_{2h}^{16}). The oxygen octahedra share edges. In the case of Mg_2SiO_4 and Ca_2GeO_4, Mg and Ca ions, respectively, occupy the octahedral positions of both types [25], whereas, in monticellite $CaMgSiO_4$, smaller Mg ions occupy the $M1$ positions and larger Ca ions occupy the $M2$ positions [26].

Upon doping forsterite, the dopant ions incorporate into the $M1$ and $M2$ octahedra mainly in the low oxidation states (up to +3). The $3d$ ions in the oxidation states higher than +3, incorporating into the olivine structure, prefer the tetrahedral positions isolated from each other and sharing vertices with neighboring octahedra. Such an incorporation is related mainly to the size and charge factors.

If the dopant ion occupies either the $M2$ octahedron (C_s) or the $M1$ octahedron (C_i), the system of regular points it forms belongs to the sp. gr. $Pnma$ or to the sp. gr. $Cmmm$, respectively [27]. In this case, the unit-cell volume being the same, the $Cmmm$ group corresponds to higher symmetry than the $Pnma$ group [25]. Thus, from the viewpoint of space-group theory and
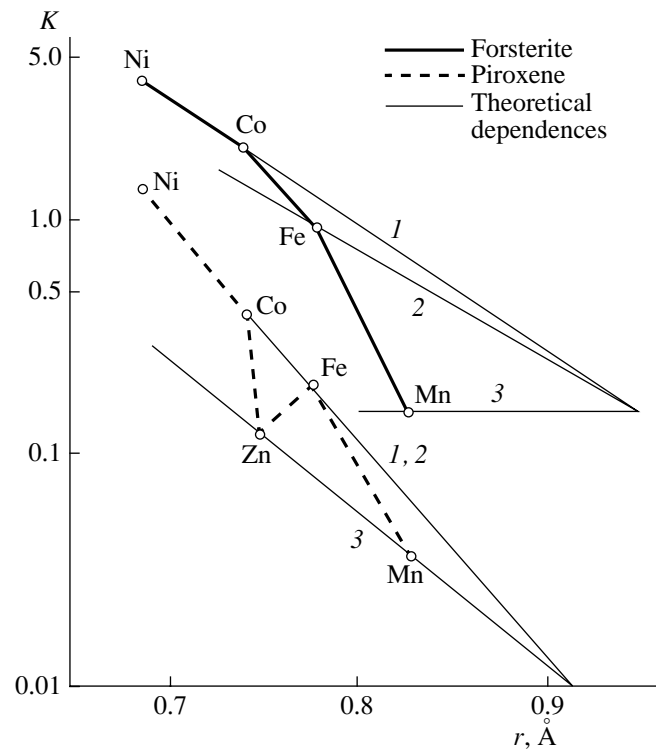

Fig. 2. Experimental dependences of the ratio of distribution of impurity divalent d ions between the octahedral cationic positions $K = C(M1)/C(M2)$ in Mg_2SiO_4 and $Mg_2Si_2O_6$ crystals on the efficient ionic radius r. The fine lines show the theoretical dependences for the (*1*) F, (*2*) D, and (*3*) S terms.

Brown's principle, the $M1$ octahedron turns out to be more preferable for location of the impurity d ion.

Let us consider how this selectivity is realized directly in a crystal. At the inversion center, the potential gradient $f = -\text{grad}U$ is zero; in the case of symmetry plane, the gradient vector lies in this plane [28]. For oxygen ions O^{2-} in the $M1$ octahedron (C_i), there are more opportunities to change their configuration when they tend to attain the minimum of the crystal-field potential, which, with the presence of edges shared with the $M2$ octahedron (C_s), decreases the volume of

Table 1. Distribution of several ions of the iron group between the $M1$ and $M2$ octahedra in forsterite Mg_2SiO_4 ($\Delta E_{st} = E_{st}(M1) - E_{st}(M2)$)

Ion	Dq, cm^{-1}	E_{st}, cm^{-1}	ΔE_{st}, cm^{-1}	K_{theor}	K_{exper}	Reference
Ni^{2+}	820	9840	680		2.92	[16]
					4.8	[17]
Cr^{3+}					2.7	[17]
Co^{2+}	840	5040	348	1.5	1.97	[16]
Fe^{2+}	1030	4120	284	1.22	1.06	[16]
					0.83	[17]
Mn^{2+}					0.16	[17]

Table 2. Ground-state terms of free d ions in a weak and strong crystal fields and experimental data [29–34] on the distribution of ions between the $M1$ and $M2$ octahedra in forsterite and pyroxene

Ion	$2s+1L(d^n)$	Weak field			Strong field	
		$\Gamma(t_2^{n_1}e^{n_2})$	E_{st}	position of preferred localization (experimental data)	$\Gamma(t_2^{n_1}e^{n_2})$	E_{st}
Ti^{3+}	$^2D(d^1)$	$^2T_2(t_2)$	2/5		$^2T_2(t_2)$	2/5
V^{3+}	$^3F(d^2)$	$^3T_1(t_2^2)$	4/5	C_i	$^3T_1(t_2^2)$	4/5
V^{2+}, Cr^{3+}	$^4F(d^3)$	$^4A_2(t_2^3)$	6/5	C_i	$^4A_2(t_2^3)$	6/5
Cr^{2+}	$^5D(d^4)$	$^5E(t_2^3 e)$	3/5		$^3T_1(t_2^4)$	8/5
Mn^{2+}	$^6S(d^5)$	$^6A_1(t_2^3 e^2)$	0	C_s	$^2T_2(t_2^5)$	10/5
Fe^{2+}	$^5D(d^6)$	$^5T_2(t_2^4 e^2)$	2/5	C_i, C_s	$^1A_1(t_2^6)$	12/5
Co^{2+}	$^4F(d^7)$	$^4T_1(t_2^5 e^2)$	4/5	C_i	$^2E(t_2^6 e)$	9/5
Ni^{2+}	$^3F(d^8)$	$^3A_2(t_2^6 e^2)$	6/5	C_i	$^3A_2(t_2^6 e^2)$	6/5
Cu^{2+}	$^2D(d^9)$	$^2E(t_2^6 e^3)$	3/5		$^2E(t_2^6 e^3)$	3/5
Zn^{2+}	$^1S(d^{10})$	$^1A_1(t_2^6 e^4)$	0	C_s	$^1A_1(t_2^6 e^4)$	0

Note: The stabilization energy E_{st} is given in Dq units.

the $M1$ octahedron. In the $M2$ octahedron, a pair of O^{2-} ions may shift only in the plane of symmetry. The deeper minimum of the crystal-field potential in the $M1$ octahedron should, all other factors being equal, lead to its preferred occupation by the activator ion in comparison with the $M2$ octahedron.

These conclusions are consistent with the experimental data on the location of a divalent impurity in the $M1$ and $M2$ octahedra with respect to both the ratio of the volumes of these cationic positions [29–34] and the force parameters of the crystal field Dq (see, for example, [35, 36]) for forsterite Mg_2SiO_4 crystals and for pyroxene $Mg_2Si_2O_6$, whose structure also contains two types of structurally nonequivalent distorted octahedral positions (Fig. 2).

Spatial distribution of the electron density of the d shell of an activator ion also affects its preferred location in one of several structurally nonequivalent cationic positions with the same coordination numbers. The effect of the radial component was discussed above. Concerning the angular component, its contribution was first noted in [21], where it was believed that it is the angular part of the spatial distribution of a dopant ion that is responsible for significant nonlinearity and presence of extrema in the experimental dependences of the coefficient of dopant distribution over the $M1$ and $M2$ octahedra on the dopant-ion radius in forsterite and

pyroxene (Fig. 2) ($K = C(M1)/C(M2)$, where $C(M_n)$ is the concentration of dopant ions in the corresponding octahedral site).

According to the experimental data [31, 33, 34], in the cases of forsterite and pyroxene, which are characterized by a weak crystal field acting on an activator ion, the value of K decreases in the following row of divalent ions: $Ni^{2+}(d^8)$, $Co^{2+}(d^7)$, $Fe^{2+}(d^6)$, $Zn^{2+}(d^{10})$, and $Mn^{2+}(d^5)$ (Tables 1, 2; Fig. 2). We should note that, in the crystal-field theory, the following relations correspond to the cases of weak and strong fields: $V_{coul} > V_{cr}$ and $V_{coul} < V_{cr}$, respectively, where V_{coul} is the energy of electrostatic interaction of the ion's electrons with each other and V_{cr} is the energy of each electron in the crystal field. In experimental practice, the following relation is used for weak and strong fields, respectively: $2.6 > Dq/B$ and $Dq/B > 2.6$. The shape of the luminescence spectrum at 300 K (a broad band or a narrow line) also serves in practice as a criterion of a weak or strong field, respectively.

According to Tables 1 and 2 and Fig. 2, the activator ions whose ground states originate from the S, D, and F terms of free ions are located in the $M2$ octahedron, equiprobably in the $M2$ and $M1$ octahedra, and in the $M1$ octahedron, respectively.

As is well known, the spherical symmetry of the electron cloud is typical of the S term. The F term, in

contrast, is characterized by significant localization of the angular component of the electron density and, therefore, by a stronger chemical bond [37]. The D term is characterized by an intermediate strength of the chemical bond and localization of the angular component of the electron density with respect to the S and F terms. The maximum values of the crystal-field stabilization energy E_{st} correspond to the term F (Table 2), whereas the minimum and intermediate values of E_{st} correspond to ions with the ground terms S and D, respectively.

The correlation between the type of the ground term and the preferable position, noted in [21], is explained as follows. In the case of weak field, the symmetry of the electron cloud of a free ion is retained near the electron core. In the case of an ion with the S term, the weaker chemical bond allows such an ion to shift in the symmetry plane of the structure. At the same time, an activator ion with a strong bond (the F term) is located in the positions with the inversion center. The reason is that the field gradient is zero at the inversion center; therefore, the shift of the ion should also be zero. Ions with the intermediate bond strength (the D term) are equiprobably located in the octahedra of both types.

Thus, the relations between the values of K_L, where L is the ground-state term of a free ion, have the form $K_F > K_D > K_S$. In addition, since in the case of localized electron density the chemical-bond strength depends on the distance between ions and on the ionic radius of the activator r stronger than in the case of extended density, the relationship $dK_F/dr > dK_D/dr > dK_S/dr$ is valid. Since the ionic radius (the oxidation state being the same) decreases with increasing number of d electrons (Fig. 1), $K_L(d^{n_1}) > K_L(d^{n_2})$ at $n_1 > n_2$, if L are identical.

Thus, the dependences of K on particular factors should be separated into the dependences for K_F, K_D, and K_S, according to the relations obtained (Fig. 2).

Let us consider the case of strong field. In a strong crystal field, the electron density of an ion is approximated within the zero-order approximation by a sum of densities of noninteracting t_2 electrons, the angular component of each density being identically equal to the angular distribution for the D term. Therefore, if we find in the zero-order approximation that the d ions tend to be equiprobably distributed over the $M1$ and $M2$ octahedra in a strong field, the account of the interaction between electrons should result in a stronger dependence of K on the number of d electrons of the ion than in the case of weak field (Table 2). Apparently, in the case of sufficiently small values of E_{st}, it is mainly the crystal–chemical factors that affect the distribution of an activator ion over the nonequivalent positions. Among these factors are the relationship between the size of the cationic position and the efficient radius of the impurity ion, the dopant concentration, the type and concentration of the charge compensator, and others. Thus, for the distribution of Cr^{3+} ions over the octahe-
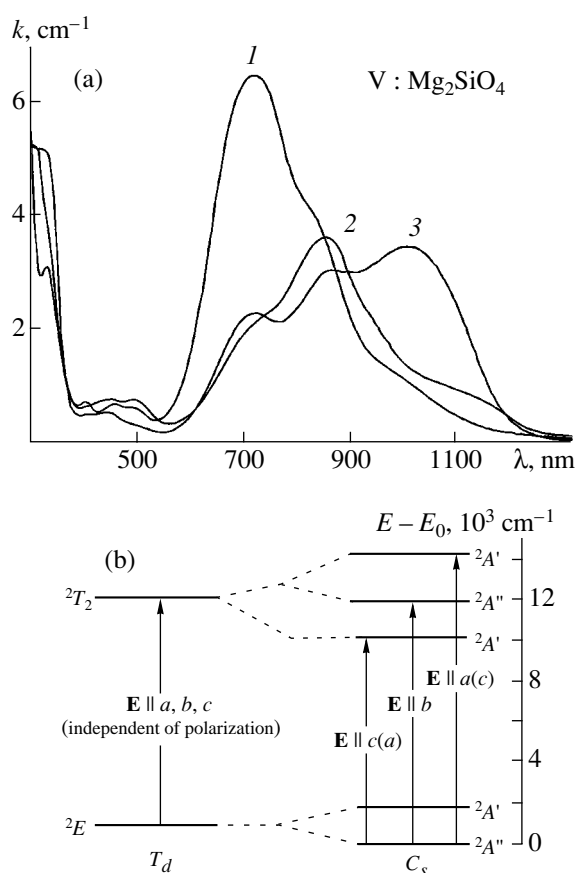

Fig. 3. (a) Experimental polarized absorption spectra of V-doped forsterite at 300 K for the polarization directions (*1*) $\mathbf{E} \parallel a$, (*2*) $\mathbf{E} \parallel b$, and (*3*) $\mathbf{E} \parallel c$; (b) allowed transitions for V^{4+} ions in distorted tetrahedra of the forsterite structure.

dral positions of forsterite (the case of weak field and maximum value of E_{st}), the values of K obtained experimentally in different studies, although being somewhat different, indicate the preferred trend for the activator ion to be located in the $M1$ octahedron [29–36, 38, 39]. At the same time, for widely studied alexandrite $Cr : BeAl_2O_4$ (the case of sufficiently strong field and small value of E_{st}), rather contradictory results are reported: specifically, the values of K range from 3.6 to 0.2 [7, 40, 41].

The conclusions made in [21] suggest that, in the case of positions with similar crystallographic characteristics, when predicting the character of distribution of an activator ion, one can compare the degree of deviation of the structure of polyhedra in which the ion can be located from the structure of the corresponding regular polyhedron to estimate the trend in the distribution of the activator ion over these positions. Apparently, for crystals with the phenakite structure, where cationic polyhedra have no symmetry elements, the preferred position is characterized by smaller deviations from a regular tetrahedron, all other factors being equal. This suggestion is being verified presently.
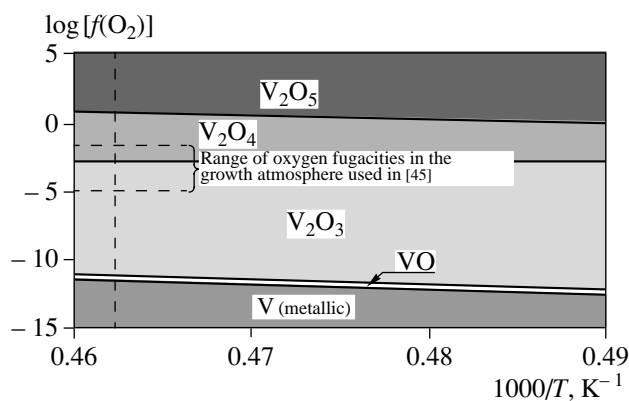
Fig. 4. Regions of thermodynamic stability of vanadium ions in different valence states (restricted by solid lines), depending on the oxygen fugacity $\log(f\mathrm{O}_2)$ and the inverse temperature $1000/T$, K^{-1}, in the range of operating temperatures and oxygen fugacities used for growing forsterite single crystals from melt by the Czochralski method. The vertical dashed line indicates the melting point of forsterite (1890°C).

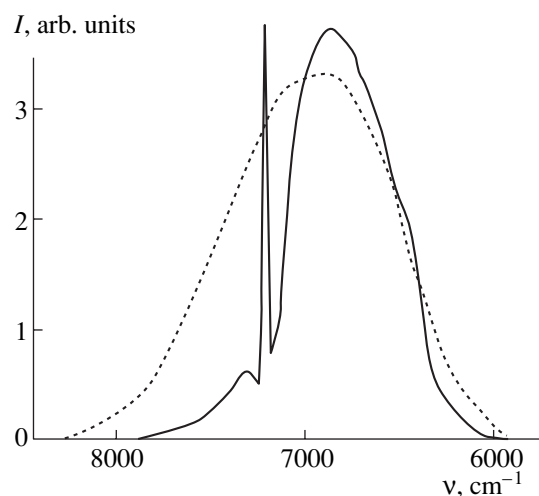**Fig. 5.** Luminescence spectrum of V : Mg_2SiO_4 single crystals at 77 (the solid line) and 300 K (the dotted line) [42].

2. SPECTROSCOPIC AND STRUCTURAL CHARACTERISTICS OF d IONS IN CRYSTALS WITH THE OLIVINE STRUCTURE

Vanadium ions in forsterite Mg_2SiO_4 are, apparently, studied experimentally most widely in view of the valence states and structural locations. The large values of absorptivity and continuous and fairly smooth shape of the absorption spectrum in the range of 600–1200 nm gives grounds to consider this crystal as a promising candidate for laser saturable absorbers in this spectral range [35, 36].

The strongest bands in the absorption spectra of V : Mg_2SiO_4 in the range of 600–1200 nm are attrib-

uted to V^{2+} and V^{3+} ions in [42] and to V^{4+} ions in [43]. On the basis of the ESR data, it was concluded in [44] that vanadium is present in forsterite mainly in the form of the V^{5+} ions. The inconsistency of the results of [42–44] may be, in particular, due to differences in the redox conditions of the crystal synthesis.

The complete picture of the structural states of vanadium ions V^{5+}, V^{4+}, V^{3+}, and V^{2+} in forsterite crystals grown by the Czochralski method is given in [35, 36, 45]. The conclusions were made on the basis of the comprehensive analysis of the absorption spectra at 300 and 77 K in a wide wavelength range (250–1600 nm) for crystals grown in various atmospheres—from slightly reducing to slightly oxidizing. Calculations of the energy-level diagrams were carried out for ions with different coordinations and valences with due regard for the spectral data. Analysis of the most thermodynamically stable charge state of the activator ion under real synthesis conditions (temperature–oxygen fugacity in the growth atmosphere) was performed. The measured dependence of the crystal density on the activator concentration was compared with the results of calculations for various combinations of the valence states and structural locations of vanadium in forsterite.

The band in the range of 300–1600 nm, which is dominant in the absorption spectra (Fig. 3) [35, 36], was assigned to the V^{4+} ion in the tetrahedral coordination. Such an assignment was based on the polarization dependences of the absorption intensities and on the high intensity of the spectrum, which correlated with the features of the electron–vibrational interaction. The assertion that this impurity center is of the main type follows from the coincidence of the regions of thermodynamic stability of the vanadium ion in the tetravalent state and the thermodynamic conditions of the crystal growth by the Czochralski method [45] (Fig. 4). The

Table 3. Experimental and calculated frequencies of the maxima of the absorption bands of V^{3+} ions in the octahedral positions of a forsterite crystal ($Dq = 1550$, $B = 500$, $C = 3150\ \mathrm{cm}^{-1}$ for $M1$ and $Dq = 1400$, $B = 800$, $C = 3000\ \mathrm{cm}^{-1}$ for $M2$)

Transition	ν_{exper}, cm^{-1}	ν_{calcd}, cm^{-1}	
		$M1$	$M2$
$^3T_1(t_2^2) \longrightarrow {}^1T_2(t_2^2)$		9540	10280
$^3T_1(t_2^2) \longrightarrow {}^1E(t_2^2)$		9640	10560
$^3T_1(t_2^2) \longrightarrow {}^3T_2(t_2e)$		14430	12640
$^3T_1(t_2^2) \longrightarrow {}^3T_1(t_2e)$	20800	20880	
	23300		23260
$^3T_1(t_2^2) \longrightarrow {}^3A_2(e^2)$	26300		26320
	30800	29940	

best agreement between the calculated and experimental dependences of the precisely measured crystal density on the concentration of impurity vanadium ions was also noted when the calculation was based on the assumption that vanadium incorporates into the tetrahedral silicon positions in the form of the V^{4+} ion [36, 45].

V^{3+} ions are located mainly in the $M1$ and $M2$ octahedra and are present in the crystals studied in relatively small amounts. The absorption of these centers manifests itself in the wavelength range below ~500 nm (Fig. 3, Table 3). The ratio of the intensities of the absorption bands of V^{3+} ions in the $M1$ and $M2$ octahedra corresponded to the distribution of the activator ion over structural positions, which follows from the considerations of the previous section. Indeed, as is well known, due to the parity forbiddenness of the d–d transitions for ions in the crystal field with the inversion center, the oscillator strengths of the electronic–vibrational transitions for the d ion in the $M1(C_i)$ position should be considerably smaller than for such transitions in the same ion located in the $M2(C_s)$ position. Thus, for equal concentrations of V^{3+} ions in the $M1$ and $M2$ positions, the absorption band corresponding to the former case should be significantly weaker. However, the observed intensities of the absorption bands of these optical centers are of the same order of magnitude (Fig. 3). This fact suggests that the concentration of trivalent vanadium in the $M1$ position considerably exceeds that in the $M2$ position.

The weak absorption at 1200 nm and the luminescence observed in the range of 1100–1700 nm (9091–5882 cm^{-1}) in [42] (Fig. 5) were assigned to the V^{3+} ion in the tetrahedral coordination with a fair degree of validity.

When the crystals were grown in the range of growth atmospheres, V^{2+} and V^{5+} ions, as well as tetrahedrally coordinated V^{3+} ions, did not arise in significant amounts [35, 36, 45]. Apparently, these states of vanadium ions may be realized when crystals are either grown or annealed after growth in more severe reducing or oxidizing conditions, respectively. Nevertheless, we failed to obtain tetrahedrally coordinated V^{3+} ions in large amounts using long reducing annealing of $V : Mg_2SiO_4$ crystals (some hundreds of hours in hydrogen atmosphere).

Chromium ions in forsterite Mg_2SiO_4 may be either in divalent, trivalent, or tetravalent states, depending on the synthesis conditions. They can be located in octahedrically coordinated positions $M1$ and $M2$, as well as in the tetrahedral position [46].

Efficient lasing tunable in the range of 1130–1370 nm, which is important from a practical point of view (for example, in fiber optics communication and ophthalmology), was obtained for Cr^{4+} ions in forsterite [47, 48]. However, the presence of chromium ions in other oxidation states (first of all, Cr^{2+} ions) in the crys-
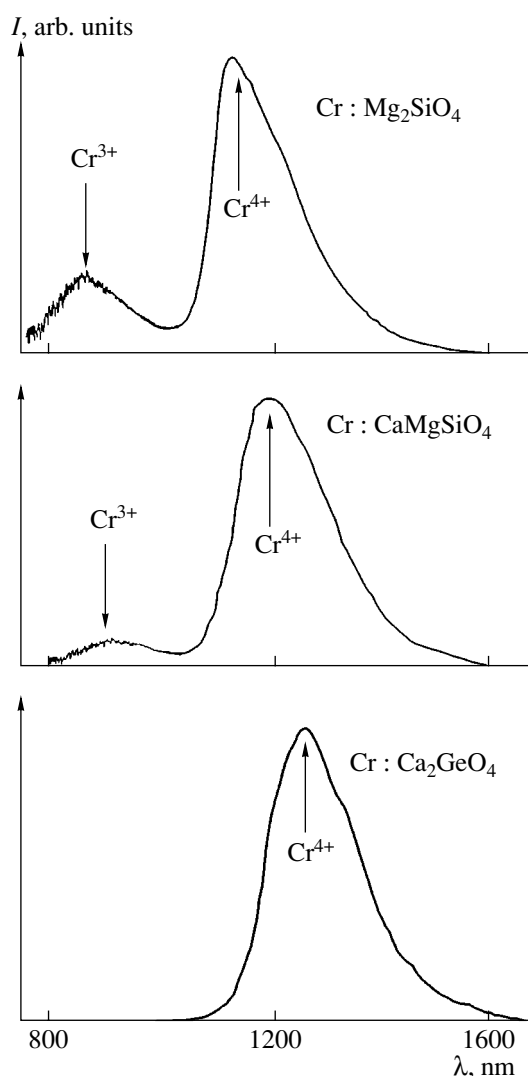

Fig. 6. Luminescence spectra of $Cr : Mg_2SiO_4$ [50], $Cr : CaMgSiO_4$ (our unpublished results), and $Cr : Ca_2GeO_4$ [66] single crystals.

tals may lead to undesirable optical absorption in the frequency range of lasing of tetravalent chromium.

Cr^{3+} ions in $Cr : Mg_2SiO_4$ crystals also exhibit luminescence, in particular, the R line at 692 nm, which is attributed to the Cr^{3+} ion in the $M1$ octahedron [49], as well as broadband luminescence with a maximum in the range of 860–890 nm (depending on the polarization, Fig. 6), corresponding to the Cr^{3+} ion in the $M2$ octahedron [50]. However, the absorption by Cr^{4+} ions at the lasing frequencies impedes efficient lasing of the Cr^{3+} ions in forsterite. Therefore, determination of conditions promoting or, vice versa, suppressing formation of particular optical centers (chromium ions in a specified state) in these crystals is of practical interest.

The absorption spectra of $Cr : Mg_2SiO_4$ crystals were also studied for various concentrations of chromium in the starting melt and different redox condi-
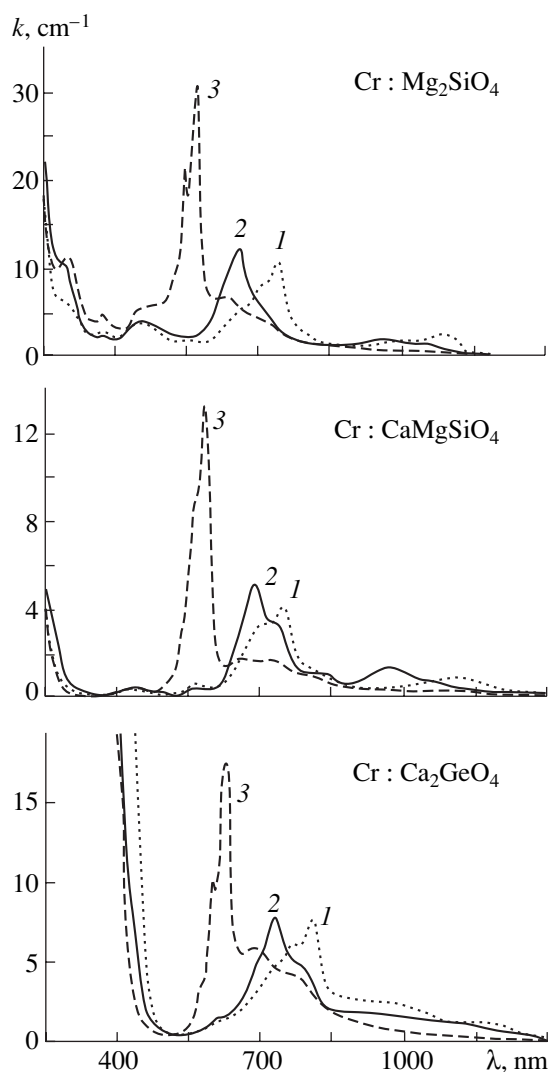
k, cm^{-1}

Cr : Mg$_2$SiO$_4$

Cr : CaMgSiO$_4$

Cr : Ca$_2$GeO$_4$

λ, nm

Fig. 7. Polarized absorption spectra of Cr:Mg$_2$SiO$_4$ [51], Cr:CaMgSiO$_4$ (our unpublished results), and Cr:Ca$_2$GeO$_4$ [56] single crystals recorded at 300 K for the polarization directions (*1*) $\mathbf{E} \parallel a$, (*2*) $\mathbf{E} \parallel b$, and (*3*) $\mathbf{E} \parallel c$.

tions of growth and subsequent annealing [46, 51]. All the bands revealed were identified and assigned to the correspondingly located chromium ions in the corresponding oxidation states.

The concentration of Cr^{2+} and Cr^{3+} ions in the octahedral coordination decreases, and the concentration of tetrahedral Cr^{4+} ions increases as the growth atmosphere becomes more oxidizing. This phenomenon is consistent with the results of [46]. However, even when crystals are grown in air, the fraction of Cr^{4+} ions in the general amount of chromium incorporated into a crystal remains rather small (no more than a few percent). Moreover, beginning with the level of 0.6 at. %, further increase in the chromium concentration does not lead to a proportional increase in the Cr^{4+} concentration in a crystal. The intensity of the absorption bands of the

Cr^{4+} ion saturates with the maximally attainable absorption coefficient at a wavelength of 1064 nm (the $^3A_2 \longrightarrow {}^3T_2$ transition) equal to 3.2 cm^{-1} [51].

Most chromium (up to 98%) incorporates into the crystal in the form of the Cr^{3+} ion [39]. Notably, the coefficient of distribution of the trivalent chromium between the *M*1 and *M*2 positions ranges from 1.5 to 4.5 according to [34, 38, 39, 52].

The Cr^{2+} and Cr^{3+} ions in the *M*1 and *M*2 octahedra rather easily transform into each other upon oxidizing and reducing annealing of crystals [46]. At the same time, even long reducing annealing fails to transform the tetrahedrally coordinated Cr^{4+} ion into a more reduced form since such a transition makes it necessary to change the structural location (from the tetrahedral to octahedral); i.e., the chromium ion should be displaced in the crystal. Apparently, the diffusivity of chromium in forsterite at the annealing temperature used in [46] is too small to initiate this process.

The chromium ions in monticellite CaMgSiO$_4$, like in forsterite, may be located in the form of octahedrically coordinated Cr^{3+} ion, although in significantly smaller amounts. This is evident from comparison of the luminescence spectra of Cr : Mg$_2$SiO$_4$, Cr : CaMgSiO$_4$ crystals in the near-infrared region (Fig. 6): the broadband luminescence in the range of 900–950 nm with relatively low intensity, which is characteristic of Cr^{3+} ions, was observed in both our experiments with single crystals grown in air and the previous experiments with polycrystalline samples prepared by melt cooling [53].

Chromium ions in calcium germanate Ca$_2$GeO$_4$ grown in air, according to the ESR data [54, 55], are not located in the form of Cr^{3+} ions or in lower oxidation states, despite the presence of octahedral cationic positions in the structure of this crystal (as well as in all the crystals with the olivine structure). The luminescence of Cr^{3+} ions was not observed in these crystals (Fig. 6). There are no data on the Cr:Ca$_2$GeO$_4$ crystals grown in less oxidizing conditions.

Cr^{4+} ions in forsterite Mg$_2$SiO$_4$, calcium germanate Ca$_2$GeO$_4$, and monticellite CaMgSiO$_4$, according to our calculations based on the spectral data [51, 56] and to our experimental results (unpublished, Fig. 7), are described by the energy-level diagrams listed in Table 4. The decrease in the crystal-field parameter *Dq* and, consequently, the long-wavelength shift of the maxima of luminescence and absorption of tetrahedrally coordinated Cr^{4+} ions in the row Cr:Mg$_2$SiO$_4$ $\longrightarrow$ Cr:CaMgSiO$_4$ $\longrightarrow$ Cr:Ca$_2$GeO$_4$ occur due to the increase in the radius of the coordination sphere around the Cr^{4+} ion. Notably, when we pass to Cr:Ca$_2$GeO$_4$, this change is more abrupt because, in this case, a smaller cation is substituted by a larger one (Si^{4+} $\longrightarrow$ Ge^{4+}) in the tetrahedral site, whereas both forsterite and monticellite are silicates. Therefore, when we pass

Table 4. Experimental and calculated frequencies of the maxima of the absorption bands of Cr^{4+} ions with tetrahedral coordination in forsterite Mg_2SiO_4, monticellite $CaMgSiO_4$, and calcium germanate Ca_2GeO_4 crystals

Transition	Mg_2SiO_4		$CaMgSiO_4$		Ca_2GeO_4	
	ν_{exper}, cm^{-1}	ν_{calcd}, cm^{-1}	ν_{exper}, cm^{-1}	ν_{calcd}, cm^{-1}	ν_{exper}, cm^{-1}	ν_{calcd}, cm^{-1}
$^3A_2(e^2) \longrightarrow\ ^1E(e^2)$	9100	8977		9574	9100	9092
$^3A_2(e^2) \longrightarrow\ ^3T_2(et_2)$	10160	10150	9500	10000	9090	9100
$^3A_2(e^2) \longrightarrow\ ^3T_1(et_2)$	15390	14854	14900	14886	13890	13420
$^3A_2(e^2) \longrightarrow\ ^1A_1(e_2)$		15393		16272		15218
$^3A_2(e^2) \longrightarrow\ ^1T_2(t_2e)$		18995	20200	19424		18066
$^3A_2(e^2) \longrightarrow\ ^1T_1(t_2e)$		21270		21880		20190
$^3A_2(e^2) \longrightarrow\ ^3T_1(t_2^2)$	22700	23096	23000	23139	20500	20856
$^3A_2(e^2) \longrightarrow\ ^1E(t_2^2)$		30063	31200	30441		28033
$^3A_2(e^2) \longrightarrow\ ^1T_2(t_2^2)$		30195	31200	30592		28159
$^3A_2(e^2) \longrightarrow\ ^1A_1(t_2^2)$		44947		46488	43000	43588
Parameters, cm^{-1}						
Dq		1015		1000		910
B		500		535		465
C		2560		2730		2755
B/C		5.1		5.1		5.9

from one of them to the other, only the composition of the octahedrically coordinated cations changes.

3. SPECTROSCOPIC AND STRUCTURAL CHARACTERISTICS OF d IONS IN CRYSTALS WITH THE PHENAKITE STRUCTURE

In this section, we will consider Zn_2SiO_4, $LiAlGeO_4$, and $LiGaSiO_4$ crystals. The spectroscopic properties of powdered samples of $Cr:Zn_2SiO_4$ were studied in [57]. $Cr:LiAlGeO_4$ and $Cr:LiGaSiO_4$ were studied in the form of single crystals. The results of these studies are reported in [58–60], and the growth technique for $Cr:LiGaSiO_4$ single crystals is described in [61].

The phenakite structure is the derivative from the β-Si_3N_4 structure [62]. In this structure (Fig. 8), all the ions are in the tetrahedrally coordinated positions. The cation–oxygen tetrahedra, sharing vertices, form columns parallel to the c axis. In this framework, channels of two types, parallel to the c axis, exist: large channels formed by six TO_4 tetrahedra combined into a ring and smaller channels formed by four TO_4 tetrahedra. All the tetrahedral cationic positions in the phenakite structure are divided into three structurally nonequivalent types ($T1$, $T2$, $T3$). In the case of $LiGaSiO_4$ crystals, each of these types is divided into two more structurally non-

equivalent subtypes ($T1_1$ and $T1_2$, $T2_1$ and $T2_2$, $T3_1$ and $T3_2$).

The division of tetrahedra into subtypes in the case of $LiGaSiO_4$ and the absence of such division in the case of $LiAlGeO_4$ is reasoned as follows [63]. In the $LiAlGeO_4$ crystal, the cationic positions of the $T1$ type are occupied by relatively large Li ions, whereas smaller Al^{3+} and Ge^{4+} ions, due to close values of their ionic radii, are randomly distributed between the $T2$ and $T3$ positions, which makes the crystal disordered. In this case, the $LiAlGeO_4$ crystal belongs to the space group with the inversion center $R\bar{3}$.

Another situation is observed in $LiGaSiO_4$ crystals, apparently due to significant differences in the sizes of all three ions. In this case, the tetrahedral positions $T1$ are occupied by gallium ions, whereas lithium and silicon ions are distributed between the $T2$ and $T3$ positions. This distribution, being now strictly regular, results in a layered structure, with the layers perpendicular to the c axis. In the first layer, Li and Si ions are located in the $T2$ and $T3$ positions, and vice versa in the next layer. Specifically this circumstance leads to division of the tetrahedral positions $T2$ and $T3$ in $LiGaSiO_4$ crystals into the subtypes $T2_1$ and $T2_2$, $T3_1$ and $T3_2$ with different sets of interatomic distances and valence angles. Gallium–oxygen tetrahedra $T1$, which have different sets of conjugate tetrahedra in different layers, are, in turn, also divided into the subtypes $T1_1$ and $T1_2$
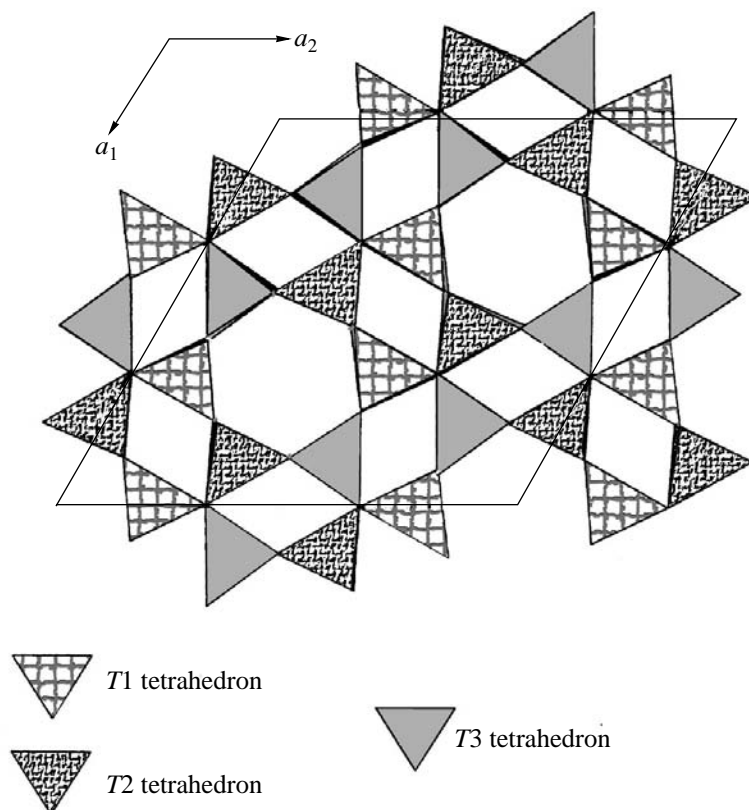
Fig. 8. Phenakite structure in the view plane perpendicular to the optical axis (cation–oxygen tetrahedra are shown entirely).

with somewhat different average values of the Ga–O distances and different character of distortion with respect to a regular tetrahedron. As a result, the inversion center in the structure of the $LiGaSiO_4$ crystal vanishes and, thus, the structure now corresponds to the sp. gr. $R3$ [64, 65].

The tetrahedral cationic positions of all structurally nonequivalent types and subtypes in $LiAlGeO_4$ and $LiGaSiO_4$ crystals are distorted so much that they have no symmetry elements at all, although the $T3$ tetrahedron in $LiAlGeO_4$ can be characterized, with some degree of approximation, by the C_S symmetry.

Cr^{4+} ions in LiAlGeO$_4$ and LiGaSiO$_4$ crystals, from the viewpoint of crystal chemistry, should obviously be incorporated primarily into the sublattices formed by tetravalent matrix ions. Thus, Cr^{4+} ions should be strictly randomly distributed between the $T2$ and $T3$ positions in $LiAlGeO_4$ crystals, and they should occupy the $T2_2$ and $T3_1$ positions in $LiGaSiO_4$ crystals. In addition, we cannot exclude from consideration the location of some (although, apparently, rather small) amount of Cr^{4+} ions in the sublattice formed by trivalent ions, i.e., also in both subtypes of the $T1$ position in $LiGaSiO_4$ crystals.

As was mentioned, the ground state $^3A_2$ of the tetrahedrally coordinated Cr^{4+} ion originates from the ^3F term, which is characterized by a high degree of localization of the angular component of the electron cloud and, therefore, by a relatively strong chemical bond. Thus, taking into account the conclusions of [21], one may expect selective incorporation of Cr^{4+} ions preferentially into more symmetric cationic positions. Indeed, the spectroscopic measurements showed that only one type of optical center formed by Cr^{4+} ions dominates in either type of the crystals. Primarily, this is evidenced by the presence of one distinct luminescence maximum even at liquid nitrogen temperatures (Fig. 9) and by the monoexponential character of the luminescence-decay kinetics in the range of 1300–1500 nm [58–60].

The absorption spectra of $LiGaSiO_4$ and $LiAlGeO_4$ single crystals (Fig. 10) also confirm the suggestion that Cr^{4+} ions form optical centers of only one type in these crystals. For example, the strongest spectral bands at a justified value of the crystal-field parameter B (from the viewpoint of bond covalence in a tetrahedrally coordinated polyhedron) can be assigned with good accuracy to the transitions in optical centers of one type formed by Cr^{4+} ions in these crystals (Table 5). We
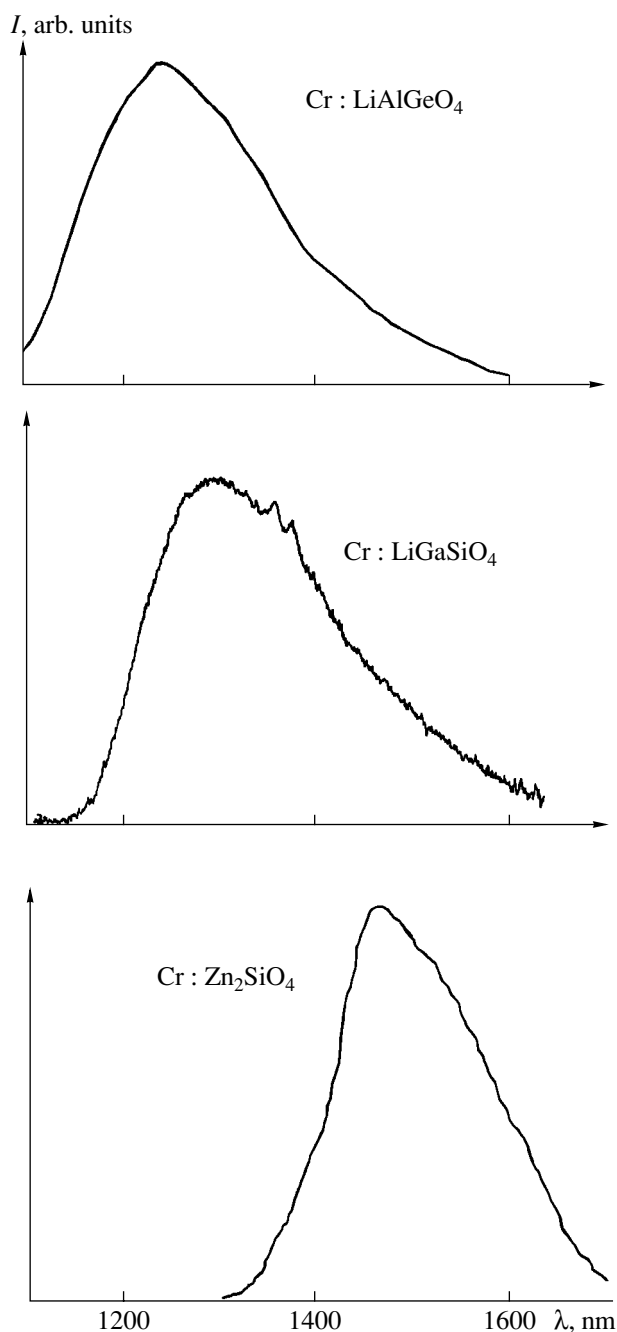
Fig. 9. Luminescence spectra of Cr^{4+} ions in $LiAlGeO_4$ [58, 59], $LiGaSiO_4$ [73], and Zn_2SiO_4 [57] single crystals recorded at 77 K.

Fig. 10. Absorption spectra of $Cr:LiAlGeO_4$ [58, 59] and $Cr:LiGaSiO_4$ [60] single crystals recorded at 300 K.

should note that the experimental frequencies of the maxima correspond to the centroids of the frequency maxima, corresponding to the spin–orbit-split components of the $^3A_2 \longrightarrow {}^3T_1$ transition.

Cr⁴⁺ ions in Zn₂SiO₄ crystals, according to [57], apparently incorporate mainly into the positions of the Zn^{2+} ion rather than the positions of the Si^{4+} ion (which one would expect since the substituent and substituted ions have the same valence). This suggestion is corrob-
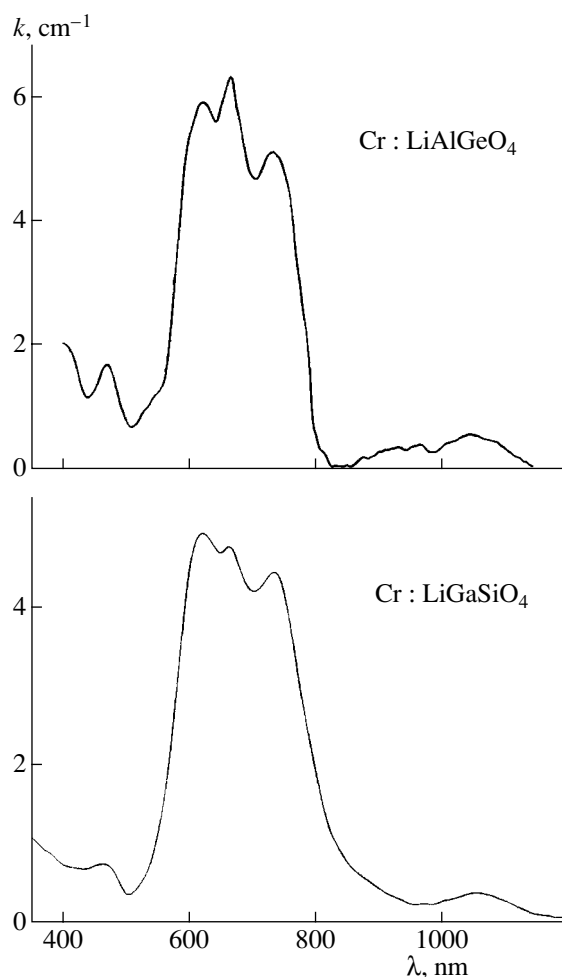
orated by the significant long-wavelength shift of the maximum of luminescence (~1480 nm) of Cr^{4+} ions in Zn_2SiO_4 crystals with respect to the maximum of luminescence of Cr^{4+} ions in Mg_2SiO_4 (1140 nm [66, 67]), $CaMgSiO_4$ (1190 nm [53, 68]), and Y_2SiO_5 (1220 nm [69, 70]) crystals and in other silicon-containing systems, in which the location of Cr^{4+} ions specifically in the silicon positions is beyond question. This shift may be caused only by a significant increase in the cation–oxygen distance in comparison with its typical value for silicon–oxygen tetrahedra.

In this context, we suppose that the preferred location of Cr^{4+} ions in silicon positions in $LiGaSiO_4$ crystals looks rather doubtful (the maxima in the absorption and luminescence spectra of $LiGaSiO_4$ (see Fig. 9, Table 5) are also significantly shifted relative to the positions of maxima typical of Cr^{4+} ions in silicate crystals.

Cr³⁺ ions in LiGaSiO₄ and LiAlGeO₄ crystals were revealed upon their pumping by the second harmonic of

Table 5. Experimental (at 300°C) and calculated frequencies of the maxima of the absorption bands of Cr^{4+} ions with tetrahedral coordination in $LiAlGeO_4$ and $LiGaSiO_4$ crystals

Transition	LiAlGeO$_4$		LiGaSiO$_4$	
	ν_{exper}, cm^{-1}	ν_{calcd}, cm^{-1}	ν_{exper}, cm^{-1}	ν_{calcd}, cm^{-1}
$^3A_2(e^2) \longrightarrow {}^1E(e^2)$		9197		9316
$^3A_2(e^2) \longrightarrow {}^3T_2(et_2)$	9500			
	10200	9400	9500	9300
	10600			
$^3A_2(e^2) \longrightarrow {}^3T_1(et_2)$	13300		13500	
	14800	14061	15000	14098
	16000		16300	
$^3A_2(e^2) \longrightarrow {}^1A_1(e^2)$		15595		15838
$^3A_2(e^2) \longrightarrow {}^1T_2(t_2e)$	18100	18449		18450
	19000			
$^3A_2(e^2) \longrightarrow {}^1T_1(t_2e)$	20900	20820		20980
$^3A_2(e^2) \longrightarrow {}^3T_1(t_2^2)$	21000	21864	21600	21977
$^3A_2(e^2) \longrightarrow {}^1E(t_2^2)$		28838		28829
$^3A_2(e^2) \longrightarrow {}^1T_2(t_2^2)$		28986		28995
$^3A_2(e^2) \longrightarrow {}^1A_1(t_2^2)$		44296		44422
Parameters, cm^{-1}				
Dq		940		930
B		515		545
C		2620		2570
B/C		5.1		4.7

the neodymium-laser emission (532 nm). Narrow-band luminescence of both crystals was detected: at 702 nm with a decay time of about 3 ms for Cr:LiAlGeO$_4$ and at 720 nm with a decay time of about 2 ms for Cr:LiGaSiO$_4$. Luminescence of this kind is typical of the spin-forbidden transition $^2E \longrightarrow {}^4A_2$ in Cr^{3+} ions. Since the broadband luminescence in the red and near-IR regions due to the electronic–vibrational transition $^4T_2 \longrightarrow {}^4A_2$ in Cr^{3+} ions was not observed, we may conclude that the $^4T_2$ level of the octahedrically coordinated Cr^{3+} ion lies much higher than the ^2E level ($\Delta E \gg kT$ at 300 K). Such a situation is typical of strong crystal fields, which excludes the tetrahedral coordination.

The question of the location of Cr^{3+} ions in these crystals also remains open to date. As was noted above, the phenakite structure contains no regular octahedral positions, and trivalent chromium ions may be either located in the channels formed by the oxygen tetrahedra (Fig. 8) or incorporated into the structure. The latter process is accompanied by the local rearrangement of regular tetrahedral cationic positions into octahedral positions. The possibility of such a rearrangement was shown previously by the example of crystals with the melilite structure [71] and LiGaO$_2$ crystals [72].

CONCLUSIONS

In this study, new laser crystals with the forsterite and phenakite structures containing ions of *d* elements are considered. The structural complexity of these materials required a complex approach to investigation of their spectroscopic characteristics and identification of active optical centers.

Complex oxides are characterized by two or three sublattice structures and often demonstrate complex isomorphism, in particular, as applied to *d* ions with variable valence. These ions exhibit diverse and sometimes unconventional structural location in complex oxides.

Ions of *d* elements may be incorporated into different sublattices in the structures of complex oxides. In this case, all other factors being the same, they occupy the most symmetric crystallographic positions, corresponding to a regular point system with higher symmetry. Such a selective trend can be considered as a manifestation of Brown's principle as applied to doping of crystals. In this case, the activator ion is located selectively in larger amounts in those positions that belong to a higher space-symmetry group (in the row of positions with similar crystallographic characteristics).

The electronic configuration of the *d* shell of the activator ion significantly affects the character of its incorporation into the structure and distribution among different structurally nonequivalent crystallographic positions (including similarly coordinated ones) by the character of distribution of the electron density in the ground state of the activator ion. The knowledge of the ground term of the ion (the *S*, *D*, *F* terms) and account of the local symmetry of positions made it possible to predict the features of this distribution with a sufficient degree of reliability. In some cases, these two factors play even more important roles than the ionic radius and formal charge, which is confirmed by the theoretical and experimental results obtained both here and in previous studies.

Finding out the laws describing the incorporation of an activator ion into a structure and its distribution over the crystallographic positions makes it possible to control the characteristics of laser crystals, in particular, to search optimal ion–matrix combinations and conditions of crystal growth, contributing to the activator localization in required positions in the specified valence state.

On the basis of the developed concepts on incorporation of an activator ion into a structure, with the use of our own experimental results and with due regard for the data in the literature, the spectroscopic characteristic of new laser crystals based on complex oxides and

doped with d ions, having olivine (Mg_2SiO_4, $CaMgSiO_4$, Ca_2GeO_4) and phenakite ($LiGaSiO_4$, $LiAlGeO_4$, Zn_2SiO_4) structures, were investigated and compared with certain optical centers formed by d ions.

ACKNOWLEDGMENTS

REFERENCES

1. E. V. Zharikov and V. A. Smirnov, *Wide Gap Luminescent Materials: Theory and Applications* (Kluwer Academic, Nowell, MA, 1997), p. 13.

2. S. Kück, Appl. Phys. B **72**, 515 (2001).

3. M. J. Hayduk and S. T. Johns, Laser Focus World **32** (12), 73 (1996).

4. S. Spalter, M. Böhm, M. Burk, *et al.*, Appl. Phys. B **65**, 335 (1997).

5. X. Zhang and S. Zhao, IEEE J. Quantum Electron. **33** (12), 2286 (1997).

6. E. V. Zharikov, G. M. Kuz'micheva, and S. G. Novikov, in *Growth of Crystals*, Ed. by E. I. Givargizov and A. M. Melnikova (Kluwer Academic, New York, 2002), 21, p. 155.

7. J. E. Walling, O. G. Peterson, H. P. Jenssen, *et al.*, IEEE J. Quantum Electron. **16**, 1302 (1980).

8. B. K. Sevast'yanov, Yu. L. Remigaĭlo, V. P. Orekhova, *et al.*, Dokl. Akad. Nauk SSSR **256** (2), 373 (1981) [Sov. Phys. Dokl. **26**, 62 (1981)].

9. B. K. Sevast'yanov, Yu. L. Remigaĭlo, T. F. Veremeĭchik, and V. P. Orekhova, Dokl. Akad. Nauk SSSR **285** (5), 1119 (1985) [Sov. Phys. Dokl. **30**, 1051 (1985)].

10. A. I. Alimpiev, G. V. Bukin, V. N. Matrosov, *et al.*, Kvantovaya Élektron. (Moscow) **13**, 586 (1986).

11. E. V. Pestryakov, V. I. Trunov, A. I. Alimpiev, and V. P. Solntsev, Izv. Akad. Nauk SSSR, Ser. Fiz. **52** (6), 1184 (1988).

12. *Physics and Spectroscopy of Laser Crystals*, Ed. by A. A. Kaminskiĭ (Nauka, Moscow, 1986).

13. A. P. Voĭtovich, A. E. Nosenko, A. G. Bazylev, *et al.*, Zh. Prikl. Spektrosk. **51** (4), 705 (1989).

14. A. A. Kaminskii, A. V. Butashin, A. A. Demidovich, *et al.*, Phys. Status Solidi **112** (1), 197 (1989).

15. Z. B. Perekalina, T. F. Veremeĭchik, K. A. Kaldybaev, and A. D. Tynaev, Kristallografiya **45** (2), 337 (2000) [Crystallogr. Rep. **45**, 304 (2000)].

16. Z. B. Perekalina, T. F. Veremeĭchik, A. D. Tynaev, *et al.*, Poverkhnost, No. 2, 67 (2001).

17. Z. B. Perekalina, V. P. Orekhova, K. A. Kaldybaev, *et al.*, Kristallografiya **46** (5), 900 (2001) [Crystallogr. Rep. **46**, 826 (2001)].

18. B. B. Dudnikova, E. V. Zharikov, V. S. Urusov, *et al.*, Mater. Élektron. Tekh., No. 2, 11 (2000).

19. E. V. Zharikov, V. V. Laptev, A. A. Maĭer, *et al.*, Izv. Akad. Nauk SSSR, Neorg. Mater. **20** (6), 984 (1984).

20. E. V. Zharikov, Tr. Inst. Obshch. Fiz., Akad. Nauk SSSR **26**, 50 (1990).

21. T. F. Veremeĭchik and R. V. Galiulin, Neorg. Mater. **38** (9), 1110 (2002).

22. I. D. Brown, Acta Crystallogr., Sect. B: Struct. Sci. **44**, 545 (1988).

23. Letter from I. D. Brown to R. V. Galiullin.

24. H. Onken, Tschermaks Miner. Petrogr. Mitteilungen **10** (1), 34 (1965).

25. *International Tables for X-ray Crystallography* (Kinoch, Birmingham, 1952).

26. G. A. Lager and E. P. Meagher, Am. Mineral. **63**, 365 (1968).

27. *International Tables for Crystallography, A: Space-Group Symmetry* (Kluwer Academic, Dordrecht, 1983).

28. R. V. Galiulin and S. E. Sigarev, Dokl. Akad. Nauk SSSR **293**, 99 (1987) [Sov. Phys. Dokl. **32**, 173 (1987)].

29. D. L. Bish, Am. Mineral. **66**, 770 (1981).

30. X. Hu, K. Langer, and D. Bostrom, Eur. J. Mineral., No. 2, 29 (1990).

31. V. Ranjamani, G. E. Brown, and C. T. Prewitt, Am. Mineral. **60** (2), 292 (1975).

32. L. Galoisy, G. Calas, and G. E. Brown, Am. Mineral. **80** (6), 1089 (1995).

33. D. Walsh, G. Donney, and J. D. H. Donney, Can. Mineral. **14**, 149 (1976).

34. T. C. McCormick, J. R. Smith, and G. E. Lofgren, Phys. Chem. Miner. **14**, 368 (1987).

35. T. F. Veremeĭchik, A. V. Gaĭster, E. V. Zharikov, *et al.*, Kvantovaya Élektron. (Moscow) **30** (5), 449 (2000).

36. T. F. Veremeĭchik, A. V. Gaĭster, V. B. Dudnikova, *et al.*, Poverkhnost, No. 3, 85 (2001).

37. B. F. Ormont, *Introduction to Physical Chemistry and Crystal Chemistry of Semiconductors* (Vysshaya Shkola, Moscow, 1982).

38. H. Rager, Phys. Chem. Miner. **1**, 371 (1977).

39. J. L. Mass, J. M. Burlitch, S. A. Markgraf, *et al.*, J. Cryst. Growth **165**, 250 (1996).

40. R. E. Newnham, R. Santoro, J. Pearson, *et al.*, Am. Mineral. **49** (3–4), 427 (1964).

41. V. N. Vazhenin, A. E. Nikiforov, and B. K. Sevast'yanov, Fiz. Tverd. Tela (Leningrad) **29** (2), 627 (1987) [Sov. Phys. Solid State **29**, 362 (1987)].

42. A. G. Avanesov, V. G. Dvornikova, V. V. Zhorin, *et al.*, Zh. Prikl. Spektrosk. **52**, 152 (1993).

43. T. C. Brunold, H. U. Gudel, and A. A. Kaminskii, Chem. Phys. Lett. **271**, 327 (1997).

44. S. J. Mackwell and D. L. Kohlstedt, Phys. Chem. Miner. **13**, 351 (1986).

45. T. F. Veremeichik, E. V. Zharikov, V. B. Dudnikova, *et al.*, Opt. Mater. **19**, 319 (2002).

46. Y. Yamaguchi, K. Yamagishi, and Y. Nobe, J. Cryst. Growth **128**, 996 (1993).

47. V. G. Baryshevsky, M. V. Korzhik, M. G. Livshits, *et al.*, in *OSA Proceedings on Advanced Solid-State Lasers*,

Ed. by G. Dub and L. L. Chase (Optical Society of America, Washington, DC, 1991), Vol. 10, p. 26.

48. V. Petricevic, A. Seas, and R. R. Alfano, in *OSA Proceedings on Advanced Solid-State Lasers*, Ed. by G. Dub and L. L. Chase (Optical Society of America, Washington, DC, 1991), Vol. 10, p. 41.

49. W. Jia, H. Liu, S. Jafe, *et al.*, Phys. Rev. B **43**, 5234 (1991).

50. V. F. Lebedev, A. V. Gaĭster, S. Yu. Tenyakov, *et al.*, Kvantovaya Élektron. (Moscow) **33** (3), 197 (2003).

51. V. F. Lebedev, A. V. Gaĭster, S. Yu. Tenyakov, *et al.*, Kvantovaya Élektron. (Moscow) **33** (3), 192 (2003).

52. I. D. Ryabov, A. V. Gaĭster, and E. V. Zharikov, Fiz. Tverd. Tela (St. Petersburg) **45** (1), 51 (2003) [Phys. Solid State **45**, 51 (2003)].

53. V. Petričevič, A. Seas, R. R. Alfano, *et al.*, in *Advanced Solid State Lasers Technical Digest* (Optical Society of America, New Orleans, 1993), Paper ATuE1, p. 238.

54. D. Reinen, U. Kesper, M. Atanasov, and J. Roos, Inorg. Chem. **34**, 184 (1995).

55. O. N. Gorshkov, E. S. Demidov, S. A. Tyurin, *et al.*, Fiz. Tverd. Tela (St. Petersburg) **44** (1), 51 (2002) [Phys. Solid State **44**, 52 (2002)].

56. V. V. Dozmarov, L. D. Iskhakova, V. N. Protopopov, *et al.*, Perspekt. Mater., No. 4, 36 (1999).

57. R. G. Pappalardo, W. J. Miniscalco, T. E. Peters, *et al.*, J. Lumin. **55**, 87 (1993).

58. K. A. Subbotin, V. A. Smirnov, E. V. Zharikov, *et al.*, Opt. Spektrosk. **89** (1), 63 (2000) [Opt. Spectrosc. **89**, 56 (2000)].

59. K. A. Soubbotin, V. A. Smirnov, S. V. Kovaliov, *et al.*, Opt. Mater. **13** (4), 405 (2000).

60. K. A. Subbotin, V. A. Smirnov, E. V. Zharikov, *et al.*, in *Technical Digest of XVII Topical Meeting on Advanced Solid-State Lasers* (Quebec City, Canada, 2002), Paper TuB19.

61. K. A. Subbotin and E. V. Zharikov, Neorg. Mater. (in press).

62. M. Behruzi and Th. Hahn, Z. Kristallogr. **133**, 405 (1971).

63. K. F. Hesse, Z. Kristallogr. **172**, 147 (1985).

64. P. Hartman, Z. Kristallogr. **187**, 139 (1989).

65. M. E. Fleet, Z. Kristallogr. **180**, 63 (1987).

66. M. F. Hazenkamp, H. U. Güdel, M. Atanasov, *et al.*, Phys. Rev. B **53**, 2367 (1996).

67. H. R. Verdun, L. M. Thomas, D. M. Andrauskas, *et al.*, Appl. Phys. Lett. **53**, 2593 (1988).

68. K. A. Subbotin, E. V. Zharikov, V. A. Smirnov, *et al.*, Kratk. Soobshch. Fiz., Nos. 11–12, 16 (1997).

69. W. M. Yen and W. Jia, J. Appl. Spectrosc. **62**, 199 (1995).

70. C. Deka, B. H. T. Chai, Y. Shimony, *et al.*, Appl. Phys. Lett. **61** (18), 2141 (1992).

71. G. M. Kuz'micheva, B. V. Mukhin, V. B. Rybakov, *et al.*, Zh. Neorg. Khim. **40** (4), 569 (1995).

72. G. M. Kuz'micheva, A. V. Gaĭster, V. B. Rybakov, *et al.*, Perspekt. Mater., No. 1, 48 (1999).

73. K. A. Soubbotin, V. A. Smirnov, V. F. Lebedev, *et al.*, in *Technical Digest of CLEO-Europe'2003, Munich, Germany, 2003*, Paper CG4W.

Translated by Yu. Sin'kov

PHYSICAL PROPERTIES
OF CRYSTALS

Dedicated to the 60th Anniversary
of the Shubnikov Institute of Crystallography
of the Russian Academy of Sciences

Excited-State Absorption Spectroscopy of Crystals Doped with Cr^{3+}, Ti^{3+}, and Nd^{3+} Ions. Review

B. K. Sevast'yanov

Shubnikov Institute of Crystallography, Russian Academy of Sciences, Leninskiĭ pr. 59, Moscow, 119991 Russia
e-mail: optcryst@ns.crys.ras.ru
Received March 30, 2003

Abstract—Basic results of the investigations of the absorption and luminescence spectra of strongly pumped crystals doped with Cr^{3+}, Ti^{3+}, and Nd^{3+} ions are considered. These investigations have been systematically carried out since 1968 in the Laboratory of Physics of Optical Crystals and the Laboratory of Spectroscopy of Crystals of the Shubnikov Institute of Crystallography of the Russian Academy of Sciences. The results obtained are compared with the data in the literature. © *2003 MAIK "Nauka/Interperiodica"*.

CONTENTS

INTRODUCTION

The ESA spectroscopy of impurity crystals is, in fact, nonlinear spectroscopy using strong light fields. This technique not only supplements and expands the fundamental ground-state absorption (GSA) spectroscopy but also opens up new lines of investigation in the spectroscopy of crystals. As is well known [1, 2], the principle of ESA spectroscopy of impurity ions in crystals is to populate, with the use of optical pumping, some (generally metastable) levels of impurity ions with the energy $E \gg kT$, which are not populated under normal conditions. Then, the spectrum of absorption from these levels is analyzed. The absorption from excited levels is often referred to as induced absorption.

Typical examples of electronic transitions considered in this review which determine the ESA spectra of Cr^{3+} and Nd^{3+} ions are shown in Fig. 1. Actually, GSA spectroscopy does not describe the structure of the energy spectrum of impurity ions in crystals quite adequately, since a large number of transitions from the ground state are forbidden by either spin or parity selection rules. If some other states with other spin or parity are populated, the forbiddenness of the transitions from these states may be partially or completely lifted. Therefore, ESA spectra are more informative than GSA spectra because they contain more absorption bands or lines. Speaking of the fundamental scientific importance of ESA spectroscopy, this technique primarily yields a great amount of experimental data for the crystal-field (CF) theory and the ligand-field (LF) theory, as well as for the theory of deep impurity levels in wide-gap insulators. When the entire energy spectrum of impurity ions in a crystal is constructed, the CF theory

needs experimental data—positions of the maxima of absorption bands and lines, their intensities, oscillator strengths, polarization dependences, kinetics, and so on [3, 4]. ESA spectroscopy provides such information.

ESA spectroscopy makes it possible to observe the high-energy states of impurity ions within the fundamental absorption band of a crystal matrix. Finally, this technique allows us to observe the absorption bands due to the charge transfer between a metal impurity ion and the nearest ligands. This circumstance is very important since it becomes possible to combine the energy spectrum of metal-impurity ions with that of the crystal matrix. The application of ESA spectroscopy to search new laser materials turns out to be quite fruitful because it allows one to determine the induced absorption in the vicinity of the laser transition, the kinetics of the population of excited states, and some other characteristics.

Vavilov and Levshin, who investigated crystal phosphors in 1926, were the first to observe nonlinear absorption [5]. In 1944, Lewis *et al.* [6] revealed nonlinear absorption in fluorescein solutions. However, it really became possible to study ESA spectra only after the laser was discovered independently by Basov and Prokhorov and by Townes. This discovery made available strong light fields. Laser experiments with ruby crystals performed by Meiman [7] revealed nonlinear absorption of light in these crystals. Gires and Mayer [8–10] carried out a series of experiments to study the ESA spectra of ruby. They suggested an experimental technique and a theoretical approach to explain the results obtained. In fact, after these studies, systematic investigation of ESA spectra of crystals began.

1. BASIC PRINCIPLES OF MEASURING ESA SPECTRA (BROAD ABSORPTION BANDS)

There are two radically different approaches to measurement of ESA spectra. One of them is used when an ESA spectrum is beyond the luminescence band, and the other is used when an ESA spectrum overlaps the luminescence band. In this section, we will consider the methods of calculating and measuring ESA spectra beyond the luminescence band.

1.1. Technique of measuring ESA spectra. The schematic of a setup for measuring GSA, ESA, and luminescence spectra of crystals is shown in Fig. 2. The measuring technique was developed at the Shubnikov Institute of Crystallography, Russian Academy of Sciences (RAS) (1970). The probe light from high-pressure arc lamp *1*, modulated with a frequency of 15 kHz by mechanical modulator *4* and shaped as a slightly converging beam, passes through sample *7*. Then, the probe light enters the slit of one of spectrographs *11–13*. A sample is installed on copper cold finger *17*, which is in thermal contact with liquid-helium bath *16*. The whole system is placed in a vacuum chamber with a residual pressure of ~10^{-6} torr. Quartz windows *21* are
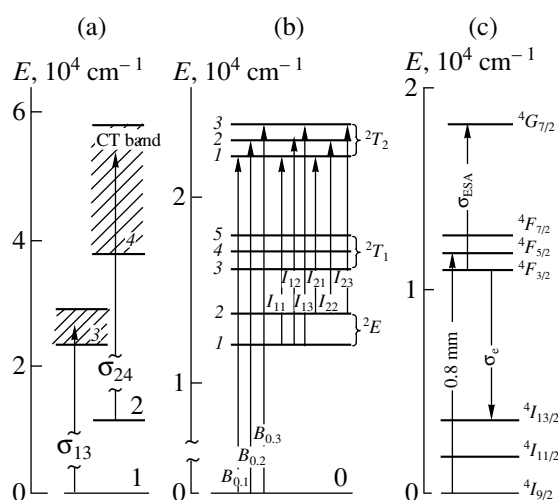

Fig. 1. (a) Simplified diagram of electronic transitions in Cr^{3+} ions in crystals. *1* and *2* stand for the $^4A_2(t_2^3)$ and $^2E(t_2^3)$ levels, respectively; band *3* includes the $^4T_2(t_2^2, e)$, $^4T_1(t_2^2, e)$, and $^4T_1(t_2^2, e^2)$ states; and band *4* includes all the doublet terms and the levels of the CT band. (b) Simplified diagram of the electronic transitions $^4A_2(t_2^3) \longrightarrow {}^2T_2(t_2^3)$ (*B* lines) and $^2E(t_2^3) \longrightarrow {}^2T_2(t_2^3)$ (*I* lines) in Cr^{3+} ions in crystals. (c) Simplified diagram of the electronic transitions in Nd^{3+} ions in crystals: $^4F_{3/2} \longrightarrow {}^4I_{13/2}$ is an emission transition (1300 nm), $^4F_{3/2} \longrightarrow {}^4G_{7/2}$ is an ESA transition, and $^4I_{9/2} \longrightarrow {}^4F_{5/2}$ is a pumping transition at 800 nm.

mounted on bellows adjusting appliances, which makes it possible to adjust windows without seal failure. Optical pumping of samples is performed by pulsed lamps *20* through glass tube *19*, which is a part of the vacuum chamber. Units *23–25* synchronize the measuring scheme, amplify, filter, and record signals. The same setup is used to measure GSA and luminescence spectra; i.e., the measurements are performed under the same conditions. Probe light of intensity $I_0(\lambda)$ with wavelength λ is incident on a unpumped sample and is absorbed in accordance with Bouguer's law:

$$I_u(\lambda) = I_0(\lambda) \exp\{(-n_0\sigma_{13}(\lambda) - K_l(\lambda))l\}. \quad (1)$$

Here, $I_u(\lambda)$ is the intensity of probe light with wavelength λ transmitted through an unpumped sample; l is the optical-path length in a sample; n_0 is the concentration of dopant ions in a sample (cm^{-3}); σ_{13} is the cross section of absorption from the ground state; and $K_l(\lambda)$ is the loss factor (cm^{-1}), which accounts for scattering, nonresonant absorption, and so on. When a sample is pumped, level 2 becomes populated (Fig. 1a). In this case, the intensity of probe light transmitted through a sample can be written as

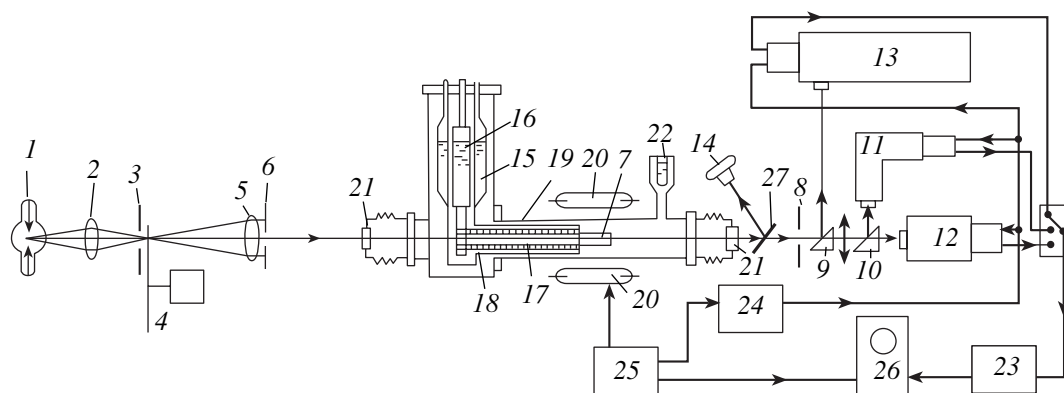$$I_p(\lambda) = I_0(\lambda)\exp\{(-n_1\sigma_{13}(\lambda) - n_2\sigma_{24}(\lambda) - K_l(\lambda))l\}, \quad (2)$$

Fig. 2. Schematic of the setup for measuring ESA spectra of doped crystals. (*1*) DKSSh 500 arc lamp; (*2*) condenser lens; (*3*) orifice plate; (*4*) mechanical modulator; (*5*) objective with f = 500 mm; (*6*) orifice plate; (*7*) sample; (*8*) orifice plate limiting pumping light scattered in a sample; (*9*, *10*) prisms; (*11*) UM-1 monochromator; (*12*) ISP-30 spectrograph; (*13*) DFS-8 spectrograph; (*14*) camera; (*15*) liquid-nitrogen bath; (*16*) liquid-helium bath; (*17*) copper cold finger; (*18*) copper screen; (*19*) glass tube; (*20*) flash lamps; (*21*) quartz windows; (*22*) liquid-nitrogen trap; (*23*) filter amplifier; (*24*) unit for applying high voltage to the photomultiplier cathode; (*25*) synchronizer; (*26*) oscilloscope; and (*27*) mirror.

where $\sigma_{24}(\lambda)$ is the cross section of absorption from level 2 to upper excited states, n_1 is the population of level 1, and n_2 is the population of level 2. Obviously, in the course of pumping, a variation in the absorption coefficient of an unpumped sample $K_u = \dfrac{1}{l} \ln \dfrac{I_u(\lambda)}{I_0(\lambda)}$ can be written as

$$\Delta K(\lambda) = \frac{1}{l} \ln \frac{I_u(\lambda)}{I_0(\lambda)} = K_u(\lambda) - K_p(\lambda) \qquad (3)$$

or

$$\Delta K(\lambda) = n_2(\sigma_{24}(\lambda) - \sigma_{13}(\lambda)). \qquad (4)$$

Note that the loss factor does not enter (4), which is an undoubted advantage of ESA spectroscopy.

If the absorption bands due to the transitions from the ground and excited states do not overlap, it is not difficult to determine n_2 and $\sigma_{24}(\lambda)$. To do this, it is sufficient to measure ΔK at some wavelength so as to satisfy the conditions $\sigma_{13}(\lambda_0) \neq 0$, $\sigma_{24}(\lambda_0) = 0$ or $\sigma_{13}(\lambda_0) = 0$, $\sigma_{24}(\lambda_0) \neq 0$, and, thus, to derive n_2, $\sigma_{13}(\lambda)$, and $\sigma_{24}(\lambda)$. Nevertheless, in the most commonly encountered case, the absorption bands due to transitions from the ground and metastable states overlap in a wide spectral range. In this case, it follows from (4) that

$$\Delta K < 0 \quad (\sigma_{24} < \sigma_{13}),$$
$$\Delta K > 0 \quad (\sigma_{24} > \sigma_{13}), \qquad (5)$$
$$\Delta K = 0 \quad (\sigma_{24} = \sigma_{13}).$$

The first and second cases correspond to a decrease and increase in the absorption of a crystal, respectively; in the third case, the absorption remains the same.

Determination of $\sigma_{24}(\lambda)$ in the case of overlapping absorption bands due to the transitions from the ground and metastable states is a complex experimental problem. Indeed, formula (4) contains two unknowns to be found, $\sigma_{24}(\lambda)$ and n_2. Therefore, another equation is necessary, which would contain either n_2 or $\sigma_{24}(\lambda)$. Attempts to derive another equation from the same measurements of ΔK were unsuccessful [8, 10]. Grechushnikov and coworkers [11, 12] used the model of additive mixing of spectra of two absorbing solutions (under the assumption that the spectrum of one solution is known) to solve the problem of mixing the absorption spectra $\sigma_{13}(\lambda)$ and $\sigma_{24}(\lambda)$. It was proved rigorously that no analysis of the entire spectrum may yield simultaneously the absorption spectrum of the other solution and the relative amounts of the solutions. In other words, it was shown that one must have another equation derived from independent experiments to determine $\sigma_{24}(\lambda)$ and n_2. For ESA spectra, such an equation follows from the dependence of $\Delta K(\lambda)$ and n_2 in formula (4) on the pumping energy.

1.2. The problem of determining the population of an excited metastable level is the central problem of ESA spectroscopy [13]. Various methods of determining the population n_2 have been suggested. In [8–10, 14–17], the ruby crystal under investigation was placed in a high-Q cavity and the relative population n_2/n_0 was determined from the value of the lasing threshold. In [18–20], amplification of emission at the R_1 line by a ruby sample was used to determine the ratio n_2/n_0. Rubinov *et al.* [21, 22] determined the ratio n_2/n_0 from the dependence of the luminescence intensity on pumping. Moos [23, 24] suggested to use the region limited by the vibrational structure of the U band in the spectrum of ruby [25] to determine n_2/n_0. Finally, in [26, 27], light of a He–Ne laser with a wavelength of 6328 Å was passed through a ruby sample and the transmittance of the sample was measured with increasing pumping power. Each of the noted methods of

determining n_2/n_0 has certain drawbacks and limitations.[1] A common drawback of all these methods is that they are strictly related to ruby. In this context, the technique suggested in [26, 27] seems to be most promising. However, this technique is based on the assumption that, at infinitely high pumping, the population of the $^2E(t_2^3)$ level becomes equal to n_0 ($n_2 = n_0$). This assumption is valid only for an ideal three-level energy diagram and, naturally, does not hold true under real conditions. One of the reasons for this is in the escape of electrons from the $^2E(t_2^3)$ level through upper excited levels mainly to the ground state $^4A_2(t_2^3)$.

The question of escape of electrons from the $^2E(t_2^3)$ level, which is of fundamental importance, was studied in [8–10, 16, 17, 28]. It was shown experimentally in [16] that escape of electrons through the channel ^2E (upper excited states) $\longrightarrow$ $^4A_2$ may even exceed the value of $0.3n_2$ found in [8–10]. However, this result was revised in [28]: the escape was found to be close to zero. According to the data of [17], the escape is also zero. In [17], a technique based on the variation in the pumping spectrum was used. The sample was exposed to light with an ultraviolet (UV) component in the spectral range of 120–240 nm. Then, the UV radiation was cut off by placing a sample in a thick-walled glass tube. Since it is the UV range where the transitions $^2E(t_2^3) \longrightarrow [^2T_2(t_2^2, e), {}^2A_2(t_2^2, e), {}^2E(t_2^2, e)]$ with very large cross sections are observed, it is reasonable to expect a noticeable difference in the populations of the $^2E(t_2^3)$ level for the cases of pumping radiation either with or without a UV component.

Unfortunately, the requirement of the optical thinness of samples in the UV range (i.e., the condition $n_2\sigma_{24}l \ll 1$) was disregarded in these experiments. The point is that standard laser ruby rods ~0.5 cm in diameter and several centimeters long with a chromium concentration of ~10^{19} cm^{-3} were used as samples in [16, 17, 28]. Under conditions of giant absorption, especially in the charge-transfer (CT) band, which should mainly control the escape from a metastable level, the UV pumping radiation is absorbed in a thin (a few micrometers) surface layer of the sample. Thus, almost the total sample volume turns out to be screened by the thin surface layer. The probe beam propagates along the cylindrical axis of the sample, i.e., in the screened region. Therefore, the difference in the values of n_2/n_0 caused by a variation in the pumping-light spectrum can hardly be detected and the conclusion

---

[1] Detailed analysis of different methods of determining the population of metastable levels can be found in [1, 2, 29].

about zero escape derived from such experiments cannot be considered convincing.

The conditions for optical thinness of samples were satisfied a fortiori in [29], where the pumping-light parameters were varied: the pumping intensity ranged from zero to maximum possible values. The measurements were carried out with two types of samples: shaped as a parallelepiped $0.2 \times 0.5 \times 0.65$ cm^3 in size with a chromium concentration of ~10^{18} cm^{-3} and as a cylinder 0.5 cm in diameter and 5.0 cm long with a chromium concentration no higher than 10^{17} cm^{-3}. In the case of parallelepiped sample, the pumping was performed through its entire surface and the probe light was passed through the sample along the direction corresponding to its largest size (0.65 cm). In the case of cylindrical sample, the probe light was passed along its geometric axis, while the pumping was carried out through its lateral surface. In both cases, the pumping intensity at a wavelength of 240 nm in the bulk of a sample was close to the intensity at its surface and, therefore, the condition for optical thinness was satisfied. The dependence $\Delta K(\lambda_0, E_p)$ on the pumping energy E_p was measured (Fig. 3). In this experiment, the width of the pumping pulse was shorter than the characteristic time of luminescence ($\tau = 3$ ms); hence, the dependence of the population n_2 on pumping energy can be expressed by the exponential dependence in the form [26]

$$n_2 = n_0(1 - \exp(-dE_p)), \qquad (6)$$

where the coefficient d has the dimension of inverse energy. If we assume that $n_0 = n_1 + n_2$, exponential (6) has the asymptote $n_2^\infty = n_0$. According to formula (4) and with due regard for the fact that $\sigma_{24}(\lambda) - \sigma_{13}(\lambda_0) =$ const, the quantity ΔK is the pumping function $\Delta K(\lambda_0, E_p)$, which represents the dependence of the population $n_2(E_p)$ on pumping energy. For either of two sets of experimental points $\Delta K_1(\lambda_0, E_p)$ and $\Delta K_2(\lambda_0, E_p)$, which correspond to either presence or absence of an ultraviolet component in the pumping radiation, the least-squares method was applied to construct the function in the form (6). The asymptotic values $\Delta K_1^\infty(\lambda)$ and $\Delta K_2^\infty(\lambda)$ differ by less than 2%. The error of the asymptotic value for each curve $\Delta K(\lambda_0, E_p)$, which is determined by the total set of experimental points, is no larger than some tenths of a percent. Thus, it was shown in [29] that the escape of electrons from the $^2E(t_2^3)$ level to the ground state $^4A_2(t_2^3)$ through upper excited states is close to zero in ruby. This result suggests that $\Delta K(E_p)/\Delta K^\infty \simeq n_2/n_0$.

Equation (6) can be applied to find the asymptote $\Delta K(E_p)/\Delta K^\infty$ if the pumping-pulse width is much shorter than the characteristic time of spontaneous radiation $\tau_{21}(\Delta t \ll \tau_{21})$. The most complex situation is when
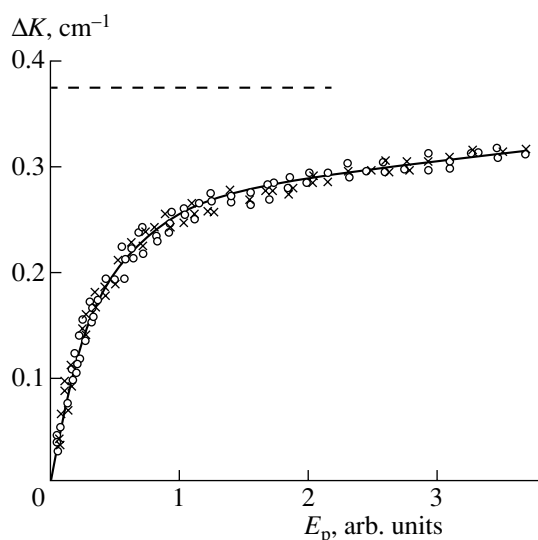
Fig. 3. Dependence of ΔK on pumping energy E_p. Solid line represents the solution to Eq. (7). Data for samples (·) in the glass tube and (×) in the quartz tube (transparent for ultraviolet light). Dashed line shows the asymptotic value of $\Delta K(\lambda)$ at infinitely high pumping level: $\Delta K^\infty(\lambda) = 0.37$ cm^{-1}.

$\Delta t = \tau_{21}$. In this case, the dependence n_2/n_0 on the pumping energy is not exponential. It is described by the solution to the equation [29]

$$\frac{dn_2}{dt} + n_2(A_{21} + (\alpha\beta + \gamma)B_{13}(\lambda)U(\lambda, t)) = n_0\gamma B_{13}(\lambda)U(\lambda, t). \quad (7)$$

Here, $\alpha = \dfrac{p_{41}}{(p_{41} + p_{42})}$; $\beta = \dfrac{\tilde{p}_{24}}{\tilde{p}_{13}}$; $\gamma = \dfrac{p_{32}}{p_{31} + p_{32}}$, and $A_{21} = 1/\tau_{21}$ is the probability of the spontaneous transition $2 \longrightarrow 1$; notably, $\tilde{p}_{13} = \dfrac{1}{\Delta\lambda}\int_{\lambda_1}^{\lambda_2} B_{13}(\lambda)\,U(\lambda, t)\,d\lambda$ and $\tilde{p}_{24} = \dfrac{1}{\Delta\lambda}\int_{\lambda_1}^{\lambda_2} B_{24}(\lambda)\,U(\lambda, t)\,d\lambda$. If $\Delta t \ll \tau_{21}$, the solution to Eq. (7) is the exponential in the form (6):

$$\frac{n_2}{n_0} = \frac{\gamma}{\alpha\beta + \gamma}\left(1 - \exp\left(-(\alpha\beta + \gamma)\int_0^{t_{max}} \tilde{p}_{13}(t)dt\right)\right). \quad (8)$$

If the pumping is continuous [22, 30], we have

$$\frac{n_2}{n_0} = \frac{\tilde{p}_{13}}{\tilde{p}_{13}(\alpha\beta + \gamma) + p_{21}}. \quad (9)$$

In intermediate cases, when $\Delta t \approx \tau_{21}$, the value of $\Delta K(E_p)/\Delta K^\infty = n_2/n_0$ is found by numerical integration of Eq. (7) and the time dependence of the pumping-pulse power is set numerically. The maximum population $(n_2/n_0)_{max}$ is attained when the instantaneous pumping power drops by an order of magnitude after passing through the maximum. This circumstance is convenient

for measurements since the fraction of pumping light scattered in a sample decreases.

Let us now consider how the accuracy in determining the population n_2 affects the ESA spectrum. According to formula (4),

$$\sigma_{24}(\lambda) = \sigma_{13}(\lambda) + \frac{\Delta K(\lambda)}{n_2}. \quad (10)$$

Obviously, at a small deviation δn_2 from the specified value of n_2, the error in determining $\sigma_{24}(\lambda)$ is expressed by the formula

$$|\delta\sigma_{24}(\lambda)| = |\Delta K(\lambda)/n_2^2\delta n_2|. \quad (11)$$

Upon changing n_2, the intensity varies and the spectrum shifts in the wavelength scale. As follows from formula (10), variation in the spectral intensity can be written as

$$\frac{\delta\sigma_{24}(\lambda)}{\delta\lambda} = \frac{\delta\sigma_{13}(\lambda)}{\delta\lambda} + \frac{1}{n_2}\frac{\delta}{\delta\lambda}[\Delta K(\lambda)]. \quad (12)$$

Thus, for each wavelength, $\delta\sigma_{24}(\lambda)/\delta\lambda$ is determined by the signs and magnitudes of $\delta\sigma_{13}(\lambda)/\delta\lambda$ and $\delta[\Delta K(\lambda)]/\delta\lambda$, as well as by the value of n_2. For example, at 453 nm, $[\delta\sigma_{13}(453$ nm$)/\delta\lambda] \sim 0$ [31] and $\delta[\Delta K(453$ nm$)/\delta\lambda] \sim 0$ for ruby. Therefore, at 453 nm, the peak in the ESA spectrum does not shift in the wavelength scale, but, with an increase in n_2/n_0, its intensity decreases. For the band at 382 nm, these conditions are not satisfied, and, with an increase in n_2/n_0, we observe not only a decrease in the band intensity $\sigma_{24}(\lambda)$ but also a shift of the band maximum to longer waves. For example, with an increase in the population n_2/n_0 by 10%, the intensity of the band at 453 nm decreases by more than 50%, but no shift of this band is observed. The intensity of the band at 382 nm decreases by about 12%, and the band shifts to longer waves by about 30 nm [1].

1.3. Ruby Al_2O_3: Cr^{3+}. Intensive studies of the ESA spectra of ruby began with the investigations of Gires and Mayer [8–10] in 1961. By the end of the 1960s, the number of publications devoted to this problem exceeded 30; i.e., ruby was investigated fairly well. Correspondingly, we consider ruby as a quite appropriate model material, in particular, for approbation of the method for determining the population n_2/n_0 developed by us [1, 2]. In this review, we do not present the detailed spectra of ruby (they are reported in [1, 2]). Some spectroscopic parameters of ruby are listed in Tables 1 and 2.

1.4. Magnesium spinel $MgAl_2O_4$: Cr^{3+} has red color and exhibits bright red luminescence at a wavelength of ~685 nm. Crystals of magnesium spinel have cubic symmetry. Its unit cell consist of eight formula units and belongs to the space group O_h^7-$Fd3m$ [32, 33]. Oxygen ions form an octahedron and two tetrahedra

Table 1. Crystal-field constants for ruby, yttrium–aluminum garnet, and magnesium spinel doped with Cr^{3+} ions

	Dq, cm^{-1}	B, cm^{-1}	C, cm^{-1}	v, cm^{-1}	v', cm^{-1}	Reference
Ruby	1800	650	3220	800	680	[46]
	1800	720	3030	756	378	[35]
	1800	740	2960			[100]
	1667	700	2800			[43]
Garnet	1725	640	3200	495	259	[57]
Spinel	1825	700	3200	−200	−1700	[33]

sharing vertices with it [34]. Aluminum (Al^{3+}) and magnesium (Mg^{2+}) ions are located in octahedra and tetrahedra, respectively. Chromium (Cr^{3+}) ions isomorphously substitute Al^{3+} ions in octahedra. The presence of tetrahedra reduces the point symmetry of the positions of Al^{3+} ions to D_{3d} [32, 33]. The symmetry group D_{3d} is isomorphic to the C_{3v} group, which is typical of the positions of Cr^{3+} ions in ruby. Hence, the entire spectrum of Cr^{3+} ions in spinel was calculated in [3, 35–38] in the approximation of the C_{3v} symmetry with the use of the energy matrix for the d^3 configuration in a trigonal field. The consideration of the second coordination shell of Cr^{3+} ions [39, 40] showed that the trigonal field in spinel may be stronger than in ruby. However, the calculation of the intensities of the U and Y absorption bands in the spinel spectra [39, 40] yielded the ratio $I(U) : I(Y) = 1 : 4$, which, as can be seen from Fig. 4, disagrees with the experiment.

The spectral properties of spinels were studied experimentally in [41–46]. Two broad absorption bands were observed in the GSA spectrum of $MgAl_2O_4 : Cr^{3+}$ spinel: the U band (18350 cm^{-1}) and the double Y band (23200 and 25200 cm^{-1}). These bands are attributed to the $^4A_2 \longrightarrow {}^4T_2$ and $^4A_2 \longrightarrow {}^4T_1$ transitions. The metastable luminescence level $^2E(t_2^3)$ is located at 14660 cm^{-1}. Its decay time is 13 and 24 ms at room temperature and at 77 K, respectively [41, 42]. When the chromium content in spinel ranges from 0.3 to 0.5%, there arises an additional luminescence transition with the characteristic time $\tau_N = 5$ ms at room temperature and 8 ms at 77 K. This transition occurs from the level lying below the ^2E level by 80 cm^{-1}. It is referred to as the N-line level. It was suggested in [33] that this level is due to the exchange interaction between Cr^{3+} ions. At the same time, we may also attribute the appearance of this level to distortion of octahedra where Cr^{3+} ions are located, which is caused by local nonstoichiometry of spinel [44]. Such a nonstoichiometry is possible since the magnesium spinel crystals we studied were grown by the Verneuil method. As is well known, this technique may yield significant stresses

and nonstoichiometric regions in grown crystals [44, 45].

The first investigation of the ESA spectra of magnesium spinel ($MgAl_2O_4 : Cr^{3+}$) crystals was performed in [41, 42]. The ESA spectrum of magnesium spinel (see Fig. 4) consists of five broad intense bands: $(U_1 + U_2)$ (32900 cm^{-1}), Y_1^a (37500 cm^{-1}), Y_1^b (40300 cm^{-1}), Y_2 (45500 cm^{-1}), and UV (54700 cm^{-1}) (the last is the strongest). The solid line in Fig. 4 represents the experimentally observed spectrum, and the dotted lines show the expansion of the spectrum in Gaussian components. The calculated terms, with which the electronic transitions responsible for the absorption bands are identified, are also shown in Fig. 4. The parameters of the crystal field in spinel are listed in Table 1. It can be seen that spinel and ruby have similar values of the cubic-field strength Dq and the parameters of electrostatic interaction B and C. Therefore, the positions of all the identical terms in the spectra of these materials are close to each other. The splitting of the $^4T_2$ term is mainly determined by the parameter v, which is four times smaller for spinel than for ruby. Hence, the splitting of the $^4T_2(t_2^2, e)$ term is only 20 cm^{-1}, and the shape of the U band is nearly homogeneous. The smallness of the parameter v accounts for the fact that the absorption cross sections for the absorption bands in the spinel spectrum are smaller than those for the absorption bands in the ruby spectrum by approximately a factor of ten. The parameter v for spinel is negative; therefore, in comparison with ruby, the components E and A of the terms shift in opposite directions in a trigonal field. The parameter v' for spinel is larger than that for ruby by a factor of 2.5. Hence, the splitting of the terms $^4T_1(t_2^2, e)$ and $^2T_1(t_2^2, e)$ for spinel is equal to 2100 and 850 cm^{-1} in magnitude, respectively. At the same time, the corresponding values for ruby are 1200 and 200 cm^{-1}, respectively. The absorption bands were identified in [46]. The ultraviolet UV band at 54700 cm^{-1} in the spectrum of spinel (Fig. 4) is 70–80 times stronger than the other absorption bands. It is suggested that the term $^2E(t_2^2, e)$, which is responsible for this band, lies in the

Table 2. Calculated and experimental energies of the terms of the $Cr^{3+}(3d^3)$ ion in ruby, magnesium spinel, and yttrium–aluminum garnet (E, cm^{-1}) [46, 57]

Term		Ruby theory	Ruby experiment	Spinel theory	Spinel experiment		Garnet theory	Garnet experiment
$(t_2^3)^4A_2$		0	0	0	0		0	0
$(t_2^3)^2E$		13900	14400 R_1 / 14429 R_2	14700	14653.5 R_1 / 14660.0 R_2		14200	14516 R_1 / 14536 R_2
$(t_2^3 {}^2T_1)^4A_2$	$^2A_2$	14650	14939 R'_3	15800	15069 R'_3		16140	15162
	^2E	15050	15150 R'_2 / 15172 R'_1	15400	14812 R'_2 / 14790 R'_1		15100	15213 / 15420
$t_2^2({}^3T_1), e: {}^4T_2$	^4E	17850	18000 $U^\perp$	18450	18350 U		17250	16700 U
	$^4A_1$	18300	18400 $U^\parallel$	18430			17450	
$(t_2^3 {}^2T_2)$	^2E	21500	20993 B_1 / 21068 B_2	22850	22100 B^*		21600	
	$^2A_1$	21900	21357 B_3	21415			21850	
$t_2^2({}^3T_1), e: {}^4T_2$	^4E	24300	24400 $Y^\perp$	26200	25200 } Y		23600	23200 Y
	$^4A_2$	25500	25500 $Y^\parallel$	24100	23200		24100	
$t_2^2({}^1E), e: {}^2A_1$		29950		30850			29400	
$t_2^2({}^3T_1), e: {}^2T_2$	^2E	31850	30100 [15700] $U_1^\parallel$	32900			31400	
	$^2A_1$	32100	30000 [15600] $U_1^\perp$	33300	32900 [18200] U_1+U_2		31500	31200 [16700] U_1+U_2
$t_2^2({}^1T_2), e: {}^2T_1$	^2E	32350	32500 [18100] $U_2^\parallel$	33600			31700	
	$^2A_2$	32500	32800 [18400] $U_2^\perp$	33200			31900	
$t_2^2({}^1E), e: {}^2E$		34200		35250			33500	
$t_2^2({}^2T_2), e: {}^2T_1$	$^2A_2$	37200	36700 [22300] $Y_1^\perp$	37850	37500 [22800] Y_1^a		36400	37800 [23300] Y_1
	^2E	37400	36400 [22000] $Y_1^\parallel$	38700	40300 [25600] Y_1^b		36500	
$t_2, e^2({}^3A_2), {}^4T_1$	^4E	39150	39200 $V^\perp$	39700	38500 V		37600	36300 V
	$^4A_2$	39200	39000 $V^\parallel$	41700			37900	
$t_2^2({}^1T_2), e: {}^2T_2$	$^2A_1$	41600	40700 [26300] $Y_2^\perp$	43700	45500 [30800] Y_2		40850	43100 [28600] Y_2
	^2E	41700	40800 [26400] $Y_2^\parallel$	42900			40800	
$t_2^2({}^1E), e: {}^2A_2$		43100	42100 [27700] $Y_3^\perp$	44750			42200	
$t_2, e^2({}^3A_2), {}^2T_1$	^2E	49800		50700			48700	
	$^2A_2$	50300		51900			48800	
$t_2, e^2({}^1E), {}^2T_2$	^2E	51500		53500			50200	
	$^2A_2$	51600		52700			50300	
$t_2^2({}^1A_1), e: {}^2E$		52000	55400 [41000] UV	53900	54700 [40000] UV		51000	55000 [40500] UV
$t_2, e^2({}^1E), {}^2T_1$	$^2A_2$	56300		58600			54900	
	^2E	56500		59300			55000	
$t_2, e^2({}^1A_1), {}^2T_2$	^2E	70700		72700			69300	
	$^2A_1$	70800		74200			69500	
$^2E(e^3 {}^2E)$		74400		77100			72700	

Note: The values in square brackets are the experimentally found positions of the excitation bands of ruby, spinel, and garnet, counted from the $^2E(t_2^3)$ level.

 * According to [45].

Fig. 4. Spectra of absorption from the ground ($^4A_2$) and metastable (^2E) states of Cr^{3+} ions in magnesium spinel $MgAl_2O_4 : Cr^{3+}$. The lower scales show the energies of transitions from the ground ($^4A_2$) and metastable (^2E) states. The calculated positions of the terms are indicated in the upper part.

CT band, due to which the $^2E(t_2^3, e) \longrightarrow {}^2E(t_2^2, e)$ transition becomes allowed. This fact accounts for the high intensity of the *UV* band. With a decrease in temperature, the behavior of the *UV* band drastically differs from the behavior of the other bands. When the temperature decreases from room to liquid-nitrogen, the *UV* band becomes narrower and its intensity decreases so that the oscillator strength decreases by more than a factor of two [1, 46].

In fact, the entire ESA spectrum of spinel $MgAl_2O_4 : Cr^{3+}$ is a superposition of two spectra due to the transitions from the $^2E(t_2^3)$ level with the characteristic lifetime 13 ms and from the *N* level, which is located below the ^2E level by 80 cm^{-1} and has a characteristic lifetime of 5 ms. All the bands, except for the *UV* band, are completely overlapped; therefore, the spectrum kinetics is controlled by the longest lifetime, specifically, 13 ms. If the absorption kinetics is measured at the edges of the *UV* band, τ = 13 and 5 ms at 230 and 280 nm, respectively. Oscillograms of these processes serve as good evidence [41, 42]. Finally, speaking of the possibility of lasing in $MgAl_2O_4 : Cr^{3+}$ spinel, our experiments do not suggest it. First, the possible lasing wavelength 682 nm (14660 cm^{-1}) is overlapped by long-wavelength wings of the *U* and (U_1 + U_2) bands. Second, the absorption and amplification cross sections of spinel are smaller by an order of magnitude than those of ruby. Therefore, both the pumping of the ^2E level and the amplification turn out to be insufficient to obtain lasing. The parameters of the crystal field and the positions of the terms in the energy-band diagram of magnesium spinel $MgAl_2O_4 : Cr^{3+}$ are listed in Tables 1 and 2.

1.5. Yttrium–aluminum garnet $Y_3Al_5O_{12} : Cr^{3+}$ became the second (after ruby) Cr^{3+}-doped material in which lasing was obtained [47, 48]. This material has green color and exhibits bright red luminescence in the vicinity of ~690 nm. Garnet has cubic symmetry and belongs to the space group O_h^{10}–$Ia3d$. In the garnet structure, Al^{3+} ions, which occupy octahedral and tetrahedral positions, are in oxygen environment. The symmetry of the environment of Cr^{3+} ions is not strictly cubic; it is characterized by weak trigonal distortion, which reduces the symmetry to C_{3i} [49–51]. The absorption and luminescence spectra of Cr-doped garnets were studied in [52–56].

Table 3. Transition frequencies, transverse cross sections, and half-widths of lines and bands in the spectra of $Y_3Al_5O_{12} : Cr^{3+}$ crystals at 300 and 77 K

Band	Transition $^4A_2 \longrightarrow$	Transition frequency ν, cm^{-1}		Absorption cross section σ, 10^{-21} cm^2		Half-width of absorption line $\Delta\nu$, cm^{-1}		Factor μ, cm^{-1}
		300 K	77 K	300 K	77 K	300 K	77 K	300 K
Y	$^4T_1$	23050	23200	37	30	3550	3070	19.4
U	$^4T_2$	16610	16780	19.6	15.4	2290	1850	10.3
R_1	$2A(^2E)$	14520	14549	1.2	9.2	14	1.3	0.64
R_2	$\bar{E}\,(^2E)$	14540	14569	0.94	8.4	12	1.2	0.56

We were the first to investigate the ESA [57, 58] and GSA [59] spectra of $Y_3Al_5O_{12} : Cr^{3+}$ crystals. The complete energy-level diagram of the Cr^{3+} ion in $Y_3Al_5O_{12} : Cr^{3+}$ was calculated in [57] in terms of strong cubic field of the C_{3v} symmetry expanded in the energy matrices of the $3d^3$ configuration with the use of the crystal-field parameters listed in Table 1. As one should expect for Cr^{3+} ions in the octahedron environment, their absorption spectrum due to the transitions from the ground state $^4A_2(t_2^3)$ in $Y_3Al_5O_{12} : Cr^{3+}$ contains two broad bands (U and Y) and three narrow lines (R_1, R_2, and B).

The complete characteristic of the absorption bands and lines in the spectra of $Y_3Al_5O_{12} : Cr^{3+}$ at room and liquid-nitrogen temperatures is given in Table 3. At room temperature, B and R lines overlap with the long-wavelength edges of the Y and U bands. Hence, it is quite a problem to find the positions of these lines. With a decrease in temperature to 77 K, the vibrational structure at long-wavelength edges of the broad bands U and U_1 freezes out, due to which these bands become narrower and shift to longer waves. At room temperature, the absorption cross section for the long-wavelength edge of the U band at the R_1 line is σ_{GSA} (300 K) = 0.5 × 10^{-21} cm^2. The absorption cross section for the long-wavelength edge of the U_1 band in the ESA spectrum at the same wavelength (the R_1 line) is σ_{ESA} (300 K) = 1.78 × 10^{-21} cm^2. At liquid-nitrogen temperatures, σ_{GSA}(77 K) ~ 0 and σ_{ESA} (77 K) = 0.33 × 10^{-21} cm^2. The luminescence of $Y_3Al_5O_{12} : Cr^{3+}$ occurs at the wavelength of the R_1 line (687.4 nm). The luminescence-decay time constant τ_{R_1} = 1.5 ± 0.1 ms at 300 K. At 77 K, this parameter increases to 9.0 ± 0.57 ms [57]. These values are close to those reported in [53, 56].

The value of the lasing threshold can be expressed by the formula [58]

$$\frac{n_2}{n_0} = \frac{1}{2} \times \frac{1}{1 + (\sigma_{13}/2\sigma_{12}) - (\sigma_{24}/2\sigma_{12})} \quad (13)$$
$$\times (1 + (\sigma_{13}/\sigma_{12}) + (\sigma_{24}/\sigma_{12})).$$

Here, σ_{12} is the cross section of amplification at the R_1 line and σ_{13} and σ_{24} are the cross sections of absorption at the R_1 line for the 1–3 and 2–4 transitions, respectively. Using the above values of absorption cross sections σ_{ESA} and σ_{GSA}, we find that the threshold value $(n_2/n_0)_{thd} > 1$ at room temperature. Hence, lasing is impossible. At 77 K, $(n_2/n_0)_{thd} = 0.51$, and lasing is quite possible. Thus, at temperatures about 100 K and below, one might expect lasing at the wavelength of the R_1 line (687.4 nm). Indeed, lasing under these conditions was obtained in [47, 48].

Yttrium–aluminum garnet (YAG) doped with Cr^{3+} ions became the second (after ruby) crystal in which we obtained lasing in 1972. It is worth noting that lasing was first predicted on the basis of the ESA-spectroscopy measurements and then obtained purposefully. This fact is significant evidence of the importance of ESA spectroscopy in predicting new laser materials.

In view of the fact that lasing had been obtained in $Y_3Al_5O_{12} : Cr^{3+}$ crystals, the dependences of the GSA and luminescence spectra of garnet crystals on chromium concentration were studied in detail [59]. It was shown that the intensities of the absorption bands Y_1 and U_1 and the R_1 and R_2 lines increase linearly with increasing chromium concentration. The dependence of the absorption coefficient K for the absorption bands and lines on the chromium concentration C (in wt %) in garnet is described well by the linear function $K = \mu C$ (Table 3).

An interesting observation was made by Pasternak [59]: when $Y_3Al_5O_{12} : Cr^{3+}$ crystals are grown by the Stockbarger method, simultaneously with the motion of the molten zone, a new phase enriched with chromium arises to move. In the luminescence spectrum of a garnet containing this phase, R_1 and R_2 lines of ruby can be clearly seen. The X-ray phase analysis corroborated the suggestion that the new phase represents ruby. It is noteworthy that, when $Y_3Al_5O_{12} : Nd^{3+}$ crystals are grown, the melt is enriched with yttrium oxide [60]. However, the situation changes when chromium oxide (Cr_2O_3) is present in the garnet melt. Cr^{3+} ions isomorphously substitute Al^{3+} ions [59, 60], and this process

leads to an excess of aluminum in the melt. As a result, Al_2O_3 phase is formed.

It is of great interest to investigate the color centers appearing in YAG : Cr^{3+} crystals during their growth, as well as the color centers appearing due to the effect of optical pumping on $Y_3Al_5O_{12}$: Cr^{3+} crystals. Special studies [61–63] were devoted to these aspects. However, since the interpretation of the results obtained is very complex, we cannot even outline them here. Therefore, we refer those who are interested in these data to [61–63]. Tables 1–3 contain the spectroscopic parameters of $Y_3Al_5O_{12}$: Cr^{3+}.

1.6. Alexandrite (BeAl$_2$O$_4$) has played a decisive role in the development of crystal lasers. It became the first crystal in which lasing at the R_1 line [64, 65] and tunable lasing in range from 700 to 815 nm at room temperature [66] were obtained.

Alexandrite has orthorhombic symmetry, which is characterized by the space group D_{2h}^{16}-P_{nma} [34]. Farrel *et al.* [67] studied the crystal structure of alexandrite and determined the unit-cell parameters: $a = 9.404$ Å, $b = 5.476$ Å, and $c = 4.427$ Å. Later [68], the atomic structure of alexandrite was refined by X-ray analysis with the use of an RÉD-4 automatic four-circle diffractometer developed at the Institute of Crystallography, RAS [69]. The following values of the unit-cell parameters were obtained: $a = 9.407(4)$ Å, $b = 5.4781(5)$ Å, and $c = 4.4285(3)$ Å. The geometric parameters of octahedra with mirror and inversion symmetry, refined in [68], confirm the conclusions drawn in [70, 71]: Cr^{3+} ions incorporate into octahedra with mirror symmetry with higher probability than into octahedra with inversion symmetry. Note that the ionic radius of the Cr^{3+} ion (0.65 Å) exceeds that of the Al^{3+} ion (0.57 Å) (the Goldschmidt ionic radii [70]). The Cr^{3+} ions incorporated into mirror- and inversion-symmetric octahedra are denoted as Cr_s^{3+} and Cr_i^{3+}, respectively.

It is Cr_s^{3+} ions that are responsible for lasing since they are characterized by high-probability electric dipole transitions. The magnetic dipole transitions in Cr_i^{3+} ions do not contribute significantly to the optical absorption and luminescence spectra. They are not only excluded from the lasing process but even serve as "sinks" for the excitation energy of Cr_s^{3+} ions. Therefore, the ratio of the concentrations of Cr_s^{3+} and Cr_i^{3+} ions is of importance. In natural deposits of chrysoberyl, the ratio of the Cr_s^{3+} concentration to the Cr_i^{3+} concentration ranges from 80 : 20 to 57 : 43 [72]. Forbes [70] found the concentration of Cr_s^{3+} ions in the samples of alexandrite studied by Walling *et al.* [66] to be 78 ± 3%. Vazhenin [73] used the fact that the linear pseudo-Stark effect is allowed for inversionless para-

magnetic centers. In the cavity of an ESR spectrometer, an electric field as strong as 300 kV/cm was applied to an alexandrite sample. Such a field did not lead to any changes in the ESR spectra of four magnetic nonequivalent centers, which are related to the Cr_i^{3+} positions. ESR signals from the two other centers either split into two components of equal intensities or broadened at all orientations of the electric and magnetic fields. According to the measurements [73], the concentration of Cr_s^{3+} ions in Czochralski grown samples studied by us [74] is 81 ± 2.5%, which is in good agreement with the results of [70]. The absorption and luminescence spectra of natural minerals (in particular, alexandrite) were investigated in [75]. Grown alexandrite crystals were studied by GSA spectroscopy in [64, 66]. The absorption spectra, which are typical of the Cr^{3+} ion in the octahedral environment [3, 4], consist of two broad bands U and Y peaked at 18182–16667 cm^{-1} (550–600 nm) and 23697 cm^{-1} (422 nm), respectively; two narrow lines R_1 and R_2 at 14700 cm^{-1} (680.27 nm) and 14739 cm^{-1} (678.46 nm), respectively; and three lines B_1, B_2, and B_3 at 21224.1 cm^{-1} (471.2 nm), 21367.5 cm^{-1} (468.0 nm), and 21413.3 cm^{-1} (467 nm), respectively [76, 77]. At 77 K, the intensities of the R_1 and R_2 lines are higher by more than a factor of five; notably, these lines shift to shorter waves by 8 Å [76, 77]. A distinct vibrational structure can be seen at the long-wavelength edge of the U band.

In the case of light polarization **E** ∥ b, a strong narrow line at 15540 cm^{-1} (643.5 nm) arises in the absorption spectrum at temperatures of 230–240 K and lower [76–78]. This line, being observed in the excitation spectrum of the R_1 line as distinctly as in the absorption spectrum, is absent in the luminescence spectrum. The integrated intensity of this line in the absorption spectrum decreases with increasing temperature, and, at room temperature, this line vanishes. We attributed this line to the zero-phonon electronic transition $^4A_2(t_2^3) \longrightarrow {}^4T_2(t_2^2, e)$ [76–78]. Indeed, the spectral position of the zero-phonon line corresponding to the $^4A_2 \longrightarrow {}^4T_2$ transition can be determined as a sum of the position of the averaged R line, i.e., $\bar{\nu}(R) = \dfrac{\nu_{R_1} - \nu_{R_2}}{2} =$ 14686 cm^{-1}, and the energy gap Δ between the $^2E(t_2^3)$ and $^4T_2(t_2^2, e)$ states. On the basis of the measurements of the temperature dependence of luminescence, the value of Δ was found to be 800 cm^{-1} [66]. Thus, the line due to the zero-phonon transition to the $^4T_2$ state is located at 15486 cm^{-1} (645.7 nm), which is in good agreement with the corresponding experimental value (15540 cm^{-1} (643.5 nm)). There is some other, more profound, evidence which corroborates the interpretation of this line as caused by the zero-phonon electronic

transition $^4A_2 \longrightarrow {}^4T_2$ [78]. A narrow line at 643.4 nm observed later was also attributed to the zero-phonon electronic transition $^4A_2 \longrightarrow {}^4T_2$ [79].

The ESA spectra of alexandrite were studied in [76–78, 80–82]. The most complete investigation was performed in [83]. Figure 5 shows the absorption spectra due to the transitions from the ground ($^4A_2$) and metastable (^2E) states of the Cr^{3+} ion for three polarizations of light. Calculated terms are also shown. The dotted line represents the expansion of the absorption bands of alexandrite in Gaussian components. The ESA spectrum of alexandrite affects its lasing characteristics. Thus, the luminescence spectrum of alexandrite, which ranges from 0.6 to about 1 μm, overlaps in the short-wavelength region (starting with 710 nm) with the induced-absorption band due to the $^2E(t_2^3) \longrightarrow {}^2T_1(t_2^2, e)$ transition. The well-known wavelength dependence of the lasing threshold of alexandrite [76–78] has a distinct peak at 715 nm. It is reasonable to attribute this peak to absorption via the $^2E(t_2^3) \longrightarrow {}^2A_1(t_2^2, e)$ channel (see Table 4). Alexandrite, as well as other chromium-doped crystals, exhibits a strong absorption band in the UV part of the ESA spectrum (at 56500 cm^{-1}). The intensity of this band exceeds the intensities of all other absorption bands in the alexandrite spectra by a factor of 30–40. As in the cases of ruby, spinel, and garnet, this absorption band may be attributed to the $^2E \longrightarrow {}^2\Gamma$ transition, where $^2\Gamma$ is the level at 56500 cm^{-1} in the CT band.

The ESA spectrum of alexandrite differs from the spectra of other chromium-containing crystals. Specifically, the $^4T_2(t_2^2, e)$ state in the energy-band structure of alexandrite is significantly populated, and the transition $^4T_2(t_2^2, e) \longrightarrow \Gamma$ (the CT band) is possible in principle. Therefore, the band at 40400 cm^{-1}, which manifests itself in the case of light polarization **E** ∥ b and is attributed to the $^4A_2 \longrightarrow b^4T_1$ transition in Fig. 5, may be even more likely due to the $^4T_2(t_2^2, {}^3T_1, e) \longrightarrow$ CT band transition. This problem could be solved using low-temperature measurements.

Farrel and Fang were the first to suggest a fundamental possibility of obtaining lasing in alexandrite crystals in 1964 [84]; however, they failed to obtain it in practice.

Lasing in alexandrite was first reported by Bukin *et al.* in 1978 [64]. These researchers observed lasing at the R_1 line in an alexandrite sample 6.4(a) × 0.46(b) × 0.3(c) cm^3 in size (a, b, and c signify the crystallographic axes) at liquid-nitrogen temperature without a dispersive element in a cavity. In addition, along with the luminescence at the R_1 and R_2 lines, strong broadband luminescence due to the $^2E \longrightarrow {}^4T_2 \longrightarrow {}^4A_2$ transition was observed in [64]. Unfortunately, as can be seen from the above parameters, the sample was incor-

rectly oriented. However, lasing at the R_1 line was observed at liquid-nitrogen temperature. At the same time, Bukin *et al.* could continue their experiments aimed at obtaining lasing at the $^2E \longrightarrow {}^4T_2 \longrightarrow {}^4A_2$ transition only after appropriate crystals were grown. The results of spectroscopic and lasing investigations of these crystals were reported in [76–78].

In 1980, Walling *et al.* [66] reported on tunable lasing at the $^2E \longrightarrow {}^4T_2 \longrightarrow {}^4A_2$ transition. At the same time as Walling's publication, we became aware of US patent 3 997 853 by Morris *et al.* [65], in which the lasing at the R_1 line in alexandrite at room temperature obtained in a cavity without a selective element was described. A cylindrical sample of alexandrite 0.5 cm in diameter and 5.8 cm long oriented along the crystallographic c axis was used in [65]. The concentration of Cr^{3+} ions was 0.03 at. %. As was noted in [65], lasing at the R_1 line (6804 Å) was observed in this sample in a cavity without a dispersive element at room temperature.

We should note that our attempts to obtain lasing at the R_1 line in alexandrite at room temperature in a cavity without a selective element were unsuccessful [76, 77, 85]. In these experiments, cylindrical samples 0.5–0.6 cm in diameter and ~7 cm long oriented along the c axis, with a chromium concentration of 0.03–0.09 wt %, were investigated. Spectrophotographs of broadband lasing in alexandrite at various temperatures (from 70 to 180°C) and pumping levels were reported in [85]. In a nonselective cavity, lasing may arise simultaneously in several spectral regions; notably, the emission bands do not shift with increasing the pumping power and only their intensity increases. The R_1 line is absent in the lasing spectrum in the case of nonselective cavity at room temperature.[2] With an increase in temperature from 70 to 180°C, the lasing spectrum shifts to longer waves.

To finish the brief description of the spectral and lasing properties of alexandrite, we should note the following. Alexandrite contains beryllium and, thus, is toxic during its growth and treatment. Presently, it is replaced by other crystals, for example, $Al_2O_3 : Ti^{3+}$. Nevertheless, alexandrite is a unique material, combining most interesting optical, spectroscopic, magnetic, and lasing properties. It is believed that alexandrite will open many new possibilities for setting up interesting experiments.

1.7. Lithium germanate $Li_2Ge_7O_{12} : Cr^{3+}$ has attracted considerable interest due to its very intense luminescence in a wide spectral range (from 650 to 800 nm). With regard to the high toxicity of alexandrite, it would be tempting to replace it with some other

---

[2] The reference in [85] to [77], where lasing at the R line was seemingly obtained in alexandrite at room temperature without using a selective element in a cavity, is incorrect. The lasing at the R line in alexandrite at room temperature could be obtained in [77] only with a selective element in a cavity.

material. At first glance, $Li_2Ge_7O_{12}$: Cr^{3+} seems to be such a material. Hence, chromium-doped lithium germanate has been a subject of study since the 1960s [86–88]. Crystalline lithium germanate undergoes the ferroelectric phase transition $D_{2h} \longrightarrow C_{2v}$ at 10°C.

$Li_2Ge_7O_{12}$: Cr^{3+} crystals are characterized by a strong cubic field. Cr^{3+} ions occupy positions in the field of octahedral symmetry. The absorption spectrum of $Li_2Ge_7O_{12}$: Cr^{3+} contains two broad bands caused by the absorption from the ground state: the U band at 600 nm (16 700 cm^{-1}) due to the $^4A_2(t_2^3) \longrightarrow {}^4T_2(t_2^2, e)$ transition and the Y band at 420 nm (23 810 cm^{-1}) due to the $^4A_2(t_2^3) \longrightarrow {}^4T_2(t_2^2, e)$ and $^4A_2(t_2^3) \longrightarrow {}^4T_1(t_2^2, e)$ transitions (Fig. 6). There are also two narrow lines: the R_1 line at 696.4 nm (14 360 cm^{-1}) and the R_2 line at 693.3 nm (14 423 cm^{-1}) due to the electronic transitions $^4A_2 \longrightarrow {}^2E(\bar{E}, 2\bar{A})$. The fundamental-absorption edge of pure $Li_2Ge_7O_{12}$: Cr^{3+} is located at 250 nm (40 000 cm^{-1}). If $Li_2Ge_7O_{12}$ is doped with Cr^{3+} ions, a strong absorption band arises in the GSA spectrum, which begins at 350 nm (28 570 cm^{-1}) and overlaps with the fundamental-absorption band in the short-wavelength region.

The dependence $\Delta K(\lambda)$ for $Li_2Ge_7O_{12}$: Cr^{3+} differs from the corresponding dependences for other crystals considered above. This dependence is observed against a strong background, which increases with decreasing wavelength. The background noted can in no way be attributed to passive nonresonant losses (see formula (4) and the note to it); its nature has not been ultimately established. A possible explanation is that the CT band is observed in a broad energy interval; specifically, this band extends, decaying, to 30 000 cm^{-1}. The spectrum $\Delta K(\lambda)$ is superposed on this background. Three maxima at 615, 480, and 390 nm and two minima at 550 and 430 nm of the function $\Delta K(\lambda)$ can be seen in the exponential falloff of the curve in Fig. 6. The ESA spectrum derived from formula (4) consists of three bands: U_1 (600 nm (32 090 cm^{-1})), Y_1 (480 nm (35 230 cm^{-1})), and Y_2 (410 nm (38 780 cm^{-1})). These bands are due to the transitions from the ^2E level to the $b^2T_2(t_2^2, e)$; $c^2T_1(t_2^2, e)$, and $c^2T_2(t_2^2, e)$ states, respectively.

In view of the observed background, the results of [87], where two-step photoionization of $Li_2Ge_7O_{12}$: Cr^{3+} crystals was realized, are of interest. A sample was irradiated simultaneously by a He–Ne and Ar laser. In this case, two-step photoionization occurred as follows: $^4A_2 \longrightarrow {}^2E \longrightarrow$ CT band. Electrodes were deposited on the sample in such a way as to record the photocurrent, which depended quadratically on the input-radiation power ($I \propto P^2$). Such a dependence corroborates the two-photon mechanism of photoionization. Powell [86] attempted to obtain lasing in $Li_2Ge_7O_{12}$: Cr^{3+} crystals but failed. Having studied the ESA spectrum, we con-
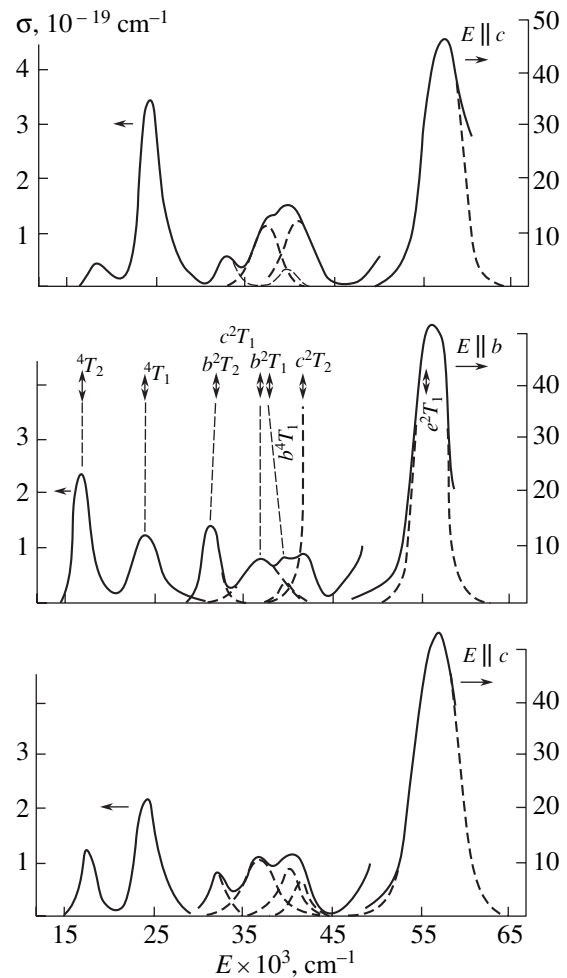

Fig. 5. Spectra of absorption from the ground ($^4A_2$) and metastable (^2E) states for Cr^{3+} ions in alexandrite $BeAl_2O_4$: Cr^{3+}.

cluded that, under the conditions of such an intense background caused by the induced absorption (which overlaps the entire spectrum), lasing in $Li_2Ge_7O_{12}$: Cr^{3+} crystals is hardly possible.

1.8. Sapphire–titanium (S–T) Al_2O_3 : Ti^{3+}. The detection of lasing in Al_2O_3 : Ti^{3+} crystals was an outstanding discovery made by Moulton [89]. Indeed, Al_2O_3 : Ti^{3+} is a unique material which combines high hardness, high thermal conductivity, wide-range transmittance, and so on. The Ti^{3+} ion only has the term ^2D, which is split by the crystal field into the components ^2E_g and $^2T_{2g}$, and no other terms, which could cause induced absorption. The only transition from the excited state ^2E_g is the transition to the CT band. Finally, the frequency of lasing in S–T crystals can be tuned in an unprecedently wide range: from 650 to 1200 nm. Naturally, such a favorable combination of properties of Al_2O_3 : Ti^{3+} crystals could not be left aside by researchers.

Table 4. Calculated and experimental energies of the terms of the $Cr^{3+}(3d^3)$ ion in alexandrite (E, cm^{-1})

Term	Calculation (E, cm^{-1})	Experiment (E, cm^{-1})
$^2E(t_2^3)$	14662	14701
		14747
$^2T_1(t_2^3)$	15291	15264
	15394	15405
	15448	15503
$^4T_2(t_2^2\ {}^3T_1, e)$	16888	16900 $\mathbf{E} \parallel b$
	17279	17500 $\mathbf{E} \parallel a$
	17617	17700 $\mathbf{E} \parallel a$
$^2T_2(t_2^3)$	21288	21184
	21347	21368
	21720	21692
$^4T_1(t_2^2\ {}^3T_1, e)$	23954	23900 $\mathbf{E} \parallel b$
	23984	23900 $\mathbf{E} \parallel a$
	24201	24100 $\mathbf{E} \parallel c$
$^2A_1(t_2^2\ {}^1E, e)$	29642	28700
$^2T_2(t_2^2\ T_1, e)$	32053	31400 $\mathbf{E} \parallel b$
	32130	
$^2T_1(t_2^2\ {}^1T_2, e)$	32672	32400 $\mathbf{E} \parallel c$
	31457	
	32212	32600 $\mathbf{E} \parallel a$
	32926	
$^2E(t_2^2\ {}^1E, e)$	33803	
	34088	
$^2T_1(t_2^2\ {}^3T_1, e)$	36967	37000 $\mathbf{E} \parallel c$
	37128	37000 $\mathbf{E} \parallel b$
	37342	37400 $\mathbf{E} \parallel a$
$^4T_1(t_2, e^2, {}^3A_2)$	36800	37500 $\mathbf{E} \parallel c$
	38310	38000 $\mathbf{E} \parallel a$
	38490	38000 $\mathbf{E} \parallel b$
$^4T_2(t_2^2\ {}^3T_1, e) \longrightarrow$ band		40400 $\mathbf{E} \parallel b$
$^2T_2(t_2^2\ {}^1T_2, e)$	42025	39700 $\mathbf{E} \parallel b$
	41745	39700 $\mathbf{E} \parallel a$
	42025	42100 $\mathbf{E} \parallel c$
$^2A_2(t_2\ {}^1E, e)$	43458	

Note: $Dq = 1726$, $B = 717$, $C = 2997$, $v = -1000$, $v' = 510$, $y = 47$, $z = 119$, $\alpha = 70$, $\beta = -328$ cm^{-1}.

After Moulton's report (December 1982), investigations of $Al_2O_3 : Ti^{3+}$ crystals began at the Institute of Crystallography, RAS. The results of these studies, specifically, the attainment of tunable lasing in the range of 720–780 nm in $Al_2O_3 : Ti^{3+}$ crystals grown by the Verneuil method, by horizontal directed crystallization, and by the Czochralski method, were reported at the IV All-Union Conference on Tunable Lasers in the beginning of December 1983 [90]. The lasing in $Al_2O_3 : Ti^{3+}$ crystals with the use of lamp pumping was obtained for the first time. A standard coaxial INK-22/250 lamp was used. A dye solution, which was used not only to cool samples but also to convert light, was pumped through the system. These investigations were developed in [91–94].

We were especially interested in quasi-continuous lasing, i.e., laser pulses with a width up to several hundred microseconds having a smooth envelope. In order to realize such a lasing, special flash lamps were designed [93] which make it possible to pass through them current pulses as wide as 600 μs with a very steep leading edge. The quartz glass of lamp bulbs contains cerium. As a result, pulses 600 μs wide with a smooth envelope were obtained [94], which can be used in a number of applications.

The ESA spectrum of Ti^{3+} ions, although not as rich as that of Cr^{3+} ions, nevertheless exhibits features related to the electronic transitions from the lower sublevel of the excited ^2E level (16700 cm^{-1}) to the CT band. Figure 7 shows the band due to the absorption from the ground state at 220 nm (45460 cm^{-1}), which overlaps with the fundamental-absorption edge, and the $\Delta K(\lambda)$ spectrum in the wavelength range from 330 nm (47000 cm^{-1}) to ~280 nm (52420 cm^{-1}). It can be seen that $\Delta K(\lambda)$ steadily increases with decreasing wavelength, which indicates the absorption from the ^2E_g level to the CT band. This result is consistent with the ESA measurements [95]. The method of two-step photoionization suggested by Kaplyanskiĭ [96, 97] showed that, upon simultaneous illumination of a $Al_2O_3 : Ti^{3+}$ sample by a N_2 laser ($\lambda = 510.2$ and 578.2 nm) and a Cu laser (510.2 and 578.2 nm), a photocurrent flows through the sample, which is caused by photoionization of Ti^{3+} ions via the intermediate level ^2E_g. The radiation of a Cu laser rapidly populates the ^2E_g level, while the N_2-laser radiation photoionizes Ti^{3+} ions from the ^2E_g state. Thus, the data of ESA spectroscopy and two-step photoionization yield similar energy-band diagrams of $Al_2O_3 : Ti^{3+}$ crystals.

2. NARROW LINES IN THE IR ESA SPECTRA OF Cr^{3+}-DOPED CRYSTALS

The ESA spectra of Cr^{3+}-doped crystals considered above consist of broad bands. At the same time, the spectra consisting of narrow lines due to the ($^2E(t_2^3)$,

$^2T_1(t_2^3)) \longrightarrow {}^2T_2(t_2^3)$ transitions, which occur without changing the electronic configuration of Cr^{3+} ions, are no less informative.

2.1. In ruby, the forbiddenness of the $^4A_2(t_2^3) \longrightarrow {}^2T_2(t_2^3)$ transition is lifted partially due to the action of a strong trigonal field. Hence, *B* lines can be observed in the absorption spectrum of ruby [98]. In crystals with higher symmetry of the Cr^{3+} positions, such as yttrium–aluminum garnet $Y_3Al_5O_{12}$: Cr^{3+} and, especially, magnesium spinel $MgAl_2O_4$: Cr^{3+}, it is very difficult (if at all possible) to observe *B* lines. ESA spectroscopy makes it possible to study the $^2T_2(t_2^3)$ state by observing the narrow lines corresponding to the spin- and parity-allowed transitions $(^2E, {}^2T_1) \longrightarrow {}^2T_2$. The *B* lines in the spectra of ruby were studied in [99–101]. According to the terminology used in [101], we will refer to them as *I* lines (infrared lines). We studied in detail the *I* lines in the spectra of ruby and, for the first time, in the spectra of garnet $Y_3Al_5O_{12}$: Cr^{3+} and spinel $MgAl_2O_4$: Cr^{3+} [102]. The measurements were performed at 300 and 77 K. Obviously, samples are heated due to pumping. The actual temperature of samples at the instant of measurements, determined from the temperature shift of the *R* lines [58], was equal to 100–120 K.

A schematic diagram of the $(^2E, {}^2T_1) \longrightarrow {}^2T_2$ transitions for chromium-doped crystals is shown in Fig. 1b. In the range of 1300–1700 nm, two narrow intense lines, I_{12} and I_{21} (6551 and 6657 cm^{-1}, respectively), are observed in the ESA spectrum of ruby at 100 K for the light polarization **E** ∥ *c*. In the case of **E** ⊥ *c* polarization, four narrow distinct absorption lines can be seen: I_{11}, I_{22}, I_{13}, and I_{23} (6580, 6623, 6907, and 6936 cm^{-1}, respectively). We failed to resolve the I_{13} and I_{23} lines as distinctly as in [100], although our measuring technique allowed us to do this. A similar result was obtained in [101]. In addition to the strong narrow *I* lines, which are due to the zero-phonon transitions, the near IR spectrum of ruby contains a great number of electronic–vibrational replicas of the *I* lines. The *I* lines and their electronic–vibrational replicas for ruby are identified in Table 5, which also lists the positions of the zero-phonon narrow lines and their electronic–vibrational replicas.

2.2. Garnet $Y_3Al_5O_{12}$: Cr^{3+}. The local symmetry of the positions of Cr^{3+} ions in garnet crystals is higher than that in ruby. Therefore, the lift of the forbiddenness of the $^4A_2(t_2^3) \longrightarrow {}^2T_2(t_2^3)$ transitions manifests itself in garnets to a lesser extent than in ruby. *B* lines cannot be observed in the spectra of garnet samples with a low chromium concentration. Only when the chromium concentration is as high as ~1% do barely distinguishable *B* lines appear. Nevertheless, Pasternak managed to measure in detail the GSA spectra of garnet in the vicinity of the *B* lines (460–480 nm) using a
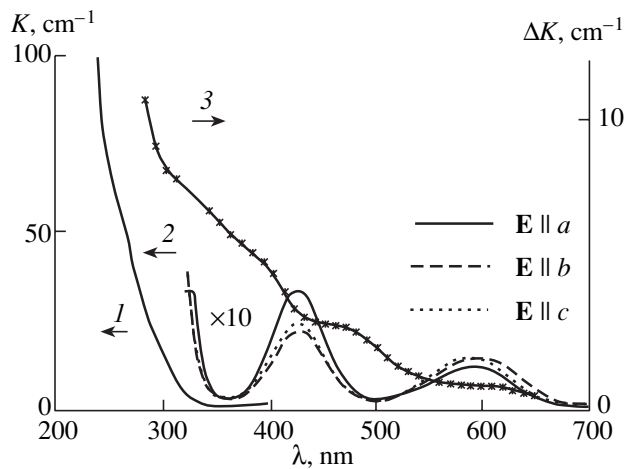

Fig. 6. Spectra of absorption from the ground state $^4A_2$ of Cr^{3+} ions in lithium germanate $Li_2Ge_7O_{12}$: Cr^{3+}. (*1*) The fundamental-absorption edge of the crystal, (*2*) the absorption spectrum of the crystal, (*3*) the spectrum of $\Delta K(\lambda)$.

method he developed [102]. At the same time, the lines due to the $^2E(t_2^3) \longrightarrow {}^2T_2(t_2^3)$ transitions can be easily observed even in the ESA spectra of garnet samples with a low chromium concentration; notably, the absorption cross sections $\sigma(^2E \longrightarrow {}^2T_2)$ exceed the absorption cross sections $\sigma(^4A_2 \longrightarrow {}^2T_2)$ by an order of magnitude. Table 6 contains the frequencies of the electronic transitions $^4A_2 \longrightarrow {}^2T_2$ and $^2E \longrightarrow {}^2T_2$ in garnet and the frequencies of corresponding electronic–vibrational replicas. It can be seen from Table 6 that the phonon frequencies we found from the ESA spectra are in good agreement with the corresponding values reported in [103, 104]. It is noteworthy that the electron–phonon spectra $(^2E, {}^2T_1) \longrightarrow {}^2T_2$ do not contain lines due to the pair and higher order interactions between chromium ions, whereas such lines manifest themselves in the luminescence spectra. This fact indicates that ESA spectroscopy can be used to determine the phonon spectra of impurity crystals. The results obtained in [102] made it possible to determine the positions of the $^2T_2(t_2^3)$ levels of the Cr^{3+} ion in ruby and garnet (Table 7).

2.3. Magnesium spinel $MgAl_2O_4$: Cr^{3+}. The energies of the $^2T_1(t_2^3)$ and $^2T_2(t_2^3)$ levels were calculated for magnesium spinel in [36, 37, 46]. The positions of the $^2T_1(t_2^3)$ and $^2T_2(t_2^3)$ levels were studied experimentally in [102]. Since the symmetry of the Cr^{3+} environment in spinel is higher than that in ruby or garnet [105], the absorption due to the $^4A_2 \longrightarrow {}^2T_2$ transition was not observed, although the chromium concentration was sufficiently high (~1.5×10^{20} cm^{-3}). In [33], where samples of natural Ceylon spinel were investigated, a slow rise in the absorption curve in the vicinity of 22100 cm^{-1}
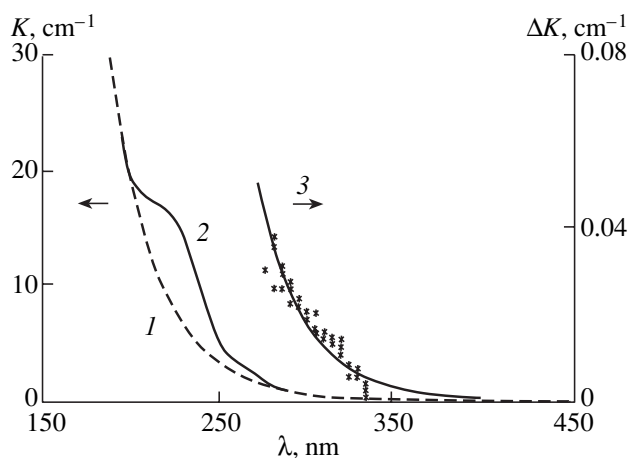
Fig. 7. Absorption spectra of $Al_2O_3 : Ti^{3+}$ crystals in the UV range. (*1*) The fundamental-absorption edge, (*2*) the absorption band at 220 nm, (*3*) the spectrum of $\Delta K(\lambda)$.

(452.4 nm) was observed. This rise was attributed to the $^4A_2 \longrightarrow {}^2T_2$ transition. Apparently, this transition is possible in natural spinel, which is corroborated by the fact that the narrow $R_{1,2}$ lines in the luminescence spectra of natural spinel are resolved well [106], even though the splitting of the $^2E(t_2^3)$ level is only ~6 cm^{-1}. In this case, one should expect the B lines to be fairly narrow and intense. In the spectra of artificial spinel, the $R_{1,2}$ and B lines are strongly broadened due to the stresses in the material and its nonstoichiometry [44]. The lines in the spectra of such crystals are weaker, and B lines cannot be observed in the absorption spectra [106].

In contrast to the GSA spectrum in the vicinity of the $^4A_2 \longrightarrow {}^2T_2$ transition, the ESA spectrum of magnesium spinel in the vicinity of the $^2E \longrightarrow {}^2T_2$ transition (1200–1700 nm) can be observed fairly easily. Unfortunately, we have no samples of natural spinel at our disposal to detect narrow R and B lines. The I lines we observed were strongly broadened and overlapped [102]. As was noted above, the ESA spectra of spinel exhibit the absorption by centers of R and N types simultaneously. Therefore, both decay times of the metastable state (20 and 5 ms) manifest themselves in the maxima of the I lines at 7690 cm^{-1} (1300 nm) and 7240 cm^{-1} (1380 nm). In the side bands at 8440 cm^{-1} (1180 nm) and 6330 cm^{-1} (1600 nm), only the contribution of the longer time (20 ms) is observed. Thus, we may conclude that the frequency of the $^2E(t_2^3) \longrightarrow {}^2T_2(t_2^3)$ transition is about 7470 cm^{-1} (1340 nm) [100].

Notably, the sum of the frequencies of the $^4A_2(t_2^3) \longrightarrow {}^2E(t_2^3)$ and $^2E(t_2^3) \longrightarrow {}^2T_2(t_2^3)$ transitions is equal to 22070 cm^{-1} (453 nm), which is in good agreement with the value 22100 cm^{-1}, obtained in [33] for the fre-

quency of the $^4A_2(t_2^3) \longrightarrow {}^2T_2(t_2^3)$ transition. The detailed ESA spectra of ruby, garnet, and spinel in the wavelength range 1300–1800 nm were reported in [102].

3. GENERAL FEATURES OF THE ESA SPECTRA OF CRYSTALS DOPED WITH CR^{3+} IONS

3.1. CT Bands. All the ESA spectra of crystals doped with Cr^{3+} ions contain a strong absorption band in the UV region at 40000–55000 cm^{-1}. The oscillator strengths of this band generally exceed those of other absorption bands by a factor of 50–150. This strong band is generally attributed to the electronic transitions between the states of metal-impurity ions and the orbitals of nearest oxygen ligands (the metal-to-ligand charge transfer).

The theoretical consideration of the CT bands in the spectra of impurity crystals was performed by McClure [107]. Tippins was the first to study them experimentally [108]. He observed the CT bands in the absorption spectra due to the transitions from the ground state of Fe^{3+}, Ti^{3+}, Cr^{3+}, Mn^{3+}, and Ni^{3+} ions in Al$_2$O$_3$ crystals. These bands are located at the fundamental-absorption edge of Al$_2$O$_3$. Hence, they manifest themselves as barely noticeable humps at the fundamental-absorption edge. For this reason, Tippins could not observe features of these bands but determine only their positions in the spectrum. On the basis of his measurements, he suggested an acceptor model of the charge transfer. According to this model, electrons pass from the orbitals of the oxygen ligands to the levels of the impurity-metal ion. However, Sabatini *et al.* [109], having measured the temperature dependence of the intensities of CT bands, revealed that the oscillator strength of the CT band decreases with decreasing temperature and its maximum shifts to shorter waves. As was believed in [109], these two phenomena indicate that electrons pass from the metal-ion levels to the ligand orbitals; i.e., the donor model is realized.

Note that CT spectra have not been investigated systematically because of the difficulties caused by overlapping of CT bands with the fundamental-absorption edge. In this context, the ESA technique may ensure significant progress. Indeed, in contrast to the GSA spectroscopy when the CT band manifested itself as very weak features against the intense fundamental absorption band, the CT band in ESA spectra is much stronger than the fundamental absorption. Moreover, the nature of the ESA technique itself [see Eqs. (1)–(3)] makes it possible to get rid of the background at the fundamental-absorption edge.

With a decrease in temperature, the oscillator strengths of CT bands decrease. For example, when the temperature decreases from 300 to 77 K, the oscillator strengths of the UV bands in ESA spectra of ruby, garnet, and magnesium spinel decrease by a factor of 1.67,

Table 5. Frequencies (cm^{-1}) of electronic ($^2E \longrightarrow {}^2T_2$) and electronic–vibrational transitions in the absorption spectrum of ruby [102]

	E ∥ c			**E ⊥ c**			
line position, cm^{-1}	possible combinations of electronic-transition frequencies with phonon frequencies		line position, cm^{-1}	possible combinations of electronic-transition frequencies with phonon frequencies			
	$\nu_{I_{12}} + \nu_{phon}$, cm^{-1}	$(\nu_{21} + \nu_{phon})$, cm^{-1}		$\nu_{I_{11}} + \nu_{phon}$, cm^{-1}	$\nu_{I_{13}} + \nu_{phon}$, cm^{-1}	$\nu_{I_{22}} + \nu_{phon}$, cm^{-1}	$\nu_{I_{23}} + \nu_{phon}$, cm^{-1}
6551		I_{12}	6623	I_{11}			
6657	I_{12}		6579			I_{22}	
6824		$I_{21} + 273(268)$*	6837	$I_{11} + 214(266)$		$I_{22} + 258(268)$	
6866		$I_{21} + 315$	6910				I_{23}
6911		$I_{21} + 360(378)$	6936		I_{13}		
6959		$I_{21} + 408(415)$	7033	$I_{11} + 410(415)$		$I_{22} + 454(457)$	
7006		$I_{21} + 455(457)$	7115	$I_{11} + 492(487)$			
7065	$I_{12} + 408(415)$	$I_{21} + 514(522)$	7145	$I_{11} + 522(522)$			$I_{23} + 235(236)$
7143	$I_{12} + 486(487)$	$I_{21} + 592(593)$	7208	$I_{11} + 585(593)$	$I_{13} + 272(268)$		
7212	$I_{12} + 555(552)$		7330				$I_{23} + 420(415)$
7313	$I_{12} + 656$		7390		$I_{13} + 454(457)$	$I_{22} + 811(815)$	$I_{23} + 480(487)$
7463	$I_{12} + 806(815)$						

* The values in parentheses are the frequencies obtained by us from the luminescence spectra of ruby.

Table 6. Frequencies (cm^{-1}) of electronic ($^4A_2 \longrightarrow {}^2T_2$, $^2E \longrightarrow {}^2T_2$) and electronic–vibrational transitions in the absorption spectrum of garnet [102]

$^4A_2 \longrightarrow {}^2T_2$, cm^{-1}	$\nu_i = \bar{\nu}_R$, cm^{-1}	Transition frequency $^2E \longrightarrow {}^2T_2$, cm^{-1}	Possible combinations of electronic-transition frequencies with phonon frequencies		
			$(\nu_{B_{01}} \pm \nu_{phon})$, cm^{-1}	$(\nu_{B_{02}} \pm \nu_{phon})$, cm^{-1}	$(\nu_{B_{03}} \pm \nu_{phon})$, cm^{-1}
20807	20809	6250	$B_1 - 263(255)[259]$	$B_2 - 326(320)$	
20890	20888	6329		$B_2 - 243[243]$	
	20928	6369			
20982	20977	6418		$B_2 - 151(148)[144]$	
21070	21073	6514	B_1		
21133				B_2	
21249	21226	6667		$B_2 + 116(123)$	$B_3 - 391(397)$
21358	21362	6803	$B_1 + 288(293)[296]$	$B_2 + 255(223)[218]$	$B_3 - 282(293)[296]$
21418	21427	6868	$B_1 + 348(346)[340]$	$B_2 + 285(293)$	$B_3 - 222(223)[218]$
21640	21640	7081			B_3
21973	21944	7385			$B_3 + 333(333)[340]$

Note: The values in parentheses and square brackets are the phonon frequencies from [103] and [104], respectively.

1.3, and 2, respectively. We detected no shift of the CT-band maximum to shorter waves for the crystals under investigation. Nevertheless, the decrease in the oscillator strengths of CT bands with decreasing temperature counts convincingly in favor of the donor mechanism of the CT process. Finally, one more important fact related to the CT band should be noted. The electronic transitions responsible for this band relate (at least, approxi-mately) the energy level diagram of an impurity ion to the edge of the conduction band of a host crystal. This circumstance reveals new possibilities, for example, of developing the theory of deep impurity levels in wide-gap insulators [110–112].

3.2. Similarity of GSA and ESA spectra. Measure-ments of the spectra of magnesium spinel

Table 7. Experimental energies of the $^2T_1(t_2^3)$ and $^2T_2(t_2^3)$ terms for ruby and garnet [102]

Term	Level*	Ruby	Garnet
		E, cm^{-1}	E, cm^{-1}
$^2E(t_2^3)$	1	14400	14559
	2	14429	
$^2T_1(t_2^3)$	3	14939	15162
	4	15150	15213
	5	15172	15420
$^2T_2(t_2^3)$	1	21002	21070
	2	21032	21133
	3	21338	21640

* The numeration of levels corresponds to Fig. 1b.

$MgAl_2O_4$: Cr^{3+} revealed that, in the wavelength scale, the maxima of the U and Y bands in the GSA spectrum coincide with the maxima of the U_1 and Y_1 bands in the ESA spectrum [42]. The intensities of the corresponding bands coincide as well. The Y band at 400 nm is complex: visually, it is a superposition of at least two bands. The Y_1 band is also complex and consists of two bands located similarly to the two Y bands. This is clearly demonstrated in Fig. 4, where the absorption bands are expanded in Gaussian components. This phenomenon was explained by Veremeĭchik [113], who also showed [114] that the similarity of GSA and ESA spectra is characteristic of a wide class of impurity crystals. The similarity of GSA and ESA spectra has a number of specific features:

(i) the frequencies corresponding to the maxima of the absorption bands U ($^4A_2 \longrightarrow {}^4T_2$) and U_1 ($^2E \longrightarrow {}^2T_2(t_2^3, e)$) coincide;

(ii) the frequencies corresponding to the maxima of the Y ($^4A_2 \longrightarrow {}^4T_1$) and $Y_1[^2E \longrightarrow {}^2T_2(t_2^3, e)]$ bands differ by $\sim Dq$;

(iii) the shapes of the bands under comparison are described by similar Gaussian functions;

(iv) the bands under comparison are characterized by similar polarization dependences; i.e., the ratio of the intensities of the bands due to the $^4A_2 \longrightarrow \Gamma$ and $^2E \longrightarrow \Gamma$ transitions in different polarizations is such that $I_{\mathbf{E} \| c}(^4A_2 \longrightarrow {}^4\Gamma) : I_{\mathbf{E} \perp c}(^4A_2 \longrightarrow {}^4\Gamma) \approx I_{\mathbf{E} \| c}(^2E \longrightarrow {}^2\Gamma) : I_{\mathbf{E} \perp c}(^2E \longrightarrow {}^2\Gamma)$.

In the approximation of a strong crystal field, the similarity of the GSA and ESA spectra is explained by the special symmetry of the wave functions of the initial terms of electronic transitions and by the similar symmetry of the orbital parts of the finite-term wave functions.

4. ESA SPECTROSCOPY IN THE LUMINESCENCE REGION OF THE MATERIAL

4.1. Theoretical grounds. We discussed above the ESA measurements in the spectral range that does not overlap with the range of luminescence of impurity crystals. However, the problem of measuring ESA spectra in the range of luminescence is no less important. Obviously, the methods developed for measuring ESA spectra beyond the luminescence range are inappropriate in this case. Generally, the luminescence intensity considerably exceeds the intensity of probe light passed through an absorbing crystal. This circumstance leads to distortion of the results of measurements or makes the measurements completely impossible. Therefore, measuring ESA spectra in the luminescence range is a separate problem of ESA spectroscopy.

If a luminescence spectrum represents a narrow line, it is not very difficult to measure the coefficients of absorption from the ground or excited states ($a_{GSA}(\lambda)$ and $a_{ESA}(\lambda)$, respectively). One can measure these quantities in the vicinity of a luminescence line either from the short-wavelength side or from the long-wavelength side and then, extrapolating the values of measured $a_{GSA}(\lambda)$ and $a_{ESA}(\lambda)$ across the range of luminescence, to obtain the corresponding values for the luminescence band itself [58].

In more common situations (when the luminescence band is broad), such an approach is, naturally, invalid. For this case, a method based on the McCumber theory was developed [115, 116]. This theory allows one to use the Einstein coefficients $A_{ij}(\nu)$ and $B_{ij}(\nu)$ [117] for broad absorption and luminescence bands. According to the McCumber theory, the spectrum of effective emission cross sections $\sigma_e(\nu)$ can be derived from the luminescence spectrum in the form

$$\sigma_e(\nu) = f(\nu)\left[\frac{2\pi}{\nu n_\lambda(\nu)}\right]^2, \qquad (15)$$

where $f(\nu)$ is determined by the formula

$$1/\tau = \int d\Omega \int f(\nu)d\nu. \qquad (16)$$

Hereinafter, $f(\nu)$ is a dimensionless function, n_λ is the refractive index for polarization λ, c is the speed of light, ν is the emission frequency, τ is the characteristic lifetime of spontaneous emission, and Ω is the solid angle of emission.

The most convenient form of the equation for determining $\sigma_e(\nu)$ in practice is as follows (see, for example, [118]):

$$\sigma_e(\lambda) = \frac{\lambda^5}{8\pi cn^2}\frac{I(\lambda)}{\int \lambda I(\lambda)d\lambda}\frac{1}{\tau}. \qquad (17)$$

Here, $I(\lambda)$ is the luminescence-power density (erg/(cm^2 s)). The integral in the denominator has the dimension of power (erg/s). A pictorial description of the application of the McCumber theory for experimental determining the cross section of stimulated emission is given in [119].

A problem of amplification of radiation in the range of 1280–1320 nm using optical amplifiers arose in the 1990s. This problem is associated with the need for transmitting light signals through fiber optic cables used in telecommunication systems. One solution was to use crystals and glasses doped with Nd^{3+} ions [118]. It is well known that the electronic transition $^4F_{3/2} \longrightarrow$ $^4I_{13/2}$ in the vicinity of 1300 nm is typical of the Nd^{3+} ion. However, the difficulty is in the presence of the induced-absorption transition $^4F_{3/2} \longrightarrow {}^4G_{7/2}$ at a wavelength close to 1300 nm, which hinders the amplification (Fig. 1c). In order to increase the amplification coefficient, one can space these transitions from each other by choosing an appropriate crystal matrix. The direct way to determine the limiting possibilities of an amplifying medium is to measure its ESA spectrum in the range of 1280–1320 nm. Preliminary experiments [118] showed that the promising candidates for amplification are SrF$_2$: Nd^{3+} and CaSrF$_2$: Nd^{3+} crystals. It was necessary to determine the spectral region in which induced absorption would not hinder the amplification of signals.

Such investigations were performed in [120, 121]. Using Bouguer's law, one can write

$$\ln \frac{I(\lambda)}{I_0(\lambda)} = (\sigma_e(\lambda) - a_{ESA}(\lambda))n_2 l, \qquad (18)$$

where n_2 is the population of the $^4F_{3/2}$ level, $\sigma_e(\lambda)$ is the amplification cross section for emission in the vicinity of 1300 nm, $a_{ESA}(\lambda)$ is the induced-absorption coefficient for this spectral range, l is the optical path length for a sample, and $I_0(\lambda)$ and $I(\lambda)$ are the power densities of the probe laser beams incident on a sample and emerging from it, respectively. Equation (18) determines the amplification spectrum for a single passage of radiation through a sample:

$$g(\lambda) = \ln \frac{I(\lambda)}{I_0(\lambda)}. \qquad (19)$$

The amplification spectrum is measured directly in the experiment. The first term on the right-hand side of Eq. (18) is found from the luminescence spectra by formula (17). Obviously, we can write

$$e(\lambda) = \sigma_e(\lambda)n_2 = A\lambda^5 L(\lambda), \qquad (20)$$

then,

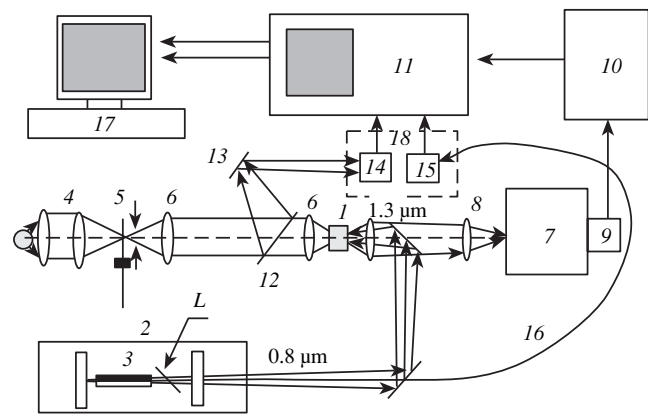$$a_{ESA}(\lambda) = A\lambda^5 L(\lambda) - g(\lambda). \qquad (21)$$

Fig. 8. Schematic of the spectrometer for measuring ESA spectra in the range of luminescence. (*1*) Sample; (*2*) tunable laser; (*3*) active sapphire–titanium element; (*4*, *8*) objectives; (*5*) modulator; (*6*) lenses; (*7*) MDR-1 double monochromator; (*9*, *14*, *15*) photodetectors; (*10*) filter amplifier; (*11*) C9-8 oscilloscope; (*12*) semitransparent mirror; (*17*) personal computer; (*18*) synchronous detector; (*L*) Lyot filter.

Here, $L(\lambda)$ is the luminescence-power density for centers of the same type in a unit solid angle and a unit wavelength range.

In the case of pulse excitation, the intensity of the emerging light $I(\lambda, t)$ after the pumping pulse is expressed by the formula

$$I(\lambda, t) = I_0(\lambda)\exp([g(\lambda, 0)]\exp(-t/\tau)). \qquad (22)$$

The experimentally measured dependence $I(\lambda, t)$ is extrapolated to $t = 0$. In the general case, the constant A can be found as in [119]. However, it turned out that, when the ESA spectra of the SrF$_2$: Nd^{3+} [120] and CaSrF$_2$: Nd^{3+} [121] crystals are measured, it is possible to use the specific spectroscopic properties of these materials. The amplification and luminescence bands of SrF$_2$: Nd^{3+} have identical shapes in the range of 1302–1308 nm. This circumstance means that ESA is absent in the noted range; therefore, the theoretical and experimental amplification spectra can be superposed. In the case of CaSrF$_2$: Nd^{3+} crystals, it is also reasonable to superpose the luminescence and amplification spectra in the vicinity of 1302 nm [121]. Thus, in the noted spectral regions, the following condition is satisfied:

$$g(\lambda) = A\lambda^5 L(\lambda). \qquad (23)$$

At other wavelengths, this equality is violated due to the ESA effect.

4.2. Measuring technique. The schematic of the spectrometer for studying the excited states of Nd^{3+} ions in crystals and glasses, which was developed at the Institute of Crystallography, RAS, is shown in Fig. 8. Sample *1* (an Nd^{3+}-doped crystal), shaped as a plate 2–8 mm thick, is pumped by pulsed tunable laser *2* based on Al$_2$O$_3$: Ti^{3+} crystal *3*. The tuning is performed by a
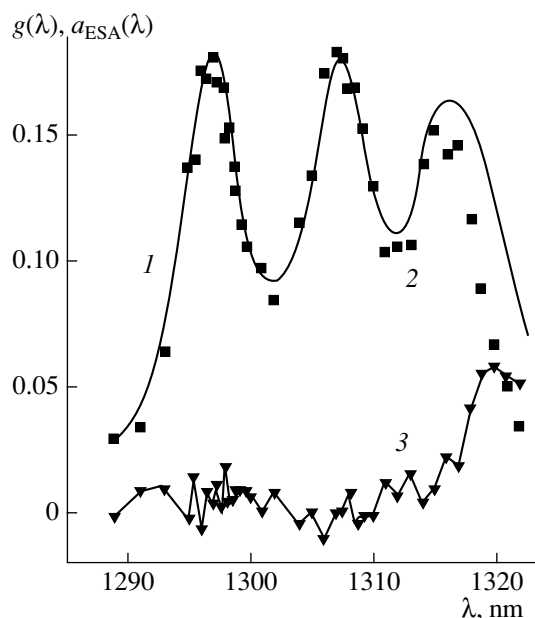
Fig. 9. Spectra of $SrF_2 : Nd^{3+}(0.8\%)$ crystals pumped at a wavelength of 800.5 nm. (*1*) Amplification calculated by formula (20), (*2*) direct measurement of amplification (formula (19)), and (*3*) the ESA spectrum (formula (21)).

Fig. 10. Spectra of $Ca_{0.6}Sr_{0.4}F_2 : Nd^{3+}(0.3\%)$ crystals pumped at a wavelength of 802.5 nm. (*1*) Amplification calculated by formula (20), (*2*) direct measurement of amplification (formula (19)), and (*3*) the ESA spectrum (formula (21)).
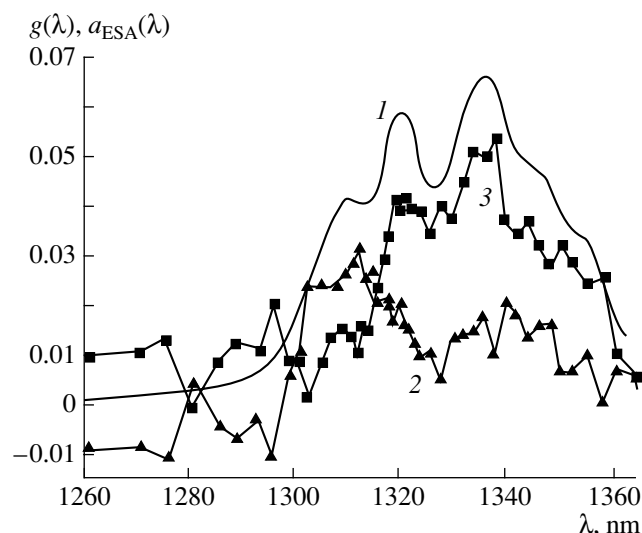
Lyot filter (*L*). In this case, the width of the lasing spectrum (at half-maximum) for an energy of an output laser pulse of 20–620 mJ is about 1.5 nm. The width of the free-lasing pulse is ~80 μs. Such a width of pumping pulse is significantly shorter than the lifetime of active centers formed by Nd^{3+} ions. Therefore, the investigation of the depletion kinetics for metastable states is simplified [29]. The pumping radiation is focused on a sample to a spot ~1 mm in diameter. Under these conditions, the energy density in an incident pulse reaches 50–60 J/cm² . A sample with a neodymium concentration of 0.8 wt % absorbs about 80% of the pumping energy. Note that the use of laser pumping with a tunable frequency makes it possible to excite active centers of different types in a sample. A halogen incandescent lamp with a power of 70 W was used as the probe-light source. Objective *4* focuses the image of the lamp filament on the plane of mechanical modulator *5*, which has an aperture of 6 mm and chops the probe light with a frequency of ~100 kHz.[3] Lenses *6* transmit the image of the modulator aperture to the sample plane (diminishing the image) and, thus, form the caustic of the probe light less than 1 mm in diameter. The probe

beam is collinear with the excitation laser beam and is directed oppositely to it. The region of a crystal exposed to the probe light is overlaps the region of excitation. Objective *8* focuses the probe light beam transmitted through a sample on the entrance slit of an MDR-1 double monochromator. The radiation emerging from the monochromator is recorded by photodetector *9* placed behind the exit slit of the monochromator. The photodetector consists of a germanium photodiode and a preamplifier. An electric signal from the output of the photodetector, which is proportional to the intensity of probe light transmitted through the sample and the monochromator, arrives at filter amplifier *10* and then at the entrance of C9-8 digital storage oscilloscope *11*.

The frequency corresponding to the center of the filter-amplifier band coincides with the chopping frequency of modulator *5* (~100 kHz). The bandwidth of amplifier *10* lies in the range of 43–230 kHz (at half-maximum). The modulation frequency of the probe beam significantly exceeds the frequencies forming the spectrum of a pulsed luminescence signal and pumping light scattered in a sample, which lie below 10 kHz. The filter amplifier suppresses these signals, as well as the high-frequency noise in the region above 200 kHz, and, thus, selects only the signal component with a modulation frequency of 100 kHz.

In order to improve the signal-to-noise ratio, lock-in detection and storage of measurable signals were used. The reference signal is formed by the probe light itself, part of which is fed to photodetector *14* by mirrors *12* and *13*. The reference and measurable signals are fed to

---

[3] The mechanical modulator with a maximum chopping frequency of 120 kHz was designed in the Laboratory of Physics of Optical Crystals (POC Laboratory) and fabricated in the Special Design Office of the Institute of Crystallography, RAS (SDO IC RAS). In order to increase the stability, the modulator was tuned to a frequency of 100 kHz. $Al_2O_3 : Ti^{3+}$ crystals were grown in the POC Laboratory; the laser was also fabricated there. The Lyot filter was calculated in the POC Laboratory and fabricated in the SDO IC RAS.

different entrances of a C9-8 two-channel storage oscilloscope. The storage oscilloscope is triggered by a signal formed at the output of photodetector *15*, which responds to a small fraction of pumping radiation passed through optical fiber *16*.

Digital signals from oscilloscope *11* arrive at personal computer *17* through a GPIB interface. Storage and processing of a signal in the computer is performed by a special program. One point in a spectrum is obtained by storage of signals from several excitation laser pulses.

When the luminescence kinetics is recorded, the probe light is switched off and a signal from the output of photodetector *9* is fed directly to the entrance of oscilloscope *11*, by-passing filter amplifier *10*. The spectral sensitivity of the measuring unit of the ESA spectrometer was calibrated against the black-body radiation.

4.3. ESA spectra of the SrF_2: Nd^{3+} and $CaSrF_2$: Nd^{3+} crystals. Several types of Nd^{3+} centers with significantly different spectral luminescence characteristics were revealed in SrF_2: Nd^{3+} crystals [118]. The amplifying properties of SrF_2: Nd^{3+} in the range of 1280–1320 nm are attributed to the so-called *L* center, which consists of an Nd^{3+} ion and an interstitial F^- ion located in the first coordination sphere. It was shown in [118] that *L* centers in SrF_2: Nd^{3+} are selectively excited at a wavelength of 743 nm. In order to find out if SrF_2: Nd^{3+} is a promising candidate for an amplifying medium in the wavelength range 1280–1320 nm, the ESA spectra of *L* centers were studied. The following values of the pumping wavelength were used: 743, 800.5, and 802 nm. Figure 9 shows the spectra of the amplification $g(\lambda)$ and induced-absorption ($a_{ESA}(\lambda)$) cross sections for the $^4F_{3/2} \longrightarrow ^4G_{7/2}$ transitions in SrF_2: Nd^{3+} crystals at a pumping wavelength of 800.5 nm. It can be seen that the induced absorption is weak in this case. The obtained ratios $a_{ESA}(\lambda)/g(\lambda)$ in the range of 1280–1320 nm are 0.12, 0.06, and 0.27 at λ_{pump} = 743, 800.5, and 802 nm, respectively. The width of the pumping spectrum is equal to 1.5 nm. The maximum amplification is obtained upon excitation of *L* centers at 800.5 nm.

The results of similar measurements of the ESA spectrum of a $Ca_{0.6}Sr_{0.4}F_2$: Nd^{3+} (0.3%) crystal [121] are shown in Fig. 10. The ratio of the ESA cross section to the amplification cross section is smallest at a wavelength of 1302 nm, which is typical of *L* centers. However, the situation with $CaSrF_2$: Nd^{3+} crystals is much more complicated than with SrF_2: Nd^{3+} crystals. Along with long-lived *L* centers (0.8–1.7 μs), there also exist short-lived centers with a lifetime of 0.3 μs in $CaSrF_2$: Nd^{3+}. The short-lived centers contribute significantly to the spectrum of $CaSrF_2$: Nd^{3+}, making it more complex. Figure 10 shows the net spectrum of the long-lived and short-lived centers. The ESA spectrum

becomes zero at 1301–1302 nm [121]. Comparison of the ESA spectra of SrF_2: Nd^{3+} and $CaSrF_2$: Nd^{3+} crystals shows that the amplification properties of the former are significantly better.

CONCLUSIONS

In spite of the fact that ESA spectroscopy has been intensively developed for more than forty years, it should be admitted that this technique, in essence, only begins to reveal its possibilities. Generally, ESA spectroscopy is used to solve a very particular problem of predicting lasing or amplification properties of various materials. However, in our opinion, the main line in developing this method is to use it as an experimental basis for developing the theory of impurity wide-gap insulators. Indeed, the theory of the energy spectrum of impurity wide-gap insulators is far from a unified physical picture to date [122].

The CF theory is semiempirical. It adequately describes the spectra of impurity transition-metal ions in wide-gap insulators but fails to predict the positions of the energy levels of impurity ions with respect to the edges of the band gap of the host crystal. The CF theory also fails to explain CT spectra [123] due to the transitions of electrons between impurity ions and their nearest ligands.

In contrast to the CF theory, the ligand-field theory [124, 125] is based on a cluster model; i.e., this theory considers a cell composed of an impurity ion and its nearest ligands in the lattice field beyond the cell. Such a cluster model allows one to describe the transfer of electrons between an impurity ion and neighboring ligands. Nevertheless, this theory fails to predict the positions of the energy levels of impurity ions with respect to the edges of the band gap.

Apparently, the most adequate approaches to solving this fundamental problem for wide-gap insulators are provided by the theory of deep levels, which was developed for impurity ions in covalent semiconductors [110–112].

Obviously, in this complex period of development of the theory of impurity wide-gap insulators, ESA spectroscopy may be considered as an effective experimental tool which may yield a large amount of useful data for developing physics of impurity wide-gap insulating crystals.

REFERENCES

1. B. K. Sevast'yanov, in *Spectroscopy of Crystals* (Nauka, Moscow, 1975), p. 122.

2. B. K. Sevastyanov, *Ruby and Sapphire* (Amerid, New Delhi, 1980), p. 354.

3. D. T. Sviridov and Yu. F. Smirnov, *Theory of Optical Spectra of Transition-Metal Ions* (Nauka, Moscow, 1977).

4. D. T. Sviridov, R. K. Sviridova, and Yu. F. Smirnov, *Optical Spectra of Transition-Metal Ions in Crystals* (Nauka, Moscow, 1976).

5. S. I. Wawilov and V. L. Lewschin, Z. Phys. **35**, 920 (1926).

6. G. N. Lewis, D. Lipkin, and T. T. Magel, J. Am. Chem. Soc. **63**, 3005 (1944).

7. T. H. Meiman, Phys. Rev. Lett. **4**, 564 (1960).

8. F. Gires and G. Mayer, J. Phys. Radium **22**, 832 (1961).

9. F. Gires and G. Mayer, C. R. Acad. Sci. **254**, 659 (1962).

10. F. Gires and G. Mayer, Ann. Radioelectr. **18**, 116 (1963).

11. B. N. Grechushnikov and I. N. Kalinkina, Zh. Prikl. Spektrosk. **29**, 929 (1978).

12. A. I. Goncharov, V. V. Volkov, and I. P. Petrov, Zh. Prikl. Spektrosk. **37**, 470 (1982).

13. T. R. Lawrence, B. Dibartolo, and C. S. Naiman, in *Proceedings of Conference on Optical Properties of Ion in Crystals, 1966*, Ed. by H. M. Crosswhite and H. W. Moos (Interscience, New York, 1967), p. 528.

14. R. L. Aagard and R. A. Daufault, Appl. Phys. Lett. **4**, 102 (1964).

15. F. J. McClung and R. W. Hellwarth, Proc. IEEE **51**, 46 (1963).

16. M. D. Galanin and Z. A. Chizhikova, Opt. Spektrosk. **17**, 402 (1964).

17. A. M. Bonch-Bruevich and T. K. Razumova, Opt. Spektrosk. **22**, 420 (1967).

18. D. F. Nelson and M. D. Sturge, Phys. Rev. **137**, A1117 (1965).

19. T. Kushida, J. Phys. Soc. Jpn. **21**, 1331 (1966).

20. T. Kushida and P. Parikh, J. Phys. Soc. Jpn. **20**, 2313 (1965).

21. A. P. Ivanov, A. N. Rubinov, and S. A. Mikhnov, Opt. Spektrosk. **17**, 597 (1964).

22. A. P. Ivanov, A. N. Rubinov, and S. A. Mikhnov, Zh. Prikl. Spektrosk. **1**, 133 (1964).

23. H. W. Moos, C. B. Opal, and J. W. Huang, Appl. Opt. **6**, 877 (1967).

24. J. W. Huang and H. W. Moos, Phys. Rev. **173**, 440 (1968).

25. B. N. Grechushnikov and P. P. Feofilov, Zh. Éksp. Teor. Fiz. **29**, 384 (1955) [Sov. Phys. JETP **2**, 330 (1955)].

26. A. N. Rosen, Appl. Opt. **7**, 1555 (1968).

27. V. Daneu, C. A. Sachi, and O. Svelto, Appl. Opt. **4**, 863 (1968).

28. M. D. Galanin, V. N. Smorchkov, and Z. A. Chizhikova, Opt. Spektrosk. **19**, 296 (1965).

29. B. K. Sevast'yanov and V. P. Orekhova, Zh. Prikl. Spektrosk. **18** (4), 641 (1973).

30. B. I. Stepanov, *Methods of Calculation of Optical Quantum Generators* (Nauka i Tekhnika, Minsk, 1966), Vol. 1.

31. T. H. Meiman, R. H. Hoskins, and I. J. D'Haenens, Phys. Rev. **123**, 1151 (1961).

32. R. M. Arlett, J. Am. Ceram. Soc. **45**, 523 (1962).

33. D. L. Wood, G. F. Imbush, R. M. Macfarlane, *et al.*, J. Chem. Phys. **48**, 5255 (1968).

34. N. V. Belov, *Structure of Ionic Crystals and Metal Phases* (Akad. Nauk SSSR, Moscow, 1947).

35. D. T. Sviridov and R. K. Sviridova, Kristallografiya **14** (5), 920 (1969) [Sov. Phys. Crystallogr. **14**, 793 (1970)].

36. R. M. Makfarlane, J. Chem. Phys. **39**, 3118 (1963).

37. R. M. Makfarlane, J. Chem. Phys. **47**, 2066 (1967).

38. F. M. Lou and D. W. Ballentyne, J. Phys. C **1**, 608 (1968).

39. V. I. Cherepanov and A. N. Men', Fiz. Tverd. Tela (Leningrad) **6**, 1939 (1964) [Sov. Phys. Solid State **6**, 1532 (1965)].

40. A. N. Men' and V. I. Cherepanov, Izv. Akad. Nauk SSSR, Ser. Fiz. **28**, 430 (1964).

41. B. K. Sevast'yanov and V. P. Orekhova, in *Spectroscopy of Crystals* (Nauka, Leningrad, 1973), p. 297.

42. B. K. Sevast'yanov and V. P. Orekhova, Kvantovaya Élektron. (Moscow) **1**, 125 (1971).

43. S. Sugano and M. Peter, Phys. Rev. **122**, 381 (1961).

44. O. N. Boksha, S. V. Grum-Grzhimaĭlo, A. A. Popova, *et al.*, in *Spectroscopy of Crystals* (Nauka, Moscow, 1970), p. 302.

45. D. L. Wood, G. F. Imbush, P. Kisliuk, *et al.*, J. Chem. Phys. **48**, 52 (1965).

46. D. T. Sviridov, B. K. Sevast'yanov, V. P. Orekhova, *et al.*, Opt. Spektrosk. **35** (1), 102 (1973).

47. B. K. Sevast'yanov, Kh. S. Bagdasarov, L. B. Pasternak, *et al.*, Pis'ma Zh. Éksp. Teor. Fiz. **17** (2), 69 (1973) [JETP Lett. **17**, 47 (1973)].

48. B. K. Sevast'yanov, Kh. S. Bagdasarov, L. B. Pasternak, *et al.*, Kristallografiya **18** (2), 308 (1973) [Sov. Phys. Crystallogr. **18**, 191 (1973)].

49. G. Burns, E. A. Geiss, B. A. Jenkins, *et al.*, Phys. Rev. **139**, A1687 (1965).

50. W. A. Wall, J. T. Karpick, and B. Dibartolo, J. Phys. C **4**, 3258 (1971).

51. I. N. Douglas, Phys. Status Solidi A **9**, 635 (1972).

52. D. L. Wood, J. Fergusson, K. Knox, *et al.*, J. Chem. Phys. **39**, 890 (1963).

53. Z. J. Kiss and R. C. Duncan, Appl. Phys. Lett. **5**, 200 (1964).

54. P. A. Arsen'ev and D. T. Sviridov, Kristallografiya **14** (4), 687 (1969) [Sov. Phys. Crystallogr. **14**, 578 (1969)].

55. P. P. Feofilov, V. A. Timofeeva, M. K. Tolstoĭ, *et al.*, Opt. Spektrosk. **19**, 817 (1965).

56. M. M. Zakharko, Ya. M. Zakharko, and V. A. Sen'kiv, Ukr. Fiz. Zh. **15**, 1726 (1970).

57. B. K. Sevast'yanov, D. T. Sviridov, V. P. Orekhova, *et al.*, Kvantovaya Élektron. (Moscow) **4** (10), 55 (1972).

58. S. Yu. Volkov, L. B. Pasternak, and B. K. Sevast'yanov, Kvantovaya Élektron. (Moscow) **2** (1), 18 (1975).

59. Kh. S. Bagdasarov, L. B. Pasternak, and B. K. Sevast'yanov, Kvantovaya Élektron. (Moscow) **3** (5), 1307 (1976).

60. B. V. Mill', Izv. Akad. Nauk SSSR, Neorg. Mater. **5**, 1604 (1969).

61. Kh. S. Bagdasarov, L. B. Pasternak, and B. K. Sevast'yanov, Kvantovaya Élektron. (Moscow) **4** (8), 1702 (1977).

62. L. B. Pasternak, B. K. Sevastyanov, V. P. Orekhova, *et al.*, J. Cryst. Growth **52**, 546 (1981).

63. Jos. Kvapil, Jiri Kvapil, B. Manek, *et al.*, Cryst. Res. Technol. **17** (2), 225 (1982).

64. G. V. Bukin, S. Yu. Volkov, V. N. Matrosov, *et al.*, Kvantovaya Élektron. (Moscow) **5**, 1168 (1978).

65. R. C. Morris, N. J. Flanders, C. F. Cline, *et al.*, US Patent No. 3997853 (December 14, 1976).

66. J. C. Walling, O. G. Peterson, H. P. Jenssen, *et al.*, IEEE J. Quantum Electron. **16**, 1302 (1980).

67. E. F. Farrel, J. N. Fang, and R. E. Newnham, Am. Mineral. **48** (7–8), 804 (1963).

68. A. P. Dudka, B. K. Sevast'yanov, and V. I. Simonov, Kristallografiya **30** (3), 480 (1985) [Sov. Phys. Crystallogr. **30**, 277 (1985)].

69. N. K. Bukhardinov, V. I. Gusev, B. T. Golovchenko, *et al.*, Kristallografiya **28** (1), 156 (1983) [Sov. Phys. Crystallogr. **28**, 86 (1983)].

70. C. E. Forbes, J. Chem. Phys. **79** (6), 2590 (1983).

71. R. E. Newnham, R. Santoro, I. Pearson, *et al.*, Am. Mineral. **49**, 427 (1964).

72. A. N. Winchell and H. Winchell, *The Microscopical Characters of Artificial Inorganic Solid Substances: Optical Properties of Artificial Minerals*, 3rd ed. (Academic, New York, 1964; Mir, Moscow, 1967).

73. V. A. Vazhenin, A. E. Nikiforov, B. K. Sevast'yanov, *et al.*, Fiz. Tverd. Tela (Leningrad) **29** (2), 627 (1987) [Sov. Phys. Solid State **29**, 362 (1987)].

74. G. V. Bukin, V. N. Matrosov, V. P. Orekhova, *et al.*, J. Cryst. Growth **52**, 537 (1981).

75. E. F. Farrel and R. E. Newnham, Am. Mineral. **50** (11−12), 1972 (1965).

76. B. K. Sevast'yanov, Yu. L. Remigaĭlo, V. P. Orekhova, *et al.*, Dokl. Akad. Nauk SSSR **256** (2), 373 (1981) [Sov. Phys. Dokl. **26**, 62 (1981)].

77. B. K. Sevast'yanov, Yu. L. Remigaĭlo, V. P. Orekhova, *et al.*, Izv. Akad. Nauk SSSR, Ser. Fiz. **45** (8), 1429 (1981).

78. Yu. L. Remigaĭlo, Candidate's Dissertation in Physics and Mathematics (Inst. of Crystallography, USSR Academy of Sciences, Moscow, 1985).

79. A. B. Suchocki, G. P. Gilland, R. C. Powell, *et al.*, J. Lumin. **37**, 29 (1987).

80. M. L. Shand, J. C. Walling, and H. P. Jenssen, IEEE J. Quantum Electron. **18** (2), 167 (1982).

81. M. L. Shand and J. C. Walling, IEEE J. Quantum Electron. **18** (7), 1152 (1982).

82. M. L. Shand and H. P. Jenssen, IEEE J. Quantum Electron. **19** (3), 480 (1983).

83. B. K. Sevast'yanov, Yu. L. Remigaĭlo, T. F. Veremeĭchik, and B. P. Orekhova, Dokl. Akad. Nauk SSSR **285** (5), 1119 (1985) [Sov. Phys. Dokl. **30**, 1051 (1985)].

84. E. F. Farrel and J. H. Fang, J. Am. Ceram. Soc. **47**, 274 (1964).

85. B. K. Sevast'yanov and Yu. L. Remigaĭlo, Dokl. Akad. Nauk SSSR **290** (1), 93 (1986) [Sov. Phys. Dokl. **31**, 735 (1986)].

86. R. C. Powell, Phys. Rev. **173**, 358 (1968).

87. S. A. Basun, S. P. Feofilov, A. A. Kaplyanskii, *et al.*, J. Lumin. **53**, 24 (1992).

88. B. K. Sevastyanov, Proc. SPIE **2498**, 223 (1995).

89. P. F. Moulton, Opt. News **8** (6), 9 (1982).

90. B. K. Sevast'yanov, Kh. S. Bagdasarov, E. A. Fedorov, *et al.*, in *Abstracts of IV All Union Conference on Tunable Lasers* (Novosibirsk, 1983), p. 8.

91. B. K. Sevast'yanov, Kh. S. Bagdasarov, E. A. Fedorov, *et al.*, Kristallografiya **29** (5), 963 (1984) [Sov. Phys. Crystallogr. **29**, 566 (1984)].

92. B. K. Sevast'yanov, Kh. S. Bagdasarov, and E. A. Fedorov, Dokl. Akad. Nauk SSSR **282** (6), 1357 (1985) [Sov. Phys. Dokl. **30**, 508 (1985)].

93. B. K. Sevast'yanov, G. S. Leonov, V. P. Orekhova, *et al.*, Élektron. Tekh., Ser. Lazer. Tekh. Optoélektron., No. 3 (55), 24 (1990).

94. B. K. Sevast'yanov, Kh. S. Bagdasarov, E. A. Fedorov, *et al.*, Izv. Akad. Nauk SSSR, Ser. Fiz. **54** (8), 1463 (1990).

95. W. C. Wong, D. S. McClure, S. A. Basun, *et al.*, Phys. Rev. B **51** (9), 5682 (1995).

96. S. A. Basun, A. A. Kaplyanskiĭ, B. K. Sevast'yanov, *et al.*, Fiz. Tverd. Tela (Leningrad) **32** (6), 1898 (1990) [Sov. Phys. Solid State **32**, 1109 (1990)].

97. S. A. Basun, S. P. Feofilov, A. A. Kaplyanskii, *et al.*, J. Lumin. **53**, 28 (1992).

98. W. Low, J. Chem. Phys. **33**, 1162 (1960).

99. G. K. Klauminzer, P. L. Scott, and H. W. Moos, Phys. Rev. **142** (1), 248 (1966).

100. T. Kushida, IEEE J. Quantum Electron. **2** (9), 524 (1966).

101. W. M. Fairbank, G. K. Klaumiuzer, and A. L. Schawlow, Phys. Rev. B **11**, 60 (1975).

102. L. B. Pasternak, Yu. L. Remigaĭlo, and B. K. Sevast'yanov, Zh. Prikl. Spektrosk. **25** (1), 110 (1976).

103. G. A. Slack, P. W. Oliver, R. M. Chrenko, *et al.*, Phys. Rev. **177** (3), 1308 (1969).

104. J. P. Hurrel, S. P. Porto, I. F. Chang, *et al.*, Phys. Rev. **173**, 851 (1968).

105. R. M. Macfarlane, Phys. Rev. B **3**, 2129 (1971).

106. V. P. Orekhova, Candidate's Dissertation in Physics and Mathematics (Inst. of Crystallography, USSR Academy of Sciences, Moscow, 1974), p. 119.

107. D. C. Mc Clure, Solid State Phys. **8**, 1 (1959).

108. H. H. Tippins, Phys. Rev. B **1** (1), 126 (1970).

109. J. F. Sabatini, A. E. Salwin, and P. S. Mc Clure, Phys. Rev. B **11**, 3832 (1975).

110. L. V. Keldysh, Zh. Éksp. Teor. Fiz. **45**, 364 (1963) [Sov. Phys. JETP **18**, 253 (1963)].

111. K. A. Kikoin and V. N. Fleurov, J. Phys. C: Solid State Phys. **10**, 4295 (1977).

112. V. N. Fleurov and K. A. Kikoin, J. Phys. C: Solid State Phys. **9**, 1673 (1976).

113. T. F. Veremeichik, Phys. Status Solidi B **124**, 719 (1984).

114. T. F. Veremeichik, Phys. Status Solidi B **143**, 283 (1987).

115. M. McCumber, Phys. Rev. **134** (2), A299 (1964).

116. M. McCumber, Phys. Rev. **136**, A954 (1964).

117. A. Yariv, *Quantum Electronics*, 3rd ed. (Wiley, New York, 1989; Sovetskoe Radio, Moscow, 1973).

118. T. T. Basiev, V. B. Sigachev, M. E. Doroshenko, *et al.*, Proc. SPIE **2498**, 179 (1994).

119. M. Sekita, Y. Miyazava, and S. Kimura, J. Appl. Phys. **58** (9), 3658 (1985).

120. B. K. Sevast'yanov, A. G. Okhrimchuk, V. V. Nabatov, *et al.*, Kvantovaya Élektron. (Moscow) **26** (2), 117 (1999).

121. B. K. Sevast'yanov, A. G. Okhrimchuk, V. S. Mironov, *et al.*, Dokl. Akad. Nauk **367** (5), 623 (1999) [Dokl. Phys. **44**, 520 (1999)].

122. V. Ya. Mitrofanov, A. E. Nikiforov, and V. I. Cherepanov, *Spectroscopy of Exchange Bound Complexes in Ion Crystals* (Nauka, Moscow, 1985).

123. L. E. Orgel, *Introduction to Transition-Metal Chemistry* (Methuen, London, 1960; Mir, Moscow, 1964).

124. C. J. Ballhausen, *Introduction to Ligand Field Theory* (McGraw-Hill, New York, 1962; Mir, Moscow, 1964).

125. I. B. Bersuker, *Electronic Structure and Properties of Coordination Compounds: Introduction to Theory*, 2nd ed. (Khimiya, Leningrad, 1976).

Translated by Yu. Sin'kov